WILEY

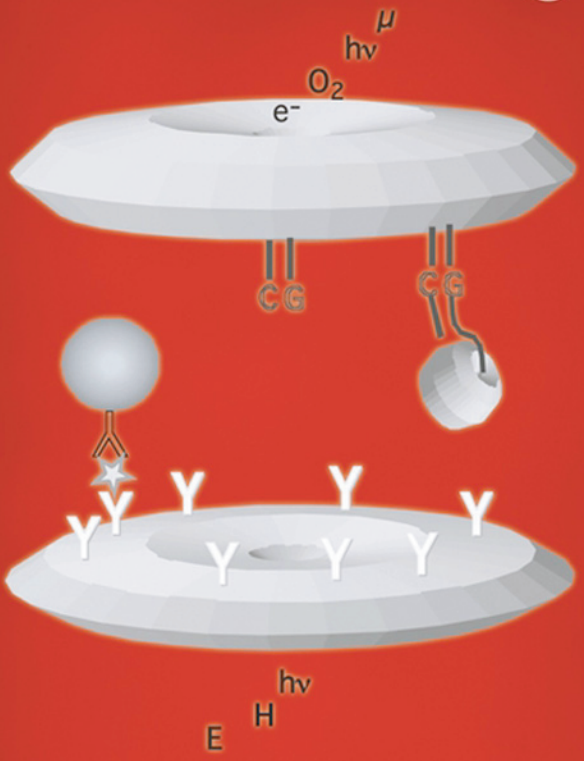

COLLOIDAL NANOPARTICLES IN BIOTECHNOLOGY

ABDELHAMID ELAISSARI

COLLOIDAL NANOPARTICLES IN BIOTECHNOLOGY

COLLOIDAL NANOPARTICLES IN BIOTECHNOLOGY

Edited by

Abdelhamid Elaissari
LAGEP Laboratory
Claude Bernard University
Villeurbanne, France

WILEY-INTERSCIENCE
A JOHN WILEY & SONS, INC., PUBLICATION

Copyright © 2008 by John Wiley & Sons, Inc. All rights reserved

Published by John Wiley & Sons, Inc., Hoboken, New Jersey
Published simultaneously in Canada

No part of this publication may be reproduced, stored in a retrieval system, or transmitted in any form or by any means, electronic, mechanical, photocopying, recording, scanning, or otherwise, except as permitted under Section 107 or 108 of the 1976 United States Copyright Act, without either the prior written permission of the Publisher, or authorization through payment of the appropriate per-copy fee to the Copyright Clearance Center, Inc., 222 Rosewood Drive, Danvers, MA 01923, (978) 750-8400, fax (978) 750-4470, or on the web at www.copyright.com. Requests to the Publisher for permission should be addressed to the Permissions Department, John Wiley & Sons, Inc., 111 River Street, Hoboken, NJ 07030, (201) 748-6011, fax (201) 748-6008, or online at http://www.wiley.com/go/permission.

Limit of Liability/Disclaimer of Warranty: While the publisher and author have used their best efforts in preparing this book, they make no representations or warranties with respect to the accuracy or completeness of the contents of this book and specifically disclaim any implied warranties of merchantability or fitness for a particular purpose. No warranty may be created or extended by sales representatives or written sales materials. The advice and strategies contained herein may not be suitable for your situation. You should consult with a professional where appropriate. Neither the publisher nor author shall be liable for any loss of profit or any other commercial damages, including but not limited to special, incidental, consequential, or other damages.

For general information on our other products and services or for technical support, please contact our Customer Care Department within the United States at (800) 762-2974, outside the United States at (317) 572-3993 or fax (317) 572-4002.

Wiley also publishes its books in a variety of electronic formats. Some content that appears in print may not be available in electronic formats. For more information about Wiley products, visit our web site at www.wiley.com.

Library of Congress Cataloging-in-Publication Data:

Colloidal nanoparticles in biotechnology / edited by Abdelhamid Elaissari.
p.; cm.
Includes bibliographical references and index.
ISBN 978-0-470-23052-7 (cloth)
1. Nanoparticles–Diagnostic use. 2. Colloids in medicine. I. Elaissari, Abdelhamid.
[DNLM: 1. Nanoparticles–chemistry. 2. Colloids–chemistry. 3. Nanomedicine. QT 36.5 C714 2008]
R857.N34C65 2008
610.28–dc22 2007035547

Printed in the United States of America

10 9 8 7 6 5 4 3 2 1

CONTENTS

About the Editor vii

Preface ix

Contributors xi

1. **Reactive Nanocolloids for Nanotechnologies and Microsystems** 1
   Christian Pichot

2. **Nanoparticles Comprising pH/Temperature-Responsive Amphiphilic Block Copolymers and Their Applications in Biotechnology** 31
   Peihong Ni

3. **Evolution in Malaria Disease Detection: From Parasite Visualization to Colloidal-Based Rapid Diagnostic** 65
   Duangporn Polpanich, Pramuan Tangboriboonrat, and Abdelhamid Elaissari

4. **Antigen-Antibody Interactions Detected by Quasi-Elastic Light Scattering and Electrophoretic Mobility Measurements – A New Concept for Latex Immunodiagnostic Test** 95
   Teresa Basinska and Stanislaw Slomkowski

5. **Biospecific Reactions by Affinity Latexes from Diagnostics to Multiplex Assay** 117
   Haruma Kawaguchi

6. **Fluorescent Colloidal Particles as Detection Tools in Biotechnology Systems** 133
   Igor Nabiev, Alyona Sukhanova, Mikhail Artemyev, and Vladimir Oleinikov

7. **Biofunctionalized Magnetic Micro/Nanoparticles for Biosensing Technologies** 169
   Nicole Jaffrezic-Renault, Claude Martelet, Yann Chevolot, and Jean-Pierre Cloarec

8. Colloids, Biotechnology, and Microfluidics **199**
Cecile Cottin-Bizonne and Rosaria Ferrigno

9. Gas Sensors Based on Ultrathin Films of Conducting Polymers and Nanocomposites **223**
Manoj K. Ram, Özlem Yavuz, and Matt Aldissi

10. Force Measurements between Emulsion Droplets As a New Tool for Medical Diagnostics **247**
Abdelhamid Elaissari, Céline Genty, and Olivier Mondain-Monval

11. Particles for Protein Analysis in Microfluidic Systems **275**
Anne Le Nel, Myriam Taverna, and Jean-Louis Viovy

12. Semicarbazide/α-oxo Aldehyde Site-Specific Ligation Chemistry: From Peptide Microarrays to the Micropatterning of Polycarbonate or Titanium Oxide Using Silica Nanoparticles **299**
Ouafâa El-Mahdi, Vianney Souplet, Olivier Carion, Clément Roux, Jean-Michel Garcia, Céline Maillet, Christophe Olivier, Oleg Melnyk and Jean-Olivier Durand

13. Electrical Detection of Antibodies from Human Serum Based on the Insertion of Gold-Labeled Secondary Antibodies into Micro- or Nanogaps **329**
Lionel Marcon, Didier Stiévenard, and Oleg Melnyk

Index **353**

ABOUT THE EDITOR

Dr. Abdelhamid Elaissari is the Director of Research at LAGEP Laboratory, Claude Bernard University, Villeurbanne, France. He received his undergraduate education from Agadir University, Morocco in 1988. In 1991, he moved to the Institute Charles Sadron at Louis Pasteur University in Strasbourg, France from where he got his PhD in chemical physics of polymers and colloids. In the same year, he got a permanent position at the Centre National de la Recherche Scientifique (CNRS), in Lyon and then joined CNRS-bioMérieux Laboratory (a semiacademic laboratory in Lyon, France) until its closing in 2007. During this period, Dr. Elaissari has developed various techniques related to colloids from synthesis to biomedical diagnostic applications. He has now moved to the Engineering Processes and Automatic Laboratory (LAGEP), which is a three-member collaboration between CNRS, Claude Bernard University of Lyon, and CPE-Engineering School. In this well-known academic laboratory, Dr. Elaissari conducts fundamental research with applications of reactive and stimuli-responsive colloids for biomedical, environmental, and bionano-technological applications.

Dr. Elaissari has been an adviser for some 30 advanced student projects, about 15 PhD projects, and various postdocs. He is the author and the co-author of some 120 papers, more than 10 chapters, and approximately 15 patents. He has also edited two books prior to *Colloidal Nanoparticles in Biotechnology.*

PREFACE

In the past decades, considerable attention has been paid to the combination of colloidal particles, biomolecules, microfluidics, multidetection and automated microsystems in order to perform powerful tools for biomedical diagnostics, food analysis, and in general way, environmental analysis. The traditional biomedical diagnostic based the capture of target biomolecules via various manual steps is now shifted to more sophisticated technologies in order to reduce time consuming, sensitivity enhancement, reduction of number of steps, analysis of small volumes (few microliter or nanoliter), and finally one use devices in integrated microsystems.

In this direction, colloidal particles are largely used in biomedical applications (diagnostic and therapy) in which they are principally used as solid-phase supports of biomolecules, nanoreators of active molecules (drug), or basically as carriers in various technological aspects. Nowadays, the colloidal particles are used not only as solid support but also as detection tools in various biomedical applications as first established in *in vivo* biomedical diagnostic in cancer diseases detection for instance. To answer the appropriate schedule of conditions for a given application, well reactive particles should be considered. The needed reactive particles relative to the target application are elaborated using many heterophase processes such as emulsion, dispersion, precipitation, self-assembly, and physical processes. In this direction various polymer-based colloids have been prepared and explored for *in vitro* biomedical applications and recently for possible integration in automated systems, nanobiotechnologies, and microsystems.

The colloidal particles are ''designed'' by considering various criteria related to the targeted applications such as particle size, size distribution, surface polarity, surface reactive groups, hydrophilic-hydrophobic balance of the surface, and also intrinsic properties for instance (nonexhaustive list). Consequently, the particles synthesis process should be well adapted in order to prepare structured particles latex particles bearing shell and core with well-defined properties. In fact, low charged polystyrene latex particles for instance are used in rapid diagnostic tests based on agglutination process. Magnetic particles are first used in immunoassays and in molecular biology for specific capture of single stranded DNA fragments. Magnetic colloids are then used as a carrier to make easy and possible biomolecules extraction, concentration, and purification as pointed out using cationic magnetic latex particles for nucleic acids extraction, purification, concentration, and amplification and more recently in viruses isolation. Labeled colloidal particles are generally used as detection tools as well studied and performed in cell sorting application and now in lab-on-chip for CCD camera detection.

The specificity and the sensitivity of the targeted biomedical application efficiency are directly related to the surface particles properties, to the intrinsic characteristics of the used materials, to the accessibility of the immobilized biomolecules and to the affinity between targeted biomolecules and the particles surface. The interaction between biomolecules and the particles surface is a complex domain, which contains various physical aspects such as the affinity, the interfacial diffusion phenomena, the immobilized biomolecules conformation, the possible exchange processes, and various anthers physicochemical properties of both biomolecules and particles surface.

The main object of this book is to report on new studies of colloids and nanoparticles in bio-nano-technologies for biomedical and environmental diagnostic. The state of the art in the elaborations and the properties of nanocolloids is presented and illustrated. Special attention is focused on new stimuli-responsive particles and reactive nanoparticles bearing intrinsic properties. The integration of reactive colloidal particles in microfluidic-based technology is a challenging field and needs to consider. In this direction, various aspects are considered and discussed in this book by considering the compatibility of reactive colloidal particles with the microfluidic based Microsystems and biosensors. The intrinsic properties of colloidal particles were also considered and special attention was focused on both magnetic particles and quantum dots fluorescent nanocrystals. Consequently, this book is prearranged in order to show to the readers the use of colloidal particles in biotechnologies

Prof. Hatem Fessi

Director,
LAGEP Laboratory

CONTRIBUTORS

Matt Aldissi, Fractal Systems, Inc., 200 9th Avenue N., Suite 100, Safety Harbor, FL 34695, USA

Mikhail Artemyev, Institute of Physico-Chemical Problems, Belarussian State University, Minsk, Belarus

Teresa Basinska, Center of Molecular and Macromolecular Studies, Polish Academy of Sciences, Sienkiewicza 112, 90-363 Lodz, Poland

Olivier Carion, Institut de Biologie de Lille, UMR CNRS 8161, 1 rue du Professeur Calmette, 59021 Lille Cedex, France

Yann Chevolot, AMPERE and INL, Ecole Centrale de Lyon, 69134 Ecully Cedex, France

Jean-Pierre Cloarec, AMPERE and INL, Ecole Centrale de Lyon, 69134 Ecully Cedex, France

Cecile Cottin-Bizonne, Université de Lyon, Université Lyon 1, CNRS UMR 5586, Laboratoire PMCN, F-69622 Villeurbanne, France

Jean-Olivier Durand, Institut Charles Gerhardt, UMR 5253 cc 1701, Université Montpellier 2, place Eugène Bataillon, 34095 Montpellier Cedex 05, France

Abdelhamid Elaissari, Claude Bernard University, LAGEP Laboratory, 43 Boulevard du 11 novembre 1918, Bât. CPE-308G 69622 Villeurbanne Cedex, France

Ouafâa El-Mahdi, Institut de Biologie de Lille, UMR CNRS 8161, 1 rue du Professeur Calmette, 59021 Lille Cedex, France

Rosaria Ferrigno, Institut des Nanotechnologies de Lyon, INL, CNRS UMR 5270, Université de Lyon, Lyon, F-69003, France, and Université Lyon 1, Villeurbanne, F-69622, France

Jean-Michel Garcia, Institut de Biologie de Lille, UMR CNRS 8161, 1 rue du Professeur Calmette, 59021 Lille Cedex, France

Céline Genty, Claude Bernard University, LAGEP Laboratory, 43 Boulevard du 11 novembre 1918, Bât. CPE-308G 69622 Villeurbanne Cedex, France, and Université Bordeaux 1, UPR 8641, Centre de Recherche Paul Pascal – CNRS, Avenue A. Schweitzer, 33 600 Pessac, France

Nicole Jaffrezic-Renault, LSA, Claude Bernard University Lyon 1, 69622 Villeurbanne Cedex, France

Haruma Kawaguchi, Graduate school of Science and Technology, Keio University, 3-14-1 Hiyoshi, Yokohama 223-8522, Japan

Anne Le Nel, Laboratoire PCC, Institut Curie (UMR CNRS/IC 168), Paris Cedex 05, France, and JE 2495 Protéines et Nanotechnologies en Sciences Séparatives, Université Paris XI, Châtenay-Malabry, France

Céline Maillet, Institut de Biologie de Lille, UMR CNRS 8161, 1 rue du Professeur Calmette, 59021 Lille Cedex, France

Lionel Marcon, Institut d'Electronique de Microélectronique et de Nanotechnologie, UMR CNRS 8520, Department of ISEN, 41 Bd Vauban, 59046 Lille Cedex, France, and Institut de Biologie de Lille, UMR CNRS 8161 (CNRS, Universités de Lille 1 et 2, Institut Pasteur de Lille), 1 rue du Professeur Calmette, 59021 Lille Cedex, France

Claude Martelet, AMPERE and INL, Ecole Centrale de Lyon, 69134 Ecully Cedex, France

Oleg Melnyk, Institut de Biologie de Lille, UMR CNRS 8161, 1 rue du Professeur Calmette, 59021 Lille Cedex, France

Olivier Mondain-Monval, Université Bordeaux 1, UPR 8641, Centre de Recherche Paul Pascal – CNRS, Avenue A. Schweitzer, 33 600 Pessac, France

Igor Nabiev, EA n°3798 Détection et Approches Thérapeutiques Nanotechnologiques dans les Mécanismes Biologiques de Défense, Université de Reims Champagne-Ardenne, 51 rue Cognacq Jay, 51100 Reims, France

Peihong Ni, College of Chemistry and Chemical Engineering, Soochow University, Suzhou 215123, China

Vladimir Oleinikov, Shemyakin-Ovchinnikov Institute of Bioorganic Chemistry, Russian Academy of Sciences, 117997 Moscow, Russia

Christophe Olivier, Institut de Biologie de Lille, UMR CNRS 8161, 1 rue du Professeur Calmette, 59021 Lille Cedex, France

Christian Pichot, CNRS-bioMérieux, Ecole Normale Supérieure de Lyon 46, allée d'Italie, 69364 Lyon Cedex, France

Duangporn Polpanich, Department of Chemistry, Faculty of Science, Mahidol University, Rama VI Rd, Bangkok 10400, Thailand, and National Nanotechnology Center (NANOTEC), National Science and Technology Development Agency (NSTDA), Thailand Science Park, Klong Luang, Pathumthani 10120, Thailand

Manoj K. Ram, Fractal Systems, Inc., 200 9th Avenue N., Suite 100, Safety Harbor, FL 34695, USA

Clément Roux, Institut de Biologie de Lille, UMR CNRS 8161, 1 rue du Professeur Calmette, 59021 Lille Cedex, France

Stanislaw Slomkowski, Center of Molecular and Macromolecular Studies, Polish Academy of Sciences, Sienkiewicza 112, 90-363 Lodz, Poland

Vianney Souplet, Institut de Biologie de Lille, UMR CNRS 8161, 1 rue du Professeur Calmette, 59021 Lille Cedex, France

Didier Stiévenard, Institut d'Electronique de Microélectronique et de Nanotechnologie, UMR CNRS 8520, Department of ISEN, 41 Bd Vauban, 59046 Lille Cedex, France

Alyona Sukhanova, EA n°3798 Détection et Approches Thérapeutiques Nanotechnologiques dans les Mécanismes Biologiques de Défense, Université de Reims Champagne-Ardenne, 51 rue Cognacq Jay, 51100 Reims, France

Pramuan Tangboriboonrat, Department of Chemistry, Faculty of Science, Mahidol University, Rama VI Rd, Bangkok 10400, Thailand

Myriam Taverna, JE 2495 Protéines et Nanotechnologies en Sciences Séparatives, Université Paris XI, Châtenay-Malabry, France

Jean-Louis Viovy, Laboratoire PCC, Institut Curie (UMR CNRS/IC 168), Paris Cedex 05, France

Özlem Yavuz, Fractal Systems, Inc., 200 9th Avenue N., Suite 100, Safety Harbor, FL 34695, USA

CHAPTER 1

Reactive Nanocolloids for Nanotechnologies and Microsystems

CHRISTIAN PICHOT

CNRS-bioMérieux, Ecole Normale Supérieure de Lyon 46, allée d'Italie, 69364 Lyon Cedex, France

1.1 INTRODUCTION

Nanoscience and nanotechnology continue to play a growing and tremendous interest, both on academic and industrial aspects. They have been applied in many systems such as in the development of nano and microdevices for nanodiagnostics, biotechnology, metrology, and molecular manufacturing. Such interest relies on the fact that it is now possible to manipulate nanometer-length atoms and molecules in order to create, according to a bottom-up technology, larger structures with outstanding properties. In biotechnology, many domains are concerned: diagnostics, microarrays, biological analysis, biochips, biominiaturization, drug delivery systems, and so forth. For instance, the development of lab-on-chips (the so-called microTAS (micro Total Analysis Systems) responds to the evolution of the bioassays toward miniaturization, which implies to deal with very small volumes of biological samples. Of course, such a drastic change raises many complex problems regarding the manipulation of fluids in confined micrometer channels integrated on a plan support (1–3).

It appeared obvious that the setup of these new systems needs appropriate tools as regards to transport, extraction, and detection. It has been found that colloidal particles, especially those having one dimension below 500 nm, proved to be very suitable and efficient tools due to their unique and versatile properties, and several examples of their use can be found in the literature (4,5). For a long time, the preparation of organic and inorganic colloids has benefited of a period of an active and fruitful research and development. A huge number of processes, more or less sophisticated, allow to carefully control the shape, particle size and size distribution, and structure and surface properties in relation to the field they have to be utilized. It

Colloidal Nanoparticles in Biotechnology, Edited by Abdelhamid Elaissari
Copyright © 2008 John Wiley & Sons, Inc.

should be reminded that in these (nano)colloids, surface aspects become more and more predominant as dimension size is decreasing. Table 1.1 provides a nonexhaustive list of various submicronic-sized mineral, organic, and composite colloids, together with some examples in which they are applied. From this table, it is worthwhile to notice, first that nano-sized colloids (such as gold and quantum particles) play a very important role in the detection step of bioassays, especially in molecular diagnostics, and second that polymer dispersions offer a wide variety of organic-based colloids as such or as composites.

The major objective of this chapter aims at giving basic information regarding the main manufacturing methods of various types of (nano)colloids involved in the

TABLE 1.1 Some Examples of (Nano)colloids Used in Microsystems and Nanobiotechnologies.

Nature of particle	Size domain	Example of applications
Inorganic particles		
Gold particles	10–30 nm	Colorimetric detection of DNA sequences (6)
Other metallic and bimetallic particles (Pt, Pd, Ru)	2–10 nm	Labels for chip-based DNA detection (7)
Metal oxides (ferrofluids, superparamagnetic particles)	5–10 nm	Medical imaging (8)
Silica nanotubes	A few nanometers wide	Probes, biological sensing (9)
Semiconductor nanocrystals (quantum dots)	2–10 nm	Detection and quantification of biological molecules (10)
Organic particles		
Carbon nanotubes and fullerens	A few nanometers	Templates, DNA targeting (11)
Dendrimers	10–50 nm	Reservoirs of drugs, DNA chips (12)
Polyelectrolyte complexes (natural and synthetic polymers)	50–200 nm	Drug targeting, vaccination (13,14)
Self-assemblies of polyethylene oxide block copolymers	50–200 nm	Stealth drug delivery systems (15)
Latexes	20–1000 nm	Solid-phase assays, vaccination, two-dimensional arrays (16)
Organic/inorganic composite particles		
Magnetic particles	100–1000 nm (and more)	Diagnostic (17), extraction of DNA, cells, virus (18)
Fluorescent nanoparticles	30–500 nm	Time-resolved fluorescence bioassay (19)
Silica-based nanoparticles	50–200 nm	Bioanalytical applications (20)
Polymer-metal nanocomposites (gold and polypyrrole)	10–30 nm	Bioassays (21)

development of nano and microsystems to be used in biotechnologies. After focusing on the special requirements that such nanoparticles should fulfill with regards to their colloidal and surface aspects, particularly their functionality, the main preparation methods will be reviewed and discussed depending on the nature of the organic or inorganic material.

1.2 WHAT CRITERIA FOR NANOCOLLOIDS IN NANO AND MICROSYSTEMS?

Due to their use in microsystems in which surface and volume effects are predominant, the design of nanocolloids needs to take into account a large number of variables with respect to molecular, surface, and colloidal properties of particles, such as those depicted in Table 1.2. It is obvious that for any application, nanocolloids should be preliminary characterized as completely as possible.

TABLE 1.2 Criteria and Related Properties to be Considered of for Nanocolloids Used in Microsystems.

Criteria	Property
Particle size and polydispersity	To determine surface area
Monodispersity	To get reproducible data
Colloidal stability	To keep nanoparticle stability against temperature, pH, shearing, and salinity
Surface charge density	To impart ionic charges at the interface
Density	To avoid sedimentation (large particles)
Cross-linking	To avoid solubilization in the solvents of organic colloids
Porosity	To favor the incorporation of dyes, small molecules, drugs, etc.
Specific functionality	
• Reactive surface groups	Covalent grafting of nanoparticles on plane surfaces or with biomolecules
• Hydrophilicity	Depletion of biomolecules, stealth effect
• Sensitivity to stimulus (T, pH, ionic strength, UV, light, electric, or magnetic fields)	To change the nature and properties of colloidal particles
• Complexation (PEO, PMAA, metal chelates, etc.)	Performing protein purification, oriented immobilization of proteins, antibodies
• Biological ligand (oligosaccharide, lipid, peptide, nucleic acid, antibody, protein)	Recognition of antigens, specific cells, DNA, RNA, protein, lectins
• Magnetic	Fast separation of colloids, imaging
• Color, fluorescence	Detection by optical methods
• Biodegradability	To be used for *in vivo* applications

PEO: polyethylene oxide; PMMA: polymethylmethacrylate.

1.2.1 Shape of Particles

Although, the spherical shape is the more thermodynamically stable form that many types of colloids usually adopt, it is worth mentioning that various and multiple other shapes can be obtained depending on the nature of material and process of preparation. This is particularly the case of inorganic colloids where ellipsoidal, rod-like, cubic, platelet, needle-like, and other shapes can be found. In the case of organic particles, it is also feasible to make colloids with nonspherical shape, but they are often in a thermodynamic metastable state, which leads, depending on the diffusion capability of the material (polymers), to a progressive evolution toward a spherical form.

1.2.2 Particle Size and Distribution

At first, the control of particle size and particle size distribution is a very important requirement since it defines the available surface area. As it will be discussed in more details in the next section, numerous appropriate preparation methods are now available, both for the synthesis of inorganic and organic nanocolloids in a large colloidal size domain (a few nanometers to 1000 nm). It is relatively easy now to produce colloids with very narrow size distribution, the so-called "monodisperse" colloids. This property will be discussed later on. The size monodispersity should be obeyed for several reasons: for the sake of reproducibility for immunoassays used in diagnostics; in drug delivery systems in which particle size should not overcome a limit; in transport in micrometer-sized channels, for the preparation of two or three-dimensional organization of particles on a surface or in a volume, and so forth.

1.2.3 Surface Charge Density and Colloidal Stability

In many cases, ionic surface charges must be imparted to the particles for different purposes. A major one is that efficient colloidal stability should be ensured to the particles for avoiding irreversible aggregation in the various steps of handling of such colloids: along their synthesis; during storage; their functionalization; and finally, in the numerous application domains, they are used: mixing either with other colloids or with biological fluids (usually exhibiting significant ionic strength) or under shearing. Since colloids, except in specific cases (microemulsions) are thermodynamically unstable, they can be made metastable for long-term periods provided an energy barrier is imparted by the presence of ionic charges (electrical stability) or of a polymer layer (steric stabilization).

The nature (anionic vs. cationic) and density of the surface charges must be taken into account for several reasons: surface properties of the device in which they could be immobilized or be transported; nature of other colloids with which they can be mixed; and physicochemical properties of the biological molecule to be fixed. Such ionic charges can be incorporated during the synthesis, especially by correctly adjusting the recipe: for instance, for polymerization in heterogeneous media

(nature and amount of the initiator usually bearing an ionic charge, addition of a surfactant, presence of ionic or ionogenic monomers or macromonomers, etc.) or by a chemical postreaction.

In general, for inorganic colloids such as metal oxides (silica, ferrite), hydroxyl groups are available at the surface and pH change can introduce anionic or cationic charges. As shown in the next section, surface modification of inorganic particles can be performed in order to incorporate organic species or various synthetic or natural macromolecules.

1.2.4 Interfacial Polarity

One major drawback when using nanoparticles as solid-phase supports (antibodies, proteins, nucleic probes, and enzymes) is that nonspecific adsorption could severely affect both the efficiency of the detecting device as well the conformation of the biomolecule and consequently its activity. In that purpose, the control of the hydrophobic–hydrophilic balance (HLB) at the particle interface is of a paramount importance to reduce this undesired adsorption. One common method is incorporating a hydrophilic layer like polyethylene oxide-based molecules.

1.2.5 Cross-Linking

In the case of organic-based nanoparticles, it is sometimes appropriate to deal with nonswellable or insoluble particles when they are handled in an organic solvent. This implies to incorporate a small amount of the so-called cross-linker able to develop a three-dimensional network. Such a network structure allows, provided colloidal stability is ensured, to make surface chemistry of the particles in organic solvents without the risk of coagulation or complete solubilization.

1.2.6 Functionality

In many applications, the use of particles offering one given or multiple functionalities is quite relevant, which requires to design the so-called *engineered particles* exhibiting physicochemical properties meeting the needs of a specific application.

One major strategy is to incorporate *reactive groups* that could be employed for many purposes: immobilization of biomolecules containing mainly carboxylic, amino, hydroxyl, or thiol groups; covalent binding of dyes; fluorescent labels or inorganic colloids (metal gold, ferrites, and quantum dots); surface binding onto plane surfaces. As it has been already extensively reviewed in many books (22,23), numerous and various reactive groups are available, depending on the chemical reaction selected to bind the molecule (which could often involve a preactivation step). In some cases, for highly reactive functions, it is necessary to keep the chemical group under protected form (aldehyde, amino, or thiol functions, for instance) and to recover them just before use. The biomolecule immobilization via molecular recognition, such as the streptavidin–biotin system, is also widely used, which implies to fix a

streptavidin molecule onto the nanoparticle surface. Other lock-and-key biomolecules can be used such as sugars moieties, antibodies, peptides, and so forth. For the sake of availability (confinement effect near the surface), the reactive function can be advantageously localized at the extremity of a spacer arm or within a hydrophilic polymer layer. Considerable amount of works has been achieved in order to identify and to quantify the amount of available reactive groups (24).

Many other functionalities can be conferred to the colloids depending on the application technique and on the type of detection (optical, electric, dielectric, and magnetism) involved for the analysis. In that respect, *magnetism* is a very important property that has been described in various review papers related to their manufacturing methodology, properties, and applications fields (25). A prerequisite when using such magnetic particles as a tool of separation is to keep the entire supeparamagnetism property of the ferrite, meaning that they can be attracted to a magnetic field but do not retain remanent magnetism when the field is removed.

Fluorescent and colored colloidal particles have also attracted much interest for many years especially in the biological and biotechnological domains in which they are used for the detection and quantization of biomolecules and pathogen agents in biological samples (26). Various nanoparticles bearing conventional dyes or fluorescent probes are currently marketed in a broad range of size and surface functionalities. However, it appears that the use of these organic dyes presents drastic disadvantages mainly because of photobleaching problems.

Recently, alternated approaches were investigated so as to develop fluorescent nanoparticles with enhanced photostability such as *quantum dots (QDs)*, lanthanide oxides, and so forth (27,28). There is a challenge for making fluorescent and magnetic nanoparticles, which was indeed partially solved in performing an appropriate encapsulation process avoiding a close contact of iron oxide nanoparticles and dyes species (29).

In the last 10 years, a great deal of efforts have been focused on the design of stimuli-responsive particles, that is, particles that are able to change their structure and therefore their size and properties by the action of an external stimuli (temperature, pH, ionic strength, electric field, light, etc.). A considerable amount of studies have been devoted to polyacrylamide derivative colloids, which concern *in vitro* biological applications only (30).

At last, for applications in living systems, it is necessary to select degradable natural (polysaccharides) or synthetic (polyglycolic or lactic acids, silicones, and polycyanoacrylates) polymers exhibiting biocompatibility, bioresorbability, and nontoxicity.

1.3 MAIN PREPARATION METHODS

Numerous methods are now available for the preparation of nano and microparticles and the general approaches whether they are inorganic, organic, or composites can be classified as depicted in Table 1.3. Although, the production of fine particles can be envisaged by comminution methods of a bulk material, they will

TABLE 1.3 Preparation Methods of Inorganic or Organic Colloids to be Used in Nano and Microsystems.

Type of preparation method	Example	References
Condensation of small molecules		
• Precipitation process	Metal hydrous oxides	(31)
• Sol-gel method	Magnetites, ferrites	(32)
• Chemical reaction in aerosols	Metal oxides (TiO_2, SiO_2)	(33)
• Ostwald ripening process	Silver halides	(34)
• Hydrolysis of silicon alkoxides	Silica	(35)
• Polyol process	Noble metals (Au, Pd, Ag, etc.)	(36)
• Dispersion polymerization	Latex particles	(37)
• Controlled hierarchical chemistry	Phosporated dentrimers (cationic)	(38)
• Other techniques	Fullerens and nanotubes	(39)
Polymerization in heterogeneous media and related techniques		
• Emulsion	Polymer latexes	(40)
• Miniemulsion	Submicronic latexes, magnetic nanoparticles	(41)
• Direct and inverse microemulsion	Functionalized nanoparticles	(42,43)
Encapsulation of organic or inorganic particles		
• Association of preformed colloids		
- Heterocoagulation	Nanostructured composite latexes (anionic latex + cationic Fe_3O_4 nanoparticles)	(29)
- Layer by layer	Composite nanoparticles (silica, Fe_3O_4)	(44)
• Radical-initiated polymerization on the surface of inorganic nanoparticles	Composite latex + silica	(45)
• Polycondensation and mineral precipitation on the surface of latex particles	Hollow nanoparticles (silica) cationic metal nanoparticles onto latex	(46)
• Simultaneous reaction of organic and inorganic precursors	Incorporation of macromolecules into organosilane networks	(47)
Formulation of colloids from preformed solutions of polymers		
• Organo-soluble polymers	Polylactic acid and poly ε-caprolactone,	(48)
• Water-soluble polymers	Polysaccharides, alginates	(49)
Surface modification of preformed particles	Hydrophobic and hydrophilic latexes	(50,51)
Self-assembly processes of polyelectrolytes and architectured polymers	PEO-based copolymers PEO–polylactic acid Dextrane sulfate–chitosan	(52–54)

not be considered since at first they require high mechanical energy for making a fine dispersion and secondly, they are not at all suitable for preparing monodisperse colloidal particles.

1.3.1 General Remarks

It is worthwhile that several common features can be found in the different manufacturing methodologies used for the synthesis of the various types of colloids. They are reviewed below.

- Many preparation methods involve the condensation of small molecules, which could be metal atoms, metal salts or oxides, silicon alkoxides for inorganic colloids, or monomers for polymer-based colloids.
- The formation of the colloids from the initial molecules usually implies either a chemical reaction (hydrolysis, reduction, polymerization, or polycondensation) or a physical transformation (Ostwald ripening, spontaneous phase separation, or gelification).
- When starting from a homogeneous solution of small molecules, the formation of particles proceeds according to a similar mechanism as schematized in Fig. 1.1. It generally encompasses the following steps:
  - A chemical reaction: reduction of a metal (Au); hydrolysis of an alkoxide (silicon alkoxide); polymerization of a monomer
  - Formation of nuclei by precipitation (oligomers) or aggregation (metal atoms), which defines the "nucleation step"

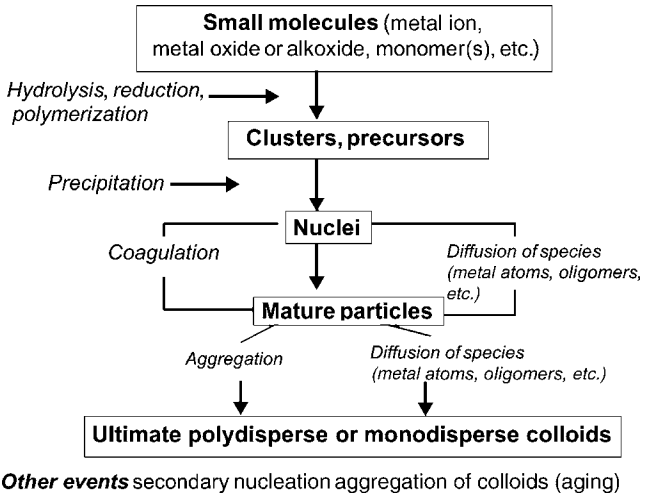

FIGURE 1.1 General schematic of the formation and growth of colloids by a precipitation process

- Growth of the nuclei to form particles by two main processes: diffusion of monomer, capture of oligomers, or metal atoms; coagulation of nuclei or clusters
- Stabilization of the final particles can be ensured by either existing surface charges, by adding hydrophilic polymer, or any surface-active agents.

- Under appropriated conditions, *monodispersed colloids* can be produced, a property that which has been formerly explained by LaMer (55), who also proposed a schematic diagram, indicating that the nucleation occurs when the species formed in solution reach a supersaturation concentration, the formed primary particles growing according to either a monomer addition or an aggregation model. Getting monodisperse colloids generally implies the control of the nucleation and growth steps; briefly, when the critical supersaturation level is reached, a fast nucleation step occurs followed by a progressive growth step. Homogeneous nucleation can be replaced by a heterogeneous nucleation process by introducing in the initial reaction medium foreign nuclei acting as a seed for capturing either elementary units or primary particles.
- The production of nanoparticles via self-assemblies of surface-active agents, especially micellar or microemulsion processes both in oil-in-water (O/W) or in water-in-oil (W/O) dispersions, has received much attention regardless of the type of colloids. Their development relies on considerable research works in the 1980, both on theoretical and practical aspects.
- The making of a microemulsion requires to use relatively high amount of an emulsifier and often with a cosurfactant (which could be an alcohol with a short alkyl chain such as *n*-pentanol, *n*-hexanol, etc.). The formulation of microemulsions is a spontaneous process, that is, it does not need mechanical shearing; they are thermodynamically stable (against coalescence and Ostwald ripening), optically transparent, and in the domain size 5–80 nm. A huge number of micelles are obtained allowing to solubilize large amounts of reactive species (metal oxides or alkoxides, monomer, etc.) offering an important surface area (of the order of 100–300 m^2/g of dispersed phase). As a result, reaction rates are considerably increased, and the synthesis of nanoparticles can elapse sometimes within a few minutes. The selection of the surfactant is obviously critical and must be adapted not only to the initial nature of the reacting system but also to the final nanoparticles (due to the modification of the interfacial and colloidal properties).

  As an example, Figure 1.2 gives a schematic representation of a pseudoternary phase diagram (water–oil surfactant) and showing that various mono and multiphasis domains can be obtained: O/W and W/O microemulsions, lamellar, and bicontinuous phases. Most of studies and developments make use of globular microemulsions; however, reactions in other phases (bicontinuous phases, for instance) give rise to interesting microstructures, as referred in the next section.
- Characterization of the colloids during the synthesis and at the ultimate stage is a very important and necessary task for any application in which they are to be

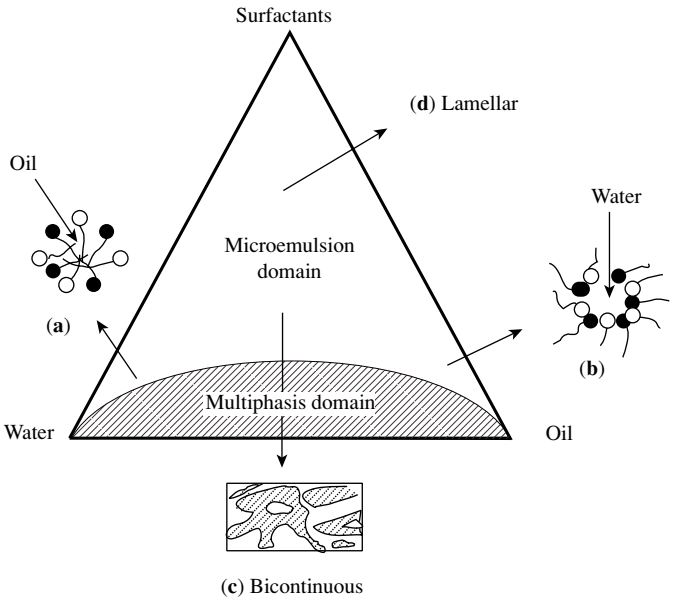

FIGURE 1.2 Phase diagram (water–oil surfactant) (adapted from (56)) (a) droplets oil-in-water; (b) droplets water-in-oil; (c) bicontinuous phase; (d) lamellar phase

involved. Many parameters should be determined among them: shape, particle size and polydispersity, surface chemistry, structure, composition. It is out of scope to detail all the techniques, which should be carried out for these analyses; the readers could consult the appropriate books and reviews on the subject.

1.3.2 Preparation of Inorganic Particles

In this section, we will describe only several important methods to produce inorganic colloids.

1.3.2.1 Precipitation Process The precipitation in homogeneous solutions of many inorganic salts has been long used for the production of various colloids in the domain size (10–100 nm). It was applied in the case of metal ions, metal (hydrous) oxides, silicon alkoxides, metal phosphates and sulfates, and so forth.

Case of Metal Ions Nanometer-sized *metal particles*, especially gold and silver, have received much increasing attention as regards to their application potentialities in various domains such as in biology for the detection of DNA or RNA (57,58). Colloidal dispersions of gold particles can be obtained by reduction of gold ions with various reactants: citrates, formaldehyde, hydrazine, and hydrogen peroxide. The mechanism of nanoparticle formation is a three-steps process following the scheme given in Fig. 1.3. After reduction of metal ions to metal atoms, aggregation of the atoms

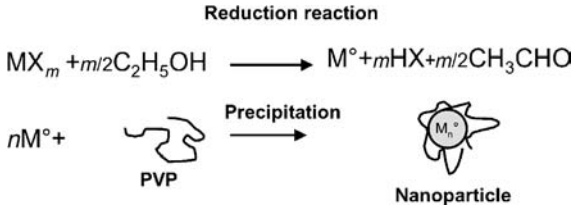

FIGURE 1.3 Formation of metal nanoparticle by reduction with an alcohol of metal salts in the presence of poly(*N*-vinyl-2-pyrrolidone) (PVP) as stabilizer

(or microclusters) leads to nuclei with an average diameter less than 1 nm. The growth of the formed nuclei proceeds by deposition of atoms or microclusters on the surface of nuclei. Stabilization is very critical in such metal nanoparticles and a steric stabilizer is usually added in the recipe. Poly(*N*-vinyl-2-pyrrolidone) (PVP) as water-soluble polymer is often employed in this purpose and showing different types of interactions with the surface metallic particle.

Semiconductor nanoparticles (the so-called quantum dots such as CdS) can be prepared by the precipitation of CdS in aqueous solution containing cadmium and sulfide ions provided stabilizer (polymer (gelatin or polyethylene glycol) or a ligand (thioacetamide) be also added to prevent the aggregation of the formed clusters. In the reaction, pH should be carefully controlled since it determines the particle size, a basic one allowing to stop the particle growth.

The hydrolysis of silicon alkoxides in homogeneous solutions also proceeds through a precipitation mechanism according to the widely described original Stöber process (59), which follows the reaction pathway, described in Fig. 1.4. It is worth mentioning as quoted by Brook (60) that silicon products and particularly silica show excellent compatibility with living systems, which explains their use in many biochemical, biological, and biotechnological applications. Obviously, silica particles have been developed not only as model systems but also as colloid supports as such or as composites with inorganic (ferric oxides) or organic polymers.

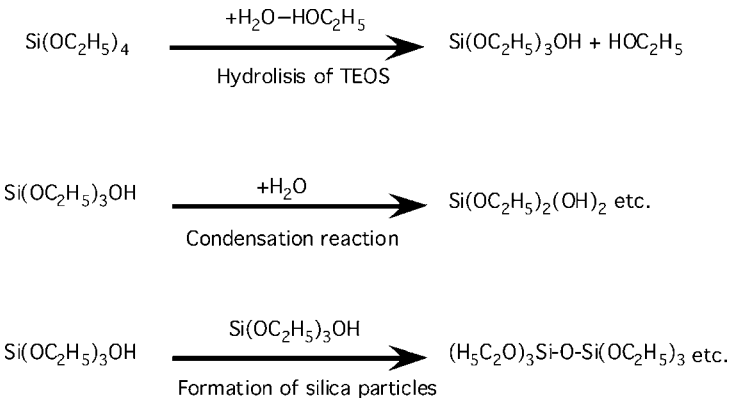

FIGURE 1.4 Schematic reaction steps leading to silica particles

Many fundamental works have been devoted to the understanding of this process owing to systematic studies investigating the influence of the nature of alkoxide and alcohol and the amount of water and ammonia on the resulting colloidal particles (in the size range from about 50 to 800 nm). Much work dealt with tetraethylorthosilicate (TEOS) upon studying the reaction rate (which encompasses both the hydrolysis and condensation reactions). Such a reaction was also examined as regards to its effect on the nucleation and growth mechanism with a view to control the particle size and monodispersity.

As it will be discussed later on, silica colloids as substrates can be surface modified. As illustrated in Fig. 1.5, extremely narrow size particles can be prepared by the Stöber process as well after surface modification to get amino-functionalized particles.

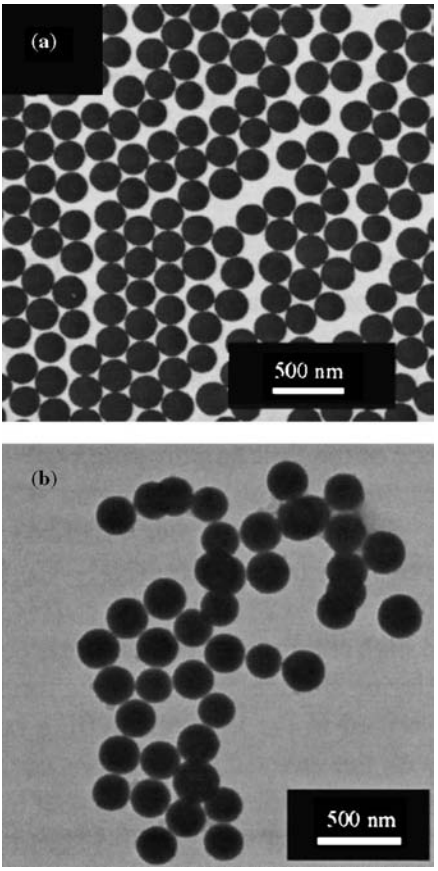

FIGURE 1.5 Transmission electron micrographs of silica particles: (*a*) native Stöber silica; (*b*) amino-silica from silanisation in acetone with a catalyst (from Reference (61))

Polyol Process (36) This process has been worked out with a view to produce metallic and bimetallic alloy particles with a controlled morphology in the micrometer and nanometer size. The preparation consists in a reduction reaction of metallic compounds dissolved in a solvent also acting as reducing agent. It has been applied to a large number of easily reducible noble metals such as Au, Ag, Ir, Pt, Os, Rd and less reducible metals such as Co, Ni, Cu (62). After dissolution of a given precursor (metal chloride or nitrate) in nonaqueous solvents like polyols such as α-diols ethylene, propylene, or tetraethylene glycols, the polyol acts to the reduction of species. The *in situ* formed metal particles proceeds, as already described, by a nucleation growth process leading to very fine nanoparticles. Experimental conditions have been well investigated so as to ensure the monodispersity of the final particles. Nanocolloids of gold, silver, and platinum were then synthesized in the size range from 5 to 30 nm.

1.3.2.2 "Gel-Sol" Method This method of preparation is based on the "gel-sol" physical process in which a highly viscous gel of a solid precursor is formed. The gel acts as a protective structure against coagulation of the solid and as reservoir of monomeric species (metal ions, for instance).

This process was applied in diluted and condensed systems to a variety of metal oxides, particularly for the preparation of magnetites and ferrites by partial oxidation of a ferrous hydroxide gel with nitrate (63). The particle formation also proceeds by a two-step nucleation/growth mechanism. Such a method leads to monodisperse and spherical particles in the colloidal size range; however, in many cases, nonspherical particles can be also produced.

1.3.2.3 Chemical Reaction in Aerosols The aerosol technique was developed as a pathway to produce valuable dispersed materials with predictable particle morphology. The main steps involved in the aerosol method are the following (64):

- generation of small droplets containing one or more reactive liquids
- use of evaporation and nucleation phenomena to favor narrow size distribution of the droplets
- exposure of the droplets to a coreactant vapor
- reaction of the liquids in the droplets with the surrounding vapor
- removal of the aerosol colloids

The process has been applied to the synthesis of various metal oxide particles (titania, silica, alumina, etc.) of size range (0.1–1.0 μm), micrometer-sized poly(*t*-butylstyrene) latex particles as well composite particle systems. It is interesting to notice that monodisperse colloids can be obtained in all cases.

1.3.2.4 Ostwald Ripening Ostwald ripening is a general process regarding the evolution of an emulsion resulting from interface energy. It includes a transfer of molecules contained in the dispersed phase through the continuous phase (aqueous one for example) provided the oil-like molecules be slightly soluble in this continuous

phase. This solubility allows the diffusion of hydrophobic molecules from the small droplets toward larger droplets with consequently a decrease in the overall interfacial area. Such a process concerns emulsions of tiny droplets about and below 100 nm, and the rate of diffusion increases with the molecular solubility of the lipophilic molecule.

We will see later on that this physical process has been utilized for making emulsions (the so-called miniemulsions) with stable submicronic sized-droplets by introducing an insoluble hydrophobic molecule (i.e., solvent) to prevent the Ostwald ripening effect.

This method was applied by Sugimoto (34) to produce monodisperse single-crystal silver halide particles by mixing tabular AgBr particles (410 nm) with fine spherical ones (42.5 nm). The growth of the large tabular grains was found to follow a spherical diffusion model proposed by the authors.

1.3.2.5 Micellar and Microemulsion Systems As already mentioned, self-assemblies of surfactants both in oil or in water continuous phases can serve as *microreactors* to induce the formation of nanocrystals. As an example, reverse micelles, obtained from the system Aerosol OT (1–4 bis-2-ethylsodium sulfosuccinate) as surfactant, isooctane as continuous phase; an aqueous solutions of cadmium and sulfide ions, were used to produce CdS and CdTe nanocrystals in the nanometer size range (about 4 nm) but with a relatively large polydispersity (65).

The microemulsion process has also been applied to the production of many metal oxide nanoparticles as reported in (66): metal oxides, silver halides, silicon oxides, and so forth. We will mostly concentrate on the case of silicon alkoxides. The hydrolysis of the alkoxide-based silica, tetraethoxysilane, takes place in micelles produced in O/W microemulsion, and many recipes can be found in the literature, a common one containing AOT as surfactant, an alcane (isooctane, cyclohexane) as continuous phase, and ammonia + water as reactant. The particle formation mechanism follows the sol-gel process with the TEOS present in the oil phase being hydrolyzed by water poles located at the boundaries of the aqueous droplets. Kinetics and mechanisms of silica nanoparticles formation have been described and a growth model was proposed (67).

1.3.2.6 Surface Modification of Preformed Particles Due to the hydrophilic nature of many inorganic colloids, it is often required to modify their functionality (mostly constituted of hydroxyl groups in silica, titania, and ferrite) by a chemical modification in order to improve the compatibility when they are combined with organic materials. The simplest modification is to bind an organic compound through the use of various coupling agents (such as those bearing a silane for silica particles), which converts the hydrophilicity of the inorganic surface into a hydrophobic character. However, for various purposes, the surface modification of inorganic colloids relies on the incorporation of a polymer phase. This can be performed according to quite a lot of methods as reported in Table 1.3. Surface polymerization can be radically initiated whether an initiating (azo or peroxy) or a polymerizable group be preliminary bound. More details related to the synthesis of organic–inorganic composite nanoparticles are given in the next section.

1.3.3 Organic Particles

The preparation of organic nanoparticles, mostly polymer based, can be performed according to three main approaches:

- polymerization in heterogeneous media
- modification of preformed particles
- formulation of colloidal dispersions from preformed polymers

1.3.3.1 Polymerization in Heterogeneous Media This technique, which has been developed for a long time, allows to produce colloidal dispersions of various nature, the so-called polymer latexes, applied in an increasing number of applications (68). Owing to the progresses at both the academic and industrial levels and due to the versatility of the process, such a technique has been more and more involved in the preparation of "high-tech" materials under dispersed form, especially for making nano and microparticles carefully controlled in terms of internal and surface structure. Figure 1.6 illustrates the range of particle sizes, which can be produced by using the main polymerization processes in heterogeneous media. Suspension polymerization, which proceeds via a bulk polymerization in initial monomer droplets (with several hundreds of micrometers size), is not a colloidal process and therefore not reported here; in addition, the obtained polymer particles are generally polydisperse in size.

On the contrary, for all other reported polymerization processes, the polymerization proceeds via a two-step mechanism involving at first the formation of the particles from (i) the continuous phase by the so-called *homogeneous nucleation* (as already mentioned) in soap-free emulsion, dispersion, and precipitation polymerization; (ii) out of the continuous phase, that is, through the presence of a

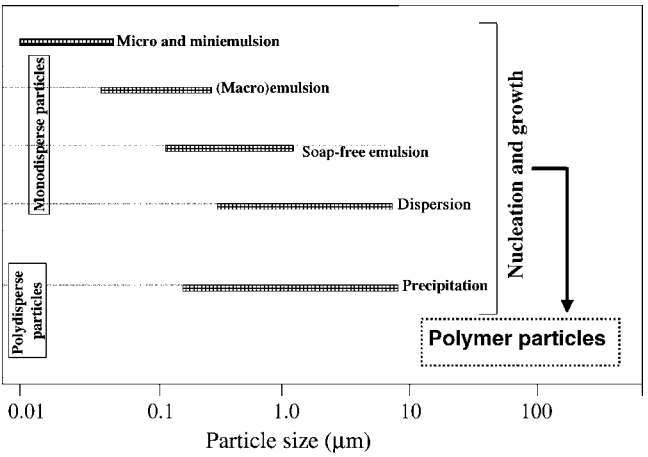

FIGURE 1.6 Nature of the heterogeneous polymerization process versus particle size and size monodispersity (adapted from Reference (15))

dispersed phase that could be micelles of surfactants (micellar nucleation), preexisting polymer, or mineral particles (*heterogeneous nucleation*).

Radical-initiated polymerizations are the more popular initiating systems; however, in the last decade, new processes have been explored based on different mechanisms than those of radical initiation, for example metathesis, or ionic polymerizations in aqueous media. It should also be emphasized on the recent introduction of controlled-radical polymerization methods, which appear highly suitable, especially for the design of latex particles with controlled surface and internal morphology (69).

Emulsion polymerization is the more developed heterogeneous polymerization process owing to the huge progresses accumulated at both the academic and industrial levels in the last 60 years. It has been widely used with numerous monomers (of various polarity) to produce latex particles applied in a continuously increasing range of domains (70). The versatility and flexibility of the process prove to be suitable for the synthesis of high-tech latex particles in the submicronic size range (down to 20 nm), to be used in biotechnology (calibration standards, diagnostic tests, solid-phase supports for biomolecules, medical imaging, synthetic vectors for drugs, biochips, etc.).

Briefly, conventional emulsion polymerization consists in dispersing a nonmiscible monomer in aqueous phase (mostly by using an emulsifier), then to initiate polymerization by a radical initiator leading to polymer particles of colloidal size much more smaller than the initial droplets. The various mechanisms involved in the formation and growth steps of the latex particles have been largely investigated, and the reader could report on many books and reviews devoted to the subject (24,40). Polymerization can be performed in the absence of surfactants, providing highly monodisperse particles but preferentially in a size range largely above 200 nm.

It has been well recognized that polymerization of two (or more) monomers, as named copolymerization, allows to produce polymer materials with physical and chemical properties more finely defined than with homopolymers. This is particularly the case of *copolymer latexes* in which surface and colloidal properties can be really tuned by taking advantage of the differences, in terms of reactivity and physicochemical properties (polarity, hydrophilicity, presence of ionic charges, etc.) of the two monomers involved in the polymerization process. In that purpose, considerable amount of work has been investigated to the kinetics and mechanisms of emulsion copolymerization in order to predict many features related to these copolymers, especially the control of the copolymer composition within the particle. In the frame of this review, it is worthwhile to focus on the potentialities of the copolymerization process to produce latex particles in which the internal morphology can be controlled (the so-called *structured latexes*) or those in which the interfacial functionality is tailored (*functionalized latexes*). It is obvious that both properties can be considered in a same latex particle.

In the case of functionalized latexes, as already mentioned in the previous section, numerous functionalities can be installed to particles. Emulsion polymerization techniques, especially those starting with a preformed batch of particles, the so-called *shot-growth* (i.e., inducing the polymerization of a functional monomer on batch particles at high conversion) and *seed* protocols (i.e., starting with a preformed population of particles), are particularly well adapted to carefully control the

incorporation of reactive groups (50). The following chemical groups can be listed containing either charges (sulfate, sulfonates, carboxylates, quaternary ammonium salts, phosphates, etc.) or not (carboxylic, aldehyde, chloromethyl, hydroxyl, amino, thiol, epoxide, acetal, activated ester, etc.) and more complex macromolecular structures (metal chelates, polyethylene oxide, polymethylmethacrylate, etc.). All these later chemical functions or macromolecules are quite useful:

- to control the particle size and monodispersity of the final latexes and especially in the case of charged monomers to allow the synthesis of stable nanoparticles (below 100 nm)
- to impart efficient steric stability (macromolecule)
- to induce subsequent reaction with biomolecules
- to incorporate a dye label, a specific ligand (oligosaccharide, lipid, peptide, nucleic acid, antibody, protein)
- to modify the surface of microsystems: two-dimensional assemblies of latex on silica wafers, microplates, biochemical devices, microfluidic channels.

Latex particles prepared with a hydrophilic layer (*hairy particles*) were found useful colloidal supports offering friendly environment when put in contact with biomolecules. Many routes can be explored to produce such particles based on different strategies: *layer-by-layer* method (LbL) (71); incorporation of a hydrophilic layer either covalently (surface polymerization of reactive surfactants (72)) or more simply by physical adsorption of amphiphilic block or graft copolymers (73). Coverage of latex particles by polyethylene oxide (PEO) proves to be quite suitable for biotechnological applications due to the immunogenicity, nontoxicity, and stealth effect of the PEO (74). The use of controlled radical polymerization methods (such as reversible addition–fragmentation transfer (RAFT), nitroxide-mediated polymerization (NMP), or atom-mediated transfer radical polymerization (ATRP)) are currently performed to tailor hairy particles with well-controlled polymer brushes.

Miniemulsion Polymerization In this process, the main difference with the emulsion process is that the monomer phase is more finely divided owing to the use of a mixture of a surfactant with a hydrophobic solvent (hexadecane, cetylic acid) together with a strong energy of agitation. In that case, the formed submicrometer-sized monomer droplets (which are prevented to coalesce by Otswald ripening) can compete with existing micelles to capture aqueous-phase radicals. Final polymer particles have almost the same size than the initial monomer droplets and exhibit a long-term stabilization. In that process, the key points are the formation of the small droplets and the influence of the various parameters (nature of the emulsifier technique, amount of emulsifier, effect of the hydrophobic molecule, and nature of the initiator), which need to be taken into account, have been thoroughly investigated (75).

Polymerization can be radically initiated using either an organic or a water-soluble initiator. Controlled radical polymerization techniques have been successfully

performed with this process since the presence of the smaller initial droplets as active sites allow to avoid the nucleation step. Such a process has been applied for polymerizing many monomers provided they are not too soluble in the continuous phase whether they are hydrophobic (MMA, styrene) or hydrophilic (MMA–acrylamide mixture, acrylonitrile).

Nonradical-initiated polymerizations have also been explored: polycondensation (polyesters, polyurethanes) ionic polymerization (for instance, the anionic polymerization of cyanoacrylates).

This method has been recently used for the synthesis of nanosized magnetic nanoparticles by preparing separately a magnetite miniemulsion and a styrene miniemulsion and mixing them before polymerization (76).

Microemulsion Polymerization As already defined in the previous section, this process consists first in preparing a highly dispersed monomer phase. Many efforts have been directed to the formulation of microemulsions having the minimal amount of surfactant (less than 10 wt%) together with high solid contents (from 10% to 40%). Polymerization initiated (by photo or radical initiation) in the formed micelles leads to nanoparticles in the size range below 100 nm.

It was investigated both with O/W and W/O systems and mostly with globular microemulsions. Mechanisms of nucleation and growth have been elucidated with styrene as hydrophobic monomer and with acrylamide as water-soluble monomer (77). Due to the large amount of monomer-swollen micelles, polymerization rate is very fast and relatively narrow size distribution could be obtained at least with the acrylamide-based system.

Functionalized nanolatexes can be produced by incorporation of hydrophilic monomers (such as hydroxyethyl or dimethylaminoethyl methacrylates) with, however, a lack of stability in the final microlatexes (42,43).

Polymerizations have also been conducted in other structures than globular microemulsions, for instance, in bicontinuous phases. Under specific conditions, the bicontinuous morphology is retained after polymerization leading to polymer presenting a nanoporous structure of potential interest in biotechnology (nanovector, membrane separation) (78).

Dispersion Polymerization In that process, the initial monomer solution is homogeneous with the presence of steric stabilizing species (mostly hydrophilic polymers like poly-*N*-vinylpyrrolidone or better with block or graft copolymers with a well defined architecture). By introduction of an initiator, an insoluble polymer phase is produced, which is dispersed as colloidal particles through the already depicted homogeneous nucleation process. Particles can be obtained in a large size range (roughly between 200 and 20 μm) but the process is more adapted to produce monodisperse micrometer-sized latexes. It can be carried out both with many different monomers (hydrophobic and water soluble) in polar and nonpolar media with preferentially a radical initiation but also by other initiation processes such as ionic, metathesis, and ring opening) (37).

Precipitation Polymerization In this process, the monomer is soluble in the continuous phase and the formed polymer phase separated with no formation of a colloidal dispersed phase.

It was found that the polymerization of several acrylamide derivatives in aqueous phase in the presence of anionically charged initiator (potassium persulfate for instance) and a small amount of a cross-linker lead to highly monodisperse and electrosterically stable latexes. This comes from the property of polyNIPAM and of many other polyacrylamide derivatives to exhibit a low critical solubility temperature (LCST) in a broad range of temperatures, which means that a drastic change in the hydrophilic–hydrophobic balance (core-globule transition) occurs at the LCST. Consequently below LCST, polyNIPAM chains are fully expanded in the aqueous phase. A huge number of studies have been investigated in the case of *N*-isopropylacrylamide (the so-called NIPAM) showing that under adjusted experimental conditions (low dilution of reactants, monomer concentration, initiator, temperature, etc.), colloidal submicronic dispersions can be produced without the presence of any surface-active agent. On the colloidal point of view, thermally sensitive polymer latex particles display unique properties as regards to the dramatic change in the size and electrophoretic mobility of the particles. They were proposed as model systems of *thermally sensitive colloids* (Fig. 1.7) with quite a lot of potential applications, especially in biotechnologies (79).

Such a property has been widely extended to the synthesis of many other polymer microspheres being responsive to other external parameters such as pH, ionic strength, light, magnetic or electric field, and biological effect, offering the possibility to envision multiresponsive particles. In addition, various particle morphologies can be now designed depending upon the recipe (with preferentially the presence of a functional and/or charged comonomer) and the type of heterogeneous polymerization process (batch, shot-growth, seed). Hairy, core-shell and microgel particles can be currently produced in a large range of size (particularly between 100 and 1000 nm) and nature of polymer.

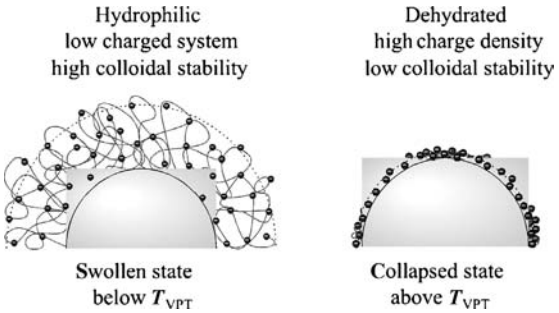

FIGURE 1.7 Illustration of thermally sensitive colloidal latex particles (polystyrene core–poly(NIPAM) shell) (T_{VPT}: volume phase transition temperature)

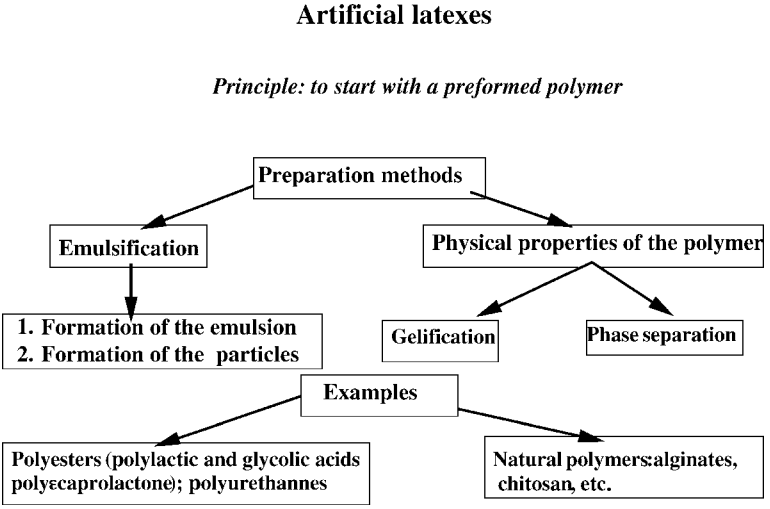

FIGURE 1.8 Main strategies followed for the preparation of polymer nanocolloids

1.3.3.2 Formulation of Polymer Colloids from Preformed Solution Polymers Depending on the nature of the polymer (lipophile vs. water soluble), two main strategies can be followed to obtain *artificial latexes* as schematically depicted in Fig. 1.8. Such techniques are now well identified (80) and widely developed in the pharmaceutical and medicine fields where they are used for *in vivo* delivery of drugs, proteins, DNA, etc.

The first method relies on a two-steps technique: formation of an emulsion, that is, a finely dispersed phase containing the polymer solubilized in a solvent in an aqueous continuous phase containing a polymer stabilizer. The formation of a polymer emulsion of small droplets usually requires high-pressure homogenizer together with ultrasonic agitation providing submicrometer size particles. The second step consists in eliminating the solvent inside the droplets and this can be conducted by different methods, which have been well described: evaporation of the solvent or extraction by depleting the solvent of the dispersed phase by another solvent.

The second method is based on the properties of the polymers: the nanoprecipitation technique allows the formation of nanoparticles due to a phase separation process induced in the polymer solution by adding a nonsolvent of the polymer or by changing pH or salinity conditions. This process can be carried out with or without stabilizer but only under very diluted systems.

1.3.3.3 Others Techniques

Controlled Hierarchical Chemistry Among the many arborescent architectures that can be produced by such chemistry, *dendrimers* constitute a class of materials, which offer quite remarkable properties in relation with their potential use as highly "engineering" nanostructure: nearly perfect monodisperse polymer tree–like,

nanometer-size (down to 10 nm), high number of functional end groups available on the molecular surface.

The synthesis of such dendrimers can be obtained by an iterative sequence of reaction steps; the divergent synthesis starts from a central reactive core such as with the polyamidoamine (38).

Dendrimers prove to be very useful in biotechnologies such as a reservoir of drugs, transfection of DNA, and immobilization of water-soluble dendrimers onto functionalized surfaces (biochips) (12).

Allotropes of Carbon It is worth mentioning the increasing interest of allotropes of carbon, the so-called fullerens and nanotubes. Both of them have a nanometer diameter size, the former being spherical in size and the second cylindrical with a length, which could reach up to millimeters. Due to their unique properties in the material science, especially in the nanotechnology domain for their applications in electronics and optics, carbon nanotubes have been widely studied in the last years with regards to their synthesis, properties, and applications (39,81). There are two main types of nanotubes the so-called single-walled nanotubes (SWNT) consisting of a single graphite sheet wrapped into a cylindrical tube and multiwalled nanotubes (MWNT), made of an array of nanotubes concentrically nested. Both of them can be obtained by carbon-arc discharge, laser ablation of carbon, or chemical vapor deposition. In the case of SWNT, the diameter of the nanotube is in the size range of 0.8–4 nm whereas the size is much larger for MWNT (from 1.4 to 100 nm). Impurities may be found in the final products, especially for the SWNT.

1.3.4 Composite Particles

Composite particles refer to colloidal dispersions in which organic and inorganic materials are intimately distributed within the particle and offering unique properties. One major effect is that at a nanometric level, surface properties predominate over volume properties. As detailed by Bourgeat-Lami in recent reviews, the synthesis of such composite systems can be classified in three main categories (82):

- assembly of organic and inorganic colloids
- synthesis by *in situ* polymerization
- simultaneous reaction in the presence of the inorganic or organic precursors

Nanocomposite particles are produced when using the two first methods, whereas the third one leads to *hybrid nanoparticles*.

1.3.4.1 Assembly of Organic and Inorganic Colloids There are many examples in the literature in which composite particles are obtained by controlling the organization of mineral core by an organic shell (polymer) or conversely. It was mainly explored with polymer latexes due to their extreme versatility as regards to nature of polymer, colloidal, and surface properties.

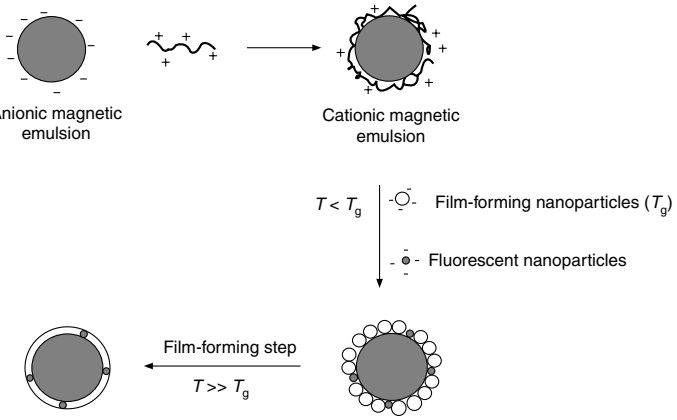

FIGURE 1.9 Stepwise heterocoagulation process used to prepare magnetic and fluorescent nanoparticles (29)

The heterocoagulation strategy (as shown in Fig. 1.9), based on the assembly of the two colloids by electrostatic interaction, has been investigated in many papers regarding the encapsulation of titania and silica. It was recently described for producing low-size (200–300 nm) magnetic nanoparticles (29). The strategy consists in inducing the flocculation of film-forming nanoparticles anionically charged (order of 40 nm) onto a preformed magnetic emulsions (containing iron oxide nanoparticles) being subsequently cationically charged by polyethylenimine. After heating the composite particles above the film formation temperature, stable magnetic nanoparticles were obtained with an average of 25% of magnetic material.

In that domain, the LbL assembly (71) has been proved quite powerful in view of preparing composite nanoparticles with outstanding properties. The process consists in adsorbing onto an organic particle a layer of inorganic nanoparticles and a polyelectrolyte of opposite sign. Figure 1.10 gives an illustration of such process in the elaboration of magnetic particles from oil in water magnetic droplets.

Such composite colloids dispersions were found to exhibit unexpected and specific properties (electric, magnetic, optic, and conductive), which are currently investigated in many places.

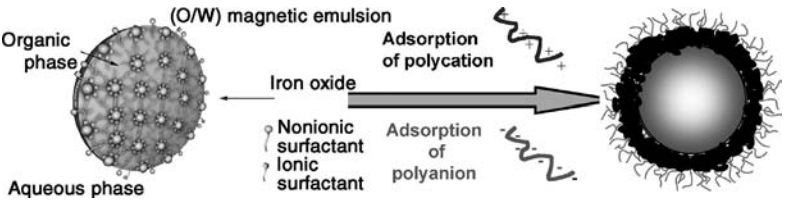

FIGURE 1.10 Schematic illustration of layer-by-layer encapsulation process of oil in water magnetic droplets

1.3.4.2 Synthesis by In Situ Polymerization Two types of particle morphology can be considered whether the inorganic phase be located in the core

or in the shell. In any cases, it is necessary to preliminary introduce functional groups at the surface of the organic or inorganic seeds.

In the case of mineral (core)-organic (shell) particles, two main strategies have been experienced:

- heterogeneous polymerization (emulsion, miniemulsion, dispersion) of various monomers in the presence of mineral colloids
- radical polymerization initiated from the inorganic particles surface

In the case of organic(core)-mineral (shell) composite particles, their synthesis relies on either the mineral polycondensation by sol-gel process or precipitation of metal salts on latex particles. Hydrolytic polycondensation via sol-gel process has been performed mostly with metal alkoxides of structure ($M(OR)_4$ using various substrates as templates, latex particles, for example. It is then possible to prepare composite latex particles with an organic layer of silica or titania, the latex particles, if correctly functionalized, are able to capture the oligomers formed in the continuous phase as polycondensation proceeds. As illustrated in Fig. 1.11, such composite particles can be transformed in hollow particles upon thermal decomposition or solubilization of the organic core.

It can be interesting to focus on a recent strategy for making low size magnetic particles containing a large amount of magnetic material. It consists in inducing styrene polymerization inside submicronic droplets of a stable and relatively monodisperse magnetic emulsion in the presence of small amount of a cross-linker and an amphiphilic polymer. The final magnetic latexes were found to exhibit a narrow size and to contain up to 60% in weight iron oxide. As shown in Fig. 1.12, a perfect core-shell morphology is observed proving the efficient encapsulation of the ferrites, which makes such particles quite adapted for diagnostic and extraction of various biomolecules (83).

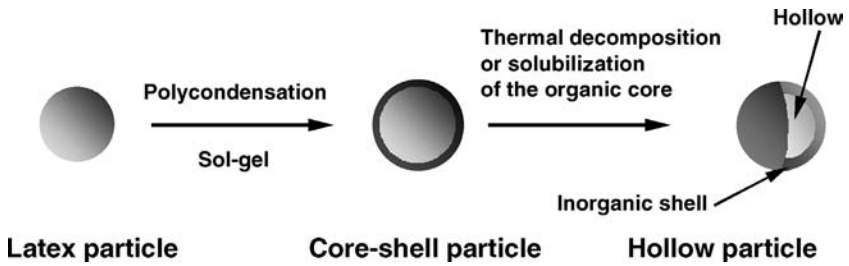

FIGURE 1.11 Principle of the preparation of hollow particles from a latex particle with an organic core and a mineral shell

1.3.4.3 Simultaneous Reaction in the Presence of the Inorganic or Organic Precursors Hybrid nanomaterials have received much interest in the last few years, and their preparation under colloid state was envisioned resulting in an intimate mixing of mineral and organic phases at a molecular level. A recent paper, for instance, reported the synthesis of such hybrid colloids by emulsion polymerization of

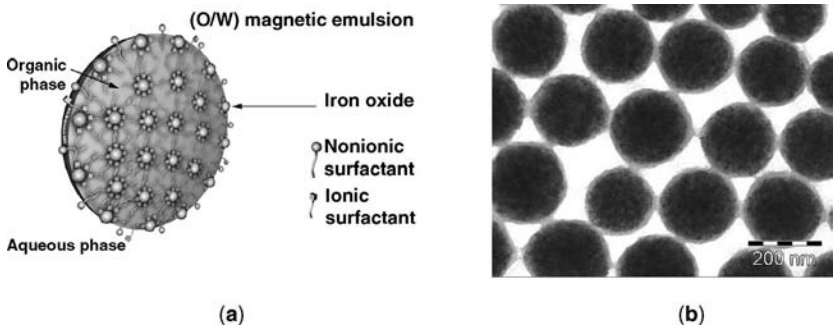

FIGURE 1.12 Transformation of oil in water magnetic emulsion (*a*) into submicronic magnetic latex (*b*) obtained by emulsion polymerization of styrene and divinylbenzene onto a ferrofluid emulsion stabilized by polyacrylic acid based amphiphilic surfactant and initiated by potassium persulfate (83)

a monomer mixture containing a comonomer, which is an inorganic precursor (an organosilane bearing a vinyl or methacrylate group). This leads to the formation of a fine dispersion of silica clusters inside the particles (49).

Finally, it should be also focused on the possibility to synthesize inorganic nanoparticles bearing a layer of stimuli-responsive polymer chains with chemical reactive end groups. For instance, the preparation of core-shell magnetic nanoparticles with a thermally sensitive biodegradable shell (dextran grafted with a poly[NIPAM]-based polymer) was recently disclosed providing *multifunctional colloids* with potential applications in drug-targeting delivery and magnetic imaging resonance (84). In the recent years, many research studies have been devoted to the synthesis of composite nanoparticles constituted of a gold or semiconductor (QDs) core surrounded by a stimuli-responsive layer that could be a synthetic (co)polymer, a biomolecule (peptide) or a polysaccharide with obvious applications in bioassays and drug delivery systems (85). In that purpose, self-assemblies of block copolymers with the polymer or the biomolecule as hydrophilic block can serve as useful templates for the encapsulation of the inorganic material.

Radical and preferentially controlled radical polymerization techniques initiated at the surface of inorganic colloids proved to be suitable to make stimuli-sensitive hairy composite nanoparticles.

1.4 CONCLUSION AND PROSPECTS

The preparation of well-characterized inorganic and organic colloids in the submicronic size (down to several nanometers in the case of metals) benefits of a considerable amount of works both on academic and practical aspects. It took advantage of the tremendous progresses accomplished in the physicochemistry of dispersed systems in aqueous media as well as in the organic and mineral chemistry (precipitation and sol-gel processes, reactions in self-assemblies, new types of heterogeneous polymerizations, controlled radical polymerization methods). All

these manufacturing techniques allow to carefully control many relevant parameters such as shape, particle size, polydispersity, morphology, and surface functionality of the particle, all of them being of importance in the design of nanobiotechnologies.

As recently quoted (86), it should be noticed the attractive interest of gold, quantum dots, and magnetic nanoparticles used as tags or labels in many applications such as in biochips, nanobiosensors with the purpose to detect DNA, or proteins in small volumes within a reduced time.

Due to the very active research in this domain, it may be anticipated that more complex materials in the nanocolloidal range are being elaborated, offering new potentialities in diagnostics and drug deliveries. It is worth mentioning several approaches dedicated to the synthesis of new kinds of nanoparticles (asymmetric, hollow, nanostructured, nanoporous). In the last few years, many studies evidenced the important role of various polymeric systems or nanotubes as colloid-size templates for the synthesis of nanostructures and superstructures. In the case of polymeric systems, self-assemblies of amphiphilic block copolymer surfactants (frozen micelles), dendrimers, vesicles, liposomes, emulsions, microemulsions, and latex particles were found appropriate (87). Polymerization can be carried out inside or at the surface of the selected template allowing to synthesize inorganic, inorganic/organic composites with tunable properties. A careful control of the association of mineral and organic material is also a challenge for creating new multifunctionalized and/or adaptive composite and hybrid nanocolloids. Due to their unique properties, stimuli-responsive nanoparticles, as smart material, should continue to offer outstanding potentialities for innovative applications.

It also appears that microfluidic reactors can be adequately designed for producing various kinds of nanocolloids (gold, nanocomposites, semiconductors, etc.) as well as to investigate particle interactions. In the domain of superstructures, there is also an attractive research to encourage the development of two or three-dimensional assemblies of nanoparticles on various surfaces or on living systems.

The development of nanosized colloids in life science activities, regardless of their nature, should not avoid systematic and independent research studies concerning their control in terms of dissemination, potential pollution, and toxic effects. This is an indispensable safety caution for people manipulating or in contact with such dispersed materials as well as for the environment.

It is obvious that multidisciplinary research on these nanocolloids would be really creative and productive, at first for elaborating new engineered materials at nanometer level and secondly for evaluating their chemical, physical, and biological properties together with their performances in nanobiotechnologies.

REFERENCES

1. Manz A, Becker H. Microsystem Technology in Chemistry and Life Sciences. New York: Springer; 1999. p. 263.
2. Jähnisch K, Hessel V, Löwe H, Baerns M. Chemistry in microstructured reactors. Angew Chem 2004;43:406–446.

3. Terray A, Oakey J, Marr DWM. Microfluidic control using colloidal devices. Science 2002;296:1841–1844.
4. Guyon S, Bílková Z, Minc N, Fütterer C, Viovy JL. Microfluidic proteolytic microreactors based on magnetic nanoparticles for proteomics. Nanobiotechnologies II. 22–24 April 2003, Grenoble.
5. Yoshinaga K. Surface modification of inorganic particles. In: Sugimoto T, editor. Fine particles, Synthesis, Characterization and mechanism of growth. Surfactant Science Series 92, New York: Marcel Dekker; 2000. pp. 626–646.
6. Park S-J, Taton TA, Mirkin CA. Array-based electrical detection of DNA with nanoparticle probes. Science 2002;295:1503–1506.
7. Fritzsche W, Taton TA. Metal nanoparticles as labels for heterogeneous, chip-based DNA detection. Nanotechnology 2003;14:63–73.
8. Tanimoto A. Magnetic resonance imaging with supermagnetic nanocapsules. In: Arshady R, editor. Microspheres Microcapsules & Liposomes. Volume, 3 Radiolabelled and magnetic particles particulates in medicine and biology. Londres: Citus Books; 2001. pp. 525–556.
9. Wang J-X, Wen L-X, Wang Z-H, Wang M, Shao L, Chen J-F. Facile synthesis of hollow silica nanotubes and their application as supports for immobilization of silver nanoparticles. Scripta Materialia 2004;51(11):1035–1039.
10. Michalet X, Pinaud FF, Bentolila LA, Tsay JM, Doose S, Li JJ, Iyer G, Weiss S. Peptide-coated semiconductor nanocrystals for biomedical applications. Proc SPIE 2005;5704: 57–68.
11. Singh R, Pantarotto D, McCarthy D, Chaloin O, Hoebeke J, Partidos CD, Briand J-P, Prato M, Brianco A, Kostarelos K. Binding and condensation of plasmid DNA onto functionalized carbon nanotubes: toward the construction of nanotube-based gene delivery vectors. J Am Chem Soc 2005;127(12):9.
12. Miska B, Slomkowski S, Chemimi MM, Delamar M, Majoral J-P, Caminade AM. Colloid Polym Sci 1999;277:58.
13. Buchhammer HM, Mende M, Oelmann M. Colloid Surf A 2003;218:151.
14. Cui Z, Mumper RJ. J Control Rel 2001;27:1039.
15. Kissel T, Li Y, Unger F. ABA-triblock copolymers from biodegradable polyester A-blocks and hydrophilic poly (ethylene oxide) B-blocks as a candidate for in situ forming hydrogel. Adv. Drug Delivery Rew, 2002; 54:99–134.
16. Pichot C, Delair T. Speciality applications of latex polymers. In: van Herk AM, editor. Chemistry and Technology of Emulsion Polymerization, Blackwell Publishing, Oxford; 2005. pp. 257–277.
17. Meza M. Application of magnetic particles in immunoassays. In: Häfeli U, Schütt W, Teller J, Zborowski M, editors. Scientific and Clinical Applications of Magnetic Carriers. New York: Plenum Press; 1997. pp. 303–309.
18. Elaïssari A, Veyret R, Mandrand B, Chatterjee J. Biomedical applications for magnetic latexes. In: Elaïssari A, editor. Colloidal Biomolecules, Biomaterials.Volume 116, Surfactant Science series, 116, M Dekker; 2004. pp. 1–29.
19. Härma H. Particle Technologies. Technol Rev 2002;126:1–30.
20. Drake TJ, Zhao XJ, Tan W. Bioconjugated silica nanoparticles for bioanalytical applications. In: Niemeyer CM, Mirkin CA, editors. Nanobiotechnology.

21. Wenguang L, Jiab QX, Wanga H-L. Facile synthesis of metal nanoparticles using conducting polymer colloids. Polym Commun 2006;47:23–26.
22. Pichot C. Surface-functionalized latexes for biotechnological applications. Curr Opin Colloid Int Sci 2004;9:213–221.
23. Ito K, Cao J, Kawaguchi S. Functional polymer colloids from functional monomers and macromonomers. In: Arshady R, Guyot A, editors. Functional Polymer colloids & microparticles. Volume IV, London: Citus; 2002. pp. 109–135.
24. Fitch RM. In: Fitch RM, editor. Polymer Colloids: A Comprehensive Introduction. Academic Press;1998. pp. 145–172.
25. Arshady R, editor Radiolabelled and magnetic particles particulates in medicine and biology. Microspheres Microcapsules & Liposomes. Volume 3, Londres: Citus Books; 2001. pp. 429–582.
26. Nichkova M, Dosev D, Gee SJ, Hammock BD, Kennedy IM. Anal Chem 2004;77: 684.
27. Murphy CJ. Anal Chem 2002;74:520A.
28. Dosev D, Nichkova M, Liu M, Guo B, Liu G-yXia Y, Hammock BD, Kennedy IM. Application of Eu:Gd03 nanoparticles to the visualisation of protein micropatterns. Proc SPIE 2005;5699:473–481.
29. Lansalot M, Sabor M, Elaïssari A, Pichot C. Elaboration of fluorescent and highly submicronic polymer particles via a stepwise heterocoagulation process. Colloid Polym Sci 2005;283:1267–1277.
30. Kawaguchi H. Temperature hydrogels microspheres. In: Arshady R, editor. Microspheres, Microcapsules, Vol 1: Preparation and Chemical Applications. Citus Books; 1999. pp. 237–251.
31. Matijevic E, Sapieszko RS, Forced hydrolysis in homogeneous solutions. In: Sugimoto T, editor. Fine Particles, Synthesis, Characterization and Mechanism of Growth. Surfactant Science Series 92, New York: Marcel Dekker; 2000. pp. 2–34.
32. Sugimoto T. Phase transformation from solid precursors. In: Sugimoto T, editor. Fine Particles, Synthesis, Characterization and Mechanism of Growth. Surfactant Science Series 92, New York: Marcel Dekker; 2000.
33. Kodas TT, Hampden-Smith MJ. Aeorol Processing of Materials. New York: Wiley-VCH; 1999.
34. Sugimoto T. Adv Colloid Interface 1987;28:65.
35. Giesche H. Hydrolysis of silicon alkoxides in homogeneous solutions. In: Sugimoto T, editor. Fine Particles, Synthesis, Characterization and Mechanism of Growth. Surfactant Science Series 92, New York: Marcel Dekker; 2000. pp. 126–146.
36. Silvert P-Y, Tekaia K. Solid State Ionics 1995;82:53.
37. Sudol ED. Dispersion polymerisation. In: Asua JM, editor. Polymeric Dispersions: Principle and Applications. NATO ASI Series E 335. Dordrecht: Kluwer Academic; 1997. pp. 141–153.
38. Caminade A-M, Majoral J-P. Nanomaterials based on Phosphorus dendrimers. Acc Chem Res 2004;37:381.
39. Murr LE, Bang JJ, Esquivel EV, Guerrero PA, Lopez DA. Carbon nanotubes, nanocrystal forms, and complex nanoparticle aggregates in common fuel-gas combustion sources and the ambient air. J Nanoparticle Res 2004;6:241–251.

40. Lowell PA, El-Aasser MS. Emulsion Polymerization and Emulsion Polymers. Chichester: John Wiley & Sons, Ltd.; 1997.
41. Tang PL, Sudol ED, Adams ME, Silibi CA, El-Aasser MS. Miniemulsion polymerization. In: Daniels ES, Sudol ED, El-Aasser MS, editors. Polymer Latexes: Preparation, Characterization and Applications. ACS Symposium Series, 492,Washington DC: 1992. pp. 72–98.
42. Antonietti M, Basten R, Lohmann S. Polymerization in microemulsion—a new approach to ultrafine, highly funcionalized polymer dispersions. Macromol Chem Phys 1995;196:441–466.
43. Larpent C, Bernard E, Richard J, Vaslin S. Polymerization in microemulsions with polymerizable cosurfactants; a route to highly functionnalized nanoparticles. Macromolecules 1997;30:354–362.
44. Caruso F, Mövhald H. Preparation and characterization of ordered nanoparticles and polymer composite multilayers on colloids. Langmuir 1999;15:8276–8281.
45. Janssen EAWG, van Herk AM, German AL. Encapsulation of inorganic filler particles by emulsion polymerization. ACS Div Polym Chem Polym Prep 1993;34:532–533.
46. Bourgeat-Lami E. Hollow particles: synthetic pathways and potential applications. In: Elaïssari A, editor. Colloidal Polymers. Surfactant Science Series, 115. New York: Marcel Dekker; 2003. pp. 189–223.
47. Vitry S, Mezzino A, Gauthier C, Cavaillé J-Y, Lefebvre F, Bourgeat-Lami E. Hybrid copolymer latexes cross-linked with methacryloxy propyl trimethoxy silane. Film formation and mechanical properties. CR Acad Sci II C 2003;6:1285–1293.
48. Fessi H, Puisieux F, Devissaguet JP, Ammoury N, Benita S. Nanocapsule formation by interfacial polymer deposition following solvent displacement. Int J Pharm 1989;55:R1–R4.
49. De S, Robinson D. Polymer relationships during preparation of chitosan–alginate and polyl-lysine–alginate nanospheres. J Control Release 2003;89:101–112.
50. Pichot C, Delair T. Functional nanospheres by emulsion polymerization. In: Arshady R, editor. Microspheres Microcapsules & Liposomes. Volume 1. Londres: Citus Books; 1999. pp. 125–163.
51. Kawaguchi K. Functional polymer microspheres. Prog Polym Sci 2000;25:1171–1210.
52. Otsuka H, Nagasaki Y, Kataoka K. Sel-assembly of polyethylene glycol-based block copolymers for biomedical applications. Curr Opin Colloid Interface Sci 2001;3–10.
53. Gref R, Couvreur P, Barratt G, Mysiakine E. Surface-engineered nanoparticles for multiple ligand coupling. Biomaterials 2003;24:4529.
54. Schatz C, Lucas JM, Viton C, Domard A, Pichot C, Delair T. Formation and properties of positively charged colloids based on polyelectrolyte complexes of biopolymers. Langmuir 2004:20 (18):7766–7778.
55. LaMer VK. Ind Eng Chem 1952;44:1270.
56. Candau F. Polymerization in Microemulsions. In: Kumar P, Mittal KL, editors. Hanbook of Microemulsion Science and Technology. New-York: Marcel Dekker;1999. pp. 679–712.
57. Li H, Rothberg. Colorimetric detection of DNA sequences based on elecrstostatic interactions with unmodified gold nanoparticles. PNAS 2004;101 (39):14036–14039.
58. Sato K, Hosokawa K, Maeda M. Non-crosslinking gold nanoparticles aggregation as a detection method for single-base substitutions. Nucleic Acid Res 2005;33 (1):1–5.
59. Stöber W, Fink A, Bohn E. J Colloid Interface Sci 1968;26:62–69.

60. Brook MA. Silicon in a biological environment. In: Silicon in Organic Organometallic and Polymer Chemistry. John Wiley & Sons, Inc.; New York: 2000. pp. 459–473.
61. Pacard E, Brook MA, Ragheb AM, Pichot C, Chaix C. Elaboration of silica colloid / polymer hybrid support for oligonucleotide synthesis Colloids Surf B Biointerface 2006;47:176–188.
62. Fiévet F, Figlarz M, Lagier J-P. Patents: Europe 0,113,281. 1987; USA 4,539,041. 1985; Finland 74,0416. 1998; Canada 1123, 5910. 1988; Norway 163887. 1988, Japan 04,024402. 1992.
63. Sugimoto T, Matijevic E. J Colloid Interface Sci 1980;74:227.
64. Matijevic E, Partch RE. Synthesis of monodispersed colloids by chemical reactions in aerosols. In: Sugimoto T, editor. Fine particles, Synthesis, Characterization and Mechanism of Growth. Surfactant Science Series, 92. New York: Marcel Dekker; pp. 147–188.
65. Gobe M, Kon-no K, Kandori K, Kitahara A. J Colloid Interface Sci 1983;93:291.
66. Pileni MP, Motte L, Petit C. Chem Mater 1992;4:338.
67. Osseo-Asare K. Hydrolysis of silicon alkoxides in microemulsions. In: Sugimoto T, editor. Fine Particles, Synthesis, Characterization and Mechanism of Growth: Surfactant Science Series 92, New York: Marcel Dekker; 2000. pp. 147–188.
68. Antonietti M, Tauer K. 90 years of polymer latexes and heterophase polymerization: more vital than ever. Macromol Chem Phys 2003;204:207–219.
69. Qiu J, Charleux B, Matyjaszewski K. Controlled/living radical polymerization in aqueous media: homogeneous and heterogeneous systems. Prog Polym Sci 2001;26:2083–2134.
70. van Herk AM, editor. Chemistry and Technology of Emulsion Polymerization. Oxford: Blackwell Publishing;2005.
71. Caruso F, Lichtenfeld H, Giersig M, Möhwald H. Electrostatic self-assembly of silica nanoparticle-polyelectrolyte multilayers on polystyrene latex spheres. J Am Chem Soc 1998;120:8523–8524.
72. Guyot A, Tauer K. Polymerizable and polymeric surfactants. In: Texter J., editor. Reactions and Synthesis in Surfactants Systems.Applied Surface Series, 100, (XXVIII). New York: Marcel Dekker;2001. pp. 547–576.
73. Riess G. Micellisation of block copolymers. Prog Polym Sci 2003;28:1107–1170.
74. Millton-Harris J. Introduction to biomedical and biotechnical applications of polyethylene glycol. ACS Polym Preprints (Div Polym Chem) 1997; 38:520–521.
75. Landfester K. Recent developments in miniemulsions—Formation and stability mechanisms. Macromol Symp 2000;150:171–178.
76. Ramirez LP, Landfester K. Magnetic polystyrene nanoparticles with high magnetic content obtained by miniemulsion process. Macromol Chem Phys 2003;204:22–31.
77. Candau F. Microemulsion polymerization. In: Asua JM, editor Polymeric Dispersions: Principles and Applications. NATO ASI Series E, 335. Dordrecht: Kluwer Academic; 1997. pp. 127–140.
78. Gan LM, Ti TD, Chew CH, Teo WK, Gan LH. Microporous polymer materials from microemulsions of zwitterionic microemulsions. Langmuir 1995;11:3316–3320.
79. Pelton R. Temperature-sensitive microgels. Adv Colloid Interface Sci 2000;85 (1):1–33.
80. Vauthier C, Fattal E, Labarre D. From polymer chemistry and physicochemistry to nanoparticular drug carrier design and applications. In: Yaszemski MJ, Trantolo DJ,

Lewamdrowski KU, Hasirci V, Altobelli DE, Wise DL. Biomaterial Handbook—Advanced Applications of Basic Sciences and Bioengineering. New York: Marcel Dekker; 2004. pp. 563–598.

81. Baughman Ray H, Zakhidov Anvar A, de Heer Walt A. Carbon nanotubes—the route toward applications. Science 2002;297:787–792.
82. Bourgeat-Lami E. Organic/inorganic nanocomposites. In: Arshady R, Guyot A, editors. Dendrimers, Assemblies and Nanocomposites. MML Series 5 London: Citus Books; 2002. pp. 149–194.
83. Montagne F, Mondain-Monval O, Pichot C, Elaïssari A. Highly magnetic latexes from submicrometer oil in water ferrofluid emulsions. J Polym Sci A Polym Chem 2006;44:2642–2656.
84. Zhang L, Srivastava RS, Misra RDK. Core-shell magnetite nanoparticles surface encapsulated with smart stimuli-responsive polymer: synthesis, characterization, and LCST of viable drug-targeting delivery system. Langmuir 2007;23:6342–6351.
85. Kim J.-H., Lee TR. Discrete thermally responsive hydrogel-coated gold nanoparticles for use as drug-delivery vehicles. Nanobiotechnology 2006;67(1):61–69.
86. Jain KK. Nanotechnology in clinical laboratory diagnostics. Clin Chim Acta 2005;358: 37–54.
87. Lui T, Burger C, Chu B. Nanofabrication in polymer matrices. Prog Polym Sci 2003;28: 5–26.x

CHAPTER 2

Nanoparticles Comprising pH/Temperature-Responsive Amphiphilic Block Copolymers and Their Applications in Biotechnology

PEIHONG NI

College of Chemistry and Chemical Engineering, Soochow University, Suzhou 215123, China

2.1 INTRODUCTION

Stimuli-responsive polymers have drawn much attention due to their various promising potential applications for the biomedical fields. There are chemical or physical stimuli. The chemical stimuli, such as pH, ionic factors, and chemical agents, will change the interactions between polymer chains or between polymer chains and solvents at the molecular level. The physical stimuli, such as temperature, electric or magnetic fields, and mechanical stress, will affect the level of various energy sources and alter molecular interactions at critical onset points. These responses of polymer systems are very useful in biorelated applications such as drug delivery, biotechnology, and chromatography (1–3). In particular, the pH and temperature-responsive block copolymers are considerably important because they can form nanoparticles, for example, polymeric micelles, vesicles, or hollow nanospheres, in aqueous media via the changing environment, and further provide a variety of applications for the biomedical fields. Recent reviews have summarized research progress in pH/temperature-responsive polymers, including poly(*N*-isopropylacrylamide) (PNIPAAm), poly(methacrylic acid) (PMAA), and Pluronic specious.

This chapter focuses on recent progress made in pH/temperature polymers, with special emphasis on recent advances in understanding the structure-property relationship in amphiphilic block copolymers consisting of poly(ethylene glycol) (PEG),

Colloidal Nanoparticles in Biotechnology, Edited by Abdelhamid Elaissari
Copyright © 2008 John Wiley & Sons, Inc.

poly(ethylene oxide) (PEO), polyvinylethers, tertiary amine methacrylates, and phosphorylcholine-based polymers. These copolymers can self-organize in aqueous media to form micelles and give the potential applications in biomedicine, pharmacy, and biotechnology, such as drug delivery, cell culture, immobilizing biocatalysts, bioseparation, and biosensor.

2.2 pH-RESPONSIVE AMPHIPHILIC BLOCK COPOLYMERS

pH-Responsive amphiphilic block copolymers contain a number of ionizable groups in their main chains and pendants. When the pH value is changed, these groups can accept or donate protons in aqueous solution to yield polyelectrolytes, weak polyacid or weak polybase, depending on their structures and the pH values. For example, poly (acrylic acid) (PAA) and poly(methacrylic acid) (PMAA) can release protons in neutral or basic medium, whereas poly[2-(dimethylamino)ethyl methacrylate] (PDMAEMA or PDMA) can accept protons due to the substituted amino group in the pendants (4).

2.2.1 Self-Assembly of Block Copolymers of Tertiary Amine Methacrylates

A series of tertiary amino methacrylate monomers, including 2-(dimethylamino)ethyl methacrylate (DMAEMA), 2-(diethylamino)ethyl methacrylate (DEAEMA), 2-(di*iso*propylamino)ethyl methacrylate (DPAEMA), and 2-(*N*-morpholino)ethyl methacrylate (MEMA) can be polymerized via various methods (5–8). These polymers show good pH/temperature response in aqueous solution, which is useful for the design of drug-delivery systems and for modification of biomedical polymer surfaces (9,10). Armes and coworkers prepared a zwitterionic block copolymer comprising PDMAEMA and PMAA via group-transfer polymerization (GTP) of DMAEMA and 2-tetrahydropyranyl methacrylate (THPMA), and subsequent acid hydrolysis of 2-tetrahydropyranyl group, as shown in Fig. 2.1 (11). They found that the isoelectric points for the PDMAEMA-*b*-PMAA vary with block copolymer composition, with higher isoelectric point being obtained for the more DMAEMA-rich copolymers. Reversible aggregations of these AB block copolymers containing a DMAEMA hydrophobic core and ionized MAA hydrophilic corona were produced at pH 9.5 and 50°C. The aggregates have a large hydrodynamic diameter of ~400 nm (12).

Stuart et al. (13) reported similar DMAEMA-*b*-NaMAA diblock copolymers. Precursor diblock copolymers of DMAEMA-*b*-TBMA were synthesized by anionic polymerization, with subsequent acid hydrolysis of *tert*-butyl methacrylate (TBMA) residues. Patrickios and coworkers (14) have also synthesized the ABC, ACB, and BAC topological triblock isomers of DMAEMA, THPMA, and MMA via GTP. The THPMA residues were converted to MAA residues by mild acid hydrolysis, yielding the triblock polyampholytes. De Schryver and Jérôme et al. investigated the synthesis and aggregation behavior of a series of poly[(dimethylamino)alkyl methacrylate-*b*-sodium methacrylate] diblock copolymers (15). They focused on the influence of

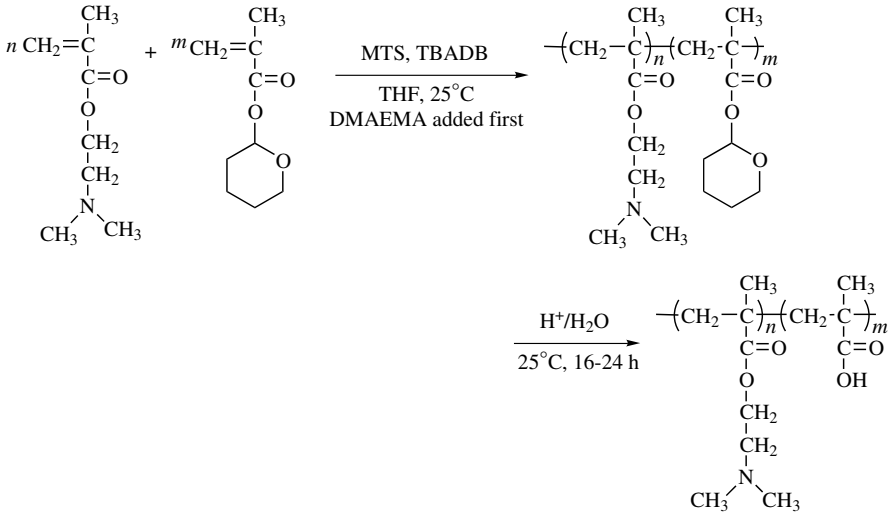

FIGURE 2.1 Reaction scheme for the synthesis of PDMAEMA-*b*-PMAA zwitterionic block copolymers via group-transfer polymerization (GTP) (11)

the relative composition of the block copolymers on the exchange process of block copolymer molecules between the micellar aggregates, and the possibilities for tuning the exchange rate by changing the composition or architecture of the block copolymer.

The preparation of block copolymer micelles in aqueous solution by adjusting the solution pH has been reported by several groups (5,16). Jérôme et al. synthesized a series of poly(2-vinylpyridine-*block*-PDMAEMA) diblock copolymers (P2VP-*b*-PDMAEMA). At low pH, loose aggregates are formed, although both the P2VP and PDMAEMA blocks are protonated. At intermediate pH, micelles are observed that consist of an uncharged hydrophobic P2VP core surrounded by a protonated PDMAEMA corona. At higher pH, the PDMAEMA corona is essentially uncharged and collapses at temperatures higher than 40°C, which results in unstable micelles (16).

The author and coworkers prepared DMAEMA homopolymer with different degrees of polymerization (4) and a series of di- or triblock copolymers or macromonomers containing PDMAEMA, for example, PDMAEMA-*b*-PPO-*b*-PDMAEMA (17), PDMAEMA-*b*-PMMA (18), PEO-*b*-PDMAEMA-*b*-POFPMA (2,2,3,3,4,4,5,5-octafluoropentyl methacrylate) (19), and the PDMAEMA-based macromonomer (20). These polymers have pH-responsive properties and micellization in acidic and neutral media.

In recent years, nonlinear amphiphilic copolymers containing DMAEMA segment with complex architectures such as star-block $(AB)_n$ (21–23), and hyperbranched star-block copolymers (24) have been synthesized and studied in selective solvents. An interesting feature of star-shaped block copolymers with a high number of arms and high hydrophilic content is that they can form unimolecular micelles as their architecture mimics a micellar structure (25). Liu et al. investigated the phase transition behavior of unimolecular dendritic three-layer nanostructures with dual

thermoresponsive coronas, which was prepared by a successive reversible addition–fragmentation transfer (RAFT) polymerizations of *N*-isopropylacrylamide (NIPAAm) and DMAEMA, using fractionated fourth-generation hyperbranched polyester (Bolton H40) based macroRAFT agent (21). The star-block copolymers exist as unimolcular core-shell-corona nanostructures with hydrophobic H40 as the core, swollen PNIPAAm as the inner shell, and swollen PDMAEMA as the corona. PNIPAAm and PDMAEMA homopolymers undergo phase transitions at their lower critical solution temperatures (LCST), which are found to be 32°C for PNIPAM and 40–50°C for PDMAEMA, respectively.

From the point view of the structure, multicompartment micelles have water-soluble shells for stabilizing nanoparticles, and multicompartment hydrophobic cores for accommodating two or more incompatible drugs simultaneously (24–27). In order to obtain the multicompartment micelles, our group designed and synthesized a kind of hyperbranched star-block copolymer (HP-*star*-PDMAEMA-*b*-POFPMA) via oxyanion-initiated polymerization process, using hydroxyl-terminated hyperbranched poly[3-ethyl-3-(hydroxylmethyl)oxetane] (HP) as a macroinitiator precursor with multireactive sites, as shown in Fig. 2.2 (24). Theoretically, the unimolecular micelle is composed of hyperbranched poly[3-ethyl-3-(hydroxymethyl) oxetane] as a core, and PDMAEMA-*block*-poly(2,2,3,3,4,4,5,5-octafluoropentyl methacrylate) (POFPMA) as the block arms. However, the multicompartment micelles and partial associated micelles with different morphologies, such as round in shape or long threadlike nanofiber, were obtained in acidic aqueous solution or in dimethylformamide (DMF)/water (pH 3.0) mixture, as shown in Fig. 2.3 (24).

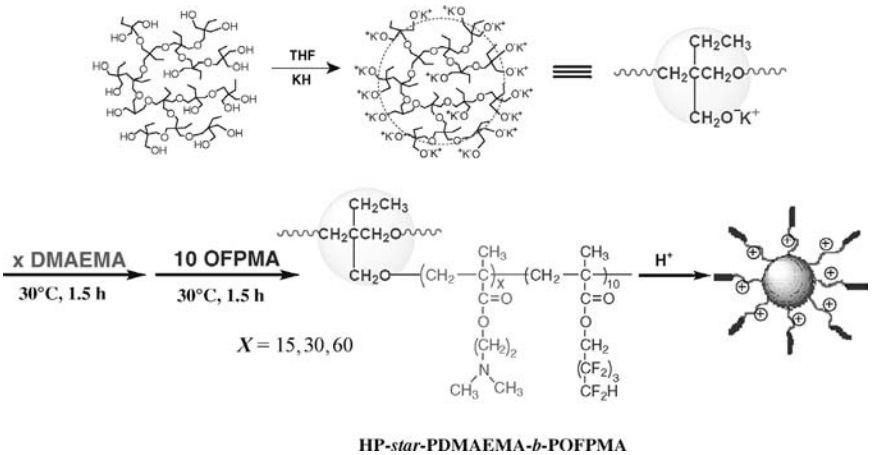

FIGURE 2.2 A representative reaction route for the preparation of the HP-*star*-PDMAEMA-*b*-POFPMA copolymers via oxyanion-initiated polymerization with a multireactive-site macroinitiator. The dimethylamino groups of PDMAEMA can be protonated in acidic medium. Reprinted with permission from Reference (24). Copyright 2007 American Chemical Society (24)

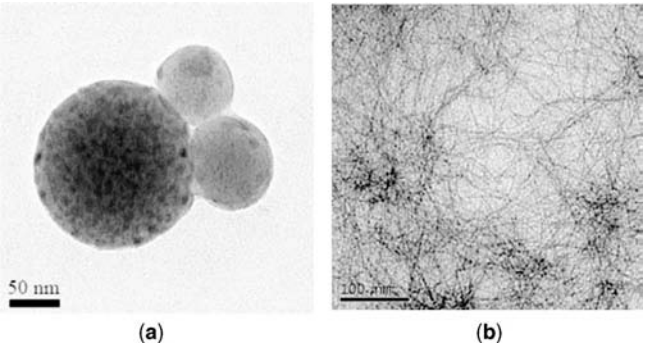

FIGURE 2.3 TEM images of (**a**) partial associated multicompartment micelles via self-assembly of HP-*star*-PDMAEMA$_{30}$-*b*-POFPMA$_{10}$ in aqueous solution (pH 3.0) and (**b**) the threadlike nanofibers self-assembled by HP-*star*-PDMAEMA$_{60}$-*b*-POFPMA$_{10}$ in dimethylformamide/water (pH 3.0) mixture ($v/v = 1:2$), bar = 100 nm. Reprinted with permission from Reference (24). Copyright 2007 American Chemical Society (24)

Poly[2-(diethylamino)ethyl methacrylate] (PDEAEMA or PDEA) is the higher hydrophobicity as compared to PDMAEMA at high pH. Both can be protonated at low pH, making their segment hydrophilic and biocompatibility and have the potential for drug-delivery applications. Armes and coworkers reported on the synthesis of poly[4-vinyl benzoic acid-*block*-2-(diethylamino)ethyl methacrylate] (PVBA-*b*-PDEA) (28). This diblock copolymer exhibits pH reversible micellization properties. Micelles with a hydrophobic VBA core and hydrophilic PDEA shell were produced at low pH, whereas PDEA formed the hydrophobic core with PVBA as the hydrophilic shell at high pH, as shown in Fig. 2.4.

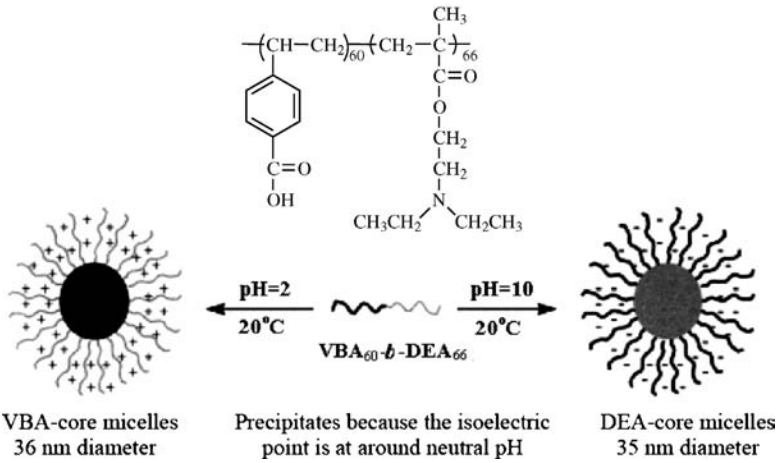

FIGURE 2.4 Chemical structure of VBA$_{60}$-*b*-DEA$_{66}$ diblock copolymer and its pH-induced "schizophrenic" micellization behavior in aqueous solution. Reprinted with permission from Reference (28). Copyright 2002 WILEY-VCH Verlag GmbH (28)

Subsequently, Tam and coworkers synthesized PMAA-*b*-PDEA via the atom transfer radical polymerization (ATRP) technique using protected group chemistry of *tert*-butyl methacrylate, followed by hydrolysis in acidic conditions (29). This copolymer system is believed to have the potential for drug-delivery applications because of the biocompatibility of PMAA and PDEA. PMAA is a weak acid ($pK_a = 5.4$), which can be ionized and becomes soluble at high pH, whereas PDEA is a weak base ($pK_a = 7.3$), which can be protonated at low pH and makes the block hydrophilic. Because both blocks have different pK_a values and different chain lengths, the hydrophile–lipophile balance (HLB) values of the block copolymer at high or low pH values are different.

Armes et al. reported on the reversible formation of block copolymer micelles using either methoxy-capped poly(ethylene glycol) (MePEO) or poly[2-(dimethylamino)ethyl methacrylate] (PDMA) as the hydrophilic block, combined with PDEA, poly(2-(di*iso*propylamino)ethyl methacrylate) (PDPAEMA or PDPA), or poly[(2-(*N*-morpholino)ethyl methacrylate] (PMEMA) as the hydrophobic block. In each case, micellization was fully reversible and depended on the solution pH, temperature, and/or salt concentration (30).

Shell cross-linked "knedel" (SCK) micelles are potentially useful nanosized vehicles for the delivery of various actives (e.g., drugs, fragrances, and pesticides) (31–34). The first example of SCK micelle was described by Wooley and coworkers, who oligomerized pendent styrene groups by using radical chemistry (31). Armes and coworkers prepared SCK micelles that consisted of PEO-*b*-PDMA-*b*-PMEMA, as shown in Fig.2 5. When a bifunctional cross-linker, 1,2-bis(2-iodoethoxy) ethane (BIEE), is added into the PEO-*b*-PDMA-*b*-PMEMA aqueous solution at 60°C, the PMEMA block is above its cloud point and forms the micelle core. On cooling to 20°C, the hydrophobic PMEMA micelle cores become hydrated. Thus, the cores of these SCK micelles can be reversibly hydrated or dehydrated, depending on the solution temperature (35).

The shell cross-linked (SCL) micelles with pH-responsive core were also reported by Liu and Armes et al. (36). The PEO-PDMA-PDEA triblock copolymers dissolved molecularly in aqueous solution at low pH; on addition of NaOH, micellization occurred at pH 7.1 to form three-layer "onionlike" micelles comprising PDEA cores, PDMA inner shells, and PEO coronas, as shown in Fig. 2.6. Above pH 7.3, dynamic

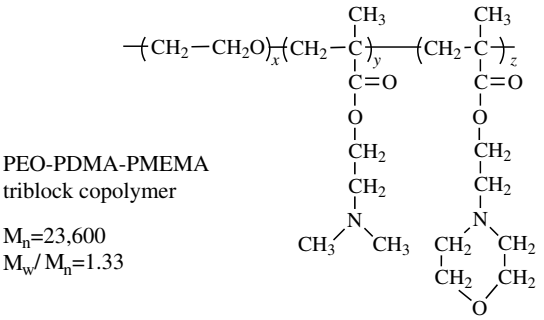

FIGURE 2.5 Chemical structure of PEO-*b*-PDMA-*b*-PMEMA triblock copolymer (35)

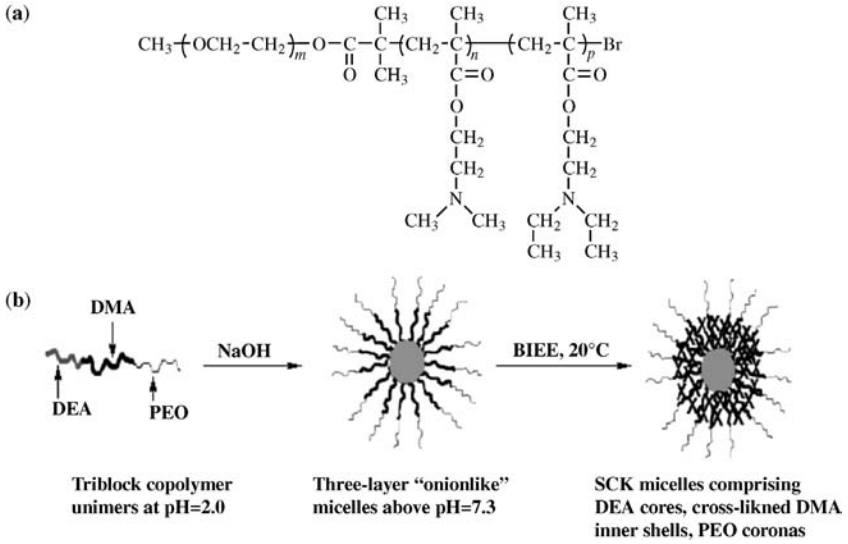

FIGURE 2.6 (**a**) Chemical structures of PEO-PDMA-PDEA triblock copolymers. (**b**) Schematic illustration of the formation of three-layer "onion" micelles and shell cross-linked micelles from PEO-PDMA-PDEA triblock copolymers. Reprinted with permission from Reference (36). Copyright 2002 American Chemical Society (36)

light scattering studies indicated unimodal, near-monodisperse populations, with mean micelle diameters of 27–84 nm. The PDEA cores of the SCL micelles with BIEE as a bifunctional cross-linker have tunable hydrophilicity depending on the solution pH. Reversible swelling is observed on lowering the solution pH from 9 to 2 due to protonation of the PDEA chains in the micelle core.

However, in view of its cost, toxicity, limited water solubility, and likely mutagenicity, BIEE is unlikely to be employed in commercial applications of SCL micelles, particularly in the biomedical field. Armes and coworkers explored the feasibility of synthesizing SCL micelles by using either an anionic sodium sodium 4-styrenesulfonate (NaStS) homopolymer or PEO_{113}-*b*-$NaStS_{34}$ diblock copolymer as an ionic cross-linker for a cationic PEO_{113}-*b*-[$QDMA_{33}$/DMA_5]-*b*-DEA_{54} triblock copolymer, in which the cationic charge density resides in the central quaternized DMAEMA (QDMA) block (37). The experimental results showed that excess diblock copolymer PEO_{113}-*b*-$NaStS_{34}$ is an efficient cross-linker for the formation of SCL micelles of PEO_{113}-*b*-[$QDMA_{33}$/DMA_5]-*b*-DEA_{54} triblock copolymer.

Considering that PEG-based block can form a permanently hydrophilic corona and the hydrophobic drug can enter into hydrophobic core, Billingham et al. investigated a series of novel micelle-forming ABC triblock copolymers MePEO-*b*-PDMA-*b*-PDEA to control the release of a hydrophobic drug, dipyridamole (DIP) (38). The drug dissolves in acid but is insoluble above pH 5.8, which was incorporated into the micelles by increasing the pH of an aqueous drug/copolymer mixture to 9. On adjusting the pH with base, micellization occurred at pH 8, with the water-insoluble, deprotonated PDEA block forming the hydrophobic cores, and the PMPEG and

PDMA blocks forming the hydrophilic micellar coronas and inner shells, respectively. The DIP-loaded MePEO-*b*-PDMA-*b*-PDEA micelles act as a drug carrier, giving slow release to the surrounding solution over a period of days. Such pH-induced micellization could be exploited for the triggered release of hydrophobic drugs in a low pH environment (e.g., in the gut or within a cell).

2.2.2 Self-Assembly of Block Copolymers having 2-Methacryloyloxyethyl Phosphorylcholine

For the purposes of drug-delivery vehicles, it is imperative that micelles have good blood compatibility and biocompatibility properties. Synthetic copolymers containing the phosphorylcholine (PC) have been shown excellent blood compatibility, that is, suppression of protein adsorption and platelet adhesion (39–42). Phosphorylcholine-based polymers mimic the surface of natural phospholipids membrane bilayers through the formation of a thermodynamic hydration barrier over the surface as a consequence of the highly hydrophilic nature of the phosphorylcholine head groups, which in turn inhibits surface biofouling (43). The leading works have been done by Ishihara's group (44,45), who found that 2-methacryloyloxyethyl phosphorylcholine (MPC) polymers effectively reduced protein adsorption and denaturation, and inhibited cell adhesion, even when the polymer was in contact with the whole blood in the absence of any anticoagulants (46). They grafted the water-soluble MPC polymer on PE sheet and studied on platelet function. The results showed that the modification with the PMPC on PE reduces the activation and adhesion and decreases the aggregation ability of platelets (47).

However, the limitation of the living polymerization of MPC is that such betaine monomers are normally insoluble in organic solvent (i.e., THF) typically used for conventional ionic living polymerizations, which is the traditional method for producing controlled-structure, near-monodisperse copolymers. Armes and co-workers first achieved the controlled homopolymerization of MPC via aqueous or methnolic ATRP (48,49). Subsequently, they synthesized various block copolymers containing MPC segment, including the incorporation of polyethers with MPC (e.g., PEO-MPC, PPO-MPC, and poly(dimethylsiloxane)-MPC diblock copolymers, with three macroinitiators), and the combination of MPC with tertiary amine methylacrylates (MPC-DMA, MPC-DEA, and MPC-DPA diblock copolymers, with the sequential monomer addition approach) (50). The chemical structures of these block copolymers are shown in Fig. 2.7, where the DMA, DEA, and DPA represent 2-(dimethylamino)ethyl methacrylate, 2-(diethylamino)ethyl methacrylate, and 2-(di*iso*propylamino)ethyl methacrylate, respectively.

The MPC-*b*-(tertiary amine methacrylate) diblock copolymers form well-defined, stimulus-responsive micelles in aqueous solution. Above pH 8, the MPC-DMA diblock copolymers also exhibited thermoresponsive behavior, forming DMA-core aggregates at elevated temperature. Spontaneous dissociation occurred on cooling to ambient temperature as the hydrophobic DMA block became hydrophilic again. The MPC-DMA, MPC-DEA, and MPC-DPA diblock copolymers proved to be pH-responsive polymeric surfactants at ambient temperature: molecular dissolution

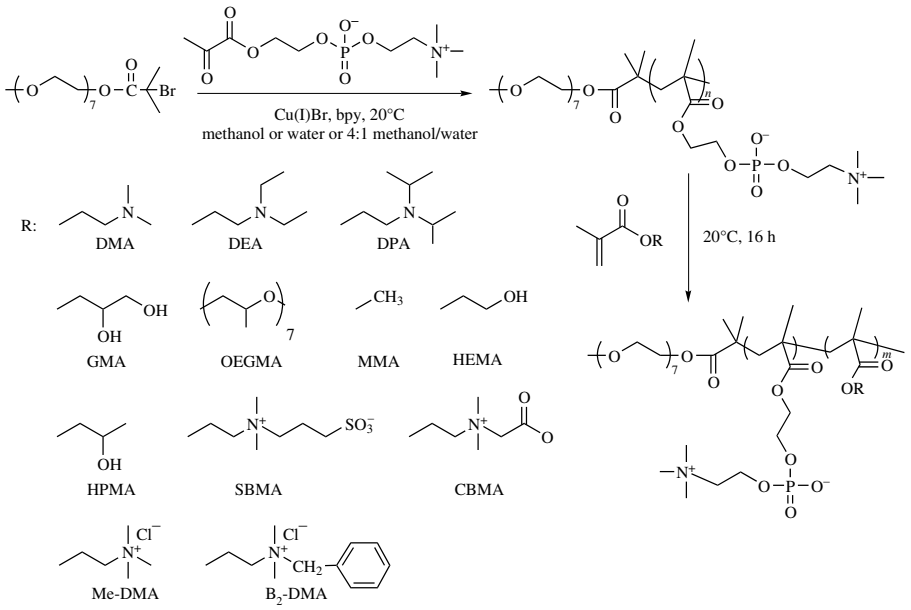

FIGURE 2.7 Reaction scheme for the block copolymerization of MPC via ATRP in protic media at 20°C using the sequential monomer addition route. Reprinted with permission from Reference (50). Copyright 2003 American Chemical Society (50)

occurred in dilute acidic solution with well-defined, near-monodisperse micelles being formed at around neutral pH. In each case, the MPC block formed the biocompatible micelle coronas, and the tertiary amine methacrylate block formed the hydrophobic micelle cores. In the case of the MPC-DPA diblock copolymer, the pyrene partition constant for the DPA-core micelles at pH 9 was similar to that reported previously for polystyrene-core micelles. These new MPC-based diblock copolymers are evaluated as new nonviral vectors for DNA condensation and "stealthy" nanocapsules for the delivery of hydrophobic drugs and also for the synthesis of biocompatible shell cross-linked micelles (50).

Using dipyridamole (DIP) as a model hydrophobic drug, the drug delivery of DPA-MPC-DPA and DEA-MPC-DEA gels with pH-responsive behavior was studied by Armes et al. (51). These triblock copolymers were prepared via ATRP, using a commercially available bifunctional ATRP initiator. Gelation occurs at around neutral pH, suitable for possible drug-delivery applications (52). Figure 2.8 shows the flower micelles at low and high polymer concentrations by DPA-MPC-DPA triblock copolymer.

Lloyd and coworkers further explored the MPC-DEA and MPC-DPA diblock copolymers as the novel biocompatible drug-delivery vehicles (53). They used Orange OT dye as a model hydrophobic compound to evaluate the drug loading capacities of these micelles and found that MPC-DEA micelles were not stable at physiological pH. In contrast, MPC-DPA diblock copolymers formed micelles of circa 30 nm diameter at physiological pH and had negligible cytotoxicities.

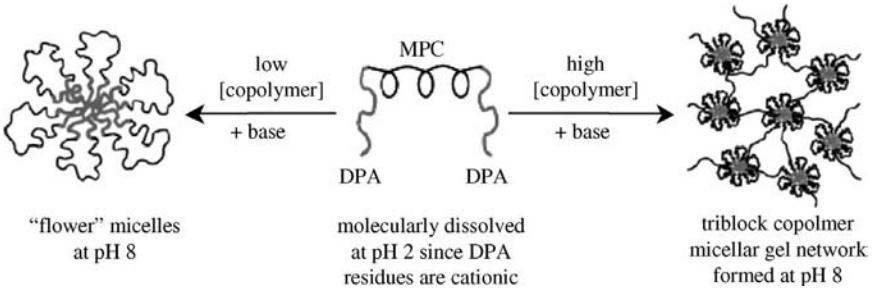

FIGURE 2.8 Schematic representation of the formation of the so-called "flower" micelles at low copolymer concentration and macroscopic gels at high copolymer concentration by DPA-MPC-DPA triblock copolymers. Reprinted with permission from Reference (51). Copyright 2003 American Chemical Society (51)

Double-hydrophilic and biocompatible diblock copolymers containing MPC can also stabilize superparamagentic magnetite noanoparticles. For example, poly[2-(methacryloyloxy)ethyl phosphorylcholine]-*block*-poly(glycerol monomethacrylate) ($PMPC_{30}$-$PGMA_{30}$) was prepared by Armes et al. via ATRP and evaluated for the synthesis of these magnetite sols (see Fig. 2.9) (54).

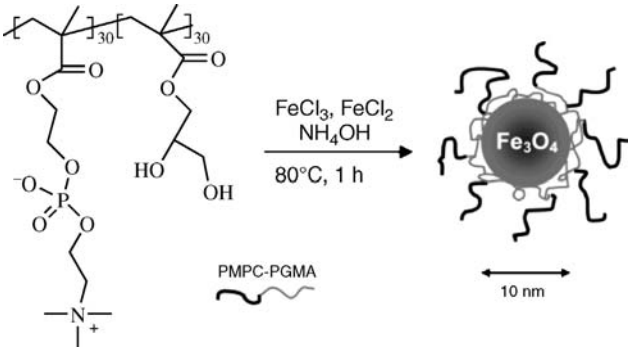

FIGURE 2.9 Schematic representation of the synthesis of sterically stabilized magnetite sols prepared using a $PMPC_{30}$-$PGMA_{30}$ diblock copolymer stabilizer. Reprinted with permission from Reference (54). Copyright 2006 American Chemical Society (54)

2.2.3 Self-Assembly of Folate-Functionalized Block Copolymers

In recent years, targeted gene and drug delivery via cellular receptors has emerged as a novel approach to enhance the efficacy of tumor-selective strategies (55). The receptor for folic acid (FA; vitamin M) is overexpressed by a number of human tumors, including cancer of the ovaries (56) (in over 90% of ovarian carcinoma), kidney, uterus, testis, brain, colon, lung, and myelocytic blood cells (57). When attached via its

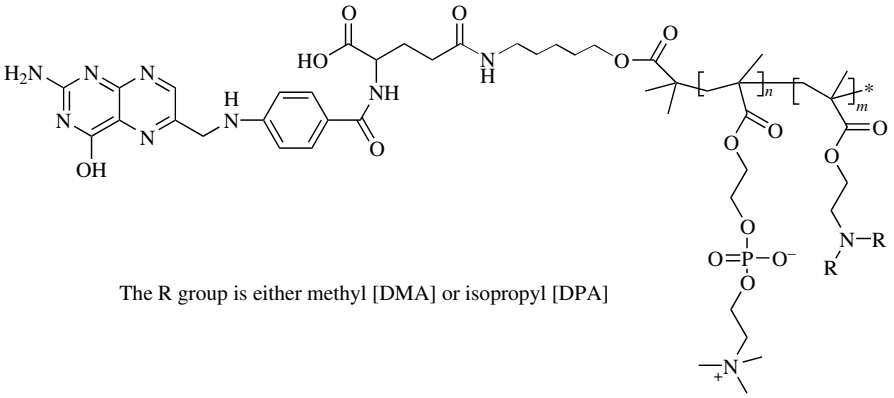

FIGURE 2.10 Chemical structures of the folate (FA)-functionalized biocompatible diblock copolymers. Reprinted with permission from Reference (60). Copyright 2005 American Chemical Society (60)

γ-carboxyl site, folate retains its normal receptor-binding affinity and can, therefore, enter receptor-decorated cells by endocytosis (58,59).

Licciardi et al. synthesized FA-functionalized biocompatible diblock copolymers based on 2-(methacryloyloxy)ethyl phosphorylcholine (MPC) and either 2-(dimethylamino)ethyl methacrylate (DMA) or 2-(di*iso*propylamino)ethyl methacrylate (DPA). The MPC-DMA and MPC-PDA diblock copolymers containing terminal primary amine groups were first prepared via ATRP, and then conjugated with FA (60). The chemical structures of the FA-MPC-DEA and FA-MPC-DPA diblock copolymers are as shown in Fig. 2.10. At pH 3, FA-MPC-DPA diblock copolymer could be molecularly dissolved in dilute acidic solution because the DPA block was protonated and therefore hydrophilic under these conditions, whereas the DPA residues were only partially protonated at pH 6. Under physiological conditions (pH 7.4), the deprotonated DPA block became fully dehydrated. ^{1}H NMR studies proved the formation of well-defined micelles with the uncharged DPA blocks forming the hydrophobic cores, the MPC blocks forming the hydrophilic coronas, and the terminal FA groups presumably being located on the micelle periphery. Thus, the FA-MPC-DPA copolymers have been evaluated as pH-responsive micellar vehicles for the delivery of highly hydrophobic anticancer drugs (61).

Poly(L-histidine) (polyHis) has multifunctionality to pH sensitivity (62), biodegradability, and fusogenic activity (63,64). Bae and coworkers investigated the polymeric micelles based on poly(L-histidine) (polyHis) as a potential pH-sensitive anticancer drug carrier (65). The micelles were composed of polyHis/PEG and poly(L-lactic acid) (PLLA)/PEG block copolymer with or without folate conjugation. The folate conjugation aimed at folate-receptor-mediated endocytosis. The introduction of folate into mixed micelles enhanced the cell killing effect by active internalization. The fusogenic activity of polyHis in endosomes facilitated cytosolic delivery of adriamycin (ADR) and explained the improved cytotoxicity of the micelles to tumor cells.

2.3 TEMPERATURE-RESPONSIVE BLOCK COPOLYMERS

Temperature-responsive polymers have received much attention because of their unique characteristics such as the presence of a critical solution temperature. Critical solution temperature is the temperature at which the phase of polymer and solution (or the other polymer) is discontinuously changed according to their composition. If the polymer solution (mostly water) has one phase below a specific temperature, which depends on the polymer concentration, and are phase separated above this temperature, the polymer generally has a lower critical solution temperature (LCST), the lowest temperature of the phase-separation curve on concentration–temperature diagram. Otherwise, it is called a higher critical solution temperature (HCST) or upper critical solution temperature (UCST). However, most applications are related to LCST-based polymer systems (1).

A new type of complex, switchable diblock polymers with double thermoresponsivity, *N*-isopropylacrylamide-*block*-3-[*N*-(3-methacrylamidopropyl)-*N*, *N*-dimethyl]ammoniopropane sulfonate (PNIPAm-*b*-PSPP), were first synthesized by Laschewsky and coworkers via RAFT polymerization (66,67). The typical chemical structure of PNIPAm-*b*-PSPP diblock copolymer is shown in Fig. 2.11. One of the block (PNIPAm) presents a LCST, whereas the other (PSPP) presents an UCST. Depending on the relative positions of the UCST and the LCST, such a design can result in polymers that are either associated at low and at high temperatures, but are insoluble at intermediate temperatures, or form colloidal aggregates at low and at high temperatures, while being dissolved at intermediate temperatures.

Unlike the report by Lanschewsky and coworkers, Armes and coworkers synthesized a series of methacrylate-based diblock copolymer, such as MEMA-DEA and DMA-MEMA, with near-monodisperse and in high yield via group transfer polymerization (GTP) (68,69). They referred to these block copolymers in aqueous solution as schizophrenic micellization. The DMA residues in the precursor of DMA-MEMA diblock copolymer was selectively quaternized using 1,3-propane sultone to yield sulfobetaine-based diblock copolymers SBMA-MEMA, as shown in Fig. 2.12. The diblock copolymers dissolved molecularly in water at 30–40°C. SBMA-core micelles were obtained below 20°C. In contrast, MEMA-core micelles were formed above 50°C (69).

Other thermoresponsive "schizophrenic" diblock copolymers reported in literature include (1) selectively betainized DMA-*b*-*N*, *N*-diethyl acrylamide (70) that forms A-core micelles below the lower consolute solution temperature (LCST) and B-core micelles above the consolute solution temperature (UCST); (2) PEO-PDEA-PHEMA

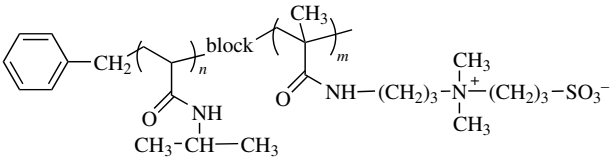

FIGURE 2.11 Chemical structure of PNIPAAm-*b*-PSPP diblock copolymer (66)

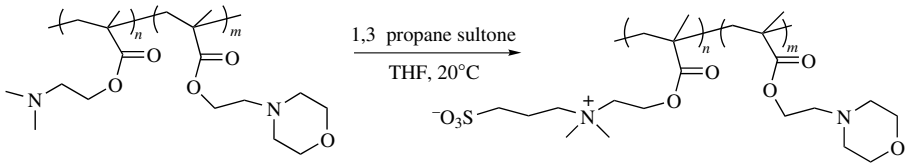

FIGURE 2.12 Selective quaternization of the GTP-synthesized DMA-*b*-MEMA diblock copolymers using 1,3-propane sultone under mild conditions to give the thermoresponsive SBMA-MEMA diblock copolymers. Reprinted with permission from Reference (69). Copyright 2002 The Royal Society of Chemistry (69)

triblock copolymer precursors and corresponding PEO-PDEA-PSEMA zwitterionic triblock copolymers converted by esterification of the hydroxyl groups on the HEMA block using succinic anhydride (71), and (3) PDEA-PDMA-PMEMA triblock copolymer synthesized by Bütün et al. very recently (72). More "schizophrenic" water-soluble block copolymers were reviewed by Armes et al. (73).

Polymers showing a sol-to-gel transition by temperature change have been proposed for an injectable drug-delivery depot (74). The sol-to-gel transition behavior of triblock PEO-PPO-PEO copolymers (Pluronics® or Poloxamers®) has been utilized for the delivery of labile drugs such as polypeptides and proteins because such drugs can be formulated in an aqueous solution (75). Although PEO_{100}-PPO_{65}-PEO_{100} (F127) has been reported to be the least toxic of the commercial available Pluronics, applications of Pluronics in drug delivery have disadvantage due to its nonbiodegradability *in vivo* (76,77), toxic side effect, and dissolution of the gel after administration (78). Kim and coworkers proposed that some biodegradable aliphatic polyesters, for example, poly(L-lactic acid) (PLLA), poly(DL-lactic acid) (PDLA), poly(lactic acid-*co*-glycolic acid) (PLGA), and poly(DLLA-*co*-ε-caprolactone (CL)), can be used as injectable drug delivery if they are connected with other pH/temperature responsive segment to form di- or triblock copolymers, such as PEO-PLLA (79), PEO-P(DLLA/CL) (79), PEO-PLLA-PEO (79), and PEO-PLGA-PEO (80). A novel star-shaped PLLA-*b*-PEO was synthesized by Kim (81).

2-Hydroxyethyl methacrylate (HEMA) copolymers exhibit excellent biocompatibility and good blood compatibility. Other biomedical applications for HEMA-based materials include an embedding substrate for the examination of cells using light microscopy and inert matrices for the slow release of drugs (82). Weaver et al. reported the synthesis of PEO-*b*-PHEMA-*b*-PDEAEMA block copolymers. Below 7°C, the HEMA block forms the hydrophilic inner shell of the micelle corona at pH 11. Above 7°C, the HEMA block forms the hydrophobic outer layer of the micelle core.

Poly(vinyl ether)s with side oxyethylene units and ω-alkyl groups obtained by living cationic polymerization were found to exhibit reversible and highly sensitive thermally induced phase-separation behavior (83) and are potential stimuli-responsive segments in a block copolymer (84). Also, the self-assembled structures of these block copolymers were evaluated using small angle neutron scattering (SANS) and

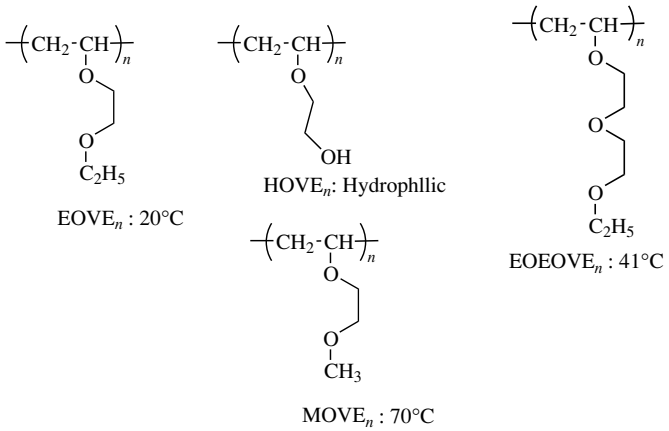

FIGURE 2.13 Chemical structures of various vinyl ether polymers and the phase-separation temperatures of the homopolymers. Reprinted with permission from Reference (87). Copyright 2004 Wiley Periodicals, Inc. (87)

dynamic light scattering (DLS) (85,86). Aoshima and coworker synthesized a series of poly(ethylene oxide)-based block copolymers having three thermosensitive and a hydrophilic (poly(HOVE)) segment, as shown in Fig. 2.13, where EOVE is 2-ethoxyethyl vinyl ether (denoted A), MOVE is 2-methoxethyl vinyl ether (denoted B) and EOEOVE is 2-(2-ethoxy)ethoxyethyl vinyl ether (denoted C) (87). They demonstrated that ABC triblock copolymers with multiple thermosensitive segments in a specific arrangement are effective for realizing multistage, stimuli-responsive self-assemblies. For example, an aqueous solution of EOVE$_{200}$-*b*-MOVE$_{200}$-*b*-EOEOVE$_{200}$ underwent multiple reversible transitions from sol (20°C) to micellization (20–41°C) to physical gelation (physical crosslinking, 41–64°C) and finally, to precipitation (64 °C).

Very recently, Sugihara and coworkers synthesized a series of random copolymers containing poly(4-hydroxybutyl vinyl ether) and 2-(vinyloxy)ethyl methacrylate,

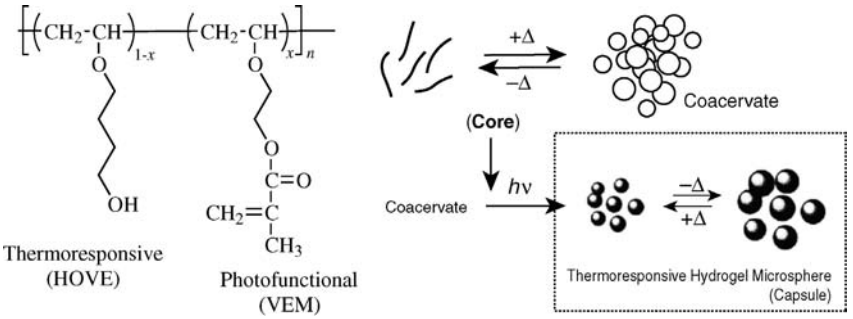

FIGURE 2.14 Synthesis of thermoresponsive hydrogel microspheres (capsules). Reprinted with permission from Reference (88). Copyright 2007 American Chemical Society (88)

that is poly(HOBVE$_{1-x}$-*ran*-VEM$_x$), and obtained thermoresponsive coacervate droplets (88). These initially formed coacervate droplets slightly above phase-separation temperature was cross-linked by UV irradiating in water, to form fine hydrogel microspheres, as shown in Fig. 2.14.

2.4 pH/TEMPERATURE/SALT MULTIRESPONSIVE BLOCK COPOLYMERS

Polymer systems that demonstrate a phase transition in response to more than one variable, in particular pH/temperature and salt, have been investigated (30,35). *N*-isopropylacrylamide was used as the temperature-sensitive component and ionic monomers such as (*N*, *N*-dimethylamino)ethyl methacrylate (DMAEMA) or acrylic acid (AA) were used as the pH-sensitive component (9,89). Yuk et al. reported on pH/temperature-sensitive polymer systems, such as poly[(DMAEMA)-*co*-acrylamide (AAm)] and poly[(DMAEMA)-*co*-ethylacrylamide (EAAm)]. For the latter, glucose-controlled insulin release can be achieved (90). As Armes et al. reported, poly [DMAEMA-*b*-methacrylic acid (PMAA)] was synthesized by group transfer polymerization (GTP) using 2-tetrahydropyranyl methacrylate (THPMA) as a protected monomer for the acid block. The PDMAEMA-*b*-PMAA zwitterionic copolymer can form micelles with PDMAEMA core and PMAA corona at 50°C in 0.01 M NaCl at pH 9.5 (12).

Nowakowska et al. reported a series of terpolymer copolymers of acrylic acid, *N*-isopropylacrylamide (NIPAM), and cinnamoyloxyethyl acrylate poly(AA-*co*-NIPAAm-*co*-CEA). The polymers were responsive to four stimuli: UV light, temperature, pH, and ionic strength (91). The chemical structure is as shown in Fig. 2.15.

In recent years, sulfonamide and sulfadimethoxine (SD) were found as efficient pH-sensitive groups in block copolymers for polymeric micelles (92) and injectable hydrogels (93–95). These groups show weak acidic nature, which is caused by readily ionizable hydrogen atom in amide bond (N^1-amide) in water. It has known that the extracellular pH of tumors is lower than that of normal tissues; pH value of about 7.0 in tumors and 7.4 in normal tissues (96,97). This small but clear difference in pH has been

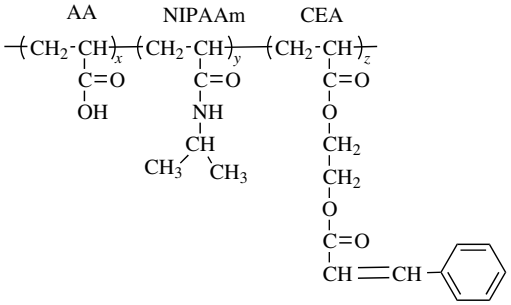

FIGURE 2.15 The chemical structure of poly(AA-*co*-NIPAAm-*co*-CEA) (91)

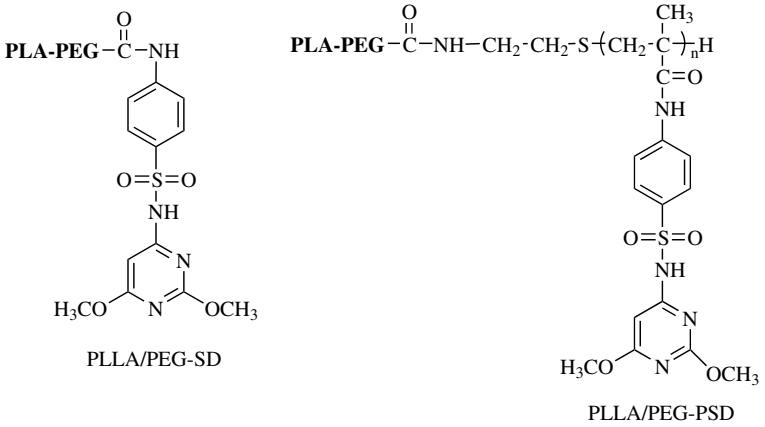

FIGURE 2.16 The chemical structures of PLLA/PEG-SD and PLLA/PEG-PSD (92)

an interesting subject for tumor targeting and various efforts has been devoted to construct pH-sensitive micelles or liposomes. The p*K*-values of polymers bearing carboxylic group range typically from 4 to 6, and their polymeric micelles have limitation in pH-based tumor targeting. Therefore, by introducing approximate sulfonamide groups to amphiphilic block copolymer, polymeric micelles responsive to physiological pH are expected. Bae et al. (92) introduced sulfadimethoxine [4-amino-*N*-(2,6-dimethoxy-4-pyrimidinyl) benzenesulfonamide] (SD; $pK_a = 6.2$) or its polymer (PSD) to the poly(ethylene glycol) (PEG) end of poly(L-lactide) (PLLA)/PEG diblock copolymer and investigated the pH-sensitive polymeric micelles thereof. The structures of PLLA/PEG-SD and PLLA/PEG-PSD are as shown in Fig. 2.16. The mean diameter of all polymeric micelles was smaller than 60 nm with a unimodal size distribution. The polymeric micelle prepared in this study sharply responded to the change in pH around the physiological pH.

Although the block copolymer hydrogels consisting of hydrophilic PEG and hydrophobic biodegradable polyesters, such as poly(D,L-lactic acid) (PDLLA), poly(D,L-lactic acid-*co*-glycolic acid) (PLGA), and poly(L-lactic acid) (PLLA) have been widely studied as controlled release drug carriers, they still have the disadvantage in their potential biomedical application when the heat transfer of the body tends to cause gels to form the needle, making them difficult to inject into the body. In order to overcome these problems, the temperature-sensitive block copolymers were modified by introducing a pH-sensitive moiety. For example, Lee and coworkers reported the incorporation of sulfonamide or sulfamethazine oligomer end groups with PEG-PCLA block copolymer to form OSM-PCLA-PEG-PCLA-OSM copolymer (94,95). This block copolymer solution showed a reversible sol-gel transition by a small pH change in the range of pH 7.4–8.0 and also by the temperature change in the region of body temperature.

A novel pentablock copolymer, OSM-PCLA-PEG-PCLA-OSM, was synthesized using Br-PCLA-PEG-PCLA-Br as a macroinitiator of atom transfer radical

polymerization (ATRP), in which sulfamethazine methacrylate monomer (SM) was used as a pH responsive moiety, and PCLA-PEG-PCLA was used as a biodegradable, as well as a temperature sensitive one, amphiphilic triblock copolymer (98). The block copolymer solution shows a sol-gel transition in response to a slight pH change in the range of 7.2–8.0.

The other multiresponsive copolymers consisted of "schizophrenic" diblock copolymers (73) or zwitterionic polymers (99) were summarized by Armes et al. and Lowe et al., respectively.

2.5 APPLICATIONS OF POLYMERIC MICELLES IN BIOTECHNOLOGY

Numerous studies on the application of polymeric micelles as drug carriers, bioreactors, diagnostic tools, and nonviral gene vectors have recently been reported (3,100). Polymer nanoparticles are widely used in the life science fields for separation technologies, histological studies, clinical diagnostic systems, and drug delivery (73). Here, we present a brief overview of recent trends and future perspectives on the applications of polymeric micelles comprising pH/temperature block copolymers in the field of bionanotechnology.

2.5.1 Drug Delivery of Anticancer Doxorubicin (DOX)

In aqueous solution, amphiphilic copolymers self-assemble in a core-shell structure that provides a loading space to accommodate mainly hydrophobic drugs. Additionally, the nanoscaled polymer micelles exhibit prolonged systemic circulation times and reduced uptake by the mononuclear phagocyte system. Anticancer drugs that are incorporated into micelles were shown to improve their stability and efficiency.

The first report on the effectiveness of a polymeric micelle system in cancer chemotherapy was PEG-poly(α,β-aspartic acid)-doxorubicin (an anticancer drug) conjugate (PEG-P(Asp)-DOX) by Kataoka et al. (101–103). The therapeutic effect on the solid tumors was attributed mainly to the physically entrapped DOX, which is considered to be stabilized in polymeric micelles through strong intermolecular interaction, mainly aromatic p-stacking with conjugated DOX moieties (104). Subsequently, they synthesized poly(ethylene glycol)–poly(amino acid) block copolymer and two derivers for the release of a water-insoluble anticancer drug, KRN 5500 (KRN), by physical entrapment utilizing hydrophobic interactions between this drug and the poly(amino acid) chain block (105). Recently, Kataoka et al. reported the design of polymeric micelles exhibiting environment-sensitive drug release (106). They synthesized PEG-poly(aspartate-hydrazone-adriamycin) block copolymer [PEG-P(Asp-Hyd-ADR)] (Fig. 2.17). It was confirmed that the micelles released DOX both in a time- and pH-dependent manner as the pH was decreased from 7.4 to 5.0. Further, the ADR release from the micelles inside cellular compartment was directly observed using confocal laser scanning microscopy. These results indicate

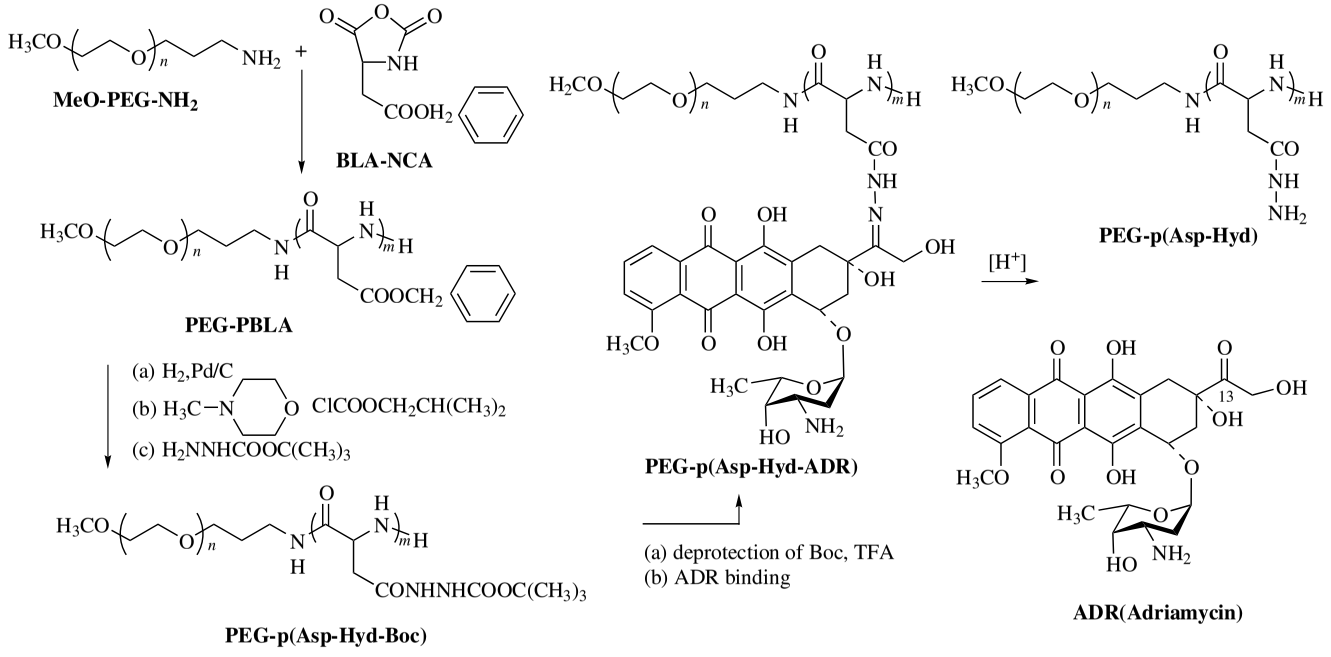

FIGURE 2.17 Synthesis of PEG-P(Asp-Hyd-ADR) block copolymer. The Schiff base formed between the C13 ketone of ADR and the hydrazide groups of the PEG–p(Asp–Hyd) block polymer are most effectively cleavable under acidic conditions around pH 5.0, which correspond to that of the lysosomes in the cells. Boc = tert-butoxycarbonyl, TFA = trifluoroacetic acid. Reprinted with permission from Reference (106). Copyright 2003 Wiley-VCH Verlag GmbH & Co. KGaA, Weinheim (106)

that such micellar systems have capacities as smart drug releasing devices responding to change in intracellular environment.

Okano et al. reported modulated release by temperature of adriamycin from thermoresponsive polymeric micelles composed of poly(*N*-isopropylacrylamide)/poly(butyl methacrylate) block copolymer (107). For the polymeric micelle system using PLA as the hydrophobic block, they achieved significant enhancements in drug release and cytotoxicity (108). However, the obtained drug release rate was too low for strong cytotoxic action (only 15% release in 6 days when the temperature exceeded the phase transition temperature). In recent report, they tried to use PLA or other biodegradable polyesters as hydrophobic block, for example, poly(ε-caprolactone) or poly(D,L-lactide-*co*-ε-caprolactone), to obtain an appropriate design of thermoresponsive polymeric micelles for both quick drug release and sharp thermoresponsiveness. These biodegradable polymeric micelles exhibited a quick thermoresponsive and drug release of the incorporated DOX (109).

Caliceti et al. proposed that poly(hydroxyethylaspartamide) (PHEA) derivatives bearing at the polyaminoacidic backbone poly(ethylene glycol) (2000 or 5000 Da) or both poly(ethylene glycol) and hexadecylalkylamine as pendant moieties can be used as new polymeric colloidal drug carriers (110), which is biodegradable, biocompatible, and multifunctional character. The macromolecular carrier can extend the drug permanence in the bloodstream and provide for slow drug release with great advantage in the drug delivery as compared to traditional formulations.

Bae (65,92,111) reported a series of pH/temperature-sensitive polymeric nanoparticles for doxorubicin release. The composition of a comb-type graft copolymer (PNDSP) included a thermosensitive cotelomer of *N*-isopropylacrylamide and *N*, *N*-dimethylacrylamide (MNDT, $M_n = 4600$, clouding temperature; 40°C), and a pH-sensitive sulfamethoxypyridazine telomere (MSPT, $M_n = 3600$, solubility transition; pH 7.4) (111). PNDSP can accelerate DOX release rate by the switching conditions. The results indicate that the drug release pattern by local tumor pH, hyperthermic condition, or both can be modulated by manipulating the nanoparticle forming condition.

Pluronic® block copolymers have been used extensively in a variety of pharmaceutical formulations including delivery of low molecular mass drugs, polypeptides, and the treatment of multidrug-resistant cancer (MDR) tumors (112). A system contains mixed micelles of L61 (0.25%) and F127 (2%) with an effective diameter of ca. 22 to 27 nm, which do not aggregate in the presence of the serum proteins. Prior to administration, doxorubicin is mixed with this system, resulting in the spontaneous incorporation of the drug into micelles, that is, new doxorubicin formulation (SP1049C) (113). Further mechanistic studies have revealed that SP1049C has higher activity than doxorubicin due to the following: (i) increase in the drug uptake; (ii) inhibition of the energy-dependent drug efflux, and (iii) changes in intracellular drug trafficking.

The experiments on *in vivo* tumor models have confirmed high efficacy of SP1049C against drug-resistant tumors, as well as suggested that this product has considerably broader efficacy than doxorubicin. The analysis of pharmacokinetics and biodistribution of SP1049C has shown that it accumulates in tumor tissue more effectively than

doxorubicin, while distribution of the formulation in normal tissues is similar to that of doxorubicin.

Hatton et al. reported the microgels based on Pluronic copolymers representing the most hydrophobic (L92) and relatively hydrophilic (F127) extremes of this class of block copolymers, grafted with light cross-linking poly(acrylic acid) (114). The former containing Pluronic L92 exhibited highly porous structure in the microgel, which affects the capacity of the microgels to absorb weakly basic anticancer drugs such as mitomycin, mitoxantrone, and doxorubicin.

Chilkoti and coworkers (115,116) have reported the use of two thermally responsive polymeric drug carriers, elastinlike polypeptide (ELP), and poly(NIPAAM-*co*-AAm), to target tumors. Their working hypothesis is that polymeric drug carriers that undergo a lower critical solution temperature (LCST) phase transition could be designed so they remain in solution *in vivo* after systemic injection, until they reach tumor that is locally heated above the LCST. The temperature of the LCST was chosen at 40°C, because this is higher than the physiological body temperature (37°C) but lower than 42°C, a temperature that is regularly used for hyperthermia treatments in cancer patients. Using rhodamine as a model compound, they examined the effects that an LCST transition had on the accumulation of polymer-bound drug in tumors that were locally heated.

Very interestingly, Yang et al. reported core/shell nanoparticles that display a pH-sensitive thermal responsive, self-assembled from the amphiphilic tercopolymer, poly(*N*-isopropylacrylamide-*co*-*N*,*N*-dimethylacrylamide-*co*-10-undecenoic acid) (P(NIPAAm-*co*-DMAAm-*co*-UA)), in which folic acid is conjugated to the hydrophilic segment of the polymer through the free amine group (for targeting cancer cells that overexpress folate receptors) and cholesterol is grafted to the hydrophobic segment of the polymer (Fig. 2.18) (117). This polymer also self-assembles into core/shell nanoparticles that exhibit pH-induced temperature sensitivity, but they possess a more stable hydrophobic core than the original polymer P(NIPAAm-*co*-DMAAm-*co*-UA) and a shell containing folate molecules. An anticancer drug, doxorubicin (DOX), is encapsulated into the nanoparticles. DOX release is also pH dependent.

Conventional pH-sensitive polymers work limitedly under acidic and alkaline conditions. Poly(2-ethyl-2-oxazoline) (PEOz) was used as a pH-sensitive functional polymer because of its low toxicity and favorable pK_a value near neutral pH (118). poly (L-lactic acid) (PLLA) is an extensively investigated biodegradable polymer in the field of drug delivery (65,119). Following intravenous administration, polymeric micelles are taken up to cells via endocytosis. The pH value of endocytic vesicles is gradually decreased from 7.4 to 5 because protons are pumped into endocytic vesicles (120). The content of flowerlike micelles based on poly(L-lactide)-*b*-poly(2-ethyl-2-oxazoline)-*b*-poly(L-lactide) (PLLA-PEOz-PLLA) can be protected in the hydrophobic inner core when they circulate in blood. The experiments on *in vitro* release have confirmed that the release of doxorubicin (DOX) from micelles was successfully inhibited at pH 7.4. In contrast, an accelerated release of DOX from micelles was observed at acidic conditions (121).

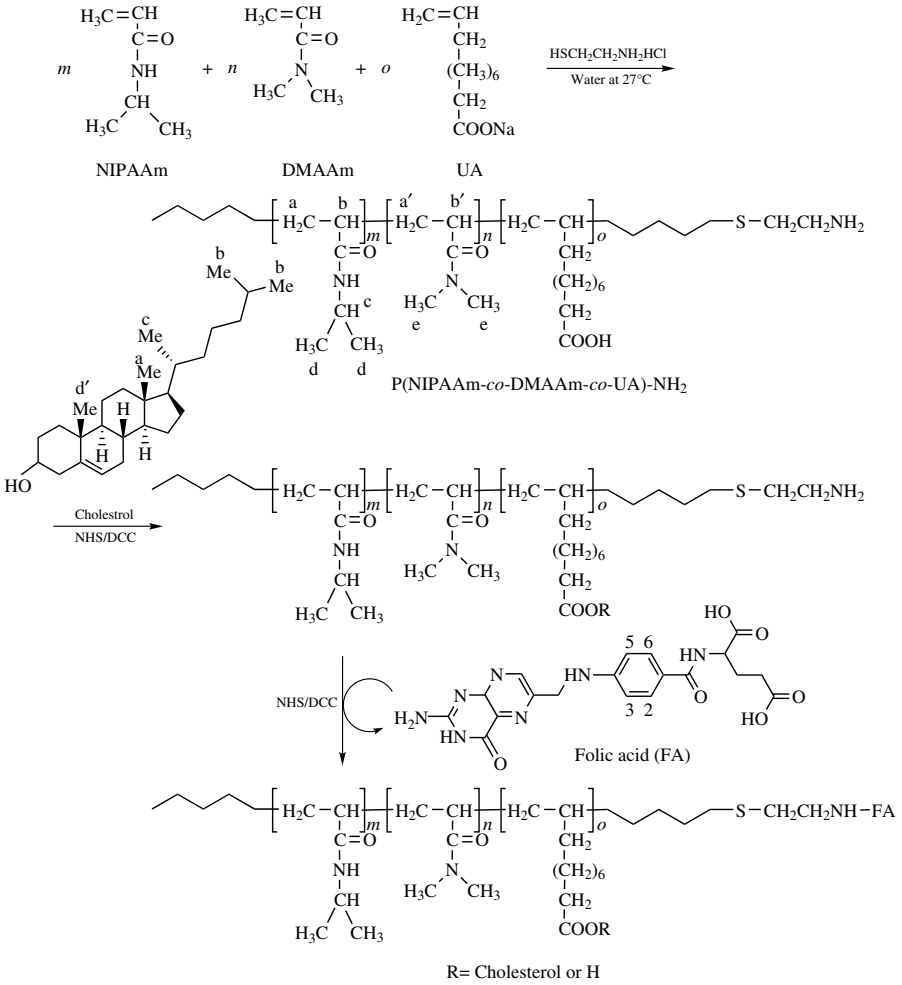

FIGURE 2.18 Synthesis of folate-conjugated P(NIPAAm-*co*-DMAAm-*co*-UA)-*g*-cholesterol. DCC: *N*,*N*′-dicyclohexylcarbodiimide. Reprinted with permission from Reference (117). Copyright 2007 Wiley-VCH Verlag GmbH & Co. KGaA, Weinheim (117)

2.5.2 Complex from Cationic Copolymer and Plasmid DNA System

Block copolymers with the oppositely charged polyelectrolyte segment, for example, PEG-*b*-poly(L-lysing) and PEG-*b*-poly(aspartic acid) (P(Asp)), spontaneously associate to form micelles with a core composed of the polyion complex of poly(L-lysine) and poly(aspartic acid) segments. The polyion complex (PIC) micelles opened the way to incorporate charged macromolecules of synthetic and biological origins including proteins and nucleic acids into the micelles (122,123).

Nucleic acid-based drugs have emerged as a potential new drug that can control the gene expression. In gene therapy, plasmid DNA is introduced into cells of patients to express the pharmaceutical proteins. On the contrary, an digonucleotide is used to suppress the expression of the disease causing genes in antisense therapy. The instability in biological fluids, the low cellular uptake efficiency due to the large molecular weight, and polyanionic nature of the nucleic acids make the applications of the gene delivery to be hindered. It has known that viral vectors are the most efficient gene delivery systems and most widely used in clinical trials. However, the use of viral vectors would bring the limitation of safety problems (122). Block copolymer micelles entrapping plasmid DNA and oligomucleotides have been developed as nonviral DNA delivery systems (123–125).

Langer et al. described a series of linear-dendritic hybrid polymers based on poly (ethylene glycol) (PEG) and poly(amidoamine) (PAMAM) dendrimers, which also contain a targeting moiety for a cell surface receptor (126). These hybrid polymers self-assemble together with DNA to nanoparticles of around 200 nm diameter, which have a PEGylated outer shell bearing cell surface receptor targeting moieties (Fig. 2.19). The results demonstrate a certain relationship between transfection efficiency and size and polymer architecture. This indicates that there is potentially a multitude of factors responsible for an efficient cellular uptake with low toxicity. Moreover, through the presentation of an outer shell of targeting ligands, these particles can transfect cells bearing targeted surface receptors with low toxicities and efficiencies that exceed the best commercially available polymer poly(ethylenimine) (PEI).

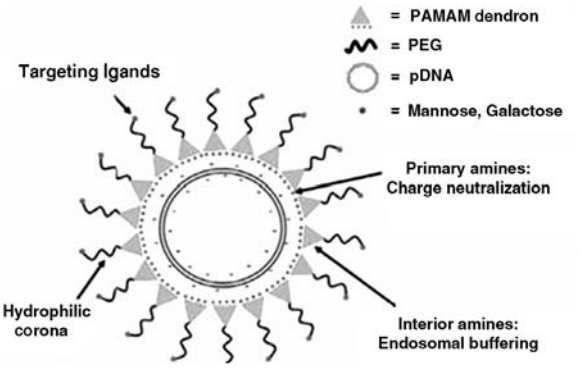

FIGURE 2.19 Self-assembly of PAMAM-PEG-mannose (G3.0 system) dendritic-linear hybrid polymer with mannose targeting moiety; the system contains primary amines buffering ($pK_a = 6.9$) for complexation of plasmid DNA and tertiary amines ($pK_a = 3.9$) for endosomal buffering, PEG stabilises the polyplex. Reprinted with permission from Reference 126. Copyright 2005 Wiley-VCH Verlag GmbH & Co. KGaA, Weinheim (126)

2.5.3 Applications of Polymer Gels in Microsystems

Flow control in microfluidic devices is critical to the development of microdevices for biochemical analysis or as chemical reactors. Such systems allow one to reduce the

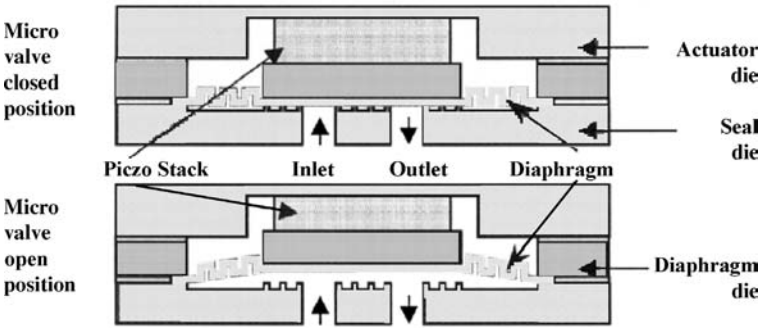

FIGURE 2.20 Microvalve cross sections. Reprinted with permission from Reference 129. Copyright 2000 Elsevier Science S.A (129)

amount of sample and chemical consumables required during operation, increase sensitivity and speed of analysis, offer portability, and potentially mean reduced manufacturing costs through high volume production and batch fabrication.

Over the past few years, a range of strategies and designs for microvalves has been explored. These include active microvalves actuated via electrostatic, piezoelectric, thermopneumatic, and electromagnetic means, as well as passive microcheck valves (127–130). Figure 2.20 shows a typical scheme of microvalve cross sections (129). As described by Chakraborty et al., the valve begins as three separate parts: the seat, the diaphragm, and the actuator. The base of the valve is known as the seat. This is the part that will interface with the rest of the microfluidic system. The seat contains the inlet and the outlet, as well as a set of seal rings around each opening inside the device. The center section of the valve is known as the diaphragm wafer. It has a circular corrugated diaphragm, with a circular boss in the center, covering both openings in the seat. The boss is either fully suspended by the diaphragm, or is also supported by four silicon bridges. Finally, the actuator consists of a piezoelectric disk in a rigid housing. All three parts are bonded together using a gold-to-gold thermo-compression bond (129).

Microvalve is an important component in many microfluidic systems or micro total analysis systems (microTAS). Some interesting active microvalves include hydrogel valves (131,132) and a pneumatically actuated poly(dimethylsiloxane) (PDMS) valve (133,134). The former used a pH-sensitive hydrogel as an actuator. Stimuli-responsive hydrogels have a significant advantage over conventional microfluidic actuators owing to their ability to undergo abrupt volume changes in response to the surrounding environment without the requirement of an external power source. Materials that undergo a significant volume change in response to temperature, pH, or an electric field can be used as actuators. These materials hold particular promise for use in microdevices, since the small characteristic lengths of the devices insure that the propagation time for the stimulating field—including thermal and concentration fields—will be short and thus relatively rapid response times may be achieved.

Fréchet and coworkers (135,136) grafted a temperature-sensitive polymer, poly(*N*-isopropylacrylamide), to the pore surfaces of a porous polymer monolith in a microchannel. The rapid and reversible swelling and collapse of the grafted polymer

chains as the temperature was cycled through the lower critical solution temperature was then used to open and close the channel to flow. Beebe and coworkers subsequently created hydrogel-based microvalves from pH-sensitive hydrogels that have been prepared by copolymerization of acrylic acid, 2-hydroxyethyl methacrylate, and ethylene dimethacrylate. These hydrogels respond to changes in the pH of the contacting stream (131,132,137): hydrogel actuators of varying designs were fabricated in microdevices and changes in pH caused the gel to swell or shrink as the solvent diffuses into or out of the cross-linked polymer network. Mastrangelo et al. (138,139) have used the high volumetric expansion of a sealed reservoir of paraffin upon heating to effect actuation and valving. This latter approach has the advantage that it can be used in nonaqueous environments.

For blood analyses, blood must be sampled frequently, particularly if the patient has a serious case of diabetes. To minimize the patient's physical and psychological burden, a miniaturized blood analysis system that imitates a mosquito has been a longstanding dream in clinical medicine and remains a challenge even now (140). Polymer gels are very promising for the realization of devices, which function autonomously in response to physical or chemical stimuli. Because they can also be used as basic building blocks in constructing very inexpensive devices, Suzuki et al. have used polymer gels to construct microactuators for use in measuring glucose concentrations (140).

Muller et al. used water-soluble, symmetric triblock copolymers of poly(ethylene oxide)$_x$-poly(proplyene oxide)-poly(ethylene oxide)$_x$ (PEO-PPO-PEO) to control flow manipulation in microfluidic systems (141). A schematic illustrating such a valve is shown in Fig. 2.21. The thermally responsive polymer is dissolved in the entire

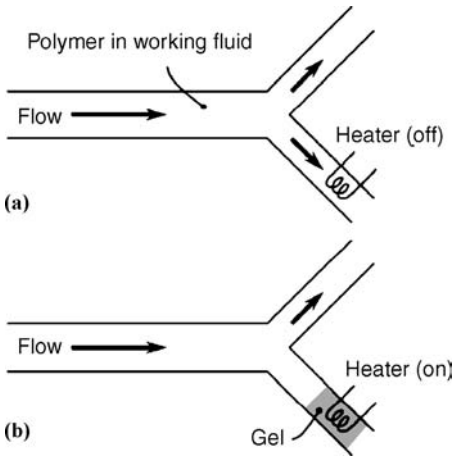

FIGURE 2.21 Microvalve using heat-induced gel formation of a thermally responsive triblock copolymer solution. (**a**) When the heater is off, the working fluid containing the polymer flows from the main channel into both downstream branches. (**b**) Upon activation of the heater, the polymer solution gels at the heater and flow into the lower branch stops. Reprinted with permission from Reference (141). Copyright 2005 IEEE (141)

working fluid. An integrated heater is recessed in one of the channel walls. When the heater is off, the working fluid flows from the main channel into both downstream branches as shown in Fig. 2.21a. On activation of the heater, the polymer solution gels at the heater and flow into the lower branch stops [see Fig. 2.21b].

The unique properties of these biocompatible materials—in particular this reversible gelation, which can occur near physiological temperatures and the accompanying dramatic change in properties—have led to their proposed use in a range of applications from electrophoresis to injectable drug-delivery systems.

2.6 SUMMARY

This chapter aims to demonstrate that nanoparticles can be obtained by the self-assembly of pH/temperature-responsive, amphiphilic block copolymers. They have many biotechnology applications in pharmaceutics, drug delivery, microfluid analysis, and so on. Nanoparticles designed in various ways have been widely investigated for application to cancer therapy and diagnosis. In all cases, nanoparticle targeting in the body is the most critical requirement for achieving excellent outcome. Various micelles, vehicles, and microgels, which are formed from the pH/temperature-responsive amphiphilic block copolymers mentioned in this chapter, will be benefit for the development of bionanotechnology.

ACKNOWLEDGMENT

The author gratefully acknowledges the financial support from the National Natural Science Foundation of China (20474041), the Key Laboratory of Molecular Engineering of Polymers, Ministry of Education of China, Fudan University, and the Natural Science Foundation of Educational Department of Jiangsu Province (03KJD150188).

REFERENCES

1. Gil ES, Hudson SM. Stimuli-responsive polymers and their bioconjugates. Prog Polym Sci 2004;29:1173–1222.
2. Jeong B, Gutowska, A. Lessons from nature: stimuli-responsive polymers and their biomedical applications. Trends Biotechnol 2002;20:305–311.
3. Harada A, Kataoka K. Supramolecular assemblies of block copolymers in aqueous media as nanocontainers relevant to biological applications. Prog Polym Sci 2006;31:949–982.
4. Liu QQ, Yu ZQ, Ni PH. Micellization and applications of narrow-distribution poly[2-(dimethylamino)ethyl methacrylate]. Colloid Polym Sci 2004;282:387–393.
5. Vamvakaki M, Billingham NC, Armes SP. Synthesis of controlled structure water-soluble diblock copolymers via oxyanionic polymerization. Macromolecules 1999;32: 2088–2090.

6. Zeng FQ, Shen YQ, Zhu SP, Pelton R. Synthesis and characterization of comb-branched polyelectrolytes. 1. Preparation of cationic macromonomer of 2-(dimethylamino)ethyl methacrylate by atom transfer radical polymerization. Macromolecule 2000;33: 1628–1635.
7. Lee SB, Russell AJ, Matyjaszewski, K. ATRP synthesis of amphiphilic random, gradient, and block copolymers of 2-(dimethylamino)ethyl methacrylate and *n*-butyl methacrylate in aqueous media. Biomacromolecules 2003;4:1386–1393.
8. Fournier D, Hoogenboom R, Thijs HML, Paulus RM, Schubert US. Tunable pH- and temperature-sensitive copolymer libraries by reversible addition-fragmentation chain transfer copolymerizations of methacrylates. Macromolecules 2007;40:915–920.
9. Hinrichs WLJ, Schuurmans-Nieuwenbroek NME, van de Wetering P, Hennink W.E. Thermosensitive polymers as carriers for DNA delivery. J Control Release 1999;60: 249–259.
10. Yang JM, Jong YJ, Hsu KY. Preparation and properties of SBS-g-DMAEMA copolymer membrane by ultraviolet radiation. J Biomed Mater Res 1997;35:175–180.
11. Lowe AB, Billingham NC, Armes SP. Synthesis and aqueous solution properties of novel zwitterionic block copolymers. Chem Commun 1997;11:1035–1036.
12. Lowe AB, Billingham NC, Armes SP. Synthesis and characterization of zwitterionic block copolymers, Macromolecules 1998;31:5991–5998.
13. Goloub T, de Keizer A, Cohen Stuart MA. Association behavior of ampholytic diblock copolymers. Macromolecules 1999;32:8441–8446.
14. Patrickios CS, Lowe AB, Armes SP, Billingham NC. ABC triblock polymethacrylates: Group transfer polymerization synthesis of the ABC, ACB, and BAC topological isomers and solution characterization. J Polym Sci Part A: Polym Sci 1998;36:617–631.
15. Creutz S, van Stam J, De Schryver FC, Jérôme R. Dynamics of poly((dimethylamino) alkyl methacrylate-*block*-sodium methacrylate) micelles. Influence of hydrophobicity and molecular architecture on the exchange rate of copolymer molecules. Macromolecules 1998;31:681–689.
16. Gohy JF, Antoun S, Jérôme R. pH-Dependent micellization of poly(2-vinylpyridine)-*block*-poly((dimethylamino)ethyl methacrylate) diblock copolymers. Macromolecule 2001;34:7435–7440.
17. Ni PH, Pan QS, Zha LS, Wang CC, Elaïssari A, Fu SK. Syntheses and characterizations of poly[2-(dimethylamino)ethyl methacrylate]-poly(propylene oxide)-poly[2-(dimethylamino)ethyl methacrylate] ABA triblock copolymers. J Polym Sci Part A: Polym Chem 2002;40:624–631.
18. Zhao Q, Ni PH. Synthesis of well-defined and near narrow-distribution diblock copolymers comprising PMMA and PDMAEMA via oxyanion-initiated polymerization. Polymer, 2005;46:3141–3148.
19. Xu J, Ni PH, Mao J. Synthesis and characterization of a novel triblock copolymers containing double-hydrophilic blocks and poly(fluoroalkyl methacrylate) block via oxyanion-initiated polymerization. e-Polymers 2006; no. 015:1–14.
20. Ni PH, Zhang MZ, Ma LH, Fu SK. Poly(dimethylamino)ethyl methacrylate for use as a surfactant in the miniemulsion polymerization of styrene. Langmuir 2006;22: 6016–6023.
21. Xu J, Luo SZ, Shi WF, Liu SY. Two-stage collapse of unimolecular micelles with double thermoresponsive coronas. Langmuir 2006;22:989–997.

22. Hong HY, Mai YY, Zhou YF, Yan DY, Cui Jun. Self-assembly of large multimolecular micelles from hyperbranched star copolymers. Macromol Rapid Commun 2007; 28:591–596.
23. Triftaridou AI, Vamvakaki M, Patrickios CS, Stavrouli N, Tsitsilianis C. Synthesis of amphiphilic $(ABC)_n$ multiarm star triblock terpolymers. Macromolecules 2005;38:1021–1024.
24. Mao J, Ni PH, Mai YY, Yan DY. Multicompartment micelles from hyperbranched star-block copolymers containing polycations and fluoropolymer segment. Langmuir 2007;23:5127–5134.
25. Stavrouli N, Triftaridou AI, Patrickios CS, Tsitsilianis C. Multi-compartment unimolecular micelles from $(ABC)_n$ multi-arm star triblock terpolymers. Macromol Rapid Commun 2007;28:560–566.
26. Li ZB, Kesselman E, Talmon Y, Hillmyer MA, Lodge TP. Multicompartment micelles from ABC miktoarm stars in water. Science 2004;306:98–101.
27. Kubowicz S, Baussard J-F., Lutz J-F., Thünemann AF, von Berlepsch H, Laschewsky A. Multicompartment micelles formed by self-assembly of linear ABC triblock copolymers in aqueous medium. Angew Chem, Int Ed 2005;44:5262–5265.
28. Liu SY, Armes SP. Polymeric Surfactants for the New Millennium: A pH-responsive, zwitterionic, schizophrenic diblock copolymer. Angew Chem, Int Ed 2002;41:1413–1416.
29. Dai S, Ravi P, Tam KC, Mao BW, Gan LH. Novel pH-responsive amphiphilic diblock copolymers with reversible micellization properties. Langmuir 2003;19:5175–5177.
30. Bütün V, Armes SP, Billingham NC. Synthesis and aqueous solution properties of near-monodisperse tertiary amine methacrylate homopolymers and diblock copolymers. Polymer 2001;42:5993–6008.
31. Thurmond KB, Kowalewski T, Wooley KL. Water-soluble knedel-like structures: The preparation of shell-cross-linked small particles. J Am Chem Soc 1996;118:7239–7240.
32. Huang HY, Kowalewski T, Remsen EE, Gertzmann R, Wooley KL. Hydrogel-coated glassy nanospheres: A novel method for the synthesis of shell cross-linked knedels. J Am Chem Soc 1997;119:11653–11659.
33. Huang HY, Remsen EE, Kowalewski T, Wooley KL. Nanocages derived from shell cross-linked micelle templates. J Am Chem Soc 1999;121:3805–3806.
34. Zhang Q, Remsen EE, Wooley KL. Shell cross-linked nanoparticles containing hydrolytically degradable, crystalline core domains. J Am Chem Soc 2000;122:3642–3651.
35. Bütün V, Wang XS, de Paz Bánez MV, Robinson KL, Billingham NC, Armes SP, Tuzar Z. Synthesis of shell cross-linked micelles at high solids in aqueous media. Macromolecule 2000;33:1–3.
36. Liu SY, Weaver JVM, Tang YQ, Billingham NC, Armes SP. Synthesis of shell cross-linked micelles with pH-responsive cores using ABC triblock copolymers. Macromolecule 2002;35:6121–6131.
37. Weaver JVM, Tang YQ, Liu SY, Iddon PD, Grigg R, Billingham NC, Armes SP, Hunter R, Rannard SP. Preparation of shell cross-linked micelles by polyelectrolyte complexation. Angew Chem, Int Ed 2004;43:1389–1392.
38. Tang YQ, Liu SY, Armes SP, Billingham NC. Solubilization and controlled release of a hydrophobic drug using novel micelle-forming ABC triblock copolymers. Biomacromolecule 2003;4:1636–1645.

39. Ishihara K, Oshida H, Endo Y, Ueda T, Watanabe A, Nakabayashi N. Hemocompatibility of human whole blood on polymers with a phospholipid polar group and its mechanism. J Biomed Mater Res 1992;26:1543–1552.
40. Nakaya T, Li YJ. Phospholipid polymers. Prog Polym Sci 1999;24:143–181.
41. Lloyd AW, Dropcova S, Faragher RGA, Gard PR, Hanlon GW, Mikhalovsky SV, Olliff CJ, Denyer E, Letko E, Filipec M. The development of *in vitro* biocompatibility tests for the evaluation of intraocular biomaterials, J Mater Sci: Mater Med 1999;10:621–627.
42. Lewis A.L, Cumming ZL, Goreish HH, Kirkwood LC, Tolhurst LA, Stratford PW. Crosslinkable coating from phosphorylcholine-based polymers. Biomaterials 2001;22: 99–111.
43. Lewis AL. Phosphorylcholine-based polymers and their use in the prevention of biofouling. Colloids Surf, B Biointerfaces 2000;18:261–275.
44. Konno T, Kurita K, Iwasaki Y, Nakabayashi N, Ishihara, K. Preparation of nanoparticles composed with bioinspired 2-methacryloyloxyethyl phosphorylcholine polymer. Biomaterials 2001;22:1883–1889.
45. Uchida T, Furuzono T, Ishihara K, Nakabayashi N, Akashi M. Graft copolymers having hydrophobic backbone and hydrophilic branches. XXX. Preparation of polystyrene-core nanospheres having a poly(2-methacryloyloxyethyl phosphorylcholine) corona. J Polym Sci, Part A: Polym Chem 2000;38:3052–3058.
46. Ishihara K, Nomura H, Mihara T, Kurita K, Iwasaki Y, Nakabayashi N. Why do phospholipid polymers reduce protein adsorption? J Biomed Mater Res 1998;39:323–330.
47. Iwasaki Y, Nakabayashi N, Ishihara K. Preservation of platelet function on 2-methacryloyloxyethyl phosphorylcholine–graft polymer as compared to various water-soluble graft polymers. J Biomed Mater Res 2001;57:72–78.
48. Lobb EJ, Ma I, Billingham NC, Armes SP, Lewis AL. Facile Synthesis of well-defined, biocompatible phosphorylcholine-based methacrylate copolymers via atom transfer radical polymerization at 20°C. J Am Chem Soc 2001;123:7913–7914.
49. Ma IY, Lobb EJ, Billingham NC, Armes SP, Lewis AL, Lloyd AW, Salvage J. Synthesis of biocompatible polymers. 1. Homopolymerization of 2-methacryloyloxyethyl phosphorylcholine via ATRP in protic solvents: An optimization study. Macromolecules 2002;35:9306.
50. Ma YH, Tang YQ, Billingham NC, Armes SP, Lewis AL, Lloyd AW, Salvage JP. Well-defined biocompatible block copolymers via Atom transfer radical polymerization of 2-methacryloyloxyethyl phosphorylcholine in protic media. Macromolecules 2003; 36:3475–3484.
51. Ma YH, Tang YQ, Billingham NC, Armes SP, Lewis AL. Synthesis of biocompatible, stimuli-responsive, physical gels based on ABA triblock copolymers. Biomacromolecules 2003;4:864–868.
52. Castelletto V, Hamley IW, Ma YH, Bories-Azeau X, Armes SP, Lewis AL. Microstructure and physical properties of a pH-responsive gel based on a novel biocompatible ABA-type triblock copolymer. Langmuir 2004;20:4306–4309.
53. Salvage JP, Rose SF, Phillips GJ, Hanlon GW, Lloyd AW, Ma IY, Armes SP, Billingham NC, Lewis AL. Novel biocompatible phosphorylcholine-based self-assembled nanoparticles for drug delivery. J Control Release 2005;104:259–270.

54. Yuan JJ, Armes SP, Takabayashi Y, Prassides K, Leite CAP, Galembeck F, Lewis AL. Synthesis of biocompatible poly[2-(methacryloyloxy)ethyl phosphorylcholine]-coated magnetite nanoparticles. Langmuir 2006;22:10989–10993.
55. Meyer F, Finer M. Gene therapy: progress and challenges. Cell Mol Biol 2001;47:1277–1294.
56. Campbell IG, Jones TA, Foulkes WD, Trowsdale J. Folate-binding protein is a marker for ovarian cancer. Cancer Res 1991;51:5329–5338.
57. Weitman SD, Lark RH, Coney LR, Fort DW, Frasca V, Zurawski VRJr, Kamen BA. Distribution of the folate receptor GP38 in normal and malignant cell lines and tissues. Cancer Res 1992;52:3396–3401.
58. Lee RJ, Low PS. Delivery of liposomes into cultured KB cells via folate receptor-mediated endocytosis. J Biol Chem 1994;269:3198–3204.
59. Dauty E, Remy JS, Zuber G, Behr JP. Intracellular delivery of nanometric DNA particles via the folate receptor. Bioconjug Chem 2002;13:831–839.
60. Licciardi M, Tang Y, Billingham NC, Armes SP, Lewis AL. Synthesis of novel folic acid-functionalized biocompatible block copolymers by atom transfer radical polymerization for gene delivery and encapsulation of hydrophobic drugs. Biomacromolecules 2005;6:1085–1096.
61. Licciardi M, Giammona G, Du JZ, Armes SP, Tang YQ, Lewis AL. New folate-fuctionalized biocompatible block copolymer micelles as potential anti-cancer drug delivery systems. Polymer 2006;47:2946–2955.
62. Patchornik A, Berger A, Katchalski E. Poly-L-histidine. J Am Chem Soc 1957;79:5227–5230.
63. Benns JM, Choi JS, Mahato RI, Park JS, Kim SW. pH-sensitive cationic polymer gene delivery vehicle: *N*-Ac-poly(L-histidine)-graft-poly(L-lysine) comb shaped polymer. Bioconjug Chem 2000;11:637–645.
64. Putnam D, Gentry CA, Pack DW, Langer R. Polymer-based gene delivery with low cytotoxicity by a unique balance of side-chain termini. Proc Natl Acad Sci 2001;98:1200–1205.
65. Lee SC, Na K, Bae YH. Polymeric micelle for tumour pH and folate-mediated targeting. J Control Release 2003;91:103–113.
66. Arotçaréna M, Heise B, Ishaya S, Laschewsky A. Switching the inside and the outside of aggregates of water-soluble block copolymers with double thermoresponsivity. J Am Chem Soc 2002;124:3787–3793.
67. Virtanen J, Arotçaréna M, Heise B, Ishaya S, Laschewsky A, Tenhu, H. Dissolution and aggregation of a poly(NIPA-*block*-sulfobetaine) copolymer in water and saline aqueous solutions. Langmuir 2002;18:5360–5365.
68. Bütün V, Billingham NC, Armes SP. Unusual aggregation behavior of a novel tertiary amine methacrylate-based diblock copolymer: Formation of micelles and reverse micelles in aqueous solution. J Am Chem Soc 1998;120:11818–11819.
69. Weaver JVM, Armes SP, Bütün V. Synthesis and aqueous solution properties of a well-defined thermo-responsive schizophrenic diblock copolymer. Chem Commun 2002;18:2122–2123.
70. Maeda Y, Mochiduki H, Ikeda I. Hydration changes during thermosensitive association of a block copolymer consisting of LCST and UCST blocks. Macromol Rapid Commun 2004;25:1330.

71. Cai YL, Armes SP. A zwitterionic ABC triblock copolymer that forms a "trinity" of micellar aggregates in aqueous solution. Macromolecules 2004;37:7116–7122.
72. Bütün V, Top RB, Ufuklar S. Synthesis and characterization of novel "schizophrenic" water-soluble triblock copolymers and shell cross-linked micelles. Macromolecules 2006;39:1216–1225.
73. Bütün V, Liu S, Weaver JVM, Bories-Azeau X, Cai Y, Armes SP. A brief review of "schizophrenic" block copolymers. React Funct Poly 2006;66:157–165, and references therein.
74. Jeong BM, Bae YH, Lee DS, Kim SW. Biodegradable block copolymers as injectable drug-delivery systems. Nature (London) 1997;388:860–862.
75. Alexandridis P. Amphiphilic copolymers and their applications. Curr Opin Colloid Interface Sci 1996;1:490–501.
76. Laughlin RG, editor. The aqueous phase behavior of surfactants. London: Academic Press; 1994.
77. Hatefi A, Amsden B. Biodegradable injectable in situ forming drug delivery systems. J Control Release 2002,80,9–28.
78. Jeong B, Choi YK, Bae YH, Zentner G, Kim SW. New biodegradable polymers for injectable drug delivery systems. J Control Release 1999;62:109–114.
79. Jeong B, Lee DS, Shon JI, Bae YH, Kim S.W. J Polym Sci Part A: Polym Chem 1999;37: 751–760.
80. Jeong B, Bae YH, Kim SW. Thermoreversible gelation of PEG-PLGA-PEG triblock copolymer aqueous solutions. Macromolecules 1999;32:7064–7069.
81. Park SY, Han BR, Na KM, Han DK, Kim SC. Micellization and gelation of aqueous solutions of star-shaped PLLA-PEO block copolymers. Macromolecule 2003;36:4115–4124.
82. Weaver JVM, Bannister I, Robinson KL, Bories-Azeau X, Armes SP, Smallridge M, McKenna P. Stimulus-responsive water-Soluble polymers based on 2-hydroxyethyl methacrylate. Macromolecules 2004;37:2395–2403.
83. Aoshima S, Sugihara S. Syntheses of stimuli-responsive block copolymers of vinyl ethers with side oxyethylene groups by living cationic polymerisation and their thermosensitive physical gelation. J Polym Sci Part A: Polym Chem 2000;38:3962–3965.
84. Sugihara S, Hashimoto K, Okabe S, Shibayama M, Kanaoka S, Aoshima S. Stimuli-responsive diblock copolymers by living cationic polymerization: precision synthesis and highly sensitive physical gelation. Macromolecules 2004;37:336–343.
85. Okabe S, Seno KI, Kanaoka S, Aoshima S, Shibayama M. Small-angle neutron scattering study on block and gradient copolymer aqueous solutions. Polymer 2006;47:7572–7579.
86. Okabe S, Seno KI, Kanaoka S, Aoshima S, Shibayama M. Micellization study on block and gradient copolymer aqueous solutions by DLS and SANS. Macromolecules 2006;39: 1592–1597.
87. Sugihara S, Kanaoka S, Aoshima S. Stimuli-responsive ABC triblock copolymers by sequential living cationic copolymerization: Multistage self-assemblies through micellization to open association. J Polym Sci, Part A: Polym Chem 2004;42: 2601–2611.
88. Sugihara S, Ohashi M, Ikeda I. Synthesis of fine hydrogel microspheres and capsules from thermoresponsive coacervate. Macromolecules 2007;40:3394–3401.

89. Chen GH, Hoffman AS. Graft copolymers that exhibit temperature-induced phase transitions over a wide range of pH. Nature 1995;373:49–52.
90. Yuk SH, Cho SH, Lee SH. pH/Temperature-responsive polymer composed of poly(*N*,*N*-dimethylamino)ethyl methacrylate-*co*-ethylacrylamide). Macromolecules 1997; 30:6856–6859.
91. Szczublalka K, Moczek L, Blaszkiewicz S, Nowakowska M. Photocrosslinkable smart terpolymers responding to pH, temperature, and ionic strength. J Polym Sci Part A: Polym Chem 2004;42:3879–3886.
92. Han SK, Na K, Bae YH. Sulfonamide based pH-sensitive polymeric micelles: physicochemical characteristics and pH-dependent aggregation. Colloids Surf Part A: Physicochem Eng Aspects 2003;214:49–59.
93. Kang SI, Bae YH. pH-Induced volume-phase transition of hydrogels containing sulfonamide side group by reversible crystal formation. Macromolecules 2001; 34:8173–8178.
94. Shim WS, Yoo JS, Bae YH, Lee DS. Novel injectable pH and temperature sensitive block copolymer hydrogel. Biomacromolecules 2005;6:2930–2934.
95. Shim WS, Kim SW, Lee DS. Sulfonamide-based pH- and temperature-sensitive biodegradable block copolymer hydrogels. Biomacromolecule 2006;7:1935–1941.
96. Stubbs M, McSheehy PMJ, Griffiths JR, Bashford CL. Causes and consequences of tumour acidity and implications for treatment. Mol Med Today 2000;6:15–19.
97. Tannock IF, Rotin D. Acid pH in tumors and its potential for therpeutic exploitation. Cancer Res 1989;49:4373–4384.
98. Dayananda K, Pi BS, Kim BS, Park TG, Lee DS. Synthesis and characterization of pH/temperature-sensitive block copolymers via atom transfer radical polymerization. Polymer 2007;48:758–762.
99. Lowe AB, McCormick CL. Synthesis and solution properties of zwitterionic polymers. Chem Rev 2002;102:4177–4189, and references therein.
100. Schmaljohann D. Thermo- and pH-responsive polymers in drug delivery. Adv Drug Deliver Rev 2006;58:1655–1670, and references therein.
101. Yokoyama M, Miyauchi M, Yamada N, Okano T, Sakurai Y, Kataoka K, Inoue S. Polymer micelles as novel drug carrier: Adriamycin-conjugated poly(ethylene glycol)-poly(aspartic acid) block copolymer. J Control Release 1990;11:269–278.
102. Yokoyama M, Miyauchi M, Yamada N, Okano T, Sakurai Y, Kataoka K, Inoue S. Characterization and anticancer activity of the micelle-forming polymeric anticancer drug adriamycin-conjugated poly(ethylene glycol)-(aspartic acid) block copolymer. Cancer Res 1990;50:1693–1700.
103. Kwon GS, Kataoka K. Block copolymer micelles as long-circulating drug vehicles. Adv Drug Deliver Rev 1995;16:295–309.
104. Kwon G, Suwa S, Yokoyama M, Okano T, Sakurai Y, Kataoka K. Enhanced tumor accumulation and prolonged circulation times of micelle-forming poly(ethylene oxide-aspartate) block copolymer adriamycin conjugates. J Control Release 1994;29:17–23.
105. Yokoyama M, Satoh A, Sakurai Y, Okano T, Matsumura Y, Kakizoe T, Kataoka K. Incorporation of water-insoluble anticancer drug into polymeric micelles and control of their particle size. J Control Release 1998;55:219–229.

106. Bae Y, Fukushima S, Harada A, Kataoka K. Design of environment-sensitive supramolecular assemblies for intracellular drug delivery: Polymeric micelles that are responsive to intracellular pH change. Angew Chem, Int Ed 2003;42:4640–4643.

107. Chung JE, Yokoyama M, Okano T. Inner core segment design for drug delivery control of thermo-responsive polymeric micelles. J Control Release 2000;65:93–103.

108. Kohori F, Sakai K, Aoyagi T, Yokoyama M, Yamato M, Sakurai Y, Okano T. Control of adriamycin cytotoxic activity using thermally responsive polymeric micelles composed of poly(*N*-isopropylacrylamide-*co*-*N*, *N*-dimethylacrylamide)-*b*-poly(DL-lactide). Colloids Surf B; Biointerfaces 1999;16:195–205.

109. Nakayama M, Okano T, Miyazaki T, Kohori F, Sakai K, Yokoyama M. Molecular design of biodegradable polymeric micelles for temperature-responsive drug release. J Control Release 2006;115:46–56.

110. Cavallaro G, Licciardi M, Giammona G, Caliceti P, Semenzato A, Salmaso S. Poly (hydroxyethylaspartamide) derivatives as colloidal drug carrier systems. J Control Release 2003;89:285–295.

111. Kang SI, Na K, Bae YH. Physicochemical characteristics and doxorubicin-release behaviors of pH/temperature-sensitive polymeric nanoparticles. Colloids Surf A: Physicochem Eng Aspects 2003;231:103–112.

112. Kabanov AV, Batrakova EV, AlakhovVY. Pluronic block copolymers for overcoming drug resistance in cancer. Adv Drug Deliver Rev 2002;54:759–779.

113. Alakhov V, Klinski E, Li SM, Pietrzynski G, Venne A, Batrakova E, Bronitch T, Kabanov A. Block copolymer-based formulation of doxorubicin. From cell screen to clinical trials. Colloids Surf B: Biointerfaces 1999;16:113–134.

114. Bromberg L, Temchenko M, Hatton TA. Smart microgel studies. Polyelectrolyte and drug-absorbing properties of microgels from polyether-modified poly(acrylic acid). Langmuir 2003;19:8675–8684.

115. Meyer DE, Shin BC, Kong GA, Dewhirst MW, Chilkoti A. Drug targeting using thermally responsive polymers and local hyperthermia. J Control Release 2001;74:213–224.

116. Chilkoti A, Dreher MR, Meyer DE, Raucher D. Targeted drug delivery by thermally responsive polymers. Adv Drug Deliver Rev 2002;54:613–630.

117. Soppimath KS, Liu LH, Seow WY, Liu SQ, Powell R, Chan P, Yang YY. Multifunctional core/shell nanoparticles self-assembled from pH-induced thermosensitive polymers for targeted intracellular anticancer drug delivery. Adv Funct Mater 2007;17:355–362.

118. Wang CH, Hsiue GH. New amphiphilic poly(2-ethyl-2-oxazoline)/poly(l-lactide) triblock copolymers. Biomacromolecules 2003;4:1487–1490.

119. Kissel T, Li YX, Unger F. ABA-triblock copolymers from biodegradable polyester A-blocks and hydrophilic poly(ethylene oxide) B-blocks as a candidate for in situ forming hydrogel delivery systems for proteins. Adv Drug Deliver Rev 2002;54:99–134.

120. Godbey WT, Wu KK, Mikos AG. Poly(ethylenimine) and its role in gene delivery. J Control Release 1999;60:149–160.

121. Wang CH, Wang CH, Hsiue GH. Polymeric micelles with a pH-responsive structure as intracellular drug carriers. J Control Release 2005;108:140–149.

122. Kakizawa Y, Kataoka K. Block copolymer micelles for delivery of gene and related compounds. Adv Drug Deliver Rev 2002;54:203–222.

123. Kataoka K, Togawa H, Harada A, Yasugi K, Matsumoto T, Katayose S. Spontaneous formation of polyion complex micelles with narrow distribution from antisense oligonu-

cleotide and cationic block copolymer in physiological saline. Macromolecules 1996;29:8556–8557.

124. Katayose S, Kataoka K. Water-soluble polyion complex associates of DNA and poly (ethylene glycol)-poly(L-lysine) block copolymer. Bioconjug Chem 1997;8:702–707.
125. Katayose S, Kataoka K. Remarkable increase in nuclease resistance of plasmid DNA through supramolecular assembly with poly(ethylene glycol)-poly(L-lysine) block copolymer. J Pharm Sci 1998;87:160–163.
126. Wood KC, Little SR, Langer R, Hammond PT. A family of hierarchically self-assembling linear-dendritic hybrid polymers for highly efficient targeted gene delivery. Angew Chem, Int Ed 2005;44:6704–6708.
127. Shoji S, Esashi M. Microflow devices and systems. J Mechan Microeng 1994;4:157–171.
128. Bosch D, Heimhofer B, Mück G, Seidel H, Thumser U, Welser W. A silicon microvalve with combined electromagnetic/electrostatic actuation. Sens Actuators A: Phys 1993;37–38:684–692.
129. Chakraborty I, Tang WC, Bame DP, Tang TK. MEMS micro-valve for space applications. Sens Actuators A: Phys 2000;83:188–193.
130. Rich CA, Wise KD. A high-flow thermopneumatic microvalve with improved efficiency and integrated state sensing. J Microelectromech Syst 2003;12:201–208.
131. Beebe DJ, Moore JS, Bauer JM, Yu Q, Liu RH, Devadoss C, Jo B-H. Functional hydrogel structures for autonomous flow control inside microfluidic channels. Nature 2000;404:588–590.
132. Liu RH, Yu Q, Beebe DJ. Fabrication and characterization of hydrogel-based microvalves. J Microelectromech Syst 2002;11:45–53.
133. Unger MA, Chou H, Thorsen T, Scherer A, Quake SR. Monolithic microfabricated valves and pumps by multilayer soft lithography. Science 2000;288:113–116.
134. Samel B, Griss P, Stemme G. A thermally responsive PDMS composite and its microfluidic applications. J Microelectromech Syst 2007;16:50–57.
135. Peters EC, Svec F, Fréchet JMJ. Thermally responsive rigid polymer monoliths. Adv Mater 1997;9:630–633.
136. Yu C, Mutlu S, Selvaganapathy P, Mastrangelo CH, Svec F, Fréchet JMJ. Flow control valves for analytical microfluidic chips without mechanical parts based on thermally responsive monolithic polymers. Anal Chem 2003;75:1958–1961.
137. Liu RH, Yu Q, Bauer JM, Moore JS, Beebe DJ. Hydrogel microvalves fabricated using *in situ* polymerization. Technical Digest of the Solid-State Sensor and Actuator Workshop. Hilton Head Island, SC; June 2000. pp.222–226.
138. Carlen ET, Mastrangelo CH. Electrothermally activated paraffin microactuators. J Microelectromech Syst 2002;11:165–174.
139. Carlen ET, Mastrangelo CH. Surface micromachined paraffin-actuated microvalve. J Microelectromech Syst 2002;11:408–420.
140. Suzuki H. Stimulus-responsive gels: Promising materials for the construction of micro actuators and sensors. J Intelligent Material Syst Struct 2006;17:1091–1097.
141. Stoeber B, Yang ZH, Liepmann D, Muller SJ. Flow control in microdevices using thermally responsive triblock copolymers. J Microelectromech Syst 2005;14:207–213.

CHAPTER 3

Evolution in Malaria Disease Detection: From Parasite Visualization to Colloidal-Based Rapid Diagnostic

DUANGPORN POLPANICH

Department of Chemistry, Faculty of Science, Mahidol University, Rama VI Rd, Bangkok 10400 Thailand
National Nanotechnology Center (NANOTEC), National Science and Technology Development Agency (NSTDA), Thailand Science Park, Klong Luang, Pathumthani 12120, Thailand

PRAMUAN TANGBORIBOONRAT

Department of Chemistry, Faculty of Science, Mahidol University, Rama VI Rd, Bangkok 10400, Thailand

ABDELHAMID ELAISSARI

Claude Bernard University LAGEP Laboratory, 43 Boulevard du 11 novembre 1918, Bât. CPE-308G 69622 Villeurbanne Cedex, France

3.1 INTRODUCTION

Malaria continues to be a threat in more than 100 countries in Africa, South and Central America, and Asia including Thailand. Each year 300–500 million cases of malaria occur worldwide and over one million people die, most of them are children under five year of age (1,2). Global distribution of malaria in 2004 is presented in Fig. 3.1.

The malaria disease is caused by protozoa of the genus *Plasmodium*, that is, *P. falciparum*, *P. vivax*, *P. malariae*, and *P. ovale* and is transmitted via an infected *Anopheles* mosquito. Among the four species, *P. falciparum* is the most important parasite causing severe and frequently fatal form of the disease.

Colloidal Nanoparticles in Biotechnology, Edited by Abdelhamid Elaissari
Copyright © 2008 John Wiley & Sons, Inc.

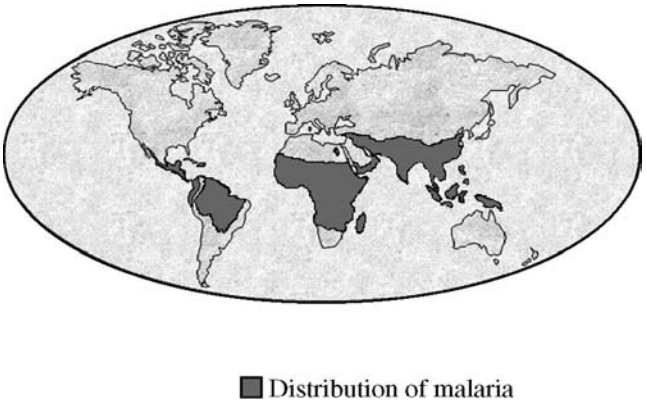

FIGURE 3.1 Global distribution of malaria in 2004 (3)

3.1.1 Life Cycle of P. falciparum

The life cycle of *P. falciparum*, shown in Fig. 3.2, is composed of two distinct phases, that is, an asexual phase within a vertebrate host and a sexual phase within an insect vector.

Infection in human host begins when an infected female mosquito feeds on the host and sporozoites are navigated through the bloodstream to the liver. These sporozoites rapidly invade liver cells, where they multiply extensively and form exoerythrocytic schizonts, each containing up to 30,000 merozoites. After bursting from the infected liver cell, the merozoites invade red blood cells (RBCs) to commence the asexual erythrocytic cycle. Through an active invasion process, merozoites enter RBCs and mature intracellularly from ring stage to trophozoite and

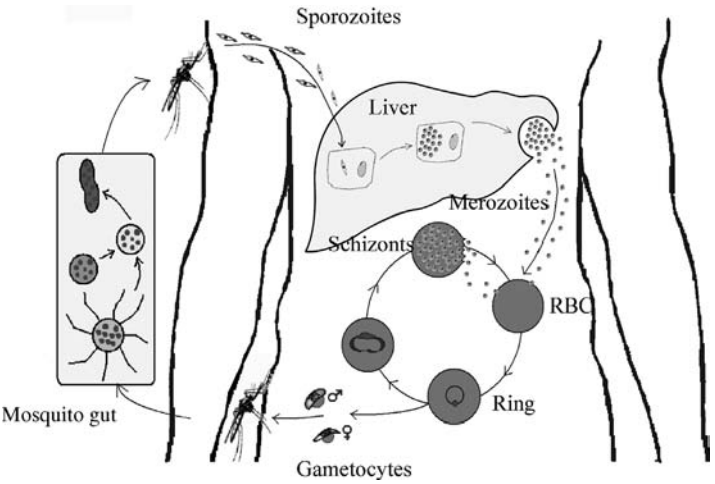

FIGURE 3.2 Life cycle of *P. falciparum* parasite (4)

finally into schizont stage. When the schizont ruptures, the merozoites are liberated into bloodstream to initiate another round of intraerythrocytic development. Some asexual parasites convert to sexual forms, male and female gametocytes, which can be taken up by *Anopheles* mosquito. After the fertilization, the zygote migrates across the mosquito midgut wall and matures within the body cavity. The resulting oocyst produces sporozoites that migrate to the mosquito salivary glands, ready for inoculation (5,6).

The enormous variability in *P. falciparum* proteins, which express from the multistage life cycle, is critical to the parasite's survival, enabling it to evade the host immune defense. At present, there is no commercially available vaccine for the parasite. In addition, the parasite is increasingly resistant to current antimalarial drugs, chloroquine and antifolate sulfadoxine/pyrimethamine, as are the *Anopheles* mosquito vector to insecticides (1,7,8). All of these have made malaria a global health problem.

Besides the development of effective vaccines and antimalarial drugs, the method of fast and accurate diagnosis is a very important aspect of malaria control (9–11). In fact, fast detection and treatment of the disease itself is enough to control the epidemic in its early stages (12,13). This reduces the parasite load in the community, thereby reducing the transmission of the disease. Among several approaches to the diagnosis of malaria, the cost, ease of performance and accuracy are important factors to determine their applicability in different situations.

3.1.2 Current Techniques in Malaria Diagnosis

3.1.2.1 Clinical Diagnosis The most widely used approach to the detection of malaria is clinical diagnosis based on patients' symptoms (9,14,15). In the areas with high rates of transmission, mostly in Africa (South of the Sahara), treatment based on clinical manifestation is the diagnostic of choice (9). This technique is inexpensive, easy to perform, and requires no special equipment. However, the symptoms of malaria are not specific (16) and overlap with a number of other febrile illnesses, such as encephalitis, dengue, and typhoid (9). The diagnosis of malaria relied on clinical ground alone is therefore unreliable. It should be confirmed by microscopic or alternative tests.

3.1.2.2 Microscopic Diagnosis Microscopic diagnosis of malaria is known as the current universal "gold standard." This involves the preparation and the examination of Giemsa- or Field-stained blood smear under light microscope (17–19). A fingerprick blood specimen is the ideal sample because the density of developed trophozoite or schizont is greater in blood from this capillary-rich area (18). However, blood obtained by venipuncture and collected in heparin or ethylenediaminetetraacetic acid (EDTA) anticoagulant-coated tube is acceptable if used shortly after being drawn, otherwise the possibility of alteration of the morphology of the malaria parasites might take place. Both thick and thin blood smears should therefore immediately be prepared. The thick smear, which concentrates the layer of RBCs on a small area of glass slide by a factor of 20–30, provides the sensitivity of the technique. However, the thin smear gives its specificity,

being much better for species identification and estimation of parasite density or parasitemia (9,17,18).

The microscopic diagnosis offers many advantages such as the cost and sensitivity. When a skilled microscopist conducts this technique, the density as low as 5–10 parasites per μL of blood can be detected (9). The parasites are able to be characterized in terms of their species and of the circulating stage (17,18). However, this technique is labour intensive and takes up to 60 min of preparation time. The interpretation of result requires considerable expertise, particularly at the low level of parasitemia (20). In addition, in patient with *P. falciparum* infection, the parasites can be sequestered in the deep capillaries (spleen, liver, and bone marrow) and are not confined to peripheral blood. Because of insufficient numbers of parasites for detection in the blood smear, *P. falciparum* infection may easily be missed (21).

3.1.2.3 Rapid Diagnostic Tests Rapid diagnostic tests (RDTs), based on the detection of antigen derived from malaria parasite in lysed blood, using an immunochromatographic method (17), open a new and exciting avenue in malaria diagnosis, particularly for use in the field. Several products that frequently employ dipsticks or strips bearing monoclonal antibody directed against the target parasite antigens have been developed and marketed (22). The most common of these products can be divided into two groups according to *P. falciparum*-specific antigen: histidine-rich protein II (HRP II) and parasite lactate dehydrogenease (pLDH) enzyme. The RDTs are uniformly reported to be easy to perform and interpret. They do not require electricity, special equipment, or training. The complete test can be performed within 15 min. The component of RDTs strips before use and the general procedure are depicted in Fig. 3.3.

In general, a fingerprick blood specimen is collected (2–50 μL) by using anticoagulated blood or plasma (9). The specimen is mixed with a buffer solution containing a hemolyzed compound as well as a specific antibody that is labeled with a visually detectable marker, such as gold particle. If the target antigen is present, an antigen–antibody complex formed migrates up the test strip by capillary action. It is then captured by the predeposited antibody that is specific against the antigen and the labeled antibody (as a procedure control). After the addition of the washing buffer to remove hemoglobin, the colored line formed by the immobilized antigen–antibody complex on the strip is visualized in the case of blood containing antigen under investigation.

The sensitivity of greater than 90% is generally achieved in the detection of *P. falciparum* at the density greater than 100 parasites per μL. However, below the level of 100 parasites per μL, the sensitivity markedly decreases. Although the specificity of RDTs is high, false-positive result has been reported in the patient's blood with rheumatoid factor (24–26). Moreover, the test based on HRP II detection can remain positive for up to 2 weeks following chemotherapy in a substantial proportion of individuals, even though the patients no longer have symptoms or parasitemia (17,18). While the clearance of parasites and pLDH appears to parallel each other, the RDTs targeting pLDH is comparatively reliable.

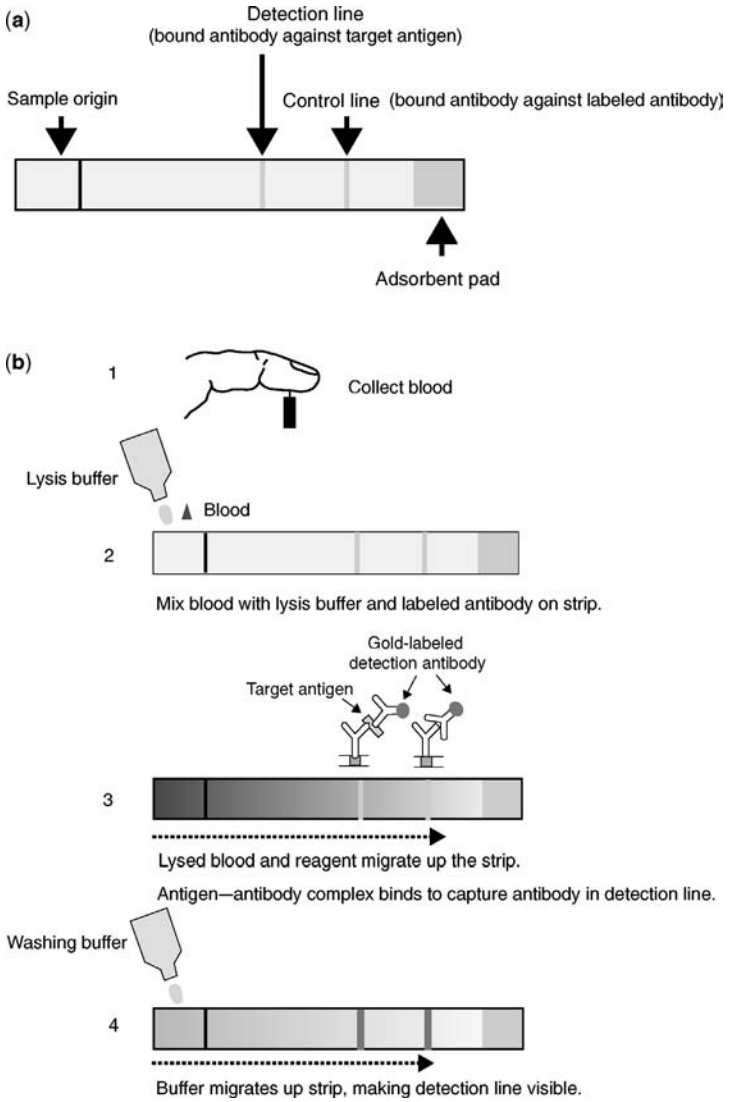

FIGURE 3.3 Component of RDTs strips before use (**a**) and the general procedure of test (**b**) (23)

In spite of many advantages of RDTs, the available tests are still expensive for developing countries where the majority of malaria cases occur.

3.1.2.4 Automated Hematology Analyzer Currently, there is an attempt to exploit an automated hematology analyzer (Cell-Dyn series) for the detection of hemozoin (or malaria pigment), which is a heme polymer resulting from the

breakdown of hemoglobin by *Plasmodium* species (27–30). The instrument, incorporating the flow cytometry-based principle, specifically discriminates between eosinophil and neutrophil. This characteristic can be plotted as a scatter diagram where eosinophils are displayed in green dots above a threshold line, while the other white blood cell are presented below (29,31). In the malaria patient, as a consequence of depolarizing hemozoin ingestion by phagocytic monocyte, atypical event of monocyte as purple dots appeared in eosinophil area is detected. Sensitivity and specificity of this method to diagnose malaria are ranged from 52% to 95% and from 72% to 100%, respectively (30).

The automated hematology analyzer is an alternative method for malaria diagnosis in the medical center where an expert microscopist is not available (29). It permits the detection of unsuspected malaria cases in which clinical suspicion does not lead to malaria testing (30). However, it has been reported that quantification and differentiation of *Plasmodium* species cannot be obtained by this automated malaria detection (30). Additionally, because of the high maintenance costs and the requirement of laboratory conditions, the automated hematology analyzer is out of reach for malaria endemic area and is not suitable for use in the field.

3.2 LATEX AGGLUTINATION TEST

Latex agglutination test (LAT) has been widely used in medicine for detection of substances (hormones, drugs or proteins) in biological fluids including saliva, urine, or blood (32–37). Because of many advantages over other tests, that is, fast, easy, highly selective, and inexpensive, LAT is applied to detect over 100 infectious diseases (38–40).

In LAT, the latex is mediated by specific reaction between antibody and antigen, which is immobilized onto the surface of latex particle, hence it is referred to as immunolatex. In the test, the immunolatex, appeared as smooth suspension (Fig. 3.4a), is mixed and incubated with the fluid to be analyzed. The presence of complementary antigen (or antibody) in the analyte creates link between particles resulting in the agglutination or clumping of the microspheres such as a curdled milk, as demonstrated in Fig. 3.4b.

The agglutination reaction can be categorized into two different modes, that is, direct and indirect LAT with respect to the ligand of interest as described below.

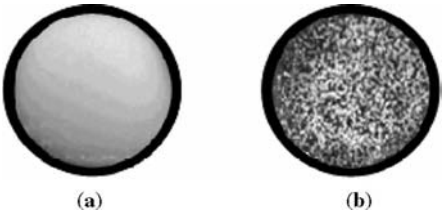

FIGURE 3.4 Immunolatex particles (**a**) before and (**b**) after agglutination (41)

3.2.1 Direct Latex Agglutination Test

The direct LAT, shown in Fig. 3.5, is based on the detection of specific antigen in biological sample by using antibody-coated latex particle. If the specific antigen is present in the sample, it will react with the antibody to form aggregates.

This method is applicable to the detection of polyvalent antigen such as proteins and microorganisms (38). The most familiar application of this method is the pregnancy test in which human chorionic gonadotropin (HCG) protein in the blood and urine is detected by polystyrene (PS) latex coated with monoclonal antibody leading to the visible agglutination within 3 min (42,43).

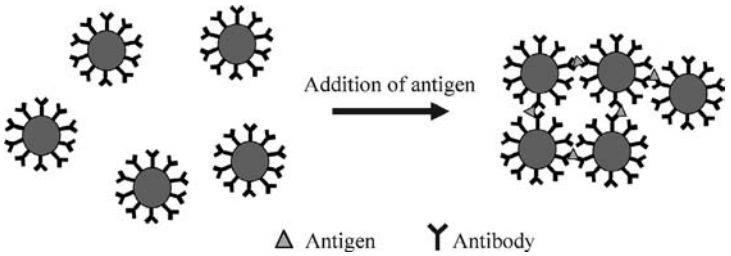

FIGURE 3.5 Direct LAT; antibody-coated particles agglutinated by the specific antigen molecules

3.2.2 Indirect Latex Agglutination Test

This method relies on the principle similar to the direct LAT whereby antigen molecules are bound to the latex particle surface. The specific antibody in the sample can be detected, by this method as schematically presented in Fig. 3.6.

This approach is applicable to mono and polyvalent antigens, that is, drugs, hormones, and proteins (38). Currently, many infectious diseases including leptospirosis, amebiasis, and *Entamoeba histolytica* Cyst Passage can be diagnosed with high sensitivity and specificity (>90%) by using the indirect LAT (32,34,44).

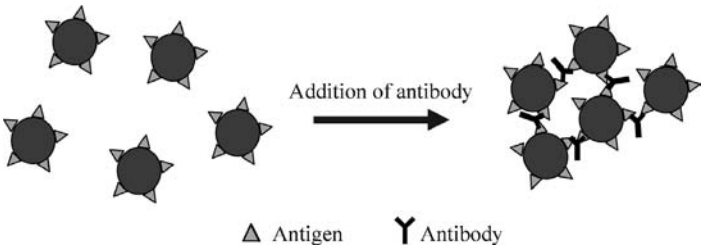

FIGURE 3.6 Indirect LAT; antigen-coated particles agglutinated by the specific antibody molecules

3.3 PREPARATION OF IMMUNOLATEX

Latex particle is used as a solid support for antigen (or antibody) molecules instead of other solid supports such as erythrocyte and metal sol (45). This is due to the following reasons: (1) the surface/volume ratio of particle is extremely large, (2) it can be produced with high degree of monodispersity, and (3) the surface properties of latex particle including hydrophilicity can be varied relatively easily.

Recently, a variety of new latex particles potentially suitable for LAT have been synthesized, and emulsion polymerization has proved to be the most appropriate technique to tailor the particles with required characteristics (46–49). For diagnostic test, the monodisperse particles are required to provide simultaneous latex agglutination. The particle diameter, ranging from 100 nm to 50 μm (49), is suitable for the selected detection system. To keep the particle a long shelf-life time before use, the chemical and colloidal stability of the particle within the specific ranges of pH, ionic strength, and temperature is demanded.

3.3.1 Conventional Emulsion Polymerization

A typical polymerization recipe consists of four major ingredients, that is, a water-insoluble monomer, for example, styrene (St); a water-soluble initiator, for example, potassium persulfate (KPS); an oil-in-water surfactant, for example, sodium dodecyl sulphate (SDS); and dispersed medium, usually water (50,51). The ratio of water to monomer is generally in the range from 70/30 to 40/60 (by weight). The reaction system is characterized by the emulsified monomer droplet (ca. 1–10 μm in diameter, 10^{12}–10^{14} dm^{-3} in number) dispersed in continuous aqueous phase with the aid of a surfactant at the very beginning of polymerization. Above the critical micelle concentration (CMC) of the surfactant, monomer-swollen micelles (ca. 5–10 nm in diameter, 10^{19}–10^{21} dm^{-3} in number) are formed in the reaction system. Because of the low water solubility of the monomer, for example, 0.07 and 0.8 g/L (at 25°C) for St and butadiene, respectively, (52), most of the monomers dwell in monomer droplets and a giant monomer reservoir. Only a small amount of monomer is present in the micelle or dissolved in the aqueous phase.

Since the particle nucleation takes place in micelle, the conventional emulsion polymerization also proceeds with the micellar nucleation mechanism proposed by Harkins, Smith, and Ewart (50). The schematic representation of the conventional emulsion polymerization is shown in Fig. 3.7.

The mechanism of emulsion polymerization can be divided into two stages, that is, particle nucleation and growth (51). In the nucleation stage, the radical initiator (denoted R•) is generated by the thermal decomposition of the initiator, for example, KPS ($K_2S_2O_8$).

$$S_2O_8^{2-} \xrightarrow{\Delta} 2SO_4^{\bullet-}$$

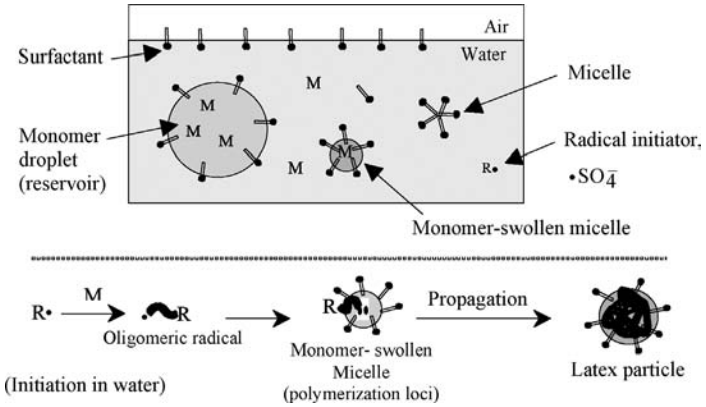

FIGURE 3.7 A simplified schematic representation of conventional emulsion polymerization or micellar nucleation mechanism

The sulphate radicals propagate with the monomer units (denoted M) in the aqueous phase to produce oligomeric radicals.

$$\overset{\bullet}{SO_4^-} + M \rightarrow \bullet MSO_4^-$$
$$\bullet MSO_4^- + M \rightarrow M_2SO_4^- \xrightarrow{nM} \bullet M_{n+2}SO_4^-$$
$$\bullet M_{n+2}SO_4^- + \text{monomer} - \text{swollen} \rightarrow \text{Entry}$$

When these oligomeric radicals become hydrophobic, they show a strong tendency to enter monomer-swollen micelles and then continue to propagate by reacting with the monomer molecules therein. As a result, monomer-swollen micelles are successfully transformed into the particle nuclei. To maintain adequate colloidal stability of the growing particle, noninitiated micelles disband to supply the increasing demand for surfactant (50). The particle nucleation stage ends with the disappearance of the free micelles. In the growth stage, the particles continue to grow in size with the progress of polymerization by acquiring the monomer from the monomer droplets. The polymerization continues at a steadily decreasing rate as the monomer concentration in the particles decreases. Final conversions of essentially 100% are usually achieved, and the spherical latex particles having diameters of 50–200 nm are obtained.

It is worth noting that the feature of latex particle is decided not only by the monomer used but also by surfactant and initiator. Several novel initiators have been employed to give some functions to the resulting latex particles. For example, a phosphatidycholine-containing azo-initiator formed particle having a phospholipid-like surface was applied for the adsorption of bovine serum albumin (BSA) (53). Unlike initiator residues on a particle surface, surfactant molecules do not necessarily deposit tightly on the surface but repeatedly desorb and adsorb. Desorbed surfactant molecules act as the impurity when the latex is used in biomedical applications. To overcome this problem, surfactant-free emulsion polymerization is a good choice for the elaboration of surface-clean latex particle.

3.3.2 Surfactant-Free Emulsion Polymerization

Since 1965, when Matsumoto and Ochi (54) first proposed that the monodispersed particle could be prepared by the surfactant-free emulsion polymerization based on St/KPS/water system, the technique has become of significant interest. It appears to be a convenient and versatile method for producing well-characterized particle with a large surface area in a wide range of size and surface characteristics for biomedical applications, such as protein separation and purification, drug delivery, and LAT. The mechanism of the surfactant-free emulsion polymerization is described on the basis of the homogeneous nucleation mechanism proposed by Priest (55), Roe (56), Fitch and Tsai (57), as schematically shown in Fig. 3.8.

In Fig. 3.8, radical initiators generated in aqueous medium by thermal decomposition of the water-soluble initiators can grow in size via the propagation reaction with those monomers dissolved in the aqueous phase to form oligomeric radicals. It is assumed that nucleation occurs when the chain length of water-soluble oligomeric radicals (j) has reached a critical value (j_{cr}). A value of $j > j_{cr}$ leads to the precipitation of the now water-insoluble oligomeric chain as particle or primary particle where the polymerization takes place (58,59). The primary particles continuously propagate to become latex particles, which are stabilized by ionic fragments of radical initiators that become end groups of the polymer chain on the particle surface. It is important to note that, in this system, a high amount of initiator is required to efficiently prepare the colloidally stable latex.

Alternatively, small amounts of functional monomers such as acrylic acid (AA) (60,61) and methacrylic acid (MAA) (61) are commonly incorporated into the surfactant-free emulsion polymer to improve the colloidal stability during polymerization. Many studies have focused on the effect of type and concentration of the functional monomer on the polymerization kinetics and mechanism, or the colloidal and surface properties of the final latex. Chemical structure of the functional monomer also plays an important role in the polymerization mechanism, especially during the

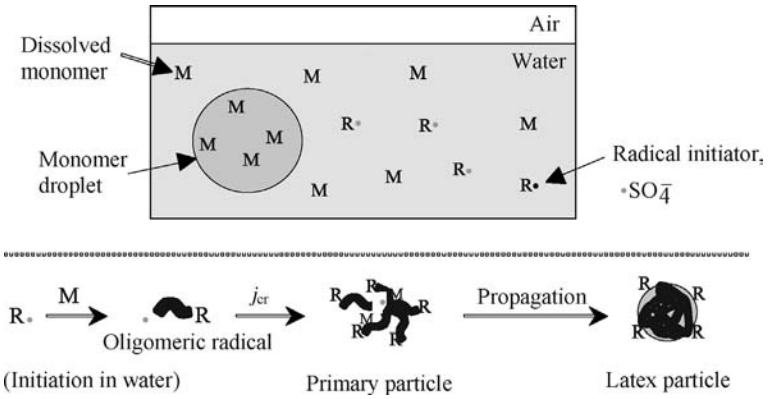

FIGURE 3.8 A simplified schematic representation of the surfactant-free emulsion polymerization or homogeneous nucleation mechanism

nucleation period and consequently on the final particle properties (62). Previous study of the surfactant-free emulsion polymerization of St and methyl methacrylate (MMA) in the presence of functional monomer AA indicated the increase in the rates of both particle nucleation and polymerization with increasing concentration of AA (63). In addition, it was reported that the rate of copolymerization of St with itaconic acid (IA), AA, or MAA in separate reactions increased with the presence of carboxylic monomer in the order IA < AA < MAA; that is, the more the hydrophilicity of functional monomer used, the lower the rate of copolymerization (64).

3.3.3 Functionalized Latex

Functionlization of latex has become a common method for the modification of its superficial and colloidal properties. It allows an increase in the interaction of the particle with different organic, mineral or metal substrates, and also enhances the immobilization of biomolecules such as protein and nucleic acid for biomedical purposes (45,62). The functionlization is carried out by incorporating reactive chemical groups contributed by the radical initiator (KPS, nitrosulphonated, carboxylated, or cationic derivatives), the surfactant (anionic, cationic, zwitterionic; or nonionic), and the functional monomer. The last one is the most preferred method due to the availability and the variety of functional monomers such as AA, MAA, and aminoethyl methacrylate, which are generally used in very low concentration (0.1–5.0%). Unlike surfactant, the covalent attachment of reactive group of functional monomer is notified. Table 3.1 highlights the chemical functional groups and the main monomers used.

Among several functional groups in Table 3.1, carboxyl (−COOH) and amino ($-NH_2$) groups are commonly used to produce functional surfaces for attachment of protein due to the following reasons (38):

TABLE 3.1 Various Chemical Functional Groups and the Main Monomers Used (62).

Functional group	Monomer used
−COOH	Acrylic acid Methacrylic acid Itaconic acid
−CHO	Acrolein
$-CH_2Cl$	Chloromethylstyrene
-CH – CH_2 \ / O	Glycidyl methacrylate
$-NH_2$	Aminoethyl methacrylate
$-NCH_2OH$	*N*-Methyloacrylamide
$-N(CH_3)_3{}^{+}Cl$	*N*-Trimethyl-*N*-ethyl methacrylate ammonium
−OH	Hydroxyethyl methacrylate

1. These groups have proven to be very stable over time.
2. The chemistry involved in the attachment of protein to either of these groups is well known.
3. The existence of terminal amino and carboxyl groups on protein molecules is universal, ensuring their availability for complementary attachment to the functional groups on the latex surface.

It was reported that, for latex diagnostic test, the immunolatex prepared from the functional latex produced a low level of nonspecific interaction compared to the hydrophobic surface. Konings et al. (65) proposed the synthesis of particle composed of a hydrophilic shell with an aldehyde group for use to detect the presence of HCG in urine. On comparing with the hydrophobic latex particle coated with the same antibody, it was found that the functionalized latex presented low nonspecific interaction and high detection limit. However, as Okubo et al. (66) pointed out, it was essential to optimize the ratio of hydrophobic/hydrophilic monomer in the synthesis to obtain appropriate particle for immunoassay.

3.3.4 Protein Immobilization onto Latex Particle

The natural habitat of most proteins is an aqueous environment. Nevertheless, when a protein solution is brought in contact with another phase (solid, liquid, or gas) that it is immiscible, the protein molecules tend to interact at the interface between two phases, leading to the adsorption of protein.

An ideal polymer latex for protein immobilization should allow the attachment of protein molecules in a controlled manner, resulting in a colloidally stable system with the required surface concentration of the immobilized protein. In addition, it should retain a maximum of biological activity, while simultaneously preventing a nonspecific binding of nontarget protein (67,68). The immobilization process can be achieved by physical adsorption, covalent grafting, or chelation.

3.3.4.1 Physical Adsorption Physical adsorption of protein on a solid surface, the longest established technique for the noncovalent immobilization, is controlled by the property of the support surface, the nature of the protein molecule, and the medium conditions, such as solution pH, ionic strength, and temperature (in the case of thermosensitive particles). Whatever the mechanism and the kinetics of protein adsorption, the process (at constant pressure and temperature) can occur only if the Gibbs free energy (G) of the system decreases:

$$\Delta_{\text{ads}}G = \Delta_{\text{ads}}H - T\Delta_{\text{ads}}S < 0 \tag{3.1}$$

where H, S, and T refer to enthalpy, entropy, and absolute temperature, respectively. The Δ_{ads} indicates the change of thermodynamic functions of state resulting from the adsorption process.

Norde et al. (69,70) originally proposed the basis of qualitative theory of protein adsorption process. They indicated that four effects, namely structural rearrangements

in protein molecule, dehydration of the sorbent surface, redistribution of charged groups in the interface layer, and protein-surface polarity usually make the primary contributions to the overall adsorption behavior. However, many important questions remain unanswered and predictive theory is not insight.

The effective control of protein adsorption process requires an understanding of its driving force. In general, carboxylated microsphere is used as the model colloid for explaining the protein adsorption process. Figure 3.9 shows schematically the interaction forces at the interface between protein and St/MAA microsphere.

The interaction forces in Fig. 3.9 involving the adsorption process are classified into four interactions, that is, (1) hydrophobic interaction, (2) electrostatic interaction, (3) hydrogen bonding, and (4) van der Waals interaction. The hydrophobic interaction has a major role in protein adsorption phenomena, especially in the adsorption of proteins onto the low charge particle surface. The maximum amount of adsorbed protein by this interaction force is near its isoelectric point (pI), and the pH shifts to more acidic region with an increase of ionic strength (72,73). In the case of microspheres having anionic functional groups, such as the sulphate groups (decomposed from an initiator), and carboxyl groups (originated from hydrophilic comonomers), they electrostatically interact with positively charged protein molecules. The hydrogen bond is frequently formed between hydroxyl–carbonyl or amide-carbonyl bond and hydroxyl–hydroxyl or amide-hydroxyl bond, whereas van der Waals interaction is operative over small distances, that is, only when water has been excluded and two nonpolar groups come close to each other. Lewin's calculation shows that it is negligible in comparison of the forces involved in the entropy increase, that is, hydrophobic interaction (74).

For such protein molecules, the adsorption is primarily governed by the electrostatic interaction and the dehydration of hydrophobic area of the sorbent and/or the protein molecule. Under most conditions, the contribution of dehydration of a

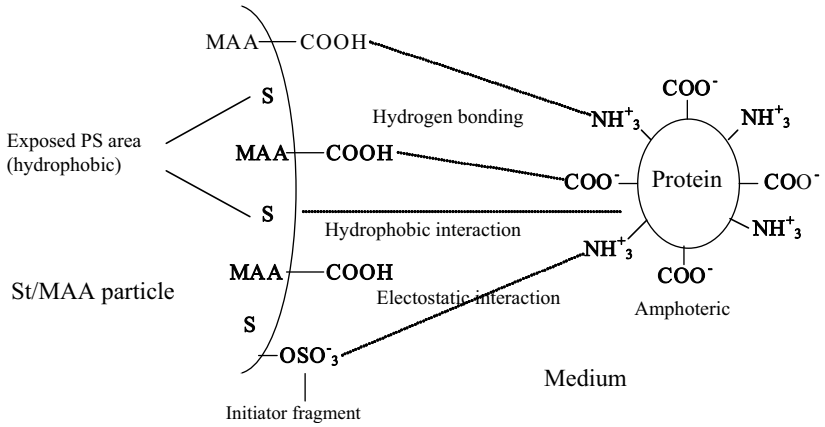

FIGURE 3.9 Schematic representation of the interaction forces at the interface between protein and St/MAA microsphere (71)

hydrophobic surface to the overall Gibbs free energy of adsorption is much larger than that of electrostatic interaction between the protein and the sorbent (69). Indeed, protein is found to adsorb onto the hydrophobic surface even if the protein and the substrate electrostatically repel each other (75,76), while it adsorbs on hydrophilic surface only if electrostatically attracted (76). However, protein molecules having a much less stable native structure also tend to adsorb on electrostatically repelling surface (76). It is plausible to relate this additional driving force to structure rearrangement in the protein molecule. Both protein adsorption and desorption would be affected by conditions that influence the strength of the interaction between support and protein. Therefore, parameters such as pH, ionic strength, and temperature must be controlled. The manipulation of these parameters would allow a simple and cost-effective method for immobilization.

3.3.4.2 Covalent Coupling Immobilization of proteins on solid support by the covalent coupling has, in principle, several advantages such as no desorption of physically adsorbed protein, minimal protein denature on the surface, and minimal nonspecific interaction (38,68). With suitable chemical manipulation, the immobilized protein molecules can be made to orient properly resulting in an improvement in the activity of the bound proteins (38).

The functional latex can covalently bind to the protein molecule via the amine group, and hence has been employed in the development of immunoassay (38,62). In the case of carboxylated latex, the covalent binding takes place at the –COOH functionality. However, for this purpose chemical activation by using carbodiimide, a condensing agent such as 1-cyclohexyl-3-(2-morpholinoethyl)-carbodiimide-metho-*p*-toluene-sulphonate (CMCI), or 1-ethyl-3-(3-dimethylaminopropyl)-carbodiimide hydrochloride (EDCI) is required (77). Figure 3.10 shows that carbodiimide reacts with carboxyl group at slightly acidic pH value to give *O*-acylisourea derivatives (I), and the activated carboxyl group subsequently rearranges to an acyl urea (II) or react with amino group of the protein molecule to yield the corresponding amide (III).

Bastos-Gonzalez et al. (78) reported the preparation of carboxylated latex by soap-free emulsion polymerization using an azo-initiator that directly provided carboxyl end groups on the latex surface. The activation of the carboxyl end groups was

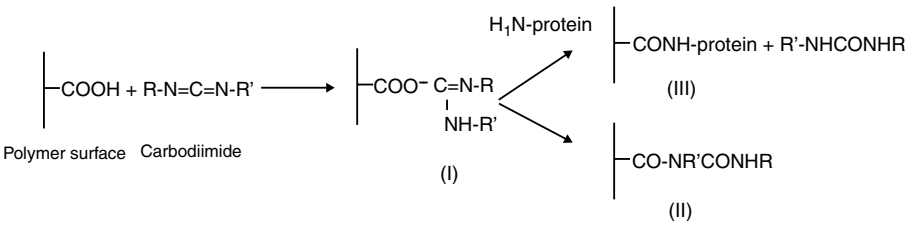

FIGURE 3.10 Chemical reaction of protein immobilization using carbodiimide as a condensing agent (77)

performed using carbodiimide method resulting in a superior condition for covalent coupling of immunoglobulin G (IgG).

The use of latex carrying an aldehyde group on its surface could simplify the formation of covalent bond with the primary amino group of protein molecule (79). However, the aldehyde group tends to decompose with time, losing the capability to bind with the protein molecule. To avoid this problem, the particle surface having an acetal group which can be transformed to the aldehyde functionality under acidic pH medium, is introduced. Peula et al. (80,81) prepared the acetal latex, that simply permitted the coupling of IgG anti-C-reactive protein (anti-CRP) by changing the mixture to pH 2. The latex–protein complex showed a good immunological response and stability with time.

3.3.4.3 Chelation Recently, protein immobilization method has been developed by using Pluronic surfactant, [poly(ethylene oxide)–poly(propylene oxide)–poly(ethylene oxide); (PEO–PPO–PEO) triblock copolymer] (82). The protein-repelling property formed from hydrophilic PEO of Pluronic was used as an activity-preserving foundation for specific protein immobilization onto the PS bead. Li et al. (83) demonstrated that protein could chemically couple to the terminal hydroxyl group of PEO chain of Pluronic F108 adsorbed onto PS beads. The method was adapted by coupling a metal-chelating nitrilotriacetic (NTA) group to the terminal group of Pluronic F108, as displayed in Fig. 3.11. Metal ion, chelated by the NTA group, possesses the coordination site that is free to bond with the electron-donating side chain, particularly histidine residue, on the protein surface. Protein can be made to have high affinity for chelation with metal ion by genetically adding terminal histidine residues. By using recombinant firefly luciferase (FFL) as a test protein, it was found that the immobilized FFL onto the chelating Pluronic retained at least 93% of its bioluminescence activity.

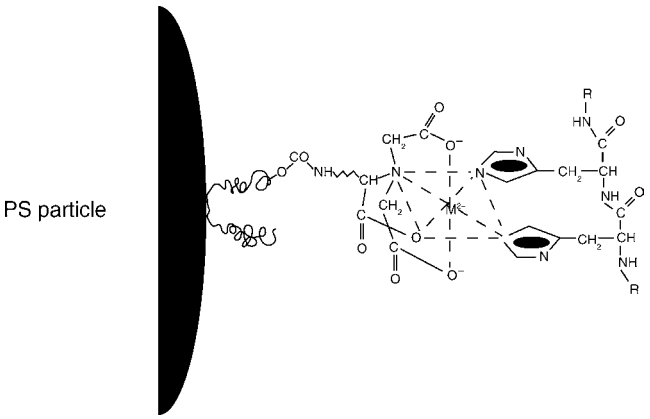

FIGURE 3.11 Immobilization scheme for histidine-tagged protein using metal chelating Pluronic F108 (82)

3.4 FACTORS AFFECTING PROTEIN ADSORPTION ONTO PARTICLE SURFACE

Besides the nature and the characteristics of protein and latex particle, external conditions, that is, incubation time, protein concentration, pH, and ionic strength of adsorption medium play important roles in the adsorption process. These factors should be optimized to gain the proper amount of adsorbed protein onto the particle.

In view of LAT, when the antigen is bound to the particle surface, for example, desired agglutination begins when the two recognition sites on the IgG molecule react with the antigen on the separate particles (Fig. 3.12a). If the antigen is densely packed

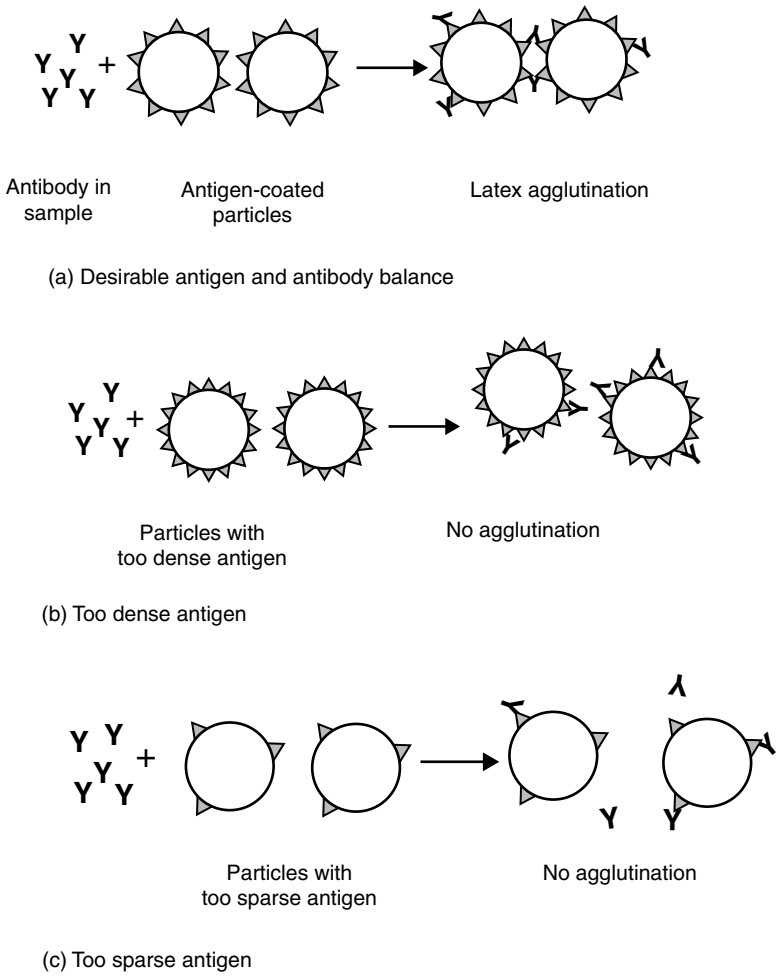

FIGURE 3.12 Diagram summarizing antigen and antibody balance affecting the probability of agglutination reaction: (**a**) desirable balance of antigen and antibody, (**b**) too dense antigen, and (**c**) too sparse antigen (84)

on the surface, the antibody can bridge between adjacent antigens on a single particle rather than on separate particles (Fig. 3.12b); as a result, the agglutination will be less likely to occur. Or, if the antigen is sparsely distributed onto the surface (Fig. 3.12c), it would prevent the agglutination reaction (84,85).

Effects of incubation time, protein concentration, pH, and ionic strength of the adsorption medium on the amount of adsorbed protein (Γ_{ads}) onto the latex particle are described as follows.

3.4.1 Incubation Time

The protein transports toward the interface and starts the adsorption via one point attached onto the substrate's surface. This process is driven by the partial dehydration of hydrophobic parts of both protein and surface resulting in an increase in entropy from the freedom gained by water molecules, which lowers the Gibbs free energy of the system, and hence favors adsorption (70). As the incubation time increases, the structure rearrangement of the protein takes place, which encourages the increase in the number of contact points (86). The representation of events following protein adsorption onto substrate's surface is illustrated in Fig. 3.13. It was found that the value of Γ_{ads} increases with an increase in the incubation time and then attains the constant value (87–89).

Although the protein in an aqueous medium tends to bury the hydrophobic amino acid residues in its interior, it often exposes these residues when the molecules are transferred to a hydrophobic surface (69). These two contributions are not independent; that is, a higher flexibility in the protein structure enables a more efficient coverage of the sorbent surface by the protein (90). It was suggested that if the incubation time was sufficient for the occurrence of the structure alteration of protein molecule, it does not readily desorb by latex dilution or changing pH medium (88,91).

3.4.2 Protein Concentration

When the protein adsorption occurs, it takes a given time for the Γ_{ads} value and protein concentration to reach their equilibrium values. The value of Γ_{ads}, determined as a function of equilibrium protein concentration (C_{eq}), is defined as an adsorption isotherm whose initial slope relates to the affinity of the protein for substrate's surface, that is, steeper slope, higher affinity. Typically, the Γ_{ads} value increases sharply at low

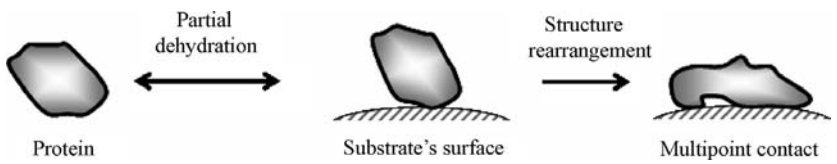

FIGURE 3.13 Representation of events following protein adsorption onto substrate's surface (86)

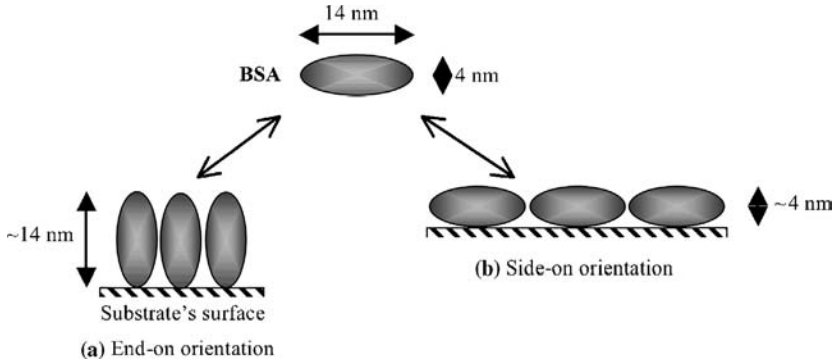

FIGURE 3.14 Orientation of adsorbed BSA onto the substrate's surface (**a**) end-on and (**b**) side-on orientations (93)

C_{eq}, tapers off at higher C_{eq} and then approaches plateau, indicating the adsorption saturation (38). The plateau is assumed to correspond to close-packed monolayer of native protein in end-on and side-on orientations. By using BSA (ellipsoid dimension $14 \times 4 \times 4$ nm) (92) as a protein model, its orientations onto the substrate's surface are demonstrated in Fig. 3.14.

3.4.3 pH of Adsorption Medium

According to the former works, it was reported that the maximum Γ_{ads} value of various proteins onto the particle surface is obtained when the medium pH coincides with pI of the protein (38,88,91,94). At pH equals to pI, the minimal lateral interaction between neighboring adsorbed protein molecules renders the maximum Γ_{ads} value. Shifting pH of the adsorption medium to lower or higher than pI of the protein tends to decrease the Γ_{ads} value. It can be explained that, away from pI, the excess of either positive or negative charge of the protein increases the intramolecular repulsion leading to the more expanded structure, and consequently less protein molecules can be adsorbed onto a given surface area. In addition, the strong repulsive electrostatic force among the adsorbed protein molecules themselves is also responsible for the low Γ_{ads} value (38,94).

3.4.4 Ionic Strength of Adsorption Medium

The ionic strength has a pronounced effect on the protein adsorption onto the charged particle. A dramatic reduction in the value of Γ_{ads} with increasing ionic strength is expected under the condition of electrostatic attraction between the opposite charges of protein and sorbent due to the charge screening effect. On the contrary, for the adsorption system in which electrostatic repulsion exists between the same charge of protein and latex particle, the increase in ionic strength would increase the Γ_{ads} value (91,94). It was noticed that, for the sorbent having hydrophilic layer on its surface (hairy particle), the increase of the ionic strength led to a shrinkage of the interfacial

hydrophilic layer (87,95), and accordingly the reduction in the accessible surface for protein adsorption (87).

3.5 DETECTION OF LATEX AGGLUTINATION

The progress of latex agglutination caused by antigen–antibody immunoreaction can be detected by various methods, such as, naked eyes and those based on instrumental techniques including, turbidimetry, nephelometry, and photon correlation spectroscopy (PCS) (38,96). With any of these instruments, the degree of agglutination plotted as a function of agglutinant concentration follows a bell-shaped curve similar to the familiar precipitin curve (96–99). It was suggested that the particle size should have a diameter of 0.1–1.0 μm for observation of agglutination under naked eyes, whereas the diameter covers the range of 0.01–0.3 μm if the instrument is used (38).

Without any special equipment required, the direct observation of LAT by naked eyes is the simplest and most convenient method. It provides the qualitative test result that helps to identify or indicate the presence of antibody (or antigen) of interest in the test sample. To detect the agglutination by naked eyes, about 100 clumps of aggregated particles are required, and each clump must be of about 50 μm (100). If the single particle is 1.0 μm in diameter, then close to 10^5 particles will be essential for the visible aggregate, and close to 10^7 particles are needed to detect agglutination in a given test (100).

3.5.1 Turbidimetry

Turbidimetry works on the measurement of reduction in intensity of the transmitted light or increase in absorbance at 180° by using a spectrophotometer. When the light of suitable wavelength passes through a suspension, it may be adsorbed or scattered by the suspended particles (Fig. 3.15) and, consequently, the intensity of light is declined, which is defined as turbidity (τ) (38,101).

For nonabsorbing particle, the relationship between the value of τ and the intensity of light is expressed by Equation (3.2).

$$\tau = \frac{1}{l} \ln \frac{I_o}{I} \tag{3.2}$$

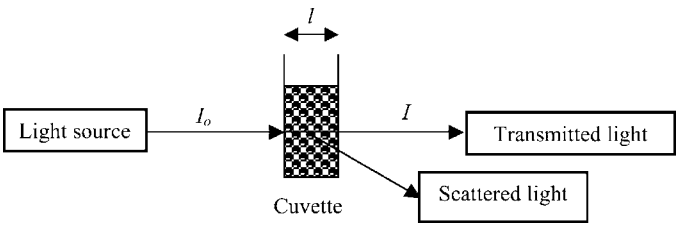

FIGURE 3.15 Behavior of light passing through the suspension

Where I_o and I are the intensities of initial and transmitted beams, respectively, and l is the length of the light path (38). In LAT, when the light is passed through a reaction solution containing latex–antigen (or antibody) conjugate, the measured absorbance is minimum. Subsequently, the reagent containing the antibody (or antigen) is added to the immunolatex and allowed to react, and this leads to the formation of the immune complex. As the reaction time increases, the particle aggregation becomes larger resulting in an increase in τ value (97,101).

The optimum wavelength for detection of the immune complex can be varied according to the initial particle size of the immunolatex to be measured. Heller and Pagonis (102) optimized the particle size to the wavelength (λ) ratio in turbidimetric assay. They reported that the sharp absorbance changed during the agglutination process would be obtained when the value of the term $2\pi a/\lambda$ was in range of 1–2, where a is the particle's radius.

Polpanich et al. (103) has recently measured the absorbance change of poly (styrene-*co*-acrylic acid) (St/AA) conjugated with malaria antigen or St/AA–malaria antigen conjugate ($a = 163$ nm) as a function of concentrations of naive control and *P. falciparum*-infected plasma at wavelength 570 nm (Fig. 3.16). As can be seen, the shape of curves was similar to the immunoprecipitin curve explained by Heidelberger and Kendall (104). The curve reached the maximum value at 4.9 μg/mL when the number of antibody in individual plasma was equivalent to the amount of antigen adsorbed onto the latex surface. Meanwhile, a detection limit of the immunolatex in *P. falciparum* plasma was 0.34 μg/mL. However, in the antigen and antibody excess zones, the size of immune complexes remained small and no distinct absorbance change could be detected (103).

Although the turbidimetry measurement requires higher particle number when compared to other optical techniques, this offers the lower reaction time needed to observe the significant change of absorbance before and after the agglutination. In

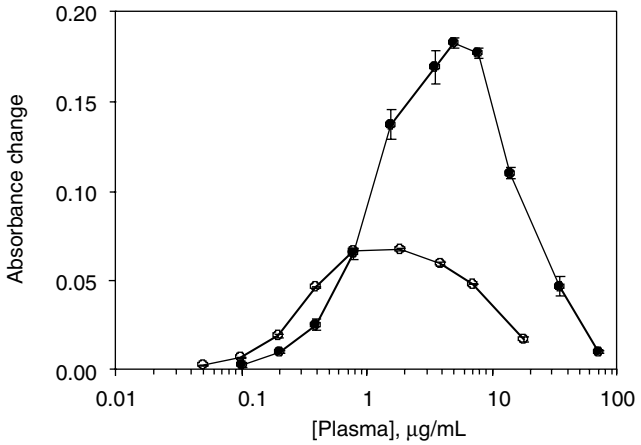

FIGURE 3.16 Absorbance changes of the St/AA–malaria antigen conjugate when mixing with various concentrations of *P. falciparum* plasma (•) and naive control (○) (103)

practice, routine clinical laboratory monitors the agglutination process for 300 s (97). The use of an automated spectrophotometer to perform particle-enhanced turbidimetric assay has also been reported (105,106). The automatic sample processing, pipetting steps, and measurements offer the advantages of being precise, easy to perform, and decreased operative time. Nishimura and Sawai (105) used PS particle immobilized with adiponectin-specific antibody to determine adiponectin in human serum using a Hitachi 7170 automated analyzer. They claimed that the detection limit of the turbidimetric assay was 0.20 μg/mL, which was comparable to the lower detection limit of commercially available enzyme-linked immunosorbent assay (ELISA) (0.28 μg/mL).

3.5.2 Nephelometry

It should be noted that the nature of immunochemical reaction is exactly the same for turbidimetry and nephelometry. However, the detection principle applied for the measurement is different from that of turbidimetry.

The nephelometry measures light scattered toward the detector, and most nephelometers measure light scattering at 90° (Fig. 3.17) (38,101). To take advantage of the increased forward scattering intensity caused by light scattering from large particle, scattered light at an angle lower than 90° is needed.

An example of nephelometer that has been specially invented to operate with LAT is the Behring Nephelometer Analyzer in which its detector is a photodiode that allows the measurement of the increment of scattered light in the forward direction at small angles (13°–24°). It is advisable that if the size of the aggregate (or the initial single particle) is increased, the smaller angle is preferred (38).

3.5.3 Photon Correlation Spectroscopy

Photon correlation spectroscopy technique, also called "dynamic light scattering," is based on the principle that the intensity of light, scattered from a latex particle when it

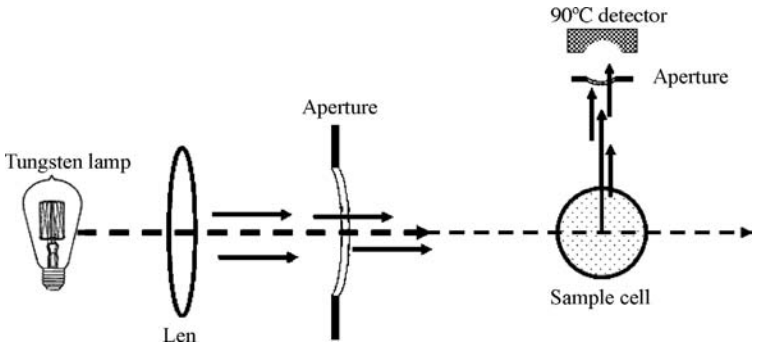

FIGURE 3.17 The basic design of nephelometer (107)

is illuminated with a laser light, fluctuates with time, depending on Brownian motion and, therefore, on the average diffusion coefficient D (38). For the spherical particle, the D value is related to the mean hydrodynamic diameter (D_h) by the Stoke–Einstein equation as shown in Equation (3.3) (96).

$$D_h = \frac{k_B T}{3\pi\eta d} \tag{3.3}$$

where k_B is Boltzman's constant (1.38×10^{-23} J/K), T is absolute temperature (K), and η is viscosity of medium (Pa s). When the immunolatex particles begin to aggregate after mixing with the analyte, the D value would be diminished due to the increase in the D_h. Figure 3.18 presents the values of D_h and D of immunoaggregates of St/AA–malaria antigen conjugate as a function of concentration of *P. falciparum*-infected plasma (108). The bell-shaped curve was noticed from the plot of D_h values of St/AA–malaria antigen conjugate versus plasma concentrations, whereas the relationship between D and plasma concentration exhibited the opposite trend. Owing to the antigen–antibody reaction, the immunoaggregates of several St/AA immunolatex particles would diffuse slower than that of the individual particles. The equivalent zone indicated from the maximum value of D_h or the minimum value of D was reached at the plasma concentration of 0.46 μg/mL. At the plasma concentration higher than 0.46 μg/mL, the system lost the immunoreactivity probably due to the saturation of the adsorbed antibody (108).

The PCS-based immunoassay generally has greater sensitivity than turbidimetric and nephelometric detection techniques. However, a longer reaction time is needed due to the reduction of particle number in the dispersion (38). Unfortunately, owing to the relatively high cost, this sophisticated and extremely delicate PCS instrument is not widely used in clinical laboratory (38,96).

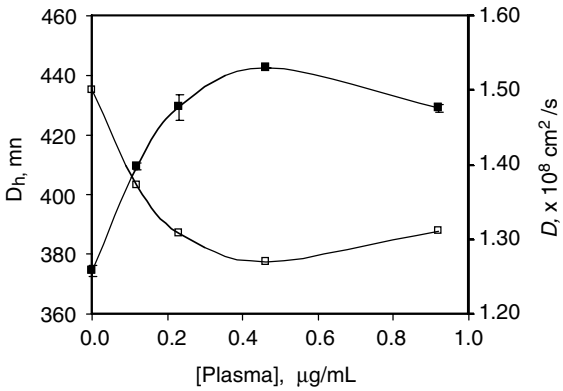

FIGURE 3.18 Hydrodynamic diameter (D_h) (■) and average diffusion coefficient (D) (□) of aggregates of the St/AA–malaria antigen conjugate as a function of *P. falciparum*-infected plasma concentration (108)

3.6 CONCLUSION

The development of prompt and accurate diagnosis is a key to effective malaria control management. Clinical diagnosis is unreliable due to nonspecific symptoms of malaria. Microscopic examination, which involves the detection of malaria parasites within red blood cells, requires expert microscopist that cannot be met, especially in remote area. The effort to replace the microscopic examination of blood smear by rapid diagnostic tests and an automated hematology analyzer is, therefore, of significant interest. While the sensitivity and specificity of RDTs and the automated hematology analyzer are rather high, the cost are still expensive and out of reach of poor, developing countries. Latex agglutination test has consequently been introduced as an alternative approach for malaria diagnosis. Not only it is quick and easy but it is also less costly, portable, and suitable for use in the field. However, further development is needed due to lack of reliable discrimination between *P. falciparum* and *P. vivax* infections. Preparation of immunolatex by immobilization of antigen (or antibody) molecule onto the latex particle surface is a very delicate process. Several factors must be cautiously controlled to finally obtain the immunolatex with high immunoreactivity. Selection of malaria antigen (or antibody) to be immobilized onto the particle is also of importance to reduce the false-positive result.

REFERENCES

1. Hoffman S. Save the children. Nature 2004;430(7002):940–941.
2. World Health Organization. The World Health Report. Geneva, 2002.
3. http://www.cdc.gov/malaria/distribution_epi/distribution.htm
4. Cowman AF, Crabb BS. A parasite genome sheds light on an old enemy. Nature Biotechnol 2002;20:1098–1099.
5. Eleanor MR, Lars H, Thor GT. *Parasitic Infections and the Immune system*. Academic Press, Inc.;1994.
6. Jones MK, Good MF. Malaria parasites up close. Nature Med 2006;12 (2):170–171.
7. Ridley RG. Medical need, scientific opportunity and the drive for antimalarial drugs. Nature 2002;415(6872):686–693.
8. International Artemisinin Study Group. Artesunate combinations for treatmen of malaria: meta-analysis. Lancet 2004;363:9–17.
9. World Health Organization. Report of a joint WHO/USAID informal consultation. New Perspectives Malaria Diagnosis. 2001.
10. World Health Organization. Meeting report of malaria rapid diagnosis: Making it work. 2003.
11. World Health Organization. Meeting report of WHO informal consultation on laboratory methods for quality assurance of malaria rapid diagnostic tests. 2004.
12. http://malaria.wellcome.ac.uk/doc_WTD023887.html
13. http://www.malariasite.com/malaria/ControlOfMalaria.htm

14. Bojang KA, Obaro S, Morison LA, Greenwood BM. A prospective evaluation of a clinical algorithm for the diagnosis of malaria in Gambian children. Trop Med Int Health 2000;5 (4):231–236.
15. Chandramohan D, Jaffar S, Greenwood B. Use of clinical algorithms for diagnosing malaria[I]. Trop Med Int Health 2002;7(1):45–52.
16. Luxemburger C, Nosten F, Kyle DE, Kiricharoen L, Chongsuphajaisiddhi T, White NJ. Clinical features cannot predict a diagnosis of malaria or differentiate the infecting species in children living in an area of low transmission. Trans R Soc Trop Med Hyg 1998;92: 45–49.
17. Moody A. Rapid diagnostic tests for malaria parasites. Clin Microbiol Rev 2002;15(1): 66–78.
18. Makler MT, Palmer CJ, Ager AL. A review of practical techniques for the diagnosis of malaria. Ann Trop Med Parasit 1998;92(4):419–433.
19. Coleman RE, Maneechai N, Rachaphaew N, Kumpitak C, Miller RS, Soyseng V, Thimasarn K, Sattabongkot J. Comparison of field and expert laboratory microscopic for active surveillance for asymptomatic *Plasmodium falciparum* and *Plasmodium vivax* in western Thailand. Am J Trop Med Hyg 2002;67(2):141–144.
20. Warhurst DC, Williams JE. Laboratory diagnosis of malaria. J Clin Pathol 1996;49: 533–538.
21. Dondorp AM, Desakorn V, Pongtavornpinyo W, Sahassananda D, Silamut K, Chotivanich K, Newton PN, Pitisuttithum P, Smithyman AM, White NJ, Day NPJ. Estimation of the total parasite biomass in acute falciparum malaria from plasma PfHRP2. Plos Med 2005;2 (8):788–797.
22. http://www.rapid–diagnostics.org/rti-malaria-com.htm
23. http://www.wpro.who.int/sites/rdt/what_is_rdt.htm
24. Grobusch MP, Alpermann U, Schwenke S, Jelinek T, Warhurst DC. False-positive rapid tests for malaria in patients with rheumatoid factor. Lancet 1999;353(9149): 297.
25. Iqbal J, Sher A, Rab A. *Plasmodium falciparum* histidine-rich protein 2-based immunocapture diagnostic assay for malaria: cross-reactivity with rheumatoid factors. J Clin Microbiol 2000;38(3):1184–1186.
26. Bartoloni A, Strohmeyer M, Sabatinelli G, Benucci M, Serni U, Paradisi F. False positive *Para*Sight™-F test for malaria in patients with rheumatoid factor. Trans R Soc Trop Med Hyg 1998;92:33–34.
27. Hanscheid T. Current strategies to avoid misdiagnosis of malaria. Clin Microbiol Infec 2003;9(6):497–504.
28. Mendelow BV, Lyons C, Nhlangothi P, Tana M, Munster M, Wypkema E, Liebowitz L, Marshall L, Scott S, Coetzer TL. Automated malaria detection by depolarization of laser light. Br J Haematol 1999;104:499–503.
29. Wever PC, Henskens YMC, Kager PA, Dankert J, van Gool T. Detection of imported malaria with the Cell-Dyn 4000 Hematology Analyzer. J Clin Microbiol 2002;40(12): 4729–4731.
30. de Langen AJ, van Dillen J, de Witte P, Mucheto S, Nagelkerke N, Kager P. Automated detection of malaria pigment: feasibility for malaria diagnosing in an area with seasonal malaria in northern Namibia. Trop Med Int Health 2006;11(6):809–816.

31. Hanscheid T, Valadas E, Grobusch MP. Automated malaria diagnosis using pigment detection. Parasitol Today 2000;16(12):549–551.
32. van Doorn HR, Hofwegen H, Koelewijn R, Gilis H, Peek R, Wetsteyn JCFM, van Genderen PJJ, Vervoort T, van Gool T. Use of rapid dipstick and latex agglutination tests and enzyme-linked immunosorbent assay for serodiagnosis of Amebic Liver Abscess, Amebic Colitis and *Entamoeba histolytica* Cyst Passage. J Clin Microbiol 2005;43 (9):4801– 4806.
33. Bänffer JRJ, van Zwol-Saarloos JA, Broere LJ. Evaluation of a commercial latex agglutination test for rapid detection of salmonella in fecal samples. Eur J Clin Microbiol Infect Dis 1993;12:633–636.
34. Hull-Jackson C, Glass MB, Ari MD, Braggs SL, Bragg SL, Branch SL, Whittington CU, Edwards CN, Levett PN. Evaluation of a commercial latex agglutination assay for serological diagnosis of leptospirosis. J Clin Microbiol 2006;44 (5):1853–1855.
35. Cruz I, Chicharro C, Nieto J, Bailo B, Canavate C, Figueras MC, Alvar J. Comparison of new diagnostic tools for management of pediatric Mediterranean visceral leishmaniasis. J Clin Microbiol 2006;44 (7):2343–2347.
36. Xu X, Jin M, Yu Z, Li H, Qiu D, Tan Y, Chen H. Latex agglutination test for monitoring antibodies to avian influenza virus subtype H5N1. J Clin Microbiol 2005;43 (4):1953–1955.
37. Smits HL, van der Hoorn MAWG, Goris MGA, Gussenhoven GC, Yersin C, Sasaki DM, Terpstra WJ, Hartskeerl RA. Simple latex agglutination assay for rapid serodiagnosis of human leptrospirosis. J Clin Microbiol 2000;38(3):1272–1275.
38. Molina-Bolivar JA, Galisteo-Gonzalez F. Latex Immunoagglutination Assays. In: Elaissari A, editor. Colloidal Biomolecules, Biomaterials, and Biomedical Applications. New York: Marcel Dekker, Inc.; 2004.
39. Gella FJ, Serra J, Gener J. Latex agglutination procedures in immunodiagnosis. Pure Appl Chem 1991;63 (8):1131–1134.
40. Bangs LB. New developments in particle-based immunoassay: introduction. Pure Appl Chem 1996;68 (10):1873–1879.
41. Musyanovych A, Adler HJP. Grafting of amino functional monomer onto initiator-modified polystyrene particles. Langmuir 2005;21:2209–2217.
42. Ouali L, Stoll S, Pefferkorn E, Elaissari A, Lanet V, Pichot C, Mandrand B. Coagulation of antibody-sensitized latexes in the presence of antigen. Polym Adv Technol 1995;6 (7):541–546.
43. Stoll S, Ouali L, Pefferkorn E. The Agglutination Test. In: Elaissari A, editor. Colloidal Biomolecules, Biomaterials, and Biomedical Applications. New York: Marcel Dekker, Inc.; 2004.
44. Pradutkanchana S, Nakarin J. The use of latex agglutination for the diagnosis of acute human leptospirosis. J Med Assoc Thai 2005;88 (10):1395–1400.
45. Kawaguchi H.Functional polymer microspheres. Prog Polym Sci 2000;25:1171–1210.
46. Ramos J, Martin-Molina A, Sanz-Izquierdo MP, Rus A, Borque L, Hidalgo-Alvarez R, Galisteo-Gonzalez F, Forcada J.Amino-functionalized latex particles obtained by a multistep method: development of a new immunoreagent. J Polym Sci A: Polym Chem 2003;41:2404–2411.
47. Gasparyan VK. Preparation and sensitization of polystyrene latex beads by some antigens and antibodies. Factors affecting sensitivity and specificity of latex agglutination tests. J Immunoassay Immunochem 2002;23(3):399–406.

48. Rosado E, Caroll H, Sanchez O, Peniche C. Passive adsorption of human antirrabic immunoglobulin onto a polystyrene surface. J Biomater Sci Polymer Edn 2005;16 (4):435–448.
49. Radomska-Galant I, Basinska T. Poly(styrene/α-*tert*-butoxy-ω-vinylbenzyl-polygylcidol) microspheres for immunodiagnositcs. Principle of a novel latex test based on combined electrophoretic mobility and particle aggregation measurements. Biomacromolecules 2003;4:1848–1855.
50. Chern CS. Emulsion polymerization mechanisms and kinetics. Prog Polym Sci 2006;31 (5):443–486.
51. Gilbert RG. *Emulsion Polymerization: A Mechanistic Approach*. London: Academic press; 1995.
52. Gardon JL. Emulsion polymerization. In: Schildknecht CE, editor (with Skeist I). Polymerizaton Processes. New York: Wiley Interscience; 1977.
53. Sugiyama K, Ohga K, Kikukawa K. Preparation of surface-modified polystyrene microspheres by an azo-initiator having analogous structure to the head group of phosphatidylcholine. Macromol Chem Phys 1994;195(4):1341–1352.
54. Matsumoto T, Ochi A. Polymerization of styrene in aqueous solution. Kobunshi Kagaku 1965;22(244):481–487.
55. Priest WJ. Particle growth in the aqueous polymerization of vinyl acetate. J Phys Chem 1952;56:1077–1083.
56. Roe CP. Surface chemistry aspects of emulsion polymerization. Ind Eng Chem 1968; 60:20–33.
57. Fitch RM, Tsai CH. Homogeneous nucleation of polymer colloids, IV: The role of soluble oligomeric radical. In: Fitch RM, editor. Polymer Colloids. New York: Plenum Press; 1971.
58. Tauer K, Kuhn I. Modeling particle formation in emulsion polymerization: An approach by means of the classical nucleation theory. Macromolecules 1995;28:2236–2239.
59. Kuhn I, Tauer K. Nucleation in emulsion polymerization: a new experimental study. 1. Surfactant-free emulsion polymerization of styrene. Macromolecules 1995;28:8122–8128.
60. Polpanich D, Tangboriboonrat P, Elaissari A. The effect of acrylic acid amount on the colloidal properties of polystyrene latex. Colloid Polym Sci 2005;284:183–191.
61. Wang PH, Pan CY. Emulsion copolymerization of styrene with acrylic acid or methacrylic acids-distribution of the carboxylic group. Colloid Polym Sci 2001;279:98–103.
62. Wang C, Yang W, Fu S. Functionalization of Colloidal Particles. In: Elaissari A, editors. Colloidal Polymers: Synthesis and Characterization. New York: Marcel Dekker, Inc.; 2003.
63. Yan C, Cheng S, Feng L. Kinetics and mechanism of emulsifier-free emulsion copolymerization: Styrene-methyl methacrylate-acrylic acid system. J Polym Sci A: Polym Chem 1999;37:2649–2656.
64. Ceska GW. The effect of carboxylic monomers on surfactant-free emulsion copolymerization. J Appl Polym Sci 1974;18(2):427–437.
65. Konings BLJC, Pelssers EGM, Verhoeven AJCM, Kamps KMP. Covalent coupling of antibodies to hydrophilic core-shell particles. Colloids Surf B 1993;1(2):69–73.
66. Okubo M, Yamamoto Y, Uno M, Kamei S, Matsumoto T. Immunoactivity of polymer microspheres with their hydrophilic/hydrophobic heterogeneous surface sensitized with an antibody. Colloid Polym Sci 1987;265(12):1061–1066.

67. Ortega-Vinuesa JL, Bastos-Gonzalez D. A review of factors affecting the performances of latex agglutination tests. J Biomater Sci Polym Edn 2001;12(4):379–408.
68. Molina-Bolivar JA, Galisteo-Gonzalez F, Hidalgo-Alvarez R. Latex immunoassays: Comparative studies on covalent and physical immobilization of antibodies. I. F(ab') 2 fragments. J Biomater Sci Polym Edn 1998;9(10):1089–1101.
69. Norde W, Lyklema J. Why proteins prefer interfaces. J Biomater Sci Polym Edn 1991;2:183–202.
70. Haynes CA, Norde W. Globular proteins at solid/liquid interfaces. Colloid Surf B 1994;2 (6):517–566.
71. Yoon JY, Park HY, Kim JH, Kim WS. Adsorption of BSA on highly carboxylated microspheres-quantitative effects of surface functional groups and interaction forces. J Colloid Interface Sci 1996;177:613–620.
72. Shirahama H, Suzuki K, Suzawa T. Bovine hemoglobin adsorption onto polymer latices. J Colloid Interface Sci 1989;129(2):483–490.
73. Kondo A, Higashitani K. Adsorption of model proteins with wide variation in molecular properties on colloidal particles. J Colloid Interface Sci 1992;150(2):344–351.
74. Lewin S. Displacement of Water and Its Control of Biochemical Reactions. New York: Academic Press; 1974.
75. Ortega-Vinuesa JL, Bastos-Gonzalez D, Hidalgo-Alvarez R. Comparative studies on physically adsorbed and chemically bound IgG to carboxylated latexes, II. J Colloid Interface Sci 1995;176(1):240–247.
76. Arai T, Norde W. The behavior of some model proteins at solid-liquid interfaces 1. Adsorption from single protein solutions. Colloids Surf 1990;51:1–15.
77. ULTROGEL®, MAGNOGEL® and TRISACRYL®, Practical guide for use in affinity chromatography and related techniques, 2nd ed., Réactifs IBF-Société Chimique Pointet-Girard,1983.
78. Bastos-Gonzalez D, Ortega-Vinuesa JL, de las Nieves FJ, Hidalgo-Alvarez R. Carboxylated Latexes for Covalent Coupling Antibodies, I. J Colloid Interface Sci 1995;176 (1):232–239.
79. Charleux B, Fanget P, Pichot C. Radical-initiated copolymers of styrene and p-formylstyrene, 2. Preparation and characterization of emulsifier-free copolymer latexes. Makromol Chem 1992;193(1):205–220.
80. Peula JM, Hidalgo-Alvarez R, de las Nieves FJ. Covalent binding of proteins to acetal-functionalized latexes. I. Physics and chemical adsorption and electrokinetic characterization. J Colloid Interface Sci 1998;201(2):132–138.
81. Peula JM, Hidalgo-Alvarez R, de las Nieves FJ. Covalent binding of proteins to acetal-functionalized latexes. II colloidal stability and immunoreactivity. J Colloid Interface Sci 1998;201(2):139–145.
82. Ho CH, Limberis L, Caldwell KD, Stewart RJ. A methyl-chelating Pluronic for immobilization of histidine-tagged proteins at interfaces: immobilization of firefly luciferase on polystyrene beads. Langmuir 1998;14:3889–3894.
83. Li JT, Carlsson J, Lin JN, Caldwell KD. Chemical modification of surface active poly (ethylene oxide)-poly(propylene oxide) triblock copolymers. Bioconjug Chem 1996;7:592–599.
84. TechNote 201. Working with microspheres. Bang Laboratories, Inc.

85. Bangs LB. Particle-based tests and assays-pitfalls and problems in preparation. Am Clin Lab 1990;9(4):16–17.
86. Kawaguchi H, Duracher D, Elaissari A. Interaction of Proteins with Thermally Sensitive Particles. In: Elaissari A, editor. Colloidal Biomolecules, Biomaterials, and Biomedical Applications. New York: Marcel Dekker; Inc.; 2004.
87. Duracher D, Veyret R, Elaissari A, Pichot C. Adsorption of bovine serum albumin onto amino-containing thermosensitive core-shell latexes. Polym Int 2004;53:618–626.
88. Lee SH, Ruckenstein E. Adsorption of proteins onto polymeric surfaces of different hydrophilicities–a case study with bovine serum albumin. J Colloid Interf Sci 1988;125 (2):365–379.
89. Kawaguchi H, Fujimoto K, Mizuhara Y. Hydrogel microspheres III. Temperature-dependent adsorption of proteins on poly-N-isopropyl-acrylamide hydrogel microspheres. Colloid Polym Sci 1992;270:53–57.
90. Vermeer AWP, Giacomelli CE, Norde W. Adsorption of IgG onto hydrophobic teflon. Differences between the F_{ab} and F_c domains. Biochimica et Biophysica Acta 2001;1526:61–69.
91. Serra J, Puig J, Martin A, Galisteo F, Galvez MaJ, Hidalgo-Alvarez R. On the adsorption of IgG onto polystyrene particles: Electrophoretic mobility and critical coagulation concentration. Colloid Polym Sci 1992;270:574–583.
92. Soderquist ME, Walton AG. Structure changes in protein adsorbed on polymer surfaces. J Colloid interf Sci 1980;75(2):386–397.
93. Puskas JE, Dahman Y, Margaritis A. Novel thymine-functionalized polystyrenes for applications in biotechnology. 2. adsorption of model proteins. Biomacromolecules 2004;5:1412–1421.
94. Suzawa T, Shirahama H. Adsorption of plasma proteins onto polymer latices. Adv Colloid Interface Sci 1991;35:139–172.
95. Guo X, Weiss A, Ballauff M. Synthesis of spherical polyelectrolyte brushes by photoemulsion polymerization. Macromolecules 1999;32:6043–6046.
96. Ortega-Vinuesa JL, Molina-Bolivar JA, Peula JM, Hidalgo-Alvarez R. A comparative study of optical techniques applied to particle-enhanced assays of C-reactive protein. J Immunol Methods 1997;205:151–156.
97. Ortega-Vinuesa JL, Molina-Bolivar JA, Hidalgo-Alvarez R. Particle enhanced immunoaggregation of $F(ab')_2$ molecules. J Immunol Methods 1996;190:29–38.
98. Quesada M, Puig J, Delgado JM, Peula JM, Molina JA, Hidalgo-Alvarez R. A simple kinetic model of antigen-antibody reactions in particle-enhanced light scattering immunoassays. Colloid Surf B 1997;8:303–309.
99. Molina-Bolivar JA, Galisteo-Gonzalez F, Quesada-Perez M, Hidalgo-Alvarez R. Agglutination kinetics of $F(ab')_2$ coated polymer colloids. Colloid Polym Sci 1998;276:1117–1124.
100. Bangs LB. New developments in particle-based tests and immunoassays. JIFCC 1990;2 (4):188–193.
101. Technical series: Turbidimetry. Tulip Group, TULIP DIAGNOSTICS (P) LTD.
102. Heller W, Pangonis WJ. Theoretical investigations on the light scattering of colloidal spheres. I. The specific turbidity. J Chem Phys 1957;26(3):498–506.

103. Polpanich D, Tangboriboonrat P, Elaissari A, Udomsangpetch R. Rapid detection of malaria infection via Immunological agglutination assay. Anal Chem 2007;79(12):4690–4695.

104. Steward MW. Immunological Techniques. In: Roitt I, Brostoff J, Male D, editors, Immunology. 6th ed.London: Mosby; 2001.

105. Nishimura A, Sawai T. Determination of adiponectin in serum using a latex particle–enhanced turbidimetric immunoassay with an automated analyzer. Clin Chim Acta 2006;371:163–168.

106. Guaita S, Simo JM, Ferre N, Joven J, Camps J. Evaluation of a particle-enhanced turbidimetric immunoassay for the measurment of immunoglobulin E in an ILab 900 analyzer. Clin Chem 1999;45(9):1557–1561.

107. Sadar M.Introduction to laser nephelometry: an alternative to conventional particulate analysis methods, Hach company, 1999.

108. Polpanich D. Latex-Peptide Conjugates for Diagnosis of Malaria Infection. Ph.D. Thesis, Mahidol University, 2007.

CHAPTER 4

Antigen-Antibody Interactions Detected by Quasi-Elastic Light Scattering and Electrophoretic Mobility Measurements—A New Concept for Latex Immunodiagnostic Test

TERESA BASINSKA AND STANISLAW SLOMKOWSKI

Center of Molecular and Macromolecular Studies, Polish Academy of Sciences, Sienkiewicza 112, 90-363 Lodz, Poland

4.1 INTRODUCTION

Chapter provides a short summary of information on most common traditional diagnostic tests based on polymer nano- and microparticles used as a main reagent. Subsequently there are discussed ideas of diagnostic tests based on the changes of properties of isolated microspheres exposed to contact with analytes. Synthesis and brief characteristics of poly(styrene/α-*tert*-butoxy-ω-vinylbenzyl-polyglycidol) microspheres (P(S/PGL))—a new type of particles with interfacial properties tailored for application in medical diagnostics are described. Diameters of P(S/PGL) particles were in the range from 220 to 650 nm, depending on fraction of polyglycidol in their interfacial layer. These particles are suitable for easy and efficient covalent immobilization of proteins with elimination of undesirable and not controlled protein adsorption. Particles with swelling polyglycidol layer, containing covalently immobilized antibodies (antigens), exposed to contact with biological fluids containing complementary antigens (antibodies) should change their electrophoretic mobility, diameters (due to change of the degree of swelling of interfacial layer) and may aggregate due to the multipoint antigen-antibody interactions. Design of a new type of diagnostic tests based on combination of changes of electrophoretic mobility and changes of average size of particles (primary particles

Colloidal Nanoparticles in Biotechnology, Edited by Abdelhamid Elaissari
Copyright © 2008 John Wiley & Sons, Inc.

and their aggregates) is described. Principles of assays for determination of anti-HSA and anti-*H. pylori* in blood sera are also presented—assays especially sensitive at low analyte concentrations.

4.2 INSTEAD OF INTRODUCTION—TRADITIONAL DIAGNOSTIC TESTS WITH MICROSPHERES USED AS BASIC COMPONENT

Important class of diagnostic tests is based on recognition systems developed by nature. Namely, in bodies of vertebrates, in particular mammals, there are specific antibodies present—proteins named immunoglobulins, constituting an important component of defense system protecting organism against invasion of viruses, bacteria, fungi, as well as potentially harmful macromolecules. The simplest immunoglobulin—immunoglobulin G (IgG)—is built from four polypeptide chains; two long (heavy) and two short (light) linked together by disulfide bridges (1). In every molecule of IgG there are two sites able to bind complementary "foreign" macromolecule. In every organism there is a large variety of IgG types with various binding sites suitable for specific binding potentially harmful invading molecules. Similar functions are fulfilled by the more complex immunoglobulins resembling dimers and pentamers of IgG (IgE and IgM). Structures of immunoglobulins are schematically shown in Fig. 4.1.

Introduction to an animal organism of molecules (antigens—an acronym from *anti*body *gen*erator) results in increased production of specific antibodies. This process named immunization allows for a relatively simple production of immunoglobulins suitable for specific binding selected molecules, viruses or cells. Isolation of appropriate immunoglobulins from animal blood samples provides specific elements for various diagnostic tests.

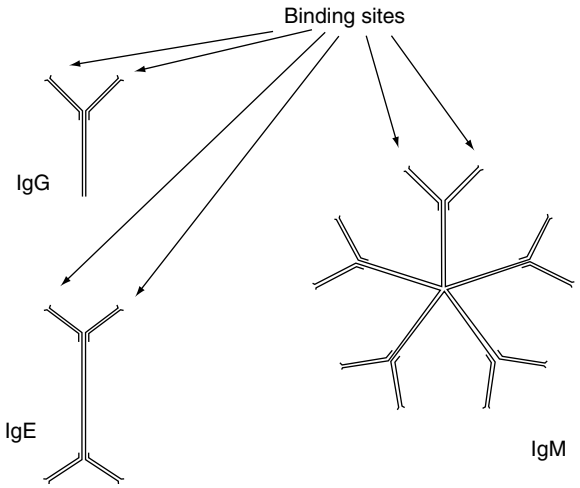

FIGURE 4.1 Schematic structure of immunoglobulins: IgG, IgE, and IgM

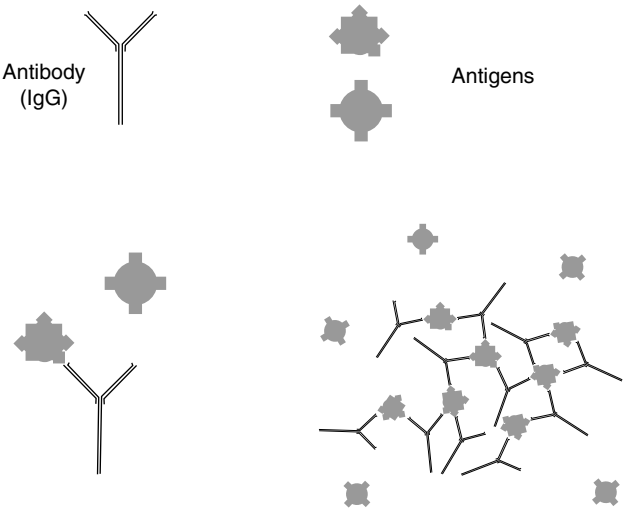

FIGURE 4.2 Schematic illustration of specific binding of complementary antibodies by IgG leading to formation of macromolecular aggregates

Following events occur when antigens are added to solution containing immunoglobulins. First, antigens are bound to binding sites of antibodies; then, in case of antigens with more than one recognition site, binding of other antibodies results in the formation of macromolecular aggregates. The described above processes are illustrated in Fig. 4.2.

It is worth noting that antigen–antibody interactions are highly specific. Antibodies that do not fit to immunoglobulin binding centers are essentially not bound whereas the equilibrium constant of binding the complementary ones is very high (in a range from 10^6 to 10^8 mol/L (2)). Thus, a diagnostic test detected toward detection of a given compound is based on observation of binding its molecules with appropriate immunoglobulins or on formation of relevant macromolecular aggregates. Direct observation of these events is very difficult due to very small size of these objects dissolved or suspended (in case of aggregates) in a "soup" of analyzed liquid, which usually also contain many other proteins, carbohydrates, and other molecules. However, more than 50 years ago it was found that by binding immunoglobulins to polymeric microspheres (polymeric particles with diameters from about 0.1 to 100 μm), there is possible better visualization of these events. Simply, aggregates of microspheres with immobilized IgG that occur in the presence of complementary antibodies (see Fig. 4.3) are much larger and scatter visible light much more efficiently than macromolecular aggregates.

In spite of many years passed from the development in 1956 of the first diagnostic test based on aggregation of microspheres (3) (often called *latex tests* after the term latex used for suspensions of microspheres in liquid), the new tests of this type are still being developed due to their attractive simplicity and short time of analysis.

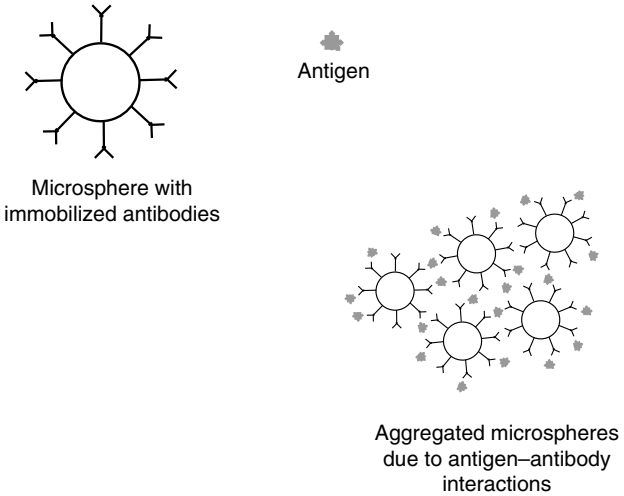

FIGURE 4.3 Formation of aggregates of microspheres bearing immobilized IgG that occurs in presence of complementary antibodies

Aggregation of microspheres can be observed even by naked eye or determined quantitatively by such techniques like turbidimetry or nephelometry (4), Coulter counter (5), and flow cytometry (6–8). The latter method allows discrimination between original particles and aggregates composed of 2, 3, and more parent particles (9). Degree of aggregation is quantified by determination of size distribution of individual particles and their aggregates (10).

Many efforts are directed toward increasing sensitivity of tests and decrease time needed for analysis. It has been found, for example, that an exposure of a mixture containing microspheres with immobilized immunoglobulins and complementary antigens to ultrasonic waves (11,12) or to alternating electric current (13) significantly reduces aggregation time and increases test sensitivity (aggregation occurs at lower antigen concentration).

Addition of appropriate additives to analyzed sample can also increase the sensitivity of latex immunoassay. For example, the addition of cationic surfactant, tetramethylammonium hydroxide, significantly increased aggregation rate, and sensitivity of test for C-reactive protein (CRP) (14).

Aggregation latex tests are sometimes preferred over other biochemical techniques like enzyme linked immunosorbent assay (ELISA). ELISA consists of few steps of analysis and requires separation of antigen–antibody complexes from the medium. After separation of not bound species during the washing step, the amount of analyte (antigen/antibody) is determined using specific antibodies conjugated with enzymes converting colorless or not fluorescent substrates to the colored or fluorescent ones. Aggregation latex tests are much simpler and faster. For example, determination of morphine in urine performed by ELISA lasts for 90 min, similar determination by latex

aggregation test needed only 20 min (15). Both tests gave close results for similar range of morphine concentration in urine.

In some instances a combination of ELISA and latex aggregation test was developed in order to increase sensitivity of analysis. Bowden et al. elaborated a turbidimetric agglutination-inhibition test allowing for detection of smooth lipopolysaccharide (S-LPS) content in *Brucella* cells. The cell lysates were adsorbed in flat bottom multiwell plates and incubated with specific antibodies against S-LPS. The amount of bound antibodies was determined by ELISA assay whereas, the amount of the unbound antibody was determined by aggregation of S-LPS-coated particles carried on in presence of rheumatoid factor added with purpose to enhance aggregation. Fraction of aggregated particles was estimated spectrophotometrically by measuring the difference between absorbance at 405 nm for the sample of not aggregated particles (blank) and the analyzed one containing aggregated particles (16).

An interesting principle of diagnostic test consists on using polyester plates with surfaces covered with antibodies and magnetic microparticles with bound antibodies of the same type (17). Polyester plate is placed at the bottom of a vessel containing suspension of magnetic microspheres with immobilized antibodies. Addition of a sample containing antigens complementary to antibodies immobilized on the polyester disk and on microspheres results in binding microspheres to the disk via antigen-antibody interactions (disk-antibody· · · · ·antigen· · · · ·antibody-microsphere). Presence and quantification of magnetic miscrospheres is detected by determination of resonance frequency of electric current in a small coil placed just below the vessel containing the polyester disk.

4.3 PRINCIPLES OF DIAGNOSTIC TESTS BASED ON PROPERTIES OF ISOLATED MICROSPHERES

Tests described in the previous section were based on aggregation of microspheres or on their binding to solid supports that occurs in presence of detected antigens. However, one should take into consideration a possibility of another class of diagnostic tests. Namely, tests based on changes of properties of single microspheres with immobilized antibodies, that occur upon binding antigens and, if needed, other reagents added to the mixture. For example, binding of antigens to microspheres with antibodies, followed by binding antibodies labeled with fluorescent tags results in the formation of fluorescent microspheres (microsphere-antibody· · · · ·antigen· · · · ·antibody-fluorophore) that may be detected using various spectroscopic techniques (18,19) Fig. 4.4.

Systems composed of mixtures of microspheres (each type of particles specifically marked with fluorophores and each type bearing antibodies against particular antigens) and antibodies labeled with another fluorophores were used for development of multiplex cytometric assays allowing for simultaneous determination of several (in some instances up to 60) antigens (20–22).

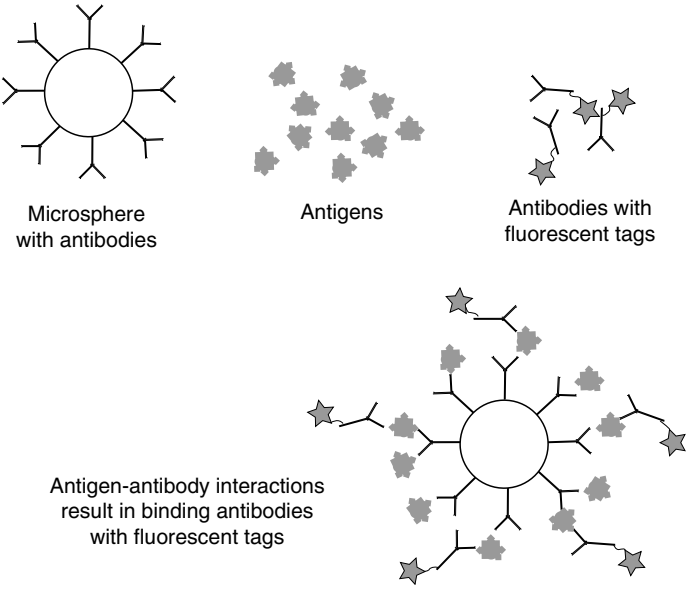

FIGURE 4.4 Formation of fluorescent microspheres (microsphere-antibody· · · · ·antigen · · · · ·antibody-fluorophore)

Many types of antigens are polyelectrolytes (e.g., proteins, oligopeptides, nucleic acids, and oligonucleotides). Thus, attachment of these compounds to microspheres should change particles' charge and in effect their behavior in electric field, in particular, their electrophoretic mobility (see Fig. 4.5). These changes may be used as a principle of diagnostic tests described in the following part of this chapter.

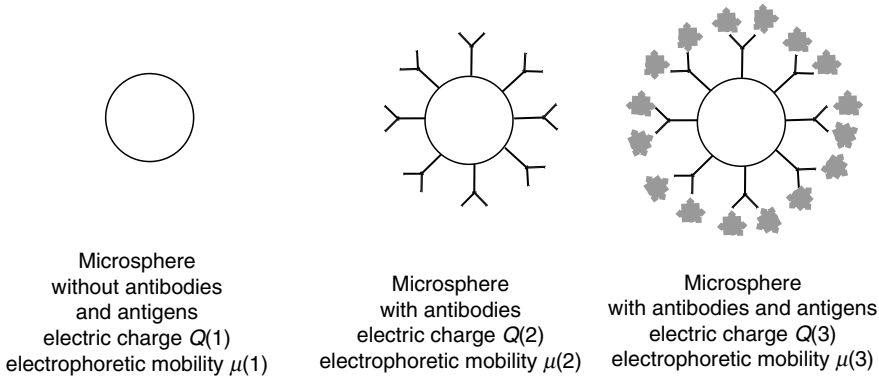

FIGURE 4.5 Microspheres (bare, with immobilized antibodies and with immobilized antibodies and attached antigens) with different electric charge (Q) and electrophoretic mobility (μ)

4.4 MICROSPHERES FOR APPLICATION IN DIAGNOSTIC ASSAYS BASED ON CHANGES OF PARTICLES' ELECTROPHORETIC MOBILITY

Microspheres used for diagnostic assays based on changes of particles' electrophoretic mobility, should allow for controlled, specific, and irreversible binding of proteins (antibodies or antigens). Thus, these properties are in principle the same as for microspheres used in other diagnostic tests. Specificity is needed to avoid an adventitious attachment of another proteins present in the analyzed mixture that would result in an interference in detection of the searched analyte. Irreversibility eliminates an uncontrolled detachment of antigens or antibodies from microspheres during storage, before using them in assays.

The above mentioned properties characterize microspheres with hydrophilic interfacial layer containing chemical groups allowing for covalent immobilization of proteins. It was established that the hydrophilic interfacial layer eliminates (or at least reduces) the nonspecific adsorption of proteins (23). Particles with hydrophilic interfacial layer could be obtained either by emulsion or dispersion homo- or copolymerization of such hydrophilic monomers as 2-hydroxyethylmethacrylate and acrylic acid (24), acrolein (25), *N*,*N*-isopropylacrylamide (26) or by copolymerization of hydrophobic monomers (e.g., styrene) with hydrophilic monomers: acrolein (25), poly(ethylene oxide) macromonomers (26,27), surface active monomers with sugar moiety, or polysaccharide containing macromonomers (28–33). Particles with hydrophilic surfaces could also be obtained by grafting hydrophilic chains from hydrophobic particles (e.g., by grafting poly(acrylic acid) from polystyrene particles with *p*-(2-hydroxy-2-methylpropiophenone) groups in the shell (34)).

Recently, there was developed synthesis of poly(styrene/α-*tert*-butoxy-ω-vinylbenzyl-polyglycidol) microspheres with core enriched in polystyrene and a shell enriched in hydrophilic polyglycidol (35). These microspheres were used for development of diagnostic assays based on monitoring both, changes of electrophoretic mobility and aggregation occurring in presence of searched analytes.

4.5 SYNTHESIS AND BASIC PROPERTIES OF POLY(STYRENE/α-*TERT*-BUTOXY-ω-VINYLBENZYL-POLYGLYCIDOL) MICROSPHERES

P(S/PGL) microspheres were obtained by emulsifier-free emulsion-dispersion copolymerization of styrene and α-*tert*-butoxy-ω-vinylbenzyl-polyglycidol macromonomer (35). α-*tert*-Butoxy-ω-vinylbenzyl-polyglycidol macromonomer(VB-polyGL) was synthesized by anionic polymerization of 1-ethoxyethylglycidyl ether with subsequent end-capping with *p*-choromethylstyrene. 1-Ethoxyethylglycidyl ether was obtained according to the procedure developed by Fitton et al (36). Reactions leading to P(S/PGL) microspheres are illustrated in Schemes 4.1– 4.5.

Typical synthesis of P(S/PGL) microspheres is given below. Briefly, microspheres were synthesized by using styrene (10 g), α-*tert*-butoxy-ω-vinylbenzyl-polyglycidol macromonomer (1.0 g, $\overline{M}_n = 2700$, $\overline{M}_w/\overline{M}_n = 1.03$), and $K_2S_2O_8$ initiator (0.2 g) in

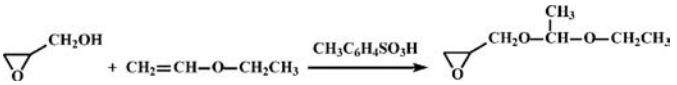

SCHEME 4.1 Protection of hydroxyl group in glycidol

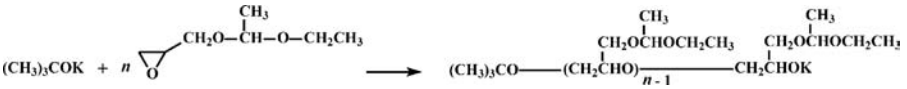

SCHEME 4.2 Synthesis of poly(1-ethoxyethylglycidyl ether)

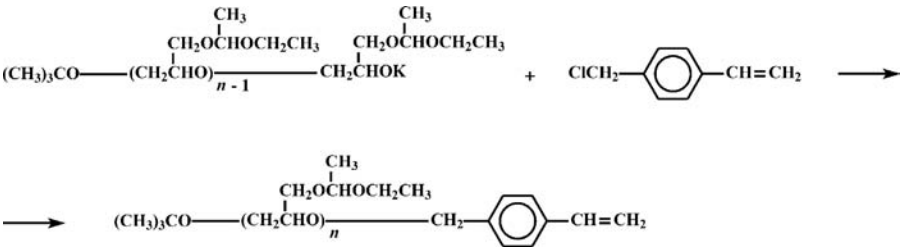

SCHEME 4.3 Synthesis of α-*tert*-butoxy-ω-vinylbenzyl-poly(1-ethoxyethylglycidyl ether) macromonomer

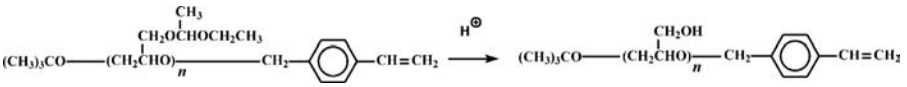

SCHEME 4.4 Deblocking of hydroxyl groups in α-*tert*-butoxy-ω-vinylbenzyl-poly(1-ethoxyethylglycidyl ether) macromonomer

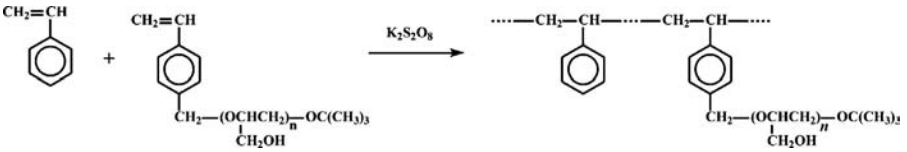

SCHEME 4.5 Emulsion copolymerization of styrene and α-*tert*-butoxy-ω-vinylbenzyl-polyglycidol macromonomer yielding microspheres

water (125 ml, three-times distilled, pH adjusted to 6.5 by addition of K_2CO_3). Polymerization was carried on for 24 h at 65°C, content was stirred at 60 rpm. The synthesized microspheres were purified by steam stripping and four times repeated isolation by centrifugation and resuspension in pure water. Particles with diameters in a range from 220 to 650 nm were obtained, depending on styrene:α-*tert*-butoxy-ω-vinylbenzyl-polyglycidol macromonomer ratio in the monomer mixture at the beginning of polymerization. Number average diameters ($\overline{\mathbf{D}}_\mathbf{n}$), diameter dispersity parameter ($\overline{\mathbf{D}}_\mathbf{w}/\overline{\mathbf{D}}_\mathbf{n}$) and surface concentration of acidic groups [SO_4^-] (polymer end-groups formed during initiation) are given in Table 4.1.

Interfacial layer of all P(S/PGL) microspheres was strongly enriched in hydrophilic polyglycidol units. This is evident from Table 4.2 showing relation between molar ratio of polyglycidol and polystyrene units in microspheres and in the microsphere interfacial layer.

Segmental mobility of polyglycidol chains in interfacial layer of microspheres dispersed in water is so high that allows registration of its ^{13}**C** NMR spectra at conditions typical for registration of spectra in solution. Even more, measurements of relaxation times for polyglycidol incorporated into interfacial layer of particles and for parent polyglycidol macromonomer in solution revealed that segmental mobilities of polyglycidol chains were very close in these environments (37).

Adsorption of proteins onto particles with interfacial layer rich in hydrophilic and highly mobile polyglycidol chains should be very weak. Indeed, it has been found that for human serum albumin, human γ-globulins, and human fibrinogen adsorbed onto P(S/PGL) microspheres the adsorption equilibrium constant K_A approaches 0 when fraction of polyglycidol units in interfacial layer exceeds 0.3.

Much weaker adsorption of proteins onto P(S/PGL) microspheres than onto hydrophobic polystyrene particles is evident from comparison of adsorption adiabates of human serum albumin (HSA) onto these particles (see Fig. 4.6).

Presence of polyglycidol in interfacial layer of microspheres strongly reduces adsorption of proteins; however, the same particles upon activation with

TABLE 4.1 Number Average Diameters ($\overline{D}_n$), Diameter Dispersity Parameter ($\overline{D}_w/\overline{D}_n$) and Surface Concentration of Acidic Groups for P(S/PGL) Microspheres (Particles Obtained Using VB-polyGL Macromonomer ($\overline{M}_n = 2700$, $\overline{M}_w/\overline{M}_n = 1.03$). Reproduced from Reference 35 with kind permission of Springer Science and Business Media.

Symbol of particles	Styrene:VB-polyGL in monomer feed (mol:mol)	$\overline{D}_n$, nm	$\overline{D}_w/\overline{D}_n$	Surface concentration of acidic groups [SO_4^-], mol/m^2
2700-1	$1:3.46 \times 10^{-4}$	650	1.008	1.65×10^{-6}
2700-2	$1:6.94 \times 10^{-4}$	460	1.014	1.05×10^{-6}
2700-3	$1:1.73 \times 10^{-3}$	350	1.007	8.77×10^{-7}
2700-4	$1:2.60 \times 10^{-3}$	260	1.007	4.85×10^{-7}
2700-5	$1:3.47 \times 10^{-3}$	220	1.022	4.13×10^{-7}

TABLE 4.2 Molar Ratio of Polyglycidol and Polystyrene Units in Microspheres and in the Microspheres Interfacial Layer—Microspheres Obtained Using VB-PolyGL Macromonomer ($\overline{M}_n = 2700$, $\overline{M}_w/\overline{M}_n = 1.03$). Based on data from Reference 35.

Fraction of polyglycidol units in microspheres	Fraction of polyglycidol units in interfacial layer of microspheres
0.019	0.216
0.0215	0.334
0.0235	0.255
0.0459	0.423
0.0620	0.426

trichlorotriazine (see Scheme 4.6) are suitable for efficient covalent immobilization of these biomolecules.

Immobilization carried on according to the described above scheme allowed obtaining particles with surface concentration of immobilized proteins close to few mg/m^2. Dependence of surface concentration of human γ-globulin (γG) immobilized covalently onto P(S/PGL) microspheres ($\Gamma_{\gamma G}$) on concentration of γG in solution is shown in Fig. 4.7.

Very often covalent immobilization of proteins is accompanied with physical adsorption of some protein molecules (38). Thus, there is a fraction of attached protein

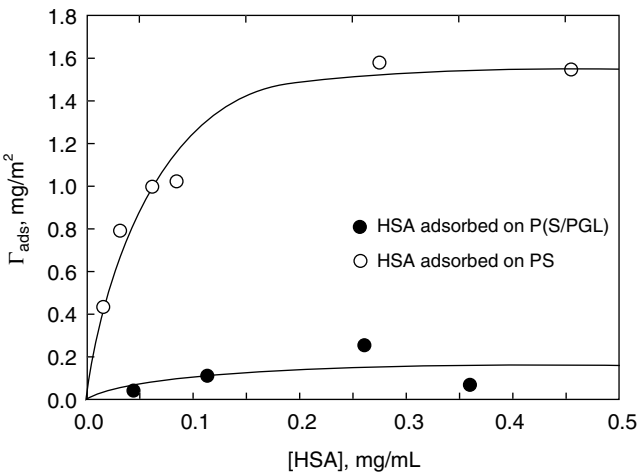

FIGURE 4.6 Surface concentration of HSA adsorbed onto P(S/PGL) and polystyrene microspheres as a function of HSA concentration in solution. Reproduced with permission from Reference 37

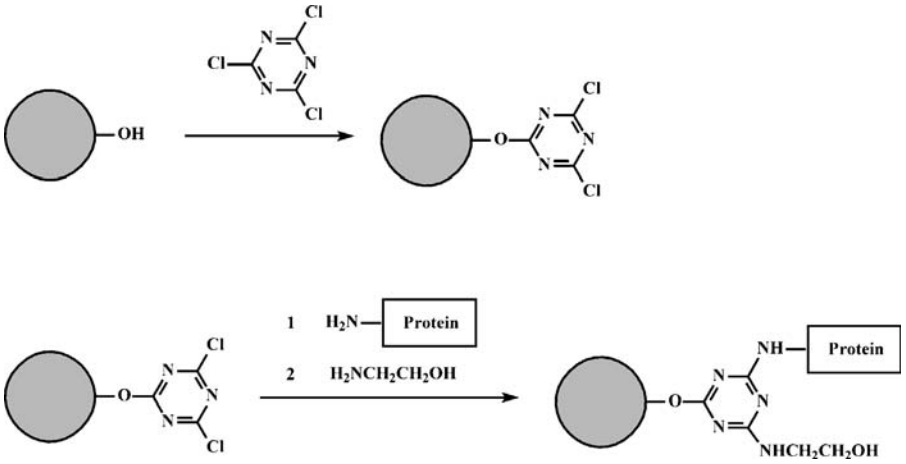

SCHEME 4.6 Covalent immobilization of proteins on P(S/PGL) microspheres activated with 1,3,5-trichlorotriazine (TCT; cyanuric chloride).

that during storage or under action of surface active compounds would leak from particles' surface to solution.

It is important to stress that P(S/PGL) microspheres are an exception and, as one could see in Fig. 4.8, the whole amount of protein bound to 1,3,5-trichlorotriazine activated particles is immobilized covalently.

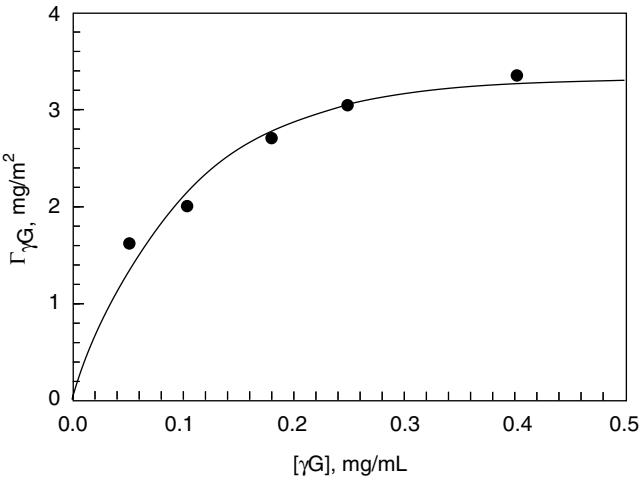

FIGURE 4.7 Dependence of surface concentration of γG covalently immobilized onto P(S/PGL) microspheres obtained using VB-polyGL macromonomer ($\overline{M}_n = 2700$, $\overline{M}_w/\overline{M}_n = 1.03$) on protein concentration in solution. Reproduced with permission from Reference 38

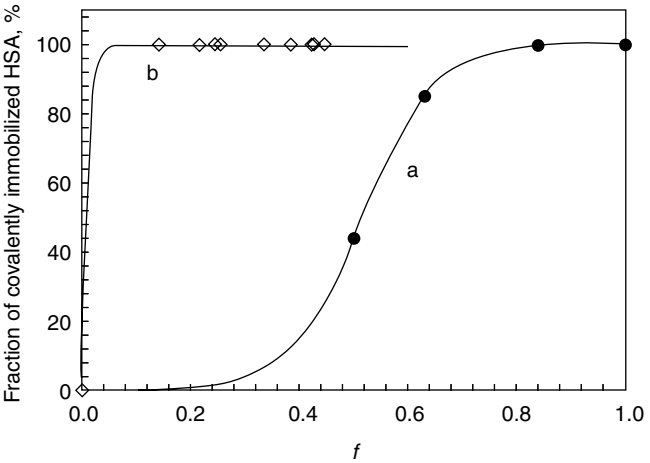

FIGURE 4.8 Fraction of covalently immobilized HSA as a function of molar fraction of polyacrolein (a) or polyglycidol (b) units in interfacial layer of poly(styrene/acrolein) (P(S/A)) and P(S/PGL) microspheres. Reproduced with permission from Reference 39

4.6 NOVEL DIAGNOSTIC TESTS BASED ON POLY(STYRENE/α-*TERT*-BUTOXY-ω-VINYLBENZYLPOLYGLYCIDOL) MICROSPHERES

Following events may happen when poly(styrene/α-*tert*-butoxy-ω-vinylbenzylpolyglycidol) microspheres with covalently immobilized antibodies (or antigens) are exposed to biological fluid containing complementary antigens (or antibodies):

1. Electrical charge and relevant electrophoretic mobility of microspheres is changed
2. Diameter of particles may change due to variation of swelling of hydrophilic interfacial layer upon attachment of antigen (or antibody)
3. Aggregates of microspheres are formed due to bridging microspheres with immobilized antibodies (or antigens) by complementary antigens (or antibodies)

Combination of these events could be used as a basis for design of diagnostic tests.

4.6.1 Principle of a Model Immunodiagnostic Assay for Anti-HSA

Poly(styrene/α-*tert*-butoxy-ω-vinylbenzylpolyglycidol) microspheres with covalently immobilized human serum albumin were used as the main reagent in the title test. Immobilization of HSA onto microspheres was performed in the following way.

Usually, 0.18 g of 1,3,5-trichlorotriazine (TCT) was added to 5 ml of aqueous suspension containing 0.4 g of P(S/PGL) microspheres (particles obtained using

VB-polyGL macromonomer with $\overline{M}_n = 2700$, $\overline{M}_w/\overline{M}_n = 1.03$); ($\overline{D}_n = 220$ **nm**, $\overline{D}_w/\overline{D}_n = 1.022$, fraction of polyglycidol units in particles' interfacial layer 0.426). The sample was incubated for 5 h at room temperature. Then, microspheres were isolated from suspension by centrifugation and resuspended in a new portion of water. The process of centrifugation and resuspension was repeated three times more. Eventually, microspheres were transferred to phosphate buffered saline (PBS, 0.2 mol/L, pH = 7.4). After that, suspension of P(S/PGL) microspheres (2 mL) was mixed with the HSA solution in PBS (3 mL, 4.0×10^{-4} g/mL). The sample was incubated overnight, and thereafter the unbound protein present in solution was removed by centrifugation and replacement of buffer. Finally, 1-aminoethanol was added (0.25 mL) to suspension of microspheres with immobilized proteins in order to saturate the binding sites not occupied by attached HSA. Surface concentration of immobilized protein was determined from the difference of protein concentration before and after incubation with activated microspheres by using a standard Lowry method (40), and in parallel, directly on microspheres, by using the developed by us modified Lowry method (41). Surface concentration of HSA on these particles was equal $\Gamma_{HSA} = 9.22 \times 10^{-4}$ mg/m^2.

Samples of suspension of poly(styrene/α-*tert*-butoxy-ω-vinylbenzylpolyglycidol) microspheres with covalently immobilized human serum albumin (P(S/PGL)-HSA, 4.5 mL, particle concentration 2×10^{-4} g/mL, surface concentration of HSA immobilized to microspheres $\Gamma_{HSA} = 9.22 \times 10^{-4}$ mg/m^2) in phosphate buffer ($I = 0.002$ mol/L, pH = 7.2, i.e., at conditions similar to physiological conditions) were mixed with samples (0.5 mL) of serum proteins containing anti-HSA (or without HSA). Protein concentrations were varied from 0 to 0.65 mg/mL. All particles treated as it was described above were characterized by electrophoretic mobility.

Electrophoretic mobility of P(S/PGL)-HSA microspheres and microsphere aggregates formed in the presence of corresponding antibodies in sera was measured using a 3000 HSa Zeta-Sizer (Malvern) apparatus. The electrophoretic mobility of particles was measured in a quartz capillary channel to which a potential equal 400 V was applied. After injection of sample containing suspension of microspheres electric field was applied to the cell that was illuminated by crossed laser beams. Interference of light from these beams created dark and illuminated stripes. Microspheres traveling through the channel scatter light when crossing illuminated areas. Fluctuations of scattered light allow determination of velocity of microspheres and eventually, their electrophoretic mobility (μ, a ratio of the average rate of microspheres and field intensity).

Figure 4.9 shows dependence of electrophoretic mobility of P(S/PGL)-HSA on serum concentration in suspension of particles. Plots in Fig. 4.9 reveal that initially the electrophoretic mobility of P(S/PGL)-HSA strongly depends on concentration of anti-HSA containing serum (for serum concentrations below 30 μg/mL). When serum concentration exceeds 60 μg/mL electrophoretic mobility approaches a plateau. At these conditions γ-globulins from anti-HSA sera are bound to all epitopes of HSA immobilized on microspheres.

In Fig. 4.9 there is also given a plot of electrophoretic mobility of P(S/PGL)-HSA microspheres as function of serum that did not contain anti-HSA. It is evident

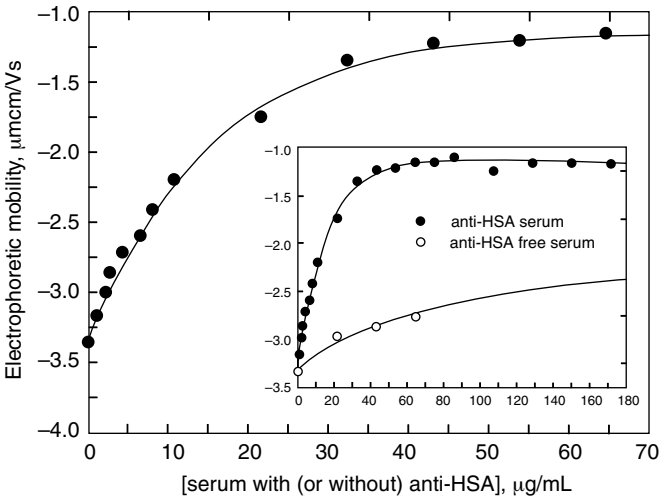

FIGURE 4.9 Dependence of electrophoretic mobility of P(S/PGL)-HSA microspheres on concentration of anti-HSA containing serum (surface concentration of HSA immobilized on microspheres $\Gamma_{HSA} = 9.22 \times 10^{-4}$ mg/m^2, concentration of microspheres 1.8×10^{-4} g/mL, phosphate buffer, PB, pH = 7.2, $I = 2 \times 10^{-3}$ mol/L). Reproduced with permission from Reference 42

that nonspecific interactions responsible for protein attachment from anti-HSA free sera result in a much weaker but clearly visible changes of particles electrophoretic mobility. This significant background may reduce accuracy of an assay based only on changes of electrophoretic mobility, especially for high concentrations of anti-HSA. However, it is worth to notice, that interactions of P (S/PGL)-HSA microspheres with anti-HSA lead to increase size of particles and at high concentration of anti-HSA serum (above 30 μg/mL) even to their aggregation. Figure 4.10 shows dependence of diameters of particles and particle aggregates (measured by quasielastic light scattering) on concentration of anti-HSA sera.

Plots in Figs. 4.9 and 4.10 indicate that changes of electrophoretic mobility are very large at low concentrations of anti-HSA whereas changes in size of particles scattering light are very significant at high serum concentration. This suggests a possibility for design of a combined function of electrophoretic mobility and size of particles that would be very sensitive to changes of anti-HSA at low and high serum concentrations. Figure 4.11 shows plot of the product ($\Phi = |\Delta\mu| \cdot D$) of absolute value of change of electrophoretic mobility ($|\Delta\mu|$)and diameter of particles scattering light (D, average diameter of P(S/PGL)-HSA particles with attached anti-HSA and particle aggregates formed by attachment of anti-HSA to more than one P(S/PGL)-HSA microspheres) as a function of concentration of anti-HSA serum. For comparison there is also shown a similar plot made for P(S/PGL)-HSA microspheres that did not contain anti-HSA.

Plot in Fig. 4.11 indicates that $\Phi = |\Delta\mu| \cdot D$ is very sensitive to changes of anti-HSA at low protein concentrations and, according to insert in this figure, for concentration

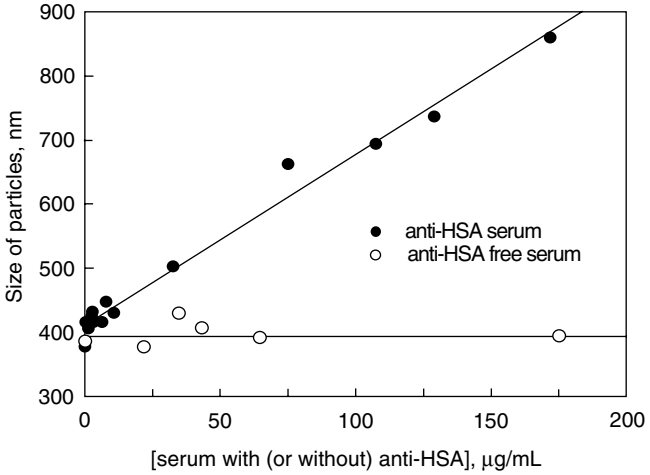

FIGURE 4.10 Diameters of particles in suspension of P(S/PGL)-HSA that were exposed to sera with and without anti-HSA (surface concentration of HSA immobilized on microspheres $\Gamma_{HSA} = 9.22 \times 10^{-4}$ mg/m^2, concentration of microspheres 1.8×10^{-4} g/mL, phosphate buffer, PB, pH = 7.2, $I = 2 \times 10^{-3}$ mol/L). Based on data from Reference 42

of anti-HSA serum below 10 μg/mL with good accuracy could be approximated with a straight line. For protein concentration higher than about 70 μg/mL, Φ as a function of concentration of anti-HSA serum could also be approximated with a straight line but with much lower slope. Thus, the plot of Φ versus concentration of serum with known content of anti-HSA can be used as calibration dependence for determination of anti-HSA sera in a broad concentration range—calibration indicated especially high sensitivity to small concentrations of the analyte.

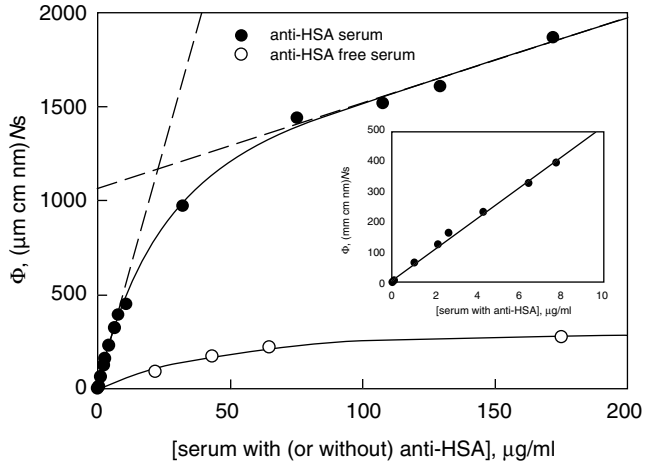

FIGURE 4.11 Parameter Φ as a function of concentration of sera containing and without anti-HSA

4.6.2 Principle of an Immunodiagnostic Assay for Determination of Antibodies against Helicobacter pylori Antigens

Helicobacter pylori is a bacteria which causes various cancer and ulcer diseases in digestion tract and concentration of the anti-*H. pylori* antibodies must be controlled in patients suffering from symptoms related to those diseases. Various commercial ELISA tests based on detection of immunoglobulins IgG, IgA, and IgM were developed for diagnosis of *Helicobacter pylori* (43–45). For fast diagnosis the rapid latex agglutination tests, especially suitable for detection of IgG in blood serum, were elaborated (46,47). In spite of advantage of short time needed for analysis, latex agglutination tests suitable for detection of anti-*H. pylori* have also some deficiencies. They are not very accurate and not enough sensitive. Thus, the new tests are still needed and a test based on combination of changes of electrophoretic mobility and aggregation of microspheres with covalently immobilized *Helicobacter pylori* antigens, developed recently in our laboratory (49) is an interesting option.

Poly(styrene/α-*tert*-butoxy-ω-vinylbenzylpolyglycidol) microspheres used in this test were the same as those used in a model immunodiagnostic assay for determination of anti-HSA—the assay described earlier in this chapter ($\overline{\mathbf{D}}_{\mathbf{n}} = 220\,\mathbf{nm}$, $\overline{\mathbf{D}}_{\mathbf{w}}/\overline{\mathbf{D}}_{\mathbf{n}} = 1.022$, fraction of polyglycidol units in particles' interfacial layer 0.426). Particles used as basic reagent in the test had covalently immobilized antigens isolated from surface of *Helicobacter pylori* bacteria.

Antigens from surface of *Helicobacter pylori* were isolated according to the known recipe (48). *H. pylori* cells were washed out from the *H. pylori* strain NCTC11637 (CCUG 17874) with phosphate buffer saline (PBS, pH = 7.2, [NaCl] = 2×10^{-3} mol/L) and then, transferred into 0.2 mol/L glycine hydrochloride buffer (pH = 2.2) in order to obtain glycine acid extract of *H. pylori* antigens (GE-*H. pylori*). After incubation for 20 min at 20°C the cells were removed by centrifugation at 12,000 g for 15 min. The supernatant was neutralized with NaOH, then dialyzed overnight against PBS at 4°C. Concentration of protein in obtained sample was determined by Coomassie Brilliant Blue (Bio-Rad protein assay). Working aliquots of the antigen were stored at −70°C.

Test was developed using sera from children patients infected with *Helicobacter pylori*. Sera were fractionated and kept at −20°C. Titer of anti-*H. pylori* IgG in patients' sera was determined by an indirect ELISA test according to description given by Montagne et al. (50).

Unit concentration of anti-*H. pylori* (1 U) in serum was defined as concentration of anti-*H. pylori* in 100-fold diluted serum with a titer 1 : 1000.

Thus, concentration of anti-*H. pylori* in serum can be calculated according to Equation 4.1:

$$[\text{anti-}H.\ \ pylori] = \frac{1}{10T\alpha}, \tag{4.1}$$

where T and α denote serum titer and dilution, correspondingly.

For example, in solution obtained by 25-fold dilution of serum with titer 1 : 16,000 the concentration of anti-*H. pylori* is equal 64 U.

Covalent immobilization of *H. pylori* antigens (GE-*H. pylori*) onto P(S/PGL) microspheres was made in the same way as it was described above in this chapter for immobilization of HSA. Amount of *H. pylori* antigens immobilized onto microspheres was determined independently by a standard Lowry method (40) and a modified Lowry method suitable for direct determination of protein immobilized and adsorbed onto microspheres (41). Surface concentration of *H. pylori* antigen immobilized covalently onto P(S/PGL) particles was equal $\Gamma_{\text{H. pylori}} = (1.6 \pm 0.3) \times 10^{-3}$ mol/L (50). It has been shown that this surface concentration did correspond to saturation conditions when whole surface of particles was covered with immobilized *H. pylori* antigen.

Measurements of electrophoretic mobility and diameters of particles in suspensions containing P(S/PGL) microspheres with immobilized *H. pylori* antigen (P(S/PGL)-*H. pylori*) and *H. pylori* antibodies were performed as follows. Concentration of particles in stock suspension of P(S/PGL) microspheres with immobilized *H. pylori* antigen was equal 640 μg/ml. Samples (100 μL) of anti-*H. pylori* containing sera with titers in a range from 1 : 500 to 1 : 32,000, diluted to various degree, were added to 3 mL of particle suspension. The mixtures were incubated for 30 min at room temperature. Thereafter, particles were isolated by centrifugation and resuspended in PBS (pH = 7.2, ionic strength 2×10^{-3} mol/L). Diameters and electrophoretic mobility of these particles were measured in the same way as it was described in previous subsection devoted to determination of anti-HSA.

Dependence of average diameters of P(S/PGL)-*H. pylori* microspheres and their aggregates formed in presence of blood sera on concentration of anti-*H. pylori* is shown in Fig. 4.12.

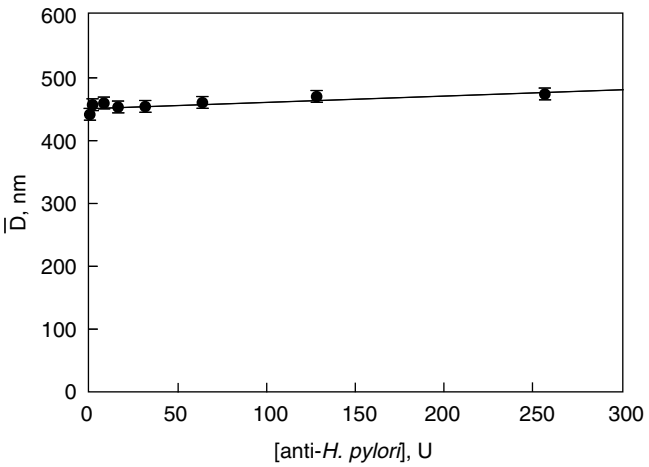

FIGURE 4.12 Average diameters of P(S/PGL)-*H. pylori* microspheres and their aggregates formed in presence of blood sera on concentration of anti-*H. pylori*

Plot in Fig. 4.12 indicates that average diameters of particles (microspheres and microsphere aggregates) are almost independent from concentration of anti-*H. pylori*, suggesting that their aggregation for concentration of anti-*H. pylori* up to 300 U is negligible.

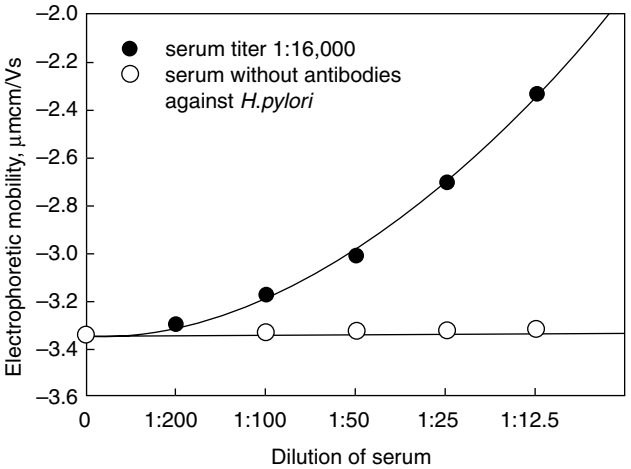

FIGURE 4.13 Electrophoretic mobility of P(S/PGL)-*H. pylori* microspheres that were in contact with serum from patient infected with *H. pylori* (serum titer 1 : 16,000) and from patient not infected. Measurements were carried on in PBS, (pH = 7.2, $I = 2 \times 10^{-3}$ mol/L). Reproduced with permission from Reference 49

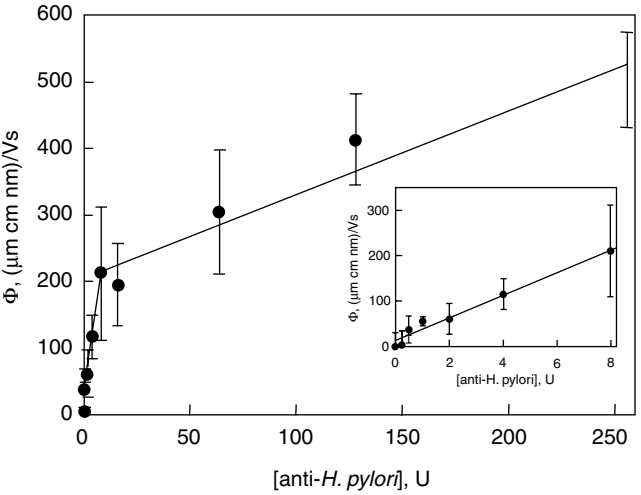

FIGURE 4.14 Parameter Φ as a function of concentration of anti-*H. pylori*

It was important to check whether electrophoretic mobility of P(S/PGL)-*H. pylori* microspheres varies with changes of anti-*H. pylori*. Plots of electrophoretic mobility of P(S/PGL)-*H. pylori* microspheres on degree of dilution of sera containing anti-*H. pylori* and without anti-*H. pylori* are shown in Fig. 4.13.

It is evident that electrophoretic mobility of P(S/PGL)-*H. pylori* microspheres does not depend on concentration of sera without anti-*H. pylori* whereas it undergoes large changes when concentration of sera containing anti-*H. pylori* is varied.

Figure 4.14 shows plot of $\Phi = |\Delta\mu| D$ (product of absolute value of change of electrophoretic mobility ($|\Delta\mu|$) and diameter of particles scattering light (D, average diameter of P(S/PGL)-*H. pylori* particles and particle aggregates formed in presence of anti-*H. pylori*) as a function of concentration of anti-*H. pylori*).

Plot in Fig. 4.14 reveals that calibration line allows determination of anti-*H. pylori* for concentrations up to 250 U. It is worth noting that like in the case of P(S/PGL)-HSA—anti-HSA system also for (P(S/PGL)-*H. pylori*—anti-*H. pylori* $\Phi = |\Delta\mu| D$ is especially sensitive to the changes of anti-*H. pylori* at low protein concentrations whereas absence of aggregation (see Fig. 4.12) makes monitoring only of variation of diameters of P(S/PGL)-*H. pylori* particles exposed to sera containing anti-*H. pylori* useless for diagnostic applications.

REFERENCES

1. Berg JM, Tymoczko JL, Stryer L. Biochemistry, 5th ed. New York, Basingstoke: W.H. Freeman Co.;2002. Chapter 33.
2. Seydack M, Biosens Bioelectron 2005;20:2454.
3. Singer JM, Plotz CM. Am J Med 1956;21:888.
4. Molina-Bolivar JA, Galisteo-Gonzalez F, Hidalgo-Alvarez R. Langmuir 2001;17:2514.
5. Stoll S, Lanet V, Peffercorn E. J Colloid Interface Sci 1993;157:302.
6. González C, García-Berrocal B, Talaván T, Casas ML, Navajo JA, González-Buitrago JM. Clin Biochem 2005;38:966.
7. Cheng T-L, Cheng C-M, Chen B-M, Tsao D-A, Chuang K-H, Hsiao S-W, Lin Y-H, Roffler SR. Bioconjugate Chem 2005;16:1225.
8. Kellar KL, Iannone MA, Exp Hematol 2002;30:1227.
9. Surovtsev IV, Yurkin MA, Shvalov AN, Nekrasov VM, Sivolobova GF, Grazhdantseva AA, Maltsev VP, Chernyshev AV. Colloids Surf B: Biointerfaces 2003;32:245.
10. Magnusson CGM, Delacoix DL, Vaerman JP, Masson PL, J Immunol Methods 1984;69:229.
11. Grundy MA, Moore K, Coakley WT, J Immun Method. 1994;176:169.
12. Jenkins P, Barnes RA, Coakley WT. J Immun Method 1997;205:191.
13. Song MIK, Iwata K, Yamada M, Yokoyama K, Takeuchi T, Tamiya E, Karube I. Anal Chem 1994;66:778.
14. Holownia P, Perez-Amodio S, Price CP. Anal Chem 2001;73:3426.
15. Aoki K, Shikama Y, Kokado A, Yoshida T, Kuroiwa Y. Forensic Sci Int 1996;81:125.

16. Bowden RA, Van Broeck J, Dubray G, Limet JN. J Microbiol Meth 1992;16:297.
17. Luxton R, Badesha J, Kiely J, Hawkins P. Anal Chem 2004;76:1715.
18. Szurdoki F, Michael KL, Walt DR. Anal Biochem 2001;291:219.
19. Waris ME, Meltola NJ, Soini JT, Soini E, Peltola OJ, Hanninen PE. Anal Biochem 2002;309:67.
20. Vignali DAA. J Immun Method 2000;243:243.
21. Dunbar SA, Vander Zee CA, Oliver KG, Karem KL, Jacobson JW. J Microbiol Meth 2003;53:245.
22. Kellar KL, Iannone MA. Exp Hematol 2002;30:1227.
23. Andrade JD, Hlady V. Adv Polym Sci 1986;79:1.
24. Miksa B, Wilczynska M, Cierniewski C, Basinska T, Slomkowski S. J Biomat Sci, Polym Edn 1995;7:503.
25. Basinska T, Slomkowski S, Delamar M. J Bioact Compat Polym 1993;8:205.
26. McPhee W, Tam KC, Pelton RH. J Colloid Interf Sci 1993;156:24.
27. Ito K, Kawaguchi S. Adv Polym Sci 1999;142:130.
28. Guyot A. Macromol Symp 2002;179:105.
29. Charreyre MT, Revilla J, Elaissari A, Pichot C, Gallot B. J Bioact Compat Polym 1999;14:64.
30. De Souza Delgado A, Leonard M, Dellacherie E. J Biomat Sci, Polym Edn 2000; 51:139.
31. Sugiyama K, Oku T. Polym J 1995;2:179.
32. Kugumiya T, Yagawa A, Maeda A, Nomoto H, Tobe S, Kobayashi K, Matsuda T, Onishi T, Akaike T. J Bioact Compat Polym 1992;7:337.
33. Charreyre MT, Boullanger P, Delair T, Mandrand B, Pichot C. Colloid Polym Sci 1993;271:668.
34. Guo X, Weiss A, Ballauff M. Macromolecules 1999;32:6043.
35. Basinska T, Slomkowski S, Dworak A, Panchev I, Chehimi MM. Colloid Polym Sci 2001;279:916.
36. Fitton AO, Hill J, Jane DE, Miller R. Synthesis 1987;12:1140.
37. Basinska T, Slomkowski S, Kazmierski S, Dworak A, Chehimi MM. J Polym Sci, A 2004;42:615.
38. Basinska T, Kowalczyk D, Miksa B, Slomkowski S. Polym Adv Technol 1995;6:526.
39. Slomkowski S, Basinska T, Miksa B. Polym Adv Technol 2002;13:906.
40. Lowry OH, Rosenbrough NJ, Farr AL, Randall RJ. J Biochem 1951;193:265.
41. Basinska T, Slomkowski S. J Biomater Sci, Polym Edn 1991;3:115.
42. Radomska-Galant I, Basinska T. Biomacromolecules 2003;4:1848.
43. Meijer BC, Thijs JC, Kleibeuker JH, van Zwet AA, Berrelkamp RJP. J Clin Microbiol 1997;35:292.
44. Megraud F. Gastroenterology 1997;113 (Suppl. 1):S93.
45. Von Wulffen H. Eur J Clin Microbiol Inf Dis 1992;11:577.
46. Westblom TU, Madan E, Gudipati S, Midkiff BR, Czinn SJ. J Clin Microbiol 1992; 30:96.

47. Fontana C, Pietroiusti A, Mastino A, Pistoia ES, Marino D, Magrini A, Galante A, Favalli C. Eur J Clin Microbiol Inf Dis 2000;19:239.
48. Rechcinski T, Chmiela M, Malecka-Panas E, Planeta-Malecka I, Rudnicka W. Microbiol Immun 1997;41:387.
49. Basinska T, Wisniewska M, Chmiela M. Macromol Biosci 2005;5:70.
50. Montagne P, Vaecin P, Culliere ML, Dureille J. Bioconjugate Chem 1992;3:187.

CHAPTER 5

Biospecific Reactions by Affinity Latexes from Diagnostics to Multiplex Assay

HARUMA KAWAGUCHI

Graduate School of Science and Technology, Keio University, 3-14-1 Hiyoshi, Yokohama 223-5822, Japan

5.1 INTRODUCTION

Development of nano- and microtechnology enabled us to prepare a variety of polymeric particles, whose size ranged from nanometer to submillimeter, with different morphologies and physical properties such as swellability, hydrophilicity/hydrophobicity, and so forth. In terms of size, the nanospheres are almost the same size as proteins and the middle sized microspheres are as large as blood cells. Therefore, colloidal particles are used for many bioreactions, which include recognition, hybridization, regulation of biofunction, modification of biomolecules, and so forth. The particles with suitable size can be selected for such bioreactions, for example, cell separation is carried out effectively using microspheres with a diameter of several micron. On the contrary, gene delivery carrier particles should be small enough to be engulfed by a cell.

The general properties for the biofunctional particles are (1) having a large surface area which is used as a stage of biospecific events, (2) being bioinert, and (3) having sufficient dispersion stability to be used in dispersion, and so forth.

The surface area of 1 g of particles D (μm) in diameter and 1.0 (g/cm^3) in specific gravity is $D/6$ (m^2), if the particles have flat surfaces and no pore. In other words, 1 g of particles 6 μm in diameter has the surface area of about 1 m^2. Small particles with high surface area are sometimes evaded because of the difficulty in handling. To increase the apparent surface area of rather large particles, micro- or macropores are given to

Colloidal Nanoparticles in Biotechnology, Edited by Abdelhamid Elaissari
Copyright © 2008 John Wiley & Sons, Inc.

them although pores are not necessarily advantageous because they cause inhomogeneity in terms of surface reactivity and adsorbability more or less.

The bioinertness is mostly controlled with the balance of hydrophilicity/hydrophobicity and degradability of the material. The details about the property (2) will be presented in the next section.

The dispersion stability of the particles is one of the crucial matters for biomedical particles. The stability is generally controlled by interparticle electrostatic repulsive force and steric stabilization effect. The former is not so dependable in living body because it is filled with salt solutions of high ionic strength.

This chapter first describes the conditions to be required for the biofunctional particles and then their preparation and applications. The outline is shown in Fig. 5.1. Applications of particles include bioseparation, single nucleotide polymorphism (SNP) analysis, protein assay, drug delivery, enzyme immobilization, cell activation, and others. Most of them are based on biospecific reaction between on-particle component and target biomolecules. Assays are divided into two categories. One is singleplex assay in which only one target is detected by a specified probe. Another one is multiplex assay, which has been developed rapidly these days because it enables quick and high throughput assay using a very small amount of sample. Multiplex assay focusing on SNP assay is described in the concluding part of this chapter.

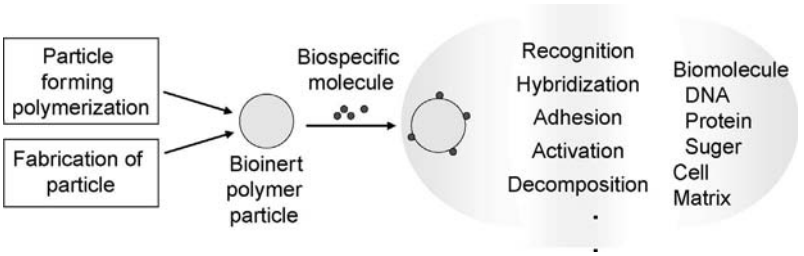

FIGURE 5.1 Preparation and applications of polymer particles as bioreactors

5.2 PREPARATION OF PARTICLES FOR BIOMEDICAL USES

5.2.1 Bioinert Surfaces

The term bioinert includes several meanings, which are (a) nontoxicity, (b) nonantigenicity, (c) nonthrombogenecity, (d) suppression of nonspecific adsorption, and so forth. In this chapter the suppression of nonspecific adsorption is mainly focused.

The particles to be used for biomedical applications should have a bioinert surface because only the aimed reaction is expected to take place at the surface of particles and any other biointeraction on particle surfaces should be avoided. Suppression of nonspecific adsorption of proteins and DNAs is a very necessary condition for such biofunctional particles. In general, particles having hydrophilic surfaces are effective in preventing nonspecific adsorption. The most commonly used hydrophilic polymer is poly(ethylene glycol) (PEG). PEG has shown good performance in various biomedical

applications such as fabrication of antithrombogenetic device, preservation of biofunction of biopolymers, drug delivery, and so forth. PEG chains in aqueous or buffer media are wavering, which contributes to prevention of nonspecific adsorption of proteins. The term "PEGulation" became common in biomaterial technology, meaning to attach PEG to materials in order to improve the surface properties of materials. Poly (acrylamide) is another representative hydrophilic polymer but this polymer is not used for biomedical purposes because it was found to rather accelerate thrombus formation. So, high hydrophilicity is not the sole condition necessary for bioinertness. In fact, moderately hydrophilic polymers such as poly(methacryloyloxyethyl phosphorylcholine) and poly(methoxyethyl acrylate) are highly evaluated as practical bioinert materials (1,2). Tanaka argued that the superiority of such polymers results from water molecules moderately bound to the polymers (2).

5.2.2 Particle Formation

PEG-carrying microspheres are prepared by soap-free emulsion copolymerization of hydrophobic monomer and macromonomer having PEG as a pendant group. Soap-free emulsion polymerization is a suitable method to prepare contaminant-free microspheres. Grafting of PEG on existing particles is another way to prepare PEG-carrying microspheres. These methods give core–shell particles, whose shell is composed of PEG chains, or so-called hairy particles. PEG chains are hydrated and the shell layer is highly swollen with water. As a result, the particle gains steric stabilization effect and is saved from aggregation and nonspecific adsorption. PEG hair nanoparticles are obtained from micelle of PEG-block-hydrophobizable polymer in which hydrophobizable polymer composes the core of nanoparticle. It may be cross-linked to make the core stiff. The example of hydrophobizable polymers is poly(*N*-isopropylacrylamide) (PNIPAM) which becomes hydrophobic above 32°C, that is, the phase transition of PNIPAM above its transition temperature enables micelle formation.

Other polymers usable at biointerface are poly(glycidyl methacrylate) (GMA) and poly(hydroxyethyl methacrylate), as well as those mentioned in the previous section. Poly-GMA particles are obtained by dispersion polymerization in ethanol using azo-bis-isobutyronitrile (AIBN) at 70°C (3). Dispersion polymerization is started from homogeneous solution of monomer and results in polymer particle dispersion. The necessary condition for dispersion polymerization is the use of good solvent for monomer but poor for polymer. Dispersion polymerization gives micron sized particles in general.

Styrene–glycidyl methacrylate copolymer particles are obtained by soap-free emulsion copolymerization (4). The resulting particle is composed of poly(glycidyl methacrylate)-rich shell and polystyrene-rich core because more hydrophilic component tends to concentrate near the surface of particle while more hydrophobic one confines itself inside the particle in the course of polymerization. This is also the case for emulsion copolymerization of styrene with hydroxyethyl methacrylate, acrylic acid, acrylamide, or its derivatives.

There is another category of bioinert polymers. It includes naturally generated polymers and related polymers, for example, a variety of cellulose derivatives, proteins, and biodegradable polyesters. These polymers are transformed to particles by the methods as described below.

a. Polymer is dissolved in organic solvent and the solution was put into water to form o/w emulsion. Then organic solvent is evaporated or extracted to get solid polymer particle.
b. Polymer solution is sprayed to evaporate solvent.
c. Polymer is phase separated or precipitated from the solution by some change in environmental conditions.

The obtained particles might be cross-linked if necessary. One of the examples for method c is the nanoaggregate formation of carboxymethyl cellulose using dodecyltrimethylammonium bromide.

5.2.3 Modification of Particle Surface

In soap-free emulsion copolymerization of styrene and glycidyl methacrylate, complete core–shell particles are not necessarily formed. If the coverage of surface with poly(glycidyl methacrylate) is imperfect and polystyrene is exposed on the surface more or less, nonspecific adsorption cannot be avoided because polystyrene is a typical hydrophobic polymer which is very susceptible to protein adsorption. To mask the polystyrene with poly(glycidyl methacrylate), additional glycidyl methacrylate was postpolymerized. Such kind of polymerization, so-called seeded emulsion polymerization, is one of the most common methods to modify the surface of particles.

New types of particles for biomolecules' carrier were proposed. They are Janus particles produced by seeded polymerization accompanied with phase separation (5). One hemisphere of the particle was composed of poly(2-hydroxyethyl methacrylate-co-methyl methacrylate) and the other was poly(styrene-co-glycidyl methacrylate) and two faces played different roles in nanobioreaction system.

Grafting of polymer chain on existing particles includes two methodologies. One of them is grafting-from and the other is grafting-to. Grafting-from is started by activation of the surface from which polymer chains grow up. Living radical graft polymerization gives to the particle the polymer chains with desirable and uniform chain lengths. It can also give block copolymer hairs onto particles. Grafting-to is a kind of coupling reaction between the surface and the chain end of polymer.

5.3 BIOFUNCTIONALIZATION OF PARTICLES

Micro- and nanoparticles can be used in the same way as they are used for some biomedical applications such as to check the ability of cell for phagocytosis, culture medium, and so forth. But, in most cases, a biospecific compound is immobilized onto

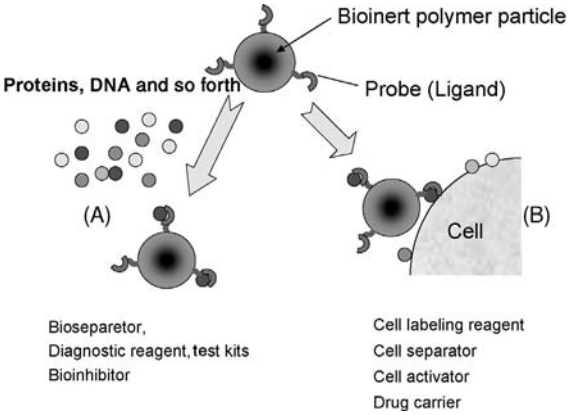

FIGURE 5.2 Biofunctions of affinity latex

the particles and then composite particles, so-called affinity beads whose dispersion is named as an affinity latex, are used for the applications shown in Fig. 5.2.

In A of Fig. 5.2, the composite particle is a catcher of target, which is the complementary counterpart of the compound immobilized on the particle. The practical applications of A are bioseparation, diagnosis, bioassay, and so forth. In B of Fig. 5.2, the composite particle is a label of cell which carries compounds complementary to the ligand on particle, cell separator, cell activator, and so forth. In both cases of A and B in Fig. 5.2, the compounds immobilized on the particles have to retain the activity to recognize their complementary partners and interact with them specifically. Physical immobilization is not suitable to satisfy these requirements because the conformation and orientation of molecule physically adsorbed on the particle are hardly controlled. In addition, physical immobilization needs an adsorption-susceptible surface for only specific compounds, but no such surface exists. When an adsorption-susceptible surface is used for adsorption of specific compound, the remaining surface must be masked with hydrophilic polymers such as albumin and poly(ethylene glycol) to prevent further nonspecific adsorption.

Chemical immobilization was carried out by many chemical reactions as shown below.

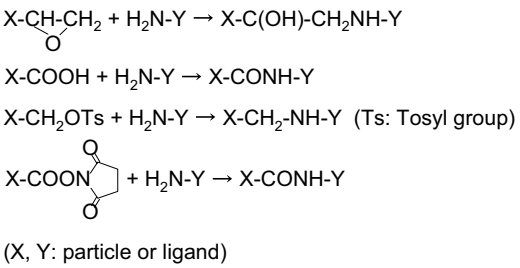

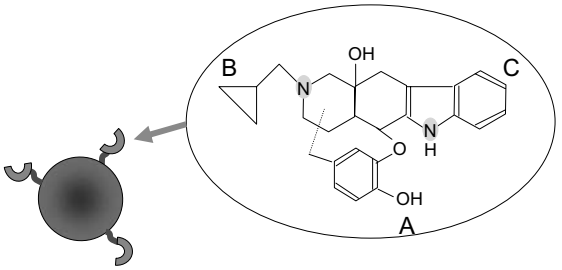

FIGURE 5.3 Importance of binding site of ligand in affinity expression (7)

When biofunctional compounds are immobilized on a polymer surface, the binding site suitable for immobilization must be carefully chosen. The ligand should be bound to the surface of particles with exposing affinity site outward. For example, antibody must be immobilized at the Fc site to keep Fab site free in order to bind antigen efficiently (6). Another example is Naltrindole (NTI, Fig. 5.3)—immobilized affinity particle (7). NTI was immobilized to a particle through a spacer in three modes, using three different binding sites A, B, and C to catch Opioide selectively. The efficiency of three composite particles to catch their target was quite different. Only the particle carrying NTI immobilized at A caught Opioide effectively. The result suggests us that the part of B and C should be kept free to catch Opioide.

Sometimes, no good result is obtained when the ligand is bound to the surface of particles directly. It is because direct binding suppresses the ability of ligand to catch target molecule due to suffering steric hindrance and loss of flexibility of ligand. To overcome these problems, spacers are inserted between ligand and a surface. The properties required for spacer are appropriate length and hydrophilicity. The representative spacers are oligo(ethylene glycol), ethylene glycol diglycidyl ether (EGDE), glycil–glycine, and so forth (Scheme 5.1).

Cleavable spacer or linker gives a merit to biofunctional particles (8). Cleavable spacer elutes the complex of species on the particle and its complementary partner without its deformation. Chung et al. bound the biospecific molecules to microparticles through UV-cleavable linker (8). The particles were packed in a microchannel and used for collecting the labeled target selectively. After that the separation microchannel was irradiated by UV to release the ligand/target complex from the particles and the concentration of target with label was determined.

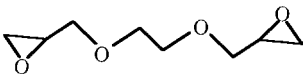

SCHEME 5.1 Ethylene glycol diglycidyl ether

5.4 BIOSPECIFIC REACTIONS ON PARTICLE SURFACE

5.4.1 Diagnosis Based on Antigen/Antibody Binding Reaction

Singer immobilized antirheumatoid factor antibody on latex particles to detect rheumatism in 1957 (9). This was the first latex diagnosis, the mechanism of which is shown in Fig. 5.4. In this case the biospecific binding of rheumatoid factor and its antibody led to agglutination of latex, which was confirmed through eyes or with a spectrometer. After Singer's trial, many antigen–antibody couples were applied for latex reagents and also several methodologies for diagnosis based on agglutination were developed in terms of the material of carrier particles, the mode of immobilization of antibody, the instruments required for test, and so forth. Optical measurements of aggregates in dispersion include spectrophotometry, nephelometry, and scanning laser microscopy. More precise measurement is carried out by using particle counting, in which the numbers of single, double, and triple particles reflecting the extent of aggregation are counted. Latex diagnostics is not limited to agglutination kits. It is also applicable to cells using antibody-immobilized particles (10), fluorescent compound- and antibody-immobilizing particles (11). More than 30 kinds of latex reagents are nowadays commercially available, including pregnancy test and HIV infection check. The application of these materials are not limited to polymer, but other ones, for example, silica particles can be applicable to latex reagent kit. Zhao et al. prepared silica nanoparticles that contained fluorescent compound inside and carried antibody on the surface and successfully detected *E. coli* O157 with them. Ugelstad used antibody-carrying magnetic particle with a diameter of several microns for cancer cell separation (12). Magnetic particles exercise their power in the particle recovery process.

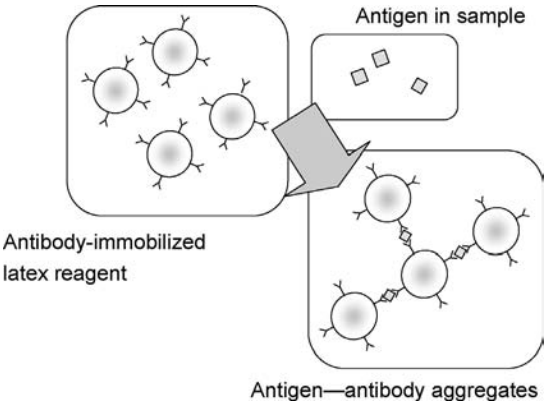

FIGURE 5.4 Latex diagnosis/latex agglutination test

5.4.2 Affinity Separation

The above-mentioned latex reagent is the first product of affinity latex, which is defined as latexes to recognize the complementary partners among the mixture of

biocompounds such as proteins and DNAs. Affinity latexes are applied to bioseparation as well as diagnosis. Single stranded DNA (ssDNA)-carrying latex was used to collect the complementary DNA or RNA from the mixture of DNA/RNA. The first example is oligo–dT carrying particle to collect mRNA, which includes PolyA sequence.

5.4.2.1 Affinity Latex for Detection of Point Mutated DNA Affinity separation was also carried out for discrimination of point mutated DNA. Two 15-mer ssDNAs that have only one different base each other were successfully discriminated by ssDNA-carrying SG particles as shown in Fig. 5.5 (13). In these studies, two kinds of DNAs were incubated with DNA-carrying affinity particles separately or as a mixture. The results are shown in Fig. 5.6a and b, respectively. As shown in Fig. 5.6a, complementary DNA hybridized quickly but mismatch one did not Fig. 5.6b shows the competitive hybridization of complementary and point mismatch DNAs with ssDNA-carrying particle. Hybridization of complementary DNA could not be suppressed by mismatch DNA even if the latter existed 100 times more than the

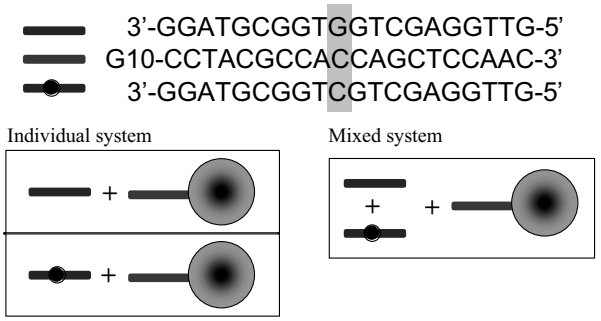

FIGURE 5.5 Discrimination of point mutant using DNA-carrying affinity latex

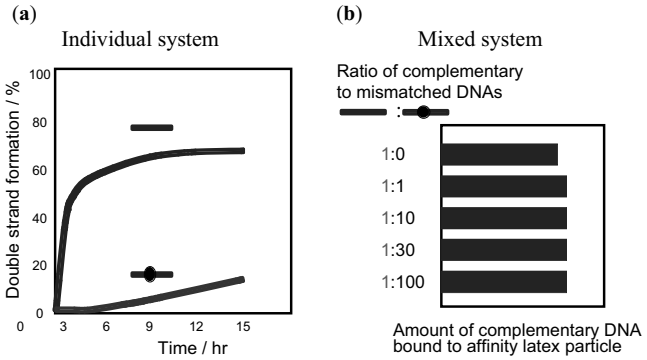

FIGURE 5.6 Hybridization of complementary and mismatch DNAs with DNA-carrying Particle (13) (**a**) individual system, (**b**) mixed system

former. Such discrimination could not be observed with free DNA. That is, immobilization gave the DNA the ability to discriminate its complementary one. This was attributed to the restricted conformational flexibility of DNA immobilized on particles. The immobilized DNA can fit only its complementary one but not point mismatch one because the immobilized DNA has less flexibility due to bound end group.

5.4.2.2 Enzyme-Participating DNA Diagnostics A new mismatch detection system was developed by the usage of functional polymer latex particles which can catch and cleave mismatched DNA selectively (Fig. 5.7) (14). The particles carry MutS, which is originally a DNA repairing enzyme and selectively catches mismatch DNA, and anthraquinone derivative (AQ), which can cleave dsDNA with the aid of UV irradiation. Therefore, the functionalized particles could discriminate between G/C complementary and G/T mismatched DNAs and cleave G/T mismatched DNA selectively upon irradiation with 365 nm UV beam. The complementary dsDNA was placed far from particles and therefore AQ could not attack it. The efficiency of photocleavage of G/T mismatched DNA increased as number of AQ bound to MutS immobilized on the particles increased and as UV irradiation time was prolonged. The system, constituted of AQ–MutS-immobilized particles with a diameter less than 100 nm and SYBR-Gold, a dsDNA-binding fluorescent dye, detect mismatched DNA with 40 base pairs. The measurement can be done without separating particles from dispersion medium because the particles are small enough to be stealth from light.

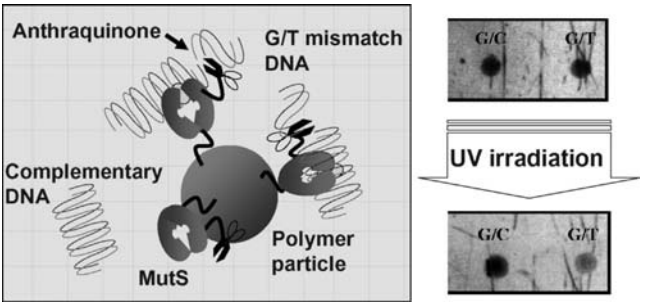

FIGURE 5.7 Novel latex reagent for mismatch detection in DNA diagnosis. Left, Schematic presentation (14). Right, Fluorescence of samples before and after incubation with MutS/AQ-particle followed by UV irradiation

5.4.2.3 Affinity Latex Reacting with A Cell Membrane Protein Arginine–glycine–aspartic acid (RGD) is a representative cell adhesive peptide located within fibronectin and other proteins. RGD was immobilized to latex particles. RGD-carrying latex was used to specifically interact with integrin, a cell membrane protein that recognizes RGD sequence. RGD-carrying particles enabled to selectively collect integrin in cell membrane extract. They also enable to stimulate the cell through the biospecific interaction between RGD and integrin (15). Such interaction did not

occur between integrin and RGE (E, glutamic acid) although the difference between D and E is only whether CH_2 group exists or not. Their specific interaction can be possible when integrin has its native conformation, which is Mg^{2+} dependent. Namely, elimination of Mg^{2+} spoils RGD–integrin binding. The efficiency of the specific reaction is controlled by the flexibility of RGD. Insertion of glycil–glycine (GG) between RGD and particle causes an appreciable improvement of efficiency in specific binding. GG serves as a spacer, which makes the probe flexible.

5.4.2.4 Drug Delivery Using Affinity Latex The main event for some drugs is to encounter their own receptor protein on cell membrane. Drug-carrying latex could identify the cell membrane proteins which have specific affinity with the drug. For example, cisplatin/DNA-carrying latex (Fig. 5.8) could catch a few proteins, which are believed to be responsible for the treatment of cancer (16).

5.4.3 Bioreaction by Immobilized Enzyme

Latex particle is one of the promising carriers for enzymes because of the huge surface area to exhibit bioreaction and the curved shape to maintain the native structure of immobilized enzyme. Self-assembled polystyrene particles were used as micropatterned enzyme support (17).

Direct immobilization of enzyme on particle sometimes causes deactivation of enzyme. In addition to insertion of enzyme into polyelectrolyte multilayers (18), entrapment of enzyme in polyelectrolyte brushes was also effective for preservation of immobilized enzyme (19). This was confirmed in the system of polyacrylic acid hair-carrying polymer colloid. Silver nanoparticles were *in situ* formed in the hairy layer and they exhibited excellent catalytic activity for reduction reaction.

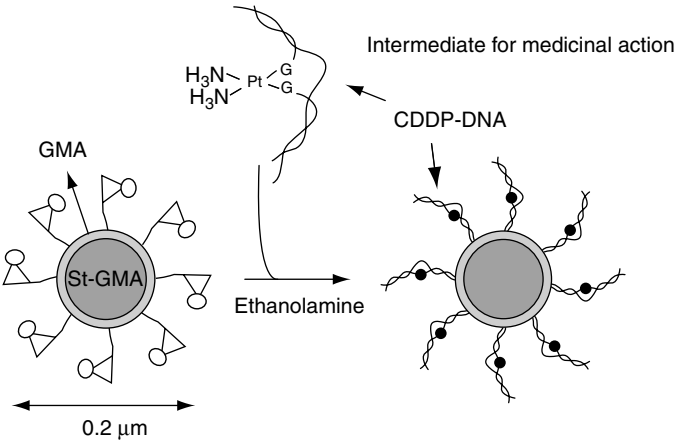

FIGURE 5.8 *cis*-platin/DNA complex-carrying latex to identify the protein responsible for *cis*-platin/DNAcomplex formation (16)

Thermally-sensitive graft chains were used as a linker or a spacer for enzyme (20). In this study, poly(*N*-isopropylacrylamide) (PNIPAM) and trypsin-bound PNIPAM chains were grafted on polystyrene particles. The transition temperature of the latter (*T*e) was several degrees higher than that of the former (*T*o). Trypsin was buried in hairy layer of particles in dispersion below *T*o, whereas it was exposed to the aqueous medium between *T*o and *T*e so that trypsin catches the substrate efficiently. The situation is almost the same above *T*e. Thus, the hair played roles not only as spacer but also as regulator of enzyme activity with temperature.

5.5 MULTIPLEX ASSAY SYSTEM

5.5.1 Two Multiplex Assay Systems

Multiplex assay is defined as the assay for simultaneous detection of multiple targets by using multiple ligands. This assay needs only a very small amount of samples and, therefore, patients suffer little anguish. Speed is another merit of multiplex assay. There are two types of multiple assay systems. One is composed of chip and the other is composed of dispersing particles. In the former, each ligand is identified by the position on a chip. In contrast, in multiplex assay using affinity particles, called as suspension array or beads array, each particle in dispersion has to carry its own sign, or bar code, to indicate its identity as shown in Fig. 5.9.

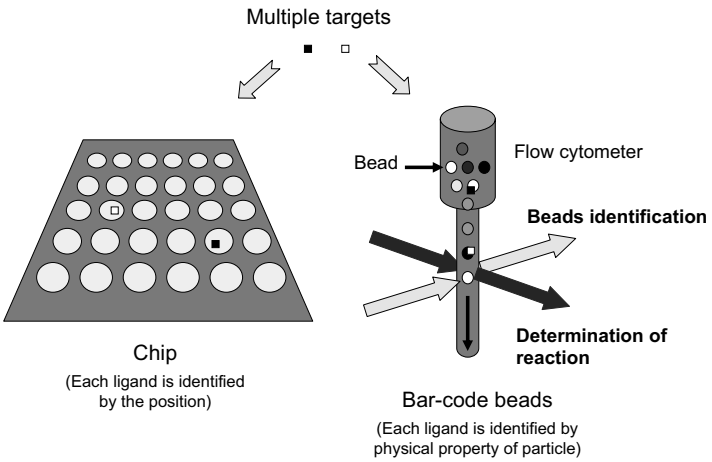

FIGURE 5.9 Multiplex assay systems

5.5.2 Coding of Particles

Color, size, density, electric charge, and so forth have been used as the bar code. A series of multiple colored particles were obtained by mixing multiple dyes or quantum dots (QD) with different mixing ratio (21). In dual fluorescent dyes system, for

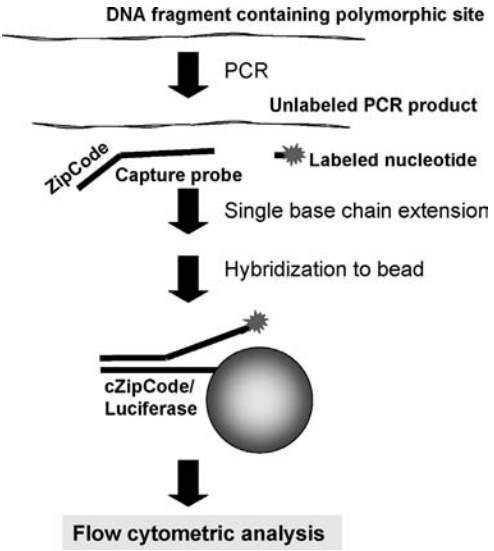

FIGURE 5.10 Multiplex beads assay of SNP using single base chain extension and ZipCode (23)

example, a hundred kinds of microbeads were prepared by putting different amount of two kinds of fluorescent dyes, ten concentrations per dye, into the beads with a diameter of 5 μm. Such beads are identified in flow cell by measuring fluorescence originated from each dye embedded in the beads. In QD-assist multiplex assay systems, some QD-carrying polymer particles are reinforced because quantum dots are apt to leak out of undependable particles. To prevent the leakage of quantum dots, silica nanoparticles were deposited on the polymer particles to form silica shell, which contributed to the improvement of bar-code stability (22).

Another code system is shown in Fig. 5.10 (23), which enables the assay of unlabeled sample DNA. The sample DNA containing SNP is first amplified by PCR. One capture oligonucleotide probe with a unique ZipCode sequence was designed for the every SNP. Multiplexed SNP analysis could be done by employing respective ZipCode sequences for different SNPs.

In the preparation of beads assay systems, functional groups should be attached on the beads in order to immobilize ligands or probes on them. The common functional groups are carboxyl group and avidin. Through these functional groups, a hundred kinds of beads having a hundred kinds of ligands are prepared.

5.5.3 Practice of Multiplex Beads Assay

Multiplex beads assay is carried out as follows. When the particles having sequence specific DNAs are mixed with labeled sample DNA, only the particle having complementary DNA hybridizes with labeled sample and the identification of the hybridized particle informs us about the DNA sequence of the sample. Then

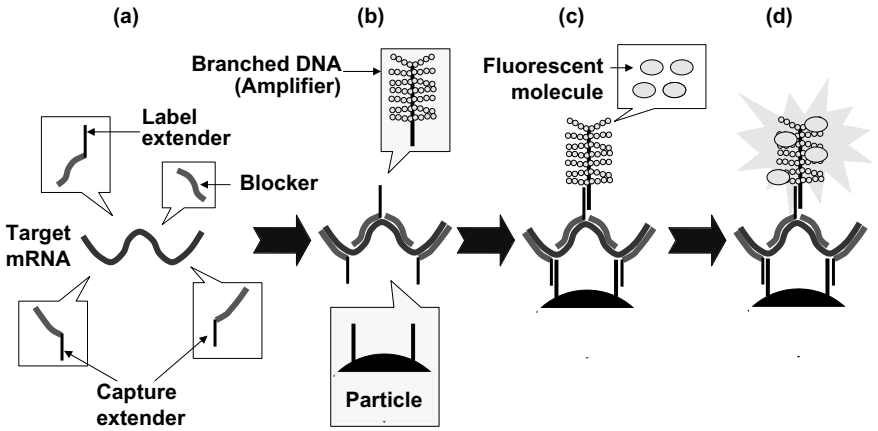

FIGURE 5.11 Constitution of multiplex beads assay system (24)

identification is done by flow cytometer as shown in the right of Fig. 5.9. The cytometer is interfaced with a personal computer carrying data processor and each DNA is quantified. This assay system prefers to chip system in terms of the speed and easy processing.

Improvement of sensitivity is the keen requirement not only in singleplex assays but also in multiplex assays. If the sensitivity is high enough, no PCR amplification followed by troublesome processes is required. Zheng et al. developed a new method to enable accurate and simple quantification of mRNA in whole blood (24). Usually the quantification of mRNA is very difficult because gene expression changes dynamically and sample preparation is complicated. Their assay system to overcome such difficulty is shown in Fig. 5.11.

As shown in Fig. 5.11a, three types of DNA blocks were prepared, that is, capture extender-carrying DNA, label extender-carrying DNA, and blocking DNA. All of them possessed specific sequences complementary to parts of target mRNA. Capture extender and label extender hybridizes with capture probe on particle and label extender hybridizes with amplifier branched DNA-carrying label probe. After three DNA fragments hybridized with mRNA (Fig. 5.11b), they were caught by capture prove-carrying particle (Fig. 5.11c). Then, amplifier was hybridized and contributed to the chemiluminescence assay (Fig. 5.11d). This system only needed 25 μL of whole blood without purification, RNA isolation, and reverse transcription for the multiplex gene expression analysis. Thus, 0.01–0.04 amol target DNA was captured from 25 μL blood.

Weissler et al. prepared a library in which 146 kinds of small molecules were attached to particles (25). The particles were used for screening cell lines. The small molecules employed were 1-adamantanemethylamine, 3-mercapto-2-methyl-propionyl-L-proline, 2-imino-1-imidazolidiaacetic acid, 1,2,4-benzenetricarboxylic anhydride, and so forth. The particles were used for differentiating cell lines, detecting distinct cellular states and targeting specific cell types.

Use of beads was focused on multiplex assay in this section. But the fact should be referred that affinity particles are usable even in chip system (26). It is because the particles give large surface area and, consequently, a large number of reaction sites to each spot on the chip. SPR imaging system enables simultaneous detection of multiple targets bound by multiple spots on a chip.

5.6 CONCLUSIONS

Biofunctional particles were designed and prepared for a variety of purposes. Studies have been done on prevention of nonspecific adsorption. The particles were employed for bioseparation, bioassay, bioreactor, and others. In terms of bioassay, high throughput process using the minimum amount of sample became more and more important. As a result, multiplex assay, including chip and dispersion systems, has made tremendous progress in the last 2 decades.

REFERENCES

1. Ye SH, Watanabe J, Takai M, Iwasaki Y, Ishihara K. Biomaterials 2005;26:5032–5041.
2. Haris P, Tanaka M. Biomed Mater Eng 2004;14:427.
3. Kawaguchi H, Asai A, Ohtsuka Y, Watanabe T, Handa H. Nucl Acid Res 1989;17:6229.
4. Inomata Y, Wada T, Handa H, Fujimoto K, Kawaguchi H. J Biomater Sci Polym Ed 1994;5:293.
5. Du YZ, Tomohiro T, Kodaka M. Macromolecules 2004;37:803.
6. Kawaguchi H, Sakamoto K, Ohtsuka Y, Ohtake T, Sekiguchi H, Iri H. Biomaterials 1989;10:225–229.
7. Hasegawa M, Ohno H, Tanaka H, Hatakeyama M, Kawaguchi H, Takahashi T. Bioorg Med Chem Lett 2006;16(1):158–161.
8. Chung WJ, Kim MS, Cho S, Park SS, Kim JH, Kim YK, Kim BG, Lee YS. Electrophoresis 2005;26:694.
9. Singer JM, Plotz CM. Am J Med 1956;21:888.
10. Rembaum A, Yen SPS, Volksen W. ChemTech 1978;182.
11. Zhao X, Hillard LR, Mechery SJ, Wang Y, Bagwe RP, Jin S, Tan W. Proc Nat Acad Sci USA 2004;101:15027.
12. Ugelstad J, Berge A, Ellingsen T, Schmid R, Nilsen TN, Mørk PC, Stenstad P, Hornes E, Olsvik O. Prog Polym Sci 1992;17:87.
13. Hatakeyama M, Iwato S, Fujimoto K, Handa H, Kawaguchi H. Colloids Surf B: Biointerface 1998;10:161–169.
14. Oba S, Hatakeyama M, Handa H, Kawaguchi H. Bioconjugate 2005;16:511.
15. Kasuya Y, Fujimoto K, Kawaguchi H, Miyamoto M. Biomaterials 1994;15:570–576.
16. Tomohiro T, Sawada, J, Sawa C, Nagura H, Yoshida S, Kodaka M, Hatakeyama M, Kawaguchi H, Handa H, Okuno H. Bioconjugate Chem 2002;13(2):163–166.
17. Yap FL, Zhang Y. Langmuir 2005;21:5233.

18. Lvov Y, Caruso F. Anal Chem 2001;73:4212.
19. Neumann T, Haupt B, Ballauff M. Macromol Biosci 2004;4:13.
20. Yasui M, Shiroya T, Fujimoto K, Kawaguchi H. Colloids Surf B: Biointerface 1995; 4:275–285.
21. Fulton RJ, McDade RL, Smith PL, Kienker LJ, Kettman JR Jr. Clin Chem 1997;43:1749.
22. Cao Y-C, Huang Z-L, Liu T-C, Wang H-Q, Zhu X-X, Wang Z, Zhao Y-D, Liu M-X, Luo Q-M. Anal Biochem 2006;351:193.
23. Chen I, Iannone MA, Li M-S, Taylor JD, Rivers P, Nelsen AJ, Slentz-Kesler KA, Roses A, Weiner MP. Genome Res 2000;10:549.
24. Zheng Z, Luo Y, McMaster GK. Clinical Chem 2006;52:1294–1302.
25. Weisslerder R, Kelly K, Sun EY, Shtaland T, Josephson L. Nat. Biotechnol 2005;23:1418.
26. Im SH, Khalil GE, Callis J, Ahn BH, Gouterman M, Xia Y. Talanta 2005;67:492.

CHAPTER 6

Fluorescent Colloidal Particles as Detection Tools in Biotechnology Systems

IGOR NABIEV and ALYONA SUKHANOVA

EA n°3798 Détection et Approches Thérapeutiques Nanotechnologiques dans les Mécanismes Biologiques de Défense, Université de Reims Champagne-Ardenne, 51 rue Cognacq Jay, 51100 Reims, France

MIKHAIL ARTEMYEV

Institute for Physico-Chemical Problems, University of Minsk, Belarus

VLADIMIR OLEINIKOV

Shemyakin-Ovchinnikov Institute of Bioorganic Chemistry, Russian Academy of Sciences, 117997 Moscow, Russia

6.1 INTRODUCTION

Proteomics, genomics, and medical diagnostics regularly require labeling of biomolecules for detection. Isotopes, enzyme-linked chromophores production, and chemiluminescence are among the most sensitive methods of biodetection. Mass spectrometry and recent advances in surface plasmon resonance technique and resonant and surface-enhanced Raman vibrational spectroscopy techniques offer label-less techniques. Even with all these methods available, the improved spatial and temporary resolution and versatility of fluorescence microscopy have found its place in the numerous biodetection applications (1). Such recent advances of fluorescence detection techniques as the development of fluorescent sensors and labeling of proteins in live cells have yielded a clearer understanding of the dynamics of intracellular networks, signal transduction, and cell–cell interaction (2). The fluorescence detection methods are characterized by fast signal acquisition where each individual label

Colloidal Nanoparticles in Biotechnology, Edited by Abdelhamid Elaissari
Copyright © 2008 John Wiley & Sons, Inc.

can provide 10^7–10^8 photons for detection; single molecule detection has become prevalent for many applications (3); the signal is localized, unlike with some enzyme-linked amplification schemes, and the labeling process is straightforward provided that appropriate functional groups are available on the target. However, the multiplexing task of elucidating the role of numerous targets simultaneously and their mutual interactions and interconversions in a real and long-lasting time, require new and emerging approaches and tools. Ultrasensitive (down to single-molecule) multiplexed methods will play a major role in this endeavor, but the complex milieu encountered inside live cells and in crude biological fluids and tissues requires substantial adaptations of current *in vitro* techniques.

Three major problems associated with fluorescence microscopy detection, diagnostics, and bioimaging include the following:

1. cell autofluorescence in the visible spectrum (which can mask signals from labeled molecules);
2. requirement of long observation times (which create a need of new probes that are more photostable than current fluorophores); and
3. the problems with a multiplexing when an absorption and fluorescence emission bands of typical organic chromophore are very close to each other, and the fluorescence emission bands are large and nonsymmetrical, thus, making difficult simultaneous biodetection of different fluorescent tags and further deconvolution of detectable signals (Fig. 6.1).

Research on fluorescent semiconductor nanocrystals (“quantum dots” or QDs) has moved over the last 10 years from electronic materials and physics to biological and biomedical areas and a literature search daily increases examples of their successful applications much exceeding the possibilities of organic dyes. The most recent examples include the observation of diffusion of individual receptors on the single molecule level, multiplexed identification of lymph nodes in live animals by near-infrared emission during surgery, ultrasensitive detection of viruses and bacteria, multiplexed detection using flow cytometry techniques, an increase of sensitivities in a lab-on-a-chip and lab-on-a-bead detection formats, and so forth. From the fundamental point of view, the new generations of QDs have far-reaching potential for the study of intracellular processes at the single-molecule level, high resolution cellular imaging, long-term *in vivo* observation of cell trafficking, tumor targeting, and diagnostics (4–6).

Colloidal semiconductor quantum dots are single crystals, a few nanometers in diameter whose size and shape can be precisely controlled by the duration, temperature, and ligand molecules used in the synthesis (6–8). This process yields QDs that have composition- and size-dependent absorption and emission (Figs. 6.1 and 6.2). Absorption of a photon results in the creation of an electron–hole pair (exciton). The absorption has an increased probability at higher energies (i.e., shorter wavelengths) and results in a broadband absorption spectrum, in marked contrast to standard fluorophores (Fig. 6.1). For nanocrystals smaller than the so-called Bohr exciton radius (a few nanometers, Fig. 6.3), energy levels are quantized, with values directly

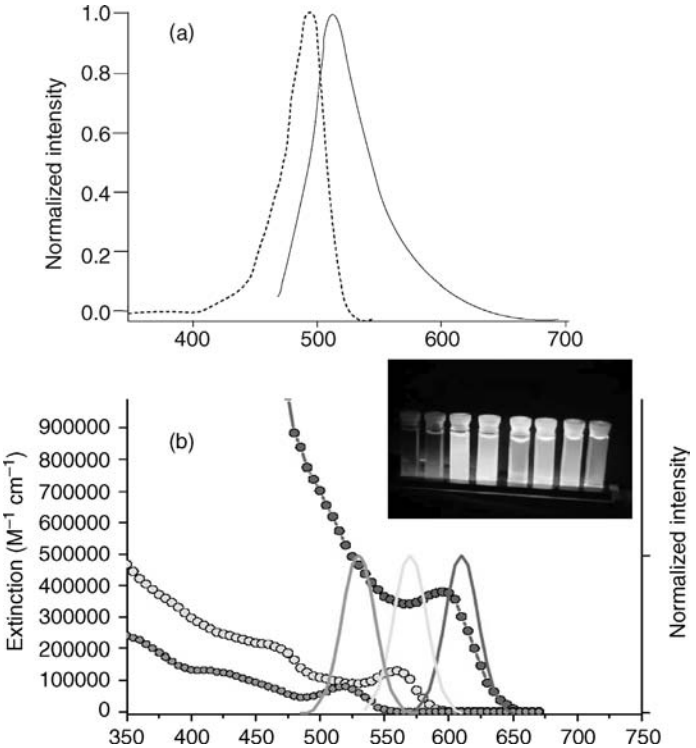

FIGURE 6.1 Typical absorption (dotted lines) and fluorescence (solid lines) spectra of organic dyes (**a**) and of semiconductor CdSe/ZnS nanocrystals quantum dots (**b**). Panel (**a**): spectra of fluorescein are presented as an example. Panel (**b**): X-axe legend: Wavelength (nm) monodispersed CdSe/ZnS QDs of diameters from 3 to 6 nm synthesized and functionalized in our laboratory are excitable with one wavelength (laser or lamp) but emit fluorescence depending from their size, from blue to red region of spectrum (insert). Absorption and fluorescence spectra of the green- (2,5 nm core diameter), yellow- (3,3 nm), and red-emitting (4,8 nm) QDs are presented as examples

related to the QDs size (an effect called quantum confinement, providing the name "quantum dots" for such nanocrystals). The radiative recombination of an exciton leads to the emission of a photon in a narrow, symmetric energy band, another difference from the red-tailed emission spectra and short lifetimes of most organic fluorophores (Fig. 6.1). The long fluorescence lifetime of QDs enables the use of time-gated detection to separate their signal from that of shorter lived species (such as background autofluorescence encountered in cells). Surface defects in the crystal structure act as temporary "traps" for the electron or hole, preventing their radiative recombination. The alternation of trapping and untrapping events results in intermittent fluorescence (blinking) visible at the single-molecule level (9) and reduces the overall quantum yield, which is the ratio of emitted to absorbed photons. One way to overcome these problems, and to protect surface atoms from oxidation and other chemical

Fluorophore	Absorption(nm)	Emission(nm)
Fast Blue	360	440
AlexaFluor 350	346	445
AMCA	350	450
Bisbenzamide	360	461
Hoechst33258	360	470
ACMA UV	412, 430	471, 474
Hoechst33342	343	483
Cy2	489	506
GFPWildtype Non UVe	475	509
GFPWildtype UVex	395	509
AlexaFluor 488	494	517
Calcein	496	517
Fluorescein (FITC/DTAF)	495	520
FluoroJade B	480	525
Lucifer yellow	425	528
JC-1	514	529
Fluoro-Gold	361	536
AlexaFluor 430	430	545
Eosin	524	545
6-Joe UV	520	548
AlexaFluor 532	530	555
Cy3	548	562
AlexaFluor 546	554	570
AlexaFluor 555	555	571
TRITC	547	572
B-phycoerythrin	545, 565	575
R-phycoerythrin	480,545,565	578
Rhodamine	539, 574	602
AlexaFluor 568	578	602
Texas Red	589	615
AlexaFluor 594	590	617
Propidiumlodide(PI)	536	617
EthidiumBromide	493	620
Feulgen	570	625
Acid Fuchsin	540	630
AlexaFluor 633	621	639
AlexaFluor 647	649	666
Cy5	650	670
PE-Cy5 conjugates	480,565,650	670
AlexaFluor 660	668	698
AlexaFluor 680	684	707
PE-Cy7 conjugates	480,565.743	767
Cy7	743	767

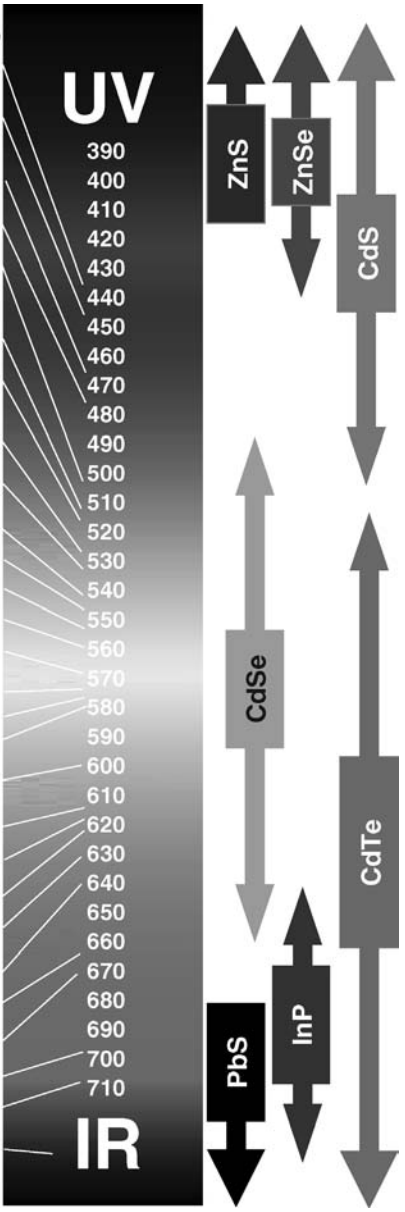

FIGURE 6.2 Fluorescence of semiconductor quantum dots of different chemical compositions and sizes cover all optical spectral region from UV to IR. QDs may replace all known organic dyes (on the left) from their actual areas of applications to detection and diagnostics

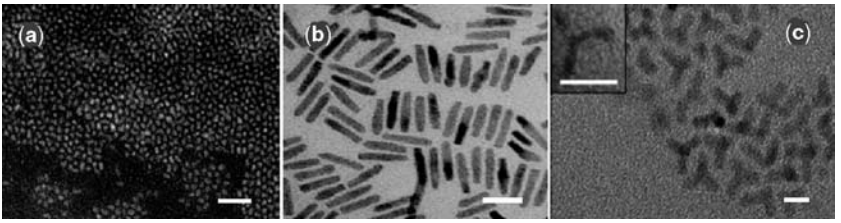

FIGURE 6.3 CdSe quantum dots of different shapes. Electron microscopy photographs of spherical nanocrystals of 3,5 nm in diameter (**a**), nanorods of 4 nm in diameter and 20 nm in length (**b**), and nano-"tetrapodes" (**c**). Bars: 20 nm

reactions, is to grow a shell of a few monolayers of a material with a larger band gap on top of the nanocrystal core (CdSe/ZnS core/shell QDs, for example). This shell can be optimized to obtain quantum yields up to 75% (10,11). Deposition of the shell also enhances QDs photostability by several orders of magnitude relative to conventional dyes (13). Additionally, the QDs have normally very large linear absorption cross-sections (or extinction coefficients) orders of magnitude bigger than that of organic dyes (Fig. 6.4). The product of the quantum yield and extinction coefficient of fluorophore determines its brightness, the key parameter of the sensitivity of fluorophores' detection with a microscope. Very big extinction coefficients and comparable quantum yields ensure at least 10-fold higher brightness of QDs over the nest organic fluorophores and enable the detection sensitivity down to a single QD level.

Single QDs can be observed and tracked over an extended period of time (up to many hours and even days) with confocal microscopy (14) or basic wide-field epifluorescence microscopy (15). Single-molecule studies of QDs have revealed

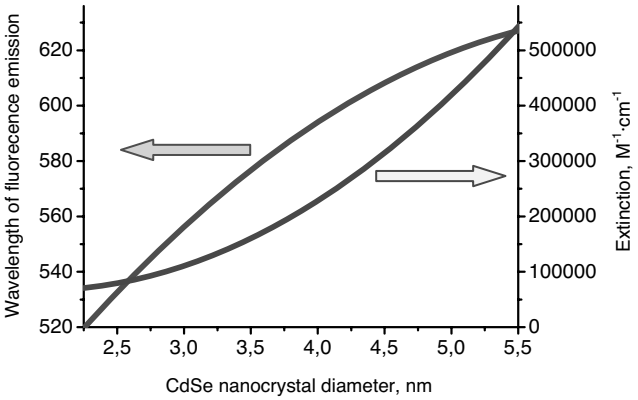

FIGURE 6.4 Dependence of position of fluorescence emission band of CdSe/ZnS core/shell nanocrystals and their extinction coefficient in a long-wavelength exciton maximum of absorption on diameter of fluorescing CdSe core

phenomena hidden in ensemble measurements, such as blinking (9) or the existence of multiple long fluorescence lifetimes (16). Single-molecule microscopy is possibly one of the most exciting new capabilities offered to the biologist. A related technique, fluorescence correlation spectroscopy, has allowed determination of the brightness per particle and also provides a measurement of the average QDs size (17).

QDs are also excellent probes for two-photon confocal microscopy because they are characterized by a very large absorption cross section (Fig. 6.4). Naturally, they can be used simultaneously with standard dyes. In particular, QDs have a largely untapped potential as customizable donors of a fluorescence resonance energy transfer (FRET) pair with organic dyes (18,19) or in the QD–QD pairs of nanocrystals of different sizes (20).

The QDs of different chemical composition and diameters cover all region of optical spectrum from UV to IR and may, in principle, replace all known for today organic dyes from their current application niches (Fig. 6.2). In this Chapter, we will start from the brief review of state-of-the-art techniques of synthesis of bioadaptable nanocrystals of different sizes and chemical compositions. We will further describe in more details CdSe/ZnS core/shell QDs as a detection and diagnostic tool in biotechnology system and will cover the current approaches to their solubilization and protection in aqueous solutions and biological fluids, functionalization and applications to ultrasensitive biodetections on molecular and cellular levels with QDs bioconjugates or with the polymer beads optically encoded with QDs of single or multiple colors. *In vivo* QDs applications and related cytotoxicity issues is an emerging area, which is not covered by this Chapter. The readers interested in this field of QDs applications are addressed to the recent comprehensive reviews presenting the rapidly growing and changing state-of-the-art in this field (21,22).

6.2 SYNTHESIS OF BIOADAPTABLE HIGHLY LUMINESCENT II–VI NANOCRYSTALS

6.2.1 History: First Generations of Semiconductor Nanocrystals

The first successful synthesis of nearly monodisperse semiconductor nanocrystals of CdE chemical composition (where E is S, Se, or Te) with intense band-edge luminescence has been published by Bawendi and coworkers in 1993 (23). The basis of this method is extremely useful and flexible and most of the highly luminescent II–VI, III–V, IV–VI nanocrystals synthesized so far have been obtained via this way. The method is based on high temperature reaction between organometallic precursors in various coordinating media. The first synthesis of highly luminescent CdSe nanocrystals involved dimethylcadmium and trialkylphosphine selenide as precursors and trioctylphosphine oxide (TOPO) as a coordinating medium. Despite their relatively high cost, TOPO was found to be nearly ideal reaction medium since, it possesses both high boiling point (above 360°C) and strong binding with various metal ions such as Cd or Zn. The general synthetic procedure involved the fast injection of

precursors into the reaction medium at high temperature (300–350°C) followed by slow growth of nanocrystals at relatively low temperature (250–300°C). All stages of synthesis must be done in the inert atmosphere (Ar or N_2) indeed. Trialkylphosphine selenide (or telluride, or sulfide) is prepared by dissolving elemental chalcogen in tributylphosphine or trioctylphosphine (TOP), and the choice of dimethylcadmium as a metal precursor is dictated by its good solubility in TOP. At room temperature, $CdMe_2$ does not react markedly with TOP:Se, but being injected into TOPO at high temperature the interaction is going quickly producing small-atom clusters of CdSe as the seeds. Subsequent lower temperature "aging" brings about the growth of CdSe nanocrystals via mass transfer from smaller particles onto bigger ones (the so-called Ostwald ripening). The final result of the process will be the CdSe nanocrystals of nearly spherical shape with the mean size and size distribution dependent mainly on the injection and growth temperature, the concentration and the sorts of reagents. The smallest CdSe nanocrystals prepared by high temperature method reach ca. 1.2 nm in diameter, while the biggest ones exceed 10 nm (Fig. 6.3). Larger CdSe nanocrystals are unstable in TOPO at high temperature and begin to precipitate out of mother solution. Due to pronounced quantum confinement effect (QCE) in CdSe nanocrystals of diameters comparable with the Bohr radius, the smaller nanocrystals have the stronger blue shift of absorption bands than the bigger QDs (24). Apart from the spectral shift in CdSe nanocrystals prepared by high temperature synthesis, the QCE produces well-resolved excitonic absorption bands clearly detected even at room temperature. It should be noted that the excitonic optical transitions in bulk CdSe may be detected only at cryogenic temperatures.

The quantum confined II–VI nanocrystals were known much earlier than the modern high temperature synthesis has been developed. Synthesized in glass matrices for optical cut-off filters or in water solutions, the first II–VI nanocrystals were suffered with too broad absorption bands and weak photoluminescence (25–27). The broadening of optical transitions arise from nonhomogeneity of early nanocrystals, while the weak photoluminescence was the indication of large number of defects and traps playing the roles of centers for nonradiative recombination of optically excited electron–hole pairs in semiconductors (24). The size distribution of semiconductor QDs was much above 10% and photoluminescence quantum yield below 1%. In addition, the origin of this weak luminescence was not purely excitonic (i.e., direct radiative recombination of excited electron–hole pairs), but rather trap-mediated recombination characterized by small efficiency, long decay time, and large Stock shift. The advantage of modern high temperature synthesis is in the formation of monodisperse semiconductor nanocrystals with accurately controllable size and high luminescence quantum yield. The fast formation of seeds just after the precursor injection followed by slow growth of nanocrystals at moderate temperature brings about nearly defect-free particles due to increased mobility and annihilation of various defects at higher temperatures. Controlling the kinetics of nanocrystals growth by the reaction temperature, duration, and concentration of components, it is possible to achieve the effect of the "focusing" in the size distribution of nanocrystals. Later, utilization of the "focusing" growth was utilized for the synthesis of CdSe nanocrystals with the standard deviation well below 10% (28).

The first high temperature synthesis of II–VI nanocrystals utilized organometallic precursors (dimethylcadmium, for example). Besides its high commercial price, dimethylcadmium is a very dangerous substance being highly volatile, pyrophoric, and highly toxic. Manipulations with $CdMe_2$, especially at high temperatures, must be done with extreme care and only in the inert atmosphere. To avoid the usage of such unpleasant material in the synthesis of CdE nanocrystals, some other precursors have been utilized successfully. High quality CdSe nanocrystals were synthesized from cadmium and organic acid salts, including cadmium stearate, laurate, acetate, and alkylphosphonic acid salts (29). More exotic precursors proposed included complexes of Cd with dialkyldiseleno (thio-) carbamates, pyridineselenolates, thioles, and so forth (30–32). The starting materials may be either commercially available salts or solid CdO and organic acids loaded together with TOPO. At moderate temperatures, CdO reacts with organic acids producing a solution of salts in TOPO, just ready for further injection of TOP:Se (or TOP:S, TOP:Te). The synthesis of CdE starting from cadmium salts was not only cheap and versatile but also gave the nanocrystals of very high optical quality with the photoluminescence quantum yield exceeding 50% and the spectral linewidth less than 30 nm (33). Additionally, this "greener" synthesis allowed achieving a multigram yield of nanocrystals per one synthesis, which is important for nanocrystals synthesis scaling and decreasing of the price of their production (34).

CdSe nanocrystals were not only a single sort of materials synthesized by high temperature method. As already mentioned above, due to QCE one may control the spectral position of both absorption and emission bands of semiconductor nanocrystals by varying their size during the synthesis. CdSe nanocrystals are of special interest, since by varying their size from ca. 2 nm to 8–10 nm, we may cover with their emission nearly full visible region from ca. 460 to 660 nm (Fig. 6.2). But, some applications, such as tissue and *in vivo* imaging, require the materials also emitting in the near-IR region. Also, the utilization of highly luminescent nanocrystals as fluorescent markers in biology and medicine would be much more expanded with nanocrystals also emitting in a deep blue-UV regions of optical spectrum. This can be done with semiconductor nanocrystals other than CdSe II–VI QDs. For example, ZnSe nanocrystals may emit a light around 360–420 nm, while CdTe fluoresce in the 550–700 nm region. Earlier, an effective method for high temperature synthesis of bright ZnSe nanocrystals was developed, based on the reaction between TOP:Se and diethylzinc (35). Here, hexadecylamine, instead of TOPO was used as a coordinating solvent, because TOPO was found to bind too strongly to Zn ions resulting in the formation of only ultrasmall ZnSe clusters. Later, "greener" synthesis of highly luminescent ZnSe nanocrystals has been developed with zinc stearate as a precursor instead of dangerous zinc organometallic compounds (35). Similar to the earlier synthesis of CdSe nanocrystals, bright CdTe nanocrystals were synthesized with the emission band between 550–650 nm depending on the size of nanocrystals (36). Interestingly, both CdTe and ZnSe nanocrystals possess cubic crystalline structure, while CdSe nanocrystals are characterized by hexagonal phase (rarely reported preparations of cubic-phase CdSe nanocrystals seem to be doubtful).

The synthesis of various alloyed II–VI nanocrystals, such as $Zn_xCd_{1-x}Se$ (37), $Zn_xCd_{1-x}S$ (38), and $CdSe_xTe_{1-x}$ (39) are of special interest indeed. With the help of

ternary alloyed nanocrystals one may tune the nanocrystals emission range very precisely, especially within the spectral region not covered by regular II–VI nanocrystals. For example, it is difficult to achieve the bright blue–green emission of CdSe nanocrystals, since the luminescence quantum yield drops sufficiently with the decrease of nanocrystal size (in this case, $d < 2$ nm) (40). From the other size, ZnSe nanocrystals still emit at much shorter wavelength. Alloyed $Zn_xCd_{1-x}Se$ nanocrystals may be synthesized with the emission bands from deep blue to yellow region. Moreover, unlike regular CdSe nanocrystals, the spectral properties of $Zn_xCd_{1-x}Se$ may be tuned not only by changing the size but also the chemical composition of nanocrystals.

The spectral properties of ternary alloyed nanocrystals are not necessarily a function of their composition. $CdSe_xTe_{1-x}$ nanocrystals demonstrate a nonlinear compositional effect: at certain Se:Te concentration (ca. $Se_{0.35}Te_{0.65}$) nanocrystals with d = 6.5 nm exhibit photoluminescence band at around 800 nm, while the maxima of emission bands of pure CdSe or CdTe nanocrystals are at 650 and 750 nm, respectively (39). This effect is of special interest for QDs applications, since one may extend now the II–VI nanocrystals' emission wavelength maxima to near-IR region, what is very important for biological and medical applications. Further shift to even longer emission wavelength requires more narrow gap semiconductors, such as HgSe, HgTe, III–V (InP, InAs) or IV–VI (PbS, PbSe) semiconductor materials.

Alloyed ternary II–VI nanocrystals may be synthesized by standard high temperature reaction using at least two different technologies. First technology is based on the simultaneous loading of both precursors, such as Zn and Cd salts, for the case of synthesis of ZnCdSe or ZnCdS nanocrystals (37,38). In this case almost homogeneous $Me^{I}Me^{II}E$ nanocrystals are formed from the very beginning stages of the synthesis. From the other side, large difference in the reactivity of different precursors, such as Se and Te in the synthesis of CdSeTe nanocrystals may produce graded nanoparticles with core enriched with fast reacted component (i.e., CdTe) and CdSe shell (39). Alternative technology of synthesis of alloyed nanocrystals (ZnCdSe, for example) is based on initial formation of secondary compound core (here, CdSe) followed by the addition of Zn precursor in reaction mixture. This high temperature reaction is very long but produces sufficiently homogeneous alloyed ZnCdSe nanocrystals. It should be noted, that the formation of homogeneous alloyed nanocrystals is sensitive to the temperature of reaction: below certain level, homogeneity is not achievable even at very long reaction time. Otherwise, graded nanocrystals with the structure close to core-shell particles may be formed.

Besides high temperature synthesis of luminescent, II–VI nanocrystals in organic media, a room temperature preparation of nanocrystals in aqueous solutions has been developed recently. The general method is based on the reaction between cadmium salts dissolved in water and gaseous precursors H_2Se (for CdSe, HgSe) or H_2Te (for CdTe) or corresponding sodium salts NaHSe, NaHTe. The main point of this method was the utilization of water-soluble thioalcohols, such as 1-thioglycerol or mercapto acids (thioglycolic acid) as stabilizers of growing nanocrystals (41). It is well known that thiols bind strongly to the surface of II–VI nanocrystals via the S–Me bonds. Surprisingly, the presence of thiols in the reaction mixture brings about the formation

of highly monodisperse nanocrystals. Both CdSe and CdTe nanocrystals prepared by this method possess strong photoluminescence in aqueous solutions, which is quite unusual, since the water molecules are known to be strong photoluminescence quenchers. It was proposed that thiols on the surface of CdSe and CdTe nanocrystals form a monolayer, which works as a protecting shell against luminescence quenchers and a potential barrier for excited electron–hole pairs. Also, the adsorption of thioles on the surface of CdSe and CdTe nanocrystals may eliminate the surface traps reducing the nonradiative recombination of excitons. Such nanocrystals may be treated as transition structures between core and real core-shell nanocrystals.

6.2.2 Synthesis of Highly Luminescent Core-Shell Nanocrystals

From the very beginning of their history, II–VI semiconductor nanocrystals synthesized in the high temperature reaction suffered from a wide range of problems, which limited their practical applications. First, their luminescence quantum yield being much higher than that for nanocrystals prepared by other methods still was much lower than that for widely used organic fluorescent dyes. Second, the photostability of these so-called "core" nanocrystals was also quite low and both these parameters even worsened when the nanocrystals were transferred to aqueous solutions. The problem arises from the surface properties of core nanocrystals. The best recent high temperature synthesizes still produces "nonideal" nanocrystals with a lot of surface defects playing a role of nonradiative recombination centers or traps for excited electron–hole pairs, thus decreasing dramatically a fluorescence quantum yield. The QCE inside nanometer-sized semiconductor nanocrystals brings about a strong quantum mechanical interaction between excited electron–hole pairs and surrounding medium. The potential barrier between nanocrystal core and surroundings might strongly isolate the electron–hole pairs inside core, increase their lifetime, decrease the nonradiative recombination, and as a consequence drastically improve the fluorescence quantum yield and photostability (12,23). Few monolayers of wide gap materials would be enough to solve this problem. However, this shell must form an epitaxial structure on the surface of semiconductor core, that is, the interface between core and shell must be homogeneous and defect-free. The requirement for epitaxial growth of shell on the surface of II–VI nanocrystals limits the sorts of materials for this purpose by wider gap II–VI semiconductors with as little as possible crystalline lattice mismatch between core and shell materials. For CdSe core nanocrystals, ZnS, ZnSe, or CdS shells may be used, while for CdS and ZnSe core nanocrystals only ZnS is possible. For CdTe core, the choice of shells is wider (ZnS, ZnSe, CdS, CdSe shells, for example), but only CdS shell has shown a really good results. Other wide gap II–VI materials such as ZnO or MgS are not appropriate due to their specific chemical properties.

First really highly luminescent II–VI core-shell nanocrystals have been synthesized only few years ago after the development of high temperature procedures for core nanocrystals. At the beginning, a ZnS shell was grown atop CdSe core nanocrystals of ca. 3 nm in diameter via one-step synthesis in the same TOPO medium with organometallic precursors (7). Then, it has been found that two-step procedure with the intermediate extraction and purification of core nanocrystals gave better and

reproducible results for both ZnS and CdS shells on the CdSe core. (42). An addition of aliphatic amines such as hexadecylamine into the reaction mixture together with TOPO further increased the quality of core-shell CdSe/ZnS nanocrystals and luminescence quantum yield to 60% (43). While a quantum yield above 50% is routinely achieved now for CdSe/ZnS core-shell nanocrystals, the best synthesis can give up to 80% quantum yields at room temperature, which is close to this parameter for the best organic fluorescent dyes (10,11). The "greener" synthesis of core-shell CdSe/CdS nanocrystals also has been developed with multigram yield of nanocrystals per synthesis (34).

6.2.3 Synthesis of III–V and IV–VI Nanocrystals Emitting in Near-IR

Interest to the synthesis of highly luminescent nanocrystals of III–V compounds was motivated by two reasons. First, III–V nanocrystals might be used in comparative study of QCE in various semiconductor nanostructures, since most of physics was done in this field using III–V epitaxially grown quantum wells, dots, and superlattices (44). Second, III–V nanocrystals, such as InP, InAs, as well as IV–VI narrow gap PbS, PbSe, PbTe nanocrystals could be promising materials with intense emission in near-IR region, important for telecommunication, laser optics, and biological applications. Fluorophores emitting in deep red and near-IR region are of especial interest for biology and medicine for *in vivo* fluorescent analysis. General synthesis of III–V and IV–VI highly luminescent nanocrystals is based on the same high temperature protocol developed before for II–VI nanocrystals. TOPO-based reaction medium was found to be suitable enough for the formation of monodisperse spherical InP or InAs nanocrystals with controllable size. As precursors, both indium inorganic compounds, such as $InCl_3$ and phosphorous or arsenic organometallic substances were used successfully (28,45,46). Strong excitonic emission with quantum yield exceeding few tens of percents was achieved especially for core-shell nanocrystals. The growth of shell on InP or InAs core is more complex and tricky procedure than for II–VI nanocrystals. The use of wide gap III–V materials such as InN or GaN is problematic and other III–V materials were examined, including ZnS and $ZnCdSe_2$ ternary compounds and InAs/InP core-shell nanocrystals.

6.3 WATER SOLUBILIZATION AND BIOCONJUGATION OF NANOCRYSTALS

As far as we have noted in the previous section, QDs are mostly synthesized in nonpolar organic solvents. In order to solubilize them in aqueous solutions, their hydrophobic surface ligands (TOPO for CdSe/ZnS QDs, for example) must be replaced by amphiphilic multifunctional molecules (Fig. 6.5). Different QDs solubilization strategies have been devised over the past few years, including (i) ligand exchange with such simple thiol-containing molecules as mercapto acids, amino acid cysteine, or cysteamine (8,13,20), oligomeric phosphines (47), dendrons (48), peptides (49), and so forth; (ii) encapsulation by a layer of amphiphilic bi- (50) or

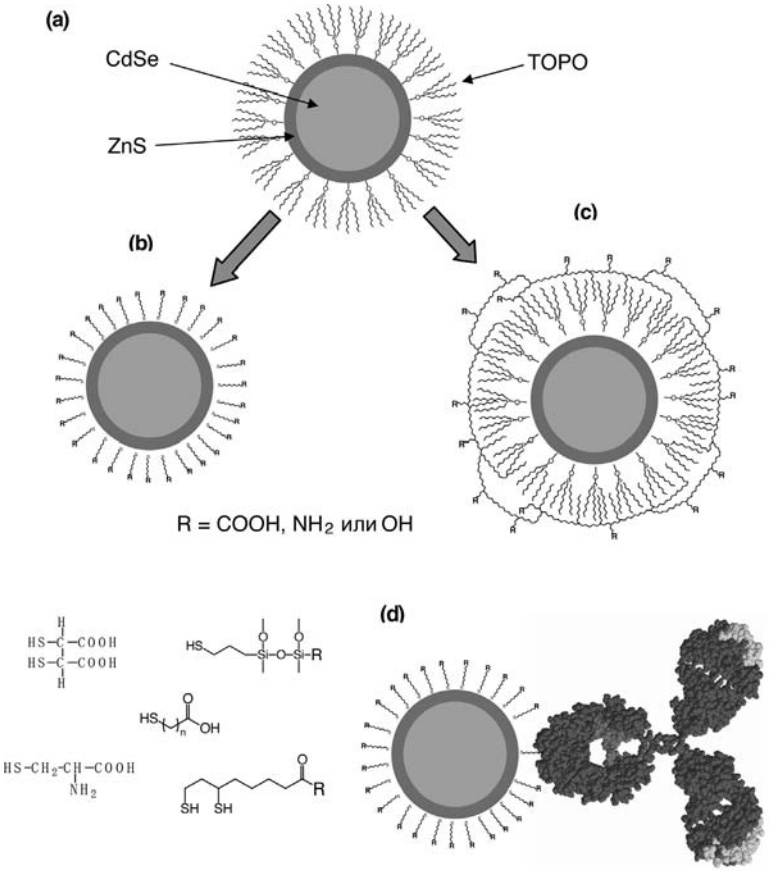

FIGURE 6.5 Examples of procedures of CdSe/ZnS core/shell nanocrystals solubilization and bioconjugation. As synthesized, QDs consists of the CdSe fluorescing core covered by a 1–2 monolayers of ZnS protecting core fluorescence from quenching; hydrophobic trioctylphosphin oxide (TOPO) covers the QDs surface after the synthesis (**a**). In order to make the nanocrystals biocompatible in aqueous solutions and adaptable for bioconjugation, we are treating the QDs surface with mercapto compounds (**b**) such as mercapto acids, cystein, cysteamine, or others. This procedure provides us with the (relatively) small water-soluble QDs adaptable for their bioconjugation through the functional COO- or NH2-groups of mercapto compounds used. Although this procedure is simple and hydrodynamic radius of resulting QDs is relatively small, the resting on the surface hydrophobic molecules of TOPO determines their potential for aggregation in a couple of the months time period. Panel (**c**) shows much more advanced procedure of QDs encapsulation within the additional organic shell formed by the mixture of a trifunctional polymers comprising (1) the groups with high affinity to QD surface; (2) the hydrophobic chains encapsulating the QD via the strong stacking interaction between these chains and with the hydrophobic TOPO chains on the QD surface; (3) the hydrophilic PEG-based functionalities ensuring solubility of nanocrystals, and terminating by the NH2- or COOH-groups available for bioconjugation. The conjugate of QD with an antibody is shown as an example (**d**)

trifunctional (11,51) polymers or in silica shells (52), phospholipids micelles (53), polymer beads (54–56), polymer shells (8,57), or amphiphilic polysaccharides (58). For simple applications such as QDs tagging of a target molecule, a single recognition moiety can be tagged to the QD (e.g., DNA oligonucleotide or aptamer, antibody, etc.) (Fig. 6.5). QD ligands containing either an amine or a carboxyl group, for instance, offer the possibility of cross-linking molecules containing a thiol group or an *N*-hydroxy-succinimyl ester moiety by means of standard bioconjugation reactions (8,13). Another approach uses electrostatic interactions between QDs and charged adapter molecules, or between QDs and proteins modified to incorporate charged domains (59). These functionalization steps can be repeated to add or change functionality. For instance, streptavidin-coated QDs can be used in combination with biotinylated proteins or antibodies. Currently, well-established procedures yield a variety of QDs with different selective functionalization, encoding their predictable cellular localization or molecular targets (nuclear localization sequences, antibody conjugates, etc.) (8,11,13,60,61). In very recent studies, evidence has been provided on the ability of CdSe/ZnS QDs to translocate 10–15 nm size peptide conjugates to the cell nucleus (62) and on the preferential nuclear targeting of 3-mercaptopropionic acid (MPA)—stabilized QDs (63).

6.4 NANOCRYSTAL CONJUGATES AS AN ALTERNATIVE TO ORGANIC FLUOROPHORES IN CELLULAR AND TISSUE RECEPTORS LABELING

Last 5 years, QDs have been tested in most biotechnological detection applications, including protein and DNA microarrays, immunofluorescence assays (4–6), and cell and animal biology (21,22). Some of the early and most successful utilizations of QDs have been achieved in immunofluorescence labeling of fixed cells and tissues and immunostaining of membrane proteins (8,13,55) or combed DNA (64). QDs are much brighter than dyes because of the multiplied effects of extinction coefficients that are the orders of magnitude larger than those of best organic dyes (Figs. 6.1 and 6.4), comparable quantum yield, and similar emission saturation levels (13,64). An additional advantage resides in their resistance to bleaching (8,13) over long periods of time (hours-scale), allowing the acquisition of images that are crisp and well contrasted (Fig. 6.6). Immunolabeling with QD-Abs conjugates was found to be 4200-, 2600-, and 420-fold more resistant to photobleaching than its labeling with fluorescein isothiocyanate-Abs, R-phycoerythrin-Abs, and AlexaFluor488-Abs, respectively (13). This increased photostability is especially useful for three-dimensional (3D) optical sectioning, where a major issue is bleaching of fluorophores during acquisition of successive *z*-sections, which compromises the correct reconstruction of 3D structures. The gain obtained with QDs was illustrated by the high resolution 3D confocal imaging of overexpressed P-glycoprotein, principle mediator of a multidrug resistance phenotype, in breast adenocarcinoma cells (13). The QDs are so bright that a very small number of QDs is necessary to detect a signal and their photostability permits the

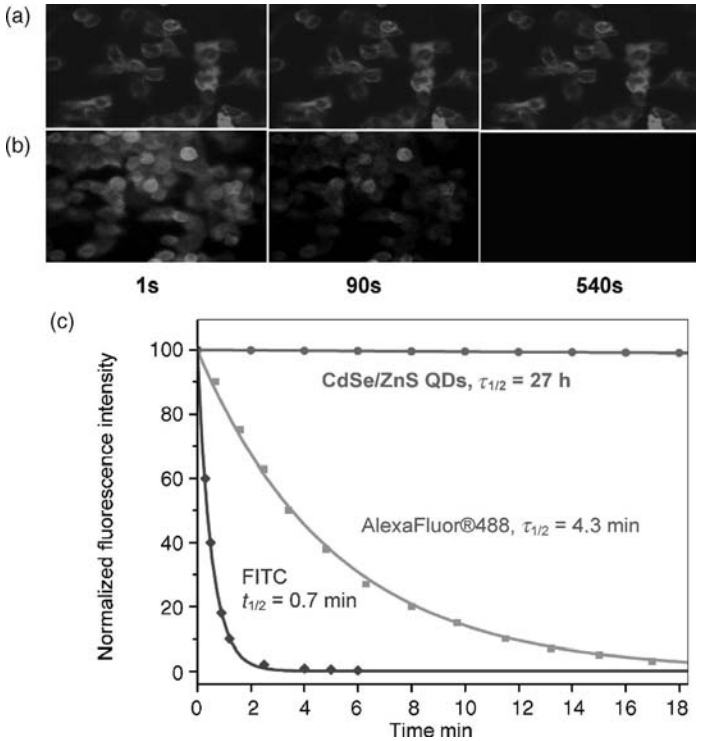

FIGURE 6.6 Semiconductor core/shell nanocrystals are rock solid against photobleaching. Fluorescence images of MCF-7r cells overexpressing *p*-glycoprotein (Pgp), mediator of a multidrug resistance phenotype, labeled with the anti-Pgp monoclonal antibodies and further stained with the QDs - (**a**) or FITC-tagged (**b**) secondary antibodies. Fluorescence images were recorded at 0, 90, and 540 s of illumination, respectively. Panel (**c**) presents time-dependent photobleaching curves of QDs-Abs, AlexaFluor-Abs, and FITC-Abs conjugates used as secondary Abs in the immunolabeling of p-glycoprotein on the membrane of MCF-7r cells. From this experiment nanocrystal-Abs conjugates have been calculated to be 4500 times as photoresistant to photobleaching ($\tau_{1/2} = 27$ h) as FITC-Abs conjugates ($\tau_{1/2} = 0{,}7$ min). Continuous wave excitation was provided by Nikon super-high-pressure mercury lamp HB10101AF

long-time signal accumulation. Several reports described detection of QDs blinking using immunodetection schemes, demonstrating that the sensitivity of QDs detection may be decreased to a single QD per target molecule (65).

We have demonstrated the first application of QDs-antibody conjugates to specific and ultrasensitive detection of antigens in paraffin-embedded formaldehyde-fixed cancer tissue specimens, using immunostaining of cytokeratin in skin basal carcinoma as an example (8). Recently, the first multiplexed detection of multiple antigens in the cancer tissue, located in a nuclear and on the cell membrane, was realized using QDs of different emission colors but at the excitation with the single wavelength (66) (Fig. 6.7).

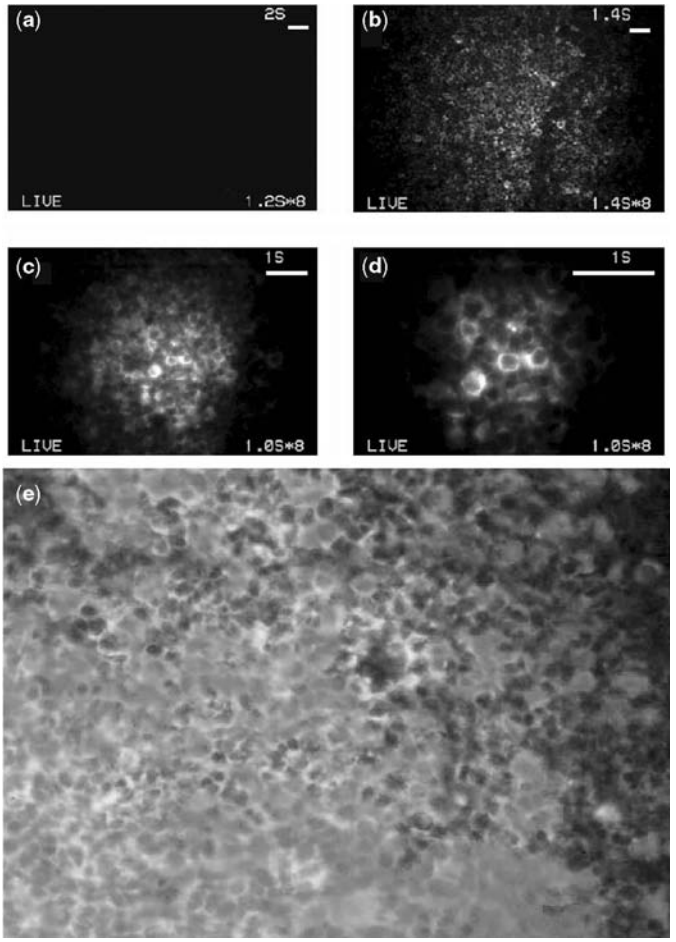

FIGURE 6.7 Fluorescence images of tonsil cancer tissue labeled with the QDs-antibody conjugates. Panels (**b**), (**c**), and (**d**): Samples were incubated with the anti-leukocyte common antigen (LCA) primary antibodies and stained with anti-mouse polyclonal immunoglobulins tagged with the CdSe/ZnS QDs. Panels (b), (c), and (d) represent fluorescence images of the same sample recorded at the $\times 10$, $\times 20$, and $\times 40$ magnifications, respectively. Panel (**a**) represents control: fluorescence image of the same sample incubated directly with the anti-mouse polyclonal immunoglobulins tagged with the QDs without preincubation with the primary antibody. Images are recorded using a Nikon Diaphot 300 fluorescence microscope equipped with the filter combination for fluorescence excitation at 480 nm and detection of emission at 590 nm. Scale bars: 50 μm. Panel (**e**): an example of a fluorescence image of double labeling of cancer tonsil tissue recorded under the excitation with the same UV-lamp. Primary anti-Ki67 antibodies were detected after staining with the secondary antibodies coupled with the red QDs (cell nuclear labeling), and the primary anti-LCA antibodies were detected with the secondary antibodies labeled with green QDs (cell membrane labeling)

Another promising application area is the use of near-infrared (NIR) QDs for *in vivo* biomedical imaging (17,51). The use of NIR light for biomedical imaging solves the problem of high tissue autofluorescence by reducing fluorescence background. Water-soluble CdSe-ZnS QDs capped with amphiphilic polymer was intravenously injected into live mice for deep multiphoton imaging (17). Not only the QD-containing vasculature was clearly visualized but also the blood flow velocity and heart rate were calculated according to the fluorescence. This new imaging technique allows the surgeons to clearly see the target lymph nodes without cutting the animals' skin, and has the potential to improve the technique even further. This noninvasive technique may open the door in medical research and drug discovery. Nie's group (51) detected tumors in the tumor-bearing mice by injecting tumor-targeting antibody conjugated with QDs to the tail vein. Simon et al. (126) used QDs to track metastatic tumor cell extravasation. DHLA-capped QDs emitting different colors (510, 550, 570, 590, and 610 nm) were each loaded into five groups of B16F10 cells with the help of cationic lipids. Then, the tumor cells labeled with QDs were injected into mice. These QDs were detectable in the lung and it was able to identify each of the five populations of cells.

QDs are available in a virtually unlimited number of well-separated colors, all excitable by a single wavelength (Fig. 6.1). Aside from simplifying image acquisition, this property could be used in confocal microscopy to perform nanometer-resolution colocalization of multiple-color individual QDs (Fig. 6.8).

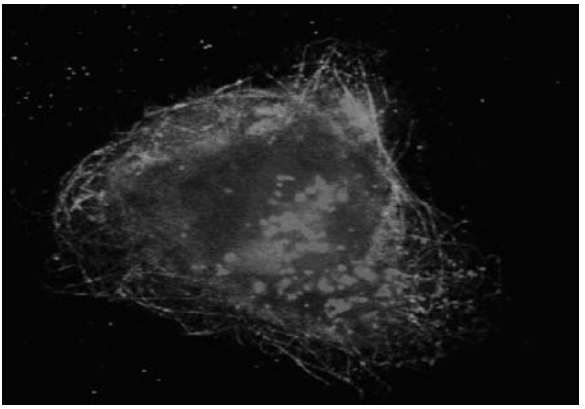

FIGURE 6.8 Multicolor intracellular detection with the QDs of different diameters. Different cellular compartments (targets) may be tagged with the functionalized QDs of different colors, excited with the single wavelength light source (lamp), and provide ultrasensitive multiplexed imaging. Here, multicolor confocal microscopic analysis of uptake and intracellular distribution of red-emitting QDs in relation to the microtubule cytoskeleton (green) in human phagocyte cell line THP-1 is presented. QDs remain photostable over the extended observation periods (>24 h) and do not perturb the cytoskeleton structure and function. Nucleus is stained blue by DAPI

6.5 DETECTION OF BACTERIA

While mammalian cells take up QDs by endocytosis, bacteria do not endocytose, and internalization of QDs by prokaryotes has so far not been observed. Such internal labeling would be desirable in many applications. Green fluorescent protein does not work in many strains, especially in anaerobes, and hence, general fluorescence labeling techniques are needed (67). Because QDs are both fluorescent and electron dense, fluorescence and electron micrographs can be directly compared for high resolution imaging of internal mechanisms in single bacteria. Three possible mechanisms through which nanocrystals could pass through bacterial cell walls and membranes are nonspecific diffusion, nonspecific membrane damage, and specific uptake.

Nonspecific diffusion is unlikely with QDs; the largest globular proteins that can pass through intact cell walls of *Bacillus subtilis* have radii of ~2 nm (68), while the smallest high quality QDs measure ~3–4 nm (representing green emission for CdSe and blue emission for CdS (69).

Entry of other types of nanocrystals into bacteria via nonspecific membrane damage has been established, particularly with highly reactive halogenated nanoparticles (70). QDs are able to transfer electrons to redox-active molecules (including oxygen) upon light exposure (71); the smaller the QD, the greater its redox potential (72). The dependence of particle entry upon light exposure would strongly suggest this mechanism.

Specific transport is the last possibility. The pore sizes for specific transport can be somewhat larger than those for nonspecific diffusion; the largest pores known, permeases for excreting proteins from bacteria, have been shown to have pore openings of up to 6 nm (73). Most pore sizes are unknown, however, as the genes for the permeases have not been cloned.

Relatively, little is known about bacterial interactions with QDs and other nanostructured materials. Strain specific and metabolism-specific QD binding to surface receptors of bacteria has been observed and is similar to that in other eukaryotic QD studies on surface receptors. Internal QD labeling has been shown on bacteria chemically treated to take up small plasmids (74). While the utility of QDs as a biological imaging tool has clearly been established for eukaryotic cells, the application of QDs to investigate microbial processes has not been fully realized.

The examples of gram-positive bacterium (*Bacillus subtilis*) and gram-negative bacterium (*Escherichia coli*) imaging were performed by using the adenine- and AMP-conjugated QDs. It was demonstrated that the QDs conjugates can be able to label bacteria only if the particles are <5 nm in diameter (75). Spectroscopy and electron microscopy suggest that QDs of <5 nm can enter the cells whole, probably by means of oxidative damage to the cell membrane, which is aided by light.

Internal bacterial labeling of *Escherichia coli* with water-soluble CdSe/CdS QDs functionalized with citrate, isocitrate, succinate, or malate, and unique intracellular interactions of these QDs within bacteria was demonstrated (76).

Despite the release of Cd^{2+} ions upon light exposure, which is cytotoxic to many mammalian cells (77,78), significant cell death or sporulation is not seen in bacterial cultures exposed to the adenine- and AMP-QDs conjugates. Slowed rates of growth are

seen in internally labeled cultures, but this is likely to reflect nonspecific mechanisms more than heavy metal release, since nanocrystals made of less toxic materials such as Ag (79) and Si (80) also slow bacterial growth in a similar fashion. However, some suggestion of heavy metal damage was seen when gram-positive (*Bacillus subtilis*) cells were incubated with bare CdSe QD conjugates under room light, which was not seen with CdSe/ZnS QDs or in the dark (75). Very low concentrations of Cd, too low to be cytotoxic or detectable in solution, are known to inhibit DNA repair enzymes and may thus inhibit cell division (81). The toxicity seen in gram-negative (*Escherichia coli*) bacterium was much less than that in gram-positive bacterium, but recovery of cell growth was accompanied by loss of fluorescence and expulsion of electron-dense material consistent with whole QDs from the cells. Gram-negative bacteria are known to be able to extrude many materials through extrusion pumps, for example, *Pseudomonas aeruginosa* was shown to expel Ag nanocrystals (82).

6.6 DETECTION OF VIRUSES

Interesting application of the QDs is the continuous tracking of viral infection (83–85), which could lead to knowledge useful to prevent the initial steps of viral infection. The remarkable photostability and brightness of QD will allow long-term tracking of single virus particles. One strategy of virus labeling is to covalently modify the outside of virus particles with QD (86,87). However, unless the position for the attachment of the QD on the capsid protein is selected carefully, the normal properties of viral infection will be affected. An alternative approach is to place the optical beacon inside the capsid, by partial or total replacement of the viral nucleic acid (88).

One of the perspective ways is using the techniques similar to the incorporation of metal, in particular, gold nanoparticles into the viruses. From an applied point of view, if the same conditions exist for different cores, then it should be feasible to encapsidate other cores with desired properties as long as basic surface chemistry specifications are met. This analysis would also confirm the hypothesis that, similar to other self-organized mesoscopic systems, such as micelles (89) the general principles underlying the virus self-assembly process can be used to control its outcome.

There are a number of challenges in working with QDs for the formation of viruslike fluorescent bioprobes (VLFB). First, upon light exposure, QDs could photorelease chemical species that would affect nearby macromolecules. For example, photoreleased Cd^{2+} ions could attack accessible cysteines in the capsid (78). Second, the QDs need to be soluble in aqueous solutions. Although several methods have been worked out to achieve solubility, the close proximity between the QD and the capsid proteins may have additional specific requirements. Third, in working with the assembly of bromoviral capsids, one needs to keep pH values approximately between 5.0 and 7.5 because this range is required to stabilize the viral particles and induce capsid assembly (90).

Comparison of water-soluble QDs coated by four different agents methods, including lipid micelles, streptavidin-biotin-DNA, DHLA (dihydrolipoic acid), and polyethylene glycol (PEG)-COOH, shows that the only last system gives stable and uniform VLFBs (91). The fluorescent bioprobes shows the highest ability in

promoting virus capsid assembly. Multiple functionalized QDs can be encapsulated by self-assembly in viral capsids, yielding a viruslike particle similar in size with the native virus. Encapsulation of several functionalized QDs inside each particle is due to the smaller size of QDs compared to similarly functionalized gold nanoparticles reported earlier. Furthermore, manipulations of the diameter of the packaged material can be used to achieve the degree of packaging, and it should facilitate additional industrial processes that require nanoparticles of uniform sizes and yet have a protein coat that can be manipulated for the desired specificity by molecular engineering.

Conjugation of QDs with the virus surfaces proteins demonstrates high potential in the understanding of molecular mechanism of cell infection. Labeling of fusion (F) and attachment (G) proteins localized on the surface of respiratory syncytial virus (RSV) permits to monitor the progression of RSV infection (92). The conjugates of antibodies anchored through streptavidin–biotin bounding with 525 and 605 nm QDs were used. High QDs photostability allowed to perform confocal microscopic image of colocalization of the F and G proteins in RSV infected HEp-2 cell monolayer cultures a few days postinfection. It demonstrated that QDs can serve as immunofluorescent labels for key viral proteins, the progression of viral infection was followed by monitoring the expression of F and G proteins over time. On the contrary, with efficacy of QDs labeling, alternative methods, which were used under similar conditions, do not give positive results (92). In particular, protein F could not be detected by Western blot analysis, using an established sensitive chemiluminescent detection protocol for at least 96 h following infection.

Several nanotechnologies, including atomic force microscopy, carbon nanotubes, and magnetite nanoparticles have been used for viral detection. While these methodologies provide detection and characterization of viral surfaces, they offer minimal insight into understanding of the molecular level of viral infections. The QDs make possible to use multiple probes to investigate the spatial distribution of several viral proteins simultaneously throughout the stages of infection. Therefore, QDs may provide a method for early, rapid detection of viral infection, and open the door for studies of the intricate spatial features and cell trafficking of viral components.

Hybrids of viruses and inorganic nanoparticles can also be used to create new types of functional nanoscale devises, such as sensors. Similar to nanowire, for which DNA molecules as template are used (64), viruses can be used as base for preparation of well-ordered nanoscaffolds. This approach was realized for preparation of 2D assembles of virus particles (compea mosaic virus) decorated with luminescent QDs (93). It was found the larger fluorescent signal than that generated by QDs immobilized on a similar "flat" surface area. This approach could have implications in designing hybrid protein assemblies. For example, the QDs on the virus scaffold can in turn act as a scaffold for other proteins.

The large surface area available on each viral particle could provide a scaffold for immobilizing an array of molecular assemblies with different functionalities and properties, so as to allow for a system with multiplexing capabilities. The different programmable chemistries of residues available on the virus surface lend themselves to these types of experiments. Inherent virus properties such as organized assembly, extensive exterior surface, enclosure of a large internal space, and propensity to form arrays, combined with the unique QD properties, make these hybrids suitable

templates for creating and investigating new nanocomposite materials with biomedical/bioelectronic applications.

6.7 NANOCRYSTAL CONJUGATES FOR MULTIPLEXED DETECTION ON TISSUE AND PROTEIN MICROARRAYS

Whereas DNA microarrays benefit from nucleic acid amplification for increased sensitivity, proteins cannot be similarly amplified. Therefore, the detection systems for protein arrays must have a built-in signal enhancement step. A variety of conventional labeling techniques, including radioactivity, chromagens, and fluorescence have been used to report the presence of proteins on arrays. However, in their current forms, they often have significant limitations in terms of their sensitivity, dynamic range, durability, speed, safety, and ability for multiplexing.

When investigating clinical specimens, a reporter system with a broad dynamic range is required so that disparate quantities of input material can be effectively measured under a single format or experiment, in which detection saturation is not easily achieved. A common means of expanding the dynamic range of a protein assay is through the use of fluorescent reporter molecules, and there is an abundance of commercially available organic fluorophores that have been used to tag biological molecules. Unfortunately, many organic fluorescent molecules lack the sensitivity of amplified chromogenic systems and are highly susceptible to photobleaching. Application of emerging nanotechnologies to biology and medicine has produced an alternative class of fluorescently labeled probes through the conjugation of QDs to biological interacting molecules. Due to their resistance to photobleaching, QDs produce signals that can be time averaged.

Tissue microarray (TMA) is an invaluable tool for simultaneous histological analysis of hundreds of archival tumor biopsies. Current research on biomarkers of tumor progression includes microscopic examination of hundreds of tissue samples and evaluation of protein expression levels. The intensity of cancer markers, as determined by visual analysis of colorimetric stains, is used to define a numerical score for staging of tumor biopsies and can be subjected to inter- and intra-observer variability. Quantification of pathology markers has been attempted using standard immunohistochemistry. The numerical categories created by this method, however, provide merely semiquantitative values and a limited range especially at a very low or high expression level. Several automated methods have also been used to determine localization and quantification of target antigens. The precept of these techniques is protein expression analysis through acquisition of fluorescence images obtained from conventional fluorescence dyes. The intensity and accuracy of this quantification method can be compromised by the photobleaching property of fluorophores. Furthermore, the sensitivity of quantitative analysis of protein expression can be affected by tissue autofluorescence.

In archival tumor samples, tissue autofluorescence is due to light absorption and scattering from endogenous proteins such as elastin, fibronectin, and collagen, from nucleic acids, and from tissue preparation processing and fixation. Given the excessive

photobleaching and low signal-to-noise ratios of fluorescent dyes, they are indeed poor candidates for antigen quantification studies. Thus, the feasibility of a sensitive expression profiling and *in situ* quantification of cancer markers in formalin fixed paraffin embedded (FFPE) biopsies, the most valuable archival tumor specimen, is restricted by the properties of fluorescent molecules and techniques currently used in the laboratory and diagnostic settings.

With the advent of nanotechnology, QDs hold a novel and promising approach for the quantification of antigen-derived markers in FFPE tissue samples. QDs allow for obtaining high signal sensitivity and thereby minimizing the autofluorescence effect in biological imaging applications. QD bioconjugates were employed in conjunction with an optical spectroscopy system with the potential to detect single molecule fluorescence, the ultimate in detection sensitivity, for high throughput analysis of target antigens on tissue microarrays (94). With this optical spectroscopy configuration, measurement of the fluorescence emission of a single QD in a localized area has been achieved (95). Overall, the use of these technologies allows for the analysis of high density tissue microarray data in an automated, accurate, sensitive, and efficient manner.

QD-based immunostaining of membrane epidermal growth factor receptor (EGFR), pan cytokeratin, and E-cadherin in lung cancer xenografts was performed on FFPE tissue microarray slides. Lung cancer xenografts were established by implanting lung carcinoma cell lines MGH7, RVH-6849, A549, H460, H1264, MGH8, H520, and H157 into ventrolateral flanks of severe combined immune deficiency (SCID) mice. Tumors of size 1–2 cm were surgically resected after 4 weeks, fixed in formalin, and embedded in paraffin according to the standard histological procedures for preservation of human tissue biopsies. The pattern of antibody expression was compared to that obtained from an organic dye, AlexaFluor 488. There was undetectable nonspecific binding observed for QD staining of tissues using this strategy (94).

The signal obtained from QD immunostaining for EGFR showed no reduction in signal intensity during continuous irradiation of a UV laser for 30 min, whereas the fluorescent signal from Alexa 488 showed 70% reduction in signal intensity during the same exposure time. In addressing these two problems, the QD signal could provide a more accurate means of measurement of signal intensity and quantification of tumor-derived antigens in cancer biopsies.

Protein microarray technologies provide means of investigating the proteomic content of clinical biopsy specimens in order to determine the relative activity of key nodes within cellular signaling pathways. A particular kind of protein microarray, the reverse-phase microarray, is being evaluated in clinical trials because of its potential to utilize limited amounts of cellular material obtained through biopsy. Using this approach, cellular lysates are arrayed in dilution curves on nitrocellulose substrates for subsequent probing with antibodies. The use of QDs conjugated to streptavidin in a reverse-phase protein microarray format for signal pathway profiling has been recently described (96). Hyperspectral imaging of the QD microarray enabled unamplified detection of signaling proteins within defined cellular lysates, which indicates that this approach may be amenable to multiplexed, high throughput

reverse-phase protein microarrays (RPPM) in which numerous analytes are measured in parallel within a single spot.

In this approach, the use of QD reporter molecules was combined with a hyperspectral imaging techniques that results in the detection of primary, unamplified signals in assays probing for the presence of signaling proteins present in cellular extracts. The detection of numerous unamplified signals within the same protein spot heralds the approach of truly multiplexed quantitative microarray assays for protein activity. This approach has potential utility in clinical settings, enabling selection of personalized therapeutic regimes.

Hence, the potential for multiplexed assays, detection of unamplified signals, expanded dynamic range, and robustness under repeated and varying exposure periods makes QD nanoparticles especially suitable for clinical proteomics applications. The hyperspectral image analyzer enables a broadened use of QDs in RPPMs because of its sensitivity and multiplexing characteristics. Technological advances such as integration of QDs and hyperspectral imaging into RPPMs for molecular network analysis will hasten the advance of personalized assessments of patient tumor cells.

6.8 MICROBEADS OPTICALLY ENCODED WITH THE FLUORESCENT NANOCRYSTALS

Bead-based assays on very large numbers of molecules in proteomics, genomics, drug screening, and clinical diagnostics require encoding of each of the microbeads according to the particular ligand bound to its surface (97). Polymeric beads optically encoded with organic dyes allow for a limited number of unique codes (98,99), whereas the use of semiconductor nanocrystals QDs as fluorescent tags improves the beads multiplexing capabilities, photostability, and sensitivity of the antigen detection (54,64,100,101).

A first proof-of-concept publication proposed to use QDs-encoded microbeads for multiplexed detection of oligonucleotide probes hybridization (54). Follow-up studies validated the QD-tagged microbeads as a sensitive tool for high throughput genotyping of single nucleotide polymorphisms (100) and for gene expression profiling (101). Although all these genomics applications of nanocrystals-encoded microbeads were demonstrated more than 5 years ago, the proteins or antibodies coupling to the beads without the loss of biological activity was still under development up to now.

The first NCs-tagged beads application to clinical proteomics for antibodies profiling and diagnostics of autoimmune diseases was demonstrated very recently for an example of QDs-tagged microbeads prepared by the method of layer-by-layer (LbL) NCs deposition on the surface of the beads using oppositely charged polyelectrolyte molecules (102,103). Preparation of QD-encoded microbeads suitable for antibodies profiling and immunodiagnostics of autoimmune diseases included (i) synthesis and functional water-solubilization of CdSe/ZnS core/shell QDs of different sizes (colors of emission), (ii) preparation, by the method of layer-by-layer electrostatic deposition of polymers in combination with infiltration of QDs (104), of optically encoded homogeneous and brightly fluorescent microbeads, and

(iii) expression and purification of enzymatically active 68-kDa fragment of human topoI followed by its adsorption on the surface of QD-encoded fluorescent microbeads. CdSe/ZnS QDs emitting in green (545 nm), orange (575 nm), or red (630 nm) with a quantum yield of 40% in aqueous solutions, were embedded into presurface layer of polymer-coated monodispersed melamine formaldehyde latex microbeads of 3 μm in diameter (Fig. 6.9a and b). The surfaces of QD-encoded microbeads where rendered specific to anti-topoI (anti-Scl-70) antibodies by passive adsorption of an

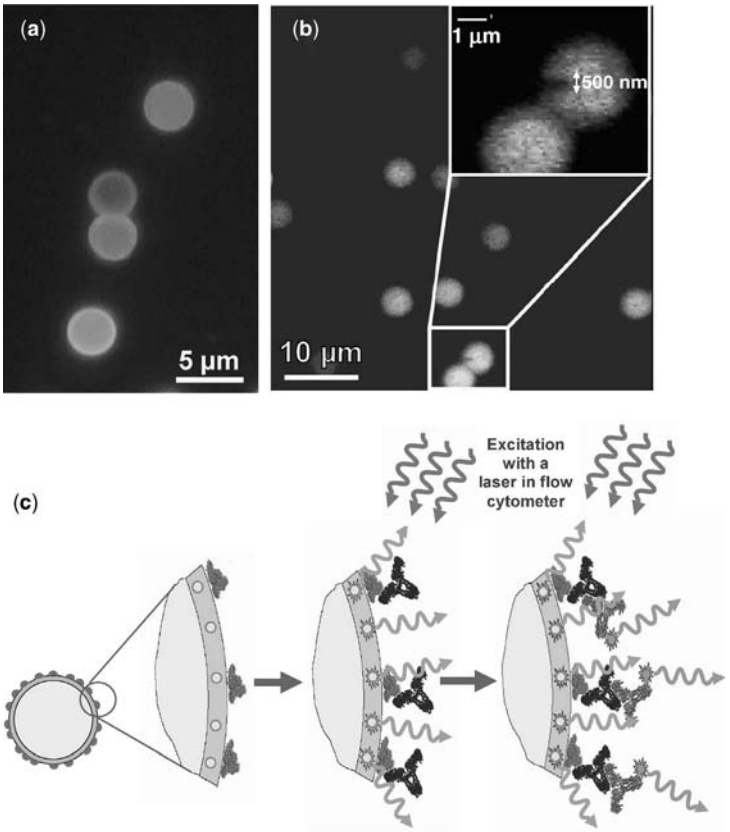

FIGURE 6.9 QDs-encoded, human DNA topoisomerase I-coated microbeads for diagnostics of autoimmune diseases. (**a**) Fluorescence micrograph of a mixture of microbeads encoded with the QDs of different emission colors. (**b**) Fluorescence image of QD-encoded beads obtained with confocal laser scanning optical microscope. Insert demonstrates a size spot of the excitation beam on the surface of a QD-encoded microbead intentionally photobleached by high power laser illumination. (**c**) Scheme of a flow cytometry assay for immunodetection of anti-topoisomerase I antibodies, markers of systemic sclerosis, with QD-encoded, topoisomerase I-coated microbeads. Microbeads optically encoded with orange-emitting QDs and coated by 68-kDa recombinant fragment of topoI are incubated with anti-topoI specific monoclonal antibodies or with the serum samples of patients, and stained with green-emitting FITC-labeled secondary antibodies. Excitation is provided by the 488 nm line of an Ar-laser

enzymatically active 68-kDa fragment of recombinant topoI produced in baculovirus system, and were back-coated with bovine serum albumin (BSA) protein.

The principle of flow cytometry detection assay used is shown in Fig. 6.9c. Flow cytometry analysis demonstrated that the QD-encoded topoI-covered microbeads were extremely bright and homogeneous (Fig. 6.10). In order to confirm the presence of topoI at the microbead's surface, they were incubated with the monoclonal anti-topoI antibodies and stained by the FITC-labeled goat F(ab′)2-fragment of antimouse

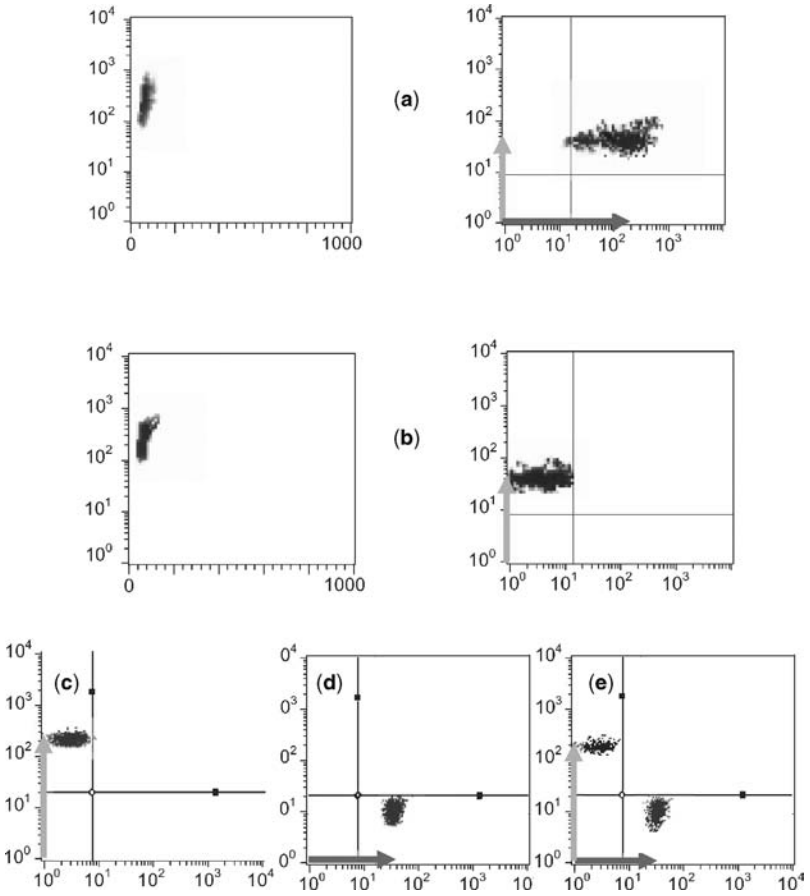

FIGURE 6.10 Flow cytometry dot plots of nanocrystal-encoded, topoisomerase I-coated microbeads used for detection of anti-ScI-70 antibodies, markers of systemic sclerosis, in the clinical serum of healthy donors and patients with systemic sclerosis (according to schematics of Figure 6.9. (a,b). Left column: light scattering measurements; right column: green (FL1) versus orange (FL2) fluorescence profiles. Right column: NCs-encoded, topoI-coated microbeads incubated in serum of a patient with systemic sclerosis (a) or in serum of a healthy donor (b) and stained with the FITC-labeled secondary antibodies. (c–e) Green (FL1) versus orange (FL2) fluorescence profiles of topoI-covered microbeads encoded with the NCs of orange (**c**) or green (**d**) emission colours, and the result of analysis of a mixture of these beads (**e**)

immunoglobulin (IgG). The shift of fluorescence signal from orange (fluorescence from the QDs on microbeads) to green area (signal from the FITC) after addition of FITC-labeled IgG, clearly approving the presence of topoI at the microbead's surface. Quantitative statistical data based on analysis of the positive and negative events in these experiments show an existing of clear discriminative criteria of anti-topoI antibodies binding. QD-encoded bead light scattering and fluorescence signals exhibited very narrow distribution peak, regardless of their surface antigen staining, particularly without any need of fluorescence compensation. For example, 90% of all the topoI-covered beads were found to be within 71 out for 10,000 channels of detector, whereas 88% of beads with two-colours immunocomplexes on their surfaces are within the 67 out of 10,000, corresponding to the microbeads heterogeneity coefficients 0.007889 and 0.007614, respectively. Hence, the QDs-encoded topoI-covered microbeads were proved to be useful for clinical immunodiagnostics of anti-Scl-70 antibodies, markers of systemic sclerosis, in the serum of scleroderma patients.

For functional clinical tests, we have used the samples of serum from scleroderma disease patients with confirmed elevated level of anti-Scl-70 antibodies and compared them with healthy controls. The sera used were characterized by standard IIF and ELISA techniques in order to correlate their results with flow cytometry assay utilizing QD-encoded microbeads. Appearance of fluorescence shift from orange to green area after incubation of topoI-covered beads with serum of positive patients compared with serum of negative patients (Fig. 6.10) provided a clear discrimination criteria and excellently agreed with the results of traditional IIF and ELISA detection techniques.

Results of a proof-of-the-concept flow cytometry experiment with a mixture of microbeads encoded with QDs emitting in green and orange regions of optical spectrum are shown in Fig. 6.10c–e. The compensation requirements in multiplexed flow cytometry assays with fluorescent microbeads encoded with organic dyes impose a strong limit on their sensitivity. Fluorescence spectra of QD-encoded beads are narrow, symmetrical, and do not trail toward longer wavelengths. These advantages of QDs over organic dyes permitted us to record the multiplexed spectra without any fluorescence compensation (Fig. 6.10c–e) ensuring maximal discrimination of multiple signals, thus, increasing additionally a sensitivity of multiplexed flow cytometry assays.

To further demonstrate the possibility of multiplexed screening and to estimate the limit of autoantibodies detection with QD-encoded microbeads, we have employed a single-bead immunodiagnostics format relying on FRET between QDs and dye molecules labels of a secondary antibody (Fig. 6.11). Microbeads encoded with orange-emitting QDs and coated by 68-kDa fragment of topoI were incubated with the anti-topoI specific antibodies and stained with the AlexaFluor633-labeled secondary antibodies. In the single-bead set up, confocal laser scanning optical microscope was equipped with a laser generating light at 532 nm and with a lamp providing a broadband excitation between 450 and 500 nm. As shown in Fig. 6.11b, AlexaFluor633 dye used as a label for secondary antibody does not absorb light at the wavelengths lower than 500 nm and cannot be excited by the lamp, whereas the QDs can be excited by both light sources. Providing sufficient spectral overlap of QD emission with dye absorption, excitation energy can be transferred from QDs to dye

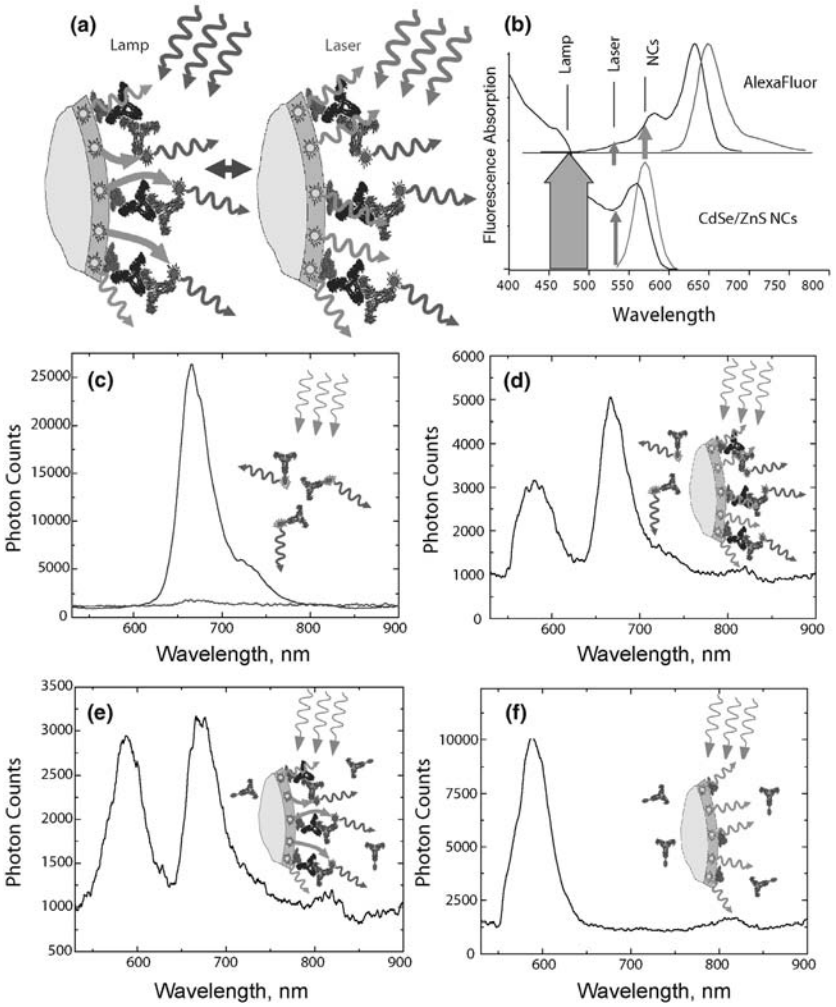

FIGURE 6.11 Single bead immunoassay for FRET detection of anti-topoisomerase I specific antibodies. (**a**) Scheme of a single bead FRET assay for immunodetection of anti-topoisomerase I antibodies, markers of systemic sclerosis, with QD-encoded, topoisomerase I-coated microbeads. Microbeads encoded with orange-emitting QDs and coated by 68-kDa recombinant fragment of topoI are incubated with the anti-topoI specific monoclonal antibodies and stained with the AlexaFluor633-labeled secondary antibodies. Excitation is provided either by the 532 nm of a laser or by the 450–500 nm broad band from a lamp. (**b**) Absorption and emission spectra of CdSe/ZnS QDs and AlexaFluor633 dye. Excitation wavelengths for the laser (532 nm) and lamp sources (450–500 nm) are indicated. The lamp source selectively excites QDs but not the dye, while the laser source excites both QDs and dye. (**c**) Emission spectra measured from solution of AlexaFluor633-labeled secondary antibody under the laser (pink line) and lamp (red line) excitations. (**d**) Emission spectrum from a QD-encoded, topoI-coated microbead incubated with the anti-topoI specific antibodies and stained with the AlexaFluor633-labeled secondary antibodies, *excitation by the laser*. (**e**) Emission spectrum from

molecules labeled on secondary antibodies, thus confirming binding effect. Large spectral distance between the emission of QDs and dye allows for easy resolution of both emission peaks, providing multiplexed detection. Fig. 6.9b shows typical fluorescence image of single QD-encoded microbeads obtained with this setup. The diameter of excitation region was ~ 500 nm (insert in Fig. 6.9b) allowing to scan over surface of single microbeads and measure emission spectra simultaneously. The fluorescence intensity statistically varied for different microbeads, but was very similar (10% variation) for different scan areas of one and the same bead, indicating homogeneous distribution of QD within the presurface layer.

Figure 6.11c shows that the red emission from AlexaFluor633-labeled secondary antibody in solution can indeed be detected upon excitation by laser, but not by the lamp. When the laser beam was focused on the surface of a single bead, both the orange emission from the QDs and the red emission from AlexaFluor633 have been detected (Fig. 6.11d), confirming the presence of specifically bound AlexaFluor633-labeled secondary antibodies at the microbead's surface. The most interesting result was obtained with a QD-selective lamp excitation focused on a single bead. Here, both the orange emission from the QDs and the red emission from AlexaFluor633 were detected (Fig. 6.11e), although the excitation by lamp falls beyond the dye absorption (Fig. 6.11b), so that AlexaFluor633-labeled secondary antibodies in solution cannot be excited by lamp (Fig. 6.11c). Hence, the QDs from presurface layer of the microbeads effectively act as FRET donors for excitation of specifically bound AlexaFluor633-labeled secondary antibodies. Fig. 6.11f shows the result of a control experiment, where no emission of AlexaFluor633 was detected under QD-tagged beads excitation by the lamp focused on a single microbead in the absence of topoI-specific antibody, where the binding of AlexaFluor633-labeled secondary antibody was not possible.

The diameter of excitation spot provided by our confocal microscope was ~ 500 nm (insert in Fig. 6.9b). In case of a monolayer coverage of the microbead's surface with topoI molecules followed by formation of sandwich-like complexes (Fig. 6.11a) with primary antibodies and dye-labeled secondary antibodies, maximum 30 complexes can be located within the fluorescence detection region on the microbead. We were, thus, able to detect less than 30 specifically bound antibodies with our setup. Selectively excited QDs transfer energy to the nearby antibody dye label allows for detection of double-peak fingerprint emission with one peak originated from the QDs on the bead and another one from the dye label on the secondary antibody (Fig. 6.11e). Specific interaction between the microbead and the antibody turns the fluorescence signal from dye label off and on (Figs. 6.11e and f), thus effectively discriminating between the occurrence and the nonoccurrence of antibody binding effect. The

◀

a QD-encoded, topoI-coated microbead incubated with the anti-topoI specific monoclonal antibodies and stained with the AlexaFluor633-labeled secondary antibodies, *excitation by the lamp*. (**f**) Negative control: No emission of AlexaFluor633 label on the secondary antibody is detected under the NC-selective *lamp excitation* focused on a single microbead in the absence of topoI-specific monoclonal primary antibody

absence of fluorescent background from noninteracting with the beads dye-labeled antibodies (Fig. 6.11f) additionally increases the sensitivity of detection and further facilitates the multiplexing capabilities of immunodetection.

Planar surface arrays currently offer the greatest per array complexities, but are limited by their methods of binding autoantigens and suffer from drying, which can distort and/or sterically interfere with immunologic epitopes (105). Liquid phase microbead-based assays utilizing minimally disruptive methods to label antigens are free from these limitations (106). These results open the way to QDs-based clinical assays with previously unachievable detection sensitivity. High throughput screening utilizing unique and robust fluorescence properties of QD-encoded beads will enable effective determination of multiple autoantibodies and enhance the clinical sensitivity and specificity of autoantibody screening for ultrasensitive multiplexed diagnostics.

6.9 PERSPECTIVES

For today, we are witnesses of prompt development of technologies and applications of QDs. Alongside with constant growth of interest to QDs as fluorescent labels, occurrence of new applications takes place: flash memory, light emitting diodes (LED) flexible displays and flexible electronics, solar cells and white LED lightning. Among these new applications are new tools for medicine and biology. Advantages of QDs is necessary to develop in order to enter in full in these areas of their applications. In synthesis, new compositions could entail QDs with properties such as (i) sensitivity to electric or magnetic fields; (ii) narrower fluorescence emission and longer lifetimes (using lanthanide-doped QDs); (iii) smaller sizes and extension to the NIR spectrum, as demonstrated by ternary alloys (41); (iv) end-specific functionalizations of nanorods; (v) suppression of blinking (15) and quantum yield enhancement (107), and (vi) built-in on–off switches or photoelectric biotransducers. An on–off switch was demonstrated for a maltose sensor (18) and can be obtained by associating the QDs to a fluorescence-quenching molecule that can be separated or cleaved upon binding to the target, or in the presence of a chemical species or enzyme. This would be of particular interest for intracellular applications, in which there is no way to get rid of unbound QDs (unlike outer cell membrane—labeling experiments). As an example of a biotransducer, light-excited QDs could transfer their charge to bound enzymes functioning as electron or hole acceptors, enabling their control by light activation.

Reciprocally, QDs could be lit up by electron or hole donor enzymes through chemiluminescence (108). Peptide coating of nanomaterials is in this respect a powerful tool for imparting novel functions to the organic–inorganic interface. The simultaneous engineering of the semiconductor's band gap (by rational design) with the peptide's redox potential (by molecular evolution) could be used to optimize QDs chemical compositions and peptide sequences for binding and desired optical, electronic, magnetic, and chemical properties. In summary, different shapes, and specificities, and compositions will lead to more complex bioinorganic architectures that could be exploited as an optoelectronic interface to the cellular machinery.

QDs have a yet untapped potential in bioelectronics. Indeed, beyond their exceptional photophysical properties, QDs also have unique electronic properties that arise from quantum confinement in such small semiconductor clusters. Many efforts have been launched to interface QDs with neurons (109,110), in an attempt to trigger neuronal functions by QDs-mediated stimulation. Although no clear proof of the feasibility of such projects has yet emerged, a thin and carefully designed surface coating together with QDs optimized for large separation of charges after excitation (e.g., type II CdTe/CdSe QDs) might indeed open the doors to a new generation of light-activated QDs probes, where photogenerated carriers (electrons or hole) may undergo electron transfer, produce heat or generate dipole moments sufficiently strong to interact with membrane proteins, and changes in local membrane potentials.

QDs functionalization is another area where new developments will be needed. Ligands of cellular proteins should be readily cross-linked to QDs by means of standard bioconjugation schemes. However, most of the potential extracellular or intracellular targets do not have any known ligands, or if they do, QDs may interfere with their interaction. The use of antibodies, which has proven successful for surface-bound proteins, may not be practical for intracellular targets because of the size of the QD-antibody construct and delivery issues. *In vivo* cross-linking strategies developed for dyes—such as the use of biarsenical ligands targeted against tetra-cysteine motifs (111), Ni2p–nitrilotriacetic acid moieties targeted against hexa-histidine motifs (112), and other similar approaches (113,114)—may be adapted for QDs functionalization. Water-soluble peptide-coated nanorods could probably be used as orientational probes for studying rotational movements of macromolecules (107).

Intracellular delivery remains a challenge, and strategies to escape the endocytosis pathways will be needed. Two recent publications indicate that peptide-coated QDs could have many untapped virtues: (i) 20-nm gold nanoparticles coated with protein transduction domains could enter live cells, and further enter the nucleus with additional adenovirus nuclear localization and integrin binding domains (117), and (ii) after microinjection into the cytoplasm, PEG-coated QDs with a nuclear or mitochondrial localization sequence were successfully targeted to the nucleus or mitochondria (118). Another interesting model system, based on adenosine triphosphate—triggered release of CdS QDs encapsulated in chaperonin molecules (119), suggests using a "Trojan horse" approach to avoid the cellular defense and recycling mechanisms.

Cell-permeable virus capsids, vaults, or other biocapsules could be used to translocate encapsulated QDs in cells, provided that a simple release-on-demand mechanism could be engineered in the vehicle, such as a photolyzable or pH-sensitive lock.

QDs photophysical properties (spectral range, brightness, long lifetimes) and their potential as single-molecule probes may justify the development of new detectors that would have the temporal resolution and sensitivity of avalanche photodiodes, and the 2D spatial resolution of cameras for widefield *in vivo* studies of protein dynamics and trafficking. Their large size and electronic density may be used for combined fluorescence and static high resolution imaging techniques such as atomic force

microscopy and electron and X-ray microscopy and tomography. Additional contrast mechanisms could be obtained by functionalization of QDs.

QDs have already fulfilled some of their promises as a class of multifunctional molecular imaging agents. Through their versatile polymer coatings, QDs have also provided a "building block" to assemble multifunctional nanostructures and nanodevices. Multimodality imaging probes could be created by integrating QDs with paramagnetic or superparamagnetic agents. Indeed, researchers have recently attached QDs to Fe_2O_3 and FePt nanoparticles. Micropositron emission tomography (microPET) shows that QDs injected into the tail vein in mice are rapidly accumulated in the liver. Fluorescence imaging of QDs for tracking combined with the quantitative capability of microPET should therefore permit the elucidation of targeting mechanisms, biodistribution, and dynamics in living animals with high sensitivity. Nuclear spin labels for magnetic resonance imaging (MRI) could also be incorporated into QDs coatings with the use of similar chelating groups. It should therefore be possible to image targeted QDs at all scales, from whole-body down to nanometer resolution, using a single probe.

Beyond biotechnological and cell-imaging applications (Fig. 6.12), and provided that cytotoxicity issues can be resolved, one can envision the use of intravenous

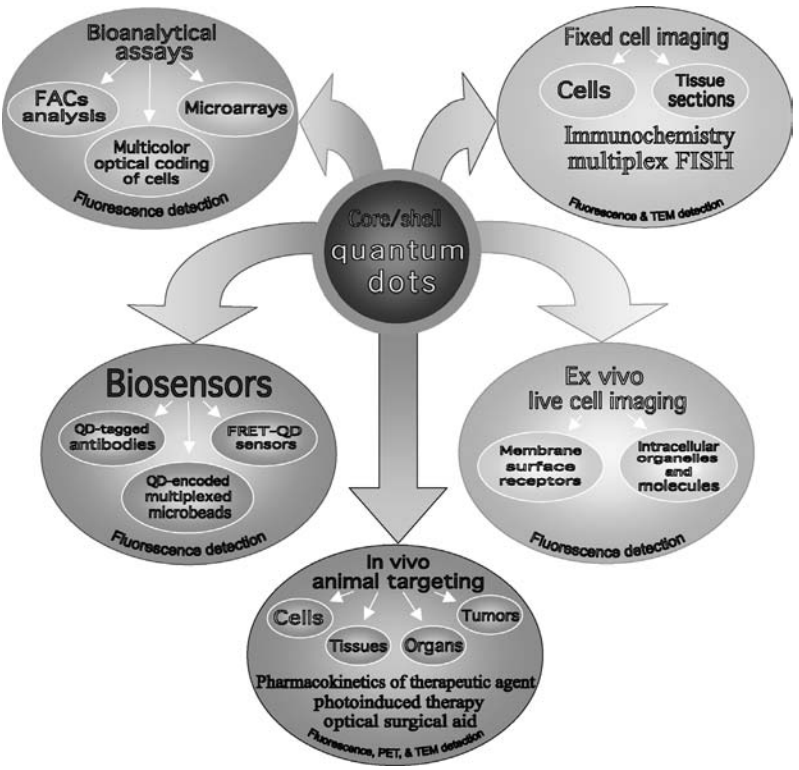

FIGURE 6.12 Fluorescent colloidal particles as a detection tools in biotechnology systems

injection of QDs to home in on and target cellular markers of diseased tissues and organs in the human body. QDs could then be used as contrast reagents for functional imaging with a combination of MRI, PET, computed tomography, and IR fluorescence imaging (the latter by direct imaging through the epidermis or by a catheter-based confocal fiber microscope). *In vivo* optical biopsy could confirm the pathology, and therapy could then be performed selectively, locally, and temporally by depositing energy (monochromatic X-rays for *k*-shell absorption or laser IR radiation) into the targeted QDs, in a manner similar to the recently reported photothermal tumor ablation with gold nanoshells (120). Alternatively, it might be possible to graft therapeutic enzymes to the QDs surface and activate them by light, or produce free radicals (such as singlet oxygen) by optically cycling the QDs.

Because the QDs have high chemical and photostability, they may become a new generation of photosensitizers. Basic principles were described in Reference 77. It was demonstrated that the combination of QD bioconjugates and UV irradiation can sensitize leukemia cells and promote the effect of the classical photosensitizers. It could be expected that photodynamic therapy based on the usage of QDs as photosensitizers will be greatly developed in near future.

QDs are good candidates for using in drug delivery carriers based on block copolymer micelles. The cellular fate of micelles is relevant for evaluating and optimizing the delivery system. The micelles distribution inside living cells can be followed by fluorescent labeling. Fluorescent dyes, which are useful for tracking micelles have several limitations, particularly if time-lapse experiments are required or if multiple laser exposures are needed. QDs represent a novel labeling strategy to follow the fate of micelles by confocal fluorescent and electron microscopy (18,53).

As we have mentioned above, the various surface chemistries developed over the years to interface ‘‘’’soft"" biological materials with inorganic QDs have not only been essential for the successful use of QDs in biological applications, but have also provided new tools in materials science for the controlled assembly of nanomaterials. Indeed, these interfaces, when used as molecular glue between inorganic nanoscaled building blocks, offer means to control 2D and 3D assemblies of nanoscaled objects by taking advantage of the unmatched ability of biological molecules to spatially and dynamically self-assemble and self-organize into complex molecular superstructures. Programmable nanomaterials scaffolding, driven by self-assembling peptides, protein domains interaction, DNA hybridisation, or carbohydrate/carbohydrate recognition, hold great promises for the creation and emergence of new biomaterials and the expansion of biomimetic nanotechnology (121–125).

6.10 CONCLUSION

QDs as ultrasensitive detection biotechnology probes have lived up to the hopes of their initial promoters. They will not replace the well-established fluorophores or fluorescent protein-fusion technologies, but will complement them for applications needing better photostability, NIR emission, or single-molecule sensitivity over long timescales. While they are not the perfect fluorophores, and more needs to be

done to better understand and improve their photophysics and to further assess their cytotoxicity, QDs have found their place in the existing repertory of bioimaging tools. They will, without doubt, be a probe of choice for long-term, high sensitivity, and multicontrast imaging of molecular dynamics in biological samples. Undoubtedly, biologists will catch on to these exciting developments and will find as yet unforeseen applications for this new toolkit, thus, enhancing and complementing their existing arsenal of biotechnology detecting tools.

REFERENCES

1. Michalet X, Kapanidis AN, Laurence T, Pinaud F, Doose S, Pflughoefft M, Weiss S. Annu Rev Biophys Biomol Struct 2003;32:161.
2. Special issue on Biological Imaging, Science 2003; 300: 75.
3. Weiss S. Science 1999;283:1676.
4. Alivisatos AP, Gu W, Larabell C. Annu Rev Biomed Eng 2005;7:55–76.
5. Nie S, Xing Y, Kim GJ, Simons JW. Annu Rev Biomed Eng 2007;9:257.
6. Somers RC, Bawendi MG, Nocera DG. Chem Soc Rev 2007;36 (4):579–591.
7. Hines MA, Guyot-Sionnest P. J Phys Chem 1996;100:468–471.
8. Sukhanova A, Venteo L, Devy J, Artemyev M, Oleinikov V, Pluot M, Nabiev I. Lab Invest 2002;82:1259–1262.
9. Nirmal M, et al. Nature 1996;383:802.
10. QY 70%.
11. Nabiev I, Sukhanova A, Artemyev M, Sharapov O, Baranov A, Jardillier JC. Ultrasensitive non-isotopic water-soluble nanocrystals, EP1366347; US2004105973; WO02073155, 09/03/2001. www.nanofm.com
12. Baranov A, Rakovich Yu, Donegan J, Perova T, Moore R, Talapin D, Rogach A, Masumoto Y, Nabiev I. Phys Rev B 2003;68:1653061–1653067.
13. Sukhanova A, Devy J, Venteo L, Kaplan H, Artemyev A, Oleinikov V, Klinov D, Pluot M, Cohen JHM, Nabiev I. Anal Biochem 2004;324:60.
14. Lacoste TD, et al. Proc Natl Acad Sci USA 2000;97:9461.
15. Hohng S, Ha T. J Am Chem Soc 2004;126:1324.
16. Kapitonov AM, et al. J Phys Chem B 1999;103:10109.
17. Larson D, et al. Science 2003;300:1434.
18. Medintz IL, et al. Nature Mater 2003;2:630.
19. Gobrbatsevich S, Kaputskaya I, Mikhnevich S, Artemyev M, Nabiev I, Strekal N, Maskevich S. J Luminesc 2004;110:24–39.
20. Wargnier R, Baranov A, Maslov V, Stsiapura V, Sukhanova A, Pluot M, Nabiev I. Nano Lett 2004;4: 451–457.
21. Gao X, Chung LW, Nie S. Methods Mol Biol 2007;374:135–146.
22. Rao J, Dragulescu-Andrasi A, Yao H. Curr Opin Biotechnol 2007;18 (1):17–25.
23. Murray CB, Norris DJ, Bawendi MG. J Am Chem Soc 1993;115:8706–8715.

24. Gaponenko SV. Optical properties of semiconductor nanocrystals. Cambridge: Cambridge University Press;1998.
25. Brus L. IEEE J Quantum Elctronics 1986;QE-22:1909–1914.
26. Wang Y. Acc Chem Res 1991;24:133–137.
27. Gurin VS, Artemyev MV. J Crystal Growth 1994;138:993–997.
28. Peng X, Wickham J, Alivisatos AP. J Am Chem Soc 1998;120:5343–5344.
29. Qu L, Peng ZA, Peng X. Nano Lett 2001;1:333–337.
30. Trindade T, O'Brien P. Adv Mater 1996;8:161–163.
31. Cheng Y, Emge TJ, Brennan JG. Inorg Chem 1994;33:3711–3714.
32. Bochman M. Chem Vap Deposition 1996;2:85–96.
33. Donega CM, Hickey SG, Wuister SF, Vanmaekelbergh D, Meijerink A. J Phys Chem B 2003;107:489–496.
34. Li JJ, Wang YA, Guo W, Keay JC, Mishima TD, Johnson MB, Peng X. J Am Chem Soc 2003;125:12567–12575.
35. Li LS, Pradhan N, Wang Y, Peng X. Nano Lett 2004;4:2261–2264.
36. Talapin DV, Haubold S, Rogach AL, Kornowski A, Haase M, Weller H. J Phys Chem B 2001;105:2260–2263.
37. Zhong X, Han M, Dong Z, White TJ, Knoll W. J Am Chem Soc 2003;125:8589–8594.
38. Zhong X, Feng Y, Knoll W, Han M. J Am Chem Soc 2003;125:13559–13563.
39. Bailey RE, Nie S. J Am Chem Soc 2003;125:7100–7106.
40. Qu L, Peng X. J Am Chem Soc 2002;124:2049–2055.
41. Harrison MT, Kershaw SV, Rogach AL, Kornowski A, Eychmüller A, Weller H. Adv Mater 2000;12:123–125.
42. Peng X, Schlamp MC, Kadavanich AV, Alivisatos AP. J Am Chem Soc 1997;119:7019–7029.
43. Talapin DV, Rogach AL, Kornowski A, Haase M, Weller H. Nano Lett 2001;1:207–211.
44. Yoffe AD. Adv Phys 2001;50:1–208.
45. Micic OI, Smith BB, Nozik AJ. J Phys Chem B 2000;104:12149–12156.
46. Cao YW, Banin U. J Am Chem Soc 2000;122:9692–9702.
47. Kim S, Bawendi MG. J Am Chem Soc 2003;125:14652.
48. Guo W, Li JJ, Wang YA, Peng XG. Chem Mater 2003;15:3125.
49. Pinaud F, King D, Moore H-P, Weiss S. J Am Chem Soc 2004;126:6115.
50. Wu XY, et al. Nature Biotechnol 2003;21:41.
51. Gao X, Cui Y, Levenson RM, Chung LWK, Nie S. Nature Biotechnol 2004;22:969.
52. Bruchez M, Moronne M, Gin P, Weiss S, Alivisatos AP. Science 1998;281:2013.
53. Dubertret B, et al. Science 2002;298:1759.
54. Han M, Gao X, Su JZ, Nie S. Nat Biotechnol 2001;19:631–635.
55. Stsiapura V, Sukhanova A, Artemyev A, Pluot M, Cohen JHM, Nabiev I. Analyt Biochem 2004;334:257–265.
56. Joumaa N, Lansalot M, Théretz A, Elaissari A, Sukhanova A, Artemyev M, Nabiev I, Cohen JHM. Langmuir 2006;22:1810–1816.
57. Pellegrino T, et al. Nano Lett 2004;4:703.
58. Osaki F, Kanamori T, Sando S, Sera T, Aoyama Y. J Am Chem Soc 2004;126:6520.

59. Goldman ER, et al. Anal Chem 2002;74:841.
60. Smith AM, Dave S, Nie S, True L, Gao X. Expert Rev Mol Diagn 2006;6:231–244.
61. Smith AM, Ruan G, Rhyner MN, Nie S. Ann Biomed Eng 2006;34:3–14.
62. Chen F, Gerion D. NanoLett 2004;4:1827–1832.
63. Lovrić J, Bazzi HZ, Cuie Y, Fortin GRA, Winnik FM, Maysinger D. J Mol Med 2005;83:377–385.
64. Stsiapura V, Sukhanova A, Baranov A, Artemyev M, Kulakovich O, Oleinikov V, Cohen JHM, Pluot M, Nabiev I. Nanotechnology 2006;17:581–587.
65. Xiao Y, Barker PE. Nucleic Acids Res 2004;32:28E.
66. Sukhanova A, Venteo L, Cohen JHM, Pluot M, Nabiev I. Ann Acad Pharm Franç 2006;64:125–134.
67. Hansen MC, Palmer RJ Jr, Udsen C, White DC, Molin S. Microbiology 2001;147:1383–1391.
68. Demchick P, Koch AL. J Bacteriol 1996;178:768–773.
69. Steckel JS, Zimmer JP, Coe-Sullivan S, Stott NE, Bulovic V, Bawendi MG. Angew Chem Int Ed Engl 2004;43:2154–2158.
70. Stoimenov PK, Klinger RL, Marchin GL, Klabunde KJ. Langmuir 2002;18:6679–6686.
71. Petruska MA, Bartko AP, Klimov VI. J Am Chem Soc 2004;126:714–715.
72. Haram SK, Quinn BM, Bard AJ. J Am Chem Soc 2001;123:8860–8861.
73. Wang HW, Chen Y, Yang H, Chen X, Duan MX, Tai PC, Sui SF. Proc Natl Acad Sci USA 2003;100:4221–4226.
74. Wenhua L, Haiyan X, Zhixiong X, Zhexue L, Jianhong O, Xiangdong C, Ping SJ. Biochem Biophys Methods 2004;58:59–66.
75. Kloepfer JA, Mielke RE, Nadeau JL. Appl Environ Microbiol 2005;71 (5):2548–2557.
76. Hirschey MD, Han Y-J, Stucky GD, Butler AJ. Biol Inorg Chem 2006;11:663–669.
77. Bakalova R, Ohba H, Zhelev Z, Ishikawa M, Baba Y. Nat Biotechnol 2004;22: 1360–1361.
78. Derfus AM, Chan WCW, Bhatia SN. Nano Lett 2004;4:11–18.
79. Sondi I, Salopek-Sondi B. J Colloid Interface Sci 2004;275:177–182.
80. Pereza L, Floresa M, Avalosa J, San Miguel L, Resto O, Fonseca L. Mat Res Soc Symp Proc 2003;737:F3.6.1–F3.6.6.
81. Hartwig A, Asmuss M, Ehleben I, Herzer U, Kostelac D, Pelzer A, Schwerdtle T, Burkle A. Environ Health Perspect 2002;110 (Suppl 5):797–799.
82. Kyriacou SV, Brownlow WJ, Xu XH. Biochemistry 2004;43:140–147.
83. Seisenberger G, Ried MU, Endre T, Buning H, Hallek M, Brauchle C. Science 2001;294:1929–1932.
84. Lakadamyali M, Rust M, Babcock H, Zhang F, Zhuang XW. Biophys J 2003;84: 583A–583A.
85. You J-O, Liu Y-S, Liu Y-C, Joo K-I, Peng C-A. Int J Nanomedicine 2006;1 (1): 59–64.
86. Agrawal A, Zhang C, Byassee T, Tripp RA, Nie S. Anal Chem 2006;78:1061–1070.
87. Agrawal A, Tripp RA, Anderson LJ, Nie SM. J Virol 2005;79:8625–8628.
88. Dragnea B, Chen C, Kwak ES, Stein B, Kao CC. J Am Chem Soc 2003;125:6374–6375.

89. Alexander M. BioEssays 2005;27:447–458.
90. Pfeiffer P, Herzog M, Hirth L. Philos Trans R Soc 1976;276:99–107.
91. Dixit SK, Goicochea NL, Daniel M-C, Murali A, Bronstein L, De M, Stein B, Rotello VM, Kao CC, Dragnea B. Nanolett 2006;6 (9):1993–1999.
92. Bentzen EL, House F, Utley TJ, Crowe JE Jr, Wright DW. Nanoletters 2005;5 (4): 591–595.
93. Medintz IL, Sapsford KE, Konnert JH, Chatterji A, Lin TL, Johnson JE, Mattoussi H. Langmuir 2005;21:5501–5510.
94. Ghazani AA, Lee JA, Klostranec J, et al. Nano Lett 2006;6 (12):2881–2886.
95. Le Gac S, Vermes I, Van den Berg A. Nano Lett 2006;6:1863–1869.
96. Geho D, Lahar N, Gurnani P, Huebschman M, Herrmann P, Espina V, Shi A, Wulfkuhle J, Garner H, Petricoin E, Liotta LA, Rosenblatt KP. Bioconjug Chem 2005;16 (3): 559–566.
97. Braeckmans K, De Smedt SC, Leblans M, Pauwels R, Demeester J. Nat Rev Drug Disc 2002;(1):447–456.
98. Robinson WH, et al. Nat Med 2002;8:295–301.
99. Naciff JM, et al. Environ Health Perspect 2005;113:1164–1171.
100. Xu H, et al. Nucl Acid Res 2003;31:e43.
101. Eastman PS, et al. Nano Lett 2006;6:1059–1064.
102. Sukhanova A, Susha AS, Bek A, Mayilo S, Rogach AL, Feldmann J, Oleinikov V, Reveil B, Donvito B, Cohen JH, Nabiev I. NanoLett 2007;7:2322.
103. Sukhanova A, Oleinikov V, Nabiev I. Proc ICONO-LAT 2007. p. 46.
104. Susha AS, et al. Colloids Surf A 2000;163:39–44.
105. Conzalez-Buitrago JM, Gonzalez C. Clin Chim Acta 2006;365:50–57.
106. Craighead H. Nature 2006;442:387–393.
107. Tsay JM, Doose S, Pinaud F, Li JJ, Weiss S. J Phys Chem B 2005;109 (5):1669–1674
108. Poznyak SK, Talapin DV, Shevchenko EV, Weller H. Nano Lett 2004;4:693.
109. Winter JO, Liu TY, Korgel BA, Schmidt CE. Adv Mater 2001;13 (22):1673–1677.
110. Winter JO, Gomez N, Korgel BA, Schmidt CE. Proc SPIE 2005;5705:235–246.
111. Adams SR. J Am Chem Soc 2002;124:6063.
112. Kapanidis AN, Ebright YW, Ebright RH. J Am Chem Soc 2001;123:12123.
113. Keppler A, Pick H, Arrivoli C, Vogel H, Johnsson K. Proc Natl Acad Sci USA 2004;101:9955.
114. Yin J, Liu F, Li X, Walsh CT. J Am Chem Soc 2004;126:7754.
115. Boder ET, Midelfort KS, Wittrup KD. Proc Natl Acad Sci USA 2000;97:10701.
116. Marks KM, Rosinov M, Nolan GP. Chem Biol 2004;11:347.
117. Tkachenko AG. Bioconjug Chem 2004;15:482.
118. Derfus AM, Chan WCW, Bhatia SN. Adv Mater 2004;16:961.
119. Ishii D, et al. Nature 2003;423:628.
120. O'Neal DP, Hirsch LR, Halas NJ, Payne JD, West JL. Cancer Lett 2004;209:171.
121. Seeman NC, Belcher AM. Proc Natl Acad Sci USA 2002;99 (Suppl 2):6451–6455.

122. Sukhanova A, Volkov Y, Rogach AL, Baranov AV, Susha AS, Kinov D, Oleinikov V, Cohen JHM, Nabiev I. Nanotechnology 2007;18:185602.
123. Stsiapura V, Sukhanova A, Baranov A, Artemyev M, Kulakovich O, Oleinikov V, Pluot M, Cohen JHM, Nabiev I. Nanotechnology 2006;17 (2):581–587.
124. Sukhanova A, Baranov AV, Klinov D, Oleinikov V, Berwick K, Cohen JHM, Pluot M, Nabiev I. Nanotechnology 2006;17:4223–4228.
125. Sukhanova A, Baranov AV, Perova T, Cohen JHM, Nabiev I. Angew Chem Intl Ed 2006;45:2048–2052.
126. Voura EB, Jaiswal JK, Mattoussi H, Simon SM. Nat Med 2004;10:993.

CHAPTER 7

Biofunctionalized Magnetic Micro/ Nanoparticles for Biosensing Technologies

NICOLE JAFFREZIC-RENAULT

LSA, Claude Bernard University Lyon, 1, 69622, Villeurbanne Cedex France

CLAUDE MARTELET, YANN CHEVOLOT and JEAN-PIERRE CLOAREC

AMPERE and INL, Ecole Centrale de Lyon, 69134, Ecully Cedex, France

7.1 INTRODUCTION

Magnetic micro/nanoparticles (MMNP) used in biosensing technologies usually present a core/shell structure. Such MMNPs have an inorganic core, for example, iron oxide, surrounded by an outer layer of shell wall that consists of long-chain organic ligands or inorganic/organic polymers. The attachment of bioactive ligands to the surface of the outer shell is the key to bioapplication of magnetic microbeads. Table 7.1 summarizes the main immobilization procedures of bioactive species, on magnetic microbeads used in this chapter. A more exhaustive view can be found in (1).

This chapter is divided into three parts covering three biosensing systems: affinity biosensors, enzymatic biosensors, bio-bar-codes.

7.2 USE OF MAGNETIC MICRO/NANOPARTICLES FOR AFFINITY BIOSENSORS

7.2.1 Electrochemical Immunomagnetic Sensors

Electrochemical immunosensors are designed through the immobilization of the specific antibody on the surface of the electrochemical transducer. The main

Colloidal Nanoparticles in Biotechnology, Edited by Abdelhamid Elaissari
Copyright © 2008 John Wiley & Sons, Inc.

TABLE 7.1 Immobilization Protocols of Biomolecules Used to Our Knowledge on Magnetic Micro/Nanoparticles.

Surface function	Cross-linker / reactive group	Biomolecule	References
Amine —NH_2	Active ester 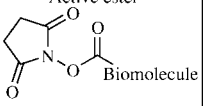	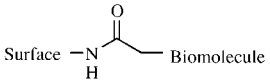	
Amine —NH_2	Glutaraldehyde 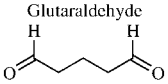	Antibody (Ab), Enzyme 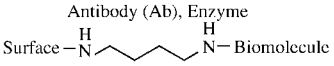	(2,3)
Amine —NH_2	Maleimide groups: SMPB 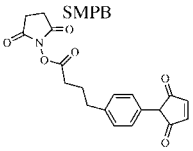 sulfo-SMCC 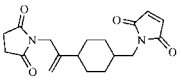	Thiol derivatives (protein, thio-DNA) 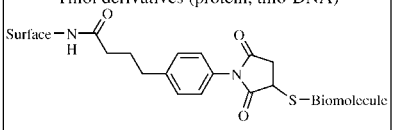 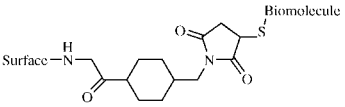	(4,5)
Gold Au	Thiol HS—DNA	Thio-DNA AuS—DNA	(6)
Active ester 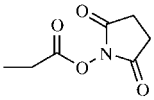	Amine H_2N-Biomolecule	Amide 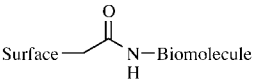 Antibody	
Avidin Streptavidin 	Biotinylated biomoleucle 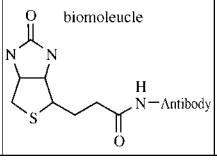	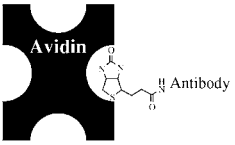	(7)

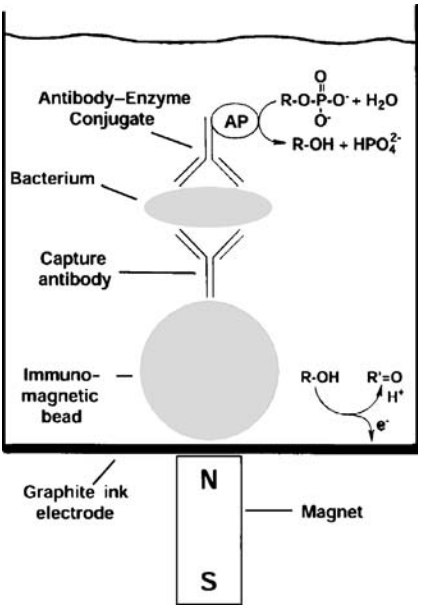

FIGURE 7.1 Schematic representation of the enzyme-linked immunomagnetic electrochemical assay (9)

problem affecting immunosensors is reproducible regeneration of the sensing surface. This renewal is a difficult task since the drastic procedures required for breaking the strong antigen-antibody interaction alter immunoreagent bound to the surface of the transducer. This drawback makes immunosensors difficult to integrate in automatic systems. An alternative approach avoiding regeneration consists of using disposable antibody-coated magnetic micro/nanoparticles and building up *in situ* immunosensing surface by localizing the immunomagnetic micro/nanoparticles on the electrode area with the aid of a magnet. Moreover, the use of immunomagnetic micro/nanoparticles is particularly evident in the detection of analytes contained in complex sample matrices (e.g., heterogeneous food mixtures) that may exhibit either poor mass transport to immunosensor or physical blockage of immunosensor surface by nonspecific adsorption. The schematic representation of the enzyme-linked immunomagnetic electrochemical assay is presented in Fig. 7.1. Immunogenic analyte (e.g., bacteria) is sandwiched between an antibody-coated magnetic microparticle (immunomagnetic particle) and an antibody-enzyme conjugate. The immunomagnetic particle is trapped magnetically on the electrode surface, exposed to the enzymatic substrate, the electroactive product is detected electrochemically. This type of immunomagnetic electrochemical assay was applied for different analytes with different transducer/enzyme combinaition gathered in Table 7.2. A good reproducibility of 2% relative standard deviation was observed (8).

TABLE 7.2 Features of Enzyme-Linked Immunomagnetic Electrochemical Assays Using Different Electrochemical Transducers and Different Enzymatic Labels.

Analyte	Transducer	Enzyme	Detection limit	Dynamic range	References
Rabbit IgG	pH-ISFET	Urease	8 nM	0–2.07 μM	(10)
Rabbit IgG	Graphite composite electrode	HR peroxidase	9×10^{-6} μg/L	0–0.26 μM	(8)
E. coli 0157: H7	Graphite ink electrode	Alkaline phosphatase	4.7×10^{3} cells per mL	$0–10^{5}$ cells per mL	(9)
2,4-D herbicide	Nafion-SPE	Alkaline phosphatase	0.01 μg/L	0.01–100 μg/L	(11)
Human IgG	Carbon paste electrode	HR peroxidase	0.18 μg/mL	0.51–30.17 μg/L	(12)

7.2.2 Label-Free Immunomagnetic Impedancemetry-Based Sensors

The impedance measurements of the electrical properties of an antibody layer immobilized on a gold electrode allows the direct monitoring of the variation of these properties when antigen-antibody interaction occurs. This technique allows label-free detection of the antigen concentration in biological samples. The problem of regeneration of the sensing surface has been solved, in this example, by using streptavidin magnetic nanoparticles for the immobilization of the antibody specific of a small pesticide molecule, the atrazine. The antibody, biotinyl-anti-atrazine Fab fragment K47, forms a quite stable layer onto the streptavidin-magnetic nanoparticles immobilized on gold electrode using a 300mT magnet, due to the high affinity of the biotin/streptavidin interaction. After the antibody layer formation, an antigen atrazine, was injected and interacted with the antibody (cf. Fig. 7.2).

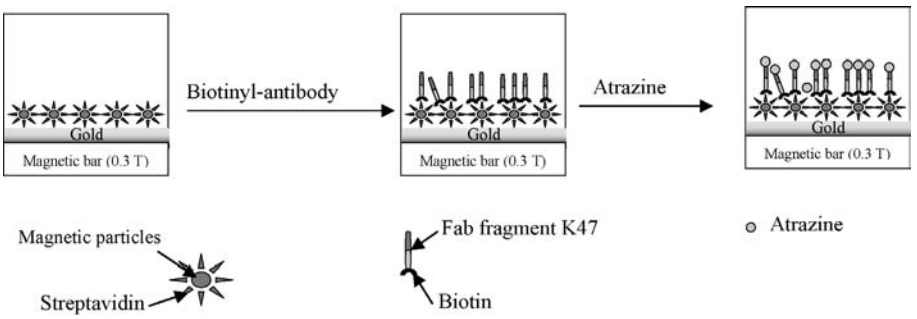

FIGURE 7.2 Different steps for building up the immunomagnetic impedancemetric sensor (7)

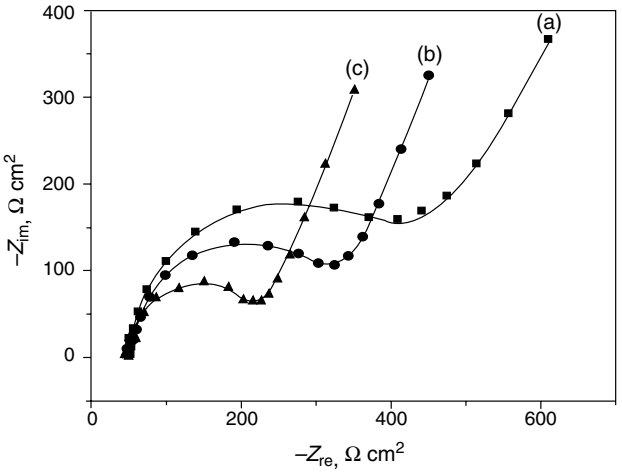

FIGURE 7.3 Nyquist diagram (Z_{re} vs. Z_{im}) for the nonfaradaic impedance measurements corresponding to: (**a**) magnetic nanoparticles/Au-electrode; (**b**)anti-atrazine-Fab fragment K47 antibody/magnetic nanoparticles/Au-electrode; (**c**) 600 ng/mL of atrazine/anti-atrazine-Fab fragment K47 antibody/magnetic nanoparticles/Au-electrode; Solid curve shows the computer fitting of the data using Randles'equivalent circuit. Symbols show the experimental data (7)

Complex impedance plots of the successive building up of the sensing layers: magnetic nanoparticles/Au-electrode, biotinyl-Fab fragment K47 antibody/magnetic nanoparticles/Au-electrode and after a 600 ng/mL of atrazine injection in cell are shown in Fig. 7.3. Using Randles' equivalent circuit model, an excellent fitting between the simulated and experimental spectra was obtained. The electron transfer resistance values were 304.6 Ω cm^2 for the magnetic monolayer, 204.5 Ω cm^2 for the antibody layer, and 188.5 Ω cm^2 after injection of 600 ng/mL of atrazine. The decreases of electron transfer resistance could be attributed to a reorganization of the nanoparticle layer as the specific capacitance decreases too. The specific capacitance, extracted from the computer fitting for the same steps was 17 μF/cm^2, 15 μF/cm^2, and 14.29 μF/cm^2, respectively. This decrease should be due to an increase in thickness.

In order to obtain a calibration data set, the values of electron transfer resistance differences ΔR_{et} versus the added atrazine concentrations were plotted in Fig. 7.4. The change of electron transfer resistance was calculated according to the equation:

$$\Delta R_{\mathrm{et}} = R_{\mathrm{et}}(\mathrm{Ab}) - R_{\mathrm{et(Ab-Ag)}},$$

where $R_{\mathrm{et(Ab)}}$ is the value of electron transfer resistance after antibody immobilization, $R_{\mathrm{et(Ab-Ag)}}$ is the value of the electron transfer resistance after antigen binding to the antibody. As it can be seen in Fig. 7.4, the plot is linear for high concentrations of atrazine and then reaches saturation. A linear relationship

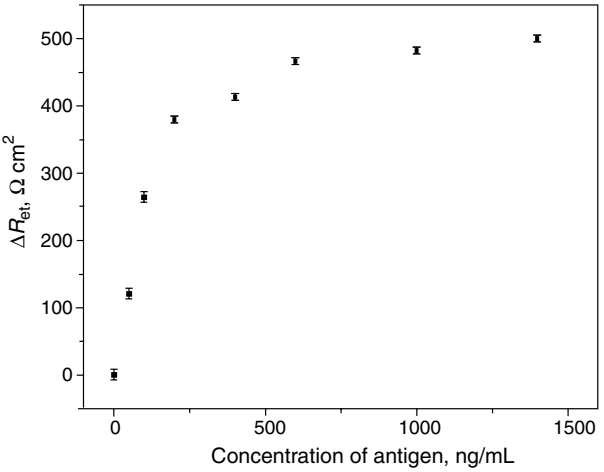

FIGURE 7.4 Calibration plot of the variation of electron transfer resistance ΔR_{et} versus concentration of atrazine (7)

between the ΔR_{et} values and the concentration of atrazine was established in the range from 50 to 500 ng/mL. A detection limit of 10 ng/mL is reached.

7.2.3 Piezoimmunosensors

A piezoelectric immunoassay based on a quartz crystal microbalance (QCM), with a renewable surface, was also proposed using immunomagnetic beads localized on the surface of a quartz using a permanent magnet (13). Human IgG as analyte was detected using goat-anti-human IgG antibody covalently bonded on amino-modified silica coated magnetic nanoparticles. A detection limit of 0.36 μg/mL and a dynamic range of 0.6–34.9 μg/mL were obtained using a 9 MHz QCM.

Another piezoelectric immunosensor based on a 5 MHz quartz crystal resonator was used for the detection of biological pathogens, such as *Salmonella typhinium* (14,15). The *Salmonella* cells were captured by antibody-coated magnetic microparticles and then these complexes were moved magnetically to the sensing quartz and were captured by antibodies immobilized on the crystal surface. An impedance analyzer measured the impedance behavior of the oscillating quartz crystal exposed to various concentrations of *Salmonella typhinium* (10^2–10^8 cells per mL). The response of the crystal was expressed in terms of equivalent circuit parameters. The motional inductance and the motional resistance increased as a function of the concentration of *Salmonella*. The viscous damping was the main contributor to the resistance and the inductance in a liquid environment. The load resistance was the most effective and sensitive circuit parameter. A magnetic force was a useful method to collect complexes of *Salmonella*-immunomagnetic microparticles on the crystal surface and enhance the response of the sensor. In this system, the detection limit, based on resistance monitoring was about 10^3 cells per mL.

7.2.4 Genomagnetic Electrochemical Assays

Currently developed DNA hybridization sensors are using single-stranded (ss) short (15–25 nucleotides) oligodeoxynucleotides (ODN, probe DNA) immobilized on an electrode. The ODN-modified electrode is immersed in the target DNA solution. When the sequence of target DNA matches that of the probe (based complementary Watson–Crick pairing), a probe-target (hybrid) duplex DNA is formed at the electrode surface. The hybridization event (DNA duplex formation) is detected electrochemically in different ways. This system works quite well with synthetic ODNs when probe target DNAs are about the same lengths. In a real DNA sequence analysis with longer PCR products, viral or chromosomal DNAs, the target DNAs are substantially longer than the probe. With longer target DNAs, difficulties connected with nonspecific target DNA adsorptions frequently arise, resulting in a loss of specificity and decreased sensitivity. Elimination of the nonspecific DNA adsorption at the electrodes (such as carbon or gold ones) usually applied for the DNA hybridization is very difficult. A new method based on separation of DNA hybridizal step (on magnetic microparticles) from the electrochemical detection step has been proposed and successfully used (16,17). One procedure of the genomagnetic electrochemical bioassay (GEME), based on a PNA probe and on a electroactive intercalator, is schematized in Fig. 7.5 (18).

The detection of target DNA can be done by label-free detection of guanine peak (16,17,19), by detection of chemically modified DNA prelabeled or postlabeled by redox probes (16), by detection of the product of the enzymatic reaction on DNA postlabeled by enzyme (20), or by detection of redox intercalators (18). The features of the different genomagnetic electrochemical assays are presented in Table 7.3.

TABLE 7.3 Features of the Different Genomagnetic Electrochemical Assays.

Analyte	Electrochemical transducer	Label	Detection limit	Dynamic range	References
Breast-cancer BRCA1 gene	Potentiometric stripping measurements Graphite pencil electrode	No	100 ng/mL, ppb	100 ppb–20 ppm	(17)
Breast-cancer BRCA1 gene	Differential pulse voltammetry	Alkaline phosphatase	100 ppb	0.25–1.0 ppm (20 min hybridization)	(20)
21-mer DNA	Square wave voltammetry	Meldola's blue intercalator	2 pM	2–20 pM	(18)
DNA Sequence from *Salmonella*	Differential pulse voltammetry Graphite composite electrodes	No	9.68 pM		(19)

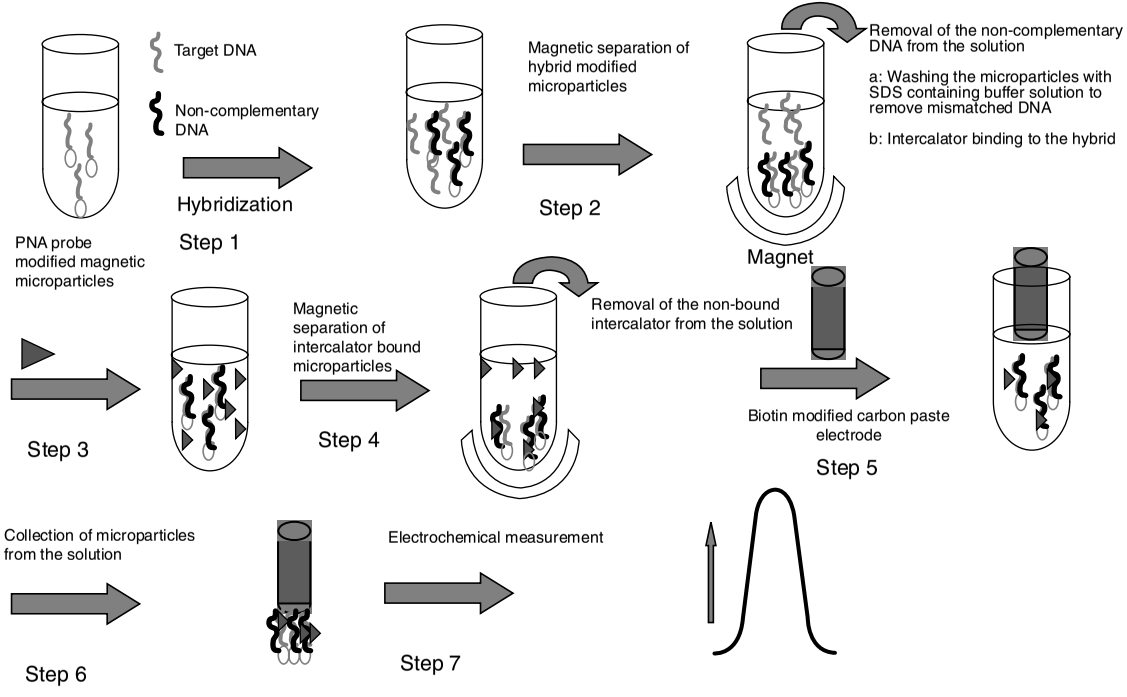

FIGURE 7.5 Procedure of the genomagnetic bioassay (18)

7.2.5 Magnetic Detection

7.2.5.1 Magnetic Permeability Measurements Magnetic nanoparticles can also be used as magnetic markers for bioassays. Measurements based on variation of magnetic permeability were performed using a transducer that comprises a coil placed in a Maxwell bridge (21) (see Fig. 7.6). The change in magnetic permeability of a compound detected using inductance measurements. Furthermore, analyte detection has been achieved directly (the analyte being labeled ferromagnetically) or competitively (competition between ferromagnetic labeled and unlabeled analytes exists for binding sites on the transducer) using the aforementioned device. The use of magnetic markers has been shown to offer advantages such as low interference, little or no background signal, no transducer fouling, and no sample treatment. The "sandwich" approach used for in the magneto binding assay, where the target analyte is bound between silica carrier particles and the magnetic marker is presented in Fig. 7.7.

Histone H1 conjugated magnetic nanoparticles were assessed for their ability to work as magnetic transducers for the detection and quantification of DNA (22). For the quantification of calf thymus DNA, a linear relationship between the DNA concentration in the sample and the relative magnetic permeability of the pellet was found for DNA concentration up to 67 μg/mL in buffered solutions as well as in a lysed cell culture. The detection limits were determined to 12 and 31 μg/mL, respectively. For the quantification of plasmid DNA in buffered solution a linear range was established for concentration up to 150 μg/mL and the detection limit was determined to 52 μg/mL.

A rapid (6.5 min) and simple one-step magnetic immunoassay has been developed for the analysis of human urinary albumin in near patient settings (23). Polyclonal rabbit antihuman was used as a capture antibody and monoclonal mouse antihuman albumin as a detection antibody in a two-site immunomagnetic assay requiring no additional washing procedures. The polyclonal antihuman albumin was conjugated to silica microparticles (cf. Fig. 7.7) and the monoclonal antibody to dextran coated magnetic nanoparticles (cf. Fig. 7.7). Quantification of human albumin in undiluted

FIGURE 7.6 The current magnetic permeability meter, a portable version of the device (21)

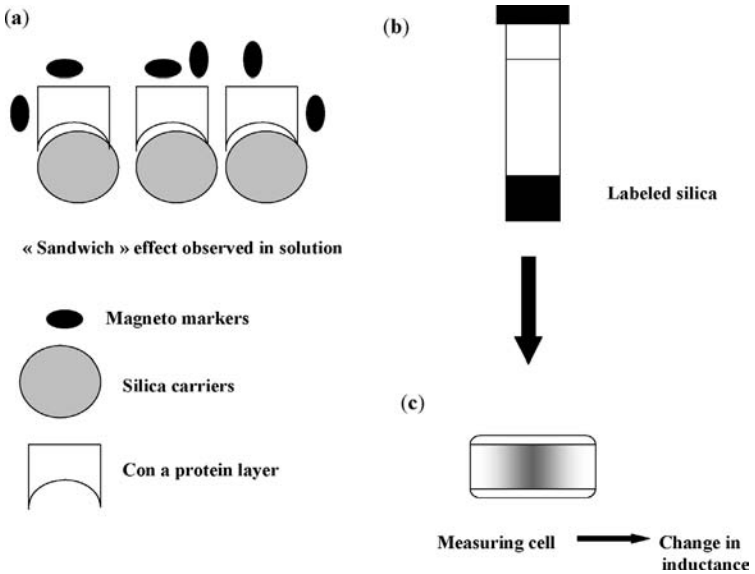

FIGURE 7.7 The "sandwich" approach used for in the magneto binding assay (21)

urine was performed by adding 2 μL urine to a measuring vial containing polyclonal Ab-silica microparticles, monoclonal Ab-magnetic nanoparticles and reaction buffer and then agitating the vial by hand for 20 s. A linear response was obtained for 0–400 μg/mL albumin with a detection limit of 5 μg/mL.

7.2.5.2 Frequency Mixing A new technique so-called frequency mixing was also used for detection of magnetic biomarkers. A two-frequency magnetic field excitation was used and the magnetic response at a third frequency was detected, which is a linear combination of the applied frequencies (24). The so-called magnetic sandwich bioassay for the detection of c-reactive protein (CRP) is presented in Fig. 7.8. The detection principle is based on two different anti-CRP antibodies (monoclonal IgG) for CRP recognition (grafted on a polyethylene PE sintered filter) and labeling. The linear detection range of this immunosensor ranged from 25 ng/mL to 2.5 μg/mL and is therefore much more sensitive than typical hsCRP-sandwich-assays. Disavantages of this system is the sample size. Sample sizes are currently 0.5 mL, which is quite high for blood serum analysis.

7.2.5.3 Magnetic AFM (25) For developing a magnetic bioassay system, an investigation to determine the presence of a specific biomolecular interaction between biotin and streptavidin was done using paramagnetic nanoparticles and a silicon substrate with a self-assembled substrate (cf. Fig. 7.9). The reaction of streptavidin-modified magnetic nanoparticles on the biotin-modified substrate was clearly observed under an optical microscope (cf. Fig. 7.10). The magnetic signals from

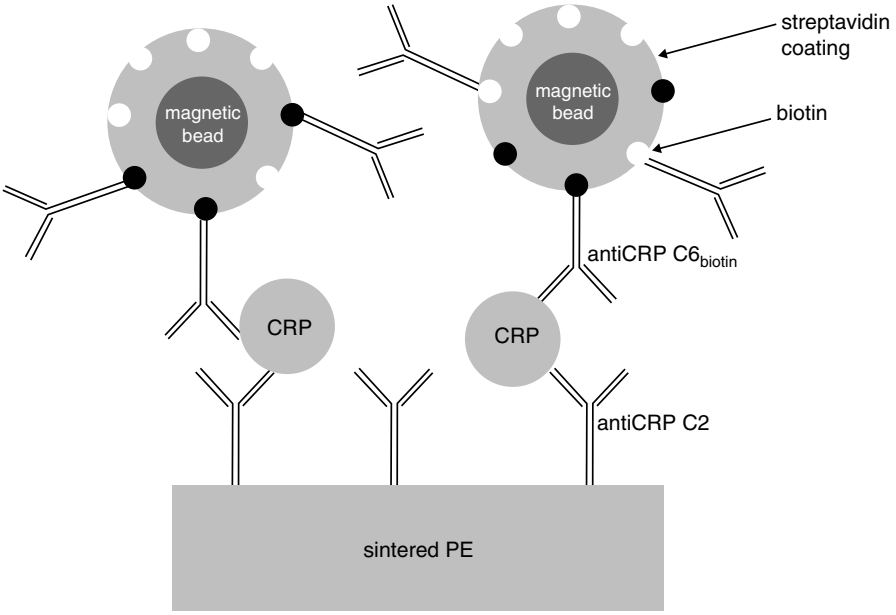

FIGURE 7.8 Magnetic sandwich bioassay for the detection of c-reactive protein (CRP) (24)

the particles were detected using a magnetic force microscope (MFM). The results of this study demonstrate that the combination of a monolayer-modified substrate with biomolecule-modified magnetic nanoparticles is useful for the detection of biomolecular interactions in medical and diagnostic analysis.

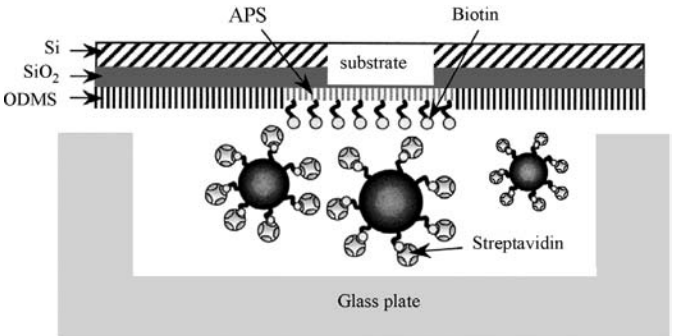

FIGURE 7.9 Schematic illustration of biotin-streptavidin reaction on a SAM-modified substrate. Biotin is attached to the aminopropyl silane (APS) patterned substrate. Streptavidin-modified magnetic nanoparticles are injected into a channel on a glass plate. The magnetic nanoparticles are bound through a specific interaction between biotin and streptavidin (25)

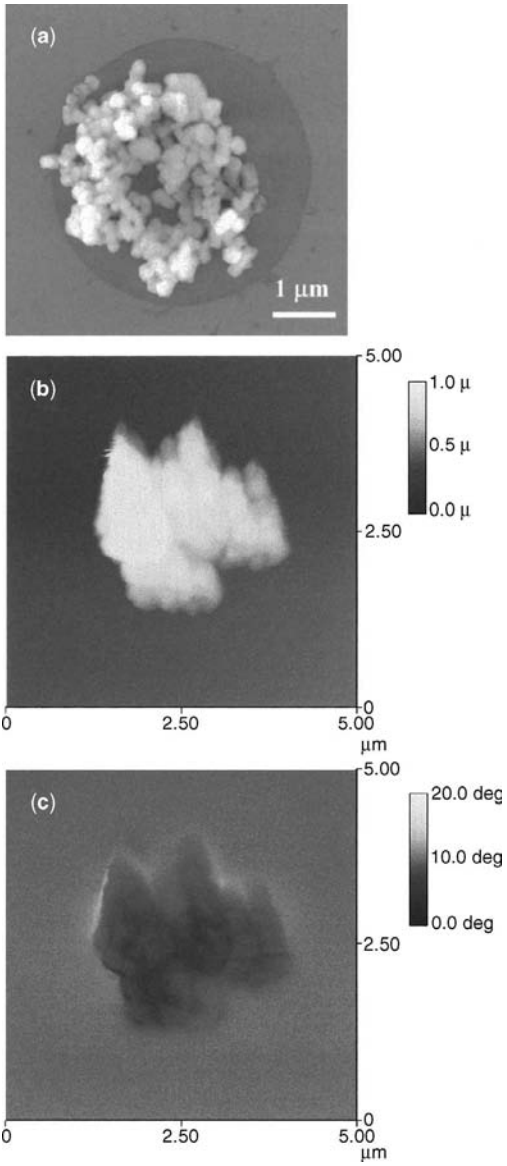

FIGURE 7.10 SEM (**a**), AFM (**b**), and MFM (**c**), images of magnetic nanoparticles immobilized on a patterned substrate by specific interaction between biotin and streptavidin. Dot size = 4 μm (25,27)

7.2.5.4 Magnetic Resonance Imaging (MRI) Biofunctionnalized magnetic nano-particles can locally and *in situ* probe the presence of biomarkers by magnetic resonance imaging (MRI) as described in the literature. The self-assembly of super paramagnetic iron oxide core nanoparticles, leads to the enhancement of the

spin–spin relaxation times $T2$ of the surrounding water molecules (26). Indeed, the spins of surrounding water protons are more efficiently dephased by the self-assembled structure. If one can design magnetic nanoparticles that would self-assemble in the presence of a biological target and detect the $T2$ relaxation time of water protons, it would be possible to build a magnetic nanosensor for magnetic resonance imaging. Proofs of concept were realized using DNA/DNA interaction, protein/protein interactions, protein/small molecules and enzyme reactions (26).

Perez et al. have reported the detection of peroxidase using such an approach (27). They showed that they could detect horseradish peroxidase and myeloperoxidase with modified magnetic iron core nanoparticle (75 nm). The presence of the latest peroxidase is related to atherosclerosis and inflammation. Amino dextran caged magnetic particles were surface modified with dopamine or serotonin using a bifunctionnal cross-linker suberic acid bis(*N*-hydroxysuccinimide ester). Surface modification was assessed by measuring fluorescence emission of serotonin. In the presence of peroxidase, hydrogen peroxide is released, serotonin or dopamine are oxidized leading to tyrosyl free radicals. The resulting cross linking leads to the formation of a self-assembled structure and to the change of $T2$ relaxation time (Fig. 7.11). The more peroxidase in the medium, the more free radicals are formed and the more the $T2$ relaxation time is changed (Fig. 7.12).

The detection of adeno virus and herpes virus (5 viral particles/10 μL) was also demonstrated (28). Antibodies directed against these viruses were immobilized at the surface of amino dextran caged iron nanoparticles (46 ± 0.6 nm) via protein G attached with *N*-succinimidyl-3-(2-pyridyldithio)propionate to the particle. The

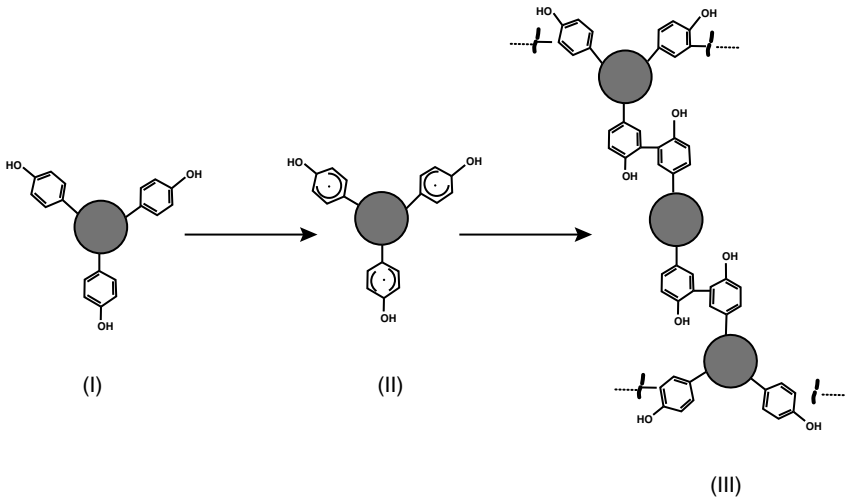

FIGURE 7.11 In the presence of peroxidase, hydrogen peroxide is released. Free radicals are formed at the surface of the magnetic particles leading to cross- linking reactions. The resulting self-assembled structure leads to a shift in water $T2$ relaxation time (27)

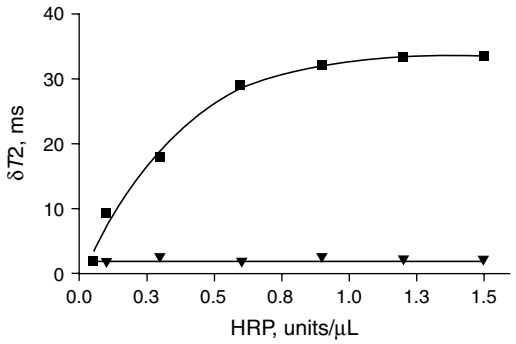

FIGURE 7.12 Variation of *T*2 relaxation time increases with the concentration of horseradish peroxidase (27)

aggregation kinetic of antibody modified magnetic particles in the presence of viruses was followed by light scattering. A plateau was reached within 2 h. The diameter increases by a factor of approximately 11 (550 ± 30 nm) due to cross linking of the magnetic and viral particles trough antigen/antibody interactions. They found a linear relationship between the variation of *T*2 relaxation time and the number of viral particles (from 50 to 250 viral particles) (Fig. 7.13). A better detection limit is obtained *versus* ELISA. They also achieved the detection of viral particle in complex media, such as cell lysates or serum but using a different surface chemistry to minimize nonspecific adsorption. They found a 50 viral particles detection limit.

Harris et al. have developed a MRI assay with nanoparticles (50 nm dextran caged iron core nanoparticles) for detecting Matrix Metalloproteinase-2 (MPP-2) activity (29). This protease activity when upregulated leads to invasive proliferation and metastasis of cell cancer. Two types of particles bearing avidin or biotin are

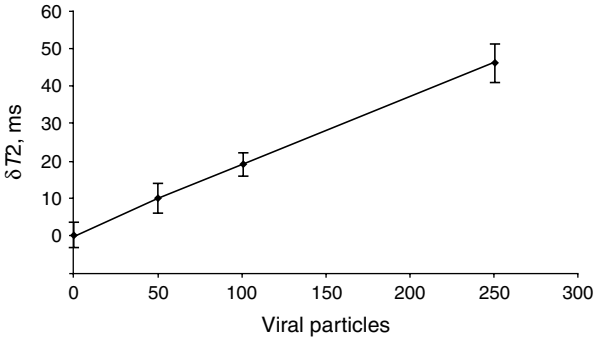

FIGURE 7.13 Variation of *T*2 relaxation time varies linearly with the number of virus particle (28)

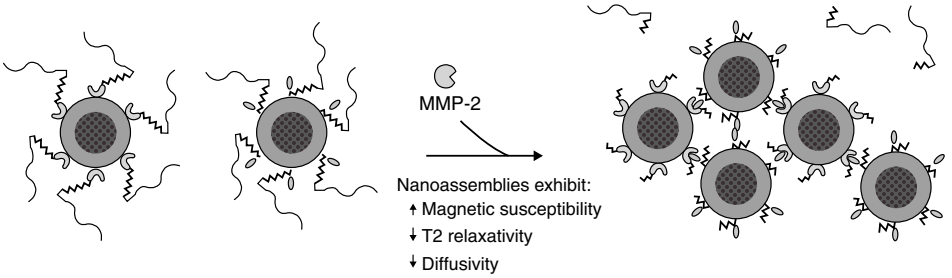

FIGURE 7.14 The PEG molecules inhibit biotine/streptavidine interactions. In the presence of MMP-2, the peptide is cleaved allowing to free the PEG molecules and leading to self-assembly of nanoparticles (29)

prepared. The presence of a PEG modified peptide at the surface of the particles inhibits the interaction between neutravidin and biotin. The peptide has an amino acid sequence, which is a substrate for MPP-2 protease activity. In the presence of MPP-2, the peptide is cleaved and the PEG is freed from the particles allowing the nanoassembling that leads to a *T*2 shift (cf. Fig. 7.14). The device could detect down to 9.2 U/mL of MPP-2. The authors have demonstrated that inhibition of biotin/neutravidin interaction increases with PEG molecular weight (10 kDa). Inversely, the rate of aggregation in the presence of MPP-2 increases with lower PEG molecular weight (cf. Fig. 7.15).

In conclusion, self-assembling of magnetic nanoparticles upon biological interaction is a promising tool for *in vivo* diagnostic as the authors have demonstrated. Indeed these authors have shown that this methodology can work in complex and turbid media. Its sensibility is below the concentration encounter in tumoral cell for instance.

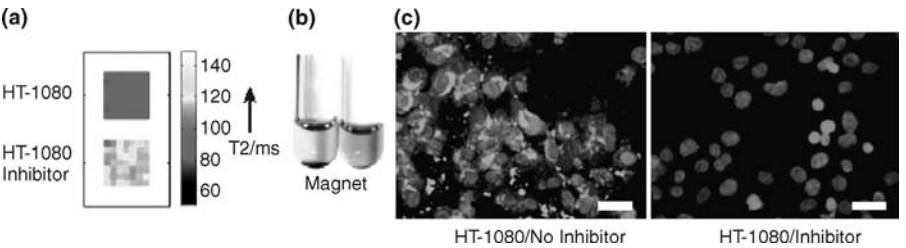

FIGURE 7.15 In the presence of tumor derived cells (HT-1080), MMP-2 is secreted. (**a**) In the absence of galardin (a MMP-2 inhibitor), *T*2 mapping of Fe_3O_4 nanoparticles demonstrated an enhancement of *T*2 relaxation time versus the *T*2 relaxation time observed in the presence of galardin. (**b**) In the absence of galardin, aggregates can be removed from the solution by a strong magnetic field. (**c**) The aggregates can be stained with biotin modified quantum dots and imaged by epifluorescent microscopy (29)

7.3 ENZYMATIC BIOSENSORS BASED ONTO MAGNETIC MICRO/NANOPARTICLES

Most of the proposed enzymatic biosensors are based on biofunctionnalization of a transducer, which is more often constituted by amperometric, potentiometric, or conductimetric devices.

Compared to classical immobilization methods used for the development of enzymatic biosensors, the use of magnetic micro/nanoparticles can bring a lot of advantages:

1. enzyme immobilization onto magnetic micro/nanoparticles, having high specific area, allows a high loading of the sensitive matrix,
2. such a matrix provides a good macroenvironment for retention of the bioactivity,
3. the most decisive advantage is a good control of the localization of the sensitive material through the use of magnets or of magnetized transducing parts allowing enzyme reactions to occur close to the detection device,
4. the sensitive transducing part can be easily renewed.

In parallel with biosensing applications, enzyme coated magnetic micro/nanoparticles have been used to facilitate the enzyme handling. By this way stock solutions containing such a material can be, when properly stored, used for more than ten months without significant activity loss. Then this immobilization method has been, for example, validated for glucose oxidase, urease, and alpha-amylase covalently immobilized onto polyacrolein magnetic microparticles (30).

Except the work of Miyabayashi et al. (31), where biomodified magnetic beads were used on a Clark electrode for glucose or *Saccharomyces cerevisiae* detection, one of the first applications of magnetic microparticles for biosensors was the combination of a covalent enzyme bonding onto magnetic microparticles with physical entrapment on the sensor surface. Latex beads, containing superparamagnetic material covalently modified with enzymes, have been patterned on a transducer by the means of screen printed thick films permanent magnets. Such a method, valuable for batch production independently of the nature of the substrate material, was evaluated for assessing glucose concentrations up to 20 mM (32).

Enzymes immobilized on magnetic nanoparticles can be trapped by magnets and retained on an electrode surface at a specific location in flow analysis devices. Thus covalent immobilization of glucose oxidase, urease, alpha–amylase on paramagnetic polyacrolein beads have been proposed to facilitate the enzyme handling.[1] But only a few number of works using magnetic microparticles have been devoted to design real enzymatic biosensors. As an example of such devices, an enzyme based electrochemical magnetobiosensor for environmental toxicity analysis can be cited. The integration of the bioactive material as urease, cholinesterases classes, significantly increases the sensitivity and allows detection limits as low as 10^{-11} M for

[1]Reference 30.

TABLE 7.4 Examples of Magnetic Nanoparticles-based Enzymatic Biosensors.

Analyte	Magnetic nanoparticles	Transducer	Enzyme	Sensitivity	Dynamic range	References
Phenol	$MgFe_2O_4$ silica coated $\phi = 120$ nm	C paste	Tyrosinase	54.2. μA/mM	10^{-6}–0.5 $\times 10^{-4}$ M	(3)
Ethanol	Precipitated Fe_3O_4 $\phi = 9.8$ nm	Screen printed C	Yeast YADH/NAD+	0.61 μA/mM	1–9 mM	(34)
Glucose	Precipitated Fe_3O_4 $\phi = 9.8$ nm	Screen printed C	Glucose oxidase	1.74 mA/mM	0–33 mM	(35)

heavy metal ions and 10^{-12} M for organophosphates and carbamates (33). In Table 7.4, characteristics of some magnetic nanoparticles-based enzymatic biosensors are gathered.

As an example, a strategy of enzyme immobilization is given in Fig. 7.16, where a covalent bonding of the biospecie can be achieved, allowing a quite good storage stability.

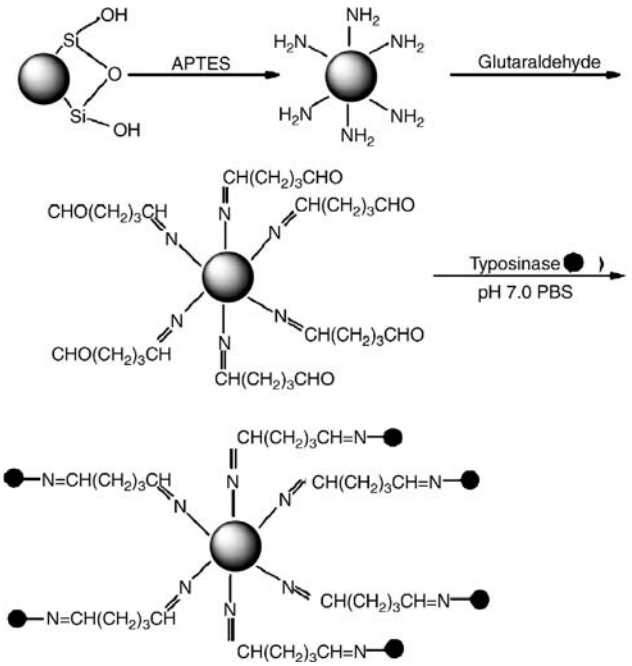

FIGURE 7.16 Preparation of magnetic bioparticles for a tyrosinase-based biosensor (3)

In the case of ferrocyanide mediated enzymatic amperometric biosensors, the use of magnetic nanoparticle can enhance the peak current of redox species.

Recently, the potentialities of nanoporous silica microparticles containing superparamagnetic defect spinel-type iron oxide nanoparticles inside their pores have been underlined for biosensors applications. This approach allows the obtaining of a high sensitivity and selectivity even in complex media. These silica-based magnetic particles also offer a new immobilization strategies, thus it was proposed a deposition of gold nanorods on magnetic nanoparticles allowing, through aminothiols, quite stable enzyme functionalization. Interest of such a support has been validated for the immobilization of horseradish peroxidase leading to hydroquinone and hydrogen peroxide biosensing at level as low as 4×10^{-7} M (36). The design of a magnetized carbon paste electrode with trapped magnetic nanoporous silica microparticles (MMPs) is given in Fig. 7.17.

A similar strategy has been used for immobilization of horseradish peroxidase with a high density of nanopores of MMPs having a diameter of 5 μm and applied for studying peroxidation of clozapine. Clozapine is a drug belonging to the dibenzoazepine class and often used to treat neurological disorders. The resulting amperometric biosensor allows the drug quantification in the micromolar range and presents a quite good stability, no significant signal loss being observed after 1 month of storage (37).

Enzymatic MMPs-based devices present also specific advantages, as silica MMPs do not act as a barrier for the diffusion of the analyte to the electrode surface. Only a decrease of few percent of the voltamperometric signal is observed in presence of microparticles compared to the bare electrode. Furthermore MMPs constitute a valuable tool for inhibition studies, immobilized enzymes on such silica microparticles being less sensitive, through a screening effect, to inhibitors than soluble enzymes. Thus, it has been recently shown that immobilized HRP, through MMP strategy, was protected from inactivation by inhibitors as thiols that can react with intermediary quinoneimine derivatives produced during the enzymatic reaction (38).

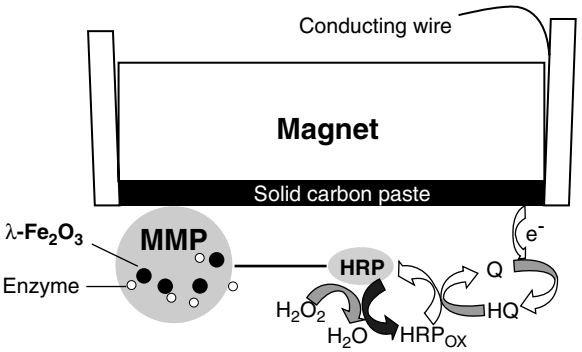

FIGURE 7.17 An enzymatic biosensor based on magnetic nanoporous silica microparticles (MMPs) where oxidation of hydroquinone (HQ) to quinone by the enzyme horseradish peroxidase (HRP) in presence of hydrogen peroxide and subsequent electroreduction of quinone (Q) is shown

Magnetoswitchable electrocatalysis and bioelectrocatalysis are accomplished by the surface modification of magnetic microbeads with redox-relay units. By the attraction of the modified magnetic microbeads to the electrode support, or their retraction from the electrode, by means of an external magnet, the electrochemical functions of the magnetic microbeads tethered relays can be switched between "ON" and "OFF" states, respectively. The magnetoswitchable redox functionalities of the modified particles activate electrocatalytic transformations, such as a biocatalytic chemoluminescence cascade that leads to magnetoswitchable light emission or the activation of bioelectrocatalytic processes (39,40).

7.4 BIO-BAR-CODE

Since the introduction of Polymerase Chain Reaction (PCR) in 1985, the detection of very low amounts of DNA (as low as 5–10 copies) has been achieved. However, its complexity, lengthy procedure time, and narrow range of targets have motivated further research to develop new technologies. Furthermore, many efforts have been devoted in the scientific community for developing new methodologies allowing for the detection of proteins with a lower detection limit than is possible with PCR.

In the early 2000s, Mirkin's group at the Northwestern University reported on a promising analytical tool for high sensitivity detection of protein (6) and DNA (4), namely, the bio-bar-code.

In the following section, the principle of bio-bar-code for protein and DNA detection will be presented, followed by examples of biological applications.

The bio-bar-code relies on sandwiching a target molecule in a biological medium between a magnetic particle and a signal amplifier nanoparticle through specific biological interactions. The magnetic particle permits the separation of reacted target molecules from unreacted ones. The nanoparticles are loaded with double stranded DNA tag encoding for a unique target. The primary interaction of the magnetic particles is amplified by the presence of numerous copies of DNA at the surface of the nanoparticles, allowing for detection in the order of zM. Therefore, the bio-bar-code approach relies on two components:

- Magnetic MicroParticles (MMP): The MMP surface is functionalized with a biological probe (DNA or antibody, Fig. 7.18) that specifically interacts with the target molecule to be detected.
- Nanoparticles (NP): The NP surface is functionalized with a target binding molecule (DNA or polyclonal antibody, Fig. 7.18), and the so-called bio-bar-code (an oligonucleotide, Fig. 7.18).

In the following, we will define the bio-bar-code complement as the oligonucleotide sequence immobilized at the surface of the nanoparticle (Fig. 7.18) and the

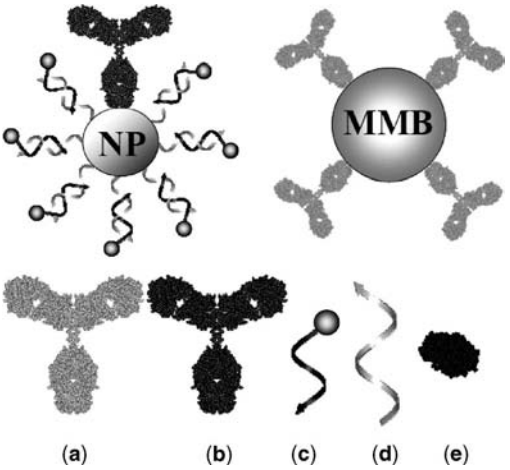

FIGURE 7.18 Components of the bio-bar code assay: MMB (Magnetic MicroBeads); NP (Nanoparticle); (**a**) monoclonal antibody or oligonucleotide; (**b**) polyclonal antibody or oligonucleotide; (**c**) bio-bar-code; (**d**) bio-bar-code; complementary oligonucleotide (**e**) target molecule (antigen or DNA)

bio-bar-code (Fig. 7.18) as the oligonucleotide that is hybridized with this immobilized sequence. The bio-bar-code sequence is captured on the DNA chip for detection after melting of the DNA duplex from the NP.

The steps involved in the bio-bar-code assay are as follows (Fig. 7.19).

First, the MMP are added to a solution of interest and allowed to interact with the biological target to be detected, generally via DNA/DNA interaction or antibody/antigen interaction (Fig. 7.19a). Next, a sandwich like structure is obtained through the interaction (via DNA/DNA interaction or Antibody/Antigen interaction) of the NP's with the biological target (Fig. 7.19b), the magnetic property of the MMP's allowing for the separation of this sandwich structure from the medium (Fig. 7.19c). After removal of the medium (Fig. 7.19d), the bio-bar-code DNA duplex is melted in pure water (Fig. 7.19e), purified from the particles by centrifugation (Fig. 7.19f) and captured on a DNA chip. The concentration of target molecules is directly related to the number of sandwich structure formed and consequently, related to the concentration of released bio-bar-codes.

Different detections have been described in the literature. Detection may be performed by fluorescence, by silver enhancement, or by electrical detection (Fig.7.19g). A promising approach is based upon using a Y-junction dendrimer DNA, carrying two fluorophores (Alexa Fluor 480 and Bodipy 630/650). The coding is not detected via a DNA chip but by intensity encoding. In consequence, no nanoparticles are required (41). So far this approach was carried out on polystyrene-based microparticles (nonmagnetic) but would be an interesting alternative in the bio-bar-code assay.

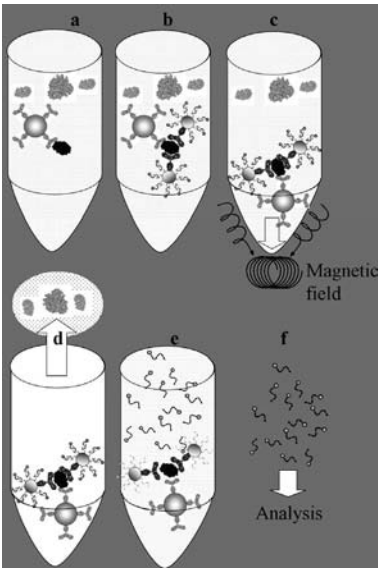

FIGURE 7.19 Steps of the bio-bar-code assay. **(a)** interaction between MMB and target; **(b)** recognition between target and particles in complex biological medium: sandwich MB/target/NP; **(c)** magnetic separation of MMB; **(d)** removal of biological medium. Only sandwiches MMB/target/NP and MMB are kept in the tube; **(e)** redispersion of sandwiches in distilled water causes dehybridization of bio-bar-codes; **(f)** removal and analysis of bio-bar-codes using DNA microarray or other methods

7.4.1 Nanoparticles (NP)

The NP amplifies the primary interaction of the MMP with the target through the so-called bio-bar-code. The ratio of bio-bar-code to target molecule per sandwich structure determines the amplification factor. The amounts of loaded bio-bar-code as well as the yield of sandwich captured target molecules will therefore determine the detection limit of the assay. The availability of immobilized biomolecules at the surface of the particles (the bio-bar-code complement and the biomolecule directed toward the target) is a key parameter. The bio-bar-code complement is typically 30 to 50 bases long, it can bear at the 3′-end an A10 spacer and an amine or thiol terminated alkyl (usually C6). 5′-thiolated ends are also described with 10-mers ethylene glycol spacer (2). The chemistry used for biomolecule immobilization depends on the materials employed for the NP's fabrication. Polyclonal antibodies are preferred for antigen detection.

Two materials are generally described, gold nanoparticles (2,6), and polystyrene (42). On polystyrene NP's, the generally described protocol for surface immobilization relies on glutaraldehyde cross-linking of amine bearing molecules. Polyclonal antibodies are immobilized through its N-termini or free amine bearing amino acid residues. The bio-bar-code complement is amine terminated that permits its

immobilization with a similar protocol (1530 ± 181 Abs). The particles are blocked with ethanol amine.

For gold NP's, the polyclonal antibody is first immobilized using a slow salt-aging methods, followed by the bio-bar-code complement using thiolated oligonucleotides through thiol/gold interactions. The surface is then blocked using BSA (43).

Sequence analysis of the complement bio-bar-code leads to the following: the GC content is near 50% with a melting temperature between 65 and 75°C (calculated with the next neighboring theory).

The number of loaded DNA strands on gold NP's is approximately 100 copies for a 10 nm particle, 300 copies for a 30 nm particle and 1000 copies for a 100 nm particle. This corresponds for approximately 0.3, 0.1, and 0.03 molecules per nm^2, respectively (5,43). It means that the surface density of bound DNA strands decreases with the diameter of the NP's. Nevertheless, Mirkin's group uses mainly 30 nm gold NP's.

The bio-bar-code is loaded by hybridization at room temperature in PBS 0.1 M. On polystyrene nanoparticles 3.5×10^5 bio-bar-code are loaded (1 μm diameter). Under these conditions of hybridization on polystyrene particles, the hybridization yield is near 10% as observed by UV spectroscopy and fluorescence (42). If the target molecule is a nucleic acid, the bio-bar-code and the target hybridizing oligonucleotide are immobilized at the surface of the particle using a solution containing the two molecules. The ratio between the two oligonucleotides provides a way to achieve signal amplification. For example, loading the particles with a 100:1 ratio of target complement DNA/bio-bar-code complement DNA leads to particles of 70:1(5).

In 2005, a simplified protocol of the bio-bar-code NP was reported where the bio-bar-code consists of single stranded thiolated oligonucleotides immobilized, on gold NP. The DNA is released for on chip DNA detection by DTT (4,44).

7.4.2 Magnetic Microparticles (MMP)

The function of the magnetic micro particles is to separate the target molecule from the medium. After interaction with the target molecule, the NP's are added leading to a sandwich like structure. MMP's magnetic properties allow for the separation of the sandwich structure from unreacted material and medium. Magnetic separation from unreacted target molecules before sandwiching is also reported (43).

Typically, MMPs are iron oxide based particles that may be encapsulated in a polymeric layer, the total particle having a diameter in the range of one to several micrometers. Amine bearing MMP are obtained by silanization of iron oxide (5) with an amine modified silane or purchased with a polyamine layer (2,5). Cross-linking reaction of glutaraldehyde with the primary amine at the surface of the particle and with free amine of the antibody, permits immobilization of monoclonal antibodies. In the case of oligonucleotide, the particle is modified with surface maleimido groups using succinimidyl 4-(*p*-maleimidophenyl) butyrate (SMPB) (4) or sulfosuccinimidyl 4-*N*-maleimidomethyl cyclohexane-1-carboxylate (sulfo-SMCC), leading to a maleimide modified surface (5). The oligonucleotide is then immobilized through thiol addition to the Carbon–Carbon double bond of the

maleimido group. The average number of DNA strands per particle is 3×10^5. In the case of antibody immobilization, the average number of immobilized molecules is 3500 per MMP (42), as estimated by optical density at 280 nm. Capping is accomplished with BSA or sulfo-NHS acetate.

Similarly to NPs, the detection limit depends on the yield of captured target molecules by the MMP, which depends among other factors upon the availability of the immobilized biomolecules.

7.4.3 Detection

Four main detection methods are described in the literature, namely, scanometric detection (45), fluorescent detection (42), electrical detection (46), and rolling circle amplification (RCA) (47).

Scanometric detection (45) is performed as follows. After collection of the sandwich structure, the DNA bar code is freed from the NP by melting of the bio-bar-code from its complement at high stringency (in DI water 55°C) or by competition between thiolated oligonucleotide and DTT (2,44). The bio-bar-code is recovered from the supernatant after centrifugation and captured on DNA chip by hybridization. The DNA chip is usually supported on maleimide modified glass slides or ester activated bearing 12-mer oligonucleotides complementary to one end of the bio-bar-code. After hybridization of the bio-bar-code (30–50-mer) on the DNA chip, the remaining free end is further hybridized with a gold nanoparticle (13 nm) labeled oligonucleotide. The 13 nm gold particles catalyze the reduction of silver salt (silver nitrate) from a modified photographic solution containing hydroquinone (reducing agent)(5,6). Light scattering due to the silver particles allow for the detection of the bio-bar-code. Mirkin's group uses an alterative method based upon the detection of a fluorophore (Alexa type) instead of silver enhancement. They found that it was best using larger NP's due to higher bio-code-bar loading (see below).

Detection limit as low as 500 zM (5) in the case of DNA targeted molecules and 3 aM is the case of protein targeted molecules (PSA) (42) are achieved. With fluorescence, the detection limit is of a few hundreds of aM using micrometer scaled NP instead of nanoscaled ones. As described above, the surface density of bound bio-bar-code complement strains decreases with the diameter of gold NP's. One might think that smaller diameter NPs would allow for a greater ratio of NPs per MMP. This may suggest that the limiting factor in the assay is the yield of sandwich structure formed per MMP.

Finally when using complex media or when multiplexing, the detection limit is increased by one to five orders of magnitude, probably due to cross reactivity and nonspecific adsorption (4).

An electrical-based detection device has also been reported (46). The device comprises of a gold layer with nanogaps containing SiO_2. These SiO_2 windows are functionalized with a thiolated silane allowing the immobilization of gold nanoparticles bearing DNA that comprises a sequence partially complementary to

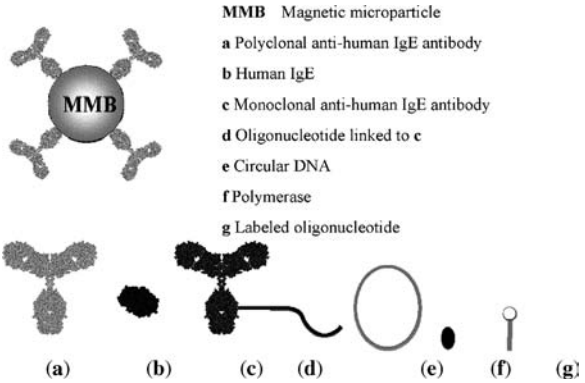

FIGURE 7.20 Components of rolling circle amplification on magnetic particle

the bio-bar-code. The bio-bar-code DNA after purification from unreacted material by magnetic field, is melted and hybridized on the the immobilized gold nanoparticles through hybridization and sandwiched through a second hybridization with a second gold nanoparticle. The resulting current is then detected producing a detection limit in the femtomolar range.

Other authors have reported rolling circle amplification (RCA) for detection (47). This method allows an antibody/antigen interaction to be revealed and amplified via DNA polymerase reaction. The detection of human IgE is achieved with polyclonal anti-human IgE functionalized magnetic particles (Fig. 7.20a). The target molecules are sandwiched between the MMP and oligonucleotide (Fig. 7.20d) tagged monoclonal anti-human IgE antibodies (Fig. 7.20c). Next the oligonucleotide tag is extended using a complementary circular DNA (Fig. 7.20e), and a DNA polymerase reaction (Fig. 7.20f). Fig. 7.21 is a schematic of the rolling circle amplification.

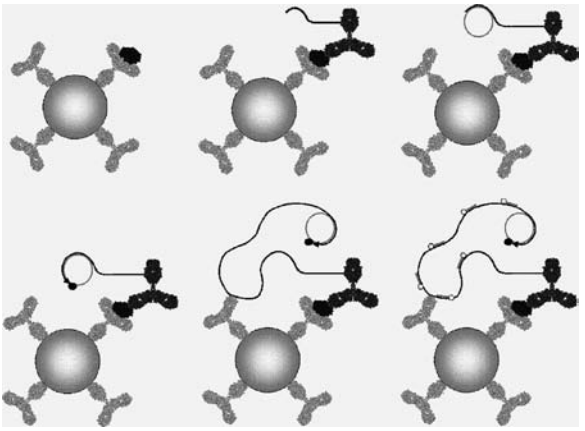

FIGURE 7.21 Rolling circle amplification with magnetic particle

TABLE 7.5 Summary of Biological Target Detected by Means of a Bio-Bar-Code assay.

Target	Disease	Recognition event	Detection	Lower detection limit	References
PSA	Breast and prostate cancer	Ab/Ag	Scanometric	30 aM	(6)
PSA	Breast and prostate cancer	Ab/Ag	Fluorescence	300 aM	(42)
Cardiac troponin I (cTnl)	Acute myocardial infarctions	Ab/Ag	RTPCR HRP	500 fM 3.35 pM	(48)
ADDL	Alzheimer disease	Ab/Ag	Scanometric	100 aM	(2)
Hepatitis B, Variolas virus, Ebola, HIV	Viral	DNA/DNA	Scanometric	500 fM	(4)
Anthrax lethal factor	Bacterial	DNA/DNA	Scanometric	500 zM	(5)
Mock RNA		RNA/DNA	Scanometric	700 aM	(44)

The analysis of this DNA is achieved using a labeled oligonucleotide probe (Figure 7.20g) that hybridizes on the extended DNA strand. Such an assay has been compared to a more classical immunoassay using magnetic particles and an anti-IgE alkaline phosphatase conjugate. The RCA amplification gave approximately 75-fold more signal than the classical immunotest, for a quantity of 25 ng/mL of IgE to be detected. The limit of detection of the RCA assay was reported as 1 pg/mL (Table 7.5).

7.4.4 Biological Application

Most applications concern the diagnosis of cancer (PSA), pathogens (bacteria or viruses), and the detection of Alziemer disease maker (ADDL). In brief, bio-bar-code allows the detection of biomolecules in the aM range when dealing with a model solution. When detection is performed with a complex mixture or when multiplex detection is performed, the lower detection limit raises up to 500 fM. In the particular case of PSA, Bao et al. (49) have demonstrated a linear dose response over at least four orders of magnitude and a 1000-fold improvement of the detection limit with regards to ELISA. Mirkin's group has been reporting an integrated system for bio-bar-code assay (50). The reported lab-on-a-chip is based on two major types of components: passive microfluidics (channels and reactive chambers) and electromechanical control structures (actuators and sensors). They reported the analysis of free PSA, as low as 500 aM using volumes in the microliter range. The free PSA is first allowed to react with the MMP. The mixture is then introduced into the lab-on-a-chip with all

subsequent operations being performed on-chip. Optical detection is performed on a DNA array as usual after silver reduction. It has been demonstrated that for concentrations of total PSA below 118 pM, the ratio of free PSA/total PSA is more sensitive than the analysis of only total PSA (51). Achieving ultra sensitive detection would allow for early diagnosis of the disease.

Another example is the detection of single polymorphism (43). However, this assay was performed with two separated solutions at concentration of 500 aM. The cross reactivity was not assessed.

7.4.5 Conclusion

The bio-bar-code appeared in the early 2000s as an analytical assay for proteins with detection limit similar to PCR. It is particularly useful for antigen detection where it improved the detection limit by many orders of magnitudes compare to classical ELISA (at the fM range) allowing for early diagnosis of diseases. Future works will focus on development of integrated systems as well as new detection procedures. Furthermore, it appears that work on surface chemistry may help to increase the capture yield as well as reducing nonspecific adsorption. Indeed, most of the work have been performed on model systems. In complex mixtures the detection limit increases by many orders of magnitude.

7.5 CONCLUSION

This chapter reports the applications of magnetic micro/nanoparticles in biosensors and bio-bar-code assays. Affinity biosensors are presented through different types of transducing systems: electrochemical, piezo electric or magnetic ones, applied to immunodetection and genodetection. Enzymatic biosensors are based on biofunctionalization through magnetic micro/nanoparticles of a transducer, more often amperometric, potentiometric or conductimetric. The bio-bar-code assays rely on a sandwich structure based on specific biological interaction of a magnetic microparticles and a gold nanoparticle with a defined biological molecule. The magnetic microparticle allows the separation of the reacted target molecules from unreacted ones. The nanoparticles aim at the amplification and the detection of the target molecule. The bio-bar-code assays allow the detection at very low concentrations of biological molecules, similar to PCR sensitivity.

REFERENCES

1. Hermanson GT, Mallia AK, Smith PK. Immobilized affinity ligand techniques. Academic Press;1992. Hermanson GT. Bioconjugate Techniques. Academic Press, London, 1996.
2. Georganopoulou DG, Chang L, Nam J-M, Thaxton CS, Mufson EJ, Klein WL, Mirkin CA. Fluorescent and scanometric ultrasensitive detection technologies with the bio-bar-code assay for alzheimer's disease diagnosis. PNAS 2005;102:2273–2276.

3. Liu Z, Liu Y, Yang H, Yang Y, Shen G, Yu R. A phenol biosensor based on immobilizing tyrosinase to modified core-shell magnetic nanoparticles supported at a carbon paste electrode. Anal Chimica Acta 2005;533 (1):3–9.
4. Stoeva SI, Lee J-S, Thaxton S, Mirkin CA. Multiplexed DNA detection with biobarcoded Nanoparticle probes. Angew Chem 2006;45:3303–3306.
5. Nam J, Stoeva SI, Mirkin CA. Bio-bar-code-based DNA detection with PCR like sensitivity. JACS 2004;126:5932–5933.
6. Nam J, Taxton CS, Mirkin CA. Nanoparticle-based bio-bar-codes for the ultrasensitive detection of proteins. Science 2003;301:1884–1886.
7. Helali S, Martelet C, Abdelghani A, Maaref MA, Jaffrezic-Renault N. A disposable immunomagnetic electrochemical sensor based on functionalized magnetic beads on gold surface for the detection of atrazine. Electrochim Acta 2006;51 (24):5182–5186.
8. Santandreu M, Sole S, Fabregas E, Alegret S. Development of electrochemical immunosensing systems with renewable surfaces. Biosens Bioelectron 1998;13:7–17.
9. Gehring AG, Brewster JD, Irwin PL, Tu SI, Van Houten LJ. 1-Naphtyl phosphate as an enzymatic substrate for enzyme-linked immunomagnetic electrochemistry. J Electroanal Chem 1999;469:27–33.
10. Sole S, Alegret S, Cespedes F, Fabregas E. Flow injection immunoanalysis based on a magnetoimmunosensor system. Anal Chem 1998;70:1462–1467.
11. Dequaire M, Degrand C, Limoges B. An immunomagnetic electrochemical sensor based on a perfluorosulfonate-coated screen-printed electrode for the determination of 2,4-dichlorooxyacetic acid. Anal Chem 1999;71:2571–2577.
12. Liu ZM, Yang HF, Li YF, Liu YL, Shen GL, Yu RQ. Core-shell magnetic nanoparticles applied for immobilization of antibody on carbon paste electrode and amperometric immunosensing. Sensor Actuator B 2006;113:956–962.
13. Li J, He X, Wu Z, Wang K, Shen G, Yu R. Piezoelectric based on magnetic nanoparticles with simple immobilization procedures. Anal Chim Acta 2003;481:191–198.
14. Kim GH, Rand AG, Letcher SV. Impedance characterization of a piezoelectric immunosensor. Part I: antibody coating and buffer solution. Biosens Bioelectron 2003;18:83–89.
15. Kim GH, Rand AG, Letcher SV. Impedance characterization of a piezoelectric immunosensor. Part II: Salmonella typhinium detection using magnetic enhancement. Biosens Bioelectron 2003;18:91–99.
16. Palacek E, Fojta M, Jelen F. New approaches in the development of DNA sensors: hybridization and electrochemical detection of DNA and RNA at two different surfaces. Bioelectrochem 2002;56:85–90.
17. Wang J, Kawde AN, Erdem A, Salazar M. Magnetic bead-based label-free elecrochemical detection of DNA hybridization. Analyst 2001;126:2020–2024.
18. Kerman K, Matsubara Y, Morita Y, Takamura Y. Peptide nucleic acid modified magnetic beads for intercalator based electrochemical detection of DNA hybridization. Sci Technol Adv Mater 2004;5:351–357.
19. Erdem A, Pividori MI, Lermo A, Bonanni A, Del Valle M, Alegret S. Genomagnetic assay based on label-free electrochemical detection using magneto-composite electrodes. Sensor Actuat B 2006;114:591–598.
20. Wang J, Xu D, Erdem A, Polsky R, Salazar MA. Genomagnetic electrochemical assays of DNA hybridization. Talanta 2002;56:931–938.

21. Kriz K, Gehrke J, Kriz D. Advancements toward magneto immunoassays. Biosens Biolectron 1998;13:817–823.
22. Abrahamsson D, Kriz K, Lu M, Kriz D. A preliminary study on DNA detection based on relative magnetic permeability measurements and histone H1 conjugated superparamagnetic nanoparticles as magnetic tracers. Biosensors Bioelectron 2004; 19:1549–1557.
23. Lu M, Ibraimi F, Kriz D, Kriz K. A combination of magnetic permeability detection with nanometer-scaled puperparamagnetic tracer and its application for one-step detection of human urinary albumin in undiluted urine. Biosens Bioelectron 2006;21:2248–2254.
24. Meyer MHF, Hartmann M, Krause HJ, Blankenstein G, Mueller-Chorus B, Oster J, Miethe P, Keusgen M. CRP determination based on a novel magnetic biosensor. Biosens Bioelectron 2007;22 (6):973–979.
25. Arakaki A, Hideshima S, Nakagawa T, Niwa D, Tanaka T, Matsunaga T. Detection of biomolecular interaction between biotin and streptavidin on a self-assembled monolayer using magnetic nanoparticles. Biotechnol Bioeng 2004;88:543–546.
26. Perez JM, Josephson L, O'Loughlin T, Högemann D, Weissleder R. Magnetic relaxation switches capable of sensing molecular interactions. Nat Biotechnol 2002;20:816–820.
27. Perez JM, Simeone FJ, Tsourkas A, Josephson L, Weissleder R. Peroxidase substrate nanosensors for MR imaging. Nanoletters 2004;4:119–122.
28. Perez JM, Simeone FJ, Saeki Y, Josephson L, Weissleder R. Viral-induced self-assembly of magnetic nanoparticles allows the detection of viral particles in biological media. JACS 2003;125:10192–10193.
29. Harris TJ, von Maltzahn G, Derfus AM, Ruoslahti E, Bhatia SN. Proteolytic actuation of nanoparticles self assembly. Angew Chem Int Ed 2006;45:3161–3165.
30. Varlan AR, Sansen W, Van Loey A, Hendrickx M. Covalent enzyme immobilization on paramagnetic polyacrolein beads. Biosens Bioelectron 1996;11 (4):443–448.
31. Miyabayashi A, Mattiasson B. An enzyme electrode based on electromagnetic entrapment of the biocatalyst bound to magnetic beads. Anal Chim Acta 1988;213:121–130.
32. Varlan AR, Suls J, Jacobs P, Sansen W. A new technique of enzyme entrapment for planar biosensors. Biosens Bioelectron 1995;10 (8):XV–XIX.
33. Solé S, Merkoci A, Alegret S. New materials for electrochemical sensing III. Beads. TrAC-Trends in Anal Chem 2001;20 (2):102–110.
34. Liao MH, Guo J-C, Chen WC. A disposable amperometric ethanol biosensor based on screen-printed carbon electrodes mediated with ferricyanide-magnetic nanoparticle mixture. J Magn Magn Mater 2006;304 (1):e421–e423.
35. Lu B-W, Chen WC. A disposable glucose biosensor based on drop-coating of screen-printed carbon electrodes with magnetic nanoparticles. J Magn Magn Mater 2006;304 (1):e400–e402.
36. Elyacoubi A, Zayed S, Blankert B, Kauffmann J-M. Development of an amperometric enzymatic biosensor based on gold modified magnetic nanoporous microparticles. Electroanalysis 2006;18:345–350.
37. Yu D, Blankert B, Bodoki E, Bollo S, Viré J-C, Sandulescu R, Nomura A, Kauffmann J-M. Amperometric biosensor based on horseradish peroxidase-immobilised magnetic microparticles. Sensor Actuat B 2006;113 (2):749–754.

38. Kauffmann J-M, Yu D, El Yacoubi A, Blankert B. Magnetic nanoporous microparticles for biosensors and bioreactors. LabPlus Int 2006;20 (3):6–8.
39. Willner I, Willner B. Functional nanoparticles architectures for sensoric, optoelectronic and bioelectronic applications. Pure Appl Chem 2002;74 (9):1773–1783.
40. Willner I, Katz E. Magnetic control of electrocatalytic and bioelectrocatalytic process. Angew Chem Int Ed 2003;42:4576–4588.
41. Li Y, Hong Cu YT, Luo D. Multiplexed detection of pathogen DNA with DNA-bases fluorescence nanobarcodes. Nat Biotechnol 2005;23 (7):885–889.
42. Oh B-K, Nam JM, Lee SW, Mirkin CA. A fluorophore-base bio-bar-code amplification assay for proteins. Small 2006;2:103–108.
43. Khan S, Klein W, Mirkin CA, Chang L, Georganopoulou D. Fluorescent and scanometric ultrasensitive detection technologies with the bio-bar-code assay for alzheimer's disease diagnosis. Nanoscape 2005;2 (1):7–15.
44. Thaxton CS, Hill HD, Georganopoulou DG, Stoeva SI, Mirkin CA. A bio-bar-code assay based upon dithiothreitol-induced oligonucleotide release. Anal Chem 2005;77:8174–8178.
45. Taton T, Mirkin AC, Letsinger AR. Scanometric DNA array detection with nanoparticles probes. Science 2000;289:1757.
46. Chang T-L, Tsai C-Y, Sun C-C, Uppala R, Chen C-C, Lin C-H, Chen P-H. Electrical detection of DNA using gold and magnetic nanoparticles and bio-bar-code DNA between nanogap electrodes. Microelectron Eng 2006;83:1630.
47. Schweitzer B, Wiltshire S, Lambert J, O'Malley S, Kukanskis K, Zhu Z, Kingsmore SF, Lizardi PM, Ward DC. Immunoassays with rolling circle DNA amplification: a versatile platform for ultrasensitive antigen detection. PNAS 2000;97 (18):10113–10119.
48. Lee A, Mirkin C, Georganopoulos D. Real-time polymerase chain reaction completed detection of cardiac tropin I with the bio-bar-code assay. Nanoscape 2005;2 (1):17–25.
49. Bao YP, Wei TF, Lefebvre PA, An H, He L, Kunkel GT, Muller UR. Detection of protein analytes via nanoparticles-based bio-bar-code technology. Anal Chem 2006;78:2055.
50. Shaikh KA, Ryu KS, Goluch ED, Nam J-M, Liu J, Thaxton CS, Chiesl TN, Barron AE, Lu Y, Mirkin CA, Liu C. A modular microfluidic architecture for integrated biochemical analysis. Proc Natl Acad Sci USA 2005;102:9745.
51. Stephan C, Jung K, Lein M, Sinha P, Schnorr D, Loening S. Molecular forms of prostate-specific antigen and human Kallikrein 2 as promising tools for early diagnosis of phosphate cancer. Cancer Epidem Bioma Prev 2000;9:1133.

CHAPTER 8

Colloids, Biotechnology, and Microfluidics

CECILE COTTIN-BIZONNE,

Université Claude Bernard, CNRS UMR 5586, Laboratoire PMCN, F-69622 Villeurbanne France

ROSARIA FERRIGNO

Institut des Nanotechnologies de Lyon, INL, CNRS UMR5270; Université Claude Bernard, Villeurbanne, F-69622, France

8.1 INTRODUCTION

Microfluidics is the field of manipulating subnanoliter volumes of fluids in a controlled way (1,2). This area has expanded very rapidly in the past 10–15 years because of its direct applications not only in the fields of Lab-on-chip (3,4) and microreaction devices (5,6), but also in the fields of proteomics and genomics (7). The success of this miniaturized approach is due to its unique features, such as the reduction of solvent/sample consumption and the improvement of mass and heat transfer due to a high surface-to-volume ratio. This last feature is very interesting from a synthesis standpoint as it allows achieving better control of the reaction conditions. Another important aspect of microfluidic is that the dimensions of microfluidic devices are approximately the same as the dimensions of many biological cells, and it is therefore a convenient tool to manipulate them. Microfluidics is now a field in its own and detailed descriptions of microfluidic physics can be found in various reviews (1,2) and textbooks (8). The first microdevices were mainly fabricated using methods issued from microelectronics industry and were made of Si and glass (9). More recently, polymers were used to fabricate devices for chemical or biological applications. Therefore, alternative techniques such as hot embossing (10,11) and soft lithography (12,13) have been developed. These techniques present the advantages of being less complex and also cheaper than technologies derived from microelectronic industries.

Colloidal Nanoparticles in Biotechnology, Edited by Abdelhamid Elaissari
Copyright © 2008 John Wiley & Sons, Inc.

The integration and coupling of colloids and microfluidic devices present many advantages and opportunities for biotechnology. Micro- and nanoparticles are becoming increasingly important for biomedical applications. In diagnosis, micro- and nanoparticles can be used as labels for selective and specific detection in immunoassays (14–16). For example, semiconductor nanoparticles can be used as fluorescent labels for fluorescence detection, and metallic (gold and silver) nanoparticles are appropriate for Raman detection due to their resonance light scattering properties (17). Integration of these immunoassays in microfluidic devices is of great interest and many examples can be found now in literature (14–16). These microdevices present the advantage of being able to minimize time and cost associated with routine biological analysis while improving reproducibility. Nevertheless, the integration of existing nanoparticle-based analytical approaches in Lab-on-chip is an obvious move when looking for improved analytical performances.

However, coupling of microfluidics and colloids can lead to less straightforward applications resulting in new perspectives for biologists or analytical chemists. In therapeutics, nanoparticles are important as they can be used for drug delivery (18–20). The development of such drug-encapsulated nanoparticles, which are able to deliver drugs to specific diseased cells in a controlled way, may maximize the therapeutic efficacy of drugs (21,22) while minimizing side effects. However, surface properties, size, and morphology of these particles can influence cell–particle interactions and should be investigated separately. Therefore, the development of devices used as *in vitro* models of biological environment is essential for the screening of these parameters. For example, microfluidic devices were introduced as *in vitro* models of biological microvasculature and were used to evaluate the interaction of polymeric particles with cells seeded in microchannels (23).

For both the above-cited applications, therapeutics and diagnosis, size and morphology of the particles are very important. Therefore, there is a need for the production of a large amount of micro- and nanoparticles with small-dimension dispersion. Microfluidics can also offer unique opportunities in the field of colloid synthesis due to the improved control of the operating conditions such as temperature and concentration in microreactors.

Microfluidic devices can also be used for *in situ* self-assembly and separation of colloids or cells. For example, one of the advantages of these devices is that due to their small dimensions, small amounts of particles can be easily handled, which can be very useful when involving precious objects (antibodies, . . .).

Finally, micro- and nanoparticles can be integrated with microfluidic devices such as "Lab-on-chip" and "Cell-on-chip" for what we will call nonstandard applications, where colloids can be part of the functionalization of the microdevices. Functions such as pumping, valving, or separation can be achieved by the integration of colloids (24).

The objective of this review is to give the reader a summary of the integration and coupling of colloids and microfluidic in the field of biotechnology. We will focus here on three fields: (1) the use of microreactors for the production of nanoparticles, (2) the use of microfluidic for colloid arrangement, and finally (3) the actuation possibilities in microfluidic devices using colloids.

8.2 NANOPARTICLE SYNTHESIS IN MICROFLUIDIC REACTORS

The concept of preparing nanoparticles in a microfluidic reactor is of very recent interest and it regroups a handful of studies (~40 papers). This concept has recently been the subject of a minireview by DeMello and DeMello (25), where they presented the potential benefits that microfluidic systems can offer, namely, producing monodispersed nanoparticles in a continuous flow mode, therefore, reaching a larger yield than that of standard production approaches. Recently, Sounart, et al. (26) also demonstrated that microsystems can offer unique opportunities to investigate the nucleation mechanism of nanoparticles. Indeed, they were able to spatially resolve nucleation and growth of cysteine-stabilized CdS nanoparticles in a microfluidic reactor and showed that the homogeneous reaction and particle nucleation are diffusion-limited processes. Microfluidic routes can, therefore, also be used as a tool to investigate kinetic and mechanism when detection techniques are coupled online to the microreactor.

To date, various types of microreactors have been described in the literature. These microreactors can be divided in two main classes based on the number of liquid phases that are used: single-phase or two-phase reactors. These microfluidic reactors have demonstrated successful production of mainly spherical nanoparticles of metal (Au, Ag, Cu, and Pd), semiconductors (CdS, Cd/Se), metal oxides (TiO_2, SiO_2), and polymers. Very recent papers demonstrated that microfluidic routes are well suited for the production of Janus (27), ternary (27), and nonspherical nanoparticles with anisotropic properties (28). Tables 8.1 and 8.2 present a brief description of the various microreactors devoted to particle synthesis.

TABLE 8.1 Main Features of Single-Phase Microfluidic Reactors Described in the Literature.

Types of nanoparticles	Microreactor	Details	References
Au	Pyrex glass/Si microreactor	Diameter between 5 and 50 nm,	(42)
	No seeds	Standard deviation 13%	
Au	Pyrex glass/Si microreactor	Diameter >12 nm	(82)
	With 12 nm seeds	Deviation >10%	
Ag	Tubular microreactor	Thermal reduction	(83)
Ag–Au nanorods	Tubular microreactor	Cylindrical particles ~100 nm long, 50 nm diameter	(84)
CdSe	Glass tubing with heated parts	Radii between 1.5 and 2.7 nm	(35)
CdSe	Silica glass capillary	245–275°C	(35,36)
CdSe	Glass microreactor	Diameter 2.23–2.55 nm	(34)
CdS			(31)
CdSe–ZnS	Tubular microreactor		(37)
Co	Polymeric microreactor	Diameter 3.9–4.7 nm Different crystal structures	(85)

TABLE 8.2 Main Features of Two-Phase Microfluidic Reactors Described in the Literature.

Types of nanoparticles	Microreactor	Details	References
UV-curable photopolymer	Two-phase droplet-based (liquid/liquid)	Nonspherical particles: plugsand disks (diameter >10 μm)	(86)
	PDMS microreactors	UV photopolymerization	
Acrylate	Two-phase droplet-based (liquid/liquid)	Core and core/shell particles (diameter >50 μm)	(55)
	PU microreactors		
Acrylate	Two-phase droplet-based tubular microreactor	Spherical microgel shell and spherical microgel particles	(53)
CdS and CdS/CdSe	Two-phase droplet-based (liquid/liquid)	Core and core/shell particles	(50)
	PDMS microreactors	From aqueous precursors at room temperature	
		No size given (wavelength)	
CdSe	Two-phase droplet-based (liquid/liquid)	High temperature (300°C)	(87)
	Glass microreactors	Diameter 3.4 nm	
CdS	Two-phase droplet-based PDMS microreactor	Diameter 4.2–8.2 nm	(88)
TiO_2	Two-phase laminar interface (liquid/liquid)	Diameter <10 nm	(43)
	Ceramic microreactor		
SiO_2	Two-phase droplet-based (gas/liquid)	Diameter >200 nm	(49)
	PDMS microreactor		
SiO_2	Two-phase droplet-based (gas/liquid) and (liquid/liquid)	10 nm–1 μm	(89)
	PDMS microreactor		
$CaCO_3$, $Mn_{1-a}Ni_a(C_2O_4)\cdot 2H_2O$, $BaTiO_3$	Two-phase laminar interface (liquid/liquid)		(47)

In this paragraph, we will first introduce some general aspects concerning the synthesis of nanoparticles and then, present some microfluidic routes that were investigated for the preparation of these nanoparticles.

8.2.1 Nanoparticle Synthesis—General

Physical properties of nanoparticles are generally defined by quantum size effects and they substantially differ from bulk material properties. For example,

characteristics such as surface plasmon resonance and optical bandgap of novel metal and semiconductor particles depend strongly on the particle dimensions (29). As a result, optical or electronic properties of nanoparticles can be tuned by particle dimensions. Bulk Au appears in a yellow color in reflected light, whereas thin films or small particles of Au appear in a large range of colors (from blue to orange) in a transmitted light. One of the most ancient examples of the use of this phenomenon is the Lycurgus Cup produced at the time of the Romans, where small amounts of Au and Ag nanoparticles (70 nm) were found in the glass and gave various colors to the cup. Another important parameter is the aspect ratio of nanoparticles. A slight deviation from spherical particles can also result in very impressive color changes (30).

There is a great interest in developing synthesis routes that are able to control particle dimensions, distribution, and also morphologies. After the synthesis, solutions containing nanoparticles are subjected to posttreatments, such as electrophoresis, to separate nanoparticles based on their size and obtain more monodispersed nanoparticles. These additional treatments are usually time consuming and also result in a lower yield of the particle production. There are two main routes to produce nanoparticles: the so-called "top-down" and "bottom-up" approaches. The latter approach is probably the one mostly used due to its versatility and ease of use.

The formation of nanoparticles can be described by two distinct processes. The nucleation phase is the formation of new particles from a supersaturated solution. These seeds can then grow by incorporation of monomers via the particle/solution interface. In a classical reactor, the nucleation and growth steps can take place at the same time and result in a broad range of particle diameters. To obtain narrow size distribution, it is necessary to discriminate in the reactor between the nucleation stage and the growth step. The nucleation stage needs to take place very fast, and then the growth condition needs to impede further nucleation.

The conditions to obtain monodispersed particles can be summarized here: (i) it is necessary to have a nucleation step occurring in a short time scale compared to the growth step and also (ii) all particles need to grow in the same chemical environment (same temperature and concentration, for example). These conditions are not always fulfilled in a standard reaction chamber. The preparation of this kind of particles is usually carried out in a batch reactor in which the precursors are rapidly injected and mixed with the solvents and the coordinating ligands at high temperature. During this process, various parameters need to be controlled to obtain nanoparticles of good quality and with low diameter dispersion. This control is obviously more difficult to be attained with a batch reactor compared to a flow microreactor.

8.2.2 Nanoparticle Synthesis—Microfluidic Route

Because of their reduced dimensions, microreactors are characterized by rapid and efficient thermal and mass transfer (5,6), conditions that are advantageous for the production of monodisperse nanoparticles. Using microreactors it is possible (i) to control temperature and concentration gradients, (ii) to efficiently mix reactants, and (iii) to operate in a continuous flow regime.

Various types of microreactors have been suggested for the synthesis of a large variety of nanoparticles: Ag, Au, CdS, CdSe, TiO_2, SiO_2, and polymers. To date, the benefits demonstrated are essentially the continuous production of particles, at least as monodisperse as in batch reactors. The lower dispersion is not always demonstrated, as strict comparisons are not shown. Nevertheless, the continuous production, the ease of scalability, and the possibility to finely tune the particle sizes are characteristics that explain the attractiveness of the microfluidic approach presented here.

8.2.2.1 Single-Phase Microfluidic Reactor The use of microfluidic reactor for nanoparticle synthesis was first reported by Edel et al. in 2002 (31). In their work, they used a continuous flow micromixer (600 nL) developed by Bessoth et al. (32) (Fig. 8.1) and based on diffusive mixing to carry out the synthesis of CdSe nanoparticles with diameter from 12 to 3.2 nm. They demonstrated by recording absorption spectrum (Fig. 8.2) that the use of a miniaturized and flow reaction vessel improved CdSe nanoparticle monodispersity compared to standard bulk reactor and that the homogeneity can further be improved by increasing the volume flow rate (31). After this first demonstration, several studies were devoted to the synthesis and characterization of several nanoparticles materials, such as CdSe, Au, Ag, Cu, Pd and TiO_2, using single-phase microfluidic reactors.

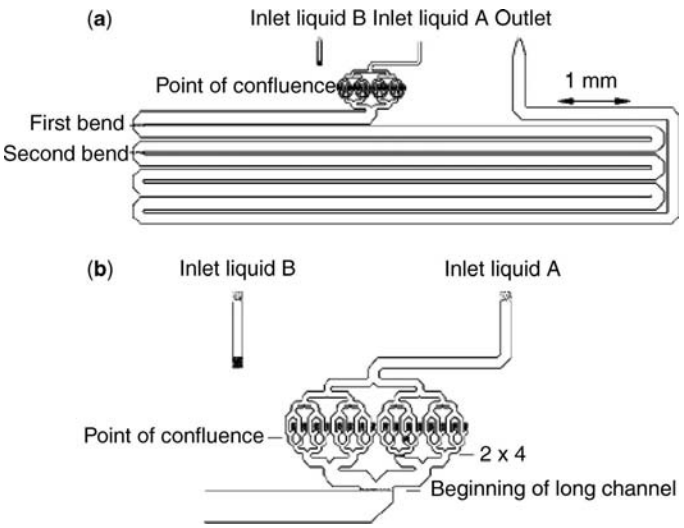

FIGURE 8.1 Schematic representation of a continuous flow micromixer (**a**) layer 1 (**b**) detail of layer 1 (32) (reproduced by permission of The Royal Society of Chemistry)

Semiconductor Nanoparticles Preparation of semiconductor nanoparticles such as CdSe has gained a lot of interest because of their potential use for fluorescence tags of biological molecules. When size of CdSe nanoparticle is smaller than the exciton Bohr radius (<7 nm), fluorescence from these particles shift toward shorter wavelength due to the reduction of their bandgap. It is therefore possible to tune fluorescence color

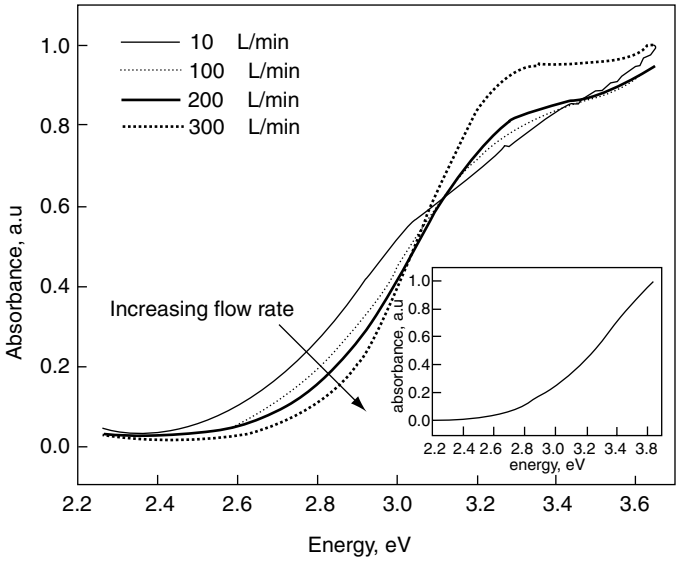

FIGURE 8.2 Absorption spectra of fluid streams exiting the micromixer after contact between cadmium nitrate and sodium disulfide solutions as a function of flow rate. Inset: absorption spectrum of nanoparticles produced using a bulk synthesis (31) (reproduced by permission of The Royal Society of Chemistry)

by controlling the particle dimensions. The continuous preparation of CdSe nanoparticles using a microfluidic approach has therefore been demonstrated by various authors (33–36), but unfortunately they do not always compare their results (particle dispersion) with macroscopic production. Nevertheless, they investigated the influence of various parameters, such as temperature, precursor concentration, and residence time (by varying the flow rate), on the particle quality and the size distribution. They demonstrated that a wide range of nanoparticle diameters is accessible, but this can be at the expense of polydispersity. As a general trend, nanoparticle dispersion usually decreases not only by increasing temperature and mixing but also by reducing microreactor dimensions. The influence of the flow rate and therefore residence time was found to be very important. The increase of the dispersion of the particle dimensions (from 6% to 11%) was observed with increasing the flow rate (35). Nakamura et al. (33) prepared CdSe nanoparticles by mixing solutions of Se trioctyl phosphine and Cd trioctyl phosphine oxide at high temperature (230–300°C), and they obtained CdSe nanoparticles with diameters from 2 to 4.5 nm. The mixing was performed outside of the microreactor and the mixture was then introduced into glass syringe connected to a glass capillary (200–500 μm diameter). These authors were the first to demonstrate the interest of segmented flow (solution plugs separated by N_2 gas injected into the capillary) for the reduction of particle dispersity. Yen et al. (35) proposed a more detailed study of the influence of reaction conditions on the quality of nanoparticles. They obtained CdSe nanoparticles by mixing two solutions containing Cd oleate and Se trioctyl phosphine using a convective

micromixer connected to a glass capillary (250 μm diameter) and maintained at a constant temperature (180–320°C). They prepared nanoparticles with diameters from 1.52 to 2.7 nm by varying the solution composition, the residence time and, the operating temperature. In their study, they also identified the main drawback of the single-phase microfluidic approach, namely, the residence time distribution due to the parabolic profile of the velocity in a microchannel or a capillary. This residence time discrepancy was identified as being responsible for particle dispersion at low flow rate.

The possibility of running successive reactions was also demonstrated by the production of composite core/shell nanoparticles, such as CdSe particles coated with ZnS (37). The authors used a three-section system where the CdSe particles were first produced in a capillary at high temperature, mixed to ZnS raw material, and then the mixture was introduced into a second capillary to carry out ZnS coating on CdSe nanoparticles. Recording the UV spectra, they demonstrated the redshift of the absorption peak due to ZnS coating of CdSe nanoparticles. They also noticed that ZnS coating thickness can be controlled by changing the flow rate and the residence time in the coating section.

Metal Nanoparticles Production of metal nanoparticles in microreactors have also been demonstrated. These kinds of particles have a great potential for analytical chemistry in applications such as colorimetric gene detection (38), nanoparticles-enhanced microchip capillary electrophoresis (39), surface-enhanced Raman spectroscopy (40), and optical detection (41). Silver nanoparticles were prepared in a continuous flow (0.08–0.7 mL/min) stainless steel tubular microreactor using thermal reduction of silver pentafluoropropionate. This synthesis was carried out at mild temperature (100–140°C) and with various molar ratios between surfactant and precursor resulting in Ag particle size from 7.4 to 8.7 nm with standard deviation between 1.4 and 0.9 nm. As for CdSe particle synthesis, polydispersity of Ag nanoparticles increases at high flow rate. Residence time of at least 60 s was required to obtain monodisperse particles.

Gold nanoparticles were obtained from the mixing of chloroauric acid with ascorbic acid using a static micromixer (42). The authors obtained nanoparticles ranging between 5 and 50 nm (with a standard deviation of ~13% at the best) by adjusting experimental parameters such as flow rate, pH, and excess of reducing agents. They also carried out comparable experiments in batch reactors and obtained particles of lower quality (standard deviation approximately two times larger).

8.2.2.2 Two-Phase Microfluidic Reactor The first report presenting a multiphase approach for the production of nanoparticles in microfluidic devices was made by Wang et al. (43) in 2002. They used the interface between two liquids as a nanoreaction chamber. The authors took advantage of the thin interface (<1 nm) between immiscible liquids to control the size of the particles. They used a ceramic microreactor composed of 9 cm long microchannel (360 μm wide and 200 μm deep) where they flowed two insoluble liquid systems: 1-hexanol/formamide and cyclohexane/water. They prepared TiO_2 nanoparticles at these interfaces, which were

less than 10 nm in size and possessed an anatase structure. In this report, immiscible liquids were flowed as two adjacent streams. However, a second configuration based on the formation of droplet nanoreactor is more widely used than the latter one.

Single-phase microfluidic reactors present two intrinsic drawbacks: (i) the parabolic profile of the velocity distribution introduces sample dispersion and (ii) the main mixing phenomenon at low Re number is diffusion, which is a slow process compare to convection (high Pe number). These two characteristics are detrimental for fast—millisecond time scale—mixing. Ismagilov et al. (44,45) recently demonstrated that it is possible to achieve millisecond mixing by using a droplet-based system. In this architecture, drops of water (organic solvents or oils, respectively) containing the reactants are transported in a flow of organic and immiscible solvents (oil or water respectively). This system solved the two previously described drawbacks: (i) dispersion is eliminated by transport in droplets and (ii) efficient mixing is achieved within droplets through winding channels by chaotic advection. The efficiency of nL reactors was demonstrated by carrying out protein crystallization (46) and was also successfully applied to nanoparticle synthesis by various groups as described below.

The first report of the droplet configuration used for colloid production was made in 2003 and the reactor was entitled "Continuous Segmented Flow Tubular Reactor" (47). This microreactor was applied to the production of $CaCO_3$, $BaTiO_3$ and $Mn_{1-a}Ni_a(C_2O_4)\cdot 2H_2O$ powders. The authors demonstrated that they were able to obtain calcite particles with a median diameter of 1.32 μm, compared to 2.35 μm for high quality commercial powder, and with a narrower particle size distribution. The span of the powder produced in the microreactor was reduced to 1.09 compared to 1.63 for commercial powder.

Silica nanoparticles were also prepared using segmented flow reactors by Jensen et al. (48). The microchannels used in their work were 400 μm wide and 150 μm deep and were fabricated using standard soft-lithographic techniques (Fig. 8.3). The synthesis was carried out using Stober (49) process and was based on the mixing of a dilute solution of TEOS in ethyl alcohol and a solution of ammonia, water, and ethyl alcohol. In this work, air was used as the segmenting fluid and a detailed characterization of the flow regimes, mixing efficiency, and residence-time distribution is presented before demonstrating the silica synthesis. They produced particles ~200–300 nm in diameter and with size distribution of ~10%. In comparison, the same particles obtained by carrying out the synthesis in a single-phase microreactor had a size dispersion of ~20–25% (Fig. 8.4).

Successful production of CdS and CdS/CdSe nanoparticles using droplet-based microreactors was also achieved by Ismagilov et al. (50) at room temperature. In their work, aqueous droplets were formed in a continuous stream of fluorinated oils. They also demonstrated that they were able to add a quenching step after synthesis to avoid particle aggregation.

Microfluidic biphasic reactors are also widely used to generate monodisperse polymer particles (27,28,51–54) that are usually in the micrometer range. In this approach, flow-focusing reactors are used and immiscible streams of monomer and perfluorinated oil solutions are flowed to create droplets of monomers inside an oil

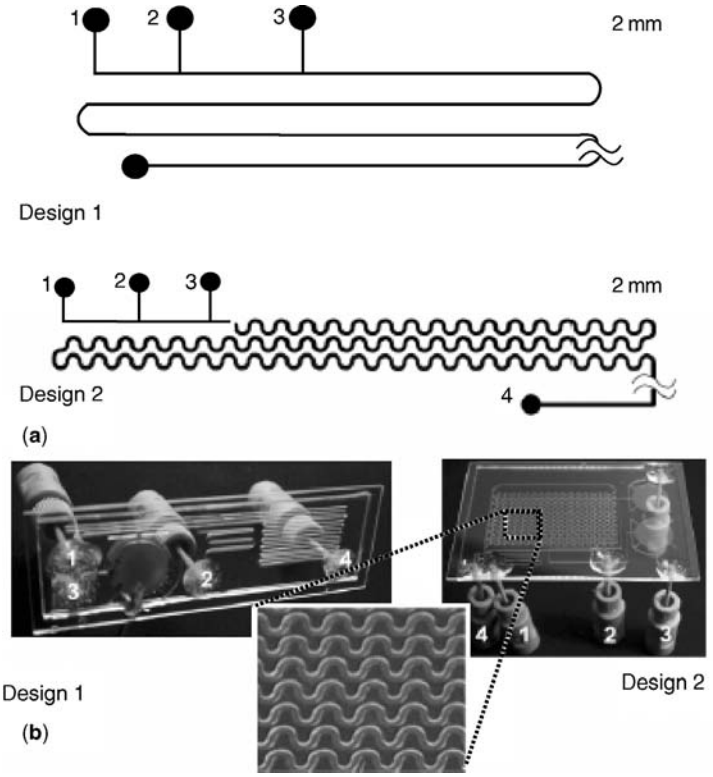

FIGURE 8.3 (**a**) Schematic representation of the microfluidic reactors used for nanoparticle synthesis. (**b**) Examples of microreactor designs in PDMS and bonded to glass slides (48) (reproduced by permission of The Royal Society of Chemistry)

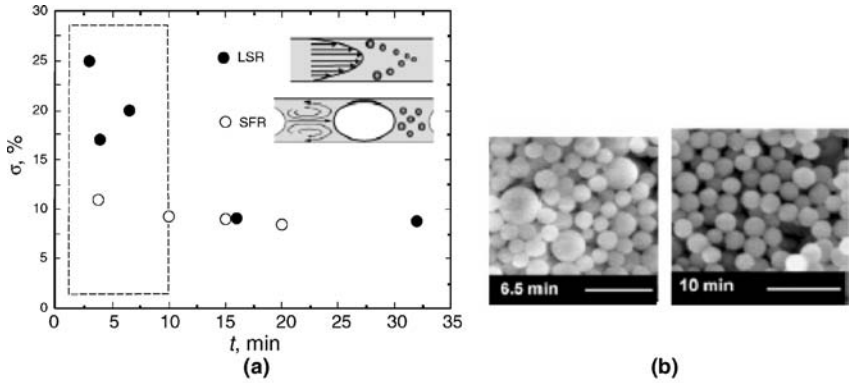

FIGURE 8.4 (**a**) Plot of variance of particle size distribution expressed as a percentage of the mean diameter for the two reactor types operating under various conditions. Inset are the schematics of flow patterns in laminar flow reactors (LFRs) and segmented flow reactors (SFRs). (**b**) SEM micrographs of typical product from an LFR (left) and a SFR (right) (48) (reproduced by permission of The Royal Society of Chemistry)

stream. The UV photopolymerization of the monomer droplets is also carried out directly in the microreactor. This approach was used to obtain various types of particles: core–shell particles with different number of cores (55), nonspherical particles (28,55), Janus and ternary particles (27).

8.3 ORGANIZATION AND SEPARATION OF COLLOIDS IN MICROFLUIDIC DEVICES

8.3.1 Microfluidic: A Tool for Crystallisation and Colloidal Assembly

One of the main current issues with colloids is to create *uniform assemblies*. These assemblies have a number of potential applications such as paper-like displays, photocatalyst supports, and 3D photonic bandgap materials. For biotechnology, they can also be used as membranes to filter elements, as supports for size-exclusion chromatography, or as nanobar codes for the recognition of biological molecules. Periodic colloidal assemblies (2D or 3D) have been grown within microfluidic devices that are used *as templates for the growth of colloidal assemblies*. Microfluidic allows an easy integration of the assembly with other functionalities. For example, photonic crystals fabricated inside microfluidic devices can be easily integrated with other planar optical components (waveguides or fiber optics). Another advantage is that it is possible to *actively control the formation of the self-assembled colloidal crystals* and to finely tune their thicknesses, areas, and orientations.

We will now describe different techniques used to create colloidal assemblies with microfluidic devices:

8.3.1.1 Microfluidic Devices: Templates for Evaporation-Induced Colloidal Assemblies Evaporation is often used at a macroscopic scale to assemble colloids. Ozin and collaborators (56) have employed *evaporation-induced self-assembly* to grow colloidal crystals *inside microchannels*. Their microchannels consist of a V-shaped groove in a silicon substrate covered by a PDMS slab. An aqueous solution containing monodisperse colloidal microspheres is driven inside the microchanel by capillary forces, and the microspheres are closely packed inside the grooves upon water evaporation through the PDMS. Over spatial surfaces of around 40 μm^2, areas sufficiently large for photonic applications or chromatographic microdevices, they were able to grow defect-free crystals. This method is a straightforward, fast (the whole process takes 2 hours), reproducible, and inexpensive tool to pattern defect-free opals on silicon wafers. The attractiveness of this method, in comparison with usual macroscopic methods, is the possibility of controlling defects in colloidal crystals (by controlling the template) as well as the number, area, orientation, and registry of close-packed layer planes of microspheres in the colloidal crystals embedded within a single-crystal silicon (100) wafer. Kuo et al. (57) have also studied convective self-assembly of colloids on structured microchannels. Using a novel approach based on a combination of sedimentation

and hydrodynamic particle removal in partially sealed microchannels, they generated assemblies of microparticles on predefined locations of the microchannels.

8.3.1.2 Evaporation of Emulsions Created inside Microfluidic Devices Assemblies resulting from spontaneous evaporation are face centered cubic crystals. More *complex nonplanar structured materials* are useful for photonic applications, chromatography, or catalysis. Yi et al. (58) have made spherical colloidal assemblies called photonic balls (Fig. 8.5). *Emulsions* created inside *microfluidic devices* were used to generate these uniform photonic balls. Yi et al. (59) have made a water-in-oil emulsion containing monodisperse spheres. The number of particles captured inside the emulsion controls the internal structure of the colloidal assembly. By slowly removing the water from the aqueous suspension droplets, they have created uniform assemblies of identical colloidal particles. The advantage of using microfluidic devices is that the emulsions generated inside these devices can be really uniform, providing uniform nanoliter crystallization chambers.

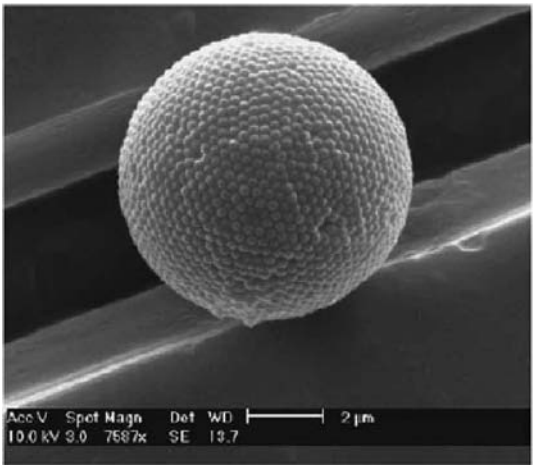

FIGURE 8.5 Typical scanning electron micrograph of colloidal assemblies that were generated in soft-microfluidic devices. This figure was published in Reference (58), Copyright Elsevier (2003)

8.3.1.3 Active Control of the Formation of Colloidal Crystals inside Microfluidic Devices: A Combination of Electrocapillary Forces and Evaporation The formation of self-assembled colloidal crystals in microfluidic devices can also be *actively controlled* by using a combination of *electrocapillary forces and evaporation-induced self-assembly* (60) (Fig. 8.6). The crystalization vessel consists of a microfluidic channel where three walls are made of PDMS while the fourth was an electrode. The electrocapillary forces drive the colloidal solution into the predesigned position in the microfluidic channels by applying a specific voltage. The colloidal crystals can then be obtained after solvent evaporation that occurs naturally through the PDMS. It is also possible to

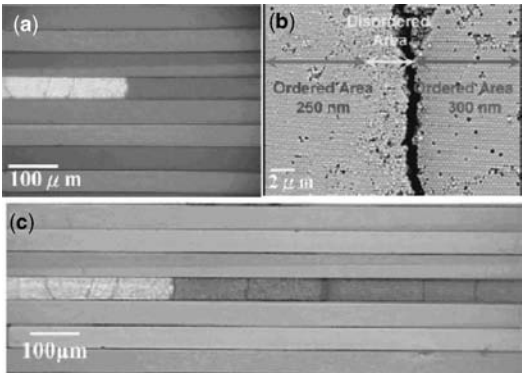

FIGURE 8.6 (**a**) Two adjacent colloidal crystals formed in the same microchannel using 250 and 300 nm diameter polystyrene beads. (**b**) SEM image of the boundary between two adjacent colloidal crystals. (**c**) Three adjacent colloidal crystals formed in the same microchannel using 250-, 300-, and 198-nm diameter polystyrene beads. Reprinted with permission from (60) Copyright (2004) American Chemical Society

address simultaneously or individually multiple channels using different configurations for the electrodes. One can selectively fabricate colloidal crystals in desired channels and also build colloidal crystals with different optical properties (by using colloids of different sizes, for example) in different channels or in the same channel. The same principle can be employed to guide microcapsules through three-dimensional networks of channels or to produce other novel functional materials using the self-assembly process.

The use of electrocapillary forces in microfluidic devices can also lead to the *patterning of biological solutions and cells in a programmable manner*. Shiu and Chen (61) have shown that it is possible to pattern and grow cells in addressable microchambers arrays using electrocapillary forces and evaporation.

8.3.1.4 The Use of the Confinement and the Geometry of Microfluidic Devices to Create Colloidal Assemblies Microfluidic devices can also be used to control precisely the formation of self-assemblies and create reproducible structures. The environments need to be controllable on the dimension of the self-assembly itself. Microfluidic systems have several characteristics that allow process control at this level; one cannot usually have such a control with conventional bulk production of self-assembly.

Kumacheva et al. (62) generated 2D colloidal lattices in microchannels by *coupling the laminar flow of dispersions of spherical colloids and geometrical confinement in microfluidic devices*. They present convective mechanism leading to the formation of close-packed and non-closed-packed structures. In their case, the number and types of possible lattices is determined by the ratio of the width of the microfluidic channel to the diameter of the particle.

Very homogeneous biological self-assemblies can be made using microfluidic devices. For example, liposomes are composed of a lipid bilayer membrane that

encapsulates an aqueous volume. To use these liposomes *in vivo* for applications such as *targeted drug delivery*, it is important to *control the liposome size* as size influences the clearance rate from the body and ultimately determines the drug dosage. In bulk the local environment is not well controlled, so a bulk fabrication of liposomes leads to inhomogeneous population. Using microfluidic devices Jahn et al. (63) created monodisperse liposomes: a stream of lipids is hydrodynamically focused at a microchannel junction between two aqueous buffers. They controlled the formation of the liposomes better than the spontaneous self-assembly in bulk. They have also determined that one can control the liposome size by changing the flow rates inside the microfluidic channel.

Microfluidic devices can also be used to create patterns of colloids. Lim et al. (64) have formed *patterns of colloids within the steady-state recirculation flow of a microvortex* generated in a microfluidic system. The mechanism at the origin of the formation of these patterns could be exploited for the separation and concentration of biological particles in analytical applications, such as in flow cytometry.

8.3.1.5 Fabrication of Patterned Colloidal Photonic Structures in Centrifugal Microfluidic Chips Lee et al. (65) report a method for fabricating colloidal photonic crystals inside microchannels using centrifugal force. Colloids are driven to flow through the channels under the action of a centrifugal force and then they assemble quickly into face-centered cubic arrangement. The colloidal photonic crystals can be used *in situ* inside the microfluidic channel, for example, as light filters for integrated adaptive optical devices.

8.3.2 Microfluidic: A Tool to Manipulate, Collect, and Separate Species

The true potential of microfabricated devices lies in their ability to integrate a complete analysis system "on chip," and those "lab on a chip" have to integrate different functionalities. It is important to control fluid flow within these microfluidic devices.

To analyze species (colloids, biological particles) from a solution, it is necessary to be able to collect and concentrate particles from this solution. As described below, some groups have developed noninvasive techniques that are perfectly suited for sorting and fractioning particles inside a microfluidic device, making it easy to integrate those steps within a "lab-on-chip." For some applications, for example, the one involving precious cells, such as primary cells that cannot be expanded to large populations, the microfluidic sorting devices are very important because it is possible to handle a small number of cells (100–100,000) with high yield. In classical macroscopic sorting techniques such as flow cytometry (characterization of single cells as they pass at high speed through a laser beam), a much higher number of cells are required.

Different noninvasive techniques have been used to create microfluidic cell sorters: some based on dielectrophoresis process, others based on optical process and still others based on hydrodynamic phenomena. Some techniques based on a CMOS/

microfluidic hybrid system make the manipulation of single cells easy. We will first describe these techniques briefly.

8.3.2.1 Integrated Cell Manipulation Lee et al. (66) have designed hybrid CMOS/microfluidic devices to control of the motion of individual biological cells that are tagged with magnetic beads. The control is assured by a CMOS chip (lying under a microfluidic device) that generates microscopic magnetic field patterns using an on-chip array of microelectromagnets. Furthermore, the CMOS chip allows programmable reconfiguration of the magnetic fields, increasing the manipulation capability of the hybrid system.

8.3.2.2 Dielectrophoresis Process An electrokinetic methodology that exploits dielectrophoresis (DEP) in microfluidic channels has been used to actively control the trajectories of some particles. Dielectrophoresis is based on the translational motion of charge-neutral matter caused by polarization effects in nonuniform electric fields. By using miniaturized electrode arrays (driven with high frequency ac) housed in a microchannel, Fiedler et al. (67) were able to actively control some particle trajectories: a laminar liquid flow carries the particles past the electrodes, and a modification of the ac drive changes the particle trajectories.

More recently, DEP in microfluidic has also been used to sort colloids (or cells) and, for example, isolate rare cells from complex mixture (68). Some target cells are labeled with particles that differ in polarization response, which changes the dielectrophoretic amplitude response of the target cells. Electric fields are engineered inside the microfluidic device to achieve an efficient separation between the dielectrophoretically labeled and unlabeled cells. With this kind of device, Hu et al. (68) have enriched rare cells by 200 in a single round of sorting. The main drawbacks of this technique are that the approach is sometimes incompatible with the buffers used for biological cells and it is also a very slow sorting process. We can also mention the work of Bhatt et al. (69): by combining electrohydrodynamic effects and EDP, they were capable of focusing latex particles and collecting, for example, yeast cells from buffer solutions.

8.3.2.3 Optical Separation

Microfluidic-Based Fluorescence-Activated Cell Sorting The principle of fluorescence-activated cell sorting (FACS) is the following: cells first pass through an analysis region and then through an optical switching region. When a cell is detected and determined to be a target cell, a focus laser spot deflects the cell to the target output channel. For applications involving precious cells, where only a small amount of cells can be used, it is very important to develop a microfluidic version of these FACS. The first microfluidic-based FACS (μFACS) cell sorters sorted cells via electrokinetic flows (70). However, the electrokinetic sorter suffers from the same drawbacks as all the electrokinetically actuated microfluidic devices, such as buffer incompatibilities and frequent change of voltage settings due to ion depletion, pressure

imbalance, and evaporation. By incorporating valves and pumps to control sorting by pneumatic actuation, the cell sorter developed by Fu et al. (71) has a better capability of fine tuning the flow and is less harmful to the cells than the devices that use electrokinetic flow. They can also create complete analytical microsystems by integrating various modules on the same chip. Different strains of *Escherichia coli* and different types of bacteria, including magnetotactic bacteria, could be pumped through the integrated cell sorter in their own suspending media. In this device, for example, two populations of *E. coli* cells were separated, one expressing EGFP and the other expressing *p*-nitrobenzyl (pNB) esterase; 480,000 cells were sorted in 3 h at the rate of 44 cells per second. Wolf et al. (72) have also developed a microfabricated fluorescent-activated cell sorter (μFACS) with several integrated functional structures. A novel structure for hydrodynamic focusing of sample in flow cytometry and cell sorting was designed. An advanced microfluidic-based fluorescence-activated cell sorter (μFACS) has also been developed by Wang et al. (73). With this device, cell populations (from 1000 up to 280,000 cells) can be sorted in less than an hour. This number is still smaller than what can be achieved with conventional macroscopic flow cytometer, but the device would be very useful for rare cells. These techniques should also facilitate a variety of more integrated and complex cell handling functions.

Optical Trapping Some optical techniques used for sorting and fractioning elements can be integrated within microfluidic devices, providing a way to sort colloidal, molecular, or biological elements that could later be used for other analysis. Macdonald et al. (74) have achieved microfluidic sorting in an optical lattice (Fig. 8.7). Their optical sorter is based on the interaction of colloids (or biological elements) with a dynamically reconfigurable 3D optical lattice. The optical trapping would hold a particle in a tightly focused light beam. Their optical technique is noninvasive and can sort particles or cells without physical contact. The sole use of optical forces simplifies surface interaction and sterility issues by

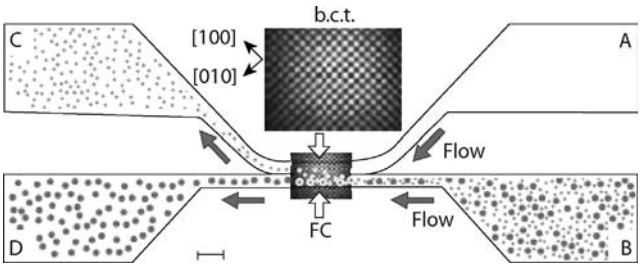

FIGURE 8.7 The concept of optical fractionation. Low Reynolds number flows will be laminar: Without an actuator all particles from chamber B would flow in chamber D. By introducing a 3D optical lattice into the fractionation chamber (FC), one species of particle is selectively pushed into the upper flow field. The reconfigurability of the optical lattice allows for dynamic updating of selection criteria. Reprinted by permission from Macmillan Publishers Ltd: *Nature* (74), copyright (2003)

removing the extremely high surface area associated with any physical sieve or gel. When a flow of mixed particles is passed through the lattice, selected particles are strongly deflected from their original trajectories while others pass straight through largely unhindered, depending upon their sensitivity to the optical potential. They can separate particles of different sizes or of different index of refraction—that is to say, of different chemistry. With their device, they have a sorting efficiency higher than 96% and their technique is often faster than the classical techniques used to separate elements.

8.3.2.4 Hydrodynamic Flow-Based Control to Sort Colloids or Cells To separate particles of different sizes, Tagaki et al. (75) have developed *microfluidic devices presenting asymmetric pinched flow fractionation*. Liquids with and without particles are introduced into a microchannel having a pinched segment obtained by using different flow rates for the two solutions (see Fig. 8.8); the particles are separated perpendicularly to the direction of flow according to their sizes by hydrodynamic force. Separated particles can be collected independently by making multiple branch channels at the end of the pinched segment. This device is really advantageous because it realizes a purely geometrical separation, which is suitable for preparative separation of particles. Their system is suitable for the *separation of biological species*. They could, for example, separate erythrocytes from blood.

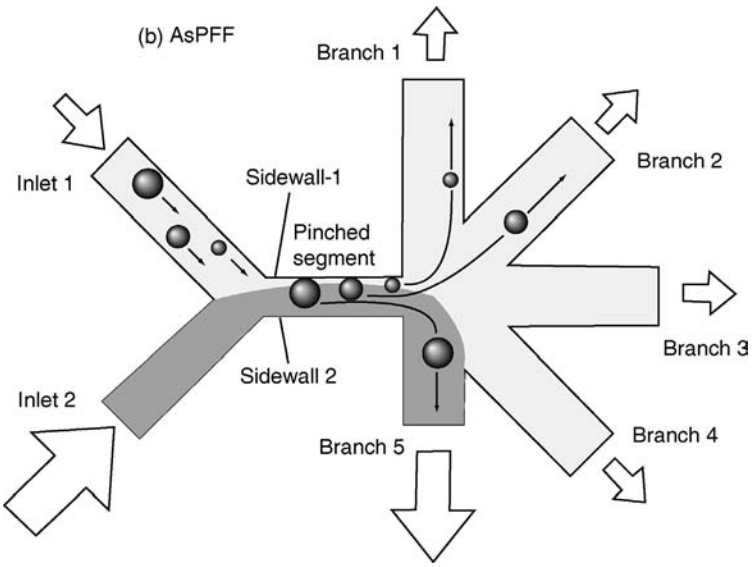

FIGURE 8.8 Schematic diagram of an asymmetric pinched flow fractionation. The size of an arrow represents the flow rate. One branch channel is designed to be short and or broad, and liquid flow is asymmetrically distributed (75) (reproduced by permission of The Royal Society of Chemistry)

8.4 COLLOIDS USED TO CONTROL FLOW MOTION IN MICROFLUIDIC DEVICES

The control of fluid motion is very important for chemical processing in "lab-on-a-chip." To integrate analysis platforms and microchemical reactors, it is necessary to use on-chip valving and pumping. Classical pump designs that employ inertial or centrifugal action are inappropriate for microfluidic applications due to the very small Reynolds number. Pumping and valving are usually realized in microfluidics by electroosmosis. Electrokinetic pumping is sensitive to surface conditions, and electrokinetic valving can leak. For biological applications, it is sometimes difficult to maintain cell viability under high electric fields. Most of those devices including control elements based on electroosmosis require complex fabrication and they also impose unique constraints on potential device capability, flexibility, and performance. Those microsystems have also never been directly integrated with microfluidic devices. Thus people have looked for other ways of valving and pumping.

Few groups have worked on controlling flows by the forced motion of colloidal microparticles in a microchannel. This seems to be a promising way to control *in situ* microfluidic flows, though there have been only a few studies on this up till now. The use of colloidal valves and pumps allows easy device integrations, and colloids can be easily transported through microfluidic channels to their target position.

8.4.1 Microfluidic Electrophoresis

Viovy and collaborators (76) have developed a microfluidic tool for the separation of DNA. They confine a solution of paramagnetic colloids in a microfluidic channel, and then they apply a constant magnetic field. The paramagnetic particles self-organize into a fixed quasi-regular array of columns. The column spacing can be tuned from submicrometer to about 100 μm by changing the concentration of the particles. They have shown that this kind of device can be used to achieve fast microfluidic separation of large DNA on a routine basis (77). One can refer to Chapter 11 for more details on this technique.

8.4.2 Peristaltic and Gear Colloidal Micropump

Terray et al. (24,78) have developed micropumps by using colloidal microspheres as the active flow control element. They remotely manipulate their colloids using optical trapping; the colloids could also be manipulated using electric or external magnetic fields. Remote activation techniques are really attractive in controlling microdevices: those noninvasive techniques do not require physical connection to macroscopic hardware, a major drawback in most of the other techniques used to control the flows.

By manipulating colloidal microspheres within customized channels, Terray et al. have created micrometer-scale fluid pumps and particulate valves. Their designs are based on positive-displacement pumping techniques that operate by imparting forward motion to individual plugs of fluid. For example, we describe one of their pumps consisting of six particles forming a chain along the channel. The chain of six

microspheres is activated by optical trapping that induces a smooth traveling-wave motion.

With this system, they can reach flow rate of about 1 nL/h. They have also used this process to create microfluidic valves capable of both restricting and directing flow of cells or colloids within microfluidic networks.

Liu et al. (79) have developed continuum-based methods to model those colloidal micropumps. They used the force coupling method. For example, they simulated a peristaltic micropump (following the design of Terray et al.) based on a chain of six colloidal microspheres in a channel. To produce a pumping effect, they applied a transverse traveling wave motion on the microspheres. They have studied the stability of the flexible chain of colloidal microspheres that provide the positive displacement that leads to net flow rate. They have also investigated the robustness of the peristaltic pump in the presence of a parasitic force. From the simulation results, a flow rate of 1 nL/h can be achieved (at an excitation frequency of about 10 Hz). However, achieving the higher flow rates in the higher frequency range that the simulation predicts may be challenging in the physical laboratory: the particles could tend to fall out of the trap, thus disrupting the pumping motion.

8.4.3 Ferrofluid Pumps and Valves

Hartshorne et al. (80) have developed pumps and valves based on the use of ferrofluids plugs that can be actuated by external magnets. Ferrofluids conform to the channel shape, potentially providing very good seals and responding to external localized magnetic forces, resulting in an easy actuation. These features offer advantages over other methods of fluid control. The ferrofluid used is a colloidal suspension of ferromagnetic colloids (the particle size is typically 10 nm) in a fluorocarbon liquid immiscible in water.

Ferrofluidic devices may have utility in microchip applications where more conventional fluid control, such as electroosmosis, is difficult. Similarly, devices may be used in complex on-chip processing as an adjunct to electroosmosis by providing channel-priming pumps or valves that can isolate specific areas of a chip to prevent leakage or contamination. These ferrofluidic systems can withstand pressure of 12 kPa.

8.4.4 Colloidal Microstirrer

Mixing of small volumes of liquid in microfluidics is difficult due to the fact that at low Reynolds number turbulent flow is suppressed. Nevertheless, the fast mixing of two fluids is important for the performance of integrated lab-on-a-chip devices. Tierno et al. (81) have achieved active colloidal microstirrers. They use for this paramagnetic colloidal particles dispersed in water and deposited above magnetic bubble domains of a uniaxial ferromagnetic garnet film. The solution is subjected to relatively small external rotating magnetic fields, and the speed of the rotating colloid can be precisely tuned up to angular frequencies of 250 s^{-1}. The stirrer's rotation is limited by the size of the magnetic bubble domain.

8.5 CONCLUSIONS

The combination of microfluidics and colloids presents many opportunities in the field of biotechnology. This coupling has already demonstrated successful applications, such as monodispersed colloid synthesis in a continuous mode, controlled *in situ* colloid crystallization, and easy separation of small volumes of colloids and cells. Microfluidic is also a very promising tool to understand precisely nanoparticles synthesis mechanism and to carry out combinatorial studies. The use of colloids can also be successfully applied to create advanced microfluidics functions. However, these reports are limited to proof-of-concepts and have not yet been really integrated or used into more complex devices with real applications. For example, reports on the production of nanoparticles only dealt with the demonstration of the syntheses but never demonstrated the possibility to directly use those nanoparticles.

We have presented in this chapter only a handful of examples as it is an emerging field. Nevertheless, we can expect that biotechnology will benefit even more from future advances in the fields of both microfluidic and colloids.

REFERENCES

1. Beebe DJ, Mensing GA, Wallor GM. Annu Rev Biomed Eng 2002;4:261.
2. Stone HA, Stroock AD, Ajdari A. Annu Rev Fluid Mech 2004;36:381.
3. Manz A, Effenhauser C, Bruggraf N, Harrison J, Seiler K, Fluri K. J Micromech Microeng 1994;4:257.
4. Tian H, Emrich CA, Scherer JR, Mathies RA, Andersen PS, Larsen LA, Christiansen M. Electrophoresis 2005;26:1834.
5. Hessel V, Lowe H. Microchemical engineering: Component, plant concepts user acceptance-Part I. Chem Eng Technol 2003;26:13.
6. Jahnisch K, Hessel V, Lowe H, Baerns M. Chemistry in microstructured reactors. Angew Chem Int Ed 2004;43:406.
7. Sanders GHW, Manz A. Trends Anal Chem 2000;19:364.
8. Tabeling P. Introduction to Microfluidics. Oxford University Press;2005.
9. Madou MJ. Fundamentals of Microfabrication. CRC Press;2002.
10. Narasimhan J, Papautsky I. J Micromech Microeng 2004;14:96–103.
11. Becker H, Gartner C.Electrophoresis, 2000;12:12–26.
12. Zhao X-M, Xia Y, Whitesides GM. Soft lithographic methods for nano-fabrication. J Mater Chem 1997;7:1069–1074.
13. Xia Y, Whitesides GM. Soft Lithography. Angew Chemie Int Ed 1998;37:550–557.
14. Shaikh KA, Ryu KS, Goluch ED, Nam J-M, Liu J, Thaxton CS, Chiesl TN, Barron AE, Lu Y, Mirkin CA, Liu C. A modular microfluidic architecture for integrated biochemical analysis. Proc Natl Acad Sci 2005;102:9745.
15. Luo C, Fu Q, Li H, Xu L, Sun M, Ouyang Q, Chen Y, Ji H. PDMS microfluidic device for optical detection of protein immunoassay using gold nanoparticles. Lab Chip 2005;5:726.

16. Lin FYH, Sabri M, Alirezaie J, Li D, Sherman PM. Development of a nanoparticle-labeled microfluidic immunoassay for detection of pathogenic microorganisms. Clinical Diag Lab Immunol 2005;12:418.
17. Desiree SG, Roberts JL, Hye YP, Jeremy D, Marc DP. Anal Chem 2003;75:5936.
18. Gu FX, Karnik R, Wang AZ, Alexis F, Levy-Nissebaum E, Hong S, Langer RS, Farokhzad OC. Targeted nanoparticles for cancer therapy. Nanotoday 2007;2:14–21
19. Couvreur P, Vauthier C. Nanotechnology: Intelligent design to treat complex disease. Pharm Res 2006;23:1417–1450.
20. Koo OM, Rubinstein I, Onyuksel H. Role of nanotechnology in targeted drug delivery and imaging: a concise review. Nanomed Nanotechnol Biol Med 2005;1:193–212.
21. Langer R.Nature 1998;392:5.
22. Langer R.Science 2001;293:58.
23. Farokhzad OC, Khademhosseini A, Jon S, Hermmann A, Cheng J, Chin C, Kiselyuk A, Teply B, Eng G, Langer R. Microfluidic system for studying the interaction of nanoparticles and microparticles with cells. Anal Chem 2005;77:5453.
24. Terray A, Oakey J, Marr DWM. Microfluidic control using colloidal devices. Science 2002;296:1841–1844.
25. Demello J, Demello A. Microscale reactors: nanoscale products. Lab Chip 2004;4:11N–15N.
26. Sounart TL, Safier PA, Voigt JA, Hoyt J, Tallant DR, Matzke CM, Michalske TA. Spatially-resolved analysis of nanoparticle nucleation and growth in a microfluidic reactor. Lab Chip 2007;7:908–915.
27. Nie Z, Li W, Seo M, Xu S, Kumacheva E. Janus and ternary particles generated by microfluidic synthesis: design, synthesis and sel-assembly. J Am Chem Soc 2006; 128:9408–9412.
28. Kim J-W, Larsen RJ, Weitz DA. Synthesis of nonspherical colloidal particles with anisotropic properties. J Am Chem Soc 2006;128:14374–14377.
29. Kreibig U, Vollmer M. Optical properties of metal clusters. Berlin: Springer; 1995.
30. Link S, El-Sayed MA. J Phys Chem B 1999;103:8410.
31. Edel JB, Fortt R, Demello JC, Demello AJ. Microfluidic routes to the controlled production of nanoparticles. Chem Commun 2002;1136–1137
32. Bessoth FG, deMello AJ, Manz A. Anal Commun 1999;36:213–215.
33. Nakamura H, Yamaguchi Y, Miyazaki M, Maeda H, Uehare M, Mulvaney P. Preparation of CdSe nanocrystals in a micro-flow-reactor. Chem Commun 2002;23:2844–2845.
34. Chan EM, Mathies RA, Alivisatos AP. Size controlled growth of CdSe nanocrystals in microfluidic reactors. Nano Letters 2003;3:199–201.
35. Yen BKH, Scott NE, Jensen KF, Bawendi MG. A continuous flow microcapillary reactor for the preparation of a size series of CdSe nanocrystals. Adv Mater 2003;15:1858–1862.
36. Nakamura H, Tashiro A, Yamaguchi Y, Miyazaki M, Watari T, Shimizu H, Maeda H. Application of a microfluidic reaction system for CdSe nanocrystal preparation: their growth kinetic and photoluminescent analysis. Lab Chip 2004;4:237–240.
37. Wang H, Li X, Uehara M, Yamaguchi Y, Nakamura H, Miyazaki M, Shimizu H, Maeda H. Continuous synthesis of CdSe-ZnS composite nanoparticles in a microfluidic reactor. Chem Commun 2004;48–49

38. Kohler JM, Csaki A, Reichert J, Moller R, Straube W, Fritzsche W. Sensor and Actuators B 2001;76:166.
39. Wang J, Grushka E, Polsky R, Pumera M. Anal Chem 2001;73:5625.
40. Shipway AN, Katz E, Willner I. Chem Phys Chem 2000;1:18.
41. Henglein A.Chem Mater 1998;10:444.
42. Wagner J, Kohler JM. Continuous Synthesis of Gold nanoparticles in a microreactor. Nano Letters 2005;5:685–691.
43. Wang H, Nakamura H, Uehara M, Miyazaki M, Maeda H. Preparation of titania particles utilizing the insoluble phase interface in a microchannel reactor. Chem Commun 2002;1462–1463.
44. Song H, Tice JD, Ismagilov RF. A microfluidic system for controlling reaction networks in time. Angew Chem Int Ed 2003;42:768.
45. Song H, Ismagilov RF. Millisecond kinetics on a microfluidic chip using nanoliters of reagents. J Am Chem Soc 2003;125:14613.
46. Zheng B, Roach LS, Ismagilov RF. Screening of protein crystallization conditions on a microfluidic chip using nanoliter-size droplets. J Am Chem Soc 2003;125:11170.
47. Jongen N, Donnet M, Bowen P, Lemaitre J, Hofmann H, Schenk R, Hofmann C, Aoun-Habbouche M, Guillemet-Fritsch S, Sarrias J, Rousset A, Viviani M, Buscaglia MT, Buscaglia V, Testino A, Herguijela JR. Development of a continuous segmented flow tubular reactor and the "scale-out" concept—In search of perfect powders. Chem Eng Technol 2003;26:303–305.
48. Gunther A, Kahn SA, Thalmann M, Trachsel F, Jensen KF. Transport and reaction in microscale segmented gas-liquid flow. Lab Chip 2004;4:278–286.
49. Stober W, Fink A, Bohn E. J Colloid Interface Sci 1968;26:62.
50. Shestopalov I, Tice JD, Ismagilov RF. Multi-step synthesis of nanoparticles performed on millisecond time scale in a microfluidic droplet-based system. Lab Chip 2004;4:316–321.
51. Jeong W, Kim J, Lee S, Mensing G, Beebe DJ. Lab Chip 2004;4:576–580.
52. Dendukuri D, Tsoi K, Hatton TA, Doyle PS. Langmuir 2005;21:2113–2116.
53. Kim J-W, Utada AS, Fernandez-Nieves A, Hu Z, Weitz DA. Fabrication of monodisperse gel shells and functional microgels in microfluidic devices. Angew Chem Int Ed 2007;46:1819–1822.
54. Xu S, Nie Z, Seo M, Lewis P, Kumacheva E, Stone HA, Garstecki P, Weibel DB, Gitlin I, Whitesides GM. Generation of monodisperse particles by using microfluidics: control over size shape and composition. Angew Chem Int Ed 2005;44:724–728.
55. Nie Z, Xu S, Seo M, Lewis PC, Kumacheva E. Polymer particles with various shapes and morphologies produced in continuous microfluidic reactors. J Am Chem Soc 2005;127:8058–8063.
56. Yang SM, Ozin GA. Opal chips: vectorial growth of colloidal crystal patterns inside silicon wafers. Chem commun 2000;2507–2508.
57. Kuo C-J, Lam KY, Vengallatore YPS. Colloidal self-assembly on internal surfaces of partially sealed microchannels. J Micromech Microeng 2006;16:1667–1673.
58. Yi G-R, Jeon S-Y, Thorsen T, Manoharan VN, Quake SR, Pine DJ, Yang S-M. Generation of uniform photonic balls by template-assisted colloidal crystallisation. Synth Met 2003;139:803–806.

59. Yi G-R, Thorsen T, Manoharau VN, Hwong M-J, Jeon S-J, Pine DJ, Quake SR, Yong S-M. Generation of uniform colloidal assemblies in soft microfluidic devices. Adv Mater 2003;15:1300–1304.
60. Shiu J-Y, Kuo C-W, Chen P. Actively controlled self-assembly of colloidal crystals in microfluidic networks by electrocapillary forces. J Am Chem Soc 2004;126:8096–8097.
61. Shiu J-Y, Chen P. Active patterning using an addressable microfluidic network. Adv Mater 2005;17:1866–1869.
62. Kumacheva E, Garstecki P, Wu H, Whitesides GM. Two-dimmensional colloid crystals obtained by coupling of flow and confinement. Phys Rev Lett 2003;91:128301.
63. Jahn A, Vreeland WN, Gaitan M, Locascio LE. Controlled vesicle self-assembly in microfluidic channels with hydrodynamic focusing. J Am Chem Soc 2004;126:2674.
64. Lim DSW, Shelby JP, Kuo JS, Chiu DT. Dynamic formation of ring-shaped patterns of colloidal particles in microfluidic systems. Appl Phys Lett 2003;83:1145–1147.
65. Lee S-K, Yi G-R, Yang S-M. High-speed fabrication of patterned colloidal structures in centrifugal microfluidic chips. Lab Chip 2006;6:1171–1177.
66. Lee H, Liu Y, Ham D, Westervelt RM. Integrated cell manipulation system—CMOS/microfluidic hybrid. Lab Chip 2007;7:331–337.
67. Fiedler S, Schnelle T, Fuhr G. Dielectrophoretic sorting of particles and cells in a microsystems. Anal Chem 1998;70:1909–1915.
68. Hu XY BP, Qian JR, Meinhart CD, Daugherty PS, Soh HT. Marker-specific sorting of rare cells using dielectropohoresis .2005;102:15757–15761.
69. Bhatt KH, Grego S, Velev OD. An AC electrokinetic technique for collection and concentration of particles and cells on patterned electrodes. Langmuir 2005;21:6603–6612.
70. Fu SC, Scherer A., Arnold FH, Quake SR. A microfabricated fluorescence-activated cell sorter. Nat Biotechnol 1999;17:1109–1111.
71. Fu AY, Chou HP, Spence C, Arnold FH, Quake SR. An integrated microfabricated cell sorter. Anal Chem 2002;74:2451–2457.
72. Wolff A, Perch-Nielsen IR, Larsen UD, Friis P, Goranovic G, Poulsen CR, Kutter JP, Telleman P. Integrated advaced functionality in a microfabricated high-throughput fluorescent activated cell sorter. Lab Chip 2003;3:22–27.
73. Wang Mm TE, RaymondDE, Yang JM, Zhanh HC, Hagen N, Dees B, Mercer EM, Forster AH, Kariv I, March PJ, Butler WF. Microfluiding sorting of mamalian cells by optical forces switching. Nat Biotechnol 2005;23:83–87.
74. Macdonald MP, Spalding GC, Dholakia K. Microfluidic sorting in an optical lattice. Nature 2003;426:421–424.
75. Takagi J, Yamada M, Yasuda M, Seki M. Continuous particle separation in a microchannel having asymmetrically arranged multiple branches. Lab Chip 2005;5:778–784.
76. Doyle PS, Bancaud JBA, Viovy J-L. Self-assembled magnetic matrices for DNA separation chips. Science 2002;295:2237.
77. Minc CFN, Dorfman KD, Bancaud A, Gosse C, Goubault C, Viovy J-L. Quantitative microfluidic separation of DNA in self-assembled magnetic matrixes. Anal Chem 2004;76:3370–3776.
78. Terray A, Oakey J, Marr DWM. Fabrication of linear colloidal structures for microfluidic applications. Appl Phys Lett 2002;81:1155–1557.

79. Liu D, Maxey M, Karniadakis GE. Modeling and optimization of colloidal micro-pumps. J Micromech Microeng 2004;14:567–675.
80. Hartshorne H, Backhouse CJ, Lee WE. Ferrofluid-based microchip pump and valve. Sens Actuators B 2004;99:592–600.
81. Tierno P, Johansen TH, Fischer TM. Magnetically driven colloidal microstirrer. J Phys Chem B 2007;111:3077–3080.
82. Wagner J, Kirner T, Mayer G, Albert J, Kohler JM. Generation of metal nanoparticles in a microchannel reactor. Chem Eng J 2004;101:251–260.
83. Lin XZ, Terepka AD, Yang H. Synthesis of silver nanoparticles in a continuous flow tubular microreactor. Nano Lett 2004;4:2227–2232.
84. Boleininger J, Kurz A, Reuss V, Sonnichsen C. Microfluidic continuous flow synthesis of rod-shaped gold and silver nanocrystals. Phys Chem Chem Phys 2006;8:3824–3827.
85. Song Y, Modrow H, Henry LL, Saw CK, Doomes EE, Palshin V, Hormes J, Kumar CSSR. Microfluidic synthesis of cobalt nanoparticles. Chem Mater 2006;18:2817–2827.
86. Dendukuri D, Tsoi K, Hatton TA, Doyle PS. Controlled synthesis of nonspherical microparticles using microfluidics. Langmuir 2005;21:2113–2116.
87. Chan EM, Alivisatos AP, Mathies RA. High-Temperature microfluidic synthesis of CdSe nanocrystals in nanoliter droplets. J Am Chem Soc 2005;127:13854–13861.
88. Hung L-H, Choi KM, Tseng W-Y, Tan Y-C, Shea KJ, Lee AP. Alternating droplet generation and controlled dynamic droplet fusion in microfluidic devices for CdS nanoparticle synthesis. Lab Chip 2006;6:174–178.
89. Khan SA, Gunther A, Schmidt MA, Jensen KF. Microfluidic synthesis of colloidal silica. Langmuir 2004;20:8604–8611.

CHAPTER 9

Gas Sensors Based on Ultrathin Films of Conducting Polymers and Nanocomposites

MANOJ K. RAM, ÖZLEM YAVUZ, and MATT ALDISSI
Fractal Systems Inc, 200 9th Avenue N., Suite 100, Safety Harbor, FL 34695, USA

9.1 INTRODUCTION

Much of the welfare of modern societies relies on the combustion of fossil fuels. To a greater or lesser extent, all energy production processes are associated with the generation of toxic by-products such as CO, NO_x and aromatic hydrocarbons (1). A significant part of CO and NO_x emission originates from the exhaust of motor vehicles due to their increasing number each year. The interaction of CO and NO_x with sunlight tends to produce O_3, which, due to its strongly oxidizing behavior, is believed to be harmful to plants and to the respiratory system of human beings (2). In order to be useful as an air monitoring system, a sensor, device, and/or technique should be able to detect the gases (CO, NO_x, CO_2) at environmentally relevant concentrations (3,4). The United States Environmental Protection Agency (EPA) and the European Union (EU) have set Ambient Air Quality Standards for such pollutants, which are listed in Table 9.1 (5).

Metal oxide-based gas sensors are known to be widely used for such combustion products. Their poor selectivity is typically bypassed partially by forming arrays of sensors distinguished by their cross sensitivity (6). The disadvantages include baseline drifts upon interaction with poisoning species such as SO_2 and NO_2 and the dual response of oxides used in the automotive field, particularly SnO_2, to oxidizing (NO_2) or reducing (CO) gases (7,8). Doping with metals in SnO_2 was shown to significantly increase sensitivity (9,10). Such gas sensors, however, still lack selectivity and sensitivity at ambient humidity, which increases its conductivity. Conducting polymers (polypyrrole [PPy], polythiophenes, and polyaniline (PAn)) have shown very

Colloidal Nanoparticles in Biotechnology, Edited by Abdelhamid Elaissari
Copyright © 2008 John Wiley & Sons, Inc.

TABLE 9.1 Standard Set for Maintaining the Quality of Air.

Pollutant	EPA standard value	EU standard attention level (ppm)
Carbon monoxide (CO)		
8-h average	9 ppm (10 mg/m^3)	12.5
1-h average	35 ppm (40 mg/m^3)	
Nitrogen dioxide (NO_2)		
Annual arithmetic mean	0.053 ppm (100 μg/m^3)	0.1
Ozone (O_3)		
1-h average	0.12 ppm (235 μg/m^3)	0.09
8-h average	0.08 ppm (157 μg/m^3)	
Sulfur dioxide (SO_2)		
Annual arithmetic mean	0.03 ppm (80 μg/m^3)	
24-h average	0.14 ppm (365 μg/m^3)	
3-h average	0.50 ppm (1300 μg/m^3)	

promising results for application in gas sensors and are currently used in electronic nose systems (11). There has also been considerable interest in the use of conducting polymers, particularly, in the form of thin films, blends, or composites as sensors for airborne volatiles such as alcohols, ethers, NH_3, NO_2, and CO (11). Films of polythiophene were successfully used for the detection of ppb levels of hydrazine gases (12). Langmuir–Blodgett (LB) films of PAn were used to measure NO_x and CO at low concentrations (13). Electrochemically synthesized conducting polymers, such as PPy and poly-3-methylthiophene, doped with copper and palladium accurately detected CO gas (14). PAn is unique among the class of electrically conducting polymers in that its electrical properties can be reversibly controlled by changing the oxidation state through protonation of amine nitrogen of the main chain (15). Electrical and electrochemical characterization of LB PAn films has shown good reproducibility in sensing characteristics (16). LB films of poly(*ortho*-anisidine) were successfully used for sensing of protonic acids (HCl, H_2SO_4) in water at a sensitivity of less than 0.1 ppm (17). The sensing, ageing, and mechanical characteristics of the conducting polymer films have been improved by composite fabrication (18,19), similarly to what was observed in the case of inorganic composites that resulted in better exhaust gas detection accuracy (20,21).

In this work, we describe the fabrication and characterization of gas sensors based on highly organized ultrathin films of conducting polymers and their nanocomposites with inorganic oxides. The films were characterized using conductivity, electrochemical impedance spectroscopy (EIS), UV-visible spectra, electrochemistry, and AFM techniques. The effect of temperature and SO_2 gas sensing on film properties as well as gas specificity are also discussed.

9.2 EXPERIMENTAL

9.2.1 Substrate Activation

The substrate preparation for ultrathin film deposition is an important task for obtaining the desired number of layers and thickness of the polymer or nanocomposite films, which were prepared according to published work (22,23). The first layer of the activated surface is deposited using a sulfonated polystyrene (PSS, $M_w = 70{,}000$) solution for 15 min, prepared by using 2 mg/mL of PSS in water, which provided the charges necessary to adsorb the first layer of the polycation. In some instances, poly (diallyldiamine) (PDDA) was used as a polycation when a second activation layer was needed. As an example of polymer film deposition, the active solution contained 0.026 M aniline monomer, 0.012 M ammonium perdisulphate, and 0.026 M para-toluenesulfonic acid (*p*-TSA) for PAn films; or 0.006 M $FeCl_3$, 0.026 M *p*-TSA, and 0.02 M pyrrole monomer for PPy films. The solution was stirred for 15 min after the addition of the monomer and filtered, and then used for the deposition of the polymer or the polymer nanocomposite films.

9.2.2 Fabrication of Conducting Polymer-SnO_2 Composite Films

The SnO_2 particles were prepared using a standard procedure. $SnCl_4$ was dissolved in 1 M HCl and then added to 400 mL of deionized water. Aqueous ammonia was added dropwise to this solution to obtain a dispersion of fine SnO_2 particles. The solution was centrifuged to remove excess ammonia and unreacted $SnCl_4$. The pH of the dispersion medium was adjusted by addition of water, followed by the addition of appropriate amounts of aniline monomer and ammonium persulfate ($(NH_4)_2S_2O_8$) oxidant to start the polymerization of aniline in the aqueous medium. The PSS-treated substrate was then introduced in the resulting solution for film deposition.

9.2.3 Fabrication of Conducting Polymer TiO_2 Composite Films

The colloidal TiO_2 was prepared using tetra-2-propoxy titanate obtained by the dissolution of $TiCl_4$ in 2-propanol. An amount of 0.5 mL of this 8.65% solution was injected in 5 mL of a 0.05 M aqueous $HClO_4$ solution (24). The resulting solution was then bubbled with nitrogen for a few hours until a transparent solution was obtained. This TiO_2 sol was stabilized by mixing with 5 mL of 0.2 wt% aqueous solution of poly (vinyl alcohol). The TiO_2-conducting polymer nanocomposite films were fabricated by *in situ* self-assembly. PAn–TiO_2 films were fabricated on a PSS-treated substrates. The chemical oxidative polymerization of aniline in the presence of colloidal TiO_2 was carried out in HCl at pH 2 using drop-by-drop addition of 0.5 M $(NH_4)_2S_2O_8$. The pH of the reaction mixture remained constant throughout the reaction. The deposition of alternating PSS and nanocomposite layers was repeated as many times as needed to get the desired thickness. The same procedure was used for fabrication of PAn–SnO_2 multilayered films.

9.3 RESULTS AND DISCUSSION

9.3.1 Effect of Surface Treatment

Conductivity of the self-assembled nanocomposite films was measured using a two-probe technique. The PSS-treated surface (protonated) shows better conductivity than the nontreated one (hydrophilic), indicating that protonation leads to better coatings. This effect is demonstrated in the results summarized in Table 9.2.

TABLE 9.2 Optical Absorption Bands for the Various Polymers and Treatments.

		UV-visible bands (nm)
Self-assembled films of polyaniline		
	HCl-doped	341, 424, 809–880
	NO_2-treated	309, 709
	Undoped	632, 330
Self-assembled films of PPy		
	As-made	442, 898
	NO_2-treated	455, 1048
Self-assembled films of regioregular polyhexylthiophene		
	As-made	523, 553, 608
	NO_2-treated	513, 544, 598
Self-assembled films of chemically synthesized polyhexylthiophene		
	As-made	520, 561, 600
	NO_2-treated	460, 535, 350, 407
Hexylthiophene and ethylene-dioxy-thiophene copolymer		
	As-made	478, 510, 601
	NO_2-treated	412, 319

9.3.2 Optical Characterizations

Optical spectroscopy of conducting polymers is a well-known technique for characterization of the conducting states that correspond to the absorption bands of inter- and/or intragap states. The UV-visible absorption spectra of PAn/PSS with bands at 340, 425, and 860 nm are shown in Fig. 9.1 (plot 1). Fig. 9.1 (plot 2) depicts the UV-visible spectra of PAn–SnO_2 composite self-assembled films deposited on a PSS/glass substrate. Since PSS does not absorb in the spectral region of concern, the absorption is due to nanocomposite only. Similarly to the PAn film, although it is shifted, this spectrum has three distinct absorption bands: 320, 425, and 900 nm. Fig. 9.1 (plot 3) shows the optical spectrum of self-assembled PAn–TiO_2 film, which exhibits two absorption bands at 340, 425, and 800–850 nm for the film made at a pH of 2.8.

Figure 9.2a depicts the UV-visible spectra of PDDA/PAn-SO_3 deposited on a PSS/glass slide as a function of the number of bilayers. As PDDA or PSS does not

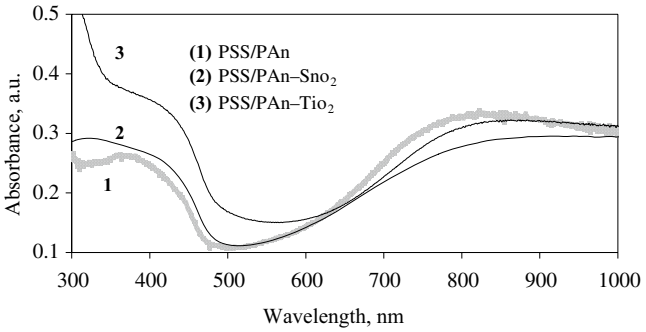

FIGURE 9.1 UV-visible spectra of *in situ* self-assembled conductive films

absorb in the spectral region of concern, absorption can only be due to the sulfonated PAn. A typical absorption spectrum has three distinct absorption bands at 340, 383, and 477 nm. The 340 nm band is attributed to the π–π^* transition. The 477 nm band is due to the polaron state, with the 383 nm band being that of an intermediate state. The deposited bilayer films were first undoped using 0.1 M NaOH solution and redoped using 1 M HCl. The deposition of bilayers was monitored by the change in absorption magnitude at 477 nm. The linear variation in absorbance versus the number of bilayers indicates a regular deposition of LBL films (Fig. 9.2b). Similar results were obtained for PPy, polyhexylthiophene, and other polymers as well as their nanocomposites with SnO_2 and TiO_2. The UV-visible absorption spectra of PPy films deposited on PSS surface at different deposition times exhibited typical bands of the doped polymer at 466 and 800–940 nm. A single layer typically results in films with a thickness in the range of 60–200 Å. The *in situ* fabrication of PPy films is a dynamic process where the film thickness initially increases linearly with time, and then gradually departs from linearity after 60 min. LBL films of both poly(hexylthiophene) (PHTh) forms (regioregular and regiorandom) were characterized as well. A redshift of the π–π^* transition is observed for the regioregular form relative to the regiorandom one (526 and 518 nm, respectively), and the appearance of more distinct shoulders at 555 and 606 nm suggests that the regioregular form has a more rod-like conformation with extended π-conjugation in the condensed phase, as reported earlier in the literature (25).

9.3.3 Annealing Effect on the Conductive Films

Figure 9.3 shows the UV-visible absorption of PAn–SnO_2 self-assembled films treated with NH_4OH and annealed at different temperatures from 100°C to 800°C. Unlike the surface topography or morphology of the film, the optical absorption spectra (except for the absorption intensity) seem unchanged, which reflects the stability of the electronic structure of the material. The PAn–SnO_2 film deposited on glass (10 min deposition) was initially treated with aqueous ammonia to yield the

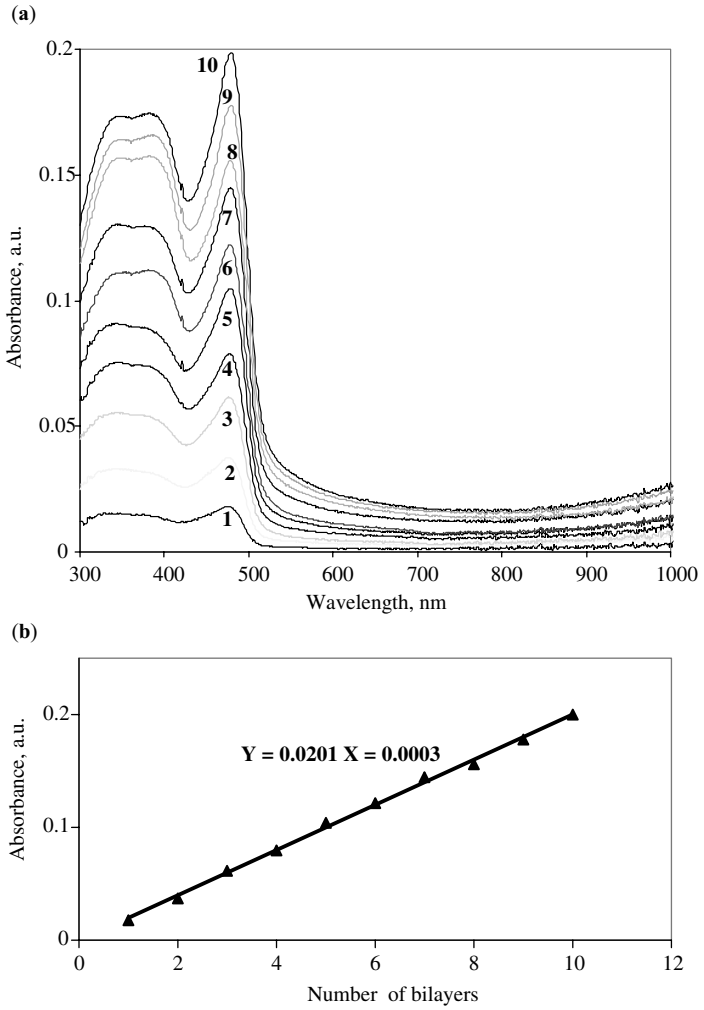

FIGURE 9.2 (**a**) UV-visible spectra of PAn-SO_3/PDDA LBL films (1–10 layers) and (**b**) absorption maximum at 477 nm versus numbers of layers for PAn-SO_3/PDDA LBL films

emeraldine base and then annealed at various temperatures up to 800°C for 2 h at each temperature. On the basis of the optical spectra of the material at the different stages, the material exhibits an excellent stability up to 200°C. Plot 1 shows characteristic absorption bands of PAn that are redshifted (320, 385, and 850 nm) due to the interaction with the oxide nanoparticles. Treatment with ammonia yields characteristic bands of the emeraldine base (plot 2). The film treated at 100–500°C (plots 3–5) shows a 600 nm band (n–π^*) with a reduced intensity due to the loss of water and restructuring. The film annealed at 800°C (plot 6) shows a change in

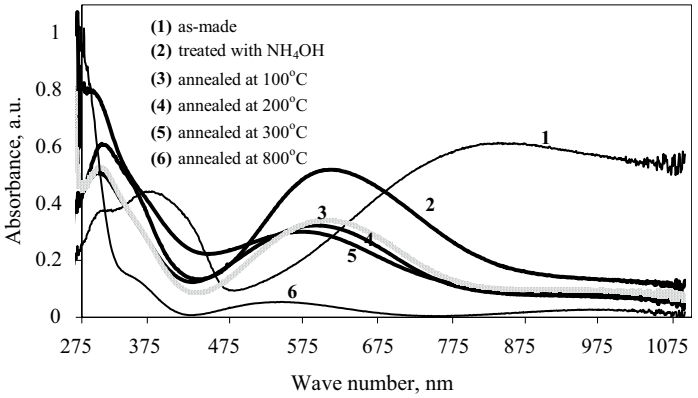

FIGURE 9.3 UV-visible absorption of PAn-SnO_2 before and after annealing

absorption characteristics due to the degradation of PAn and is characteristic of the oxide only. Also, at this temperature, SnO_2 nanoparticles undergo an ordering process. PAn–TiO_2 films exhibit a similar behavior.

9.3.4 Atomic Force Microscopy

The surface morphology of self-assembled films treated at different temperatures was examined using atomic force microscopy (AFM) (in tapping mode in air at a constant contact force) because it is important that the film morphology remains intact at elevated temperatures. A granular structure is typically obtained with such nanocomposites, as shown in Fig. 9.4 for PAn–SnO_2: initial (plot a) annealed at 100°C for 20 min (plot b). The granular structure of the film is maintained up to 250°C. However, a partial deformation of the granular structure is observed at higher temperatures, probably due to the restructuring of the film upon removal of intrinsic water and particle fusing. The annealed PAn–SnO_2 particles are aggregated into clusters in the range of several hundred nanometers. As with optical absorption, annealing results in the removal of traces of moisture and some restructuring of the material at 500°C (plot c). Annealing at 800°C shows an ordered structure of SnO_2 particles (plot d). Similar results were obtained for PAn–TiO_2.

9.3.5 Cyclic Voltammetry

Figuere 9.5 shows the cyclic voltammograms of PAn–TiO_2 film in 0.1 M HCl with three main redox couples at 0.14, 0.48, and 0.63 V. The first peak is due to the surface electron transfer, which has almost identical characteristics as that of PAn (0.15 V). However, it is slightly more anodic than that of PAn, and this behavior suggests that the incorporation of TiO_2 into PAn does not decrease its conductivity,

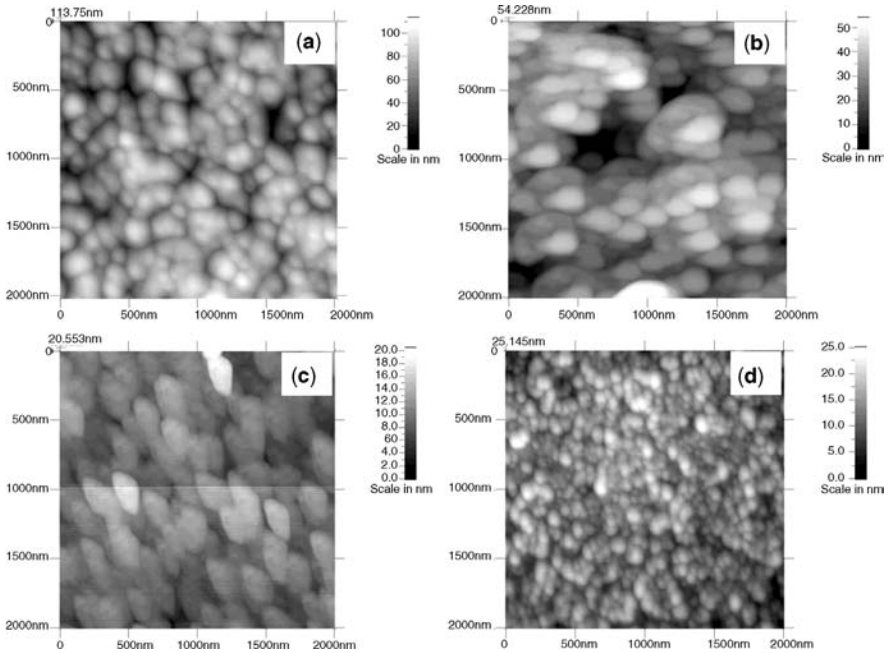

FIGURE 9.4 AFM of self-assembled PAn–SnO_2 (**a**) as-made (**b**) annealed at 100°C (**c**) annealed at 500°C and (**d**) annealed at 800°C

indicating the formation of a high conductivity composite. Interestingly, the second peak, which is due to the quinoid structure in PAn, has a higher potential than that observed for PAn (0.48 V versus SCE). The third peak due to protonation is observed at 0.64 V.

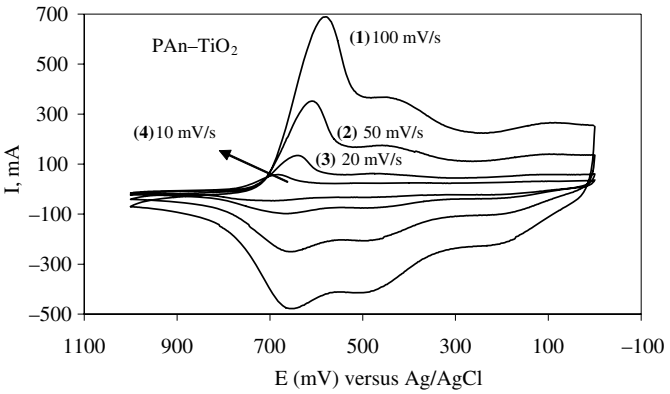

FIGURE 9.5 CV of PAn–TiO_2 films as a functional of scan rate

9.3.6 Effect of Gas Exposure on the Optical Characteristics of Films

We wanted to first examine the conducting polymer films to establish the optical absorption characteristics as a baseline for comparison with the nanocomposites. Figure 9.6a shows the optical spectra of PSS/PAn self-assembled films on glass as prepared and after *ex situ* gas treatment. As-prepared films are doped with HCl and exhibit characteristic bands at 340, 424, and 810–880 nm that are attributed to the π–π^* transition, polaron, and bipolaron (doped) states, respectively, as mentioned earlier. Treatment with NO_2 gas, for example, results in a blue shift of the π–π^* transition (309 nm) and the emergence of a new peak at 710 nm as a result of the formation of an intermediate state between the emeraldine salt (doped, conductive) and the emeraldine base (reduced, nonconductive). Dedoping the films by dipping in 1 M NaOH solution for 5 min results in an absorption peak at 330 nm and a broad band at 630 nm, indicating the formation of the emeraldine base form of PAn with its characteristic blue color. Figure 9.6b shows the optical absorption of PPy films deposited on PSS surface for 1 h. The as-prepared film exhibits the 440 nm π–π^* transition band and a broad free-carrier-tail band at 900 nm, indicating a high degree of doping. No significant shift is observed upon treatment with NO_2 gas, indicating that no structural changes takes place and thus reversibility (gas desorption) can be easily attained when desired. Figure 9.6c shows the optical spectra of regioregular

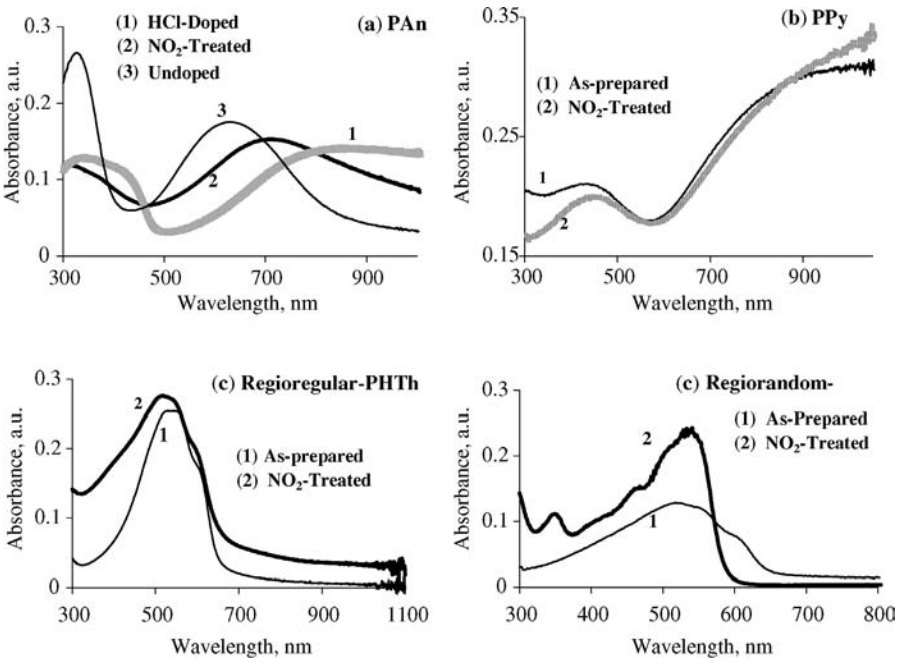

FIGURE 9.6 UV-visible spectra of self-assembled conducting polymers: (**a**) PAn, (**b**) PPy, (**c**) regioregular PHTh, and (**d**) regiorandom PHTh

TABLE 9.3 Resistance of Self-Assembled PAn–SnO_2 Films on Protonated and Nonprotonated Substrates.

Nonpropotaned substrate		Protonated substrate	
Polymerization time, min	Resistance, kΩ	Polymerization time, min	Resistance, kΩ
15	100	15	62.9
30	20.7	30	20.3
40	40.7	45	40.7
60	47.2	60	16.5
90	28.6	90	10.0

poly(hexylthiophene) (PHTh) layered films (30 layers). The observed π–π^* transition at 523 nm and the two more distinct shoulders at 555 and 606 nm are characteristics of the rod-like conformation with extended π-conjugation in the condensed phase. Similar to PPy, no change in the absorption spectra has been observed when exposed to NO_2 gas. Absorption bands at 520, 560, and 600 nm observed for the regiorandom PHTh layered films (Fig. 9.6d) are basically similar to the regioregular equivalent. However, exposure to NO_2 results in several bands at 350, 460, 535, and 407 nm. The 350 nm band indicates a structural change in the polymer. Similar to the regiorandom polymer, the PEDT–PHTh copolymer undergoes a structural change when treated with NO_2, as evidenced by the formation of bands at 320 and 410 nm. Table 9.3 shows the bands of ultrathin films as a function of NO_2 gas treatment.

9.3.7 Effect of Exposure to Gas on Morphology

Morphology of multilayered films of the various polymers has been investigated using AFM at the nanometer level. The morphology of self-assembled films on a PSS surface for 1 h is shown in Fig. 9.7. AFM images of PPy (Fig. 9.7a) reveal a granular surface topography with an average size of 70 nm and a surface roughness of 17 nm. No significant change occurs in particle size upon exposure to NO_2, except for a slight decrease in surface roughness to 15 nm due to slight doping of the polymer. Self-assembled PAn films on a PSS surface (35 min) exhibit a morphology with particles in the range of 30–100 nm (Fig. 9.7b). The particle size in PSS/PAn is known to increase with the number of layers. The change in particle size observed in this polymer due to gas treatment is more significant than that observed in other polymers without necessarily changing the surface roughness (45 nm before and after gas treatment). This correlates with the optical absorption results that a reaction (doping/undoping) takes place. The surface morphology of 30-layer films of the regioregular PHTh had particles in the size range of 50–100 nm (independent of the number of layers) with no change after exposure to gases, as shown in Fig. 9.7c.

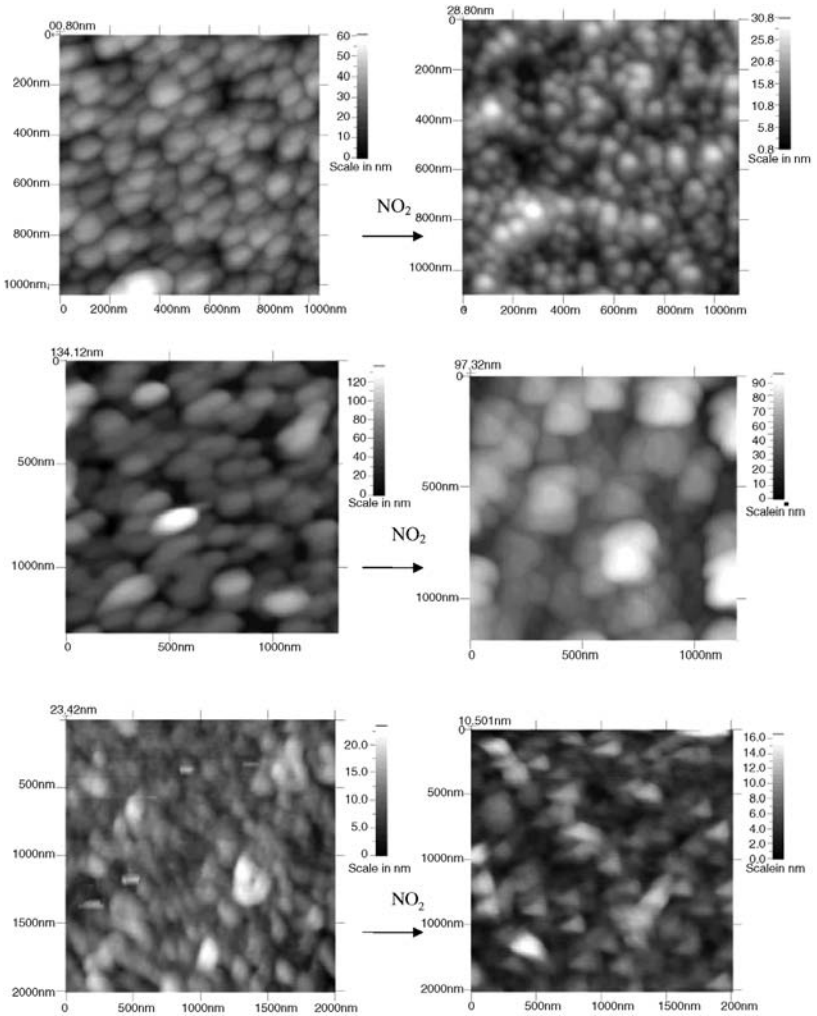

FIGURE 9.7 AFM of self-assembled (top) PPy, (middle) PAn, and (bottom) regioregular PHTh films before and after exposure to NO_2

9.3.8 Gas Detection via Resistance and Impedance Measurements

The sensor element consists of interdigitated electrodes (50 μm spacing, 50 μm wide, and 40 μm thick) made of platinum-coated quartz. The gas sensing system consisted of a Parr pressure chamber equipped with the necessary valves to achieve vacuum, introduce gases, and perform *in situ* four-probe conductivity measurements at room temperature. The film is connected to a digital multimeter or an impedance analyser, with the change in resistance being recorded as gas pressure is varied. Real-time resistance changes are monitored using a computer-interfaced electrometer upon exposure to gas.

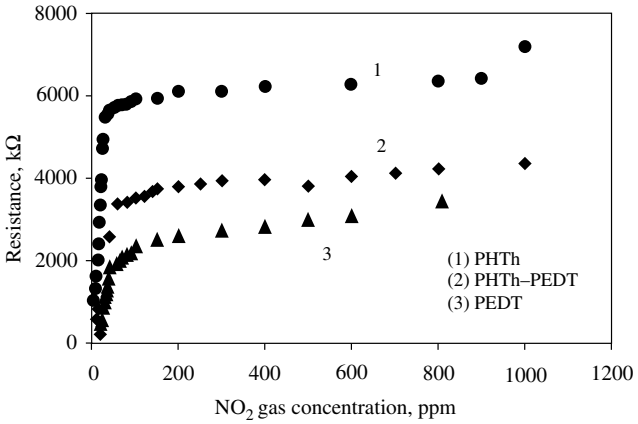

FIGURE 9.8 Resistance change versus NO_2 gas concentration for various materials with a similar thickness

Resistance values obtained for three different polymers (regioregular PHTh, PEDT, PHTh–PEDT copolymer) as a function of NO_2 concentration are shown in Fig. 9.8. The resistance decreases continuously and exponentially upon exposure to NO_2, indicating that the gas acts as a dopant for the polymer. The change in resistance was dramatic at all concentrations, which made detection of small quantities easy with a good resolution. It is worth noting that the response was instantaneous due to the thin nature of films, which has an excellent reproducibility.

We wanted to study the effect of number of bilayers on gas sensing. Figure 9.9 shows the results obtained for four films of PHTh with different layer thicknesses. All films behave similarly as a function of gas concentration, with a semidoping effect that consists of one gas molecule per thiophene repeat unit. The two-layer films have a higher resistance than that of thicker ones. However, the thin films are better for low

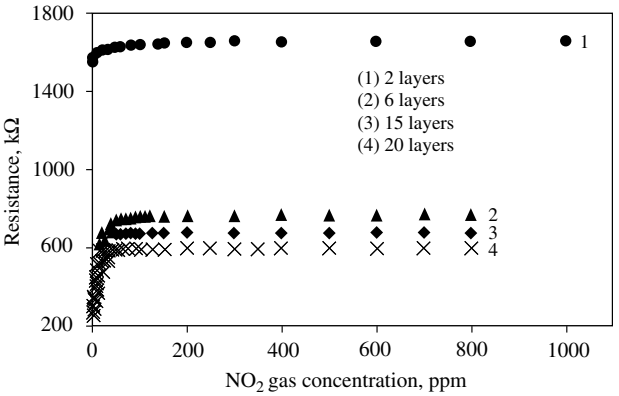

FIGURE 9.9 Resistance change versus NO_2 gas concentration and number of layers of PHTh

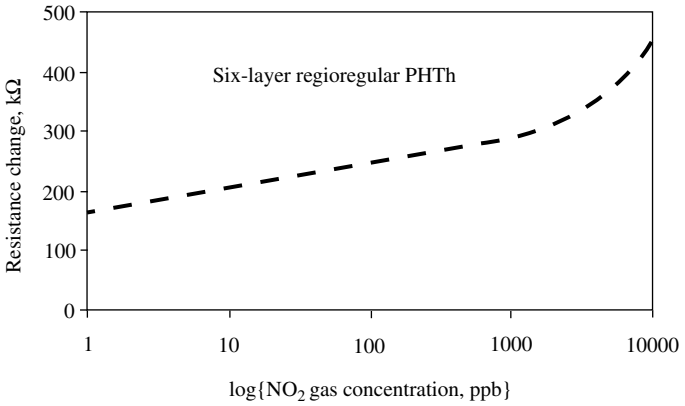

FIGURE 9.10 Resistance change at ppb levels of NO_2 gas using six-layer PHTh films

gas (ppb) detection levels. Figure 9.10 shows the lower end of the concentration range for the six-layer film with an excellent sensitivity in the ppb range.

Self-assembled PPy films exhibited a decrease in resistance when exposed to NO_2, however, with less sensitivity. The polymer is highly conductive, and therefore further doping by the gas results in a weak effect on resistance. In the case of PAn, a large change in resistance was observed (from few kΩ to 110 MΩ) upon exposure to 100–200 ppm of NO_2, with a concomitant structural and color change to the emeraldine base. Evacuation of the gas does not lead to a change in resistance unless heat (50–60°C) is applied to the sample. Therefore, we concentrated mostly on the thiophene-based materials for NO_2 gas measurements. SnO_2-based nanocomposites films with poly(ethylene-dioxythiophene) (PEDT) and PHTh (Figs. 9.11 and 9.12, respectively) exhibited good detection characteristics, with the former having better

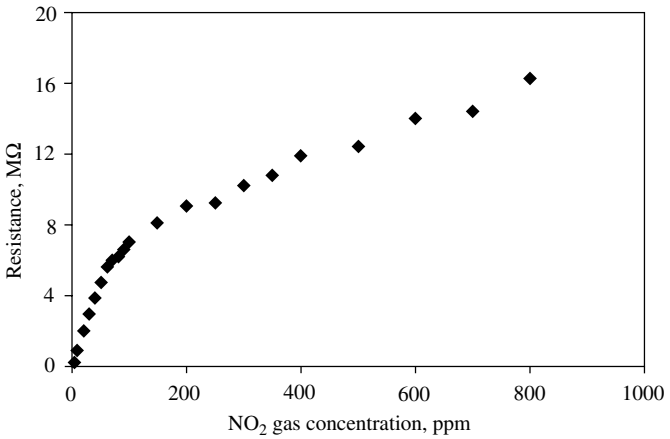

FIGURE 9.11 Resistance change of PEDT-SnO_2 nanocomposite versus NO_2 gas concentration

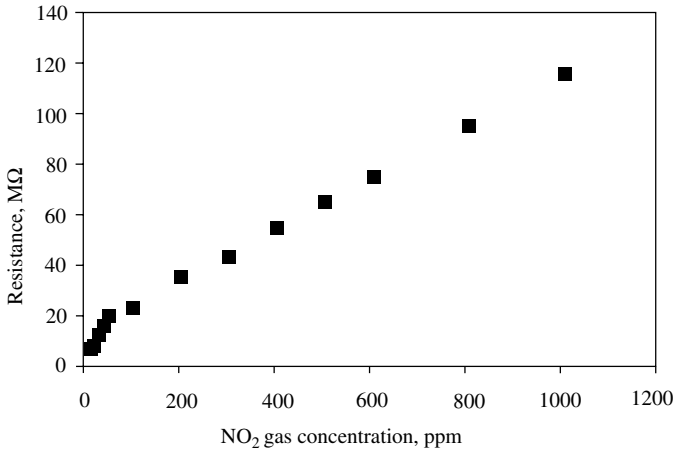

FIGURE 9.12 Resistance change of PHTh–SnO_2 nanocomposite versus NO_2 gas concentration

sensitivity. Furthermore, detection occurred instantaneously by the composite as opposed to a delayed response with the oxide alone. The resistance results for NO_2 gas are tabulated in Tables 9.4 and 9.5.

The change in resistance (ΔR) obtained for three different types of PAn–metal oxide films in the case of PAn-CO films are shown in Fig. 9.13a and b. $\Delta R = R_0 - R_x$, where R_0 is the initial resistance and R_x the resistance at gas concentration x. The CO gas acts as an oxidant, and exposure results in a decrease in the resistance value (in kΩ range) as CO concentration increases (Fig. 9.13a). This is probably because interaction between the polymer and the SnO_2 nanoparticles results in the reduced form of PAn, which becomes easily oxidizable. It is important to note that reversibility of gas adsorption can easily take place under vacuum at room temperature for few minutes. Similar results were obtained with TiO_2 (Fig. 9.13b).

TABLE 9.4 DC Resistance before and after NO_2 for Various Polymers and Number of Layers.

Polymer	Number of layers	R; MΩ (before NO_2)	R; MΩ (after NO_2)
PHTh	1	24.43	8.08
PHTh	6	0.34	0.68
PHTh	15	1.70	3.08
PHTh	24	99.2	0.15
PHTh	143	67.3	0.19
PEDT	—	9.61	3.67
PAn		2.90	>100
PEDT-PHTh	150	5.91	2.42
PPy	—	0.001	0.002
PAn	—	0.028	2.78

TABLE 9.5 Comparison between Different Materials Tested for the Various Gases.

Structure	NO_2, ppm	Comments
$SnTiO_2$ thin films (at 400°C)	1.7	Thin films are more sensitive than thick films
SnO_2 (crystalline, RF sputtered) (300°C)	5000	Highly selective but effected due to influence of water
SnO_2-reactive evaporated, measured at 450°C	0.92	Poor selectivity and stability
Pd-doped SnO_2	2.5	Stability
WO_3 thin films at 300°C	2.6	1–2 mins response time
Pt–Pd/Si/Al	6	No response with NO detection
Pt/SnO_2/n-Si/p-Si/Al	1000	The barrier height change or conductivity change of SnO_2
CoO/SiO_2 nanocomposite		Selective to NO
Our work	<100 ppb	<1 s response time, material-based selectivity

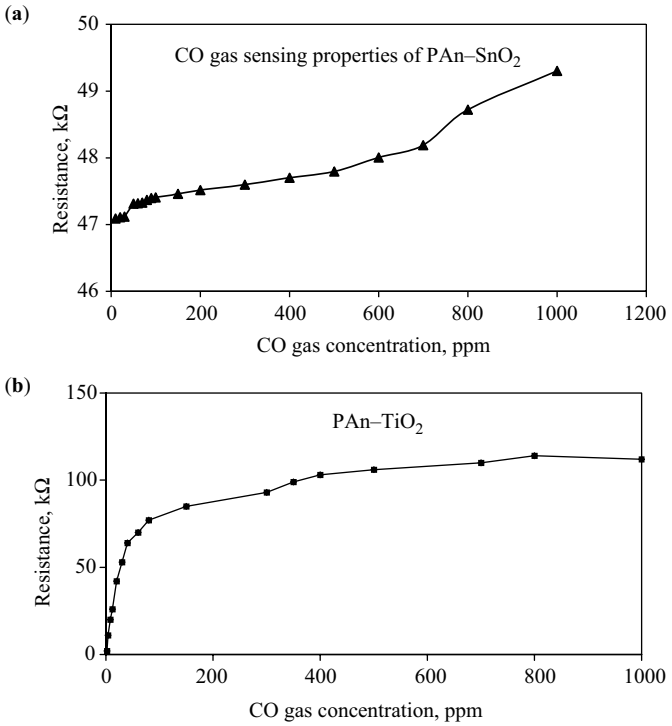

FIGURE 9.13 Resistance change of self-assembled PAn–SnO_2 (**a**) and PAn–TiO_2 (**b**) films versus CO gas concentration

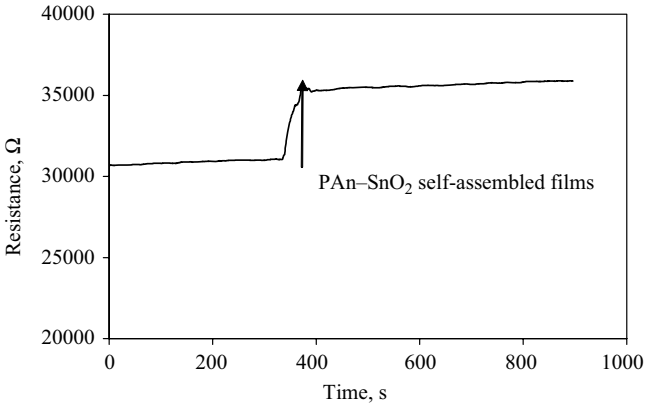

FIGURE 9.14 Response curve with SO_2 introduction to PAn–TiO_2 composite films

9.3.8.1 Effect of SO_2 Gas on the Nanocomposite Films Figure 9.14 shows that there is little or no variation in conductivity of PAn–SnO_2 or PAn–TiO_2 composite films, respectively, after exposure to SO_2 gas (1000 ppm). In other words, the nanocomposite films should not be affected by SO_2 gas poisoning during CO gas detection measurements, as is the requirement for motor vehicle exhaust detection.

9.3.8.2 The Sensitivity in the Measurement The resistance of the nanocomposite films typically changes by at least one order of magnitude after 50–100 ms of exposure to the gas. The change is readily observed after a few seconds with saturation taking place after 80 s of exposure in such thin films. Such effect is readily reversible by subjecting the films to vacuum created, as shown in Fig. 9.15.

9.3.8.3 Gas Detection Specificity Evaluation of specificity was performed by using gas mixtures. The response of PHTh, PHTh-TiO_2, and PHTh-SnO_2 films to a mixture of NO_2 and CO in equal amounts indicates high specificity for NO_2, as

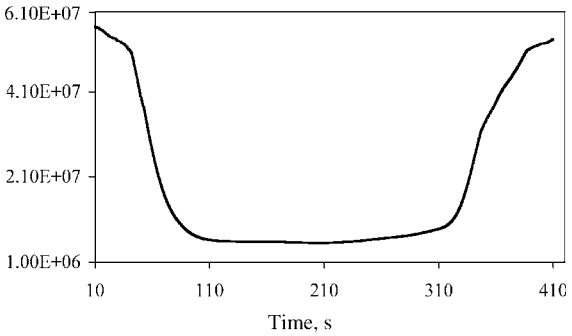

FIGURE 9.15 Response time of PAn-SnO_2 membrane with 1ppm CO gas

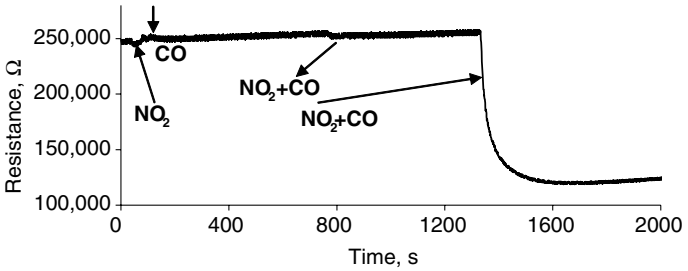

FIGURE 9.16 Resistance change of PHTh films versus time in the presence of CO and NO_2

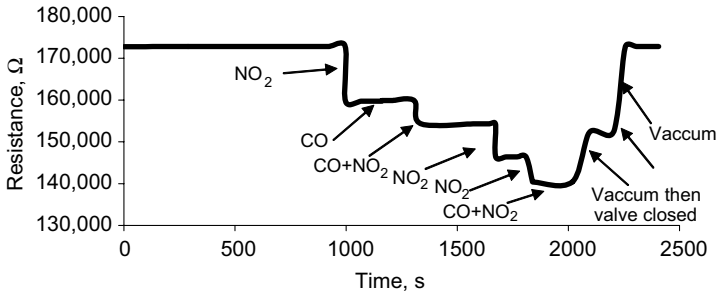

FIGURE 9.17 Resistance change of PHTh-TiO_2 films versus time in the presence of CO and NO_2

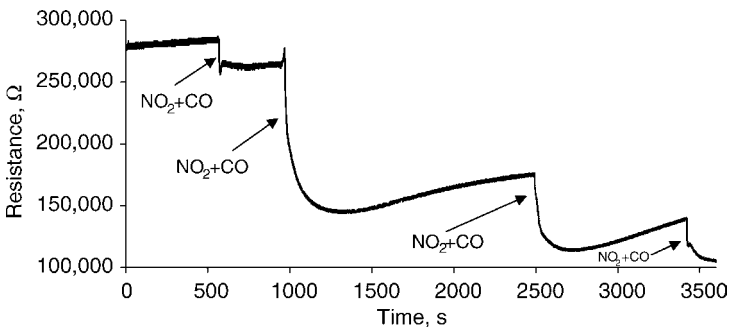

FIGURE 9.18 Resistance change of PHTh-SnO_2 films versus time in the presence of CO and NO_2

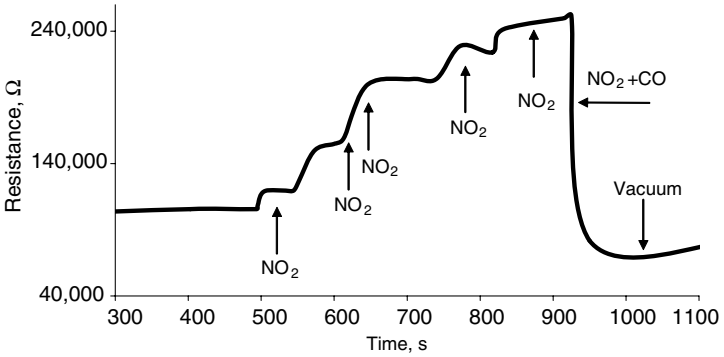

FIGURE 9.19 Resistance change of PAn–TiO_2 films versus time in the presence of CO and NO_2

shown in Figs. 9.16–9.18. The data show that the nanocomposites are much more specific than the polymer itself. A sharp decrease in resistance is observed when NO_2 is introduced in the chamber, while no significant change takes place when CO is introduced. The gases are introduced in to the chamber with 10 ppm increments each time. The sharp decrease in resistance indicates an excellent sensitivity of such films. In addition, total reversibility was observed upon removal of the gas mixture by vacuum. Similar effects for the specific recognition of CO gas by PAn–TiO_2 can be seen in Fig. 9.19 where the gases were introduced into the chamber in the same manner using the same amount and ratio. Here, resistance of the sensing layer increases in response to the presence of CO and practically no change in resistance is observed upon introduction of NO_2. In the case of PAn–SnO_2 films (Fig. 9.20), a slight change in resistance is observed compared to that of PAn–TiO_2 films. This means that although both materials are CO specific, the latter composite has a higher sensitivity.

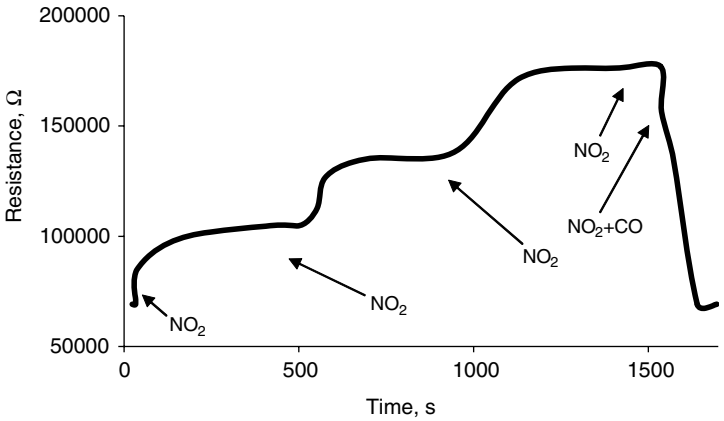

FIGURE 9.20 Resistance change of PAn-SnO_2 films versus time in the presence of CO and NO_2

9.3.9 Gas Sensing Mechanism in the Materials

9.3.9.1 Conducting Polymers It is important to understand the change of physical parameters using conducting polymers and their nanocomposites. The resistance decreases continuously and exponentially upon exposure to NO_2, indicating that the gas acts as a dopant for the polymer, as shown in Fig. 9.21. The change in resistance is dramatic at all concentrations, which makes the detection of small quantities easy with a good resolution. It is worth noting that the response was instantaneous due to the thin nature of the films with excellent reproducibility.

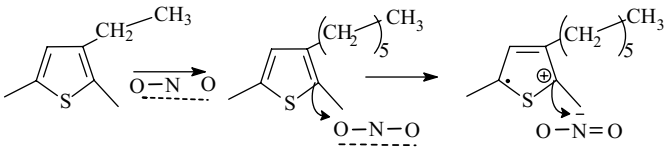

FIGURE 9.21 Schematic of the NO_2 reaction with PHTh conducting polymer

9.3.9.2 Oxide Nanoparticles Such nanoparticles (i.e., SnO_2) exhibit good sensory characteristics only at high temperatures of the order of 400°C. The dominant species in tin oxide surfaces is O^-, that is, the atomic surface oxygen ion. Such ions form in a sequence of physisorption and charge exchange reactions with the bulk of the SnO_2 grains. With significant amounts of O^- ions now available on the surface, oxidation reactions, such as those sketched in Fig. 9.22 should become possible. This kind of interaction clearly gives rise to a reducing interaction as observed at high temperatures for the low concentration regime. At higher NO_2 concentrations, the reaction is likely to deplete the SnO_2 surface from O^- sites.

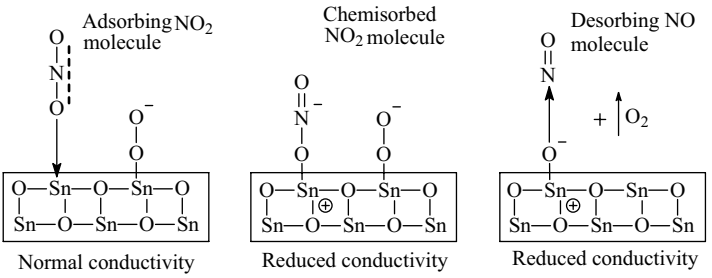

FIGURE 9.22 Operating mechanism of SnO_2 semiconductor (200°C to 400°C)

9.3.9.3 Conducting Polymers/Oxide Nanocomposites Conducting polymer-SnO_2 or -TiO_2 films exhibit interesting nanostructured materials with excellent optical, dielectric, and catalytic properties. The n-type SnO_2 forms a p-n heterojunction with the p-type conducting polymer with a depletion region as shown in its energy band diagram (Fig. 9.23). The device resembles a field effect transistor

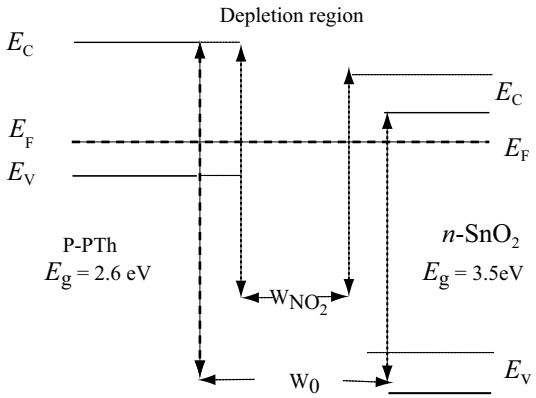

FIGURE 9.23 Energy band diagram of PHTh-SnO_2 p-n heterojunction before and after NO_2 exposure

(FET). The gas effects a change of the depletion region and thus modulates conductivity of the junction. Exposure to NO or NO_2 causes a depletion of the SnO_2 carrier concentration. Less carriers in the SnO_2 layer causes a reduction of the channel electric field of the junction. The width of the depletion region decreases and the conductivity of the thiophene channel increases before and after the exposure to NO_2. NO_2 causes an increase in $E_c - E_F$ in the n-region, involving the reduction of the width of the depletion region. This corresponds to the observed large difference in the value of conductivity between the layered PHTh and the PHTh-SnO_2 films for detection of ppb levels of NO_x gas.

9.4 CONCLUSIONS

We have performed numerous experiments using a variety of materials that have been well characterized using spectroscopic, microscopy, and electrical techniques. The use of ultrathin films of conducting polymers and their nanocomposites with certain inorganic oxides, processed via the LBL self-assembly technique, has proved to be an effective way for simple, fast, and cost-effective sensing of gases. The self-assembled films are typically deposited on precleaned surfaces that are then modified by a polyanion or polycation as a necessary step before the deposition of the active layer to ensure that the proper sequence of deposition is followed and for adhesion purposes. We have fabricated the films with a different number of layers (thickness) of the same material during our optimization effort and found that 2–10 monolayers are sufficient to form a cohesive film with excellent gas detection capability.

The synergy between the conducting polymer and the inorganic oxide leads to the formation of novel materials with gas detection capability beyond that of the conducting polymer and the inorganic oxide used separately. With this technology, sensitivity and selectivity have been dramatically improved compared to commercial systems. For example, sensitivity levels exceed those of oxide-based materials by >2

orders of magnitude with good reversibility in most cases without requiring difficult and costly processes used in commercial systems. Selectivity has been addressed by looking into using different materials that respond differently to gases. Furthermore, conducting polymer films are known to perform $>10^6$ of doping/undoping cycles in similar applications, such as capacitors and electrochromics. With gases that do not form a strong charge transfer complex with the polymers, cycling, and therefore, multiple uses of our sensors will be a natural outcome without using heat activation or deactivation.

We have evaluated the stability of the films *in situ* and *ex situ* versus temperature and gases. The stability versus time and temperature of these films has been tested and found to be appropriate at temperatures > 200°C and in some cases up to 400°C. We have optimized gas detection properties of several materials for several gases. The sensors were tested in the presence of mixed gases for specificity and sensitivity studies with excellent results. For example, SO_2 gas did not change the conductivity of the nanocomposite films, indicating that our sensing layers that are specific to NO_2 or CO will not be affected by the presence of SO_2 gas.

In order to address viability of this technology, we have fabricated the sensing layers onto interdigitated electrode arrays. The electrodes were characterized for their gas detection capability, which proved to be more effective than their planar electrode counterparts used at the beginning of this effort.

ACKNOWLEDGMENTS

This project was supported by the Environmental Protection Agency (EPA) and NASA Ames Research Center.

REFERENCES

1. Becker Th, Mühlberger St, Braunmühl, Bosch-v Chr, Müller G, Ziemann Th, Hechtenberg KV. Air pollution monitoring using tin-oxide-based microreactor systems. Sens Actuators B 2000;69:108–119.
2. Santos J, Serrini P, O'Beirn B, Manes L. A thin film SnO_2 gas sensor selective to ultra-low NO_2 concentrations in air. Sens Actuators 1997;43:154–160.
3. Pijolat C, Pupier C, Sauvan M, Tournier G, Lalauze R. Gas detection for automotive pollution control. Sens Actuators B 1999;59:195–202.
4. Meixner H, Gerblinger J, Lampe U, Fleischer M. Thin-film gas sensors based on semiconducting metal oxides. Sens Actuators B 1995;23:119–125.
5. Pijolat C, Pupier C, Sauvan M, Tournier G, Lalauze R. Sens Actuators B 1995;59:195.
6. Lim J-W, Kang D-W, Lee D-S, Huh J-S, Lee D-D. Heating power-controlled micro-gas sensor array. Sens Actuators B 2001;77:139–144.
7. Zhang W, de Vasconcelos EA, Uchida H, Katsube T, Nakatsubo T, Nishioka Y. A study of silicon Schottky diode structures for NO_x gas detection. Sens Actuators B 2000;65: 154–156.

8. Rickerby DG, Horrillo MC, Santos JP, Serrini P. Microstructural characterization of nanograin tin oxide gas sensors. Nanostruct Mater 1997;9:43–52.
9. Melendez J, de Castro AJ, Lopez F, Meneses J. Spectrally selective gas cell for electrooptical infrared compact multi-gas sensor. Sens Actuators A 1995;46(47): 417–421.
10. Koshizaki N, Yasumoto K, Sasaki T. Mechanism of optical transmittance change by NO_x in CoO/SiO_2 nanocomposites films. Sens Actuators B 2000;66:122–124.
11. Bartlett PN, Ling-Chung K. Conducting polymer gas sensors Part III. Sens Actuators 1989;20:287–292. Gardner JW, Bartlett PN. *Electronic Noses, Principles and Applications*. Oxford: Oxford Science Publications; 1999.
12. Bauerle P, Scheib S. Adv. Mater 1993;5:848. McQuade DT, Pullen AE, Swager TM. Conjugated Polymer-Based Chemical Sensors. Chem Rev 2000;100:2537–2574.
13. Monkman AP, Petty MC, Agbor NE, Scully MT. Polyaniline gas sensor, U.S. Patent 5,536,473. July 16,(1996).
14. Torsi L, Pezzuto M, Siciliano P, Rella R, Sabbatini L, Valli L, Zambonin PG. Conducting polymers doped with metallic inclusions: New materials for gas sensors. Sens Actuators B 1998;48:362–367.
15. Chiang JC, MacDiarmid AG. Polyaniline: a new concept in conducting polymers. Synth. Met 1986;13:193.
16. (a) Dhawan SK, Kumar D, Ram MK, Chandra S, Trivedi DC. Application of Conducting Polyaniline as Sensor material for Ammonia. Sens Actuator, B 1997;40(2–3):99–103. (b) Paddeu S, Ram MK, Nicolini C. Investigation of Processable poly(ortho-anisidine) Ultra -Thin Films obtained by Langmuir- Blodgett Technique. J Phys Chem B 1997;101:4759–4766.
17. Paddeu S, Ram MK, Nicolini C. Langmuir-Schaefer films of a poly(o-anisidine) conducting polymer for sensors and displays. Nanotechnology 1998;9:228–236.
18. Endres F, Schwitzgebel G. Morphological and electrochemical studies of polypyrrole/Nafion®. Synth Met 1997;88:73–78. Selampinar F, Toppare L, Akbulut U, Yalçin T, Süzer S. A conducting composite of polypyrrole: II. As a gas sensor. Synth Met 1995;68:109–116. Selampinar F, Akbulut U, Toppare L. Conducting polymer composites of polypyrrole and polyimide. Synth Met 1997;84:185–186.
19. Tai W-P, Kim J-G, Oh J-H. Humidity sensitive properties of nanostructured Al-doped ZnO: TiO_2 thin films, Sens Actuators B 2003;96:477–481.
20. Gerlich M, Kornely S, Fleischer M, Meixner H, Kassing R. Selectivity enhancement of a WO_3/TiO_2 gas sensor by the use of a four-point electrode structure. Sens Actuators B 2003;93:503–508.
21. (a) Cao Y, Zhang XT, Yang WS, Du H, Bai YB, Li TJ, Yao JN. A bicomponent TiO_2/SnO_2 particulate film for photocatalysis. Chem Mater 2000;12(11):3445–3448. (b) Tada H, Hattori A, Tokihisa Y, Imai K, Tohge N, Ito S. A Patterned-TiO_2/SnO_2 Bilayer Type Photocatalyst. J Phys Chem B 2000;104(19):4585–4587.
22. Ram MK, Salerno M, Adami M, Faraci P, Nicolini C. Physical Properties of Polyaniline Films: Assembled by the Layer-by-Layer Technique. Langmuir 1999;15:1252–1259.
23. (a) Ram MK, Adami M, Faraci P, Nicolini C. Physical insight in the in-situ self-assembled films of polypyrrole. Polymer 2000;41(20):7499–7509. (b) Nicolini C, Erokhin V, Ram MK. Supramolecular Layer Engineering for Industrial Nanotechnology. In: Rosoff M, editor. Nano-Surface Chemistry. New York: 2001. pp. 141–212.

24. Ding H, Ram MK, Nicolini C. Nanofabrication of organic/inorganic hybrid of TiO_2 with substituted phthalocyanine or polythiophene. J. Nanosci Nanotechnol 2001;1:207–213.
25. McCullough RD. Adv Mater 1998;10:1. Bjørnholm T, Hassenkam T, Greve DR, McCullough RD, Jayaraman M, Savoy MS, Jones CE, McDevitt JT. Adv Mater 1999;11:1218.Bjørnholm T, Greve DR, Reitzel N, Hassenkam T, Kjaer K, Howes PB, Larsen NB, Bøgelund J, Jayaraman M, Ewbank PC, McCullough RD. J Am Chem Soc 1998;120:7643.

CHAPTER 10

Force Measurements between Emulsion Droplets As a New Tool for Medical Diagnostics

ABDELHAMID ELAISSARI

Claude Bernard University, LAGEP Laboratory, 43 Boulevard du 11 november 1918, Bât. CPE-308G 69622 Villeurbanne Cedex, France

CÉLINE GENTY

Université Bordeaux 1, UPR 8641, Centre de Recherche Paul Pascal – CNRS, Avenue A. Schweitzer, 33 600 Pessac, France

OLIVIER MONDAIN-MONVAL

Université Bordeaux 1, UPR 8641, Centre de Recherche Paul Pascal – CNRS, Avenue A. Schweitzer, 33 600, Pessac, France

10.1 INTRODUCTION

The specific capture and detection of nucleic acid molecules (DNA or RNA) in biomedical diagnostic have attracted special interest in the last 20 years. In order to enhance the specificity and the sensitivity of molecular diagnostic, special attention has been paid to the possible automation of samples preparation, specific or generic extraction of DNA molecules, and specific target detection in new biotechnological devices (1–3). To answer the variability of conditions encountered by the different types of nucleic acids, various supports have been used and widely explored (4–6). Several devices (such as planar silica wafers and colloids) were used as solid supports for biomolecules immobilization. In this direction, the chemical grafting of single stranded DNA (ssDNA) fragments (capture probes) on selected solid support (1) has been applied to the capture of nucleic acid molecules. The specificity of this capture is controlled by the hydrogen binding between complementary basis. The

Colloidal Nanoparticles in Biotechnology, Edited by Abdelhamid Elaissari
Copyright © 2008 John Wiley & Sons, Inc.

detection is hereafter performed by coupling a complementary ssDNA bearing enzyme sequence to a given part of the target. Then, the addition of a chemical specie that is transformed by the enzyme results in a coloring of the system. A colorimetric titration leads directly to the target captured amount. As a general tendency, the specific capture efficiency is related to (i) the accessibility and the reactivity of the capture probes, (ii) the surface properties of the solid support, (iii) the affinity between the solid support surface and the target probes, and (iv) the amount of target in the biological sample.

Using magnetic colloids, various problems have been solved or at less circumvented as evidenced by the numerous reported works (6–8). Such colloids have been used in various levels of bionanotechnologies. Apart from their large specific area, their main advantage is their ability to move under the application of a single magnetic field, which allows for their separation from the surrounding medium. Magnetic particles have been widely used in various biomedical applications, such as immunoassays, bacteria isolation, cell sorting, virus extraction, and finally generic nucleic acids (6–8). In this direction, magnetic emulsions (9,10) were used as seed in emulsion polymerization processes. The advantages of magnetic emulsions are their narrow size distribution, high iron oxide content, and their ability to be turned into magnetic latex particles as an appropriate polymerization process occurs (11).

In the last decade, it was shown that the repulsive forces between magnetic emulsion droplets could be measured (12) and used to determine the presence of charges (13) or adsorbed macromolecules (14) at the particles surface. More precisely, it was demonstrated that even the conformation and density number of adsorbed macromolecules could be determined using such measurements (15).

The main objective of this chapter is to review the various results obtained with this method when simple ionic and nonionic surfactants, polymers, and finally biomolecules are adsorbed at the droplets surfaces. In Section 10.2, we present the technique and its experimental aspects. In Sections 10.3 and 10.4, we review the results that were obtained with emulsions stabilized by simple surfactant molecules and polymers, respectively. In Section 10.5, we then summarize the recent studies on systems containing proteins and ssDNA molecules. As a further prospect of this work, we present, in Section 10.6, some recent results obtained with ferrofluid droplets covered by a silica shell.

10.2 FORCE MEASUREMENTS BETWEEN MAGNETIC PARTICLES

10.2.1 Description of the Experimental System

A ferrofluid is dispersion of small paramagnetic iron oxide grains (Fe_2O_3, of size around 10 nm) that are dispersed and chemically stabilized in octane using a mixture of oleic and phosphoric acid (OPA) as surfactant within the oil. OPA adsorb at the surface of the oxide grains that are thus sterically stabilized (16). A magnetic emulsion is

obtained by shearing the ferrofluid oil in a mixture of water and surfactant. Using the analog of a fractionated crystallization technique (17), a monodisperse population of oil droplets can be obtained from the initially crude emulsion. The final emulsion contains both a watersoluble surfactant (of high Hydrophile/Lipophile Balance (HLB) (18)) and the oil soluble only OPA (of low HLB).

10.2.2 Description of the Technique and Theoretical Aspect

The droplets align into an external magnetic field and form linear chains aligned along the field direction (Fig. 10.1). The applied field induces a magnetic dipole in each drop, causing them to form chains. At low particles volume fractions, the chains are well separated.

Intense Bragg scattering is observed (12–15) due to the presence of this one-dimensional ordered structure. The interdroplet spacing can be measured since it is very simply related to the Bragg peak wavelength λ through the following relation:

$$2d = \lambda/n, \tag{10.1}$$

where d is the center to center separation distance between the particles in the chain and n is the refractive index of the suspending medium ($n = 1.33$ in the case of water). The distance h is related to the droplets radius R,

$$h = d - 2R, \tag{10.2}$$

R is determined independently using light scattering measurements. The attractive magnetic force is a function of the radius R, the amount of ferrofluid grains in each

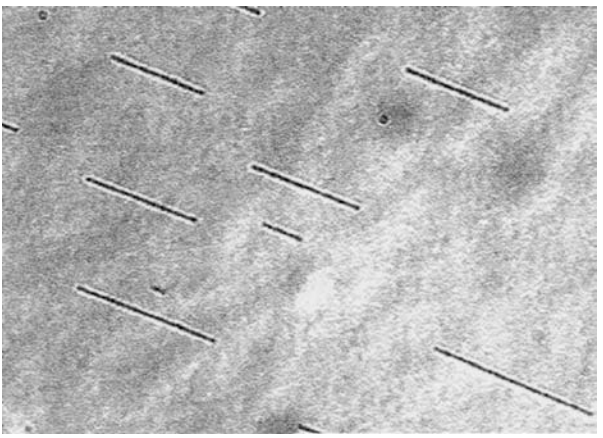

FIGURE 10.1 Light microscopy picture of a monodisperse magnetic emulsion enduring a magnetic field. The droplets chains align in the direction of the applied field (width of the pictures 100 μm)

droplet, the magnetic susceptibility of the ferrofluid (measured with a SQUID susceptometer), the adjustable intensity of the applied field, and h. The calculation of this attractive force is fully described by Zhang et al. (19). Inside the chains, the mechanical equilibrium takes place between the droplets. This means that, for a given equilibrium distance h_{eq}, one gets

$$F_{att}(h_{eq}) = F_{rep}(h_{eq}), \tag{10.3}$$

where $F_{att}(h_{eq})$ and $F_{rep}(h_{eq})$ are, respectively, the attractive and the repulsive force between the droplets. $F_{att}(h_{eq})$ can be calculated leading to the value of $F_{rep}(h_{eq})$ (Eq. 10.3). The full force–distance profile can be determined by varying the field and measuring the consequent Bragg peak's wavelength.

10.3 FORCE MEASUREMENTS IN SURFACTANT SOLUTIONS

In this section, we review the force–distance profiles obtained in surfactant solutions (13).

The force–distance profile measured when droplets are stabilized by a nonionic surfactant (Nonylphenol Ether of commercial name NP10) is shown in Fig. 10.2. At such small droplet separation, the attractive van der Waals forces are significant and have been taken into account in the calculation of F_{att}. The measured surface separation h is found to be independent of the magnetic field strength. Within the experimental uncertainty, h is found to be around 2 nm, very close to zero. The contact is almost achieved between droplets and the repulsion is of the hard sphere type. This profile

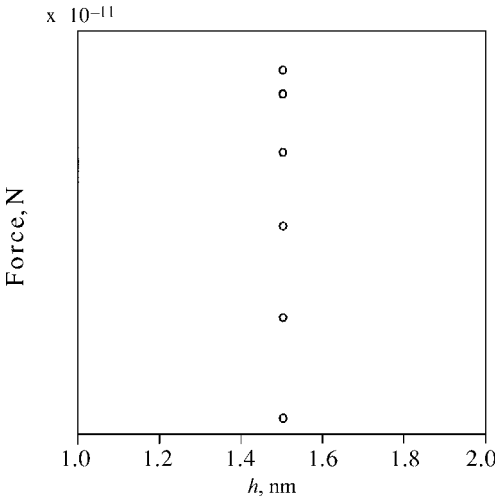

FIGURE 10.2 Force–distance measurement between ferrofluid droplets in a nonionic surfactant solution ([NP10] = 10 CMC). The profile is of the "hard sphere" type indicating that the interfaces are not significantly charged (from Reference 13)

evidences the absence of any long-range double layer repulsion or any significant deformation of the droplets.

When an ionic surfactant sodium dodecyl sulfate (SDS) is added in the bulk phase (Fig. 10.3a) the behavior changes drastically, going from hard sphere to exponentially

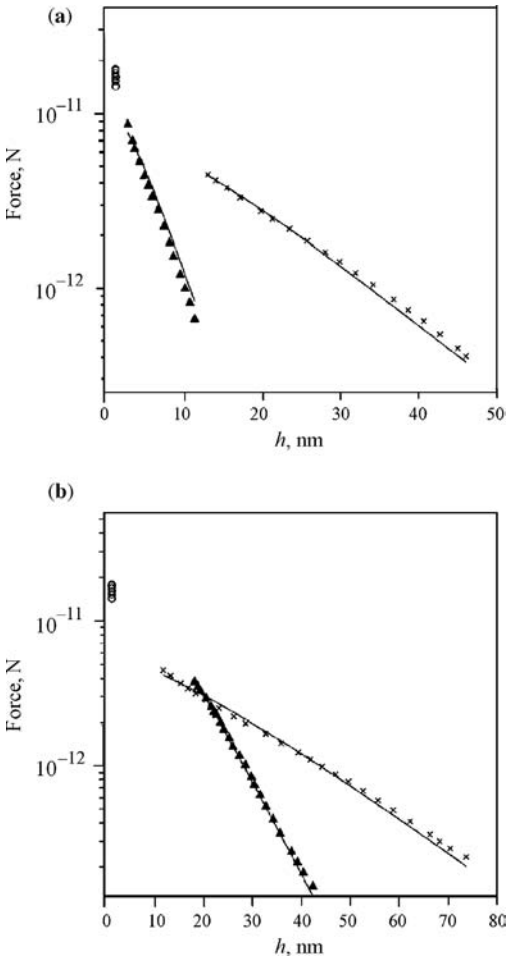

FIGURE 10.3 Evolution of the force–distance profile from a typically "hard sphere" to an electrostatic exponentially decaying behavior. (**a**) Evolution of the force–distance profile when SDS is introduced in an initially nonionic ferrofluid emulsion at low pH (5.5). Empty circles: [NP10] = 10 CMC, no SDS; cross: [NP10] = 10 CMC, [SDS] = 7.1×10^{-4} M; black triangles: [NP10] = 10 CMC, [SDS] = 8×10^{-3} M; continuous lines: best fits of our data to Equations (10.4), (10.5), and (10.6), respectively in the text. (**b**) Evolution of the force–distance profile with increasing pH. Empty circles: [NP10] = 10 CMC, pH = 5.5; cross: [NP10] = 10 CMC, [NaOH] = 2.9×10^{-4} M; black triangles: [NP10] = 10 CMC, [NaOH] = 1.3×10^{-3} M; continuous lines: best fits of our data to Equations (10.4), (10.5), and (10.6), respectively, in the text (from Reference 13)

decaying. The obtained profiles reveal the appearance of a long-range repulsion that is caused by the adsorption of charged molecules at the oil-water interface.

A similar behavior (Fig. 10.3b) is observed when the pH is increased in the continuous phase. Indeed, the acid molecules that are contained in the oil droplets are also present at the oil-water interface and are ionized at large pH. In that case, the droplets are stabilized by the surfactant contained in the oil and the addition of any other surfactant in the bulk aqueous phase is not needed. The profiles of Fig. 10.3b clearly reveal the appearance of long-range exponentially decaying double layer forces.

These profiles can be successfully described using a theoretical expression of the double layer repulsion that is derived from Poisson–Boltzmann theory. Between two charged spheres (of radius R) of low surface charge densities immersed in a continuous phase of ionic concentration C_s, the force reads (12,20)

– when $\kappa R < 5$

$$F_r(h) = 4\pi\varepsilon\psi_0^2 R^2[\kappa/(h+2R)+1/(h+2R)^2]exp(-\kappa h) \tag{10.4}$$

– when $\kappa R > 5$

$$F_r(h) = 2\pi\varepsilon\psi_0^2 R\kappa[exp(-\kappa h)/(1+exp(-\kappa h))], \tag{10.5}$$

where ε is the water dielectric permittivity and ψ_0 the droplet surface potential. κ^{-1} is the Debye length that is connected to the electrolyte concentration C_s. In the case of symmetric 1:1 electrolytes, κ^{-1} reads (20)

$$\kappa^{-1} = [(4\pi q^2/\varepsilon kT)2C_s]^{-1/2}, \tag{10.6}$$

where q is the ion charge and kT the thermal energy. From Equations 10.4 and 10.5, it is clear that the intensity of the electrostatic force is mostly fixed by the surface potential while its range is determined by κ^{-1}. The data are compatible with Equation 10.5 (see Fig. 10.3) since the screening lengths κ^{-1} (computed through Equation 10.6) that determine the slopes of the semilogarithmic plots are in all cases in good agreement with the experimental slopes. In these fits, the Debye lengths are never treated as adjustable parameters and the only free parameter is the droplet surface potential. This agreement between the measured and the theoretical slope is our main proof for the accuracy of that experimental technique (12).

Interestingly, our technique can evidence the cooperative effect between a nonionic and an anionic surfactants. As a nonionic surfactant is added into an emulsion containing initially only an ionic one, the force intensity increases (Fig. 10.4). From the two sets of profiles, we can deduce several conclusions. First, the characteristic range κ^{-1} of the repulsion remains unchanged as NP10 is introduced since the bulk ion concentration is kept at a constant value (see Equation 10.6). This is evidenced by the parallel evolution of the force profiles on the semilogarithmic scale. Second, we observe that the intensity of the repulsive forces is always larger in the presence of

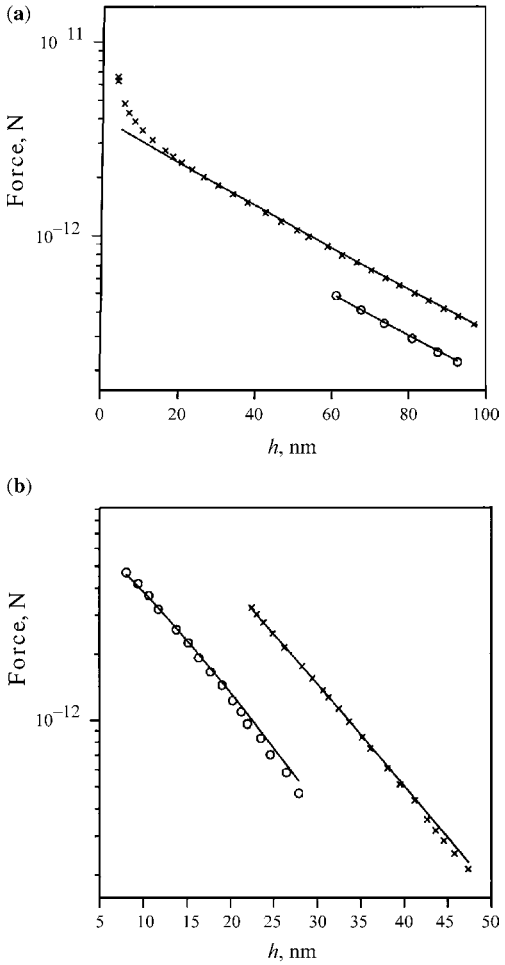

FIGURE 10.4 Compared force–distance profiles of the simple and the mixed surfactant systems at constant ion concentration in the bulk phase: (**a**) SDS-NP10 system (pH = 5.5). Empty circles: simple SDS system ([SDS] = 3.7×10^{-5} M, no NP10); cross: mixed SDS-NP10 system ([SDS] = 3.7×10^{-5} M, [NP10] = 4.2×10^{-5} M); continuous lines: best fits of our data to Equations (10.4) and (10.5) in the text ($\psi_{0,\text{simple}} = 15.2$ mV, $\psi_{0,\text{mixed}} = 20$ mV). (**b**) AOP-NP10 system. Empty circles: simple AOP system ([NaOH] = 1.1×10^{-3} M, no NP10); cross: mixed AOP-NP10 system ([NaOH] = 1.1×10^{-3} M, [NP10] = 10 CMC); continuous lines: best fits of our data to Equations (10.4) and (10.5) in the text ($\psi_{0,\text{simple}} = 18.6$ mV, $\psi_{0,\text{mixed}} = 30.5$ mV). (from Reference 13)

NP10. This indicates that the surface charge densities are always larger in the mixed surfactant system. It is due to an increase of adsorption of charged species caused by an attraction between ionic and neutral surfactant molecules in good agreement with earlier surface tension results (21).

TABLE 10.1 Characteristics of the Diblock Copolymers. The Polydispersity Index (Mw/Mn) was Determined by SEC with Polystyrene Standards. (from Reference 15(b)).

Reference name	Butadiene block M_W, g/mol	Oxyethylene block M_W, g/mol	M_W/M_n
7.7/8	7,700	8,000	1.06
21/9.3	21,000	9,300	1.1
58/20	58,000	20,000	1.12
98/13.5	98,000	13,500	1.19
150/30	150,000	30,000	1.3

10.4 FORCE MEASUREMENTS IN POLYMER SOLUTIONS

10.4.1 Diblock Copolymers

Emulsions can also be stabilized using diblock copolymers such as those listed in Table 10.1. In such copolymers, the hydrophobic part (polybutadiene) is larger than the hydrophilic (poly(ethylene oxide)) one. Consequently, such polymers can be used to stabilize inverted water-in-oil emulsions.

The measured profiles at various polymer concentrations are plotted in Fig. 10.5. An increase in the range of the forces that is due to the adsorption of a copolymer layer is clearly observed. The presence of the polymer generates repulsive forces with characteristic ranges larger than those obtained with a nonionic surfactant (see previous

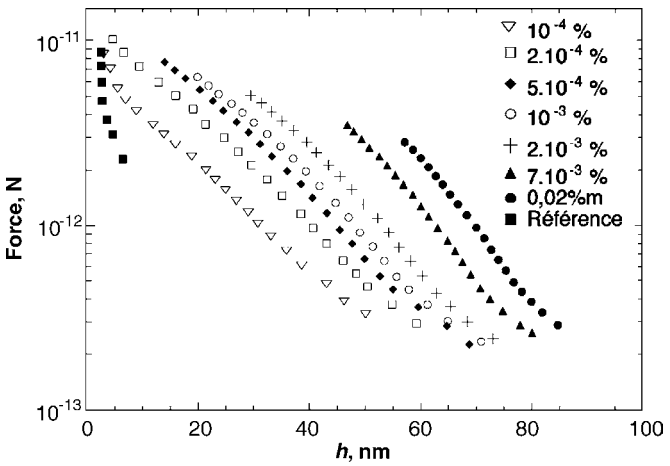

FIGURE 10.5 Evolution of the force–distance profile between aqueous ferrofluid emulsion droplets in methylcyclohexane as a function of the polymer concentration and at a constant Span 80 concentration (0.5%). The used polymer is the 98–13.5 K of Table 10.1. The concentrations are given in weight percents. The "reference" profile is the one found in the absence of any polymer when the droplets are stabilized by the "short-tail" surfactant Span 80 (sorbitan monooleate, from Aldrich) only. The scale is semilogarithmic. (from Reference 15(b))

section). We identify different regimes depending on the polymer concentrations. For the lowest one ($Cp < 0.1\%$), the force range increases with the polymer concentration to reach a plateau value.

In such concentration range, we have measured the force profile as a function of the polybutadiene block molecular weight in Fig. 10.6a. We have made the same

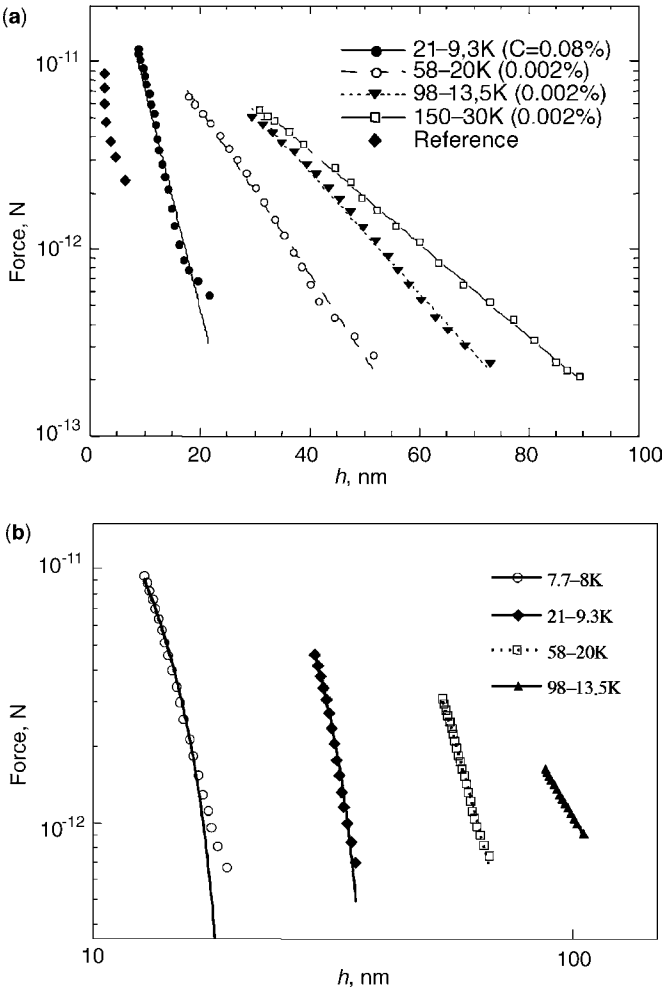

FIGURE 10.6 (**a**) Evolution of the force–distance profiles as a function of the polybutadiene block molecular weight in the low concentration regime. The solid lines are the best fits of our data to the Dolan–Edwards model described in Reference 22(a), which treats the cases of the compression of polymer "mushroom." The scale is semilogarithmic (from Reference 15(b)). (**b**) Evolution of the force–distance profiles as a function of the polybutadiene block molecular weight in the high concentration regime. The solid lines are the best fits of our data to the Alexander–de Gennes model described in Reference 22(b), which treats the cases of the compression of polymer "brushes" layers. The scale is in log-log (from Reference 15(b))

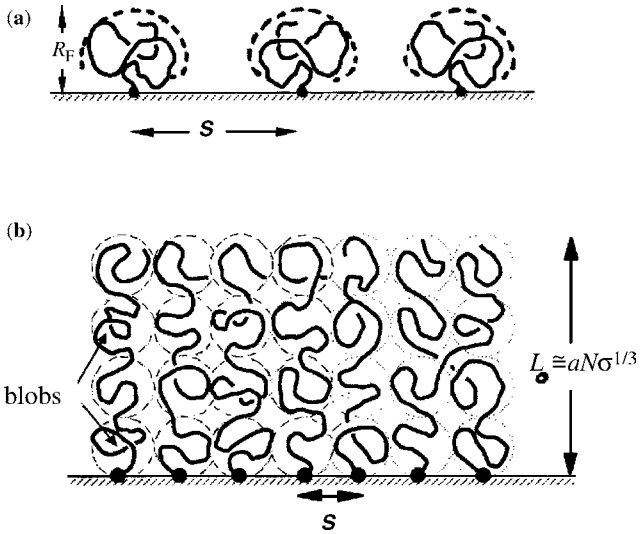

FIGURE 10.7 (**a**) "Mushroom" polymer layer. Schematic of a diblock adsorbed layer at low concentration. Since the surface concentration is low, the polybutadiene block can adopt a coil conformation and the adsorbed chains do not interact with each other (the average spacing between neighboring coils is larger than $2R_{G,PBut}$) (from Reference 15(b)). (**b**) "Brush" polymer layer. Schematic of a diblock adsorbed layer at high concentration. Since the surface concentration is large, the polybutadiene block can no longer adopt a coil conformation, and the adsorbed chains interact with each other and extend in the continuous phase (the average spacing between neighboring coils is smaller than $2R_{G,PBut}$). (from Reference 15(b))

experiment in the high concentration regime (Fig. 10.6b: $C_p = 0.5\%$). In both cases, the force range clearly increases with the polybutadiene block length. We interpret these results within the frame of the Dolan–Edwards (22(a)) and Alexander–de Gennes (22(b)) models that, respectively, describe the compression of independent random coils at low surface concentration ("mushroom" situation, Fig. 10.7a) and polymer brushes ("brush" situation, Fig. 10.7b) at high surface concentration. The data are fully consistent with this hypothesis as confirmed by the excellent agreement between the experimental results and the theoretical predictions (which are the solid lines in Fig. 10.7a and b). They are also in full agreement with earlier results obtained between solid surfaces (23). The conclusions are also confirmed by independent measurement of the polymer layer thickness using dynamic light scattering (Fig. 10.8). The polymer layer thickness is indeed proportional to the polybutadiene block gyration radius (which is itself proportional to $M_{W,PBut}^{0.6}$) at low concentration and to the polybutadiene block extended length at high concentration (about $M_{W,PBut}$).

10.4.2 Statistical Copolymers

A statistical copolymer can also stabilize an emulsion. For example, a PVA-VAc (polyvinyl alcohol (88%)-*co*-polyvinyl acetate (12%)) is shown to adsorb at the

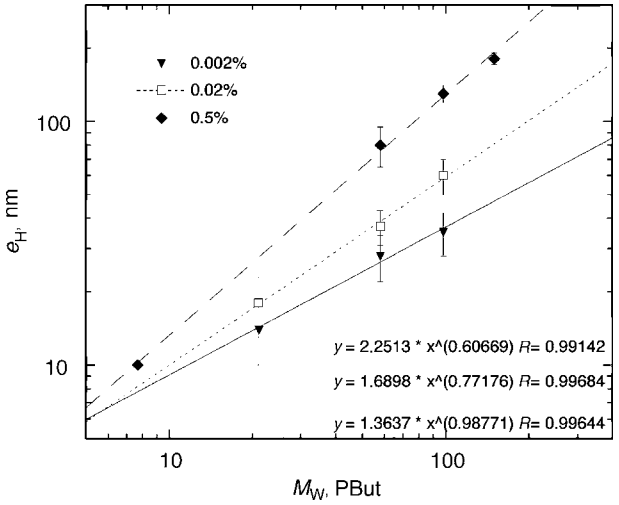

FIGURE 10.8 Log–log evolution of the characteristic layer length as a function of the polybutadiene block length (in kg/mol) and at various polymer bulk concentration. At low concentrations, the length follows a power law with an exponent of about 0.6 for $M_{W,Pbut}$, as predicted when the polymer layer adopts a coil like conformation in good solvent. At large concentration, the linear behavior (with an exponent around 1) reflects an extended conformation of the adsorbed chain, as schematized on Fig. 10.7b. (from Reference 15(b))

surface of oil droplets (14,15(a)). Here also, a long-range repulsive force is measured (Fig. 10.9).

The observed force is shown to be unchanged by the addition of ions in the bulk phase, which clearly establish the steric nature of the measured force. The measured forces decay exponentially with the distance h with ranges that increase with the polymer molecular weight. The profiles can be fitted by the following expression (24):

$$F(h) = A\,h \exp(-h/\lambda), \tag{10.7}$$

where A is a constant and λ is a distance characteristic of the adsorbed polymer layer that can be, in a first approximation, considered as proportional to the layer thickness. Interestingly, it can be shown that the polymer layer characteristic distance is proportional to the polymer coil gyration radius R_G,

$$\lambda \sim R_G. \tag{10.8}$$

Our observations (Fig. 10.10) are in good agreement with the earliest (25) as well as the more recent theories (24) on polymers at interfaces. The results are independent of the nature (liquid or solid) of the surfaces (26).

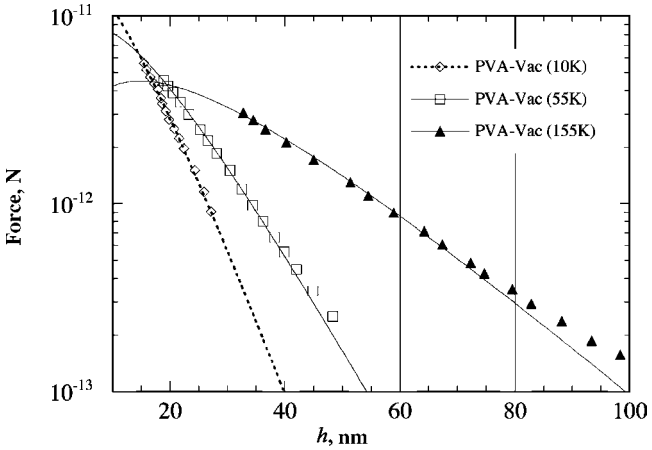

FIGURE 10.9 Evolution of the force–distance profiles between oil-in-water emulsion droplets stabilized by the statistical copolymer PVA-Vac of different molecular weights (10,000, 50,000, and 155,000 g/mol). The profiles are exponentially decaying with ranges that depend on the polymer molecular weight. The solid lines are the best fits of our data to Equation 10.7 in the text. The extracted value of λ are plotted versus the polymer gyration radius on Fig. 10.10. The scale is semilogarithmic (from Reference 15(a))

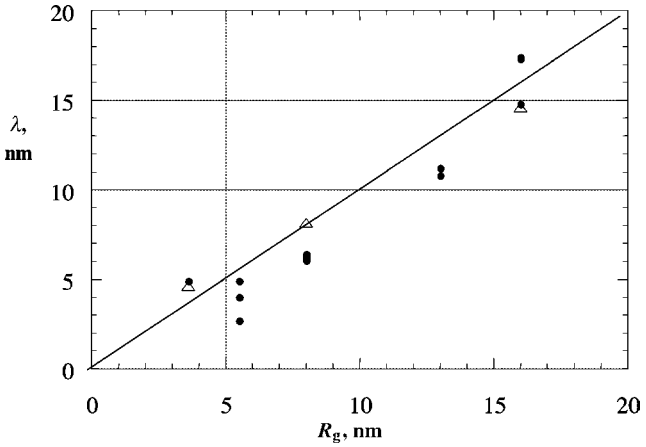

FIGURE 10.10 Evolution of the characteristic length λ deduced from the best fits of the data from Fig. 10.9 to Equation 10.7 in the text, as a function of the polymer coils gyration radii (which were deduced independently from viscometric measurements). Other points were obtained from results that are not shown here. The different symbols correspond to different sets of emulsions. (from Reference 15(a))

10.5 FORCE MEASUREMENTS IN SOLUTIONS OF BIOMOLECULES

10.5.1 Force Measurements in Protein Solutions

In the late 1990s, Dimitrova et al. (27) have used the technique to investigate the forces that take place between emulsion droplets suspended in mixtures of nonionic surfactant (polyoxyethylene (20) sorbitan monolaurate: Tween 20, and Bovine Serum Albumine BSA). When dispersed in pure BSA solution, the emulsions droplets could not be stabilized and are always flocculated. To ensure a good stability to the system, Tween 20 has to be added into the continuous phase of the emulsion. The force profiles obtained at constant Tween 20 but varying BSA concentrations are plotted in Fig. 10.11.

In the absence of BSA, the authors observe a classical exponentially decaying behavior that is characteristic of long-range double layer forces added to van der Waals attraction. However, as BSA is added in the system, the force profiles deviate from this behavior. For both Tween 20 concentrations, the resulting profiles in the

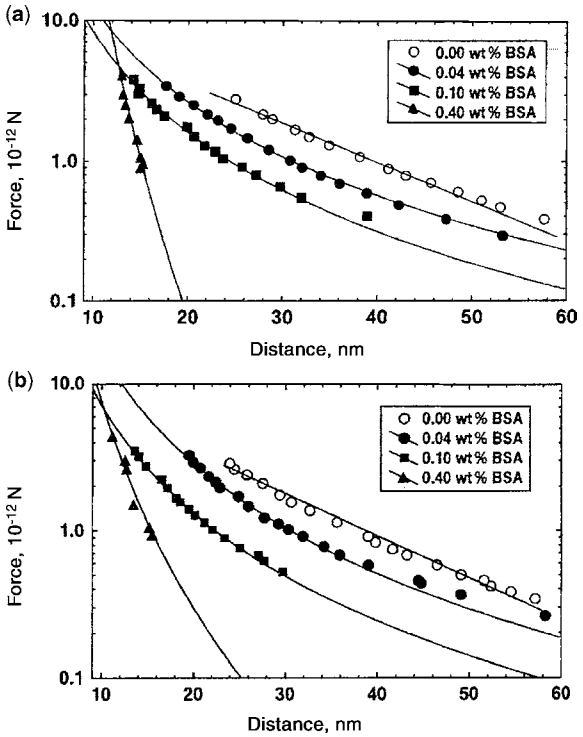

FIGURE 10.11 Force versus distance profiles for ferrofluid emulsions stabilized with mixed BSA-Tween 20 adsorption layers. The total concentration of the Tween 20 is kept constant: 5 CMC (**a**) and 50 CMC (**b**) The ionic strength is 3×10^{-4} mol/L, pH = 5.8. The solid lines are the best fits to Equation 10.9 in the text (from Reference 27)

presence of the same quantity of BSA are very similar and do not depend strongly on the Tween 20 concentration. Measurements of the ζ-potential in the mixed systems lead to some values of about 2–3 mV, which suggests that there is a negligible contribution from the electrostatic repulsion. For that reason, the authors fitted the experimental points for mixed protein–surfactant systems with a combination of van der Waals attraction and power-law steric repulsion, supposing the additivity of these two contributions using Hamaker constants from the literature (20(b), 28). The expression used for the steric force is

$$F_S = f_0^{st}(h/h_{min})^{-\alpha}, \tag{10.9}$$

where α is a parameter that accounts for the range of the interaction. The value h_{min} is the minimum distance measured in each case and serves as a scaling factor. The authors adopt this empirical expression, because it is the one that provides the best description of the experimental data (the continuous lines in Fig. 10.11). The fits are obtained leaving both f_0^{st} and α as free parameters. The force profiles for the corresponding emulsions stabilized only with Tween 20 are fitted with DLVO theory, as described in previous section are shown for comparison. In Table 10.2, the values of the fitting parameters f_0^{st} and α for different BSA concentrations are reported. It is important to notice that f_0^{st} and α are *effective* parameters characterizing the mixed adsorbed layers.

The obtained f_0^{st} values are quite similar, and the main differences come from the α factor that determines the *range* of the force. The change of its value with the increase in BSA content can be attributed to some changes in the adsorption and/or structural parameters of the protein–surfactant mixed layer present at the interface. It was proven (29) that a low molecular weight surfactant and a globular protein interact in the bulk solution forming a complex. The formation of this complex is driven by electrostatic and and/or hydrophobic interactions. Unfortunately, the lack of detailed knowledge concerning the surface/interfacial properties of protein–surfactant complexes, makes any further interpretation of our numerical results rather difficult.

From Fig. 10.11, the authors conclude that the force profiles do not vary much with Tween 20 concentration at the same BSA content. The deviations are in the frame of

TABLE 10.2 Fitting Parameters for the Mixed Layers of BSA and Tween 20 (from Reference 27).

BSA	Tween 20 concentration (CMC)							
	5		25		50		25	
Concentration, wt %	f_0^{st} pN	α	f_0^{st}, pN	α	f_0^{st}, pN	α	f_0^{st}, pN	α
0.04	3.61	2.23	3.76	1.73	3.07	2.5	4.46	2.17
0.1	3.74	2.36	3.21	1.92	3.46	2.44	3.79	2.45
0.4	3.79	8.97	3.43	3.76	4.89	4.68		

the experimental error, which suggest that the presence of the protein dominates the behavior and the properties of the systems studied. The force profiles are qualitatively identical to those reported in the literature. Indeed long-range steric repulsion between BSA covered mica sheets were observed in a previous study (30). It was found that at pH 5.5 the force (measured by means of SFA) deviates from linearity (in semilog plot) at a separation of about 50 nm, indicating the presence of long-range steric repulsion. The increased stability against coalescence of BSA-stabilized oil-in-water emulsions is also attributed to steric repulsion between the BSA adsorption layers (31).

Then the authors have also studied the behavior of casein covered emulsion droplets. Caseins are common milk proteins widely used as emulsifiers due to their excellent stabilizing properties. The caseins are disordered proteins, which (within some limits) can be treated as specific random coil polymers. Here the authors focus their attention on β-casein, which represents almost 33–35 wt %of the total casein content in cow's milk. This protein is an amphiphilic molecule that could be divided into hydrophilic and hydrophobic parts (32). The force profiles between β-casein covered droplets, at various protein concentrations in the continuous phase (from 0.1 to 0.5 wt%) are investigated. The authors explain their results by considering a repulsive electrostatic force combined to an attractive depletion contribution due to the presence of free casein in the continuous phase. This behavior is reminiscent of previous results obtained in micellar surfactant solutions where the osmotic pressure of the micelles induces a long-range depletion attractive force (13,33).

10.5.2 Force Measurements in ssDNA Solutions

10.5.2.1 Streptavidin-Magnetic Droplets Conjugates Preparation The oligonucleotides or ssDNA molecules bearing biotin at the 5′ position are immobilized onto the streptavidin containing oil in water magnetic ferrofluid nanodroplets. The streptavidin is chemically grafted onto activated carboxylic groups of the nanodroplets surface. After chemical grafting, the emulsion droplets bearing ssDNA capture probe are washed via magnetic separation-redispersion cycles using a TE buffer solution (10 mM Tris; 1 M NaCl, 10 mM EDTA, 0.05 wt %Triton X-405). In order to avoid the adsorption of the capture and detection probes on the nanodroplets, well appropriate amount of salmon DNA (low molecular weight) is introduced in streptavidin containing magnetic nanodroplets dispersion as a coating agent (34).

The capture probe (ssDNA grafted consists in 32 nucleotides complementary to HIV nucleic acid sequence used as a target model (see Table 10.3)). The obtained mixtures are then incubated at 37°C for 30 min before the washing step.

10.5.2.2 Specific Capture and Detection of the Nucleic Acid Target (i.e., ELOSA) Enzyme Linked Oligo Sorbent Assay (ELOSA) is used in biomedical diagnostic for specific detection of nucleic acid target via specific hydrogen binding as shown in Fig. 10.13. The capture probe-magnetic particle conjugates are mixed with ssDNA solution composed of HIV sequence containing 72 nucleotides as a model of target nucleic acid materials (Table 10.3). The detection process of the captured HIV

TABLE 10.3 Sequences of the Different ssDNA Used in this Study as Schematically Illustrated in Figure 10.12 (G, Guanine; T, Thymine; C, Cytosine A, Adenine) (from Reference 34).

Sequence of the capture ssDNA bearing biotin	→5′TAT GTC TAC TAT TCT TTC CCC TGC ACT GTA CC 3′→
Sequence of the target HIV ssDNA	→5′GTA TTC ATC CAC AAT TTT AAA AGA AAA GGG GGG ATT GGG GGG TAC AGT GCA GGG GAA AGA ATA GTA GAC ATA 3′→
Sequence of the detection ssDNA bearing HRD enzyme	→5′CCT TTT CTT TTA AAA TTG TGG ATG AAT AC 3′→

target is performed by adding a second ssDNA (named detection probe) of 29 nucleotides bearing HRP enzyme (Horse Radish Peroxydase) at its extremity (Table 10.4). The added substrate is oxidized by HRP leading to colored medium, which quantified by UV spectrophotometer. The intensity of the coloration is quantified using a UV spectrometer at 492 nm wavelength (34).

This study is necessary in order to evaluate the specificity and the accessibility of the capture probes. This ELOSA method clearly reveals the presence of detection ssDNA at the surface of the magnetic particles. In addition, the amount of ssDNA (capture probe) at the magnetic particles surface increases as a function of streptavidin immobilized amount on the particles before reaching the surface saturation. It is interesting to notice that ELOSA technique is not quantitative and can be used for the qualitative and comparative aspects only.

10.5.2.3 Measurement and Determination of the Force–Distance Profiles The different studied systems are schematized on Fig. 10.12. The

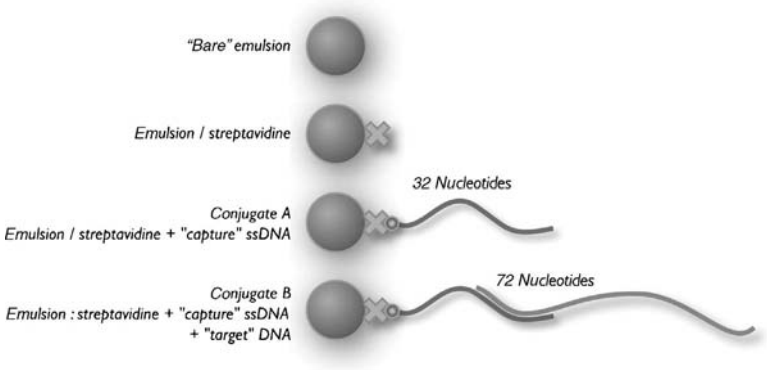

FIGURE 10.12 Schematic presentation of the system after each different step of the coupling and capture procedure (from Reference 34)

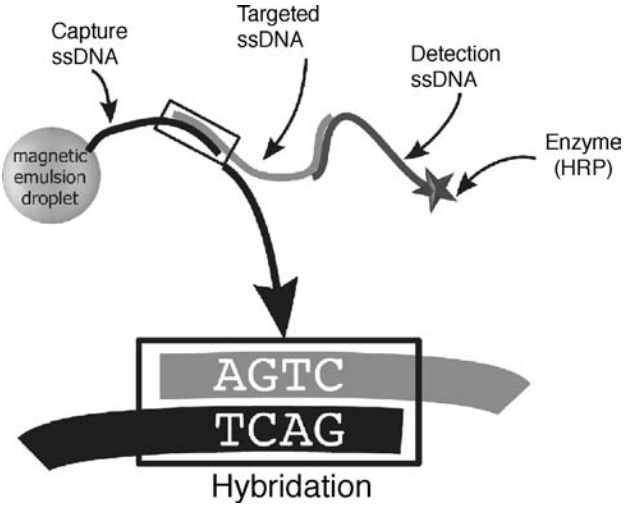

FIGURE 10.13 Schematic illustration of Enzyme Linked Oligo Sorbent Assay (ELOSA)

force–distance profiles (Fig. 10.14) of bare magnetic emulsion, streptavidin containing magnetic emulsion, capture probe containing particles (conjugate A) and target-capture probe containing particles (conjugate B) are examined in phosphate buffer (pH 8) solution of concentration 10^{-3} M (an equimolar mixture of Na_2HPO_4 and NaH_2PO_4), Triton X-405 at a concentration of 1 g/L (around CMC/2). They are exponentially decaying. Since, the droplets interfaces are charged, one can compare these data with what is expected from a double layer electrostatic type of repulsive force (Eqs. 10.4 and 10.5).

TABLE 10.4 Values of and Deduced from the Fit of the Data of Figure 10.14 Using Equation (10.5) (from Reference 34).

System	[a]κ^{-1}, nm	[b]κ^{-1}, nm	[c]Effective salt concentration, M	[d]Surface potential, mV
Bare emulsion		4	5.8×10^{-3}	26.9
Emulsion + streptavidin		3.3	8.5×10^{-3}	20.9
Conjugate A	4.1	5.4	3.2×10^{-3}	43.5
Conjugate B		5	3.7×10^{-3}	41.6
Conjugate B + "detection" ssDNA		5.26	3.3×10^{-3}	38.4

[a]Calculated using Equation (10.6).
[b]From the best fit using Equation (10.5).
[c]Concentration deduced from the fit using Equation (10.5).
[d]Surface potential deduced from the best fit using Equation (10.5).

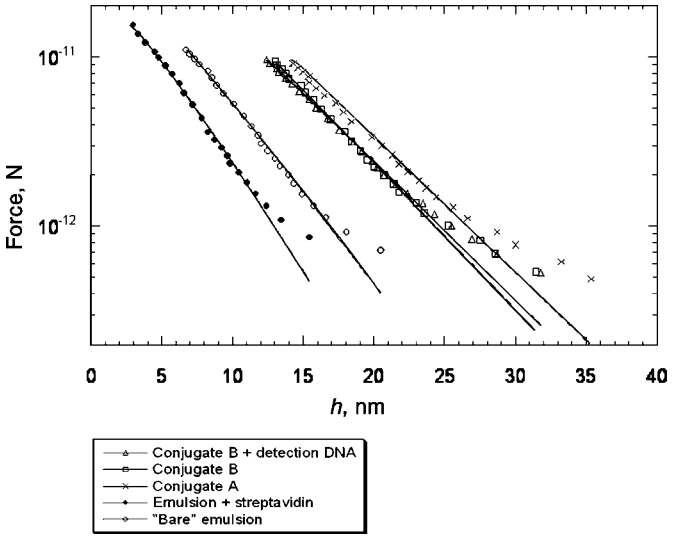

FIGURE 10.14 Force–distance profiles between emulsion droplets performed at pH 8 and at each step of the coupling procedure (from Reference 34)

In the first investigated medium, at pH 8, the effective concentration should be around 5.5×10^{-3} M if considering that the most stable state of phosphoric acid is HPO_4^{2-}. Such a concentration value leads to a Debye length of around 4.1 nm.

The best fit of the data reported in Fig. 10.14 leaving κ^{-1}, ψ_0, and C_{eff} as free parameters are reported in Table 10.4. The magnetic dispersion containing streptavidin only is found to be not as stable as the other systems under magnetic field. In fact, once a magnetic field is applied to the droplets, they remain attached one to the others. This might be due to a decrease in the droplets surface potential as streptavidin is coupled onto the surfaces. However, it is not easy to understand such an effect without additional information on the surface state.

Whereas, the profiles in the case of ssDNA containing droplets are repulsive in nature in all three cases (i.e., conjugate A, conjugate B, and conjugate B plus the detection probe). However, the values of κ^{-1} (or equivalently the values of C_{eff}) deduced from the fitting procedure are significantly different. The obtained forces can be explained not only in terms of purely electrostatic contribution but also in the presence of steric interactions. In fact, the presence of ssDNA molecules induced a significant increase in the magnitude of the force. This increase can be attributed to an increase in the surface potential and in the thickness of the adsorbed ssDNA layer (2,5).

Unfortunately, it appears very few differences between conjugate A and B, which means that, under such conditions for such surfaces, it is problematic to deduce exactly the amount of target ssDNA captured by the ssDNA capture probe using this force measurement based technique.

Such a mismatch between the expected double layer contributions is confirmed by the experiments performed with the conjugate A as a function of ionic strengths

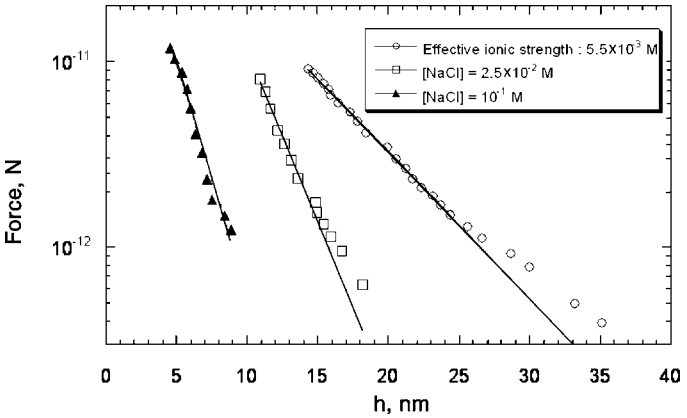

FIGURE 10.15 Force-distance profiles between emulsion droplets performed at pH 8, with conjugate A, as function of the ionic strength. (from Reference 34).

(Fig. 10.15). The solid lines correspond to the fitting of the data leaving both ψ_0 and κ^{-1} as free parameters of the fit. The differences between the obtained κ^{-1} and the one deduced from Equation 10.6 to the ψ_0 are too large to be attributed to an experimental uncertainty (see Table 10.5). The observed difference can be attributed to the macromolecular conformation of the interfacial nucleic acid molecules. In fact, the conformation of immobilized single stranded short ssDNA fragments onto colloidal particles was found to be pH and ionic strength dependent as examined by small angle neutron scattering studies (35). The thickness layer of high grafted oligonucleotide amount ($\sim$0.8 mg/m^2) was reported to be in between 6 and 12 nm as a function of pH and ionic strength (36).

The effect of pH on the repulsive forces between ssDNA-droplets conjugates was examined and is reported in Figs. 10.16 and 10.17 and the values deduced from the best

TABLE 10.5 Values Deduced from the fit of the Fata of Figure 10.15 to Equation 10.5 (from Reference 34).

System	[a]κ^{-1}, nm	[b]κ^{-1}, nm	[c]Effective salt concentration, M	[d]Surface potential, mV
Bare emulsion		3.4	8.1×10^{-3}	22.2
Emulsion + streptavidin + "capture" ssDNA	3.9	4.8	4×10^{-3}	39.2
Emulsion + streptavidin + "capture" ssDNA + "target" ssDNA		4.8	4×10^{-3}	36.6

[a]Calculated from Equation (10.6).
[b]From the best fit using Equation (10.5).
[c]Concentration deduced from the fit using Equation (10.5).
[d]Surface potential deduced from the best fit using Equation (10.5).

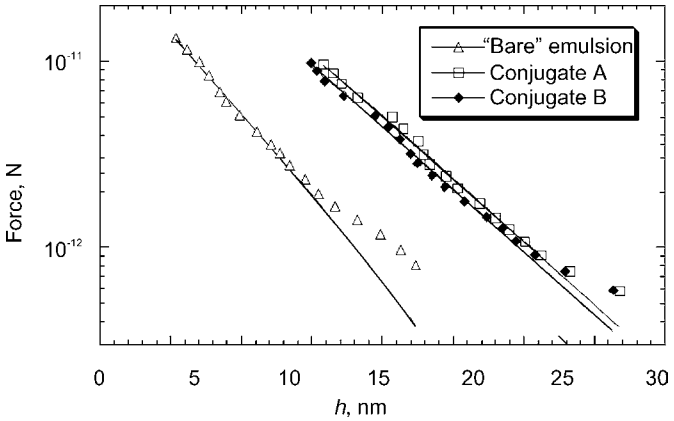

FIGURE 10.16 Force–distance profiles between emulsion droplets performed at pH 6 and at each step of the coupling procedure (from Reference 34)

fits are reported in Table 10.6. The tendency of results obtained shows no evidence of target ssDNA captured by the capture probes on the magnetic particles.

The literature on forces measurement between two surfaces coated with polyelectrolytes is rather abundant (37). In fact, various interfaces have been reported such as polyelectrolyte brushes (38), mixed surfactant-polyelectrolyte layers (39), polyelectrolytes multilayers (40), nanoparticles-polyelectrolytes systems (41). The reported forces are generally the combination of both electrostatic and steric in nature (42). When electrostatic interactions are the main forces, the calculation of the characteristic Debye length is not obvious (43) and can certainly not be performed using Equation 10.6. In the case of ssDNA-magnetic droplets conjugates, the main

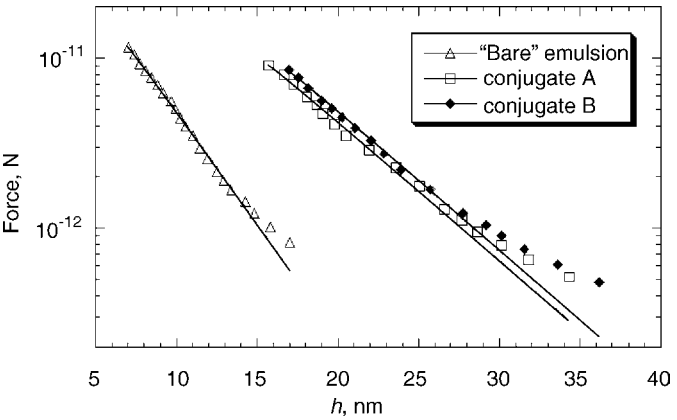

FIGURE 10.17 Force–distance profile between emulsion droplets performed at pH 11 and at each step of the coupling procedure. (from Reference 34)

TABLE 10.6 Values Deduced from the Fit of the Data of Fig. 10.16 Using Equation (10.5) (from Reference (34)).

System	[a]κ^{-1}, nm	[b]κ^{-1}, nm	[c]Effective salt concentration, M	[d]Surface potential, mV
Bare emulsion		3.2	8.4×10^{-3}	30.6
Emulsion + streptavidin + "capture" ssDNA	3.9	5.3	3.3×10^{-3}	54.1
Emulsion + streptavidin + "capture" ssDNA + "target" ssDNA		5.3	3.3×10^{-3}	53

[a]Calculated from Equation (10.6).
[b]From the best fit using Equation (10.5).
[c]Concentration deduced from the fit using Equation (10.5).
[d]Surface potential deduced from the best fit using Equation (10.5).

trends seem to follow the Debye Hückel approach presented even though the use of Equation 10.6 does not lead to the expected experimental value for the effective ionic strength of the investigated system. The possible explanation of this can be due to a possible rearrangement of the ssDNA (polyelectrolytes in nature) layer as the interdroplet distance decreases.

10.6 FURTHER DEVELOPMENTS: SILICA COVERED FERROFLUID EMULSIONS

In this section, we present the preparation of new magnetic supports that are constituted of a core made of ferrofluid embedded into a silica shell. Our idea here is to perform some new magnetic carriers exhibiting a silica surface that in principle should allow for some new possibilities for the grafting of functions different from the one usually grafted onto polymer latex particles.

10.6.1 Preparation of the Particles

To promote such a growth of the silica shell, we used the process first exploited by Schacht et al. (44). The process consists of previously adding a small amount of tetraorthosilane (TEOS) in the organic phase of the ferrofluid emulsion. Then, when suspended in the continuous aqueous phase of the system, the pH can be increased in order to trigger the hydrolysis-condensation of TEOS in water according to the following sol-gel reaction (45):

Hydrolysis step:

$$Si(OC_2H_5)_4 + xH_2O \rightarrow Si(OC_2H_5)_{4-x}(OH)_x + xC_2H_5OH$$

Condensation step:

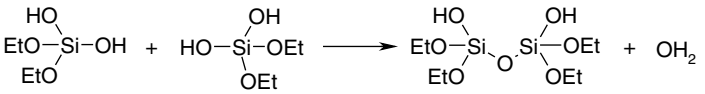

Because the reaction can occur only with water and that the initial TEOS molecules are oil soluble only, the reaction can be confined at the oil–water interface leading to the formation of a thin silica layer around the droplets. This process can also be used in inverted emulsion systems in order to perform water capsules dispersed in an organic phase (46). These reactions are catalyzed at low or high pH (45). In this case, we triggered the reaction by heightening the pH at a value of 12 by introducing NaOH in the continuous phase.

We first tested this process in a simple emulsion system with an oil phase composed of Dodecane (82 wt%) and TEOS (18 wt%) but containing no ferrofluid. To efficiently stabilize the emulsion, the droplets are suspended in an aqueous phase containing a surface-active polymer (polyvinyl alcohol, 0.5 wt%) and a cationic surfactant (tetradecyltrimethyl-ammonium bromide TTAB, CMC $= 3.6 \times 10^{-3}$ M) at a concentration of 2 CMC. Once the emulsion is performed, one increases the pH of the aqueous phase to a value around 12. This triggers the sol-gel reaction. In Fig. 10.18, we present some light microscopy picture of the system as a function of time.

Clearly, as time goes by, the surface of the emulsion droplets looks more and more crumpled as a result of the growth of the silica shell. When shearing the emulsion between two glass slides, it clearly appears that the inner part of the droplets is liquid. We then applied this process in the presence of the ferrofluid. However, the presence of the iron oxide particles gives some color to the system and prevents from the observation of the system using light microscopy. To get some insights into the structure of the system, we used freeze-fracture transmission electron microscopy. At room temperature, the samples are deposited on Cu planchettes and are afterward quenched rapidly by plunging them into liquid propane cooled to $-190°C$ by liquid nitrogen. The frozen samples are then introduced into a vacuum chamber and fractured

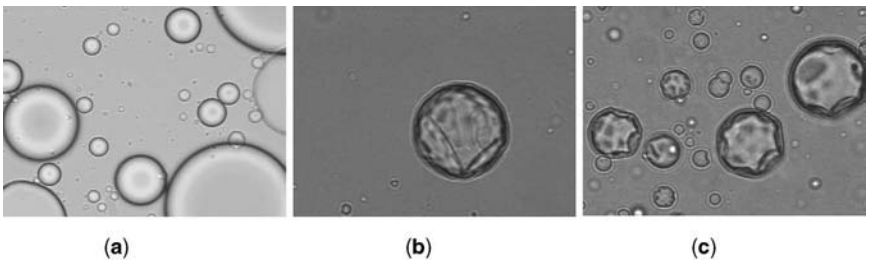

FIGURE 10.18 Light microscopy pictures of the dodecane/TEOS emulsion dispersed in the PVA/TTAB aqueous solution at pH 12 as a function of time after the addition of NaOH in the aqueous phase. (**a**) picture of the system at $t = 0$, (**b**) $t = 10$ min, (**c**) $t = 4$ days. Scale: 1 cm = 10 μm

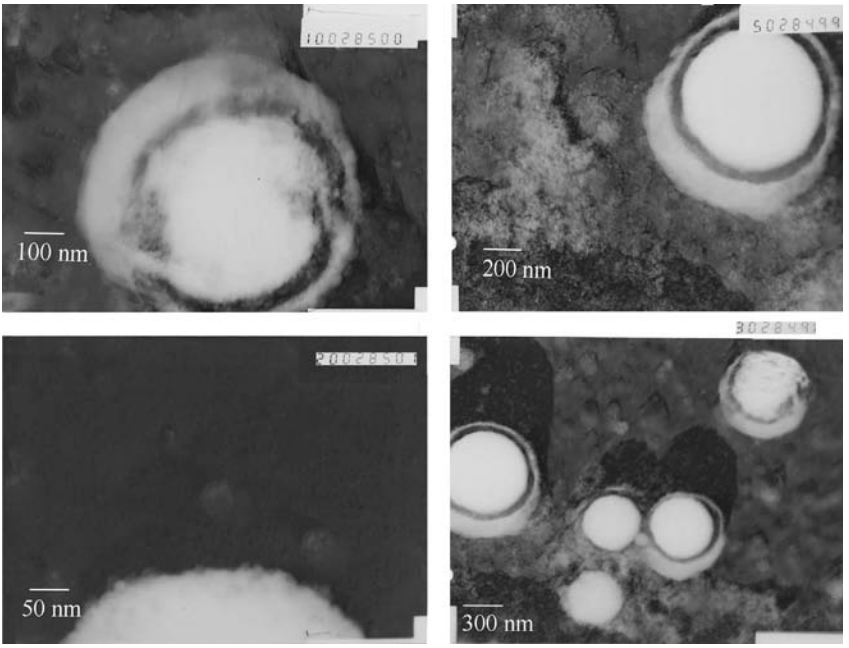

FIGURE 10.19 FF-TEM pictures of the emulsions made using the process described in the text. The ferrofluid appears as the grainy white centers of the droplets. The pictures clearly evidence the core-shell structure of the emulsions

at a temperature of $-150°C$. The replications are ensured by a shadowing of platinum, deposited at a 35° angle with respect to the fracture surface, followed by the deposition of a carbon film normal to the surface. The replicas are removed from the copper plate and cleaned in a surfactant solution to dissolve the emulsion droplets that are stuck to the replica. We observe the replica with a transmission electron microscope. This technique thus allows for the observation of fluid samples at the nanometric scale (47). The pictures obtained are presented in Fig. 10.19.

10.6.2 Force–Distance Measurements During the Sol-Gel Reaction

We have performed some force distance measurements between the droplets as the sol gel reaction takes place in the system (Fig. 10.20). First, the force–distance profile is measured in the emulsion before pH is increased but at the same ionic strength (using NaCl at 10^{-2} M) as in the emulsion containing NaOH. The observed profile is exponentially decaying. Such behavior is not due to a double layer repulsive force but to the presence of the polymer layer. Indeed, the range of the force is much larger than the one obtained at such ionic strength (using Equation 10.6, one gets $\lambda = 3.2$ nm, which is clearly much smaller than the characteristic decay length observed in Fig. 10.20). In the absence of NaCl and still without added NaOH, the range of the profile remains identical and the only change is the intensity of the force. This might be

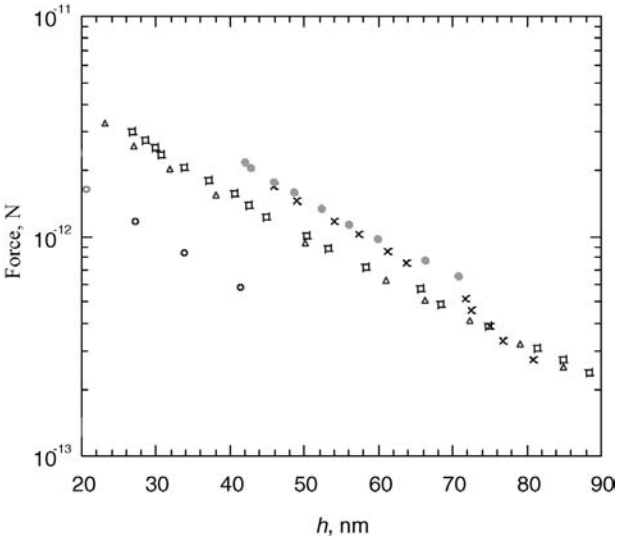

FIGURE 10.20 Force–distance profile between emulsion droplets at various pH (▲, □, at pH 5.5), (○, at pH 5.5, 0.2 M NaCl), (✗, at pH 12, min < t < 30 min) and (●, at pH 12, t > 1h)

due either to an increasing amount of adsorbed polymer in the absence of salt or to the presence of ionized oleic acid adsorbed at the droplet's surface. As NaOH is added to the system, one at the same time measures the force distance profile between the droplets. The first measured points are the one performed at large distances (low magnetic field). Interestingly, the points are on the same curve as the ones obtained at low pH. As the field is increased, the obtained profile deviates from this behavior and the higher field points are then found to lie above the one obtained at low pH. This means that, at a given forces, the surface are separated by a larger distance. Such an observation is compatible with the growth of a silica layer at the surface of the droplets. Finally, once the time exceeds 30 min, the force profile never looks back as it was before pH was increased, which is also consistent with the presence of a silica shell at the surface of the droplet.

10.6.3 Zeta Potential Measurements

In order to check the presence of silica at the surface of the particle, we measured the zeta potential of the droplets before and after modification as a function of pH (Fig. 10.21). Before the encapsulation process, the zeta potential of oil in water droplet is found to be negative irrespective of the used pH. This is due to the used negatively charged surfactant is the formulation recipe. The zeta potential of encapsulated oil in water magnetic droplets revealed the presence of the isoelectric point in between pH 4 and 5, which is attributed to the surface modification by inducing $-Si-O^-$ groups. The surface of ferrofluid core–silica shell droplets dispersed in PVA solution was modified by using (3-aminopropyl)triethoxysilane (APTS). The zeta potential analysis was found to be

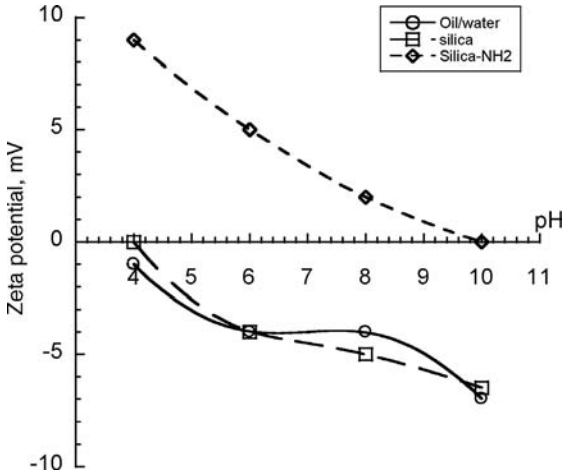

FIGURE 10.21 Zeta potential of oil in water magnetic droplets, ferrofluid core–silica shell and functionalized magnetic droplets as a function of pH

positive until pH 9. In addition, the zeta potential values increases with increasing the APTS amount used in the functional recipe. Such process revealed without any doubt, the possible preparation of liquid core bearing functionalized silica shell.

10.7 CONCLUSION

This short review shows the different possibilities of the force measurement technique between magnetic emulsion droplets. First, the determination of force profiles between emulsion droplets in the presence of surfactant molecules can be very well accounted by using the classical DLVO theory involving van der Waals and double layer forces. Then, steric forces in the presence of adsorbed polymers were explored and discussed. Depending on the architecture and on the adsorption amount of the used macromolecules, the characteristic force range is either proportional to the coil gyration radius or to their extended configuration length were discussed. In all cases, the obtained results are in agreement with the predictions from the theory. The situation is more complicated in solutions of proteins where the forces are shown to be steric in nature but do not obey the same law as the one observed for adsorbed polymers. The best possible fit of the data is shown to be an empirical power law, which is difficult to connect to any spatial conformation of the adsorbed proteins. In ssDNA-magnetic droplets systems, the results look closer to what expected for adsorbed polyelectrolytes and are not far from being understandable within the frame of the Debye theory. Only some slight deviations from the predictions are observed. The possibility of using the presented technique to measure the amount of immobilized ssDNA molecules at the interface looks promising but still requires some additional work before it can lead to any reproducible quantitative measurements for diagnostic purpose. The lack of precision might be due to the small quantities of grafted DNA at

the interface, which could in principle be improved. Finally, this short review demonstrated that magnetic emulsions (magnetic oil in water ferrofluid) can properly be turned into "isodense" silica shell—oil in water magnetic core using a sol-gel process. This process should be considered as challenging methodology for the liquid encapsulation for both *in vivo* diagnostic applications and for *in vivo* diagnostic and therapy applications.

ACKNOWLEDGMENTS

The authors thank the financial support from Le Conseil Régional d'Aquitaine. This work was financially supported by Mérieux's foundation as a grant for C. Genty.

REFERENCES

1. Elaissari A, Ganachaud F, Pichot C. Top Curr Chem 2003;227:169–193.
2. Ganachaud F, Pichot C, Elaissari A. Colloidal biomolecules, biomaterials and biomedical applications. In: Elaissari A, editor. Surfactant Science Series Volume 116. Marcel Dekker; 2003; pp.253–286.
3. Hatakeyama M, Nakamura K, Iwato S, Handa H, Fujimoto K, Kawaguchi H. Colloid surface B 1998;10:171–178.
4. Erout MN, Troesch A, Pichot C, Cros P. Bioconjugate Chem 1996;7:568–575.
5. Charles MH, Charreyre MT, Delair T, Elaissari A, Pichot C. STP Pharma Sci 2001;11: 251–263.
6. Elaissari A, Veyret R, Mandrand B, Chatterjee J. Colloidal biomolecules, biomaterials, and biomedical applications. In: Elaissari A, editor. Surfactant Science Series, Volume 116. Marcel Dekker; 2003; 1–26.
7. Häfeli U, Schütt W, Teller J, Zborowski M. Scientific and Clinical Applications of Magnetic Carriers. New York: Plenum Press; 1997; pp.1–26.
8. Arshady R. Microspheres Microcapsules & Liposomes: Radiolabeled and Magnetic Particles in Medicine & Biology 3. London: Citus Books; 2001.
9. Montagne F, Mondain-Monval O, Pichot C, Mozzanega H, Elaissari A. J Magn Magn Mater 2002;250:302–312.
10. Montagne F.Ph.D. Thesis, Claude Bernard University, 2002.
11. Montagne F, Braconnot S, Mondain-Monval O, Pichot C, Elaissari A. J Disper Sci Technol 2003;24:821–832.
12. Leal Calderon F, Stora T, Mondain-Monval O, Poulin P, Bibette, J. Phys Rev Lett 1994;72:2959.
13. Mondain-Monval O, Leal Calderon F, Bibette J. J Phys II 1996;6:1313.
14. Mondain-Monval O, Espert A, Omarjee P, Bibette J, Leal Calderon F, Philip J, Joanny, J-F. Phys Rev Lett 1998;80:1778.
15. (a) Espert A, Omarjee P, Bibette J, Leal Calderon F, Mondain-Monval O. Macromolecules 1998;31:7023.(b) Omarjee P, Hoerner P, Riess G, Cabuil V, Mondain-Monval O. Eur Phys J E 2001;4:45.

16. Rosensweig RE. Ferrohydrodynamics, New York: Cambridge University Press; 1985.
17. Bibette J. J Colloid Inter Sci 1990;147:474.
18. Lissant KJ. Emulsion and Emulsion Technology 6. New York: M. Dekker; 1974. Becher P. Emulsions: Theory and Practice. New York: Reinhold; 1965.
19. Zhang H, Widom M. Phys Rev E 1995;51:2099.
20. Israelachvili JN. Intermolecular and Surface Forces. San Diego: Academic; 1985. Hunter RJ. Zeta Potential in Colloid Science. New York: Academic Press London; 1981.
21. Ogino K, Abe M. Mixed Surfactant Systems. New York: Marcel Dekker; 1993. Poulin P. Thesis University Bordeaux I(1995) (unpublished).
22. Dolan AK, Edwards SF. Mushrooms Proc Roy Soc 1974;337:509. Alexander S. Brushes J Phys (Paris). 1977;38:983.de Gennes PG. Macromolecules 1980;13:1069.
23. Taunton HJ, Toprakcioglu C, Fetters LJ, Klein J. Macromolecules 1990;23:571. Kuhl TL, Leckband DE, Lasic DD, Israelachvili JN. Biophys J 1994;66:1479.
24. Semenov AN, Bonet-Avalos J, Johner A, Joanny J-F. Macromolecules 1996;29:2179. Semenov AN, Bonet-Avalos J, Johner A, Joanny J-F. Macromolecules 1997;30:1479.
25. de Gennes, PG. Macromolecules 1981;14:1637. de Gennes, PG. Macromolecules 1982;15:492. Scaling Concepts in Polymer Physics. London: Cornell University Press; 1979.
26. Omarjee P, Espert A, Mondain-Monval O, Klein, J. Langmuir 2001;17:5693.
27. Dimitrova TD, Leal-Calderon F. Langmuir 1999;15:8813.
28. Roth CM, Neal BL, Lenhoff AM. Biophys J 1996;70:997.
29. (a) Turro NJ, Xue-Gong L, Ananthapadmanabhan KP, Aronson M. Langmuir 1995;11:2525. (b) Guo XH, Zhao NM, Chen SH, Teixeira J. Biopolymers 1990;29: 335.
30. Fitzpatrick H, Luckham PF, Eriksen S, Hammond K. Colloid Surface 1992;65:43.
31. Narsimhan G. Colloids Surf 1992;62:41.
32. Velev OD, Campbell BE, Borwankar RP. Langmuir 1998;14:4122.
33. Mondain-Monval O, Philip J, Leal-Calderon F, Bibette J. Phys Rev Lett 1995;75:3364.
34. Montagne F, Braconnot S, Elaïssari A, Pichot C, Daniel JC, Mandrand B, Mondain-Monval O. J Nanosci Nanotechnol 2006;6:2312–2319.
35. Elaïssari A, Chevalier Y, Ganachaud F, Delair T, Pichot C. Langmuir 2000;16:1261–1269.
36. Walker HW, Grant SB. Langmuir 1996;12:3151–3156.
37. Claesson, PM. Surface Force Apparatus: Studies of Polymers, Polyelectrolytes and Polyelectrolyte-Surfactant Mixtures at Interfaces. In: Dubin P, Farinato R, editors. Calloid-Polymer Interactions: From Fundamentals to Practice. New York: John Wiley & Sons; 1999. pp. 287–330.
38. Balastre M, Li F, Schorr P, Yang J, Mays JW, Tirrell MV. Macromolecules 2002;35:9480. Abraham T, Giasson S, Gohy JF, Jerome R. Langmuir 2000;16 (9):4286–4292.
39. Anthony O, Marques CM, Richetti P. Langmuir 1998;14 (21):6086–6095.
40. Kulcsar A, Lavalle P, Voegel JC, Schaaf P, Kekicheff P. Langmuir 2004;20 (2):282–286.
41. Sennerfors, T, Fröberg, JC, Tiberg, F. J Colloid Interf Sci 2000;228 (1):127–134.
42. Pincus P. Macromolecules 1991;24:2912. Borisov OV, Zhulina EB, Birshtein TM. Macromolecules 1994;27:4795.

43. Tadmor R, Hernandez-Zapata E, Chen N, Pincus P, Israelachvili JN. Macromolecules 2002;35 (6):2380–2388.
44. Schacht S, Huo Q, Voigt-Martin IG, Stucky GD, Schüth F. Science 1996;273:768.
45. Brinker CJ, Scherer GW. Sol Gel Science: The physics and chemistry of sol-gel processing. San Diego, CA: Academic Press; 1990.
46. Fornasieri G, Badaire S, Bakov R, Mondain-Monval O, Zakri C, Poulin P. Adv Mater 2004;16:1094.
47. Mondain-Monval O. Curr Opin Colloid Interf Sci 2005;10:250–255.

CHAPTER 11

Particles for Protein Analysis in Microfluidic Systems

ANNE LE NEL

Laboratoire PCC, Institut Curie (UMR CNRS/IC 168), Paris Cedex 05, France
JE 2495 Protéines et Nanotechnologies en Sciences Séparatives, Université Paris XI, Châtenay-Malabry, France

MYRIAM TAVERNA

JE 2495 Protéines et Nanotechnologies en Sciences Séparatives, Université Paris XI, Châtenay-Malabry, France

JEAN-LOUIS VIOVY

Laboratoire PCC, Institut Curie (UMR CNRS/IC 168), Paris Cedex 05, France

11.1 INTRODUCTION

After the success of the human genome project, and the following sequencing of an increasing number of genomes of various organisms, the focus of methodological research in high throughput analysis is progressively shifting toward proteomics, the unavoidable partner of genomics in systems biology (1). The first and still widely expected applications from proteomic studies are the identification of all (or, more reasonably, the highest possible number of) proteins contained in one proteome. This task typically implies to separate the proteins with the highest resolution and sensitivity possible and identify each "spot." In many applications, it is also necessary to have a quantization of the relative concentration of proteins of interest in a sample. In particular, level of expression of specific "biomarker" proteins is extensively used for diagnosis, or for unraveling the effect of drugs on different metabolic paths, for drug discovery. More refined studies of proteins may also involve the characterization of protein posttranslational modifications (also often useful as powerful biomarkers of diseases), or studies of protein–ligand interactions.

Colloidal Nanoparticles in Biotechnology, Edited by Abdelhamid Elaissari
Copyright © 2008 John Wiley & Sons, Inc.

The increasing activity in this area makes the development of new techniques highly desirable. Several issues make the analysis of proteins much more challenging than that of nucleic acids. First, no amplification such as PCR exists in the protein world, so that one has to "live with" the quantity of a given protein in the initial sample, putting a strong challenge on the sensitivity of the detection method. This challenge is further hardened by a huge dynamic range of concentrations. One single type of protein, such as actin in the cytoplasm or albumin in blood, can represent alone more than 10% or 20% of the total proteinaous mass, and some essential other ones, such as signaling proteins, may be present at subpicomolar concentrations (down to a few hundred copies only per cell). These low abundance proteins are often the most interesting for biological and medical applications. Another difficulty lies in the hydrophobicity of numerous proteins, in particular, the biologically very important membrane proteins (they are designed to lie embedded in the lipidic membrane of cells). These proteins are difficult to dissolve and to separate in aqueous media. Overall, low abundance proteins and membrane ones (the second category mostly included in the first one) remain largely *terrae incognitae*. Still today, about one third of the proteins, the genome is expected to code for, have unknown function!

Also, most proteins lie within a relatively limited range of sizes, typically from 15,000 Da to 200,000 Da, but they present a huge chemical diversity. They can involve any of the 20 amino acids, either acidic or basic, and with very different hydrophobicities, in a specific sequence. They may adopt various complex secondary structures and are folded into tertiary structures, which give each of them a very unique pattern of recognition, signaling, and biological properties. Mass Spectrometry, with its unchallenged mass resolution, is presently the gold method in proteomics, but it can be operated with high resolution in a limited range of sizes only, typically up to a few kDa. Also, its resolution is still by far insufficient to separate all of the different proteins and peptides contained in a complex sample such as serum or a cell extract, so that in practice, MS is mostly applied in combination with electrophoresis or chromatography as a "post column" separator and detector. The method still mostly employed is two-dimensional gel electrophoresis (separation according to isoelectric point in a pH gradient, followed by separation by size thanks to migration within a sieving media of SDS–protein complexes). This method is very labor intensive, but it is still widely employed due to its still unchallenged peak capacity (several thousand). An alternative method to 2D-gel electrophoresis is 2D chromatographic separation of the proteins. It can include, for example, fractionation on a cation exchange column followed by a gradient elution on a C18 reverse phase column. After the excision of the subsequent spots (from 2D gel electrophoresis) or collection of the protein fractions (after chromatography), the proteins are submitted to proteolytic digestion by trypsin that cut proteins after specific amino acids. This yields a series of peptides that can often provide a unique "signature" of a protein. The power of peptide mapping was considerably increased by genome sequencing: knowing the entire genome of an organism, one knows the sequence of all the proteins it can code for, including those which have never been identified, or the function of which is not known. These sequences and numerous useful annotations (sequence similarities with other proteins with a known function, etc.) are now

gathered in large databases, such as the famous "SwissProt," and have accelerated considerably the identification of proteins in the last years. As a second advantage, tryptic digest yields peptides that are in the optimal range of resolution and sensitivity for MS, unlike most native proteins.

Besides these proteomic applications, in which a large number of proteins have to be treated simultaneously, numerous applications, focused on the identification or just on the quantization of a limited number of proteins, exist, in particular, for diagnosis purposes. These applications still rely heavily on immunoassay-type methods, such as agglutination or ELISA tests, using the very specific interaction of proteins with antibodies directed against them. Even in diagnosis, however, the trend is toward multiparametric analysis (involving several to several tens of different biomarkers), which bears the potential of more powerful diagnosis and more accurate treatment design. Thus, both fundamental research and diagnosis are in a need of protein analysis methods with high level of parallelism, automation and sensitivity. Microfluidic systems or "lab-on-chips" pave the route to such progress, and bear the promise of entirely new molecular analysis systems (2–4).

In addition to molecular separation or assays, briefly recalled above, the analysis of a biological sample generally involves sample preparation steps that can represent a significant cost and delay in the analysis process, and microfluidics also seems well suited to integrate such steps into a single, fully automated device ("lab on chip"). This, however, raises numerous challenges, for which micro- and nanoparticles can provide very powerful helps (as we shall now see).

The use of particles (also called beads) in analytical techniques has become a field of strong interest (5,6). Indeed, they present a lot of advantages. First, they are available within controllable sizes and with inorganic or organic polymer core composition. They can be manipulated using electric fields, pressure driven flow, gravity, or simple shaking. They can be coated with biological molecules to make them interact with or bind to a biological entity. In contrast to a direct coating of the surface of the analytical device, this biofunctionalization can be performed in a batch process, and the particles prepared and characterized in a single batch can be used to prepare thousands of different test elements. For diagnosis applications, in which cost is a major issue, this is a considerable advantage. Moreover, particles offer a much larger surface to volume ratio than functionalized planar surface (typically increased hundred fold or more, for micron-sized particles), allowing for higher sensitivity and dynamic range. Magnetic beads offer an additional advantage: because of their magnetic core, they can be magnetically manipulated with an external magnetic field and thus be easily extracted and resuspended in a different solution without centrifugation. Numerous suppliers now propose various colloids for biological assays, demonstrating the practical interest of these materials.

In this review, we describe a series of applications illustrating the wide use of particles for protein analysis in Microsystems. These applications typically raise four challenges:

- The preparation of the beads: This aspect has been extensively discussed elsewhere in this book and will not be considered here again.

- The manipulation and packing of the beads into the microchannel: This aspect is of particular importance, since the preparation of good and reproducible packed beads columns in microfluidic systems is much more difficult than in conventional chromatography microcolumns. This is due to, in particular, the smaller dimensions and weaker mechanical resistance of microchannel, as compared to tubular microcolumns.
- The manipulation of the fluids in the resulting system. In contrast to the previous point, this manipulation is in general facilitated by the microfluidic format, in which connections with no dead volume can be easily fabricated. The possibility of integrating complex protocols and steps is indeed one of the powers of microfluidic systems. Problems remain, however, associated in particular with the very small volumes of liquid to be manipulated (in the μL or nL range). The conventional tools for fluid manipulation, such as peristaltic, piston, or syringe pumps, are poorly adapted to microfluidic systems.
- The detection: The detection of proteins in microsystems is challenging for several reasons: first, the reduced volume tends to reduce the total quantity of proteins captured. Second, chips are generally fabricated in materials that are not transparent in the UV (quartz chips exist but are extremely expensive), preventing the use of UV absorption, the most common detector in chromatography or capillary electrophoresis of proteins. Finally, staining is not as easy as with gels. This latter disadvantage has to be minored, however, by the fact that staining is an expensive and slow process that the current trend of high throughput and automation tends to avoid anyway.

These different aspects must be taken into account simultaneously when designing a microfluidic system for protein analysis. In the following, we shall provide an overview on the variety of strategies proposed in the literature to integrate bead-based assays or analyses in microfluidic systems, taking into account the packing challenge.

11.2 GEOMETRIC IMMOBILIZATION OF PARTICLES

A simple strategy for bead immobilization, developed by several groups, relies on the use of geometrical obstacles. The resulting structures must satisfy the dual purpose of holding particles while still allowing sample and reagents to be delivered to the chip.

Oleschuk et al. created a chamber demarcated by two weirs and applied this device to Solid Phase Extraction (SPE) and Capillary ElectroChromatography (CEC) on chip. A 200 μm long, 580 μm wide and 10 μm deep cavity was etched into the glass, with its inlet and outlet channels obstructed by 9 μm high weirs to leave a 1 μm gap for sample and reagents introduction. Beads larger than 1 μm in diameter were introduced through a transverse channel (30 μm wide) and trapped between the weirs (see Figure 11.1). In their first experiment, these authors immobilized in the cavity octadecylsilane coated silica beads of 1.5–4 μm in diameter. Eluted fractions were analyzed by Laser Induced Fluorescence in an off-line mode. Beads packing and liquid

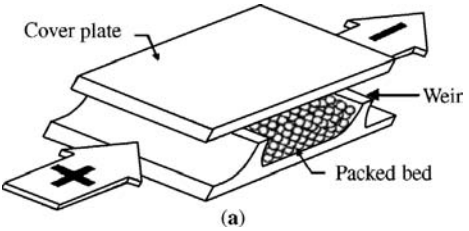

FIGURE 11.1 Scheme of the packed chamber obtained by creating weirs in a microchannel (with permission from Reference (8))

handling were performed using electroosmotic flow. The SPE was performed on BODIPY reagent and preconcentration factors of 80–500 for preconcentration times ranging from 120 to 532 s were obtained. The CEC experiments showed complete elution and separation of BODIPY and fluorescein in less than 20 s (7). Thanks to the external channel for beads handling, the chromatographic bed can be easily removed and refreshed with new beads. An additional advantage is that a wide variety of stationary phases are available, so that different retention mechanism can be used. This device is more reproducible than creating a frit (common technique in capillary format), in terms of formation and positioning of the packed beads. In later publications, this group improved the length of the chromatographic bed and added a cross injector in order to increase the efficiency of the analysis. They demonstrated, for example, that using a bead-based SPE step, they could decrease the detection limit from 30 pM to 70 fM for a fluorescent dye, with a very good reproducibility (8,9).

Along the same line, Wang et al. developed an integrated device comprising an enzymatic reactor (based on the grafting of trypsin on agarose beads of 40–60 μm in diameter) associated to electrophoresis separation and coupled to electrospray mass spectrometry (ESI-MS). The chamber for beads immobilization was 800 μm wide, 150 μm deep, and 15 mm long. The channels for sample and reagents transport and separation were 10 μm so that beads bigger than 10 μm in diameter were physically maintained in the chamber. Solutions of melittin, cytochrome C, and bovine serum albumin were passed through the trypsin reactor bed at different flow rates from 0.5 to 60 μL/min. Complete digestion was obtained faster on chip (5 s) than in a classical cuvette (15 min) for melittin, due to an increased ratio of enzyme to substrate and decreased diffusion time (10). Based on the same packing method, Li et al. (from the same group) developed another example of partly integrated device. The large channel was filled with C18 reverse phase or antibody-coated beads made of mixed bed (beads of 40 μm and 5 μm in diameter). The device integrated sequential injection, preconcentration followed by Capillary Electrophoresis (CE) separation and interface to mass spectroscopy analysis (see Figure 11.2). It led to the detection of fmol of digest peptides and a throughput of 12 samples per hour (11).

Sato et al. presented a new method to create a physical barrier in a microchip. The solid phase, made of polystyrene beads, was retained by a single microfabricated dam. The microdevice was made of glass plates and involved different technologies for its

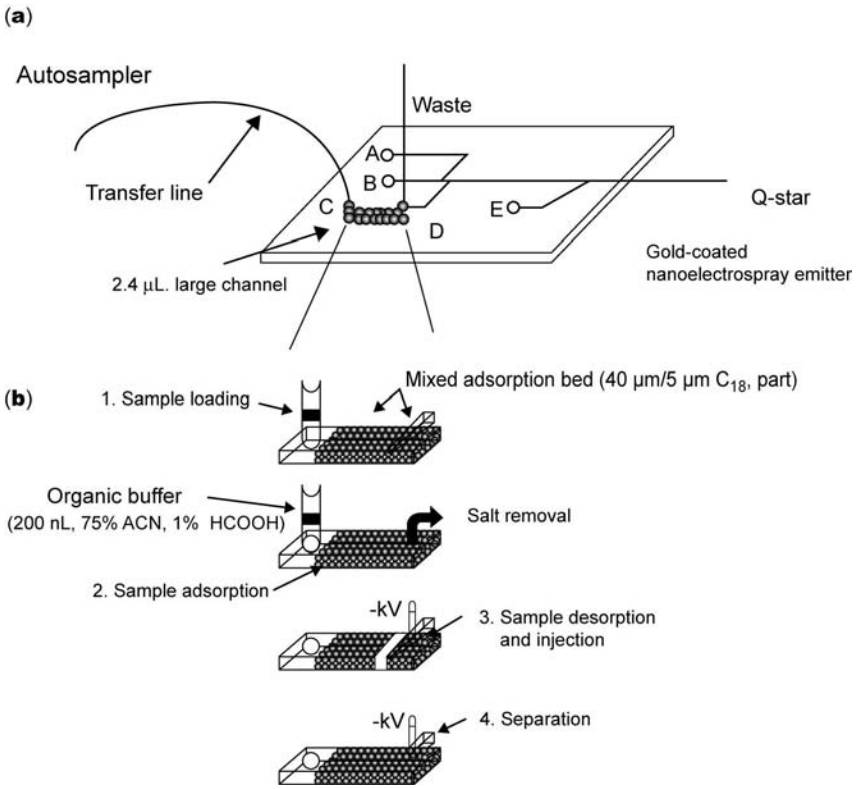

FIGURE 11.2 Scheme of the device, created by Li et al. integrating preconcentration step, electrophoretic separation, and electrospray interface (from Reference (11)). (**a**) View of the device. (**b**) Sequential steps

fabrication such as soft lithography, fast atom beam fabrication, and lamination. It used restrictions of the height of the channel from 100 to 10 μm to immobilize the beads (see Figure 11.3 left) on a well-defined region. The beads could be removed from the microchannel by applying reverse flow, and the bed reactor could be easily reformed in a reproducible manner. In their first experiment, the authors used 45 μm diameter beads on which human secretory IgA (s-IgA) was adsorbed, packed them in the microchannel, and passed solutions of anti-s-IgA labeled with colloidal gold through the beads reactor. The on-chip detection was made by thermal lens microscopy. The results showed a reduced reaction time of the complete procedure from 24 h in classical format (12) to less than 1 h. In a following study, these authors developed a sandwich immunoassay using three antibodies (for capture and detection) for the analysis of a colon cancer marker. They obtained reduced time analysis (45 h to 35 min) and detection limits more than one order of magnitude lower than conventional tests (13). Finally, they created bead-bed immunoassay systems for

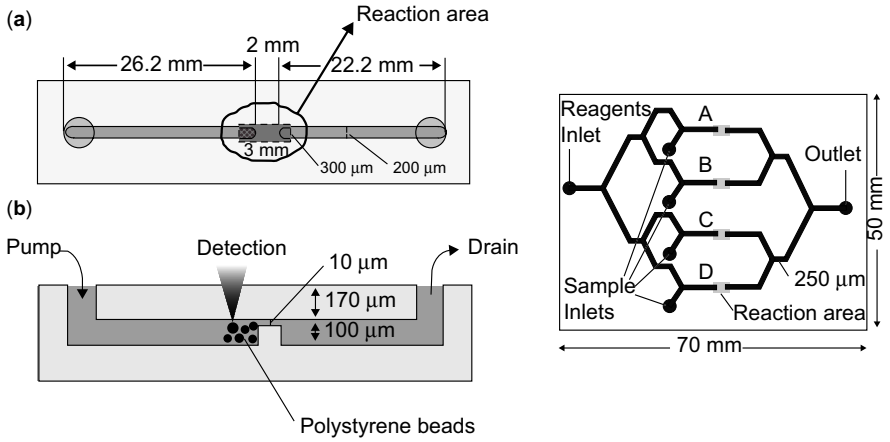

FIGURE 11.3 Scheme of the microdevice with the fabricated "dam" fixing the beads inside the microchannel, overview (left (**a**)) and a cross section (left (**b**)). Overview of the glass microchip for 4 simultaneous assays (right) (adapted from References (12,14))

simultaneous assays in high throughput reactions (see Figure 11.3 right). The glass device was composed of four reaction and detection chambers with branching channels, reducing the number of pumps needed in the process. It took only 50 min to perform the complete analysis of four samples of interferon γ, compared to the 35 min necessary for one sample (14). The main disadvantage of this approach, based on microfabricated weir, is the size of the beads (higher than 40 μm in diameter), which limits the surface to volume ratio.

Murakami et al. used antibody-coated beads of 90 μm in diameter, also immobilized by a dam, to detect, by fluorescence measurements, an immunosuppressant, FK506 labeled with HRP (Horse Radish peroxidase). A limited number of beads (1 to 10) were injected into the channel before sealing it to glass. With this microflow chip, they obtained a sensitivity about 1000-fold higher than that obtained with classical ELISA method. The major drawback of this pre-sealing immobilization method is that the beads can't be removed easily (15), leading to a single-use device.

An additional approach for creating retaining features was proposed by Andersson et al. It involved the fabrication of pillars acting as filters to retain the beads in a chamber. The device was made by deep reactive ion etching and anodic bonding; techniques allowing for uniform and reproducible fabrication process. Pictures of the reaction chamber are presented in Figure 11.4. This device presents various advantages such as the easy removal of the beads (by applying backpressure), the confined area of the packed beads, which facilitates on-chip detection (optical detection), and finally, the rare and reversible clogging of the filter. These authors tried to immobilize two types of beads, polystyrene beads (5.50 μm) and magnetic ones (2.8 μm), but the smaller beads easily passed through the filters (16). The capacity to perform biological reaction in the chamber

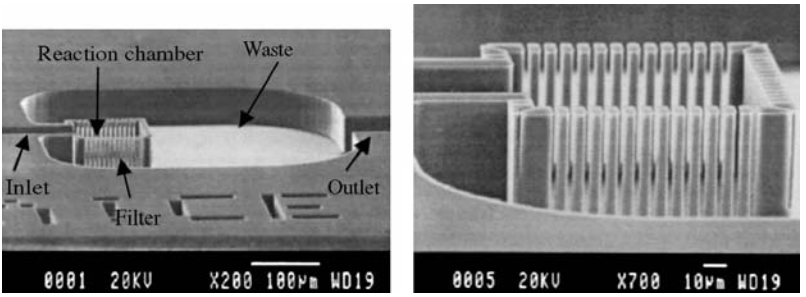

FIGURE 11.4 A SEM view of the microfabricated device with the pillars (left). A SEM image of the reaction chamber in side view (right). The dimensions are given in the pictures (adapted from Reference (16))

delimited by the pillars was demonstrated on single nucleotide polymorphism analysis (17,18) while integrating passing valves in the microchip.

Ali et al. created a device in which individual agarose microbeads (300 µm in diameter) were positioned into chemically etched microcavities patterned in a square array inside hybrid microchip of PolyDiMethylSiloxane (PDMS) and Silicon (19). Each cavity served as a miniaturized reaction vessel and analysis chamber (see Figure 11.5). They coated their beads with specific antibodies and applied their device to the detection of C-reactive protein by fluorescence measurement. They obtained a detection limit of 1 ng/mL with a device made of a single chamber. The use of a four-chamber design (in a single device) showed the same signal with an error of less than 10% for the same solution (20).

One additional example of packing beads in microchannel with a specific geometry was proposed by Ceriotti et al. They developed a miniaturized device where particles were immobilized via a tapered channel for on-chip CEC application. They created a tapered geometry in PDMS microchip to induce particles aggregation by a Keystone effect. Beads were introduced in the column from the buffer waste reservoir (by

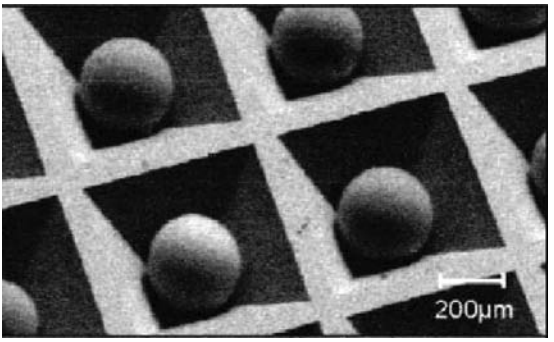

FIGURE 11.5 Scanning electron photography of the pyramidal wells designed to confine the beads (with permission from Reference (19))

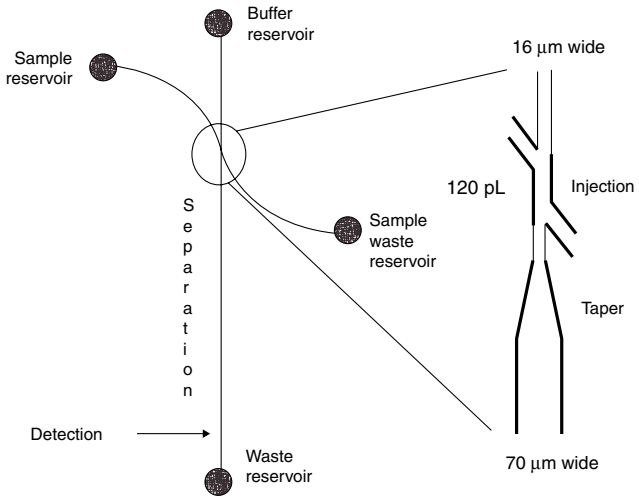

FIGURE 11.6 Chip layout for fritless CEC in PDMS microchip: the channel consisted in ≪double-T≫ injection and a gradual tapering just below the intersection (from Reference (21))

pressure) and drawn toward the intersection (see Figure 11.6). The first particles aggregated and blocked the others, allowing the growth of the packed bed in the opposite direction toward the waste. The packing beads were stabilized by a thermal treatment at 115°C. The authors packed this way porous octadecylsilanized silica microspheres of 3 μm in diameter and separated methanol and benzaldehyde (neutral compounds) in less than 15 s (21). The reproducibility of a given column was quite good (2%) but intercolumn variability was significant. However, this system presents various drawbacks. The heating stabilization step hinders the use of precoated particles and the column is not reusable, since the beads can't be released from the channel.

Numerous methods, consisted in creating filters or grids inside the microchannel to fix the beads, were developed. For example, Buranda et al. developed a miniaturized assay for performing single (or multiple) analytes detection. They designed obstruction 20 μm apart patterned as a filter to hold 30 μm beads. This blocking layer was used to hold subsequent layer of smaller beads (20 μm streptavidin-coated glass beads) (22). A third layer of 10-μm beads was used to minimize the dispersion of active beads (6.2 μm streptavidin-coated beads) into the foundation layer (23). The authors used this device for biomolecular recognition, establishing a model system for determination of the FLAG epitope (commonly used epitope tag that relies on an octapeptide). On-chip identification and quantification of analytes occurred via direct fluorescence or fluorescence resonance energy transfer measurements. They showed that the assay was able to detect subfemtomole quantities of protein. Their system presents advantages of scale, direct measurement of bound analyte on beads (no need for an elution step), and simultaneous detection of multiple analytes.

Moorthy et al. described a microfluidic device for assaying botulinum toxin by sandwich ELISA from blood sample. Multiple functions such as dilution, mixing,

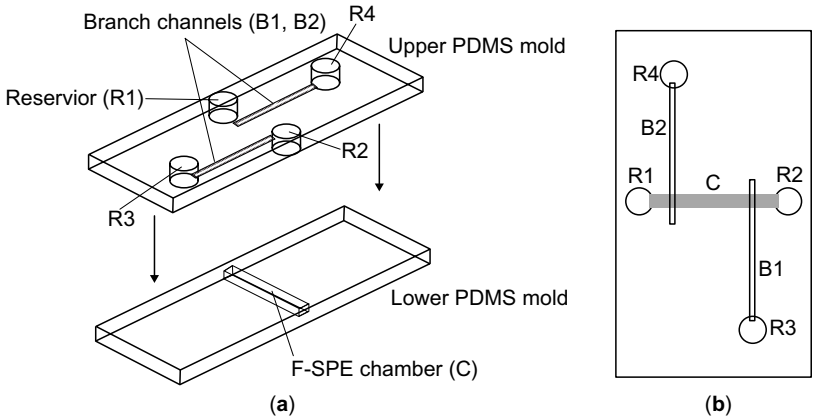

FIGURE 11.7 Simple device dedicated to SPE of aminoacids developed by Hu et al. (**a**) Two PDMS molds bonded together to create a two-level device. (**b**) Schematic representation of the final device, the gray part represents the packing chamber. R1 and R2 are used to fill the chamber with beads (C), R3 is for the introduction of the samples and R4 for collecting (with permission from Reference (26))

separation, and detection (UV–Visible absorption) were performed in the device. A filter incorporated between layers of the device enabled the trapping of antibody-grafted agarose beads (24) for readout. Clinically relevant amounts of the toxin were detected in a reduced time. In the same way, Wallman et al. created a grid inside a microchannel to trap beads (50 μm in diameter) for solid phase microextraction application prior to MS analysis (25).

Recently, Hu et al. presented a very simple device to perform solid phase extraction of amino acids. This device was made of two layers of PDMS slabs that contained channels with different depth (see Figure 11.7). Once the chamber had been filled, the reservoirs (R1 and R2 on the figure) were glued to prevent the particles (fluorous silica beads of 5 μm in diameter) from escaping. Because of the different channel depths, the beads couldn't go through the channels B2 and B1 (only 4 μm deep) while the liquid mixtures were able to travel all around the microchannel network (channels B1, B2, and C). This device was used to separate and extract fluorescently tagged amino acids. The authors obtained an average extraction efficiency of 55% by off-chip MS detection (26). The system presents a good reproducibility of the column, but is not "recyclable" (once contaminated, the whole chip must be replaced).

11.3 SURFACE MODIFICATION OF THE MICROCHIP

The use of physical barriers such as frits, weirs, or grids to retain beads inside the microchannels involves fabrication processes with multiple thicknesses, and complicates the overall process. In this paragraph, we will focus on another method for trapping particles, which consists in modifying the surface of the microchip.

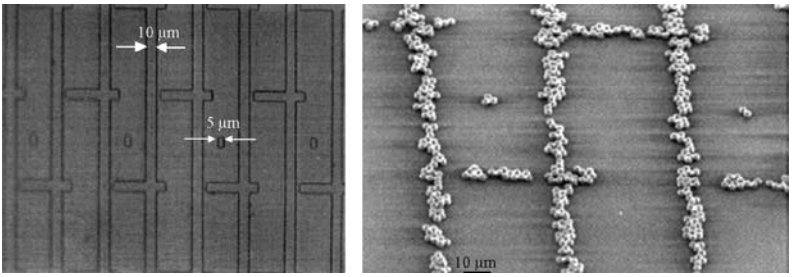

FIGURE 11.8 Immobilized streptavidin-coated beads. Photo of the stamp (left) and arrangement of the beads after microcontact printing (right) (adapted from Reference (27))

The method developed by Andersson et al. consisted in modifying the surface of one internal wall of the microchip using microcontact printing. First, it involved printing a protein (for example biotin) on a wall (in practice, generally the "bottom") of the microchip. Then, when adding beads bearing the complementary protein (for example, streptavidin), they self-assembled as a monolayer by interaction. This assembly occurred before the sealing of the channel so that the method of sealing should occur under low temperature, in order not to damage the coated beads. A picture of the immobilization of streptavidin-coated beads (2.8 µm in diameter) is shown in Figure 11.8. This method led to a surface coverage about 14 beads per μm^2, for these beads. Based on this principle, it was possible to assemble other beads using other kinds of interactions such as hydrophilic/hydrophobic interaction or antigen/antibody interaction. The coverage of beads on the channel walls was better for the bottom wall than for the top one, because of sedimentation. This method is particularly suitable to immobilize beads according to predefined patterns. It was applied on various substrates; silicon, quartz or plastic. It can be applied to several biological reactions such as those needed for proteomics analysis. The immobilized beads can be easily removed by sonication in water for 30 s (27).

Alternatively, Malmstadt et al. developed a thermal method to attach particles on the walls of a microchip. They used stimuli-responsive polymers to construct beads that were able to be reversibly immobilized on the walls of a channel made of poly (ethyleneterephtalate). For this purpose, latex beads (100 nm in diameter) were coated with a temperature sensitive polymer poly(*N*-isopropylacrylamide) (PNIPAM), which presented a hydrophilic–hydrophobic phase transition. The beads were injected into the channel at room temperature and when the temperature was increased, they aggregated and adhered to the walls of the channel, thanks to a phase transition making them more hydrophobic. When the temperature was decreased below the lower critical solution temperature of PNIPAM (26°C in aqueous conditions), the beads were quickly resuspended, and could be eluted from the walls of the channel. The system was applied to two different applications. First, the authors immobilized biotin-labeled polymer-coated beads and analyzed solutions of streptavidin labeled with a fluorophore (Alexa488) (28). Then, a model competitive assay based on the digoxin antibody–antigen interaction was performed to evaluate the performances of the

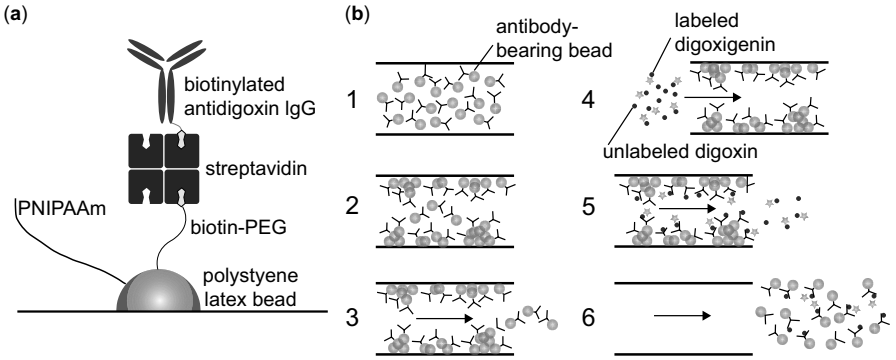

FIGURE 11.9 Schematic representation of the bead immunoassay based on temperature sensitive polymer developed by Malmstadt et al. (**a**) The assembled bead construct. (**b**) Protocol of the immunoassay. (1) Increasing of the polymer-coated beads at room temperature. (2) Temperature increasing leading to the adhesion of the particles on the channel walls. (3) Washing of the non adsorbed particles. (4) Injection of the target analyte. (5) Washing of the non immobilized analytes. (6) Temperature decreasing leading to the removal of all the materials (from Reference (29))

system (Figure 11.9) (29). Concentrations around 1 μM were detected with this system. This sensitivity is not exceptional, but this capture method nevertheless presents several advantages. The adhesion of the beads to the surface is reversible so that the removal of the beads is easy. Thanks to microfabricated heaters, it is possible to localize the beads in well-defined regions, and to determine the exact timing of the immobilization during a multistep analysis.

Another example of channel coating was given by Murrihy et al. By physical absorption, they immobilized cationic latex particles (75 nm in diameter) on the walls of a microchannel to perform ion-exchange chromatography. They studied the separation of ionic species and found increased retention factors while proceeding in microchip compared to in-capillary reactions. Detection limits of 0.5 μM were obtained (30). This method, however, presents a rather poor reproducibility. It is not possible to control the absorption of particles and consequently two successive fabrication processes lead to two different bead beds.

Ramsey et al. developed a chemical technique to immobilize beads onto channel walls. It consisted in depositing plugs of porous methacrylate polymer inside the microchannel. Monomer and initiator were injected in the microchannel, and polymerization was initiated in defined areas by UV illumination. The photopolymerization process led to the formation of a chemical frit with a pore size of 5 μm, larger than bead diameter (3 μm in this study) but the random nature of the pores prevented the beads from passing through this plug. C_{18}-coated silica beads were used to determine the concentration capacity of the column with different dyes and to separate a mixture of neutral hydrophobic dyes as a model experiment (31). The authors obtained a detection limit of 60 fM with their device integrating micro-SPE sampling, on-chip

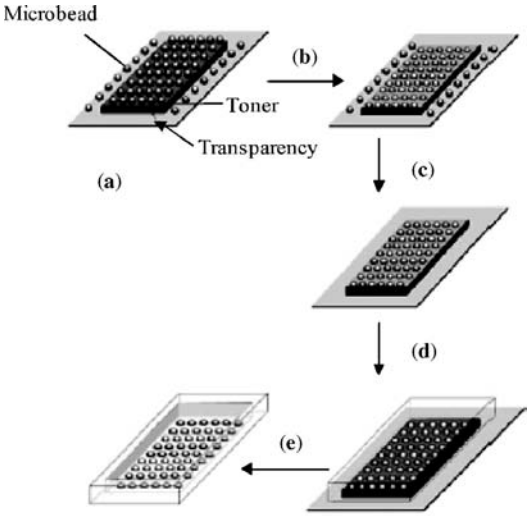

FIGURE 11.10 Procedure for the immobilization of beads on the surface of the microchips developed by Zhang et al. (**a**) After the formation of a master with toner printed where the beads should be immobilized, a suspension of particles is added to cover the toner. (**b**) The master is heated in an oven. (**c**) The master is taken out and the nonbound particles (those that are deposited on the transparency nonprinted region) are washed away. (**d**) PDMS agent and its reticulant are added to the master and cured. (**e**) Finally, the PDMS replica with the immobilized beads is peeled off (from Reference (32))

elution, sample injection, and Micellar ElectroKinetic Chromatography (MEKC). On the positive side, this method allows an accurate and easy positioning of the microcolumn, thanks to photopolymerization. This polymerization, however, renders the process irreversible.

Recently, Zhang et al. proposed a new method for retaining beads inside a channel during the fabrication process. The particles (silica-based beads of 5 μm of diameter) were first printed on a master and then transferred into microchannels of PDMS microchips (see Figure 11.10 for the different steps). The master was not only a mold to fabricate the chips but also a stamp to transfer the beads. This group compared the ability of ODS silica-modified and silica-modified PDMS chip for electrophoresis and enzymatic digestion applications. For enzymatic application, they demonstrated the feasibility of the system to immobilize Glucose Oxidase on the patterned beads and to perform digestion. For electrochromatography application, they noticed improvements in the separation of dopamine and epinephrine with the ODS silica-modified PDMS chips versus the native PDMS chips. This method simplifies considerable microfabrication, since it allows simultaneous formation of the chip and of the column. It is not possible to replace the beads, but this simple process is well suited for the fabrication of disposable chips, so this is probably a minor disadvantage (32). As another limitation, however, it is applicable only to rather large beads.

11.4 ELECTROKINETIC METHODS FOR BEADS IMMOBILIZATION

An interesting approach was presented by Lettieri et al. for the trapping and manipulation of small beads using fluid flows only. These authors created complex bidirectional flows, by a combination of opposing pressure-driven and electroosomotic flows in channels with a variable section. Electroosmosis is driven by the field strength at the wall, whereas Poiseuille flow is driven by equilibrating pressure forces (potential flow). In some regimes, this creates vortices (see Figure 11.11), in which fluorescent polymer beads can be captured and preconcentrated to form clusters of freely moving beads. The ability to perform biological assays in this device was demonstrated. After the introduction of streptavidin-coated beads (2 μm in diameter), the moving beads were continuously perfused with labeled biotin solutions and detection limits of 4 μM in 200 s incubation time for B4F (biotin-4-fluorescein), and 50 nM in 120 s for FLB (biotin-fluorescein product less prone to quenching) were obtained (33).

Auerswald et al. presented another method for dynamic trapping of beads inside a microchannel, using positive dielectrophoresis (DEP). DEP is based on polarizability and requires a strong inhomogeneous electric field. If the beads are more polarizable than the surrounding liquid medium, the DEP force moves them toward areas with a high electric field gradient. These authors proposed a simple chip layout with planar electrodes, on which particles adhered after the DEP voltage had been applied. Different fluorescent-coated beads (biotin, protein A, antimouse IgG) of various diameters were investigated. They found, in their first results, a detection limit of

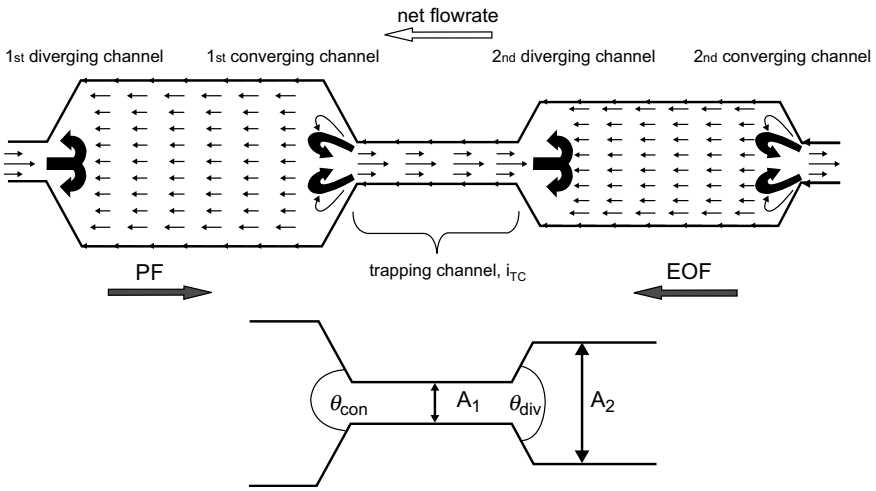

FIGURE 11.11 Schematic view of the microfluidic device, involving fluid flow only, proposed by Lettieri et al. The arrows represent the electroosmotic Flow (EOF) and the pressure-driven flow (PF). The flow recirculates between the converging and diverging channels. θ_{con} and θ_{div} are the converging and diverging channel opening angles (with permission from Reference (33))

1.6 μg/mL for mouse IgG (for nonoptimized conditions). They demonstrated the proof of concept of a parallel assay achieving the detection of different components in a multianalyte solution on the same chip (34). This method is fast, versatile, easy to fabricate, but the device with the beads can be used only once. Also, DEP requires high electric fields that can induce strong Joule heating and even bubble formation, in the highly conductive buffers required for some biological assays.

11.5 MAGNETIC BEADS

The use of magnetic beads in bioassays is becoming increasingly popular due to the simplification they bring, avoiding centrifugation steps. The manipulation of magnetic beads in lab-on-a-chip systems is also a rapidly growing activity since it is possible to manipulate them at a distance, without disrupting biochemical reactions (35,36), and without the Joule heating problems raised by, for example, DEP manipulation.

The first attempts to use magnetic particles in miniaturized systems were proposed simultaneously by Mayer et al. for DNA separation (37) and by Rashkovetsky et al. for protein assays (38). This latter group immobilized magnetic beads (polystyrene microspheres of 2.8 μm in diameter) inside a commercial capillary electrophoretic system using two permanent magnets placed in the cartridge in contact with the capillary. They demonstrated the feasibility of the technique for enzymatic digestion. For this purpose, biotinylated alkaline phosphatase (ALP) was bound to streptavidin-modified magnetic beads and solutions of ALP substrate were injected in the modified capillary (38). The product of the enzymatic degradation was detected at 405 nm. They determined the Michaelis–Menten constants and the results were in good agreement with the literature. Furthermore, they applied their system to analyze specific antigen and detected fmol amount of material. This system was reversible, since the beads could be released and flushed away when the magnets were removed. This method was easy to use (no need for frit formation) but this strategy did not lead to further applications, maybe due to difficulties in achieving reproducible bead beds by a "blind" operation in a capillary electrophoresis machine.

Magnetic immobilization regained interest thanks to the outcome of microfabricated systems. Hayes et al. developed a heterogeneous immunoassay in a microchannel using magnetic beads. The particles were packed in the microchannel by the application of a strong magnetic field created by a single permanent magnet located directly over the channel. The length of the bed was between 1 and 3 mm. Reagents were passed through the bead reactor and the bed was imaged with an epifluorescence microscope with laser-induced excitation. The bed of beads did not extend across the channel because the magnetic beads aggregated near the single magnet, which enabled fluorescence detection on the surface of the packed bed (Figure 11.12b) and the use of high flow rates. The device was optimized with the analysis of model compounds, fluorescein isothiocyanate (FITC)/anti-FITC (direct assay), and real samples such as parathyroid hormone and interleukin-5 with sandwich assay (the principle of the interaction is given in Figure 11.12a). This group used streptavidin-modified magnetic

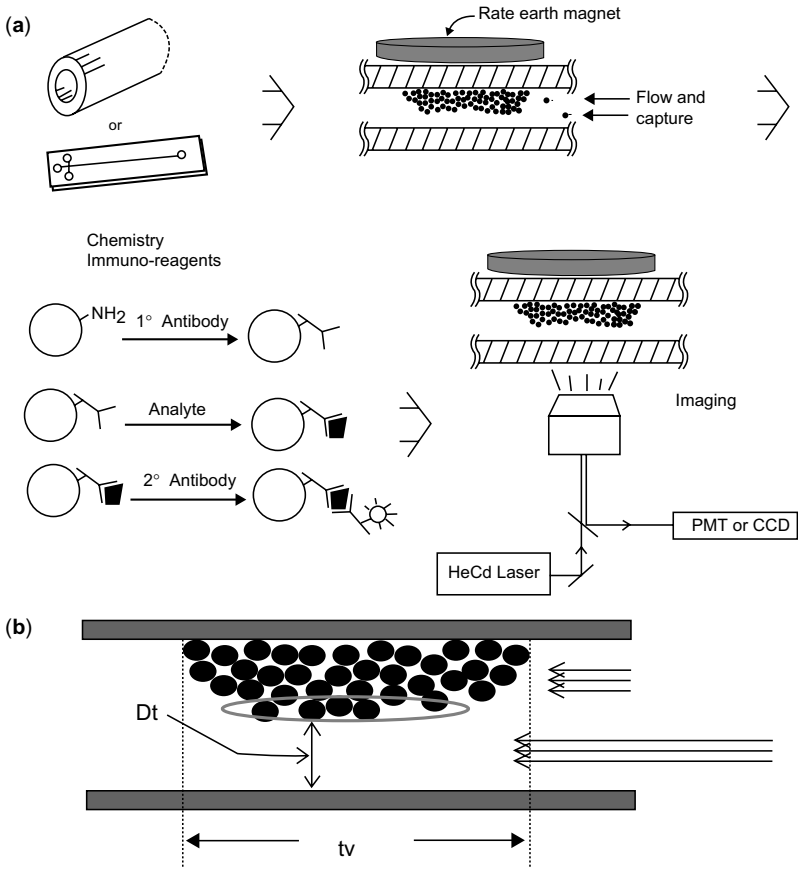

FIGURE 11.12 (**a**) Schematic representation of microsystem flow-based immunoassay based on paramagnetic particles coated with antibody, immobilized near a permanent magnet. Solutions of antigen and secondary labeled antibody are injected and passed through the beads bed. (**b**) The magnetic beads do not occupy the whole channel section. The flow rate is fixed so that Dt < tv. (from Reference (39))

beads of 1–2 μm in diameter, and demonstrated that the assay had physiologically relevant sensitivity (μg/mL). Particles could be packed, dynamically positioned, flushed, and repacked. Moreover, this system consumed low amount of reagents: 100 to 1000 times smaller than conventional assays (39).

Another use of magnetic beads was proposed by Choi et al. They presented an integrated microfluidic electrochemical detection system for protein analysis, involving several assembled modules on a microfluidic control panel. This device, made by glass etching and glass-to-glass direct bonding, contained different reservoirs and channels for introducing different solutions. The biofilter and the electrochemical sensor were integrated to the motherboard by fluoropolymer bonding technique (see Figure 11.13). The magnetic element for immobilization of the beads was a planar

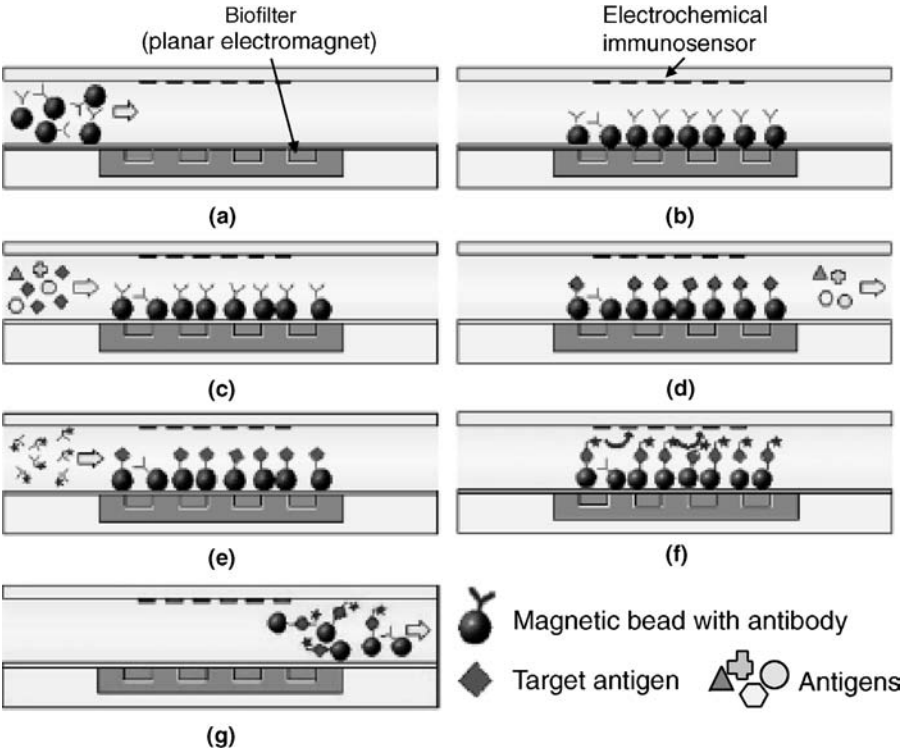

FIGURE 11.13 Principle of the microchip assay developed by Choi et al. (**a**) Introduction of the magnetic beads into the microchannel. (**b**) Immobilization of the beads on the surface of the biofilter due to magnetic field. (**c**) Introduction of the sample. (**d**) Interaction between the bead and the target analyte. (**e**) Introduction of the secondary labeled antibody. (**f**) Electrochemical detection after the introduction of the substrate. (**g**) Washing (with permission from Reference (40))

electromagnet located under the biofilter so that the beads were packed on the bottom surface of the microchannel. All the channels were 400 μm wide and 100 μm deep. With this microdevice, magnetic beads (2.8 μm in diameter) coated with primary antibody were immobilized on the surface of the biofilter. Then, solutions of antigen, secondary antibody labeled with alkaline phosphatase (ALP), and finally, ALP-substrate were introduced and incubated (see Figure 11.13). After electrochemical detection, all the materials (beads and reagents) were flown away. The immunoassay was applied to mouse IgG. Sample consumption was 10 μL, the total assay time was less than 20 min, including all steps. Its working concentration range was below 100 ng/mL (40).

To overcome the challenging microfabrication of integrated electromagnets, the same group developed another magnetic assay based on an easier microfabrication strategy, with fully on-chip sampling and detection by chronoamperometry

measurement. They performed ELISA and achieved sampling and detection of 50 ng/mL of mouse IgG in 10 min (41).

Our group developed a new approach based on the self-organization of magnetic beads under a magnetic field. The PDMS device integrated strong magnets, with specific orientation, to create a magnetic field parallel to the flow, with a strong gradient pointing through the center of the channel (Figure 11.14a)). When expose to a uniform external field, the magnetic beads self-organize into a supraparticle structure consisting of a columnar clustering in the direction of the field (Figure 11.14b,c) (42). These columns are organized in "labyrinth-like" structures if the concentration of the suspension is high enough. The distance between the columns is maintained by dipole–dipole repulsion, maintaining in the bulk of the plug, channels collinear to the flow, with a thickness of a few micrometers. As compared to previous immobilization methods involving fields perpendicular to channel's axis, this strategy yields a lower pressure drop, a better resistance to flow, and a more uniform permeation. The pores between the magnetic beads columns play the role of coated capillaries in a multiopen tubular chromatographic-like system. This concept had been applied to enzymatic digestion with trypsin or proteinase K immobilization on beads (43,44). The results showed a 100 and 50, for trypsin and PK digestion, respectively, fold increase in digestion rate on-chip as compared to digestion in solution. This system allows easy replacement of the bead matrix by the application of a strong flow, a very good reproducibility in terms of beads packing and digestion efficiency. The tryptic digestion chip was recently combined with Electrospray Mass Spectroscopy, allowing for online peptide mapping (45). Online digestion by PK beads allowed a differentiation between normal and pathogeneous (PK resistant) prion proteins, opening the route to chip-based prion diagnosis (44).

Kim et al. developed another strategy for biomolecular detection based on magnetic forces in a microfluidic channel. Small superparamagnetic particles (50 nm) and fluorescent polymer beads (1 μm) were coated with polyclonal antibodies. When the antigen was introduced in the mixture, a sandwich between the two types of beads was

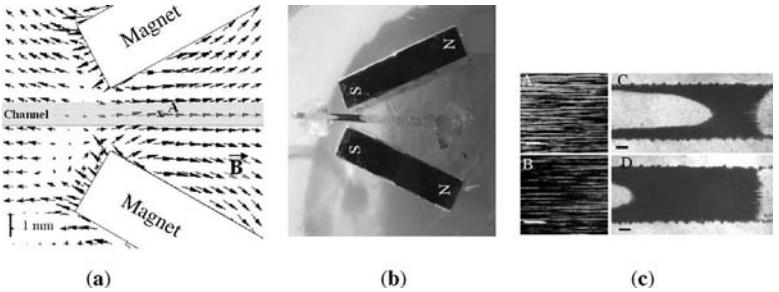

FIGURE 11.14 New immobilization approach developed by Viovy's group. (**a**) Simulation of the magnetic field created by the two permanent magnets. (**b**) View of the plug of magnetic beads immobilized between the two magnets in the microchannel. (**c**) Organization of the columns parallel to the flow (A and B) at the beginning of the plug clustering. Formation of the plug (C and D)

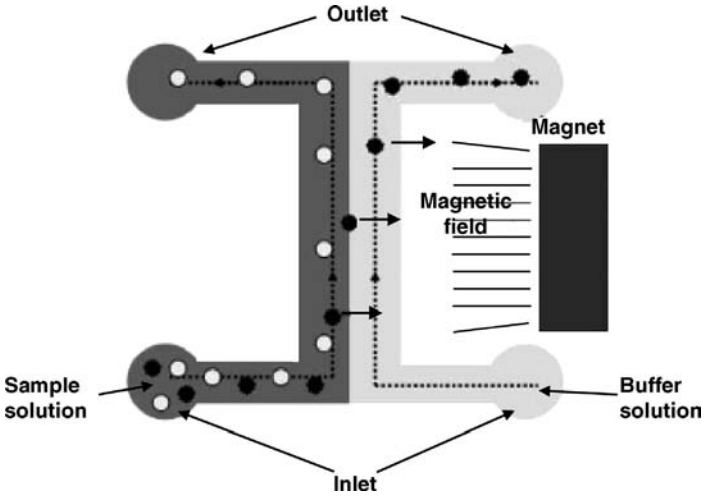

FIGURE 11.15 Principle of the detection system by Kim et al. The complex formed by interaction between microbead with superparamagnetic particle (●) is deflected by the magnetic field while the microbead (○) keep their initial way (from Reference (46))

formed. Upon application of a magnetic field, polymer beads interacting with superparamagnetic particle were deflected and detected by fluorescence, whereas naked beads were not, allowing for a separation (Figure 11.15). These authors demonstrated the ability of this system to perform sandwich immunoassay and dual analyte detection with rabbit and mouse IgG as model analytes and detected IgG at nanomolar concentration (46).

Recently, Pamme et al. developed a method for simultaneous bioassays based on plugs of magnetic particles. In a microchannel, they immobilized different plugs of beads with different biological functions. Permanent magnets, positioned around the channel, created a localized magnetic field to immobilize the beads (from 1 to 8 μm in diameter). With this technique, up to three plugs were immobilized in a 5 cm long channel. An example of dual bioassay was performed with the immobilization of both streptavidin- and glycine-coated beads (2.8 μm in diameter) and elution of fluorescent biotin solutions. The streptavidin plug became fluorescent due to the interaction between biotin and streptavidin on the beads (47). The main advantage of this system relies on its very simple way of fabrication. As discussed above, however, this kind of beads immobilization (by a field perpendicular to the channel) may lead, sometimes, to limited capture efficiencies.

Herrman et al. described an original microfluidic design to perform parallel ELISA in stop-flow conditions. The device consisted in eight independent channels composed of an inlet, a reaction chamber and a smaller channel for detection (Figure 11.16), enabling simultaneous assays. The external magnet, located near the microchip, was displaced manually in order to move the beads and consequently induce a mixing of the fluid around them. Streptavidin-coated magnetic beads

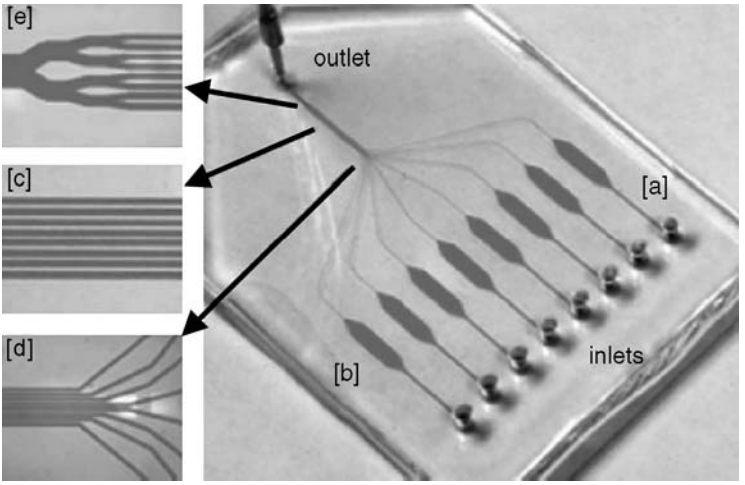

FIGURE 11.16 Picture of the PDMS chip developed by Herrman et al. (**a**) Independent channel. (**b**) Reaction chamber in which magnetic particles are introduced. (**c**) Small channels for the detection. (**d**) Gathering of the independent channels. (**e**) Merging into a unique outlet (from Reference (48))

(1 μm in diameter) were used for detection by epifluorescence and quantification of antistreptavidin antibodies. The authors found low picomolar sensitivity and a coefficient of variation for both the intra- and interassay of 15% (48). In this study, the beads acted not only as a solid support for the biological reaction but also as one mean to create an internal mixing of the solution.

11.6 CONCLUSION

In spite of their recent outcome, microfluidic systems have stimulated numerous applications, in which micro- and nanoparticles play a major role. Indeed, latexes seem particularly interesting partners of lab-on-chips. One of their major advantages is that they can be prepared in batch in large quantities. By introducing into a microchannel microparticles previously functionalized, one avoids the need to achieve this functionalization on each chip, a process that can be tedious in the lab, and often precludes industrial applications for cost reasons.

As a price to pay, one has to load and immobilize the particles in the chip in a reproducible manner. The most traditional way of packing particles in macroscopic systems, that is, pressure-driven packing of columns onto frits, proved rather disappointing in microsystems. First, the surface-size ratio is detrimental for this particular process, because interactions with the walls tend to increase defects, and because most chip systems do not withstand the high pressures necessary for achieving good packing. This difficult transposition of methods from the macroscopic world has stimulated a vivid invention activity, and we hope we provided a

reasonable, although far from complete, account of this in the previous sections. Microfluidic analysis systems will have a deep influence in the bioanalytical sciences in the next years, and we anticipate that thanks to this technology, analytical apparatuses, and laboratories 10 years from now will be dramatically different from what they are today. We also anticipate that micro- and nanoparticles will be major components of this technological revolution, and that the development of microanalysis will stimulate further developments in the field of micro- and nanoparticles. Because of the very small volume of microcolumns in microfluidic devices, they generally use a number of particles per analysis smaller than that for traditional bead assays by one to three orders of magnitude. This can not only dramatically reduce the cost of existing analysis but also help to extend the field of application of very elaborate micro- and nanoparticles that were not usable industrially because of their high production cost.

ACKNOWLEDGMENTS

This work was supported in part by the EU project "Neuro-TAS" ("Quality of Life" Program).

REFERENCES

1. Liebler DC. Introduction to Proteomics. Humana Press; 2002.
2. Lion N, Rohner TC, Dayon L, Arnaud IL, Damoc E, Youhnovski N, Wu ZY, Roussel C, Josserand J, Jensen H, Rossier JS, Przybylski M, Girault HH. Electrophoresis 2003;24:3533–3562.
3. Sanders GHW, Manz A. Trends Anal Chem 2000;19(6):364–378.
4. Schasfoort RBM. Expert Rev Proteomics 2004;1:123–132.
5. Verpoorte E. Lab Chip 2003;3:60N–68N.
6. Peterson DS. Lab Chip 2005;5:132–139.
7. Oleschuk RD, Shultz-Lockyear LL, Ning YB, Harrison DJ. Anal Chem 2000;72:585–590.
8. Jemere AB, Oleschuk RD, Ouchen F, Fajuyigbe F, Harrison DJ. Electrophoresis 2002;23:3537–3544.
9. Jemere AB, Oleschuk RD, Harrison DJ. Electrophoresis 2003;24:3018–3025.
10. Wang C, Oleschuk R, Ouchen F, Li JJ, Thibault P, Harrison DJ. Rapid Commun Mass Spectrom 2000;14:1377–1383.
11. Li J, LeRiche T, Tremblay TL, Wang C, Bonneil E, Harrison DJ, Thibault P. Mol Cell Proteom 2002;1:157–168.
12. Sato K, Tokeshi M, Odake T, Kimura H, Ooi T, Nakao M, Kitamori T. Anal Chem 2000;72:1144–1147.
13. Sato K, Tokeshi M, Kimura H, Kitamori T. Anal Chem 2001;73:1213–1218.
14. Sato K, Yamanaka M, Takahashi H, Tokeshi M, Kimura H, Kitamori T. Electrophoresis 2002;23:734–739.

15. Murakami Y, Endo T, yamamura S, Nagatani N, Takamura Y, Tamiya E. Anal Biochem 2004;334:111–116.
16. Andersson H, van der Wijngaart W, Enoksson P, Stemme G. Sens Actuators B 2000;67:203–208.
17. Andersson H, van der Wijngaart W, Stemme G. Electrophoresis 2001;22:249–257.
18. Russom A, Ahmadian A, Andersson H, Nilsson P, Stemme G. Electrophoresis 2003;24:158–161.
19. Ali MF, Kirby R, Goodey AP, Rodriguez MD, Ellington AD, Neikirk DP, McDevitt JT. Anal Chem 2003;75:4732–4739.
20. Li S, Floriano PN, Christodoulides N, Fozdar DY, Shao D, Ali MF, Dharshan P, Mohanty S, Neikirk D, McDevitt JT, Chen S. Biosens Bioelectron 2005;21:574–580.
21. Ceriotti L, de Rooij NF, Verpoorte E. Anal Chem 2002;74:639–647.
22. Buranda T, Huang J, Perez-Luna VH, Schreyer B, Sklar LA, Lopez GP. Anal Chem 2002;74:1149–1156.
23. Piyasena ME, Buranda T, Wu Y, Huang J, Sklar LA, Lopez GP. Anal Chem 2004;76:6266–6273.
24. Moorthy J, Mensing GA, Kim D, Mohanty S, Eddington DT, Tepp WH, Jonhson EA, Beebe DJ. Electrophoresis 2004;25:1705–1713.
25. Wallman L, Ekström S, Marko-Varga G, Laurell T, Nilsson J. Electrophoresis 2004;25:3778–3787.
26. Hu G, Lee JSH, Li D. J Colloid Interface Sci 2006;301:697–702.
27. Andersson H, Jonsson C, Moberg C, Stemme G. Electrophoresis 2001;22:3876–3882.
28. Malmstadt N, Yager P, Hoffman AS, Stayton PS. Anal Chem 2003;75:2943–2949.
29. Malmstadt N, Hoffman AS, Stayton PS. Lab Chip 2004;4:412–415.
30. Murrihy JP, Breadmore MC, Tan A, McEnery M, Alderman J, O'Mathuna C, O'Neill AL, O'Brien P, Advoldvic N, Haddad PR, Glennon JD. J Chromatogr A 2001;924:233–238.
31. Ramsey JD, Collins GE. Anal Chem 2005;77:6664–6670.
32. Zhang Q, Xu JJ, Chen HY. Electrophoresis 2006;27:4943–4951.
33. Lettieri GL, Dodge A, Boer G, de Rooij NF, Verpoorte E. Lab Chip 2003;3:34–39.
34. Auerswald J, Widmer D, de Rooij NF, Sigrist A, Staubli T, Stöckli T, Knapp HF. Electrophoresis 2005;26:3697–3705.
35. Gijs MAM. Microfluid nanofluid 2004;1:22–40.
36. Pamme N. Lab Chip 2006;6:24–38.
37. Mayer P, Bibette J, Viovy J-L. Mater Res Soc Symp Proc 1997;463:57.
38. Rashkovetsky LG, Lyubarskaya YL, Foret F, Hughes DE, Karger BL. J Chromatogr A 1997;781:197–204.
39. Hayes MA, Polson NA, Phayre AN, Garcia AA. Anal Chem 2001;73:5896–5902.
40. Choi JW, Oh KW, Thomas JH, Heineman WR, Halsall HB, Nevin JH, Helmicki AJ, Henderson HT, Ahn CH. Lab Chip 2002;2:27–30.
41. Do J, Ahn CH. In:Jensen KF, Han J, Harrison DJ, Voldman J, editors. Micro Total Analysis Systems. Volume 1. San Diego, California: Transducers Research Foundation, Inc.; 2005.
42. Lawrence EM, Ivey ML, Flores GA, Liu J, Bibette J, Richard J. Intl J Mod Phys B 1994;8:2765–2777.

43. Slovakova M, Minc N, Bilkova Z, Smadja C, Faigle W, Fütterer C, Taverna M, Viovy JL. Lab Chip 2005;5:935–942.
44. Le Nel A, Minc N, Smadja C, Slovakova M, Bilkova Z, Peyrin J-M, Viovy J-L, Taverna M. Accepted Lab Chip DOI,10.1039/B715238H.
45. Le Nel A, Krenkova J, Kleparnik K, Smadja C, Taverna M, Viovy J-L, Foret F. In: Viovy J-L, Tabeling P, Descroix S, Malaquin L, editors. Micro Total Analysis Systems. Volume 1. Chemical and Biological Microsystems Society; 2007.
46. Kim KS, Park JK. Lab Chip 2005;5:657–664.
47. Brown BJK, Pamme N. In: Kitamori T, Fujita H, Hasebe S, editors. Micro Total Analysis Systems. Volume 2. Society for Chemistry and Micro-Nano Systems; 2006.
48. Herrman M, Veres T, Tabrizian M. Lab Chip 2006;6:555–560.

CHAPTER 12

Semicarbazide/α-Oxo Aldehyde Site-Specific Ligation Chemistry: From Peptide Microarrays to the Micropatterning of Polycarbonate or Titanium Oxide Using Silica Nanoparticles

OUAFÂA EL-MAHDI, VIANNEY SOUPLET, OLIVIER CARION, CLÉMENT ROUX, JEAN-MICHEL GARCIA, CÉLINE MAILLET, CHRISTOPHE OLIVIER and OLEG MELNYK

Institut de Biologie de Lille, UMR CNRS 8161, 1 rue du Professeur Calmette, 59021 Lille Cedex, France

JEAN-OLIVIER DURAND

Institut Charles Gerhardt UMR 5253 cc 1701, Université Montpellier 2, place Eugène Bataillon, 34095 Montpellier Cedex 05, France

12.1 INTRODUCTION

The parallel detection of different antibodies in complex biological samples has a wide range of potential applications in the diagnosis of allergies, autoimmune and infectious diseases as well as in epitope mapping studies and the development of vaccines (1–4). Actually, the detection of antibodies is usually performed by using ELISA-based assays. However, the need for a highly parallel format allowing the study of large collections of antigens and biological samples has stimulated the development of peptide or protein microarrays, which are increasingly used in this area (5). Many groups have now reported that peptide or protein microarrays are useful devices for the detection of antibodies (6–13) and can be used for the serodetection of infections

Colloidal Nanoparticles in Biotechnology, Edited by Abdelhamid Elaissari
Copyright © 2008 John Wiley & Sons, Inc.

(14–16). This review is focused on our contribution to the preparation of peptide microarrays for the detection of antibodies.

A peptide microarray is composed of a planar substrate on which a collection of polypeptides are immobilized individually in the form of microspots. The diameter of the spots is usually comprised between 50 and 250 μm depending on the characteristics of the arrayer. The position of each peptide probe is precisely known. The peptides can be synthesized directly on the chip surface or spotted after isolation or synthesis. The microarray can be incubated with a purified target (protein, enzyme, phages, DNA, etc.) or a biological sample (cells, serum, etc.). Each arrayed probe is able to capture specifically a soluble target. Different methods are used to detect the capture events. Among them, fluorescence is probably the most frequently used detection technique (17–19).

The major advantage of microfabricated analytical devices over conventional techniques is the highly parallel, addressable, miniaturized array format that allows simultaneous detection of different targets in solution, virtual automation, and functional integration for high throughput screening. Another great advantage of miniaturization is that microspot assay sensitivities can be higher than those obtainable by conventional methods, especially if close packing of sensor molecules within the microspot can be achieved (20,21).

The substrate and the coupling chemistry used to attach the peptide probe to play a crucial role in the performance of the microarray (22). Usually, microarrays are prepared on microscope glass slides. This substrate is cheap, has a low intrinsic fluorescence and can be easily functionalized by silanization. Different methods are available for attaching polypeptides to microscope glass slides (23). A covalent bond can be formed site-specifically between the substrate and the polypeptide using native ligation (24–26) oxime (27) semicarbazone (14,28,29) Staudinger (30), or thiol chemistry (27). Random attachment of the polypeptide chain to the surface using the reactivity of α or ε-amino groups was also examined (31). Noncovalent immobilization involved Ni(II) coordination chemistry (32) or the biotin/avidin interaction (26,33,34). Another interesting method is to immobilize polypeptides by physisorption (14,15). The last strategy is of great interest owing to its simplicity and because the proteins do not need to be chemically modified before the printing procedure and are not modified after immobilization. The field has been recently reviewed by Yeo et al. (24).

This review is focused on the site-specific immobilization of peptides through α-oxo semicarbazone ligation (Scheme 12.1).

Hydrazone site-specific ligation is probably the oldest ligation reaction known to peptide chemists. This bond, which can be formed chemoselectively using very mild aqueous experimental conditions, was often used for the preparation of conjugates or for the convergent synthesis of large molecular objects. However, due to the sensitivity of the hydrazone bond to hydrolysis, the conjugates were usually stabilized by reduction with a borohydride (35). Application of this ligation chemistry to microarrays would thus require a chemical step after the printing of the probe. We have thus focused our work on semicarbazone ligation as an alternative to hydrazone ligation. As for hydrazones, the stability of semicarbazones toward hydrolysis is greatly influenced by the structure of the aldehyde partner. In 2001, Podyminogin et al. have

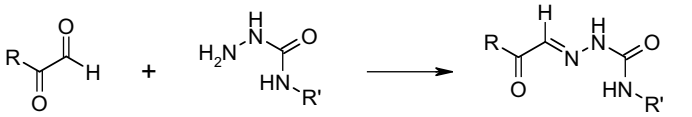

SCHEME 12.1 α-Oxo semicarbazone ligation.

described the preparation of semicarbazide-functionalized glass slides and their use for the site-specific attachment of benzaldehyde deoxyoligonucleotides (36). Forty percent of hydrolysis of this semicarbazone bond was observed at pH 7.5 (65°C) after 24 h. We have decided to explore instead the interest of the α-oxo aldehyde (COCHO) moiety in this field, since this group is resistant to oxidation, compatible with polypeptides and reacts chemoselectively in aqueous solution with hydrazine, hydroxylamine or β-aminothiol derivatives (37). Moreover, the COCHO group can be easily introduced into peptides using various solution (38) or solid-phase methods (37,39–43).

Thus, in a first approach, we have studied the stability of the α-oxo semicarbazone bond toward hydrolysis in solution using model peptides. The high stability of this bond stimulated the study of this ligation method in the context of silica particles. The reactivity and selectivity of α-oxo aldehyde (COCHO) or semicarbazide-functionalized silica microparticles was studied. The results showed the superiority of semicarbazide substrates for the site-specific immobilization of peptides. Thus, semicarbazide-functionalized microscope glass slides were prepared, characterized and used for the preparation of peptide microarrays by printing COCHO-peptides. For another application, we also describe the synthesis and characterization of semicarbazide nanoparticles. These nanoparticles were used for the chemical micropatterning of polycarbonate or titanium oxide substrates and the site-specific attachment of COCHO-peptides to the surface through the nanoparticle silica layer. The peptide micropatterns on polycarbonate were used for the specific and sensitive capture of antibodies in serum using fluorescence detection.

12.2 SEMICARBAZIDE/α-OXO ALDEHYDE SITE-SPECIFIC LIGATION CHEMISTRY FOR MAKING PEPTIDE MICROARRAYS

12.2.1 Stability of the α-Oxo-Semicarbazone Bond

Among all the criteria considered for the selection of an immobilization chemistry for microarray fabrication, the stability of the bond linking the probe to the surface is perhaps the most important. The linkage has to survive to the different incubations and washings. We have examined by reverse-phase-high performance liquid chromatography (RP-HPLC) the stability of the α-oxo semicarbazone bond to hydrolysis using peptide **1** (Fig. 12.1). Trace A and C correspond to the purified glyoxylpeptide **2** and semicarbazone **1**, respectively. Trace B, which corresponds to the coinjection of both compounds, shows that the starting glyoxylpeptide **2** was separated readily by

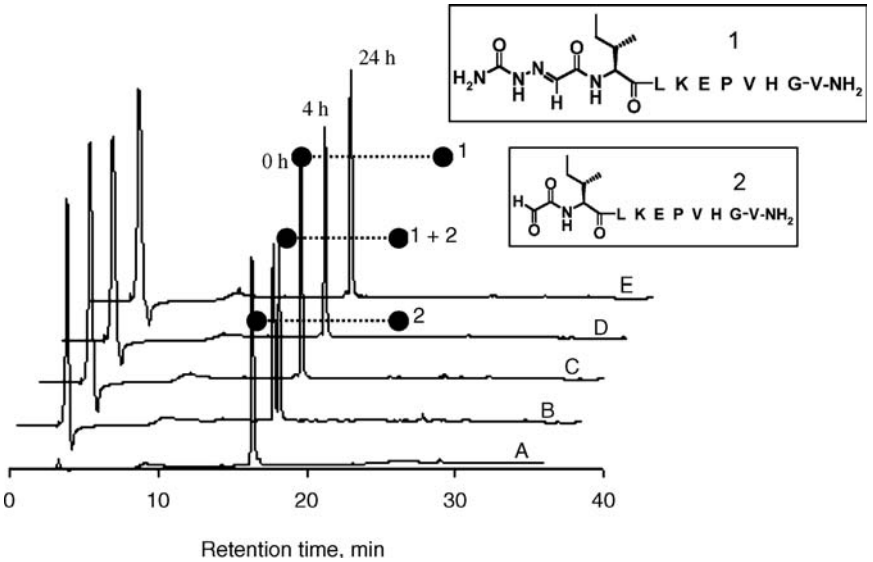

FIGURE 12.1 RP-HPLC study of the stability of semicarbazone **1** at pH 7.5 and 65°C during 24 h. Experimental conditions are identical to those described by Podyminogin et al. (36)

RP-HPLC from semicarbazone **1**. α-Oxo semicarbazone **1** was dissolved in pH 7.5 HEPES buffer using the experimental conditions described by Podyminogin et al. (36) and incubated up to 24 h at 65°C. Interestingly, neither decomposition nor hydrolysis occurred after 24 h of incubation (Fig. 12.1E) whereas Podyminogin reported about 40% of hydrolysis for a semicarbazone formed by reaction of benzyl semicarbazide with benzaldehyde-ODNs. The same resistance to hydrolysis was observed at pH 7.1 or 8.0 (data not shown), highlighting the good stability of the α-oxo semicarbazone bond.

12.2.2 Synthesis of COCHO or Semicarbazide Silica Microparticles. Reactivity Study

Immobilization of peptides through site-specific α-oxo hydrazone or semicarbazone chemistry has been scarcely studied in the context of bioorganic-inorganic materials synthesis. For this reason, we have undertaken the synthesis of COCHO or semicarbazide silica microparticles as model substrates for reactivity studies. A critical point was to select the functional group present on the substrate. The ease of formation of a functional group and its reactivity on a solid substrate can differ significantly from solution experiments (44). Should the α-oxo aldehyde group be on the substrate or on the peptide?

12.2.2.1 Synthesis of COCHO-Silica Microparticles A few methods have been proposed for the modification of surfaces by α-oxo aldehyde moieties (27,45–48) Indeed, the presence of this functionality on the surface of silica was found to be attractive due to its hydrophilicity and stability towards oxidation compared to

aliphatic or aromatic aldehydes. These properties are mainly due to the formation of a hydrate in aqueous media (49). ^{1}H NMR study of an aqueous solution of glyoxylic acid revealed the absence of aldehydic proton and the presence of a singlet at 5.4 ppm corresponding to the gem-diol moiety of glyoxylic acid hydrate. Interestingly, ^{13}C NMR spectra also revealed the presence of oligomers. For comparison, many papers have reported the synthesis of COCHO peptides, and to our knowledge no oligomerization was observed either in solution or in the lyophilized state. In the solid state, the high concentration of COCHO groups on the substrate might favor the formation of oligomers, whose reactivity might be different from that of the monomer. The complex chemistry of glyoxylic acid derivatives and the difficulty to deduce the usefulness of this group on a solid substrate from data obtained in solution stimulated the study presented in this section.

The introduction of the α-oxo aldehyde group on the surface of microscope glass slides has been performed by coupling a protected serine to amino-functionalized surfaces. The COCHO group was generated after deprotection and periodic oxidation of the β-aminoalcohol moiety (27). In an alternative approach reported by the same group, coupling of glyoxylic acid dimethoxyacetal was followed by deprotection using strong acid (23). Recently, we have described an alternative approach based upon the sol-gel chemistry of triethoxysilylpropylgluconamide (GAPS), whose polyol chain was converted into the α-oxo aldehyde group by treatment with periodate in aqueous acetic acid (50). These materials showed a good reactivity with low molecular weight hydroxylamine or hydrazine derivatives but were unable to react with α-hydrazinoacetyl peptides probably due to poor accessibility. In search for a functionalization method that could be applied to the site-specific immobilization of polypeptides, we envisaged the grafting of GAPS by silanization of the surface of silica particles (Scheme 12.2). Silica particles for flash chromatography **X** (Macherey Nagel, particle size 43–60 μm, BET surface: 450 m^2/g) were reacted with GAPS. Two types of materials were synthesized with 50 μmol (**X1-50**) or 500 μmol (**X1-500**) of GAPS per gram of silica.

IR spectroscopy showed absorptions characteristic of the gluconamide chain, in particular ν C=O gave a band at 1648/cm as in the hybrid organic-inorganic material prepared by sol-gel chemistry. Microanalysis allowed us to quantify the grafting of GAPS at the surface (solid-state NMR was not sensitive enough for this purpose).

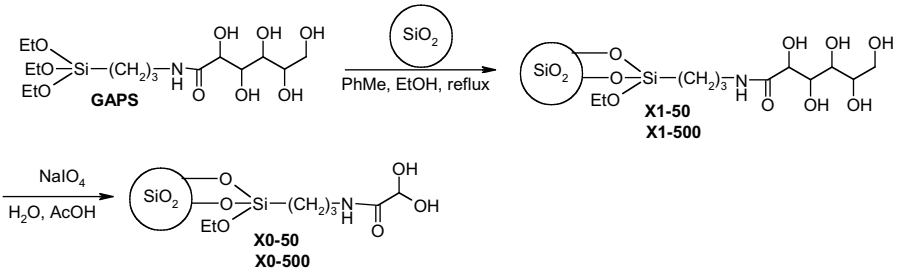

SCHEME 12.2 Synthesis of COCHO functionalized silicas using GAPS reagent and oxidative cleavage with periodate.

Loadings of 60 μmol/g and 257 μmol/g were obtained respectively. Treatment of silicas **X1-50** or **X1-500** with an excess of periodate in 10% aqueous acetic acid led to the oxidative cleavage of the polyol chain and to the glyoxylyl supported silicas (**X0**). IR analysis showed a shift for ν C=O at higher wavelength (1682/cm) after oxidation which confirmed the cleavage of the polyol chain and the successful formation of the COCHO group.

12.2.2.2 Synthesis of Semicarbazide Functionalized Silicas Silicas modified by hydrazine derivatives have been described by few authors. These materials were prepared using multistep procedures and involved the reaction of dihydrazides with supported electrophiles, such as aliphatic aldehydes or epoxides (51–53). Surprisingly, semicarbazide silica supports have been scarcely studied (14,29,36,51–54). The preparation of semicarbazide silicas required the synthesis of compound **4** according to Scheme 12.3. Reagent **4** was synthesized by reacting commercially available triethoxysilylpropylisocyanate **3** with $FmocNHNH_2$ (96% yield) (55).

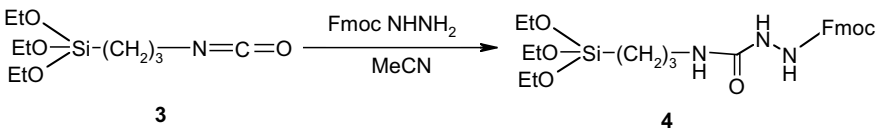

SCHEME 12.3 Synthesis of silane **4**.

Then, solid supports **XS**, could be prepared in two steps by reacting silane **4** with silica particles **X**. 50 μmol/g of **1** (**XS-50**) or 500 μmol/g of **1** (**XS-500**) were used with silica **X**. All the prepared semicarbazide silicas presented characteristic absorptions for carbonyl groups at about 1730 (ν C=O) and 1654 (ν C=O)/cm. One of the interest of the Fmoc protecting group is the possibility to determine the loading of the solid supports by treatment with piperidine followed by spectrophotometric UV analysis of the dibenzofulvene-piperidine adduct (Scheme 12.4). Loadings of 36 μmol/g and 320 μmol/g, were obtained for solid supports **XS-50**, **XS-500**, respectively.

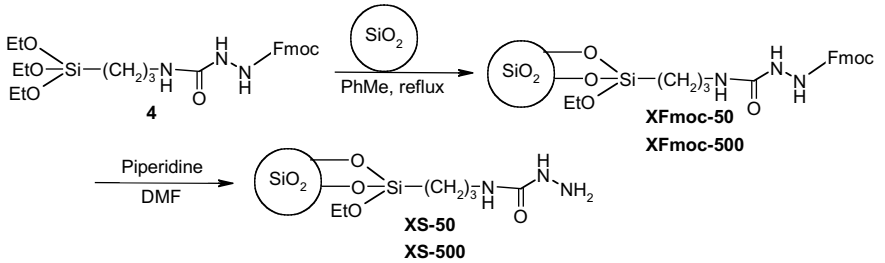

SCHEME 12.4 Synthesis of semicarbazide silicas **XS**.

12.2.2.3 Ligation Experiments The glyoxylyl peptide **5** was used to estimate the level of physisorption on COCHO silicas and the yield of site-specific ligation on

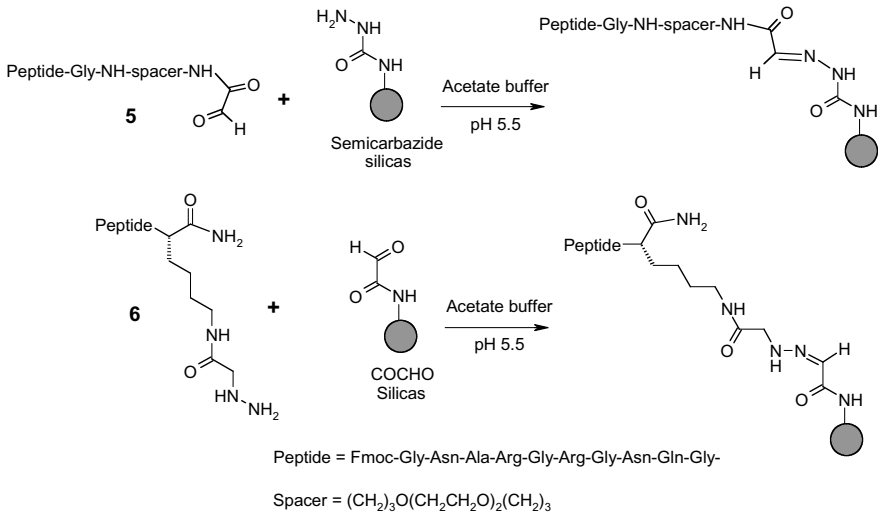

SCHEME 12.5 Reaction of peptides **5** and **6** with semicarbazide (**XS**) or α-oxo aldehyde (**X0**) silicas in sodium acetate buffer (pH 5.5).

semicarbazide silicas. Analogously, α-hydrazinoacetyl peptide **6** was utilized to estimate the level of physisorption on semicarbazide silicas and the yield of site-specific ligation with COCHO silicas (Scheme 12.5). A wiser choice would be to use a peptide derivatized by a semicarbazide group. However, unpublished data from our laboratories demonstrated the difficulty of preparing these modified peptides, mostly due to the hydrolysis of the semicarbazide group in aqueous solution at acidic pH, that is, the experimental conditions routinely used for the RP-HPLC analysis and purification of peptides. The chemistry of α-hydrazinoacetyl group and its utility in ligation reactions with COCHO peptides has been demonstrated (43,56–58). Thus, peptide **6** was considered as a good alternative to probe the reactivity of COCHO solid supports.

Ligations and control experiments were performed in pH 5.5 sodium acetate buffer at a fixed peptide concentration of about 1 mM. All the experiments were carried out by using 36 or 50 μmol of peptide per gram of silicas **X0** or **XS**. Thus, the stoichiometry of functionalized silica ranged from 1 to about 10 equiv depending on the loading of the silica particles. After the incubations, the solid supports were washed with an acetate buffer containing 0.5% of Tween® 20 and with water to remove the excess peptide. The ligation yield was determined after spectrophotometric quantification of the dibenzofulvene-piperidine adduct formed by treating the particles with 20% piperidine in DMF. The results are presented in Fig. 12.2. The yields are expressed relative to the peptide quantity engaged in the experiments.

The yields of immobilization of peptides **5** and **6** on glyoxylyl silica **X0-50** are comparable (about 20%), thus indicating that little or no site-specific ligation occurred on this solid support. Alternately, support COCHO-silica **X0-500** led to about 60% of immobilization with hydrazinoacetyl peptide **6**, whereas the Fmoc loading obtained in

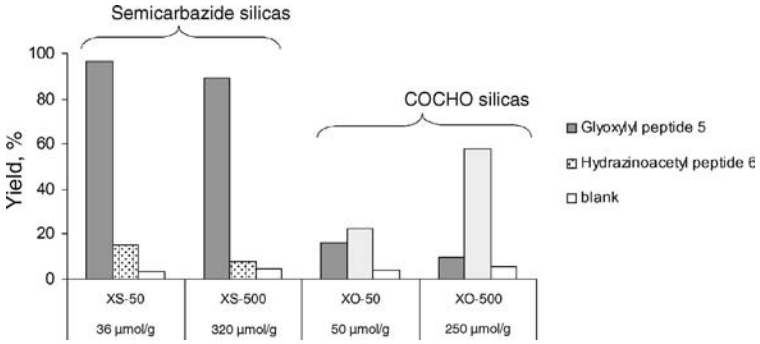

FIGURE 12.2 Immobilization yield of peptides **5** and **6** on semicarbazide (**XS**) or α-oxoaldehyde (**X0**) silicas

the control experiment with peptide **5** was below 10%, showing that site-specific ligation occurred between hydrazinoacetyl peptide **6** and COCHO-silica **X0-500**. Thus, silica **X0-500** appears as an interesting solid support for the preparation of hybrid materials owing to its ease of preparation starting from GAPS, which is a cheap commercially available reagent. The approaches presented here are interesting alternatives to the methods described in the literature (27,50).

If we now consider the semicarbazide substrates, reaction of glyoxylyl peptide **5** with a stoichiometric amount of solid support **XS-50** led to a high yield (97%) of immobilization, with only 15% of physisorption in the control experiment with hydrazinoacetyl peptide **6**. Utilization of higher loadings (support **XS-500**) led to similar results in term of ligation yield (84–90%) and physisorption (5–15%).

The behavior of the functionalized particles described in this study differ significantly from the sol-gel materials described recently (50). Indeed, hybrid organic-inorganic semicarbazide or glyoxylyl sol-gel matrices were unable to react with the corresponding functionalized peptides. Reaction with small chemical reagents was observed showing that the absence of reaction with peptides was mainly due to the inability of the polypeptide chain to diffuse into the sol-gel matrix.

The good reactivity of semicarbazide silicas toward COCHO-peptides, the low level of physisorption observed with these solid substrates and the stability and ease of synthesis of COCHO-peptides compared to semicarbazide peptides led us to select semicarbazide substrates and COCHO peptides for the preparation of peptide microarrays as described in Scheme 12.6.

12.2.3 Preparation and Characterization of Semicarbazide Microscope Glass Slides

Two methods were explored to install the semicarbazide layer on microscope glass slides. The first one is based upon the utilization of silane Fmoc-NHNHCONH $(CH_2)_3Si(OEt)_3$ **4** and is similar to the method used above to derivatize silica microparticles. This mode of functionalization led to poor results with microscope

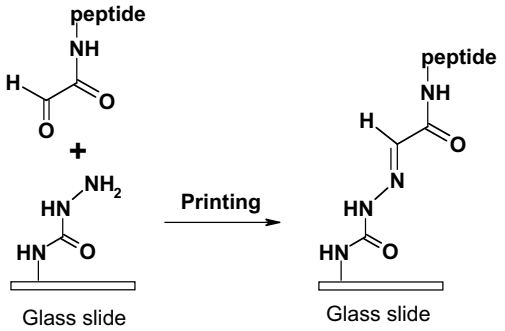

SCHEME 12.6 α-oxo semicarbazone site-specific ligation of glyoxylyl peptides onto semicarbazide functionalized glass slides.

glass slides and was abandoned. The second method involves the silanization of the microscope glass slides with 3-aminopropyltrimethoxysilane to form an amine layer and the subsequent conversion of amino groups into semicarbazide groups as described in Scheme 12.7. The amino group B was converted into isocyanate group C using triphosgene. Reaction of the isocyanate with $FmocNHNH_2$ led to intermediate D, which upon treatment with piperidine led to the formation of semicarbazide group E. The use of hydrazine instead of $FmocNHNH_2$ led to poor results.

The optimization of semicarbazide glass slides and the quality control of the different batches required a robust method for the qualitative evaluation of the surface density and homogeneity of semicarbazide groups. This characterization was performed using tetramethylrhodamine-labeled peptides **7** and **8** and fluorescence detection. (Figure 12.3) The quality control is based on the immersion of 2 slides in a solution of glyoxylyl peptide **7**, whereas two other slides are treated with the control peptide amide **8**. The slides are washed to remove adsorbed peptide and analyzed using the 532 nm channel of a standard microarray fluorescence scanner. The mean fluorescence intensity of the slides and its standard deviation is determined using

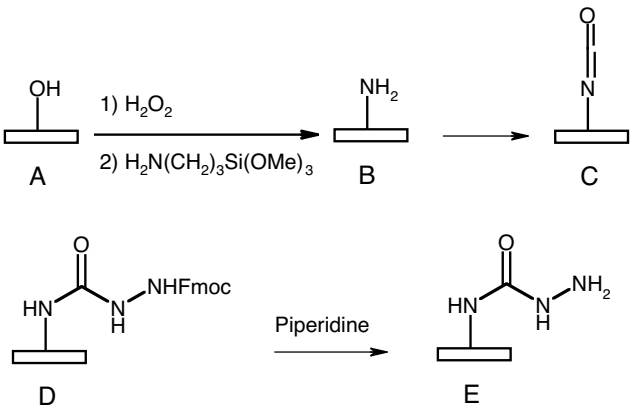

SCHEME 12.7 Preparation of semicarbazide microscope glass slides.

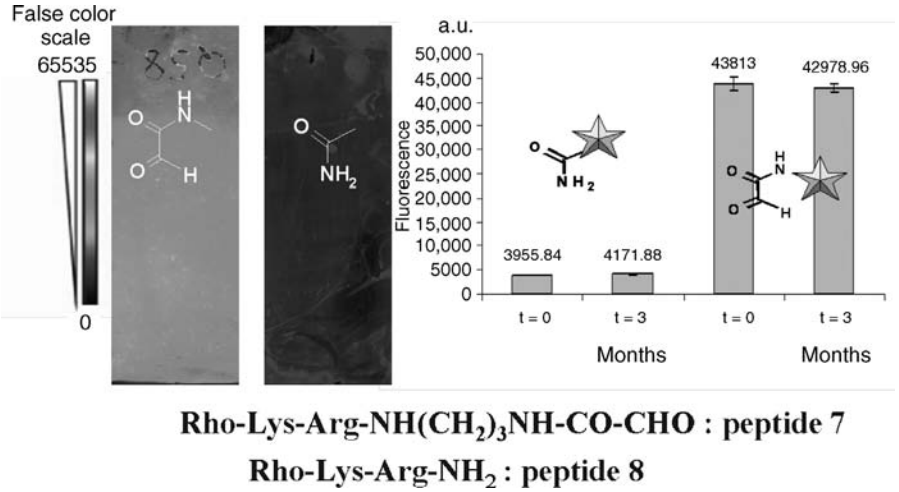

FIGURE 12.3 Quality control using glyoxylyl-peptide **7** and peptide amide **8**. On the left-hand side, false color scale images at 532 nm (Affymetrix 418 scanner, L35, PMT50) of semicarbazide glass slides reacted with peptides **7** or **8**. On the right-hand side, results after quantification. The fluorescence is expressed in arbitrary units (A.U.). The data were analyzed using ScanAlyze Software (Stanford University)

a grid of 320 virtual spots distributed upon the entire surface. If the glass surface is densely covered by accessible semicarbazide groups, the difference in fluorescence intensity between the two slides must be high. The mean fluorescence intensity and its standard deviation are a good measure of the glass slide quality.

Typical results are presented in Fig. 12.3. The fluorescence intensity obtained with COCHO peptide **7** is about 10 times higher than the fluorescence obtained with control peptide **8**. No significant difference was observed between the two peptides with underivatized microscope glass slides. Taken together, these results demonstrate the site-specific immobilization of COCHO-peptide **7** on the semicarbazide substrate. A study dealing with the immobilization of COCHO peptides labeled with a cobalt carbonyl probe at the surface of oxidized silicon wafers functionalized with the semicarbazide group was published recently. ATR-FTIR spectroscopic studies demonstrated that the peptide derivatized by the COCHO function was immobilized with a yield of 82%, whereas the control peptide was immobilized with a yield of 5% (53). Thus, roughly the same ratios of chemisorption/physisorption were obtained with peptides reacted with different semicarbazide surfaces and derivatized by tetramethylrhodamine or cobalt-carbonyl labels.

This method of characterization was also used to document the chemical stability of the semicarbazide slides upon aging. Slides of the same batch were analyzed just after preparation or following 3 months of storage at room temperature in a closed chamber. The data presented in Fig. 12.3 show that the fluorescence intensity of the slides did not change over a 3 months period for both labeled peptides ($p < 0.05$). The coefficient of variation of the fluorescence intensity was also unaffected in this experiment (4–8% for peptide **7** and 4–7% for peptide **8**). Thus, the chemical

properties of the semicarbazide slides are conserved at least 3 months even if some air pollution could be detected after 30 days of storage by contact angle measurements (see later).

From experiments using COCHO-ODNs radiolabeled with ^{32}P at the 3′-terminus and phosphorimaging, we were able to determine a semicarbazide density of 300 fmol/spot (28). The quantity of immobilized ODN obtained in this experiment is comparable to those obtained by Podyminogin et al. using benzaldehyde ODNs and corresponds to a density of $\sim 1.10^5$ molecules/μm^2 at 100 μM (36). This density is comparable to the density of ODN arrays prepared by *in situ* synthesis (59).

We have described a chemical method allowing a quality control of the semicarbazide surface reactivity based on the reaction of a semicarbazide substrate with peptide **7** or **8**. An interesting aspect of this method is the possibility to characterize the homogeneity of the surface viewed through the reactivity of solvent accessible semicarbazide groups. A complementary method allowing the rapid, simple, and cheap characterization of surfaces is to perform contact angle measurements with liquids whose surface tension is well known.

α-bromonaphtalene, dimethylsulfoxide, and ethyleneglycol were found to spread on semicarbazide slides. Diiodomethane, water, and formamide were found to be useful remove liquids. Contact angle measurements performed just after the preparation of the surfaces can be considered as reference data for a quality control. These contact angles are collected in Table 12.1. The use of the Young's equation permitted the determination of the Lifshitz-van der Waals (LW) and Lewis acid and base surface tension parameters according to the Van Oss theory (Table 12.1) (60). In addition, we have calculated the free energy of interfacial interaction of the surface in water (ΔG_{sws}) and the free energy of binding of water to the surface (ΔG_{sw}), which are good indications of the hydrophilicity of a surface (61). The data for microscope glass slides silanized with 3-aminopropyltrimethoxysilane, which is a substrate often used for polypeptide microarray preparation were included for comparison.

The Lifshitz-van der Waals surface tensions of the surfaces were close to 44 mJ/m^2, a typical γ^{LW} value for a large number of substances. Both surfaces displayed a positive free energy of interfacial interaction between the surfaces in water ΔG_{sws}. The free energy of binding of water to the surface ΔG_{sw} was found to be inferior to −113 mJ/m^2,

TABLE 12.1 Contact Angle Measurements on Semicarbazide or Amine Glass Slides.

	Contact angle (SD) degrees			γ mJ/m^{2a}					
	w	dim	fad	tot	LW	Acid	Base	ΔG^b_{sws} mJ/m^2	ΔG^c_{sw} mJ/m^2
Semicarbazide	36.3 (0.5)	30.9 (0.2)	15.6 (0.9)	56.4	43.9	1.2	33.9	4.6	−131.5
Amine	33.1 (0.5)	31.5 (0.6)	21.5 (0.7)	54.0	43.8	0.7	39.8	13.7	−133.7

[a]The surface tension parameters of diiodomethane (dim), water (w), and formamide (fad) were taken from literature (20).
[b]Free energy of interfacial interaction of the surface in water.
[c]Free energy of binding of water to the surface.

a value below which a substance is usually considered as hydrophilic. Taken together, the data demonstrate that semicarbazide microscope glass slide is a hydrophilic substrate.

Another interesting application of contact angle measurements is to follow the evolution of the surface upon aging. The silane layer covering the glass slide surface can be the subject of changes due to chemical transformation of surface functional groups (e.g., air oxidation) or to the deposition of air contaminants. For example, air pollution of amine surfaces has been well studied (62). We have studied the evolution of the contact angles of the three reference liquids diiodomethane, water, and formamide on both amine (up to 15 days) and semicarbazide microscope glass slides (up to 2 months). In accordance with literature, contact angle measurements on amine surfaces obtained by silanization with 3-aminopropyltrimethoxysilane demonstrated a rapid pollution of the surface by air impurities (Fig. 12.4). The major change was observed during the first 8 days of aging.

For semicarbazide glass slides, a significant change in the contact angles was observed after 30 days of aging for diiodomethane and 60 days for water, thus suggesting that the semicarbazide glass slides are more stable toward air pollution than amine glass slides. Interestingly, pollution of the semicarbazide surface by air contaminants did not alter the reactivity of the layer as shown previously in a 3 month chemical stability study.

Finally, we have determined the thickness of the semicarbazide layer. After removing a defined region of the glass surface by reactive ion etching so as to get the original silicon oxide substrate, the height of the step at the frontier between the silicon oxide and semicarbazide surface was determined by AFM. The thickness of the layer was ranging from 1.8 to 2.2 nm, a value superior to the length of one silane unit (about 1 nm in an extended conformation).

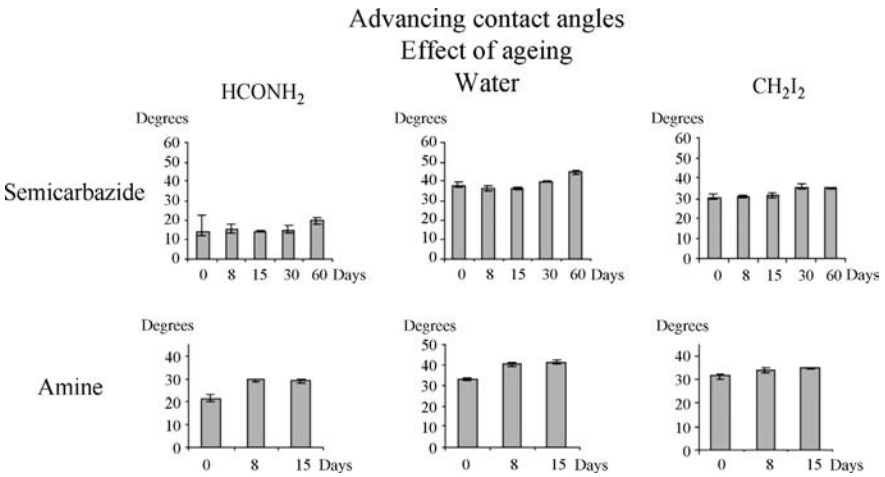

FIGURE 12.4 Stability studies on semicarbazide or amine glass slides using contact angle measurements with formamide, water, or diiodomethane at 20°C. The interquartile range is indicated at the top of the bar (median)

12.2.4 Peptide Microarrays, Model Study Using Biotinylated Peptide

The quality of the immobilization procedure was also examined using the well known biotin–streptavidin interaction. Peptides **9** and **10** were printed at different concentrations (10^{-3}–10^{-6} M) in a pH 5.5 0.1M sodium acetate buffer and the slides were incubated with tetramethylrhodamine-labeled goat antibiotin antibody in the presence of a competitor for nonspecific adsorption (5% BSA). As shown in Fig. 12.5, the signal displayed by the glyoxylyl-peptide **9** at 10^{-4} M was again about 10 times higher than those given by control peptide **10** lacking the glyoxylyl group for reacting with the substrate. This experiment demonstrates that the presence of a glyoxylyl group is important to avoid the loss of probe during the different incubation or washing steps.

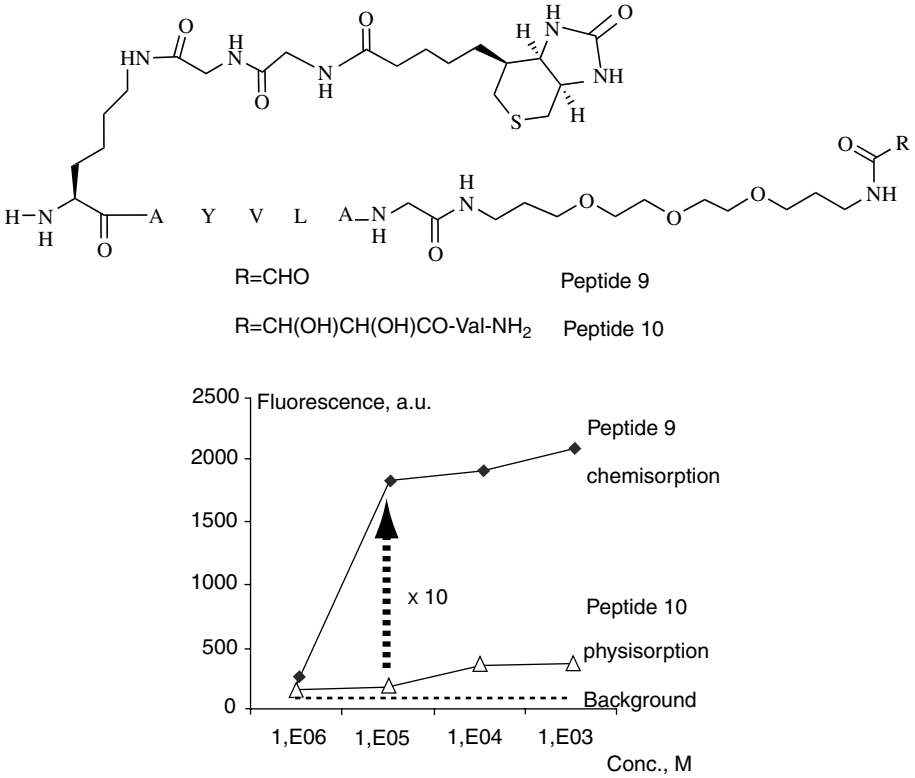

FIGURE 12.5 Printing of peptides **9** and **10** on semicarbazide slides and incubation of the arrays with tetramethylrhodamine-labeled goat anti-biotin antibodies (10^{-2} mg/mL). Incubations were performed in the presence of 5% (w/v) BSA. Affymetrix 418 scanner, 532 nm, L35, PMT50. The fluorescence is expressed in arbitrary units (a.u.). The data were analyzed using ScanAlyze Software (Stanford University)

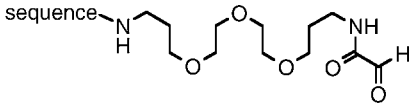

HCV p21 H-NTNRRPQDVKFPGGGQIVGGVYLLPRRGPRLG peptide 11

HCV NS4 H-AFASRGNHVSPTHYVPESDAAARG peptide 12

FIGURE 12.6 HCV peptides **11**-**12** used for the serodetection of antibodies from referenced sera

12.2.5 Peptide Microarrays for the Capture of Antibodies from Referenced Sera

The interest of the peptide microarray method presented here for the simultaneous capture of antibodies is illustrated with peptide antigens derived from HCV pathogen (HCV core p21 15-45 antigen for peptide **11**, HCV NS4 1925-1947 antigen for peptide **12**). The structure of peptides **11**-**12** is presented in Fig. 12.6. Detection of antibodies from serum was performed as illustrated in Fig. 12.7. The microarray was incubated with diluted human serum and then tetramethylrhodamine-labeled secondary antibodies. Detection was performed at 532 nm using a standard microarray scanner.

Sera were collected from the clinical laboratory of the Centre Hospitalier Régional (Lille, France). The reactivity of HCV referenced sera was determined with the AxSYM® HCV version 3.0 Abbott ELISA kit (30 HCV-negative and 40 HCV-positive individuals). For some sera an additional RIBA® HCV 3.0 SIA test (Ortho-Clinical Diagnostics) or a DECISCAN® HCV PLUS test (BIORAD) was performed.

Group 1 of Table 12.2 is composed of false-positive sera by ELISA. These sera are negative using the Western blot test. Interestingly, the sera of group 1 were also found negative for the HCV antigens in the microarray format. Western blot core, NS3 and

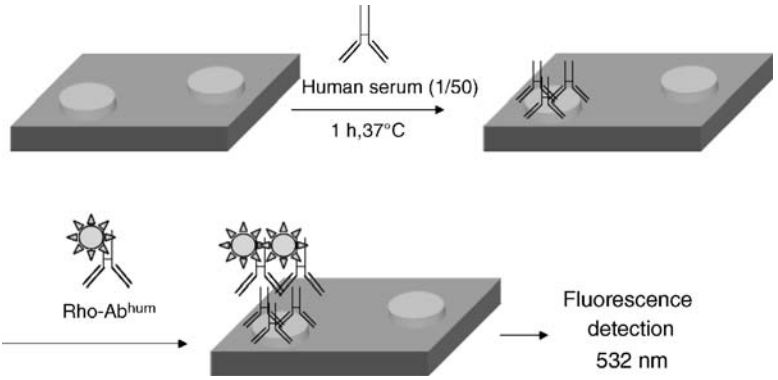

FIGURE 12.7 Detection of antibodies from referenced human serum using peptide microarrays. The microarray was incubated with diluted human serum and then with tetramethylrhodamine-labeled secondary antibodies. Detection was performed at 532 nm using a standard microarray scanner

TABLE 12.2 Sensitivity and Specificity Results Obtained with 40 HCV ELISA[a] Positive Sera. Microarray Experiment Using Peptides 11 and 12.

		Western-blot[b]				Microarray	
Group	Serum number	Core	NS3	NS4	NS5	Peptide 11	Peptide 12
1	1	—	—	—	—	0	0
	2	—	—	—	—	0	0
	3	—	—	—	—	0	0
	4	—	—	—	—	0	0
	5	—	—	—	—	0	0
	6	—	—	—	—	0	0
	7	—	—	—	—	0	0
	8	—	—	—	—	0	0
2	9	+++	++	++		15214	4658
	10	+++	++	++		22542	10684
	11	+++	++	++		29854	13654
	12	++	+++	+++		25145	9854
	13	+++	+++	+++		29854	13654
	14	+++	++	+++		34125	14985
	15	+++	+++	+		30489	4695
	16	+++	+++	++		21897	4685
	17	+++	++	++		31245	10238
	18	+++	+++	+++		20547	9584
	19	+++	+++	+++		31284	11278
	20	+++	+++	++		23654	10319
	21	+++	+++	+++		19874	15497
	22	+++	+++	+++		25421	9703
	23	++	+	+		13524	3958
	24	++	+	++		17954	10854
3	25	—	+++	+++		0	7985
	26	—	++	+		0	4625
	27	—	+++	+++		0	8547
	28	—	++	—		0	0
	29	—	++	+		0	3958
	30	++	++	—		15874	0
	31	+++	+	—		21547	0
	32	—	+	—	0.5+	0	0
4	33	—	0.5+	—	0.5+	0	0
	34	0.5+	—	—		2958	0
	35	0.5+	+	0.5+		213	428
	36	—	—	0.5+	0.5+	0	115
	37	+++	++	0.5+		19854	1654
	38	+++	++	0.5+		14528	384
	39	+++	+++	0.5+		13879	258
	40	+++	+++	0.5+		16547	215
Cut-off[c]						0	0

[a]AxSYM® HCV version 3.0 Abbott ELISA.

[b]Western blot assay: RIBA® HCV 3.0 SIA test or DECISCAN® HCV PLUS test.

[c]For the 30 HCV ELISA negative sera, the spots were indistinguishable from the background; leading to a zero output value after quantification. The cut-off value of positivity was set to zero.

NS4 positive sera are collected in group 2. In this case, both peptide antigens displayed high fluorescence signals. Group 3 includes the sera that displayed one or two western blot negative reactivities. The same sensitivity and specificity was observed with the arrayed antigens. Group 4 collects the sera that displayed at least one western blot 0.5+ intensity for core, NS3 or NS4 antigens. These sera were particularly useful since they permitted the evaluation of the performance of peptide-protein microarrays in a context, where the limit of sensitivity of the western blot was reached for at least one antigen. Interestingly, antibodies that led to a western blot 0.5+ intensity were easily and specifically detected using the peptide microarray, illustrating the ability of the miniaturized device to detect specifically low levels of antibodies in human sera. In principle, other peptide antigens can be added to improve the sensitivity of the detection and to characterize more precisely the binding properties of anti-HCV antibodies.

12.2.6 Conclusion

We have demonstrated that semicarbazide-COCHO site-specific ligation chemistry is an interesting tool for attaching peptides to microscope glass slides, for antigen-antibody recognition. In the last two parts of this article, we will describe the preparation of semicarbazide nanoparticles and their use for micropatterning polycarbonate or TiO_2 substrates.

12.3 MICROPATTERNING OF POLYCARBONATE

12.3.1 Introduction

Polycarbonate (PC) is a useful substrate for the preparation of microfluidic devices (63,64). Recently, its utility for bioanalysis has attracted much attention owing to the possibility of using compact discs as platforms for the high throughput analysis of biomolecular interactions (63,65–67). Unlike SiO_2 or gold substrates on which miniaturized devices are usually fabricated and for which various functionalization methods are available, methods for the chemical modification of the surface of PC are scarce. Indeed, PC is degraded by aqueous bases, swelled or solubilized by various organic solvents and cannot be exposed to temperatures exceeding 115°C. Thus, the design of mild functionalization methods for PC is of great interest and should widen its use for biosensor fabrication.

The method used for chemical micropatterning of polycarbonate is based on the printing of functionalized silica nanoparticles as described in Fig. 12.8. For this, silica nanoparticles functionalized with semicarbazide groups were printed on PC using a noncontact piezoelectric microarrayer to give micropatterns. The semicarbazide groups present on the micropatterns were site-specifically reacted with unprotected peptides derivatized by an α-oxo aldehyde group, featuring peptides linked to the micropatterns through a semicarbazone bond (28,29,53). The surface between the spots was left unchanged. Importantly, the use of nanoparticles of different diameters

(from 27 to 304 nm) permitted the study of the influence of surface curvature on signal strength and capture specificity.

The chemical reactivity of the nanoparticles adsorbed on PC was examined by reaction with glyoxylyl peptides **7** and **8** labeled with tetramethylrhodamine, followed by fluorescence detection as already discussed in Fig. 12.3. The capture properties of immobilized peptide probes were studied using influenza hemagglutinin (HA) or FLAG tag peptides and their corresponding murine antibodies. The principle of the detection is illustrated in Fig. 12.7. In the present case, a second incubation with secondary anti-murine antibodies labeled with tetramethylrhodamine was performed for fluorescence detection instead of secondary anti-human antibodies.

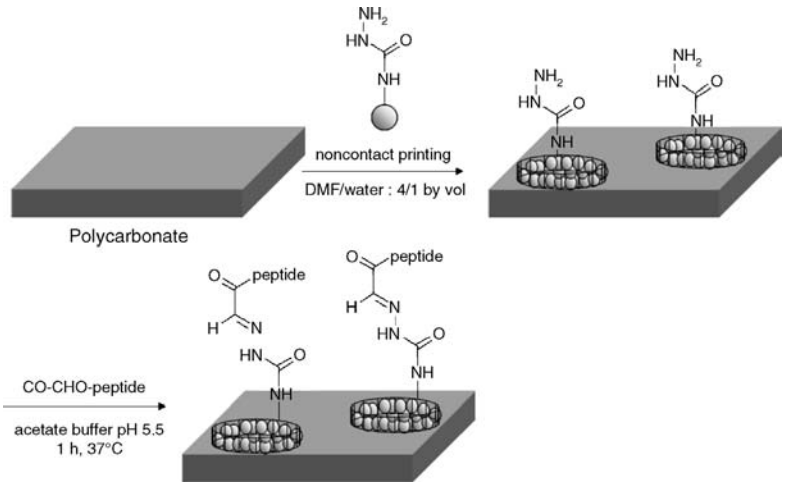

FIGURE 12.8 Chemical micropatterning of PC for the site-specific immobilization of peptides. The semicarbazide nanoparticles (27–304 nm, 1% w/v) in suspension in 20% aqueous DMF were printed on the PC slides (75 × 25 × 1 mm) using a noncontact microarrayer (3 drops, ~1 nL overall). Incubation of the micropatterns with glyoxylyl-peptide (0.1 mM in 0.1 M pH 5.5 sodium acetate buffer with 0.1% w/v BSA) led to the site-specific anchoring of the peptide to the micropattern

12.3.2 Synthesis of Silica Nanoparticles

Silica nanoparticles of different diameter (82, 151, 192, 256, 304 nm) were prepared by hydrolysis and polymerization of tetraethylsilicate in the presence of ammonia and ethanol (68). Silica nanoparticles of 27 nm are commercially available (Ludox AS-40).

Silica nanoparticles were silanized in *N,N*-dimethylformamide (DMF) with silane **4** (see Scheme 12.4) to give semicarbazide silica nanoparticles. The method used to derivatize the nanoparticles is similar to the method used above for microparticles. The experimental procedure is however vastly different because unlike microparticles, nanoparticles are prone to aggregation in organic solvents. To avoid the aggregation of silica nanoparticles during their transfer into organic solvent, traces of sodium and

chloride ions must be carefully removed. Ludox AS-40 nanoparticles contain such impurities. Thus, the commercially available suspension of Ludox nanoparticles in water was diluted with deionized water and treated with cation- and anion-exchange resins, respectively. The suspension was diluted with ethanol and DMF, and then water and ethanol were remaind by distillation (69). The ion-exchange procedure was not necessary for the nanoparticles prepared by hydrolysis of tetraethylsilicate because contamination by sodium or chloride ions in this case was negligible. Silane **4** used for the grafting of semicarbazide groups on the surface of silica nanoparticles is protected by a Fmoc group. Silanization was performed in the presence of piperidine, which permitted the *in situ* removal of the Fmoc protection but also the catalysis of siloxane bond formation. The semicarbazide nanoparticles were extensively washed with DMF and stored at 4°C as 1% (w/v) suspensions in DMF. The suspensions were stable for months.

The nanoparticles were characterized by ^{13}C and ^{29}Si NMR, FTIR, microanalysis, scanning or transmission electron microscope (SEM, TEM). ^{29}Si solid-state NMR spectroscopy gives useful information on the silanization step since the chemical shift of ^{29}Si is highly sensitive to the number and nature of groups attached to it (70). CPMAS ^{29}Si NMR spectrum of 27 nm semicarbazide nanoparticles is presented in

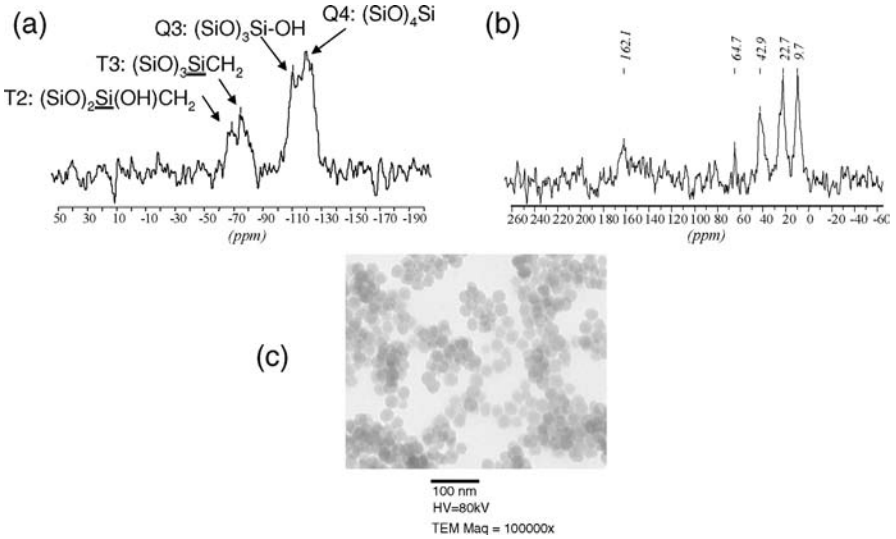

FIGURE 12.9 Characterization of 27 nm semicarbazide nanoparticles prepared starting from Ludox AS-40 nanoparticles, **(a)** ^{29}Si CP-MAS NMR spectrum of the solid 27 nm semicarbazide nanoparticles were recorded on a Bruker spectrometer at 79.49 MHz using 5 μs single pulses (60° flip angle) with 10 s repetition rate and 15 ms contact time employing magic angle spinning at 3.5 kHz; 10,000 scans were accumulated. All ^{29}Si chemical shifts were referenced to tetramethylsilane (TMS). (**b**) ^{13}C CP-MAS NMR spectrum were recorded on a Bruker spectrometer at 100.62 MHz using 10 μs single pulses ($\pi/6$) with 5 s repetition rate and 3 ms contact time employing magic angle spinning at 3.5 kHz; 50,000 scans were accumulated. (**c**) TEM image

Fig. 12.9a. Signals at −101 and −110 ppm correspond to Q3 (surface silanol $(SiO)_3SiOH$) and Q4 $(SiO)_4$ silicon species that are usually observed for bare silica. Novel signals due to the reaction with silane **4** are visible at 58.6 and 64.5 ppm that are due to the silicon atom of silane **4** implicated in 2 ($(SiO)_2SiCH_2$-, T2) or 3 ($(SiO)_3$-$SiCH_2$, T3) siloxane bonds with the surface. The presence of T2-T3 species, the absence of T1 $(SiO)Si(OH)_2CH_2$- and Q2 $(SiO)_2Si(OH)_2$ species and finally the variation in signal intensity for species Q3 and Q4 relative to bare silica demonstrate the efficient grafting of silane **4** on the surface of silica nanoparticles.

The CPMAS ^{13}C spectrum of 27 nm semicarbazide nanoparticles is presented in Fig. 12.9b. Three resonances situated at 9.7, 22.7, and 42.9 ppm correspond to the propyl chain of silane **4**. The resonance at 162.1 ppm is attributed to the carbonyl group of the semicarbazide function. Signals corresponding to ethoxy groups or Fmoc groups were not detected.

12.3.3 Micropatterning

12.3.3.1 Reactivity of the Micropatterns Sheets of molded polycarbonate were cut with a high pressure water jet to the dimension of microscope glass slides (75 × 25 × 1 mm), allowing the use of standard microarray equipment for the printing, incubation, and detection steps. The PC slides were washed with deionized water and absolute ethanol before printing. Semicarbazide nanoparticles at a concentration of 1% in 20% aqueous DMF were printed on PC slides using a noncontact piezoelectric arrayer (3 drops, ~1 nL overall).

The reactivity of the adsorbed nanoparticles was examined using peptides Rho-Lys-Arg-$NH(CH_2)_3NHCOCHO$ **7** and Rho-Lys-Arg-NH_2 **8**. For this, the printed PC slides were incubated under cover-glass with peptides **7** or **8** dissolved at 0.1 mM in 0.1 M pH 5.5 acetate buffer for 1 h at 37°C, washed with 0.01 M phosphate buffered saline pH 7.2 containing 0.05% of tween® 20 to remove the excess peptide and then analyzed with a standard fluorescence microarray scanner at 532 nm (Fig. 12.10).

The highest signals were obtained for 82 and 27 nm nanoparticles probably due to a higher specific surface area. The signal obtained with control peptide **8** was always low compared to COCHO peptide **7**. The ratio between the signals obtained with peptide **7** and **8**, indicated at the top of the bars in Fig. 12.1, was 19.3 and 12.8 for 82 and 27 nm nanoparticles, respectively. The printing of underivatized 27 nm silica nanoparticles **7** led to a ratio of 0.5 (data not shown). For comparison, a ratio of about 10 was obtained for a similar experiment performed using microscope glass slides derivatized by semicarbazide groups (see Fig. 12.3) (28). These data demonstrate that semicarbazide nanoparticles adsorb onto PC and that their ability to react chemoselectively with a glyoxylyl-peptide is preserved.

12.3.3.2 Capture of Antibodies An obvious application of the method described here for micropatterning PC could be the preparation of PC devices able to capture antibodies in biological fluids. Thus, we have examined the capacity of the peptides immobilized on PC through the nanoparticle layer to interact

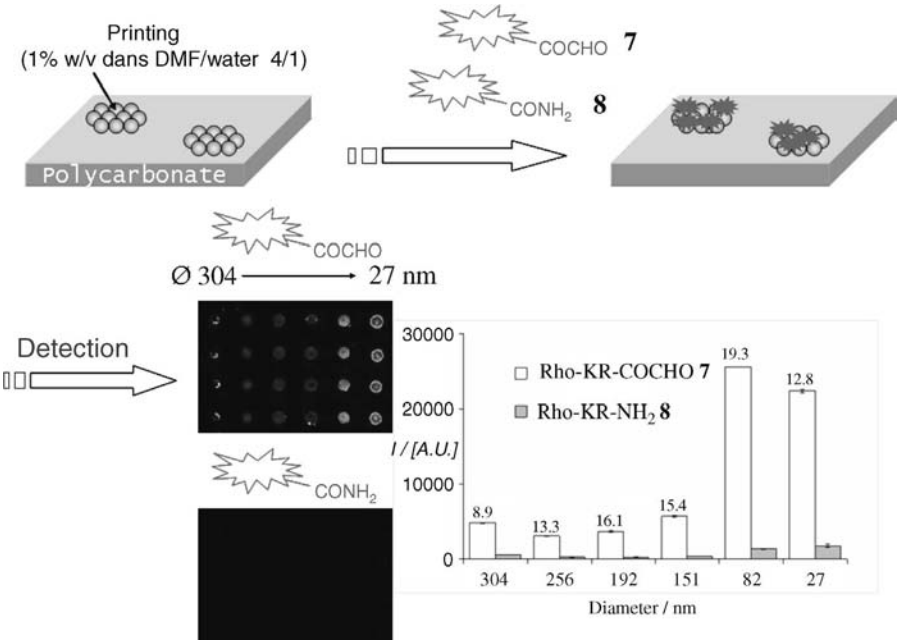

FIGURE 12.10 Reactivity of semicarbazide nanoparticles (∅ from 27 to 304 nm) printed on PC (1% w/v in 20% aqueous DMF, 3 drops, 1 nL). The PC slides were incubated with glyoxylyl peptides **7** or peptide amide **8** (0.1 mM in 0.1 M pH 5.5 sodium acetate buffer, 120 μL under cover-glass), washed and fluorescence (arbitrary units, a.u.) was determined with a confocal microarray fluorescence scanner at 532 nm (16-bit images). The data correspond to the median and interquartile range for 3 slides. The ratio between the signals obtained with peptides **7** and **8** is indicated on top of the bars

specifically with antibodies in solution. HA (71) and FLAG (72) tag peptides and commercially available anti-HA and anti-FLAG monoclonal antibodies were chosen for this study. The different semicarbazide nanoparticles were printed on PC slides as described before and the surfaces were covered for 1 h at 37°C with 120 μL of the COCHO-HA **13** or COCHO-FLAG **14** peptides dissolved at 0.1 mM in pH 5.5 sodium acetate buffer containing 0.1% BSA. BSA was used to avoid the adsorption of the peptides on the PC surface. The surfaces were washed to remove the excess of peptide and incubated for 1 h at 37°C with murine anti-HA, murine anti-FLAG, or murine IgGs antibodies used as negative control. Captured antibodies were detected by incubating the substrates with goat antibodies against murine IgGs labeled with tetramethylrhodamine. The PC slides were analyzed at 532 nm using a standard confocal microarray scanner.

Fig. 12.11 shows an image of the micropatterns obtained for 27 (A) and 82 (B) nm nanoparticles after incubating the substrates with anti-HA or anti-FLAG antibodies at a concentration of 10 μg/mL, or the buffer. The other micropatterns are not shown for clarity. The corresponding fluorescence values are presented in Fig. 12.12. High signal intensities (>10.000 a.u.) were obtained for HA or FLAG peptides in the

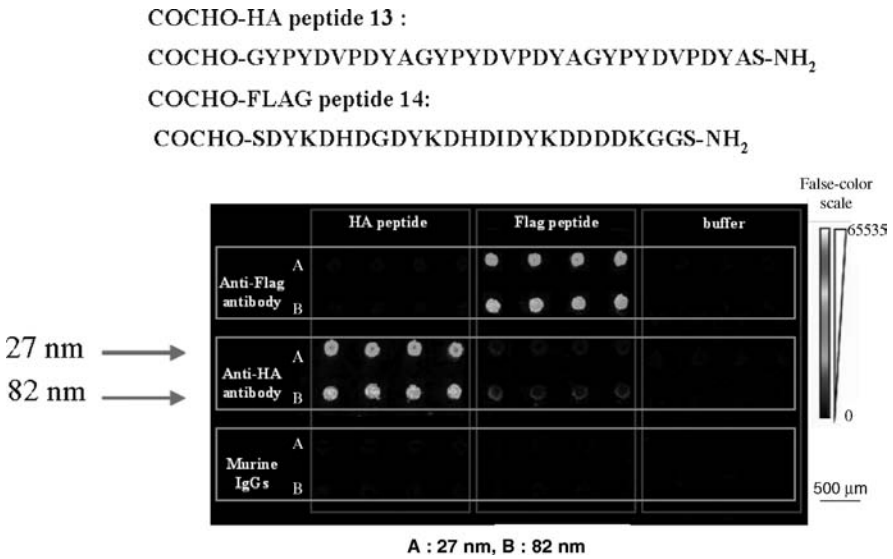

FIGURE 12.11 Semicarbazide nanoparticles were printed in quadruplicate on PC slides and each experiment was performed in triplicate. HA or FLAG peptides were ligated to the semicarbazide micropatterns (0.1 mM in 0.1 M pH 5.5 sodium acetate buffer, 1 h at 37°C, 120 µL) and then incubated with anti-HA, anti-FLAG or murine antibodies for 1 h at 37°C (120 µL). Secondary antibodies against murine IgGs labeled with tetramethylrhodamine were diluted 1/100 in PBS containing 0.05% of tween® 20 and 2% BSA (1 h at 37°C, 120 µL). The surfaces were analyzed at 532 nm using a standard fluorescence microarray scanner. The figure shows typical 16-bit images (false-color scale), line A: 27 nm nanoparticles, line B: 82 nm nanoparticles. Antibody concentration: 10 µg/mL. The other micropatterns are not shown for clarity

presence of anti-HA or anti-FLAG antibodies respectively. The signal associated with semicarbazide nanoparticles alone (buffer, Fig. 12.11) corresponded to the background for all the tested antibodies, showing that antibodies did not physisorb on the nanoparticles. Anti-HA antibody cross-reacted slightly with the FLAG peptide, probably because, unlike the anti-FLAG antibody, it was not affinity-purified. The cross reactivity between FLAG peptide and anti-HA antibodies was also observed on amine-modified microscope glass slides, a surface which is often used for the preparation of peptide microarrays (data not shown). Fluorescence displayed by HA micropatterns in the presence of anti-FLAG antibodies or of HA and FLAG micropatterns in the presence of murine IgGs corresponded to the background of the substrate, demonstrating the high specificity of the capture of anti-HA or FLAG antibodies by immobilized peptides. The arrow in Fig. 12.12 illustrates the influence of the diameter of the nanoparticles on the level of cross-reactivity of anti-HA antibody with FLAG peptide. Interestingly, the signal displayed by FLAG micropatterns incubated with anti-HA antibodies decreased when decreasing the diameter of the nanoparticles (FLAG, gray bars, Fig. 12.12), whereas the signal of the same micropatterns incubated with anti-FLAG antibodies tends to increase (FLAG, black bars, Fig. 12.12).

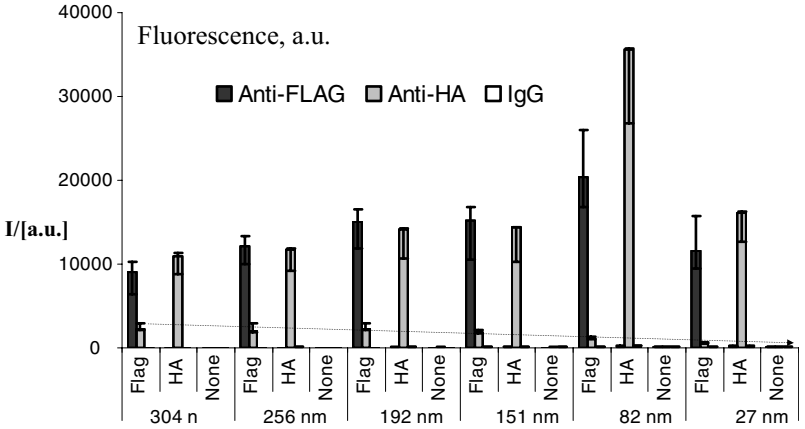

FIGURE 12.12 Fluorescence intensities corresponding to the experiment presented in Fig.12.11. The data were obtained by incubating the surfaces with anti-HA antibody (gray bars), anti-FLAG antibody (black bars), or murine IgGs (white bars) and correspond to the median and interquartile range (arbitrary units). The arrow illustrates the influence of the diameter of the nanoparticles on the level of cross-reactivity of anti-HA antibody with FLAG peptide

Obviously, the best selectivity was observed for the smallest particles. This effect is clearly visible in Fig. 12.11 that compares 27 and 82 nm nanoparticles (column FLAG peptide, row anti-HA antibody). The effect of the curvature of surfaces on the conformation of proteins and/or biomolecular interactions occurring at the solid–liquid interface is the subject of intense research. For example, the effect of the size of silica nanoparticles on the structure and function of adsorbed lysozyme (mainly through electrostatic forces) was studied by Vertegel et al. (73). These authors showed that less significant perturbation of lysozyme's secondary structure was observed when the protein was adsorbed onto smaller nanoparticles. Similarly, Roach et al. have studied the effect of surface curvature on the conformation of adsorbed BSA or fibrinogen (74). Particles with high surface curvature (small particles) were found to stabilize the native like conformation of BSA. Fibrinogen, in sharp contrast to BSA and lysozyme, becomes more denatured upon binding to smaller particles. Very recently, Mandal et al. have described the effect of the surface curvature on the secondary structure of Leucine-rich peptide adsorbed on gold nanoparticles (75). Van Oss et al. have also discussed in detail the role of surface curvature on interfacial interactions between proteins and surfaces (76). In particular, aspecific interactions are favored when the interacting surfaces present a large radius of curvature. Clearly, such phenomena may play a crucial role in the trend observed in this work. Interestingly, micropatterning of PC could be successfully realized with nanoparticles of different size from 27 to 304 nm. It is thus possible to choose the optimal diameter relative to the immobilized species and the biomolecular interaction studied.

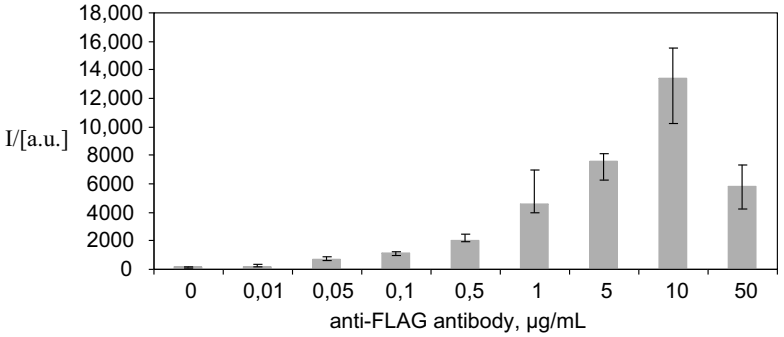

FIGURE 12.13 Incubation of FLAG micropatterns (see Figure 12.11 for experimental details) with different concentrations of anti-FLAG antibody (0–50 μg/mL). The data correspond to the median and interquartile range (arbitrary units)

Fig. 12.13 corresponds to the incubation of the FLAG-27 nm micropatterns incubated with different concentrations of anti-Flag antibody from 0 to 50 μg/mL. The signal displayed by FLAG micropattern for an antibody concentration of 0.05 μg/mL was significantly different from the background. The microspot fluorescence was found to decrease at high antibody concentration (50 μg/mL). This phenomenon can be attributed to the self-quenching of the rhodamine induced by the high concentration of anti-FLAG antibody on the micropattern. This self-quenching effect, which was already observed using peptide microarrays prepared on amine-modified microscope glass slides, is not due to the nanoparticles or to the PC substrate (77).

12.4 MICROPATTERNING OF TITANIUM OXIDE

The usefulness of semicarbazide nanoparticles for the micropatterning of polycarbonate surfaces led us to consider the application of this functionalization method to other substrates, in particular metallic ones.

We have focused our work on titanium, which is nowadays the metal of choice for biomedical applications, but also a material used for the preparation of biosensors (64,78). Thus, the development of a novel TiO_2 functionalization method should be of great interest for different applications. Various reagents are now available for titanium and titanium alloys surface modification, such as organosilanes (79) or phosphonic acids (80). The field has been recently reviewed (64). Self-assembled monolayers can then be utilized to graft polypeptides onto the titanium surface but usually the grafting method utilizes functional groups already present in polypeptides, such as thiols (81), amino- or carboxylate moieties, that may potentially result in the formation of several bonds between the polypeptide and the surface and thus impair its accessibility. We have examined the possibility to functionalize the titanium surface using the same strategy as for polycarbonate. The reactivity of adsorbed 27 nm semicarbazide nanoparticles was examined using peptides **7** and **8** and fluorescence detection.

12.4.1 Adsorption of 27 nm Semicarbazide Nanoparticles

The preparation of the substrates was performed starting from commercially available mirror-polished titanium discs (15 mm in diameter). Prior to functionalization, the discs were cleaned by immersion in 30% nitric acid, thus ensuring a uniform passivation TiO_2 layer over the whole surface, which participates to the biocompatibility of Ti and protects the surface from further oxidation (82).

The functionalization of the Ti surfaces was achieved by deposition of a layer of 27 nm semicarbazide silica nanoparticles. For this, the discs were carefully washed, dried, and then spin-coated with a 1% w/v suspension of semicarbazide nanoparticles in DMF. Spin-coating is a very fast and efficacious technique that allows relatively small surfaces (up to about 15 cm^2) to receive a uniform coating within less than a minute. The fluid deposited on the sample is spread by centrifugal force, and although DMF is not a volatile solvent, 45 s of spin coating are enough to produce uniformly coated, dry titanium surfaces. For each sample, a very low amount of colloidal suspension is required (75 μL).

12.4.2 Characterization

As it can be seen on the SEM micrographs (Fig. 12.14), the spin-coating procedure applied to a 0.1% (w/v) colloidal suspension produces surfaces with an incomplete layer of particles (Fig. 12.14a). However, when a 1% suspension is used, the surface obtained presents a uniform coverage (Fig. 12.14b).

Fig. 12.15 shows reflection infrared spectra of bare titanium and titanium coated with semicarbazide nanoparticles. Bare titanium shows no adsorption bands, apart from noise in the 2000/cm region. Coated titanium however, shows adsorption bands of semicarbazide nanoparticles. The very large asymmetric band at 1140/cm (asymmetric Si-O-Si stretching), as well as bands at 943.3/cm (νSi-OH$-H_2O$) and 803/cm (ν_sSi-O-Si) are all attributed to silica. Smaller absorption bands at 1550/cm (amide II band), 1653/cm (amide I band), and 2930/cm (propyl) are all attributed to the semicarbazide moiety. The spectrum for the modified titanium is in all parts

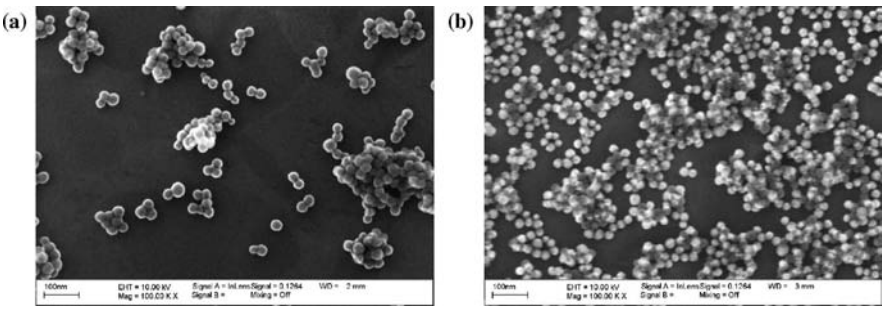

FIGURE 12.14 SEM micrographs of a Ti disc coated with a suspension of nanoparticles in DMF.(**a**)The disc was coated with a 0.1% (w/v) suspension of semicarbazide nanoparticles. (**b**) The disc was coated with a 1% (w/v) suspension of semicarbazide nanoparticles

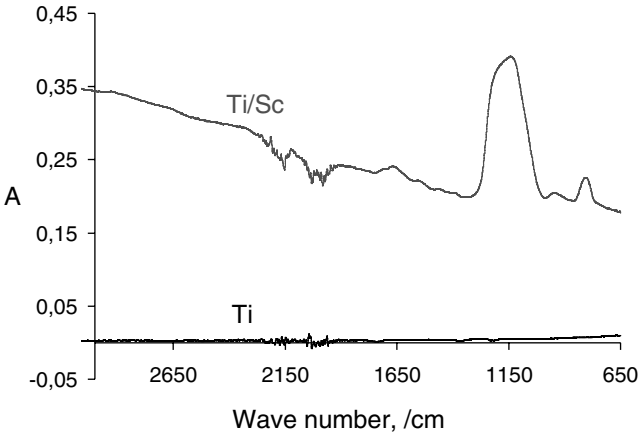

FIGURE 12.15 Reflection infrared spectra of bare Ti and Ti coated with a 1% suspension of semicarbazide nanoparticles

similar to the one for semicarbazide nanoparticles in dry KBr pellets (data not shown).

12.4.3 Reactivity and Chemoselectivity

Titanium discs were printed with an array of spots of increasing concentrations in semicarbazide nanoparticles. In order to assess the presence of accessible semicarbazide functions on the surface, we incubated the spin-coated titanium discs with peptides **7** or **8**. Results obtained from fluorescent detection are presented in Fig. 12.16. Across all printing concentrations (0.1–1% w/v), the signal obtained from glyoxylyl-peptide **7**

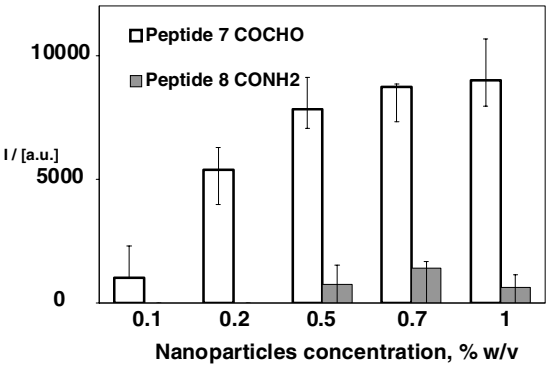

FIGURE 12.16 Reactivity of 27 nm semicarbazide nanoparticles printed on Ti discs. The nanoparticles were printed as suspensions in DMF/H_2O mixture 1/1 v/v. At 0.1 and 0.2% w/v, the fluorescence displayed by the spots after incubation with peptide **8** was below the background of the substrate. The data corresponds to the median and interquartile range of three experiments

is several fold greater than the signal from peptide **8**, as indicated by the ratios above the bars. This demonstrates that semicarbazide nanoparticles immobilized on titanium retain their reactivity and are able to react chemoselectively with aldehyde-containing polypeptides. The density of polypeptide on the surface can be controled by controling the density of nanoparticles on the titanium surface. This immobilization method opens the way to the easy modification of titanium surfaces by glyoxylyl-peptides produced by chemical synthesis or by complex polypeptides, such as oxidized glycoproteins using a simple experimental procedure (83). This work, which shows that titanium substrates can be easily modified by polypeptides, should favor the use of the material for medical and biosensor applications.

12.5 GENERAL CONCLUSION

This review focuses on the application of semicarbazide/α-oxo aldehyde ligation chemistry to the field of bioorganic-inorganic material synthesis and microarray field. We have demonstrated using silica microparticles that site-specific immobilization of peptides is best carried out by derivatizing the solid substrate with semicarbazide groups and the peptide by the α-oxo aldehyde group. Application of this ligation chemistry to microscope glass slides permitted the preparation of peptide microarrays. Model studies with HCV-derived peptide antigens and a collection of referenced sera demonstrated the specificity and sensitivity of the antibodies capture from serum. We have also presented the synthesis of semicarbazide nanoparticles. The nanoparticles can be used for micropatterning polycarbonate substrates. The reactivity of the nanoparticles is retained after printing. We have studied the capture of antibodies by peptide micropatterns and shown that the diameter of the nanoparticles has an important impact on the selectivity of the capture. The best results in term of selectivity were obtained for the smallest particles.

ACKNOWLEDGMENTS

We would like to thank CNRS, Université de Lille 1 and 2, Institut Pasteur de Lille, and ANRT for financial support. The microarray facility (Institut de Biologie de Lille) was financed by the Région Nord Pas de Calais, the European Community (FEDER), and the Ministère de la Recherche et des Nouvelles Technologies (puces nano-3D and FANSBAMED projects).

REFERENCES

1. Templin MF, Stoll D, Schrenk M, Traub PC, Vohringer CF, Joos TO. Drug Discov Today 2002;7:815–822.
2. Talapatra A, Rouse R, Hardiman G. Pharmacogenomics 2002;3:527–536.
3. Ryan TE, Patterson SD. Trends Biotechnol 2002;20:S45–S51.

4. Xu Q, Lam KS. J Biomed Biotechnol 2003;5:257–266.
5. Ekins RP. Clin Chem 1998;44:2015–2030.
6. Glokler J, Angenendt P. J Chromatogr B Analyt Technol Biomed Life Sci 2003;797: 229–240.
7. Graham KL, Robinson WH, Steinman L, Utz PJ. Autoimmunity 2004;37:269–272.
8. Hueber W, Kidd BA, Tomooka BH, Lee BJ, Bruce B, Fries JF, Sonderstrup G, Monach P, Drijfhout JW, van Venrooij WJ, Utz PJ, Genovese MC, Robinson WH. Arthritis Rheum 2005;52:2645–2655.
9. Neuman de Vegvar HE, Amara RR, Steinman L, Utz PJ, Robinson HL, Robinson WH. J Virol 2003;77:11125–11138.
10. Robinson WH, DiGennaro C, Hueber W, Haab BB, Kamachi M, Dean EJ, Fournel S, Fong D, Genovese MC, de Vegvar HE, Skriner K, Hirschberg DL, Morris RI, Muller S, Pruijn GJ, van Venrooij WJ, Smolen JS, Brown PO, Steinman L, Utz PJ. Nat Med 2002;8:295–301.
11. Robinson WH, Fontoura P, Lee BJ, de Vegvar HE, Tom J, Pedotti R, DiGennaro CD, Mitchell DJ, Fong D, Ho PP, Ruiz PJ, Maverakis E, Stevens DB, Bernard CC, Martin R, Kuchroo VK, van Noort JM, Genain CP, Amor S, Olsson T, Utz PJ, Garren H, Steinman L. Nat Biotechnol 2003;21:1033–1039.
12. Robinson WH, Steinman L, Utz PJ. Biotechniques 2002 (Suppl):66–69.
13. Robinson WH, Steinman L, Utz PJ. Proteomics 2003;3:2077–2084.
14. Duburcq X, Olivier C, Desmet R, Halasa M, Carion O, Grandidier B, Heim T, Stievenard D, Auriault C, Melnyk O. Bioconjugate chem 2004;15:317–325.
15. Mezzasoma L, Bacarese-Hamilton T, Di Cristina M, Rossi R, Bistoni F, Crisanti A. Clin Chem 2002;48:121–130.
16. Petrik J. Vox Sang 2001;80:1–11.
17. Schaferling M, Nagl S. Anal Bioanal Chem 2006;385:500–517.
18. Brecht A, Gauglitz G. Biosens Bioelectron 1995;10:923–936.
19. Ekins R, Chu F, Micallef J. J Biolumin Chemilumin 1989;4:59–78.
20. Ekins R, Chu F, Biggart E. Ann Biol Clin (Paris) 1990;48:655–666.
21. Ekins RP, Chu FW. Clin Chem 1991;37:1955–1967.
22. Angenendt P, Glokler J, Sobek J, Lehrach H, Cahill DJ. J Chromatogr A 2003;1009: 97–104.
23. Liu X, Chu PK, Ding C. Materials Science and Engineering: R: Reports 2004; 47:49–121.
24. Yeo DS, Panicker RC, Tan LP, Yao SQ. Comb Chem High Throughput Screen 2004;7: 213–221.
25. Yeo DS, Srinivasan R, Chen GY, Yao SQ. Chemistry 2004;10:4664–4672.
26. Uttamchandani M, Chen GY, Lesaicherre ML, Yao SQ. Methods Mol Biol 2004;264: 191–204.
27. Falsey JR, Renil M, Park S, Li S, Lam KS. Bioconjugate Chem 2001;12:346–353.
28. Olivier C, Hot D, Huot L, Ollivier N, El-Mahdi O, Gouyette C, Huynh-Dinh T, Gras-Masse H, Lemoine Y, Melnyk O. Bioconjugate Chem 2003;14:430–439.
29. Melnyk O, Duburcq X, Olivier C, Urbes F, Auriault C, Gras-Masse H. Bioconjugate Chem 2002;13:713–720.

30. Soellner MB, Dickson KA, Nilsson BL, Raines RT. J Am Chem Soc 2003;125:11790–11791.
31. MacBeath G, Schreiber SL. Science 2000;289:1760–1763.
32. Zhu H, Bilgin M, Bangham R, Hall D, Casamayor A, Bertone P, Lan N, Jansen R, Bidlingmaier S, Houfek T, Mitchell T, Miller P, Dean RA, Gerstein M, Snyder M. Science 2001;293:2101–2105.
33. Pritchard DJ, Morgan H, Cooper JM. Anal Chem 1995;67:3605–3607.
34. Delehanty JB, Ligler FS. Anal Chem 2002;74:5681–5687.
35. King TP, Zhao SW, Lam T. Biochemistry 1986;25:5774–5779.
36. Podyminogin MA, Lukhtanov EA, Reed MW. Nucleic Acid Res 2001;29:5090–5098.
37. Melnyk O, Fehrentz J-A, Martinez J, Gras-Masse H. Biopolymers 2000;55:165–186.
38. Geoghegan KF, Stroh JG. Bioconjugate Chem 1992;3:138–146.
39. Far S, Melnyk O. J Pept Sci 2005;11:424–430.
40. Far S, Gouyette C, Melnyk O. Tetrahedron 2005;61:6138–6142.
41. Far S, Melnyk O. Tetrahedron Lett 2004;45:1271–1273.
42. Far S, Melnyk O. Tetrahedron Lett 2004;45:7163–7165.
43. Melnyk O, Fruchart JS, Grandjean C, Gras-Masse H. J Org Chem 2001;66:4153–4160.
44. Tertykh VA, Yanishpolskii VV. Surfact Sci 2000;90:523–564.
45. Xu Q, Lam KS. Tetrahedron Lett 2002;43:4435–4437.
46. Scheibler L, Dumy P, Boncheva M, Leufgen K, Mathieu H-J, Mutter M, Vogel H. Angew Chem Int Edit 1999;38:696–699.
47. Kar S, Joly P, Granier M, Melnyk O, Durand J-o. Eur J Org Chem 2003;21:4132–4139.
48. Kar S, Durand J-O, Granier M, Joly P, Melnyk O. Tetrahedron Lett 2003;44:5617–5619.
49. Chastrette F, Bracoud C, Chastrette M, Mattioda G, Christidis Y. B Soc Chim Fr 1985;1:66–74.
50. Kar S, Durand J-O, Granier M, Joly P, Melnyk O. Tetrahedron Lett 2003;44:5617–5619.
51. Blanchet C, Joly P, Granier M, Lanneau GF, Cretin M, Persin M, Melnyk O, Durand J-O. Tetrahedron Lett 2003;44:4191–4194.
52. Olivier C, Perzyna A, Coffinier Y, Grandidier B, Stievenard D, Melnyk O, Durand J-O. Langmuir 2006;22:7059–7065.
53. Singh RP, Subbarao HN, Dev S. Tetrahedron 1981;37:843–846.
54. Zhang RE, Cao YL, Hearn MW. Anal Biochem 1991;195:160–167.
55. Bonnet D, Grandjean C, Rousselot-Pailley P, Joly P, Bourel-Bonnet L, Santraine V, Gras-Masse H, Melnyk O. J Org Chem 2003;68:7033–7040.
56. Bonnet D, Ollivier N, Gras-Masse H, Melnyk O. J Org Chem 2001;66:443–449.
57. Bonnet D, Rommens C, Gras-Masse H, Melnyk O. Tetrahedron Lett 2000;41:45–48.
58. Shchepinov MS, Case-Green SC, Southern EM. Nucleic Acid Res 1997;25:1155–1161.
59. Van Oss CJ, Chaudhury MK, Good RJ. Adv Colloid Interf Sci 1987;28:35–64.
60. Van Oss CJ, Good RJ. J Protein Chem 1988;7:179–183.
61. Siqueira RD, Petri DF, Wenz G, Schunk P, Schimmel T. Langmuir 1999;15:4520–4523.
62. Soper SA, Hashimoto M, Situma C, Murphy MC, McCarley RL, Cheng YW, Barany F. Methods 2005;37:103–113.

63. Liu J, Roussel C, Lagger G, Tacchini P, Girault HH. Anal Chem 2005;77:7687–7694.
64. La Clair JJ, Burkart MD. Org Biomol Chem 2003;1:3244–3249.
65. La Clair JJ, Burkart MD. Org Biomol Chem 2006;4:3052–3055.
66. Alexandre I, Houbion Y, Collet J, Hamels S, Demarteau J, Gala JL, Remacle J. Biotechniques 2002;33: 435–436, 438–439.
67. Stöber W, Fink A, Bohn E. J Colloid Inter Sci 1968;26:62–69.
68. Nechifor AM, Philipse AP, De Jong F, Van Duynhoven JPM, Egberink RJM, Reinhoudt DN. Langmuir 1996;12:3844–3854.
69. Mijatovic J, Binder WH, Gruber H. Mikrochim. Acta 2000;133:175–181.
70. Field J, Nikawa J, Broek D, MacDonald B, Rodgers L, Wilson IA, Lerner RA, Wigler M. Mol Cell Biol 1988;8:2159–2165.
71. Brizzard BL, Chubet RG, Vizard DL. Biotechniques 1994;16:730–735.
72. Vertegel AA, Siegel RW, Dordick JS. Langmuir 2004;20:6800–6807.
73. Roach P, Farrar D, Perry CC. J Am Chem Soc 2006;128:3939–3945.
74. Mandal HS, Kraatz HB. J Am Chem Soc 2007;129:6356–6357.
75. van Oss CJ. J Mol Recognit 1990;3:128–136.
76. Souplet V, Desmet R, Melnyk O. J Pep Sci Forthcoming.
77. Xie Y, Zhou L, Huang H. Biosens Bioelectron 2007;22:2812–2818.
78. Porte-Durrieu MC, Guillemot F, Pallu S, Labrugere C, Brouillaud B, Bareille R, Amedee J, Barthe N, Dard M, Baquey C. Biomaterials 2004;25:4837–4846.
79. Viornery C, Guenther HL, Aronsson BO, Pechy P, Descouts P, Gratzel M. J Biomed Mater Res 2002;62:149–155.
80. Xiao SJ, Textor M, Spencer ND, Wieland M, Keller B, Sigrist H. J Mater Sci Mater Med 1997;8:867–872.
81. Knob LJ, Olson DL. Metals Handbook: Corrosion, Volume 13, 9th edition. Material Park, OH: ASM International; 1987.
82. Wolfe CA, Hage DS. Anal Biochem 1995;231:123–130.

CHAPTER 13

Electrical Detection of Antibodies from Human Serum Based on the Insertion of Gold-Labeled Secondary Antibodies into Micro- or Nanogaps

LIONEL MARCON

Institut d'Electronique de Microélectronique et de Nanotechnologie, UMR CNRS 8520, Department of ISEN, 41 Bd Vauban, 59046 Lille Cedex, France
Institut de Biologie de Lille, UMR CNRS 8161 (CNRS, Universités de Lille 1 et 2, Institut Pasteur de Lille), 1 rue du Professeur Calmette, 59021 Lille Cedex, France

DIDIER STIÉVENARD

Institut d'Electronique de Microélectronique et de Nanotechnologie, UMR CNRS 8520, Department of ISEN, 41 Bd Vauban, 59046 Lille Cedex, France

OLEG MELNYK

Institut de Biologie de Lille, UMR CNRS 8161 (CNRS, Universités de Lille 1 et 2, Institut Pasteur de Lille), 1 rue du Professeur Calmette, 59021 Lille Cedex, France

13.1 INTRODUCTION

Solid-phase assays play a crucial role today in biological studies. These assays are based on the immobilization of molecular probes on a surface that are able to bind specific soluble receptors. The detection of the captured molecules is a key step in these experiments and is usually performed using optical (1–3), piezoelectric (4) or electrochemical (5) methods. However, electrical detection is emerging as a promising alternative due to its simplicity and the possibility of designing portable devices.

Some biosensors have been described that convert the information contained in the affinity between two molecular species into a measurable electrical signal. The pioneering work published by Velev in 1999 is based on the conductance change induced by silver deposition between microelectrodes catalyzed by gold nanoparticles

Colloidal Nanoparticles in Biotechnology, Edited by Abdelhamid Elaissari
Copyright © 2008 John Wiley & Sons, Inc.

(GNPs) (6). In this work, latex beads coated with protein A (pA) were immobilized between microelectrodes. The microelectrodes were incubated with IgGs labeled with GNPs leading to the capture of gold nanoparticles between the electrodes through protein A-IgG biomolecular interaction. Precipitation of metallic silver on the GNPs resulted in a conductance change of several orders of magnitude. This concept was extended to DNA probes for the detection of soluble DNA species (7). In 2002, Park et al. (8) demonstrated the binding of oligonucleotide functionalized GNPs in a 20 μm gap between two metallic electrodes. As in the work of Velev et al., a direct current was not detected due to the large spacing between the electrodes. A significant conductance change could be observed only after precipitation of silver enhancer that resulted in the filling of the gap by metal particles.

Besides the use of a very limited number of electrodes, these pioneering studies have revealed the large variation in conductivity after the silver precipitation step, thus impeding the analysis of probe molecules having different capture properties. This result was expected because (i) the conduction path between two electrodes can take any arbitrary shape, depending on the exact location of GNPs and how silver deposition occurs on these GNPs, resulting in a wide statistical distribution of the measured resistance; (ii) the resistance of the contact between the electrodes and the silver aggregate is expected to vary significantly, due to the variation in the mode of contact between the silver aggregate and the microelectrode surface, and also due to the presence of organic matter on gold arising from contaminants, chemical reagents and/or biological sample. To circumvent the large variation in conductivity due to silver precipitation, we have examined an alternative output for the device. For this, a device containing 300 pairs of microelectrode was fabricated and two probe molecules, pA and goat antimouse Ig(H+L) (goat-Ab), were printed within each microgap using a noncontact printer. The device was used to detect IgGs from human serum using secondary antibodies labeled with GNPs and silver precipitation. The output of the biosensor was defined as the percentage of short-circuited microelectrodes for a given probe, independently of the observed conductance changes. We show that probes of different affinities can be distinguished easily and that the signal is correlated with the GNP density between the electrodes. The effect of the microgap spacing (5, 10, 15 or 20 μm) on the sensitivity of the chip was examined. This novel approach is presented in the first part of the article.

The second part of the article is focused on the use of nanoelectrodes for the detection of IgGs. Indeed, the development of efficient techniques allowing the fabrication of nanoelectrodes separated by few tens of nanometers has recently stimulated the development of biosensors based on a direct change in conductance induced by the insertion of GNPs inside a nanogap. In this case, a silver precipitation step is not needed as for microelectrodes. Tsai et al. (9,10) presented an electrical detection method that permitted the detection of target oligonucleotides by using 300 nm spaced electrodes and GNPs for signal amplification. In 2004, Haguet et al. (11) reported the detection of biotin/streptavidin or biotin/antibiotin antibody interactions by combining a nanometer-sized gap (typically 100 nm) with purified receptor molecules labeled with GNPs. However, the application of the device for the detection of antibodies in serum, which requires two incubation steps with the

biological sample and the GNP-labeled secondary antibody respectively, was not described. The exact mechanism of the detection and, in particular, the role of GNPs too were not elucidated. Another point of interest was to define the output of the device, pertinent for a biological detection. Should we consider the conductivity change, the number of conducting electrodes, or both? To address these aspects, nanometer-sized gaps, ranging from 30–90 nm between two planar gold electrodes, were fabricated and functionalized to allow the immobilization of pA and goat-Ab. The devices, each one containing 90 nanogaps, were incubated with human serum and GNP-labeled secondary antibodies. Here, the detection of IgGs is based on changes in the intensity-voltage$I(V)$ curves induced by the insertion of GNP-labeled secondary antibodies directed against human antibodies. A statistical analysis of the $I(V)$ curves is presented to unambiguously distinguish current changes from noise background. The importance of GNPs on the detection efficiency was examined, as well as the use of an original quality factor correlated to the nanosensor efficiency. The resulting $I(V)$ curves allow for the proposal of a mechanism to describe the observed current changes following the insertion of GNPs into the nanogap.

13.2 EXPERIMENTAL

13.2.1 General

Protein A, phosphate buffered-saline (PBS), Tween® 20, bovine serum albumine (BSA) and 3-aminopropyltrimethoxysilane (APS) were purchased from Sigma-Aldrich, goat antihuman Ig(H+L) antibodies linked to 25 ± 3 nm diameter gold nanoparticles from Electron Microscopy Science, and goat antimouse Ig(H+L) human adsorbed antibodies from Southern Biotechnology Associates.

Serum was collected from the clinical laboratory of the Center Hospitalier Régional (Lille, France). Water was deionized using a Milli-Q purification system (Millipore). We used Si (100) substrates (Siltronix) with a 200 nm thermal oxide (SiO_2) for electrical detection and microscope glass slides (ESCO Precleaned Microslide Frosted) for fluorescence study. MF319 developer and S1818 photoresist were provided by Shipley Chemicals. Methylisobutylketone (MIBK) developer, methacrylic acid (MAA), and polymethyl methacrylate (PMMA) resists were obtained from MicroChem.

Incubations were performed using a CMT™ hybridization chamber (Corning). Silver enhancement was performed using the Silver Blue kit acquired from Advanced Array Technology; this commercial kit contains a blocking solution (block sol) and a silver enhancer solution (silver staining sol).

Glass slides fluorescence of the signals was acquired with an Affymetrix 418 Array Scanner at a resolution of 10 μm per pixel using the 532 nm channel (Cy3 channel). The average fluorescence intensity for each spot was analyzed and quantified using ScanAlyze software (v 2.32, Eisen, Standford University). The background fluorescence, determined as the mean fluorescence around each spot, was subtracted from the main fluorescence values.

AFM characterization was carried out using a Dimension 3100 Scanning Probe Microscope (Veeco Instruments, Santa Barbara, California).

Electrical measurements were performed before and after silver enhancement in a nitrogen low pressure chamber (0.2 mbar, H_2O and O_2 <0.1 ppm) at room temperature with a picoamperemeter HP4140B coupled to a mobile micromanipulator probe station. Voltages were applied between each pair of microelectrodes by placing manually two metal probe tips on contact pads leading to the sensor.

13.2.2 Electrodes Fabrication

Silicon samples were first cleaned with a freshly prepared piranha solution (H_2SO_4/H_2O_2 1/1 by vol), then rinsed with water and isopropanol (IPA) with ultrasonic agitation followed by a plasma O_2 treatment (50 s, 100W, 0.1 T). Those supports were then subjected to particular treatments depending on the gap size required.

13.2.2.1 Microelectrodes Seveny-five microelectrodes separated by 5, 10, 15, or $20 \pm 0.1\,\mu m$ were prepared on a single $0.9 \times 1.9\,cm^2$ silicon wafer (300 microelectrodes overall) by UV lithography and lift-off of a 5 nm Ti/60 nm Au bilayer stack deposited by evaporation (12). Patterned pads of $20\,\mu m^2$ were used at each electrode extremity as contacts with the picoamperemeter for the electrical measurements.

The patterns from a positive mask—prepared using the software WaveMaker, Barnard Microsystems Limited—were photographically transferred onto a 1.4 μm thick spin-coated layer of photoresist S1818. Development was carried out by immersion in MF319. The next step was to deposit titanium of 5 nm thick by a thermal deposition process followed by a deposition of 60 nm gold thin film. Liftoff was performed using ultrasonic agitation in an acetone bath for 40 min.

13.2.2.2 Nanoelectrodes A resist bilayer of EL (MAA)/PMMA was used to ensure a proper liftoff. A 500–Å thick bottom layer of EL 4% (MAA 8.5) was spin coated on a (1×1)-cm^2 substrate, followed by a 275–Å thick top layer of PMMA 3% (495 K). Both layers were baked at 170°C. E-beam exposure was performed at an accelerating voltage of 50 kV and energy dose of $220\,\mu C/cm^2$. Development was carried out in a 1:2 (by volume) mixture of MIBK and IPA. A 5–nm thick titanium layer followed by 15-nm thick gold layer were deposited. Lift off was performed using ultrasonic agitation in an acetone bath during 6 h. Connection pads and connecting structures were photographically patterned with a 1.4-μm thick spin-coated layer of photoresist (S1818) and liftoff of a 10 nm Ti/40 nm Au bilayer deposited by evaporation. Development was carried out in MF319.

13.2.3 Substrate Functionalization

Silicon samples carrying micro- and nanoelectrodes were cleaned by plasma O_2 treatment. Meanwhile glass slides were treated with a freshly prepared piranha solution. Both substrates were then washed with water (3×3 min) and MetOH (3 min), and then treated with 3% APS in MetOH/water, 95/5 by volume (30 min, under sonication). Substrates were finally washed with MetOH, water (two times), MetOH and annealed for 15 min at 110°C.

13.2.4 Immobilization of Probes

pA (2.4×10^{-2} mM), goat–Ab (1.7×10^{-4} mM), and PBS were printed over the micro- or -nanoelectrodes using a piezo-driven noncontact printer (Packard Biochip Arrayer, volume 1 nL) after appropriate dilution in PBS. The diameter of the spots was typically 370 μm. Samples were then incubated in a humid chamber overnight (60% relative humidity).

13.2.5 Incubation with Human Serum

The samples were washed successively with PBS containing 0.05% of Tween® 20 (by volume), water, and ethanol (EtOH). Substrates were then incubated for 1 h at 37°C in human serum diluted to 5% (by volume) with a PBS Tween® 0.05% BSA 2% buffer.

13.2.6 Incubation with the Secondary Antibodies

After new washings with PBS Tween® 20 0.05%, water, and EtOH, samples were incubated for 1 h at 37°C with goat antihuman secondary antibodies labeled with 25 nm gold nanoparticles that were concentrated 10-fold (final concentration $\sim 3.3 \times 10^{12}$ GNP/mL) by centrifugation or tetramethylrhodamine diluted to 5% with PBS Tween® 20 0.05% BSA 2% for the fluorescence study.

13.2.7 Precipitation of Silver for Microgaps and Electrical Measurements

Samples were washed successively with PBS Tween® 20 0.05%, water, and EtOH; rinsed for 5 min in commercial *block sol*; and incubated at room temperature with *silver staining sol*, rinsed with water and MetOH, and finally dried. Exposure time varied from 1–20 min silver enhancement. Electrical measurements were performed before and after silver enhancement. The applied voltage ranged from $-1 - +1$ V with 500 mV steps.

13.2.8 Amplification of the Antibody-Antigen Reaction for Nanogaps

After incubating with GNP-labeled secondary antibodies, samples were washed successively with PBS Tween® 20 0.05%, water, and EtOH, and then dried under N_2. SEM (Zeiss 820) analysis was carried out and combined with electrical measurements. The applied voltage ranged from $-5 - +5$ V with 500 mV steps.

13.2.9 Statistical Data Analysis

A regression analysis of the $I(V)$ data was carried out using a third-order polynomial equation of the type $y = a + bx + cx^2 + dx^3$. Considering 21 $I(V)$ data points, the null hypothesis ($I(V)$ data are not correlated) could be rejected at the 1% significance

level when the multiple correlation coefficient r^2 exceeded 0.48. r^2 was calculated using the F-test for the comparison of variance (17 and 3 degrees of freedom for the residuals and for the regression, respectively) (13).

13.3 RESULTS AND DISCUSSION FOR THE MICROGAP BASED BIOSENSOR

In most of the studies dealing with the electrical detection of immunoglobulins G (IgGs), the detection was realized using purified proteins. Detection of IgGs in a biological sample such as serum using micro-or nanoelectrodes was never examined to the best of our knowledge. Serum is of great biological, medicinal and economic importance (14). In particular, the detection of antibodies in serum is used for the diagnostic of infections by several pathogens such as HIV, HCV, and HBV. The use of miniaturized devices for specifically detecting IgGs in serum is not obvious due to its complexity. It is estimated that up to 10,000 proteins may be present in serum, which has IgGs with normal levels between 8 and 17 mg/mL in adult blood (15). Thus, model studies with purified soluble targets are for great interest but the usefulness of a device cannot be evaluated as long as the detection has not been realized using serum or a sample of relevant complexity. For this reason, the micro and nanodevices described in this article were optimized, characterized, and evaluated using human serum to be directly applicable to real detection experiments.

The fabrication of the micro- or nanodevices for IgG detection required the immobilization of probe molecules inside the micro-or nanoelectrodes. Protein A (pA) and goat antimouse Ig(H+L) antibodies (goat-Ab) were used as probes in this study. Staphylococcal pA, a 42 kDa cell wall protein from *Staphylococcus aureus*, binds strongly to IgGs from several mammalian species, and in particular, human IgG via the Fc fragment (16). Alternately, goat antimouse Ig(H+L) was found to cross react with human IgG and could be used as a probe of low affinity compared to pA. At last, phosphate buffered saline (PBS) was used as negative control. The monomeric IgGs's hydrodynamic radius is, at pH 7.6, about 5.5 nm (17,18) and the dimensions of a single complex pA-IgG were estimated by AFM observations to measure typically 10.5 nm height and 14.2 nm width (19). The sizes of human IgG and goat-Ab are similar. Thus, the size of the probes, of the human IgG/probe complexes, and the diameter of Ab^{II}-GNPs (25 nm) are below the size of the nanogaps (30–90 nm) prepared in the second part of the article.

Immobilization of the pA and goat-Ab is required to chemically derivatize the surface. Amine-modified surfaces are known to adsorb proteins and are, therefore, widely utilized for the preparation of protein microarrays (20–22). Due to its simplicity, this immobilization method was employed in this work. A silicon surface was silanized with 3-aminopropyltrimethoxysilane in a MeOH/water mixture. By this procedure, the thickness of the silane layer ranges from 1.8–2.2 nm, as determined by atomic force microscopy (23). The printing on electrodes was performed using a noncontact piezoelectric arrayer. A camera aligned with the piezoelectric tips permitted a precise positioning of the dispensed probes on the gaps that were situated at equal distance between the gold contacts used for the electrical measurements.

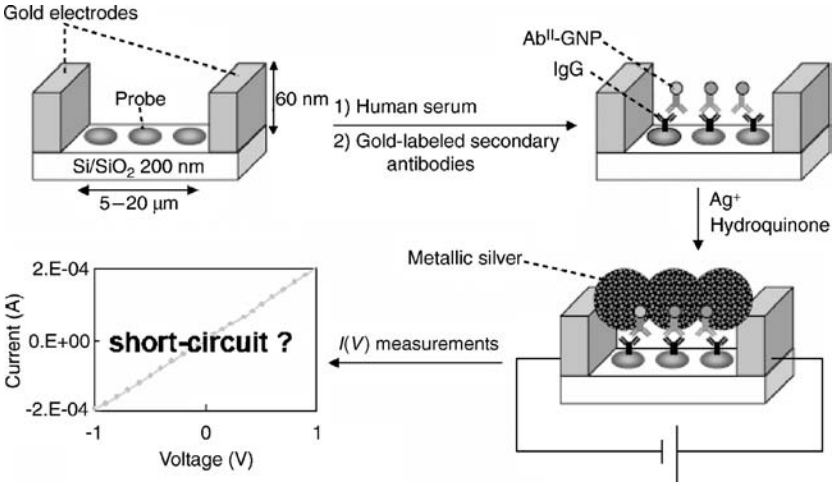

FIGURE 13.1 Schematic representation of the electrical detection of IgGs.

13.3.1 Principle of the Sensor

The principle of the biosensor is described in Figure 13.1 Seventy-five microelectrodes separated by 5, 10, 15, or 20 ± 0.1 μm were prepared on a single $0.9 \times 1.9\,cm^2$ silicon wafer (300 microelectrodes overall) by UV lithography and lift-off of a 5 nm Ti/60 nm Au bilayer stack deposited by evaporation (12). Patterned pads of 20 μm^2 were used at each electrode extremity as contacts with the pico-amperemeter for the electrical measurements. One hundred and twenty microelectrodes of different spacing were used for pA and goat-Ab against 60 for PBS.

The chips were then incubated first with diluted human serum and subsequently with antihuman antibodies (Ab^{II}) labeled with 25 nm GNPs. Precipitation of colloidal silver was performed, using a solution of silver nitrate and hydroquinone under cover glass (24). Current-voltage $I(V)$ measurements were done before and after the silver nitrate/hydroquinone treatment. Electrodes that displayed a typical ohmic current between ± 1V and low resistance ($R \sim 10^{-3}$–$10^{-9}\,\Omega$) were considered as short circuited. The output of the biosensor was defined as the percentage of short-circuited electrodes independently of the conductivity.

13.3.2 Characterization of the Probe Reactivity

Atomic force microscopy (AFM) permitted to characterize the GNP distribution and density on the spotted area after incubation with diluted human serum and Ab^{II}-GNPs. Fig. 13.2 shows typical AFM images for (a) pA, (b) goat-Ab, and (c) PBS printed areas. A dense GNP covering was obtained for pA (120 ± 10 GNP/μm^2) a sixfold lower (20 ± 5 GNP/μm^2) density for goat-Ab. In contrast, no nanoparticles could be detected for PBS. Furthermore, no nanoparticles could be detected for all the printed areas when diluted human serum was replaced by PBS (data not shown). These data demonstrate the specificity of the capture of human IgGs by pA or goat-Ab. Protein A is known to have a high affinity for human IgGs but only a low affinity

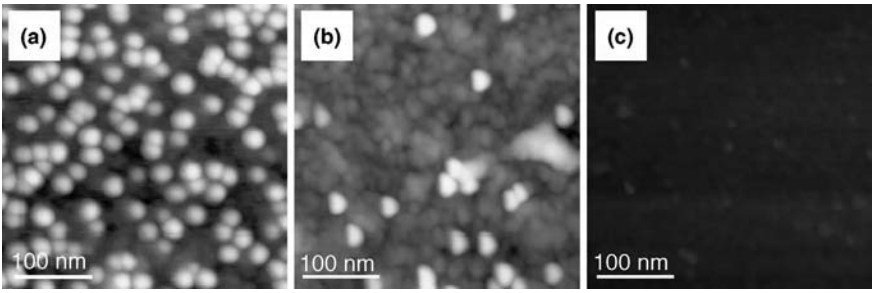

FIGURE 13.2 Characterization of probe reactivity. AFM images of the spotted areas between the microgaps after incubation with diluted human serum and Ab^{II}-GNPs. (**a**) pA, (**b**) goat-Ab, and (**c**) PBS.

for goat antihuman antibodies which are used as secondary antibodies in this experiment (25).

A similar experiment was conducted on amine-modified microscope glass slides to assess the pA, goat-Ab and PBS reactivity using fluorescence detection with a standard microarray fluorescence scanner (Fig. 13.3). In this experiment, incubation with diluted human serum was followed by incubation with antihuman Ab^{II} labeled with tetramethylrhodamine, as reported in Reference 23. The microarrays were then scanned at 532 nm. Figure 13.3 shows a typical image of the microarray. The signal intensity obtained for pA was fourbold higher than the signal obtained for goat-Ab, while PBS was close to the background of the microarray. These results are consistent with the GNP densities observed using Ab^{II}-GNPs and AFM analysis.

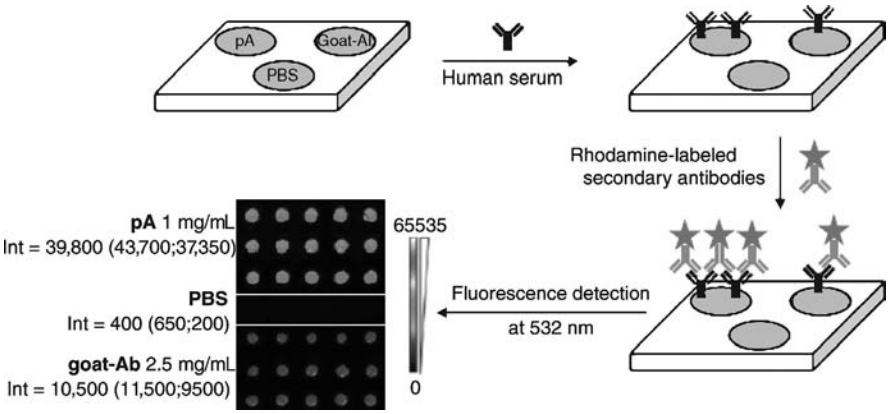

FIGURE 13.3 Printing of pA($n = 15$), goat-Ab ($n = 15$) and PBS ($n = 5$) on amine functionalized microscope glass slides was used for studying probe reactivity using fluorescence detection. The microarrays (triplicate) were incubated with diluted human serum (1/20th) and tetramethylrhodamine-labeled antihuman IgG antibody, respectively. Detection was performed at 532 nm at L35, PMT50 scanner sensitivity using, an Affymetrix 418 Array Scanner. The figure shows a 16-bit image of the resulting microarray (false-color scale) and the fluorescence intensities expressed in arbitrary units. The number in parentheses corresponds to the first and third quartiles

13.3.3 Optimization of the Silver Nitrate/Hydroquinone Treatment Time

The silver enhancement treatment results in a large amount of silver deposition on the printed areas due to the catalytic reduction of the silver ions by the GNPs. Depending on the reaction conditions, and especially for long reaction time, deposition of metallic silver on the surface can also occur in the absence of GNPs (26). It was important to adjust the reaction time before undertaking any detection process because both too short and too long development might bring excessive background noise or lack of detection sensitivity.

Optimization of the duration of the silver nitrate/hydroquinone treatment was performed by measuring the $I(V)$ curves in real time from a single pair of electrodes with 5 μm gap printed with pA 1 mg/ml. To this goal, silver enhancement was performed in a low pressure chamber by incubating the commercial solution under cover glass. $I(V)$ curves were measured through the contact pads linked to the pico-amperemeter. Measurements were performed between $+1$ V and -1 V because a too high range of voltage may damage the electrodes through a phenomenon of electromigration of gold atoms, causing a breakage of the electrodes. In our case, this phenomenon appeared since ± 3V and caused parasite short circuits visible by SEM. Consequently, the ± 1 V range turned out to be a good compromise to avoid the degradation of the structures and the easy observation of ohmic short circuits after silver enhancement.

Current less than 100 fA was obtained for treatment time below 7 min (Fig. 13.4 a). The corresponding $I(V)$ curves (Fig. 13.4b, line t_1) corresponded to the background. Current rapidly increased between 7–15 min (line t_2: 10 min. to reach a plateau beyond 15 min (line t_3: 20 min). However, for reaction time beyond 15 min, nonspecific precipitation of silver onto the entire surface of the chip was observed. The duration of the silver treatment was thus set to 15 min for the rest of the study.

13.3.4 Electrical Measurements

Optimal experimental conditions determined previously were used after incubation of a chip (pA 1 mg/mL, goat-Ab 2.5 mg/mL, and PBS printed on 5, 10 15, and 20 μm electrodes with diluted human serum (1/20th) and Ab^{II}- GNPs. Fig. 13.5 shows the optical images of 5 μm electrodes for (a) pA, (b) goat-Ab, and (c) PBS. The spot shape is clearly visible for pA and goat-Ab (Fig. 13.5a and b) due to the silver deposition leading to an important number of short-circuited electrodes. In contrast, no precipitate is observed for PBS (Fig. 13.5c).

Such observations are confirmed through the percentages of short-circuited electrodes outlined in Table 13.1. The silver connection made between the electrodes exhibited a typical ohmic current, as shown in Fig. 13.4b, with low resistance ($\sim 10^{-3}$–10^{-9} Ω). The GNP densities determined by AFM (Fig. 13.2), as well as fluorescence intensities obtained on microscope glass slides (see Fig. 13.2) are also included for comparison. The percentage of short-circuited 5-μm electrodes was 97, 27, and 0% for pA, goat-Ab and PBS, respectively. A similar trend was observed for the other electrodes but less short circuits were observed due to the inability of metallic silver to bridge an increasing gap.

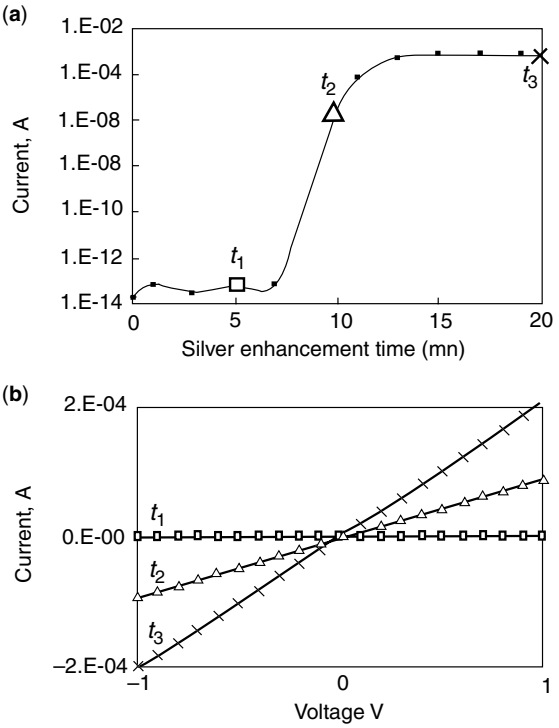

FIGURE 13.4 Effect of the silver enhancement time upon current using 5-μm-separated electrodes. (**a**) Current measured in real time and plotted on a log scale at U = 1 V as a function of the duration of the silver treatment. t_1, t_2, and t_3 correspond to 5, 10, and 20 min reaction times, respectively. (**b**) $I(V)$ measurement between ±1 V at t_1, t_2, or t_3

These experiments demonstrate that the gap width has a crucial impact on the percentage of short-circuited electrodes. Gold electrode dimensions are not expected to have any significant influence here because the gap dimensions are too large to influence the diffusion of the reagents. However, the width and height of the electrodes probably

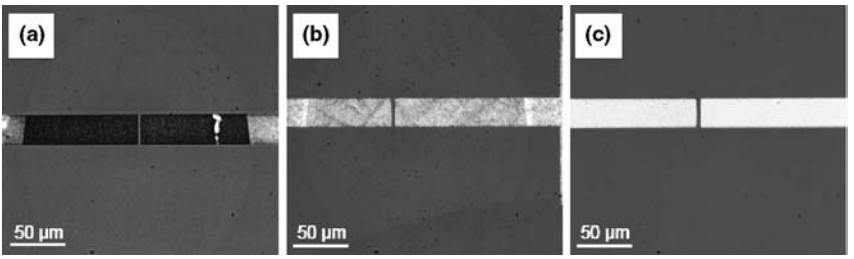

FIGURE 13.5 Optical images of the 5 μm electrodes after incubation with diluted human serum, Ab^{II}-GNPs and silver nitrate/hydroquinone. (**a**) pA, 1 mg/mL, (**b**) goat-Ab, 2.5 mg/mL, and (**c**) PBS

TABLE 13.1 Electrical Detection Results Obtained from the Three Different Probes (pA, Goat-Ab, and PBS) and the Four Fabricated Microgaps (5, 10, 15, and 20 μm). Fluorescence Intensities Expressed in Arbitrary Units were Obtained by Printing the Different Probes on Amine-Modified Microscope Glass Slides and by Using Ab^{II} Labeled with Tetramethylrhodamine (see Fig. 13.3 for details).

Probe	Gap, μm	Ratio of short circuits, %	GNP density, part/μm^2	Fluorescence intensity, a.u.
pA, 1 mg/mL	5	97	120 ± 10	39,900 (43,700; 37,350)[a]
	10	83		
	15	57		
	20	17		
goat-Ab, 2.5 mg/mL	5	27	20 ± 5	10,500 (11,500; 9500)[a]
	10	10		
	15	7		
	20	0		
PBS	5	0	0	440 (650; 200)[a]
	10	0		
	15	0		
	20	0		

[a]As the gain is calculated from statistical approach (median calculated value), the numbers in parentheses correspond to the first and third quartiles.

modify the connection path and so the conductance measured. Such consideration reinforces the interest of using a readout independent from the conductance.

The following experiments aimed to study the effect of pA concentration on the percentage of short-circuited electrodes. To this goal, serial dilutions of pA (from 1–10^{-8} mg/mL) were printed on 10 μm electrodes (15 replicates per concentration). Capture of human antibodies and detection were performed as previously described. The GNP densities on the spotted areas were determined by AFM analysis before the silver nitrate/hydroquinone treatment. The printing was also performed in parallel on amine-modified microscope glass slides for fluorescence detection, as shown in Fig. 13.3. The resulting data are collected in Table 13.2. Decreasing pA concentration led to a decrease of GNP density, of the percentage of short-circuited electrodes, and of the fluorescence intensities, confirming that different GNP densities can be distinguished by considering the percentage of short-circuited electrodes as the output of the device. Notice that fluorescence intensities displayed in Tables 13.1 and 13.2 are not comparable, given that experiments were performed upon distinct biochips with different fluorescence scanner parameters.

13.3.5 Discussion

Recently, the silver enhancement method was used for the detection of proteins (27) or DNA (26) on microarrays using optical detection. It was found that the gray level of the

TABLE 13.2 Effect of pA Concentration (from 1–10^{-8} mg/mL) on the Percentage of Short-Circuited Electrodes. pA was Spotted on Electrodes with 10 μm Gap (n = 15 for each concentration). The GNP Density Prior to the Silver Nitrate/Hydroquinone Treatment was Determined by AFM. Fluorescence Intensities Expressed in Arbitrary Units were Obtained by Using Amine-Modified Microscope Glass Slides and Ab^{II} Labeled with Tetramethylrhodamine (see Fig. 13.3 for details).

pA concentration, mg/mL	Ratio of short circuits, %	GNP density, part/μm^2	Fluorescence intensity (a.u.) ± SD
1	100	120 ± 10	42,500 ± 3,000
10^{-2}	80	25 ± 5	38,500 ± 1,690
10^{-4}	47	5 ± 2	34,000 ± 1,400
10^{-6}	7	2 ± 2	25,000 ± 3,400
10^{-8}	0	0	7,700 ± 2,620

spots was correlated with the logarithm of the sample concentration (27). Combination of the silver enhancement method and electrical detection between microelectrodes has also been reported (6–8,28). The transduction signal (current/resistance in function of the applied voltage) was dependent on the probe concentration until it reached a plateau due to the filling of the gap by metallic silver. However, none of these studies examined (i) the electrical response to different probes, i.e., the capacity of the method to distinguish different capture efficiencies toward one particular target, (ii) the detection of a target in a complex biological sample, or (iii) the reproducibility of the detection method by using a large set of microelectrodes.

The capture efficiencies of pA and goat-Ab used in this work were characterized by AFM using Ab^{II}-GNPs and also by fluorescence using Ab^{II} labeled with tetramethylrhodamine. The GNP density obtained for pA was sixfold higher than that observed for goat-Ab (Table 13.1). Similarly, the fluorescence intensity obtained for pA was fourfold higher than that observed for goat-Ab. By combining the use of Ab^{II}-GNPs and precipitation of silver, we obtained a large current increments ranging from 10^7–10^{11} (resistance in the range 10^{-3} to10^{-9} Ω) for both pA and goat–Ab, but not for PBS. Resistance measurement of the gaps alone did not enable to discriminate the different capture efficiencies of pA and goat-Ab and could not be used as a useful readout for the biosensor. This result was expected because the conduction path between the two electrodes can take any arbitrary shape, depending on the exact location of GNPs and how silver deposition occurs on these GNPs, resulting in a wide statistical distribution of the measured resistance. Alternately, discrimination between pA and goat-Ab could be achieved by considering the percentage of short-circuited microelectrodes independently of the current. The percentages of short-circuits observed for pA and goat-Ab were clearly different (83% and 10%, respectively with 10 μm electrodes) in agreement with the GNP densities determined by AFM or the fluorescence data. In the same way, the percentage of short circuits varied as a function of pA concentration (Table 13.2).

All the experiments were performed using a complex biological fluid and thus can be applied to real detection experiments. The biosensor described here is easy to construct and is opened for parallelization. This can be achieved by combining dense arrays of microelectrodes on a single chip, which can be easily prepared at low cost using circuit fabrication processes on silicon and standard noncontact printers to individually address the probes of interest. Identification of the optimal number of microelectrodes per probe will be the subject of future studies, as well as the determination of the detection limit of IgGs.

13.3.6 Conclusion

In this work, microelectrodes were fabricated on silicon wafers and presented different probes (pA, goat-Ab) to human serum. The specific capture of IgGs from serum was electrically detected by combining Ab^{II}-GNPs and silver precipitation. Through the number of short-circuited electrodes as the readout of the biosensor, different capture efficiencies could be easily distinguished; whereas the conductivity of the microgaps was highly variable and difficult to interpret. The number of electrodes displayed by the chip for a given probe determines the different values for the signal output. This new readout procedure circumvents the large variability of the conductivities observed for silver deposits and should stimulate the development of portable biosensors based on this electrical detection method.

13.4 RESULTS AND DISCUSSION FOR NANOGAP BASED BIOSENSOR

13.4.1 Principle of the Biosensor

Figure 13.6 shows the scheme of a typical chip on a silicon substrate with a 200 nm thermal oxide and the SEM image of a pair of bare nanoelectrodes with a length of 5 μm and a thickness of 20 nm (15 nm Au on 5 nm Ti), prepared by electron-beam lithography. The controlled gap width is ranging from 30–90 nm, a size compatible with the trapping of GNPs (Ø 25 nm).

The principle of the detection is illustrated in Fig. 13.7. The probe is bound to a silicon substrate by adsorption in the periphery of the nanogap and into the nanogap as well. Incubation of the device with diluted human serum leads to the capture of antibodies by the probe. Finally, incubation with secondary antihuman antibodies labeled with 25 nm gold nanoparticles (Ab^{II}-GNPs) results in the insertion of GNPs into the nanogap. Current-voltage $I(V)$ measurements were performed at 0.2 mbar before and after incubation with Ab^{II}-GNPs. To correlate $I(V)$ curves with the GNP density on the surface and between the electrodes, the device was also observed by scanning electron microscopy (SEM). We hypothesized that the insertion of 25 nm nanoparticles into the 30–90 nm nanogap would result in conductivity changes due to the small distances between the nanoparticles and the walls of the nanogap, and further leading to the possibility of tunneling effects.

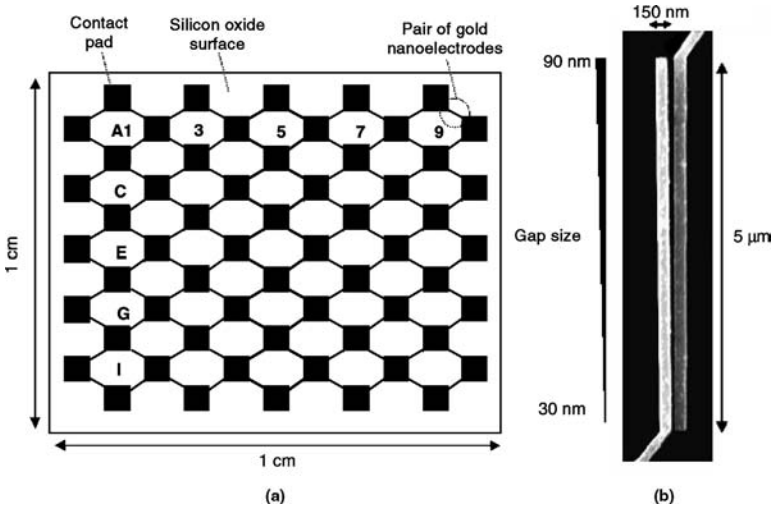

FIGURE 13.6 Fabrication of nanoelectrodes. (**a**) Scheme presenting the typical 1 cm^2 silicon chip carrying 100 pair of electrodes. (**b**) SEM image of gold nanoelectrodes with nanometer-sized gap

13.4.2 Results and Discussion

In 2004, Haguet et al. (11) reported the detection of biotin/streptavidin or biotin/antibiotin antibody interactions by combining a nanometer-sized gap (typically 100 nm) with purified receptor molecules labeled with GNPs. However, the application of the device for the detection of antibodies in serum, which requires two incubation steps with the biological sample and the GNP-labeled secondary antibody respectively, was not described. The topography of the surface is known to have a large effect on the conformation of proteins and on the adsorption or the diffusion phenomena at the solid-liquid interface (29–31). Thus, the capacity of the different species (protein used as probe, primary antibody, and GNP-labeled secondary antibody) to insert into the nanogap and to retain their binding properties had to be examined. Moreover, it was unclear if the additional protein layer inside the nanogap between the probe and the GNPs could perturbate the detection, considering that the size of the captured primary antibodies and those of the nanoelectrodes is comparable.

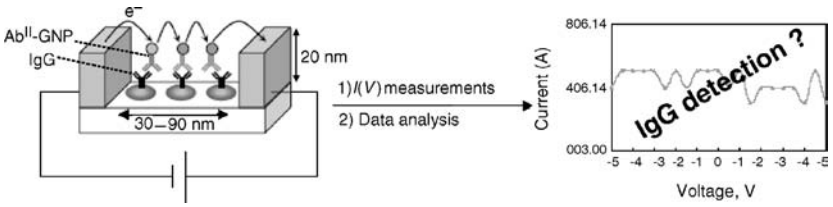

FIGURE 13.7 Schematic illustration of the electrical detection of IgGs

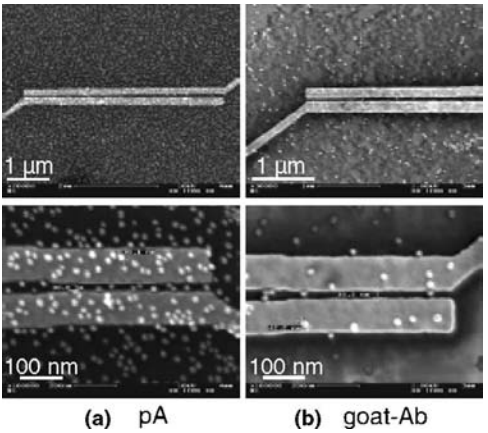

FIGURE 13.8 SEM image of the GNP layer around and between the nanoelectrodes after incubation of human serum and Ab^{II} - GNPs with (**a**) pA and (**b**) goat-Ab as probe. GNP density around the nanogap was approximately 200 and 20 GNP/μm^2 for pA and goat-Ab, respectively. An average number of 60 and 15 GNP were trapped in the nanogaps

Considering one chip carrying 100 pair of nanoelectrodes, 60 chips were spotted with pA, 30 with goat-Ab, and 10 with PBS. Incubation of the nanoelectrodes with diluted human serum and GNP-Ab^{II}, respectively, were followed by electrical measurements and then SEM observations. Fig. 13.8 corresponds to (a) pA or (b) goat-Ab nanoelectrodes, respectively. The images clearly show that the GNPs are located both outside and between the nanoelectrodes. The GNP density in the area surrounding the nanoelectrodes is 200 and 20 particles/μm^2 for pA and goat-Ab, respectively. Moreover, ~60 GNPs fill the nanogaps for pA (against ~15 for goat-Ab). In contrast, no nanoparticles were detected for the PBS printed alone (data not shown). SEM observations demonstrate the presence of GNPs between the electrodes, and consequently both the presence of the probes inside the nanogap and their accessibility to the primary and secondary antibodies. The insertion of the different species into the nanogap (probes, primary antibodies, and GNP-labeled secondary antibodies) is facilitated by the nanogap geometry. We hypothesized that the variable distance between the electrodes ranging from 30–90 nm would allow the insertion of species of variable size. Another important issue is the filling of the nanogap by the buffers used during the printing, incubation, and washing steps. Brinkmann et al. have developed recently a basic analytical model for the invasion of a liquid in a chemically heterogeneous channel (32). The essential parameters in the model are the nanogap geometry and the chemical properties of the surface leading to specific solid-liquid surface tensions. By using this model and the contact angles of the buffers on the corresponding planar surfaces, we could predict the filling of the nanogap by the different liquid used in the study.

The electrical characterization of the chip was performed on the bare surface, after APS grafting, printing of the different probes, and after incubations with the human serum and the Ab^{II}-GNPs. The current measured through bare electrodes between

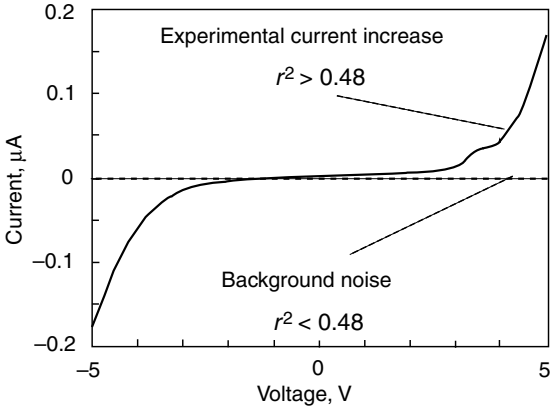

FIGURE 13.9 Typical current-voltage curves on bare electrodes and after detection of IgGs with pA and goat-Ab. The dashed curve is a typical curve obtained with the bare electrodes, or after spotting of the probes and incubation with the human serum. In contrast, the plain curve is obtained after spotting of pA and goat-Ab, incubation with the human serum, and finally incubation with Ab^{II}-GNPs

±5 V is below 10^{-13} A and exhibits a random shape (dashed line, Fig. 13.9), associated with noise background. Subsequent incubation with the serum and the Ab^{II}-GNPs was generally followed for pA and goat-Ab probes by an increase in current ranging from 10^{-11}–10^{-7} A. The plain line shows a typical nonlinear $I(V)$ curve attributed to the presence of GNPs into the nanogaps, with a threshold voltage of the order of ±2 V. Tunnel multijunctions are formed between particles and the metallic surface of the electrodes, probably induced by electronic transport in metal disordered nanocristal arrays, as discussed later.

Nevertheless, a specific data treatment is required to distinguish unambiguously the current rise from the noise background in a set of 100 pairs of nanoelectrodes. To this goal, we used a statistical analysis to filter the data according to the $I(V)$ curve shapes and current changes. We performed a nonlinear regression analysis of the $I(V)$ data using a third-order polynomial expression, characterized by the so-called multiple correlation coefficient r^2. Using 21 $I(V)$ data (17 degrees of freedom), I and V are correlated for r^2 values greater than a cutoff value $r_c^2 = 0.48$ at a 1% significance level. Above this value, a given $I(V)$ curve fits the polynomial model and is linked (correlated) to a tunnel effect into the nanogap.

In this context, the first parameter that can be considered is the proportion of nanogaps for which I and V are correlated after incubation with Ab^{II}-GNPs (see Table 13.3). The second parameter of interest is the current gain observed at 5 V for the correlated nanogaps (ratio between the current at 5 V after incubation with Ab^{II} - GNPs and the current measured for bare electrodes). Finally, a quality factor combining both data and corresponding to the product of the percent of correlated nanogaps and the average current gain at $V = 5$ V was included in Table 13.3. Such factor has been made up to ponder the relative importance of both parameters.

TABLE 13.3 Electrical Characteristics of the System after Incubation with Ab^{II}-GNPs as a Function of the Immobilized Probe (pA, Goat-Ab, and PBS). The Percentage of Correlated Gaps, the Current Gain Relative to Bare Electrodes, and the Quality Factor are Indicated. The Number of GNP per Nanogap is Also Presented as a Reminder (see Fig. 13.8) to Show the Link between the Increase in Current and the Presence of GNPs.

Step	Probe	GNP/gap	Correlated gaps, %	Current gain	Quality factor
After Ab^{II}-GNPs incubation	pA	60	68	7534 (461; 41678)[a]	5123
	goat-Ab	15	12	89 (72; 356)[a]	11
	PBS	0	0	/	0[b]

[a]As the gain is calculated from statistical approach (median calculated value), the numbers in parentheses correspond to the first and third quartiles.

[b]When the gaps are not correlated, the quality factor is set to zero.

No correlation was observed for the bare electrodes (Fig. 13.10a). The corresponding multiple correlation coefficients r^2 were all below the cutoff (mean r^2 value 0.19 ± 0.13, Fig. 13.10b). Similarly, no significant increase in current was observed after spotting of probes and incubation of the human serum compared to bare electrodes. The corresponding current is ranging from 10^{-14} to less than 10^{-12} A and the resulting r^2 (0.20 ± 0.14 and 0.19 ± 0.14, respectively) is still below the cutoff.

In contrast, Fig. 13.10c indicates that large changes in conductance were observed after incubation with the Ab^{II}-GNPs, with pA, or goat-Ab as probe. Another striking feature is the change in related r^2 values upon incubation with Ab^{II}-GNPs (Fig. 13.10d). The control experiment performing the whole process except serum incubation, did not exhibit increase in current nor in r^2 above the cutoff (data not shown), highlighting the essential role of the serum in the detection process.

At this stage, 38 of the 56 gaps (68%) were found to be correlated for pA and exhibited intensities ranging from 4.4×10^{-12}–1.7×10^{-7} A (current gain from ~17–1.3×10^6 A). For the noncorrelated nanogaps (32%), current was lower than 2×10^{-13} A. Only 3 of the 25 gaps (12%) were found to be correlated for goat-Ab with an associated current of a few pA. Finally, no nanogaps were correlated for PBS.

These data led to a quality factor of 5123 for pA, 11 for goat-Ab and 0 for PBS (Table 13.1). The quality factor is greatly dependent upon the GNP density on the surface as determined by SEM analysis and reflects the specific capture of human antibodies from serum. Using a complex biological fluid, we thus show that electrical detection based on the use of nanogaps and Ab^{II}-GNPs enable us to distinguish between different probes. Future studies will focus on demonstrating the reliability of the method. Ideally, the signal should scale with the concentration of IgGs in the sample. Consequently, the detection limit must be determined to assess the future use of our system.

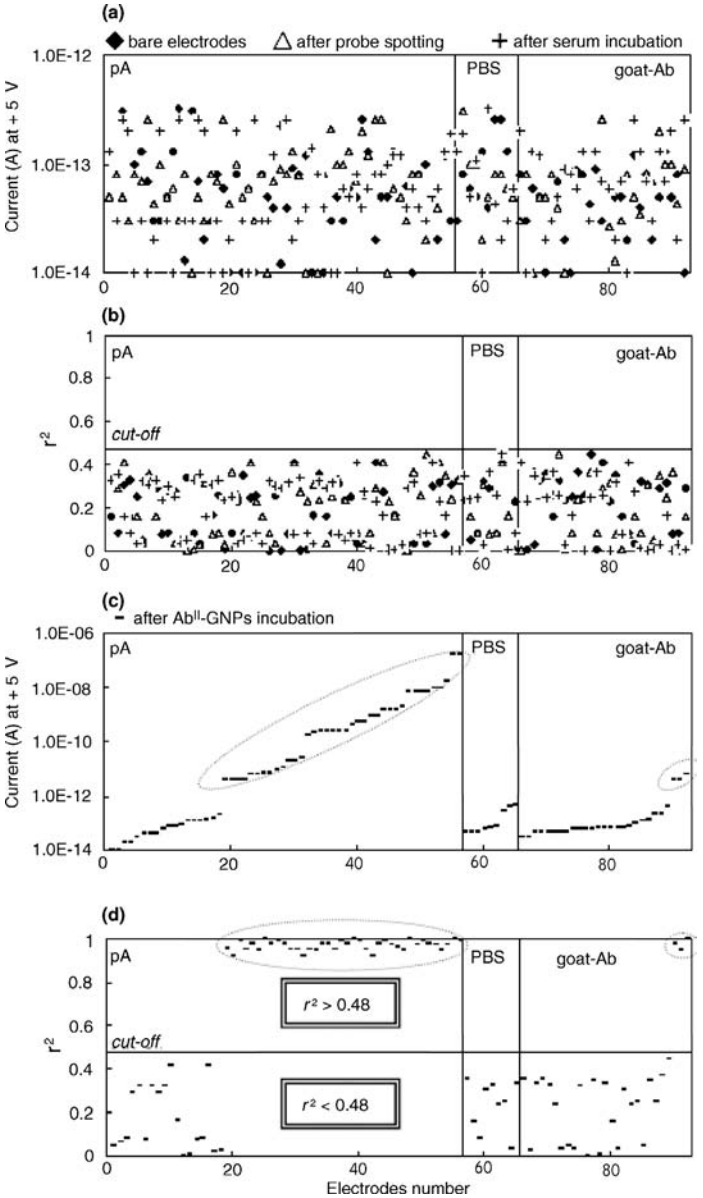

FIGURE 13.10 Application of the statistical analysis on the electrical characteristics of the device. Intensity of the detected current at $V = 5$ V (**a**) and correlation factor (**b**) for 92 nanogaps on bare electrodes (blue label), after spotting of probes (red label) and after incubation with the human serum (gray label). The same data are presented in (**c**) and (**d**) after incubation with the Ab^{II} - GNPs (black label). The cutoff is shown as an horizontal line and the correlated nanogaps (above the cutoff) are circled. Current values per probe—pA, PBS and goat-Ab—in (c) are arbitrary, ranked by increasing order

13.4.3 Analysis of the Transport Mechanism

As no significant change of the device conductance was found until the chip was exposed to the Ab^{II}-GNPs, we reasonably conclude that the use of GNPs enhances the electrical signal. SEM images prove the presence of GNPs in the gap, correlated with typical $I(V)$ curves. Therefore, we tried to analyze the $I(V)$ curves assuming that there was a narrow link between the number of nanoparticle and the measured current. Collective transport in arrays of small metallic dots has been theoretically treated by Middleton et al. (33), in the case of regular one- and two-dimensional arrays of small metal dots separated by tunnel barriers. They deine a threshold voltage V_T given by

$$V_T = N(q/C_0) \tag{13.1}$$

where q is the electron charge, C_0 is the capacitance associated with one nanoparticle, N is the number of particles, and is a factor depending on the capacitive coupling between neighbouring particles. V_T decreases as coupling increases and is lower than 0.5 in the case of very low coupling between the dots. For $V < V_T$, the array current is zero and for $V > V_T$, the array conducts with a current I varying with a power-law form associated with Coulomb blockade of transport (34) given by

$$I \propto (V/V_T - 1)\zeta \tag{13.2}$$

with $\zeta = 1.5$ or 3 in dimensions $d = 1$, 2, respectively.

Recently, Parthasarathy et al. (35) have observed such behavior on electronic transport in 1-dodecanethiol GNPs arrays, with typical size of $500\,\text{nm} \times 2\,\mu\text{m}$, corresponding to a number of particles of approximately 16,000 and a V_T value close to 9 V. In our case, V_T is near 2 V and ξ of the order of 1.2. The capacitance C_0 associated with a metallic nanoparticle of radius r is

$$C_0 = 4\pi\varepsilon\varepsilon_0 r \tag{13.3}$$

with ε_0 the vacuum dielectric constant and ε the relative dielectric constant associated with the surrounding medium. In our case, $r = 12.5$ nm.

The critical parameter is ε, ranging from a few units (e.g., two for dodecanethiol) to 10 for proteins (36). In the particular case of water, this value varies from Equation (13.2), if the dynamic dielectric constant is considered, up to 80 for the static ones. As the electrons always move, the dynamic one has to be taken into account. Taking an arbitrary value of ε from 2–10, we find an estimated value for C_0 ranging from typically 3–15 aF that leads to a product αN varying from 35–190, deduced from Equation (13.1). The number of particles located in a nanogap is of the order of 60–100 and indicates that α varies from typically 0.35–0.5 (0.5 is the maximum value associated with low coupling between the nanoparticles (33).

Although it was difficult to apply the theory developed for a large array of nanoparticles to our case where we observe only fraction of arrays lying in the nanogap, we can deduce that (i) the current shape originates from a Coulomb blockade associated with the nanoparticles and (ii) the observed threshold voltage is compatible with the

number of observed particles in the case of low interparticles coupling. The low value of ξ indicates a weak coupling between the nanoparticles (37), in agreement with the high α value.

Alternatively, several parameters other than the GNPs could be involved in the conductivity nanogap variation. An electron transfer may occur across multiple peptide chains from the antibodies covering the GNPs (38). In addition, the detected current could be due to the presence of charged proteins and buffer including several ionic species. Indeed, a local electrochemical process on the electrodes may generate an ionic current through the adsorbed water layer on top of the silicon oxide. Nevertheless, even if a careful analysis of the $I(V)$ curves is difficult to perform using transport model in arrays nanoparticles, our results demonstrate the key role played by the nanoparticles in the electrical detection through a multitunneling process.

13.4.4 Conclusion

We have demonstrated that a nanobiosensor based on the use of nanogaps and Ab^{II}-GNPs enables the selective electrical detection of human IgGs from a complex body fluid. The recognition of IgGs with probes (pA and goat-Ab) immobilized into the nanogap resulted in a significant increase in the measured current through electrodes likely due to the additional layer of conductive GNPs. Nonlinear regression analysis of the $I(V)$ data permitted us to distinguish signals correlated to a current increase from the noise background. The fraction of nanogaps displaying correlated data and an increase in conductance at 5 V enabled a quality factor to be calculated for the detection, which was linked to the GNP density around and inside the nanogap and thus to the specificity and affinity of the arrayed probes for human IgGs. The results of this study open the possibility to use the device for detecting protein-protein interactions in biological samples.

13.5 GENERAL CONCLUSION

The work presented in this article is focused on the combined use of micro- or nanoelectrodes and gold-labeled reagents for the electrical detection of antibodies from serum. In the first part of the article, the electrical detection of IgGs using microelectrodes required the precipitation of silver on the gold nanoparticles. As expected, a large variation in conductance was observed and enabled to distinguish probes of different capture efficiencies. The use of a device carrying a large number of microelectrodes permitted to consider the utility of the percent of short-circuited electrodes as an output parameter. We show that this parameter is indeed correlated with the density of gold nanoparticles between the microelectrodes and allows to sort out probes having different reactivities. This novel output does not depend on conductivity changes, which are highly variable and difficult to control experimentally. The second approach aims at demonstrating that the detection of IgGs from serum is feasible using nanoelectrodes and gold-labeled secondary antibodies. In this case, precipitation of silver is not required and leads to the overall simplification of the

detection procedure. Taken together, these results open novel possibilities for detecting IgGs from serum electrically, and thus for the design of portable devices of medical interest.

ACKNOWLEDGMENTS

This work was partly supported by the French Ministry of Research and grants from the EEC and from the Région Nord Pas-de-Calais. We also used the microarray platform facilities from the Institute of Biology (Lille, France).

REFERENCES

1. Engvall E, Perlman P.Enzyme-linked immunosorbent assay (ELISA). Quantitative assay of immunoglobulin G. Immunochem 1971;8:871–874.
2. Homola J.Present and future of surface plasmon resonance biosensors. Anal Bioanal Chem 2003;377:528–539.
3. Weiss S.Fluorescence spectroscopy of single biomolecules. Science 1999;283:1676–1683.
4. Chu X, Lin ZH, Shen GL, Yu RQ. Piezoelectric immunosensor for the detection of immunoglobulin M. Analyst 1995;120:2829–2832.
5. Ghindilis AL, Atanasov P, Wilkins M, Wilkins E. Immunosensors: electrochemical sensing and other engineering approaches. Biosens Bioelectron 1998;13:113–131.
6. Velev OD, Kaler EW. *in situ* assembly of colloidal particles into miniaturized biosensors. Langmuir 1999;15:3693–3698.
7. Xue M, Li J, Lu Z, Ko PK, Chan M. Array-based electrical detector of integrated DNA identification system for genetic chip applications. ESSDERC;2002. pp483–486.
8. Park SJ, Taton TA, Mirkin CA.Array-based electrical detection of DNA with nanoparticle probes. Science 2002;295:1503–1506.
9. Chang TL, Tsai CY, Sun CC, Uppala R, Chen CC, Lin CH, Chen PH.Electrical detection of DNA using gold and magnetic nanoparticles and bio bar-code DNA between nanogap electrodes. Microelec Eng 2006;4:1630–1633.
10. Tsai CY, Chang TL, Chen CC, Ko FH, Chen PH.An ultrasensitive DNA detection by using gold nanoparticle multilayer in nano-gap electrodes. Microelec Eng 2005;78–79:546–555.
11. Haguet V, Martin D, Marcon L, Heim T, Stiévenard D, Olivier C, El-Mahdi O, Melnyk O. Combined nanogap nanoparticles nanosensor for electrical detection of biomolecular interactions between polypeptides. Applied Physics Letters 2004;84:1213–1215.
12. Hatzakis M, Canavello BJ, Shaw JM.Single-step optical lift-off process. IBM J Res Develop 1980;24:452–460.
13. Miller JC, Miller JN. Statistics for Analytical Chemistry. New York: Ellis Horwood;1992.
14. Adkins JN, Varnum SM, Auberry KJ, Moore RJ, Angell NH, Smith RD, Springer DL, Pounds JG.Toward a human blood serum proteome: analysis by multidimensional separation coupled with mass spectrometry. Mol Cell Proteomics 2002;1:947–955.

15. Linder V, Verpoorte E, de Rooij NF, Sigrist H, Thormann W.Application of surface biopassivated disposable poly(dimethylsiloxane)/glass chips to a heterogeneous competitive human serum immunoglobulin G immunoassay with incorporated internal standard. Electrophoresis 2002;23:740–749.
16. Lindmark R, Thoren-Tolling K, Sjoquist J.Binding of immunoglobulins to protein A and immunoglobulin levels in mammalian sera. J Immunol Methods 1983;62:1–13.
17. Jossang T, Feder J, Rosenqvist E.Photon correlation spectroscopy of human IgG. J Protein Chem 1988;7:165–171.
18. Narita T, Kitazato H, Koshimura J, Suzuki K, Murata M, Ito S.Effects of protein meals on the urinary excretion of various plasma proteins in healthy subjects. Nephron 1999;81:398–405.
19. Coen MC, Lehmann R, Groning P, Bielmann M, Galli C, Schlapbach L.Adsorption and bioactivity of protein A on silicon surfaces studied by AFM and XPS. J Colloid Interface Sci 2001;233:180–189.
20. Bogatskii AV, Davidenko TI, Chuenko AV, Ianishpol'skii VV, Tertykh VA.Pronase E and P immobilization on aminoorganosilica surface. Ukr Biokhim Zh 1979;51:315–318.
21. Mezzasoma L, Bacarese-Hamilton T, Di Cristina M, Rossi R, Bistoni F, Crisanti A. Antigen microarrays for serodiagnosis of infectious diseases. Clin Chem 2002;48:121–130.
22. Robinson WH, DiGennaro C, Hueber W, Haab BB, Kamachi M, Dean EJ, Fournel S, Fong D, Genovese MC, de Vegvar HE, Skriner K, Hirschberg DL, Morris RI, Muller S, Pruijn GJ, van Venrooij WJ, Smolen, JS, Brown PO, Steinman L, Utz PJ,Autoantigen microarrays for multiplex characterization of autoantibody responses. Nat Med 2002;8:295–301.
23. Duburcq X, Olivier C, Desmet R, Halasa M, Carion O, Grandidier B, Heim T, Stievenard D, Auriault C, Melnyk O.Polypeptide semicarbazide glass slide microarrays: characterization and comparison with amine slides in serodetection studies. Bioconjug Chem 2004;15: 317–325.
24. Hayat MA. Immunogold Silver Staining: Principles, Methods and Applications. CRC Press;1995.
25. Richman DD, Cleveland PH, Oxman MN, Johnson KM. The binding of staphylococcal protein A by the sera of different animal species. J Immunol 1982;128:2300–2305.
26. Alexandre I, Hamels S, Dufour S, Collet J, Zammatteo N, De Longueville F, Gala JL, Remacle J. Colorimetric silver detection of DNA microarrays. Anal Biochem 2001;295:1–8.
27. Liang RQ, Tan CY, Ruan KC. Colorimetric detection of protein microarrays based on nanogold probe coupled with silver enhancement. J Immunol Methods 2004;285:157–163.
28. Möller R, Csáki A, Köhler JM, Fritzsche W. Electrical classification of the concentration of bioconjugated metal colloids after surface adsorption and silver enhancement. Langmuir 2001;17:5426–5430.
29. Karajanagi SS, Vertegel AA, Kane RS, Dordick JS. Structure and function of enzymes adsorbed onto single-walled carbon nanotubes. Langmuir 2004;20:11594–11599.
30. Roach P, Farrar D, Perry CC. Surface tailoring for controlled protein adsorption: effect of topography at the nanometer scale and chemistry. J Am Chem Soc 2006;128:3939–3945.

31. Vertegel AA, Siegel RW, Dordick JS. Silica nanoparticle size influences the structure and enzymatic activity of adsorbed lysozyme. Langmuir 2004;20:6800–6807.
32. Brinkmann M, Blossey R, Marcon L, Stievenard D, Dufrene YF, Melnyk O. Fluidics of a nanogap. Langmuir 2006;22:9784–9788.
33. Middleton AA, Wingreen NS. Collective transport in arrays of small metallic dots. Physical Review Letters 1993;71:3198–3201.
34. Black CT, Murray CB, Sandstrom RL, Sun S. Spin-dependent tunneling in self-assembled cobalt-nanocrystal superlattices. Science 2000;290:1131–1134.
35. Parthasarathy R, Lin XM, Jaeger HM. Electronic transport in metal nanocrystal arrays: The effect of structural disorder on scaling behavior. Phys Rev Lett 2001;87: 186807, 186801–186804.
36. Olson MA.Mean-field analysis of protein–protein interactions. Biophys Chem 1998;75: 115–128.
37. Roux S, Herrmann HJ. Disorder induced non-linear conductivity. Europhys Lett 1987;4: 1227–1232.
38. Shin YG, Newton MD, Isied SS. Distance dependence of electron transfer across peptides with different secondary structures: the role of Peptide energetics and electronic coupling. J Am Chem Soc 2003;125:3722–3732.

INDEX

Adsorption
  adsorption affinity, 81
  adsorption equilibrium constant, 81, 103
  adsorption kinetic, 76
Affinity
  affinity latex, 120
  affinity Separation, 123
Agglutination
  agglutination of latex, 123
  aggregation of microspheres, 98
  probability of agglutination, 80
Allotropes of carbon, 21
Amphiphilic polymer, 31
Anopheles mosquito, 67
Antibody
  antibody coated latex particles, 71
  antibody-Antigen reaction, 332
Anticancer
  anticancer doxorubicin, 47
  anticancer doxorubicin, 47, 50
Anticoagulant, 67, 68
Antigen
  antigen-antibody complex, 68
  antigen-antibody interactions, 95, 99
  antigen-antibody reaction, 123
  antigen-coated particles, 80
Anti
  anti-H.pylori, 110, 111
  anti-HSA, 109
Artificial latexes, 20
Assembly
  assembly layer-by-layer, 22
  assembly of inorganic colloids, 21
  assembly of organic colloids, 21
Atom
  atom Transfer Radical Polymerization, 17, 36, 39, 47
  atomic Force Microscopy, 229, 336
Automated
  automated hematology analyzer, 69
  automated malaria detection, 70
Azo-initiator polymerization, 73

Bacillus subtilis, 149
Bacteria detaction, 149
Bar-code beads, 127
Bio
  bio-analytica assay, 162
  bio-Bar-code DNA duplex, 188
  bio-Bar-code process, 187
  biochips, 1
  bioconjugation of nanocrystals, 143
  biodegradability, 3
  biodegradable polymer, 49, 120
  biodistribution, 49
  bioinert surface, 118
  biointerface, 119
  biological fluids, 4
  biological ligand, 3
  biominiaturization, 1
  bioreactors, 118
  biosensors, 162
  biospecific reaction, 117
  biotin-streptavidin reaction, 179
  biotinylated peptide, 309
Bleaching of fluorophores, 145
Blood
  blood cells, 117
  blood sera, 111
  blood, 68, 129

Colloidal Nanoparticles in Biotechnology, Edited by Abdelhamid Elaissari
Copyright © 2008 John Wiley & Sons, Inc.

Bovine serum albumin, 73, 82, 260
Bragg scattering, 249
Brucella cells, 99

Capture of antibodies, 312, 317
Carbon nantubes, 2
Cell
  cell activator, 120
  cell autofluorescence, 134
  cell for phagocytosis, 120
  cell internalization, 41
  cell manipulation, 213
  cell membrane protein, 125
  cell permeable virus capsids, 161
  cell separator, 120
  cell sorting, 213
  cell surface receptor, 52
Cellular imaging, 134
Chelation, 79
Chemical
  chemical activation, 78
  chemical immobilization, 120
  chemical micropatterining, 315
Chemoselectivity, 323
Clark electrode for glucose, 184
Clinical diagnostic, 47, 77
Colloidal
  colloidal crystals, 211
  colloidal Micropump, 216
  colloidal Microstirrer, 217
  colloidal stability, 4
Colorometric detection, 2
Composite particles, 21
Conductivity
  conducting polymer, 225, 241
  conductivity measurements, 233
  conductivity of the self-assembled nanocomposites, 226
Contact angle measurements, 309
Coomassie Brilliant, 110
Copolymer
  copolymer latexes, 16
  copolymers, 45, 51
  diblock copolymer, 35, 38, 40, 42
Core-shell
  core-globule transition, 19
  core-shell nanocrystals, 142
  core-shell particles, 19, 50, 119
  core-shell structure, 19, 50
Covalent
  covalent coupling of immunoglogulin, 78
  covalent coupling, 78
  covalent immobilization of biomolecules, 104, 105
C-reactive protein (CRP), 98, 178
Cyclic Voltammetry, 229
Cytoskeleton in human phagocyte cell, 148

Dendrimers, 20
Depletion of biomolecules, 3
Detection
  detection of DNA, 191
  detection of point mutated DNA, 124
  detection of ssDNA, 261
Diblock copolymer, 35, 38, 40, 42
Dielectrophoresis, 213
Diffusion coefficient, 86
Direct latex agglutination, 71
Dispersion polymerization, 18, 119
DNA
  DNA chip, 2, 188
  DNA delivery, 52
  DNA detection, 2, 10
  DNA hybridization, 124, 175
  DNA Sequences, 2
  DNA/DNA interaction, 180, 188
  DNA-carrying affinity latex, 124
Drug
  drug delivery using affinity latex, 47, 49, 126
  drug delivery, 1, 47, 49
  drug Doxorubicin, 49
  durg targeting, 2

Electric
  electric charge, 100
  electrical detection of antibodies, 329, 335
Electro
  electrocapillary forces, 210
  electrochemical detection, 171
  electrochemical immunomagnetic sensors, 169
  electrophoretic mobility, 95, 100, 101, 107, 108, 112
Emulsion
  emulsion copolymerization, 102
  emulsion deroplets, 247
  emulsion evaporation, 210
  emulsion polymerization, 16, 72

Entamoeba histolytica, 71
Enzyme
  enzymatic biosensors, 184, 185, 186
  enzyme Linked Immunomagnetic electrochemical assay, 171
  enzyme Linked Immunosorbent assay (ELISA), 98, 157, 182, 292, 312
  enzyme Linked Oligosorbent assay (ELOSA), 261, 263
Escherichia coli, 149, 214
Evaporation induced colloidal assemblies, 209
Ex vivo live cell imaging, 162
Exoerythrocytic schizonts, 66

Falciparum
  falciparum infection, 65, 67, 87
  falciparum life cycle, 66
  falciparum parasite, 66
  falciparum proteins, 67
Ferric oxide, 11
Film
  film of conducting polymers, 223, 227
  film of nanocomposites, 223
  film-forming nanoparticles, 22
Flow cytometry assy, 155, 156, 290
Fluorescence
  fluorescence images, 147
  fluorescence lifetime, 135
  fluorescent particles, 6, 22, 99, 100, 133, 134
  fluoresent semiconductor, 134
Force
  force between magnetic particles, 249
  force measurement in magnetic emulsion, 263
  force measurements in ssDNA, 261
  force measurements, 247
  force-distance measurement, 250
  force-distance measurements during sol-gel reaction, 269
Free enrgy, 309
Fullerens, 21
Functionality, 5

Gas
  gas detection, 233, 230
  gas sensors, 223, 241
Gel
  gelification, 8
  gel-sol method, 13
Geometry of microfluidic, 211
Geromagnetic electrochemical assays, 175
Gibbs free energy, 76, 78, 81
Global distribution of Malaria, 66
Gold particles, 2
Grafting-to, 120
Gram-positive bacterium, 149

Hairy particles, 17, 82
Helicobacter pylori, 110
Herpes virus, 181
Heterocoagnulation, 22
High luminiscent nanocrystals, 138
Histidine-tagged protein, 79
Hollow particles, 23
Homogenious nucleation, 74
Human Serum albumin (HSA), 104
Hydro
  hydrodynamic flow, 215
  hydrogels particles, 46
  hydrogels-based microvalves, 54
  hydrogen bond, 77
  hydrophilic-hydrophobic balance, 5, 19, 36
  hydrophobic aminoacid, 81
  hydrophobic interaction, 77

Immuno
  immobilization of biomolecules, 78, 170
  immunoaggregates, 86
  immunochemistry, 162
  immunochromatographic method, 68
  immunodiagnostic test, 95, 106, 110
  immunoglobulin, 96
  immunolabeling with quantom dots, 145
  immunolatex, 72, 76, 84
  immunosensors, 171
  immunostaining of cytokeration in skin, 146
Impedance
  impedance measurements, 233
  impedancemetry based sensors, 172
In-situ polymerization, 22
In-situ quantification of cancer markers, 153
In vivo
  In vivo optical biopsy
  In vivo quantum dots application, 138
  In vivo tumor, 49
Indirect latex agglutination, 71

Injectable
injectable drug-delivery systems, 44
injectable hydrogels, 45
Inorganic
inorganic colloids, 5
inorganic particles, 2
Interaction forces, 77
Interfacial polarity, 5
Intracellular detection, 148
Intravenous administration, 50
Isoelectric point (pI), 77

Lab-on-a-chip, 1, 199
Lamellar pahse, 10
Laminar flow reactor, 208
Latex
latex agglutination test, 70, 72, 80, 83, 87, 110
latex protein immobilization, 76
Layer
layer-by-layer electrostatic deposition of polymer, 154
layer-by-layer process, 17, 22
layer-by-layer Quantom dots tagged microbeads, 154
Lewin's calculation, 77
Lewis acid, 309
Lifshitz-van der Waals, 309
Ligation chemistry, 299
Lipidmicelles, 150
Liposome, 212
Living radical graft polymerization, 120
Lower Critical Solution Temperature, 19, 34, 42, 50
Lunctionalized nanolatexes, 18, 75
Lysed boold, 68

Macromolecular aggregates, 97
Magnetic
magnetic beads, 289
magnetic emulsion, 22, 24
magnetic force microscopy, 179
magnetic microbeads, 188, 190
magnetic nanoparticles, 179, 192
magnetic particles, 2
magnetic permiability measurements, 177
magnetic resonance imaging, 180, 181
magnetite sols, 40
Malaria
malaria disease, 65
malaria pigment, 69
Metal
metal nanoparticles, 2006
metal oxides, 2
Micellar electrokinetic chromatography, 287
Microactuators, 54
Microarrays, 145, 152, 299
Microchip, 282, 284, 287, 291
Microelectrodes, 332
Microemulsion, 9, 14, 18
Microfluidic
microfluidic Chip, 212
microfluidic devices, 54, 199, 209, 212, 216, 275
microfluidic Electrophoresis, 216
microfluidic Pumps, 217
microfluidic reaction, 201, 208
microfluidic valves, 217
Microgap based biosensor, 334
Microgel, 19
Micropaterning
micropaterning, 317
micropaterning of polycarbonate, 314
micropatterning of Titanium oxide, 321
Microscopic diagnostic, 67
Microsystems, 2
MicroTAS, 53
Microvalve, 53, 54
Miniemulsion polymerization, 17
Mismatch DNA, 125
Monodisperse colloids, 9
Multicompartiment micelles, 35
Multifunctional colloids, 24
Multiplex
multiplex Assay, 117, 127
multiplex beads, 128, 129
multiplex cytometric assays, 99
multiplex detection on tissue, 152
Multiresponsive polymer, 45
Multi-walled nanotubles, 21

Nano
nanoelectrodes, 332, 342
nanofibers, 35
nanogap based biosensor, 341
nanogaps, 329

Nanoparticles
nanoparticles for affinity biosensors, 169
nanoparticles synthesis, 2002
paramagnetic nanoparticles, 178, 217
Nanotubes, 21
Nitroxide Mediated Polymerization (NMP), 17
Nonviral DNA, 52
Nuclei, 8, 9
Nyquist diagram, 173

One-step magnetic immunoassay, 177
Optical
optical characterization of films, 231
optical fractionation, 214
optical measurements of aggregates, 123
optical separation, 213
optical Trapping, 214
Organic
organic fluorophores, 145
organic/inorganic composite particles, 2
Ostwald ripening, 8, 13, 17
Oxide nanoparticles, 241
Oxyanion-initiated polymerization, 34

Paramagnetic nanoparticles, 178, 217
Particles
particles colored, 6
particles degradable, 6
particles surface modification, 7
Pentablock copolymer, 46
Peptide Microarrays, 299
Peroxidase detection, 181
Pharmacokinetic, 49
Photon corelation spectroscopy, 85
pH
pH-responsive gels, 39
pH-sensitive hydrogels, 54
pH-sensitive liposomes, 46
pH-sensitive micelles, 46
pH-sensitive polymer, 31, 33, 36, 41, 45, 50
Physical adsorption of protein, 76, 78
Piezo
piezoelectric, 53, 174
piezoimmunosensors, 174
Plasmid
plasmid DNA, 51, 52
plasmodium, 65
Pluronic, 43, 49, 50, 79
Poloxamer, 43
Poly(L-histidine), 41
Polycondensation, 18
Polymer
polymer micelles, 47
polymer polyelectrolyte, 7
polymer self-assembly, 7
Polymerase Chain Reaction (PCR), 187
Polymerization
polymerization suspension, 15
polymerization, 15
precipitation polymerization, 19
Polyol Process, 13
Precipitation polymerization, 19
Preparation
preparation condensation,7
preparation of nanoparticles, 6, 7
preparation polycondensation, 7
preparation polymerization, 7
Probability of agglutination, 80
Protein
protein adsorption, 80
protein analysis in microfluidic systems, 275
protein microarray technologies, 153
protein/protein intercation, 180
Protozoa, 65
Pseudoternary phase diagram, 9

Quantification of DNA, 177
Quantum
quantum dots antibody, 146
quantum dots encoded human DNA, 155
quantum dots, 11, 127
quantum dots based immunostaining 153
quantum dots bioconjugates, 153
quantum dots for in vivo imaging, 148
Quasi-Elastic Light Scattering, 95

Rapid diagnostic, 65, 68
Reactive
reactive groups, 5
reactive surface groups, 3
Red blood cells, 66, 67
Repulsive electrostatic force, 82
Reservoirs of drugs, 2
Resistance measurements, 233
Reversible Addition Fragmentation Chain Transfer polymerization, 17, 34
RNA isolation, 129

Saccharomyces cerevisiae detection, 184
Salmonella
  salmonella cells, 174
  salmonella detection, 174
  salmonella typhinium, 174
Sandwich bioassay, 179
Seed polymerization, 16, 120
Self-Assemblies
  self-assemblies of copolymer, 28
  self-assemblies of nanofibers, 35
  self-assemblies of polymer, 32, 40
Semicarbazide functionalized silica, 304
Semiconductor
  semiconductor chemical composition, 136
  semiconductor nanoparticles, 11, 204
  semiconductor spectra, 135
  semiconductor, 2, 11, 24
Separation of biological species, 215
Shape of particles, 4
Shot-growth, 16
Silica
  silica covered ferrofluid emulsion, 267
  silica nanoparticles, 11, 299
  silica Stöber, 12
Single
  single stranded DNA, 124
  single-walled nanotubes, 21
Size distribution of quantum dots, 139
Sol
  sol-gel process, 14
  sol-gel reaction, 269
  sol-gel transition, 43, 47
Specific
  specifc capture of Nucleic Acid, 261
  specific gravity, 117
  specific surface area, 117
Sporozoites, 66
Stimuli
  stimuli-responsive hairy, 24
  stimuli-responsive polymer, 31
  stimuli-responsive sel-assemblies, 44
Stöber silica, 12
Streptavidin
  streptavidin-biotin DNA, 150
  streptavidin-biotin system, 5
  streptavidin-coated beads, 285
  streptavidin-coated quantom dots, 145
Strip, 69
Structured latex, 16
Superparamagnetism, 6
Surface
  surface area, 9
  surface charge density, 4
  surface concetration of HSA, 107
  surface modification, 14
  surface tenstion, 309
Synthesis of Silica nanoparticles, 315

Temperature
  temperature sensitive hydrogel, 44
  temperature sensitive immunoassay, 286
  temperature sensitive latexes, 19
  temperature sensitive polymer micelles, 49
  temperature-responsive polymer, 31, 42, 53
Time resolved fluorescent bioassay, 2
Tissue
  tissue autofluorescence, 152
  tissue microarray, 152
Titanium oxide nanoparticles, 299
Traditional diagnostic, 96
Transfect cells, 52
Triblock
  triblock copolymer, 37, 40, 43
  triblock polyampholyte, 32
Tumor
  tumor tissue, 49
  tumors derived cells, 183
  tumors, 153
Turbidy, 83, 84
Tyrosinase-based biosensor, 185

UV
  UV irradiation, 45, 125, 163
  UV-cleavable linker, 121
  UV-photopolymerization, 209

Vaccination, 2
Van der Waals forces, 250
Viruses detection, 150
Vitamin M, 40
Vivax, 65, 87
Volume phase transition temperature, 19

Young's equation, 309

Zeta potential 270
Zip-code, 128
Zwitterionic copolymer, 45

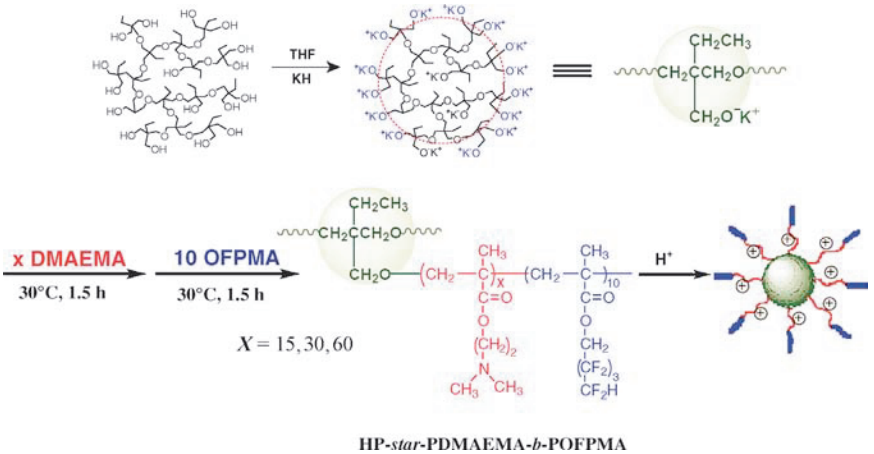

FIGURE 2.2 A representative reaction route for the preparation of the HP-*star*-PDMAEMA-*b*-POFPMA copolymers via oxyanion-initiated polymerization with a multireactive-site macroinitiator. The dimethylamino groups of PDMAEMA can be protonated in acidic medium. Reprinted with permission from Reference (24). Copyright 2007 American Chemical Society (24)

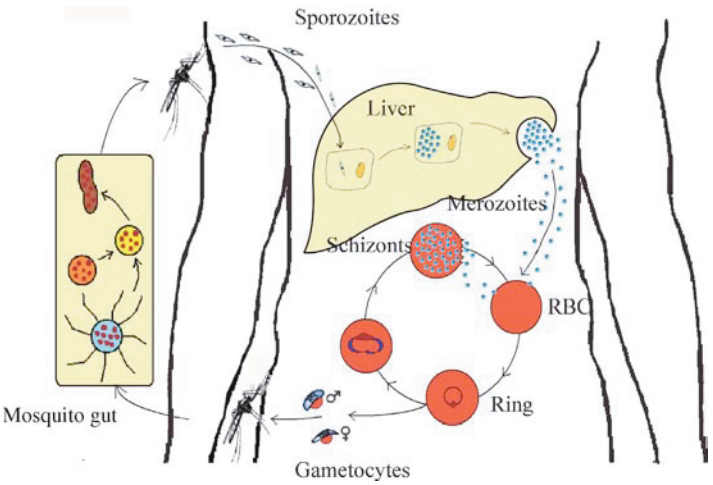

FIGURE 3.2 Life cycle of P. falciparum parasite (4)

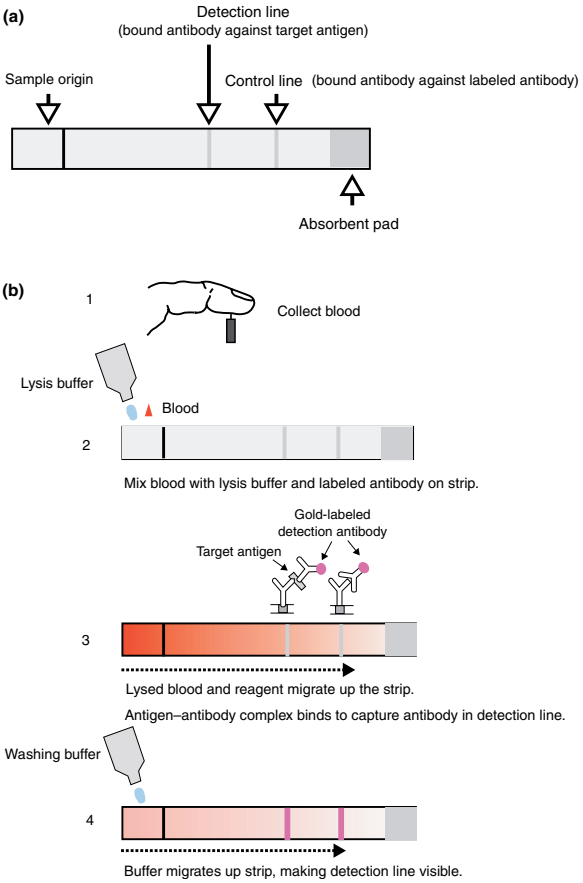

FIGURE 3.3 Component of RDTs strips before use (**a**) and the general procedure of test (**b**) (23)

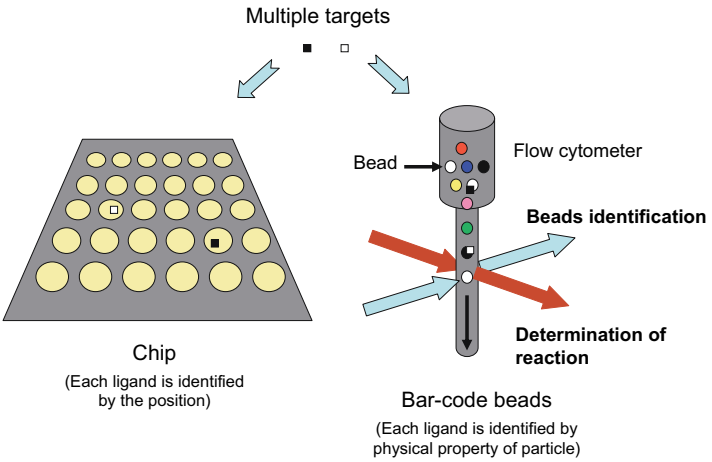

FIGURE 5.9 Multiplex assay systems

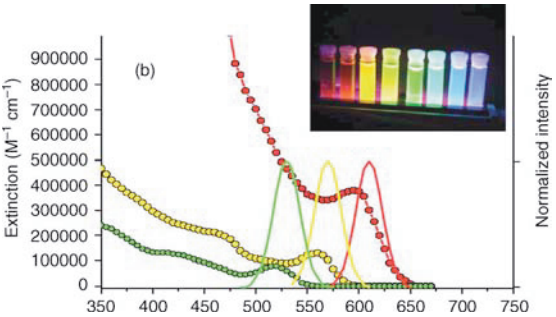

FIGURE 6.1 Typical absorption (dotted lines) and fluorescence (solid lines) spectra of organic dyes (*See text for full caption.*)

Fluorophore	Absorption(nm)	Emission(nm)
Fast Blue	360	440
AlexaFluor 350	346	445
AMCA	350	450
Bisbenzamide	360	461
Hoechst33258	360	470
ACMA UV	412, 430	471, 474
Hoechst33342	343	483
Cy2	489	506
GFPWildtype Non UVe	475	509
GFPWildtype UVex	395	509
AlexaFluor 488	494	517
Calcein	496	517
Fluorescein (FITC/DTAF)	495	520
FluoroJade B	480	525
Lucifer yellow	425	528
JC-1	514	529
Fluoro-Gold	361	536
AlexaFluor 430	430	545
Eosin	524	545
6-Joe UV	520	548
AlexaFluor 532	530	555
Cy3	548	562
AlexaFluor 546	554	570
AlexaFluor 555	555	571
TRITC	547	572
B-phycoerythrin	545, 565	575
R-phycoerythrin	480,545,565	578
Rhodamine	539, 574	602
AlexaFluor 568	578	602
Texas Red	589	615
AlexaFluor 594	590	617
Propidiumlodide(PI)	536	617
EthidiumBromide	493	620
Feulgen	570	625
Acid Fuchsin	540	630
AlexaFluor 633	621	639
AlexaFluor 647	649	666
Cy5	650	670
PE-Cy5 conjugates	480,565,650	670
AlexaFluor 660	668	698
AlexaFluor 680	684	707
PE-Cy7 conjugates	480,565.743	767
Cy7	743	767

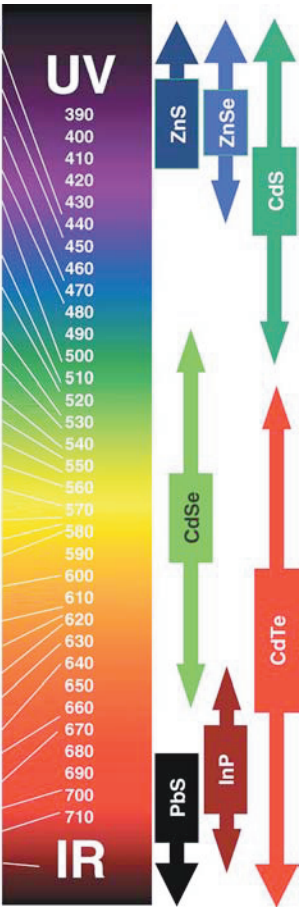

FIGURE 6.2 Fluorescence of semiconductor quantum dots of different chemical compositions and sizes cover all optical spectral region from UV to IR. QDs may replace all known organic dyes (on the left) from their actual areas of applications to detection and diagnostics

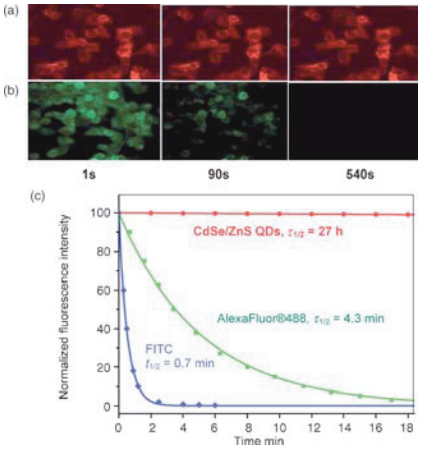

FIGURE 6.6 Semiconductor core/shell nanocrystals are rock solid against photobleaching. (*See text for full caption.*)

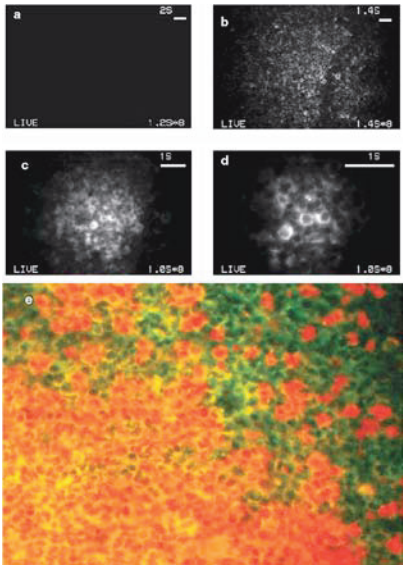

FIGURE 6.7 Fluorescence images of tonsil cancer tissue labeled with the QDs-antibody conjugates. *See text for full caption.*)

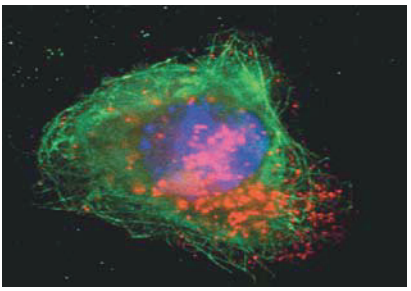

FIGURE 6.8 Multicolor intracellular detection with the QDs of different diameters. (*See text for full caption.*)

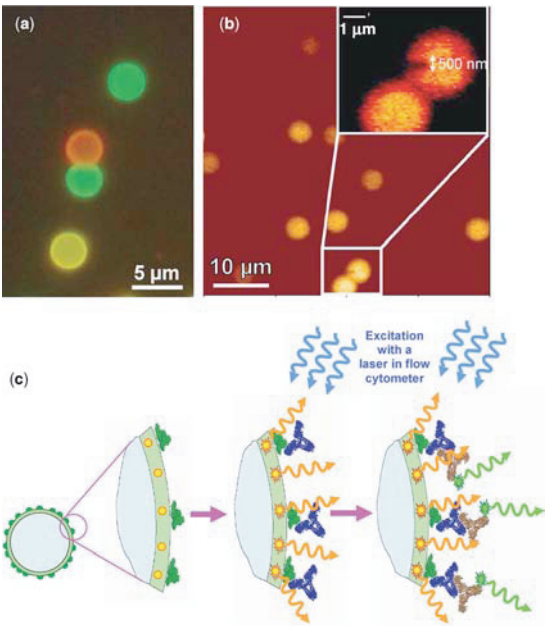

FIGURE 6.9 QDs-encoded, human DNA topoisomerase I-coated microbeads for diagnostics of autoimmune diseases. (*See text for full caption.*)

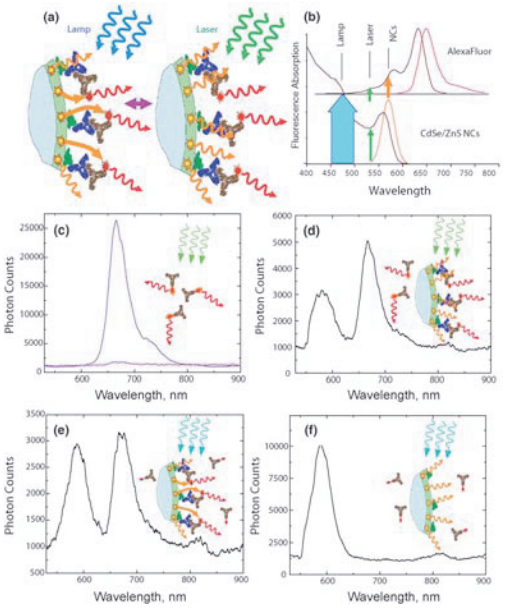

FIGURE 6.11 Single bead immunoassay for FRET detection of anti-topoisomerase I specific antibodies. (*See text for full caption.*)

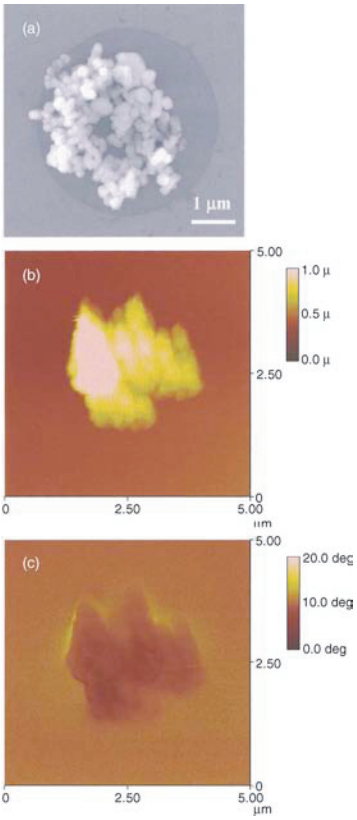

FIGURE 7.10 SEM (**a**), AFM (**b**), and MFM (**c**), images of magnetic nanoparticles immobilized on a patterned substrate by specific interaction between biotin and streptavidin. Dot size = 4 μm (25,27)

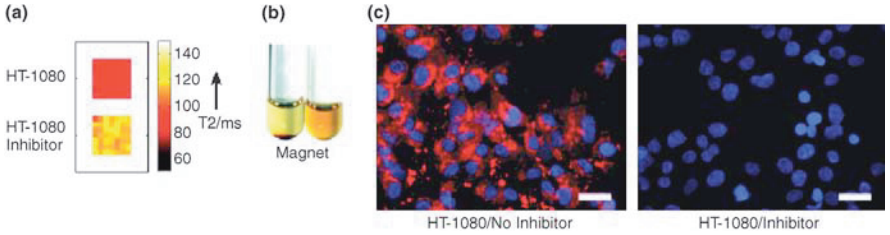

FIGURE 7.15 In the presence of tumor derived cells (HT-1080), MMP-2 is secreted. (*See text for full caption.*)

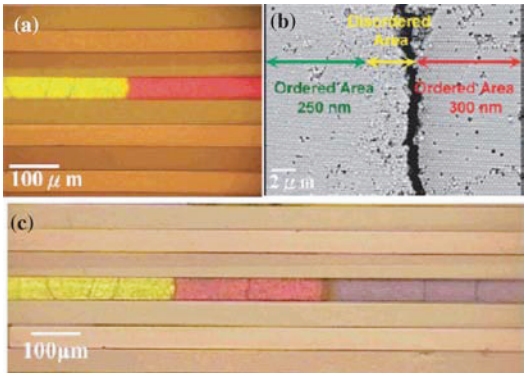

FIGURE 8.6 (**a**) Two adjacent colloidal crystals formed in the same microchannel using 250 and 300 nm diameter polystyrene beads. (**b**) SEM image of the boundary between two adjacent colloidal crystals. (**c**) Three adjacent colloidal crystals formed in the same microchannel using 250-, 300-, and 198-nm diameter polystyrene beads. Reprinted with permission from (60) Copyright (2004) American Chemical Society

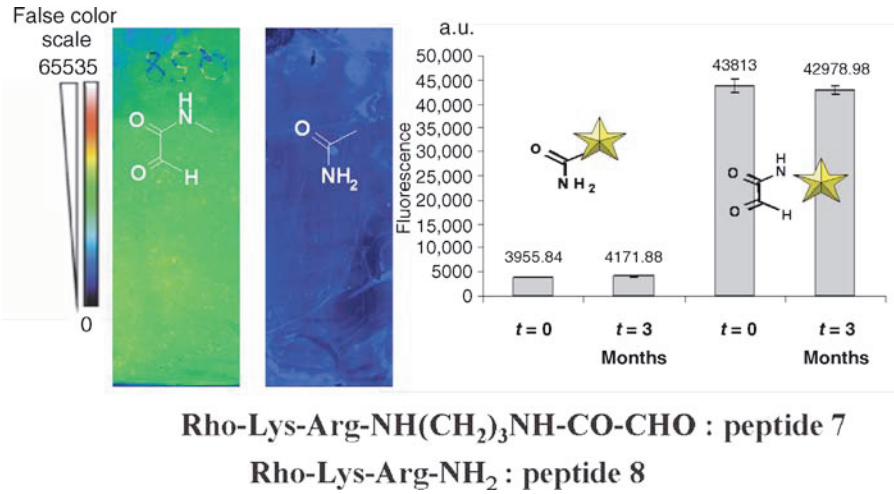

FIGURE 12.3 Quality control using glyoxylyl-peptide **7** and peptide amide **8**. On the left-hand side, false color scale images at 532 nm (Affymetrix 418 scanner, L35, PMT50) of semicarbazide glass slides reacted with peptides **7** or **8**. On the right-hand side, results after quantification. The fluorescence is expressed in arbitrary units (A.U.). The data were analyzed using ScanAlyze Software (Stanford University)

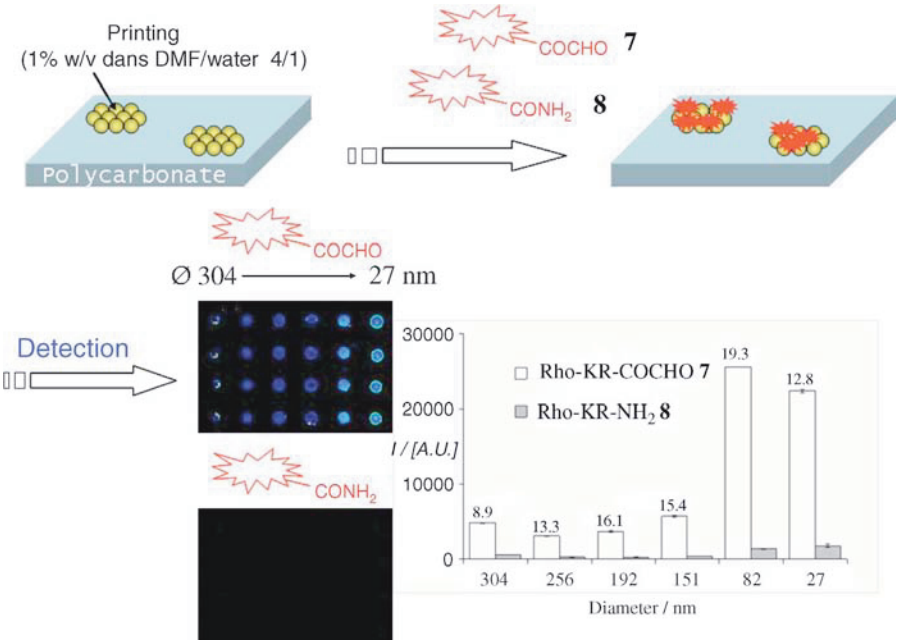

FIGURE 12.10 Reactivity of semicarbazide nanoparticles (∅ from 27 to 304 nm) printed on PC (1% w/v in 20% aqueous DMF, 3 drops, 1 nL).(See text for full Caption)

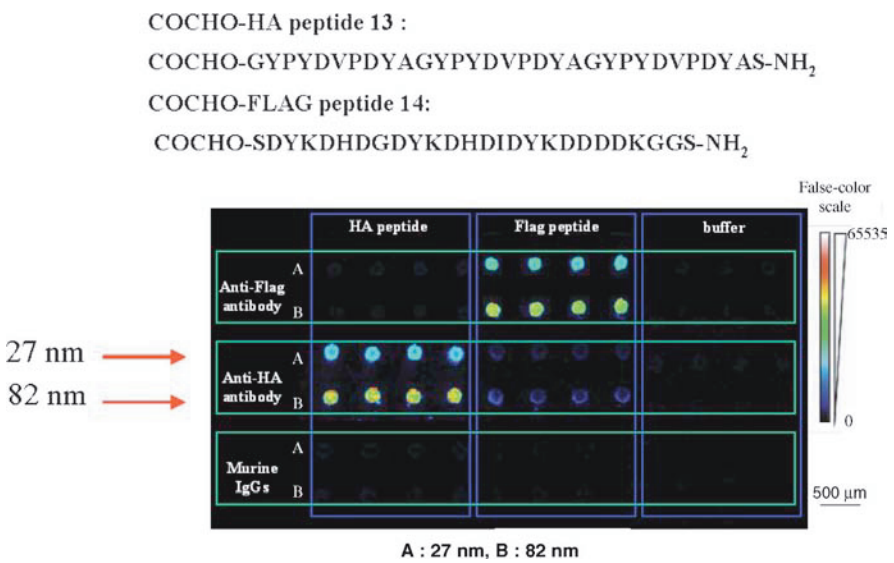

FIGURE 12.11 Semicarbazide nanoparticles were printed in quadruplicate on PC slides and each experiment was performed in triplicate.(See text for full Caption)

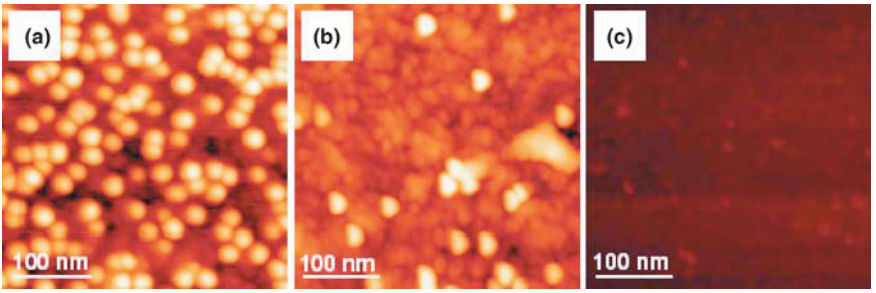

FIGURE 13.2 Characterization of probe reactivity. AFM images of the spotted areas between the microgaps after incubation with diluted human serum and Ab^{II}-GNPs. (**a**) pA, (**b**) goat-Ab, and (**c**) PBS

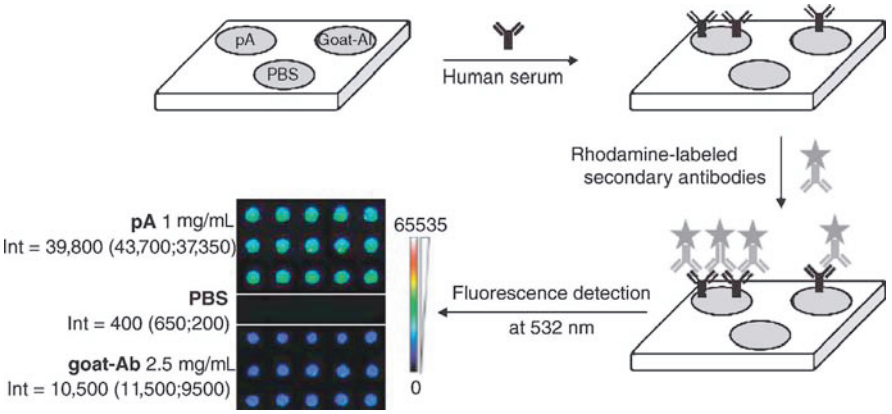

FIGURE 13.3 Printing of pA($n = 15$), goat-Ab ($n = 15$) and PBS ($n = 5$) on amine functionalized microscope glass slides was used for studying probe reactivity using fluorescence detection. The microarrays (triplicate) were incubated with diluted human serum (1/20th) and tetramethylrhodamine-labeled antihuman IgG antibody, respectively. Detection was performed at 532 nm at L35, PMT50 scanner sensitivity using an Affymetrix 418 Array Scanner. The figure shows a 16-bit image of the resulting microarray (false-color scale) and the fluorescence intensities expressed in arbitrary units. The number in parentheses corresponds to the first and third quartiles